FACULTY OF SCIENCES

DESIGNING PHOSPHORS FOR LEDs

AN EXPERIMENTAL AND THEORETICAL PERSPECTIVE

Jonas Joos

Supervisors: Prof. Dr. Philippe Smet, Prof. Dr. Dirk Poelman

A dissertation submitted to Ghent University in partial fulfillment of the requirements for the degree of Doctor of Science: Physics

Academic year: 2016-2017

GHENT UNIVERSITY

❝I thank you for those items that you sent me
The monkey and the plywood violin
I practiced every night, now I'm ready❞

— I'm Your Man, Leonard Cohen (1988)

PREFACE

Volgens aloude traditie wordt het voorwoord van een thesis gebruikt om een aantal mensen te bedanken. Meer specifiek degenen die bijgedragen hebben aan de totstandkoming van dit werk, alsook degenen die niet rechtstreeks bijgedragen hebben, maar die toevallig in de buurt waren en bovendien degenen die niet in de buurt waren, maar die de auteur niettemin van de lopende werken wisten af te leiden opdat hij met een frisse blik zou terugkomen. Kortom, het volledige entourage van de promovendus.

Teneinde de geijkte volgorde te respecteren, vangt de lofzang aan bij de promotor, degene die toezicht houdt op de vooruitgang van de arbeid: Philippe, bedankt voor alle hulp en de vele uitstekende ideeën, gaande van de projectaanvraag, het uitvoeren van het onderzoek zelf tot het afwerken en insturen van artikels. Erkentelijkheid komt je toe voor de vrijheid die ik heb kunnen genieten bij het exploreren van wetenschapsoorden die niet erg voor de hand lagen en voor het vertrouwen dat ik krijg bij mijn onderwijsopdrachten die ik overigens met veel vreugde uitvoer. Je genegenheid voor de wetenschap en het communiceren ervan naar de buitenwereld werkt erg aanstekelijk. Dirk, dankzij jou is het nooit kleurloos of stil op LumiLab en je verbeten enthousiasme weet bijzonder te motiveren. Ik dien je mijn dankbaarheid te betuigen voor je kritische wetenschappelijke houding en taalvaardigheid die menig artikel verbeterd hebben.

Wat absoluut niet verzuimd mag worden, is de enkelingen bedanken die dit boek gelezen hebben. Naast Philippe en Dirk zijn dit de achtenswaardige leden van de examencommissie. Zij worden niet enkel gelauwerd voor hun volharding, maar eveneens voor hun waardevolle commentaren die bijzonder op prijs gesteld werden en bijgedragen hebben aan de huidige vorm van dit werk.

De lofzang gaat verder en huldigt diegenen die in dezelfde modderige put ploeteren dan de promovendus, evenzeer op zoek naar een knook om aan te kluiven, de overige drie man en paardenkop die zich in dezelfde nauwe en diepe spelonk van gespecialiseerde kennis bevinden en helpen om de daar heersende meedogenloze eenzaamheid te gerieven. Met name zijn dit Katleen, Koen, Ang, Anthony, Hajieh, Heleen, Iolanda, Jiaren, Katrien, Lisa, Olivier, Reinert, Simon. Zij die talloze uren doorgebracht hebben in dezelfde ruimte als ondertekende hebben daarnevens recht op de hoogste egards voor de koenheid waarmee zij dit lot ondergingen. Andreas,

David, Jonas, Nursen en Sofie, het was een plezier om met jullie lief en leed te delen. Van ons heen gegaan, maar evengoed gedenkwaardig en derhalve bedankt zijn JB en Katrien, ambtsbroeders van het eerste uur, spitsbroeders tot op heden.

Bijwijlen komt het voor dat men de kans krijgt een blik over de haag te werpen, om zich even te laten zakken in een andere spelonk van kennis. In dit geval bevond deze spelonk zich op het CMM, de wereld der zwarte computerschermen met witte letters. Hiervoor werd bereidwillig bijstand geboden door Kurt en Karen die daarvoor uitdrukkelijk bedankt worden.

Aan ieder hierboven, het heeft mij steevast verblijd om de wetenschappelijke queeste met jullie te ondernemen.

Des avonds, wanneer de wetenschapper zijn modderlaarzen aan de haak hangt, begint het tweede leven, het leven waarvan de protagonisten de ultieme strofes van deze lofzang invullen. Prominente rollen worden ingenomen door zij die deel uitmaken van onze Fanfare van Honger en Dorst, zij die hun avondleven op ongedwongen wijze slijten in aanwezigheid van de auteur. Aan gewichtigheid zal het hen evenwel niet ontbreken zoals blijkt uit de roemrijke annalen van de Trappers van Alaska. Deze annalen zouden er niet zijn zonder Gertjan, Thomas, Tim, Sam en Renaat. Tevens dienen ook Annelise, Philippe en Kwinten gehuldigd te worden voor de gedeelde momenten.

Vervolgens arriveert de lofzang bij zijn laatste halte, daar waar degenen zijn verzameld die doorgaans geen keuze hebben, degenen die noodgedwongen een deel van hun bestaan doorbrengen in de aanwezigheid van de auteur. In het bijzonder is er dank verschuldigd aan de ouders, zij die verkeerdelijk dachten dat het vertrek van ondertekende naar de grote stad plaats zou maken voor tijd en rust. Zij worden bedankt voor de goede zorgen waarop kennelijk geen afstand staat.

De laatste noten van deze lofzang worden besteed aan de voornaamste vondst van de jarenlange zoektocht in de modder, het staaltje serendipiteit dat de auteur ten beurt viel en zijn leven verreikend veranderde. Sofie, ik bedank je voor deze opwaardering en de leuke jaren die we tezamen doorbrachten terwijl ik uitkijk naar de jaren die aan de horizon liggen.

Blijmoedig dat aan de aloude traditie kon worden voldaan, eindigt hier deze paragraaf. Nu, beste lezer, begint Uw queeste, de zoektocht naar de perfecte ledfosfor. Het belooft een waar avontuur te worden dat U voorbij kwantummechanica, lasers en andere narigheden zal brengen. Maar koestert U vooral geen vrees, beste lezer, als U hier bent geraakt, heeft U dit voorwoord overleefd. Het kan U enkel maar beter vergaan!

Mei 2017
Jonas Joos

Contents

1 Introduction

Nature exhibits many different forms of luminescence. Examples are fluorescent minerals, the polar light or luminous organisms such as jellyfish or fireflies. Almost equally diverse are the technological applications of luminescence, ranging from lighting, display technology to medical imaging. Here, the basic ideas involving luminescence, the study of luminescent materials and the application of these materials in light-emitting diodes (LEDs) are reviewed. At the end of this chapter, the reader is guided through the structure of this text.

1.1 Terminology

The German physicist and science historian Eilhard Wiedemann was, in 1888, the first to use the term *Luminescenz* or luminescence as collective name for all luminous phenomena which are not caused by thermal radiation [1]. The so-called black-body radiator for which the emission spectrum is given by Planck's law [2],

$$I(\omega_k, T) = \frac{\hbar\omega_k^3}{4\pi^3 c^2} \frac{1}{e^{\hbar\omega_k/k_B T} - 1}, \tag{1.1}$$

is hence a kind of light emission which is not considered as luminescence. The light emission of the sun, smoldering wood or the filament of an incandescent lamp is thermal radiation. In contrast to the emission spectrum of a black-body radiator that consists of a broad band of which the color drifts from red-hot via yellow and white to blue-glowing with increasing temperature, the emission spectrum of luminescent processes is characterized by several discrete lines or narrow bands, entailing a vast number of colors of *cold light* that can be found in nature as well as in laboratories.

Before a luminescent material can emit light, it requires some kind of excitation. The nature of the excitation mechanism determines the name that is given to the phenomenon. This distinction was also first made by Wiedemann [1]:

- Photoluminescence (PL): This kind of luminescence is excited by light itself. This is not necessarily visible light, but can likewise be ultraviolet light (UV).
- Thermoluminescence (TL): Light emission which is caused by heating a material. Although this phenomenon is driven by temperature, it has a completely

different origin and appearance than thermal radiation. The emitted energy was stored in the material before the heating. This can *e.g.* be effectuated by illumination, similar to PL. Temperature is hence not explicitly controlling the excitation mechanism and only causes the stored energy to be released.

- Electroluminescence (EL): When light emission is caused by an electric discharge, *e.g.* in gases or by an electric current passing through a solid or a liquid.
- Triboluminescence: Luminescence which is caused by applying pressure to crystals, possibly - but not necessarily - breaking them. Mechanoluminescence (ML), fractoluminescence and piezoluminescence are variants of this phenomenon. As in the case of TL, nondestructive ML is caused by the release of stored energy by applying pressure.
- Crystalloluminescence: This type of luminescence is found during the crystallization from a liquid solution; Lyoluminescence is the opposite phenomenon, *i.e.* when light is emitted when crystals are dissolved.
- Chemoluminescence: When light is emitted during a chemical reaction.

Later on, many other names were added. These are not necessarily all mutually independent or independent from the initial six types of luminescence of Wiedemann [1, 3]:

- Cathodoluminescence (CL): Light emission caused by the impact of an electron beam on a material.
- Anodoluminescence: Light emission caused by the impact of positively charged ions on a material. Also known as ionoluminescence.
- Radioluminescence: Luminescence which is caused by the exposure of materials to ionizing radiation. In the case of X-rays, this is often referred to as röntgenoluminescence.
- Sonoluminescence: Light emission upon the exposure of a liquid to intense sound waves.
- Pyroluminescence: Luminescence caused by a flame.
- Bioluminescence: Luminescence in a living organism. All bioluminescence phenomena can be reduced to chemoluminescence.
- Galvanoluminescence: Light emission which can be found upon steering an electric current through an aqueous solution such as in some electrolysis processes.

A luminescent material is often referred to as a *phosphor*. Furthermore, photoluminescence is typically divided into fluorescence and phosphorescence, a distinction which can also be attributed to Wiedemann [1]. The former features a "fast" transition, while the latter a "slow" transition. In the case of luminescent organic

molecules, this distinction can be straightforwardly related to the type of electronic transition, governing the luminescence. In the case of inorganic materials where the luminescence is caused by isolated metal ions, this distinction is less straightforward to make and luminescence is used in general terms (see chapter 4). For the latter class of luminescent materials, the designation persistent luminescence or *afterglow* is additionally made. This refers to photoluminescence for which the light emission can still be seen seconds to hours after the excitation stopped.

1.2 Historical overview of luminescence

Eilhard Wiedemann (1852-1928) [4].

The oldest known writings about luminescence date from 10 to 15 centuries BC and were found in China. The authors from the Shang dynasty mention the luminescence of glowworms and fireflies. In contrast, no writings on luminescence were found from the old Egyptian, Sumerian and Babylonian civilizations. This void is probably rather due to a lack of registration than due to a lack of observation. Multiple writings are found from the Greek and Roman civilizations which describe - in addition to mentioning fireflies - atmospheric discharges (a form of electroluminescence) that are known as *ignis lambens*. For the Romans this marine luminescence, which later became known as St-Elmo's fire, is a bad omen. It was moreover a Greek, Anaximenes, who was the first to mention *the light from the sea* (which is due to microorganisms, *i.e.* a form of bioluminenscence).

New types of luminescence, luminescent materials and organisms were discovered in the subsequent centuries. During the Middle Ages no systematic scientific studies of the different phenomena were undertaken. For this, humanity had to wait until the scientific revolution which took place at the end of the Renaissance.

What is now considered as the first scientific approach took place in the 17^{th} century, following the discovery of the Bologna Stone by Vincenzo Casciarolo in 1602. This Italian shoemaker and amateur-alchemist found a rock of barite ($BaSO_4$) near Bologna which he heated in an attempt to produce gold. However, instead of gold he created a material that was able to absorb the light at day which could be re-emitted later, when it was dark. This phenomenon was named phosphor, derived from the Greek *phosphorus* meaning morning star or light bearer. More recent research has shown that the persistent luminescence was most likely due to the formation of barium sulfide (BaS) during the heating. The luminescence can be activated by trace impurities of Cu^+ ions [5, 6]. A detailed description of how the Bologna Stone was prepared was given by the Frenchman Pierre Potier (Poterius) who emigrated to Italy under commission by the French king (1652). The chemical element phosphorus which was later, in 1669, isolated from urine by the German alchemist Hennig Brand received the same name because it emits light upon oxidation, *i.e.* shows chemoluminescence. This ambiguity confuses many people to date as a phosphor (a

luminescent material) does not necessarily contain phosphorus (element 15) [1].

Thanks to the discovery of the Bologna Stone, luminescence ensures its place in science. In the remainder of the 17^{th} century, new luminous life forms and phosphorescent minerals were found. Especially the latter were succesful in seeking the attention of alchemists as these minerals, given their ability to store the *golden sunlight*, might illuminate the path towards the legendary philosopher's stone. As a consequence, numerous alchemists bundled their knowledge in voluminous reports. Worth mentioning and progressive was the work of Robert Boyle, the only member of the prominent *Royal Society of London* who performed a memorable study on luminescence. He carried out exhaustive experimental research into the luminescence of diamond, rotting wood and luminous fish. Moreover, he discovered phosphorus independently from Brand. At the end of the 17^{th} century, all but one -crystalloluminescence- of the six types of luminescent of Wiedemann were discovered and described. Notwithstanding the many efforts, one did not go beyond the description and enumeration of phenomena. Furthermore, an esoteric atmosphere remained associated with luminescence. A profound understanding of the different phenomena was still far away [7].

In the 18^{th} century, the age of reason, many essays were written on luminescence and the scientific approach got more decoupled from the mystical approach. As a consequence of the development of electricity, the research into electroluminescence, *i.e.* electrical light, boomed. In 1786, a green light was observed during the crystallization of potassium sulfate (K_2SO_4) from solution, crystalloluminescence was discovered. This age can also be characterized by the disagreement between those adhering to the wave theory of light and those adhering to the corpuscular theory of light. Among those active in the field of luminescence, particle theories were very popular because persistent luminescent materials were often envisioned as a sponge for light, absorbing light particles in their pores which can be released slowly in the dark.

The 19^{th} century featured many important discoveries. However, one was in the middle of a crisis at the beginning of this century as not a single connection could be found between the large number of luminescence phenomena that were known. Driven by the famous mineralogist and founder of crystallography, René Just Haüy, the French institute for mathematics and physics promised a financial reward to the one who could find a connection between the different phenomena. This competition yielded two remarkable essays. The first, the winner of the prize, was written by the Frenchman Jean Philibert Dessaignes. He was the first to distinguish short and long-lasting luminescence. Moreover, he was able to show that the light that was produced by certain fish was the result of a chemical reaction. A second interesting work was due to the German Placidus Heinrich. He was the first to distinguish organic and inorganic luminescence.

The fact that the luminescent properties of materials could be influenced by adding metal impurities was already supposed by Benjamin Wilson in the 18^{th} century.

Wilhelm Osann succeeded in the 1830s to prepare phosphors of different colors by adding small quantities of sulfides of arsenic, antimony or mercury to his starting material, crushed oyster shells, before heating. Osann can therefore, together with Wach who added metal oxides to barite and celestite ($SrSO_4$), be considered as the "inventors" of luminescence by metal impurities. This discovery was formalized in 1886-1887 by Auguste Verneuil who investigated luminescence in calcium sulfide (CaS) and took it into his commerce of synthetic gems. His method to synthesize ruby[1] crystals is well-known to date.

Sir George Stokes (1819-1903) [3].

Thanks to the development of spectroscopy, more targeted research on light could be performed in the 19^{th} century. The Scotsman David Brewster and the Frenchman Alexandre-Edmond Becquerel[2] can be safely regarded as pioneers in the spectroscopy of phosphors. Becquerel was one of the first to acknowledge that many luminescent materials can be most effectively excited by - the at that time recently discovered - ultraviolet (UV) light. It was George Stokes who established in 1852 that the light which is emitted by luminescent materials always has a longer wavelength than the absorbed light. This important fact is now known as the Stokes shift or Stokes' law, making Stokes' name one of the most encountered in luminescence literature. He was also the first who used the term *fluorescence*, named after the mineral fluorite (CaF_2) which is often luminescent. Fluorite was already discovered in the 16th century and used as additive to melt ores, yielding its name (from the Latin *fluere*, meaning to flow). The chemical element fluorine was also named after fluorite. A landmark in the history of luminescence was the denomination of the phenomenon. For this, science had to wait until 1888 when Wiedemann published his *Uber Fluorescenz und Phosphorescenz* in *Annalen der Physik* [4].

The development of quantum theory, which was launched by Max Planck in 1900, changed the complete thinking about luminescence. A connection was found with the photo-electric effect and explanations were searched at the electronic level. The configurational coordinate model, the standard model to explain the basic characteristics of luminescent materials, was developed in the 1920-1930s by the group of Robert Pohl in Germany, in collaboration with Frederick Seitz in the United States. Besides that, the Nazi scientists Johannes Stark and Philipp Lenard supplied important and progressive work on luminescence. Next to applying the youthful quantum theory, which they later discarded for anti-Semitic reasons, to the theory of luminescence, they investigated in a systematic way the influence of different metal im-

[1] Ruby consists of aluminum oxide or corundum, Al_2O_3, contaminated with a small amount of chromium, Cr, denoted as $Al_2O_3{:}Cr^{3+}$. The Cr^{3+} ions replace Al^{3+} ions in the crystal. The notation with the colon is conventional in the discipline of luminescence.

[2] Alexandre-Edmond was the son of Antoine César Becquerel who investigated luminescence as well. This family tradition ended abruptly when Alexandre-Edmond's son Antoine-Henri Becquerel accidentally discovered radioactivity during his investigation of the luminescence of uranium salts. This made him the most famous Becquerel and also Nobel laureate.

purities in host materials. They were the first to use so-called rare earth metals[3] to activate luminescence.

After the second World War, the luminescence research evolved radically thanks to advances in solid state physics, optical spectroscopy and the understanding of the electronic structure of transition metal and lanthanide ions. The fact that lanthanides give rise to efficient luminescence caught the attention of industry. In the Dutch company Philips a young scientist George Blasse worked who paved the path for the production of lanthanide-based fluorescent lamps which were commercialized in 1980 [10]. The first *cold* light source with application in general lighting was a fact.

1.3 Towards white LEDs

Since the invention of the incandescent bulb at the end of the 19th century, several lighting technologies came and went. A recurring tendency is the quest for an efficient light source with a good color rendering. Nowadays, white light-emitting diodes (LEDs) are a mature technology superior to all other technologies. Fig. 1.1(a) shows the luminous efficacy in lumen/watt (lm/W) for different types of light sources. It demonstrates the amazing rise of LED technology after the turn of the century. The theoretical maximum for white LEDs with a good color rendering lies around 300 lm/W (for pc-LEDs, see further).

1.3.1 The LED chip

Light-emitting diodes are essentially built from a semiconductor p-n junction, called a diode[4]. In forward bias, *i.e.* when connecting a positive voltage to the anode, electrons and holes are injected in respectively the anode and cathode, provoking an electric current which grows exponentially with voltage as described by Shockley's law[5]. When the electrons and holes meet each other in the middle of the junction, recombination can occur, leading to the emission of photons. This is hence a form of electroluminescence. Since the energy that is released during the recombination

[3] Rare earths are a collective name for the lanthanides (La, Ce, Pr, Nd, Pm, Sm, Eu, Gd, Tb, Dy, Ho, Er, Tm, Yb, Lu), scandium (Sc) and yttrium (Y). Although rare earths are not really rare given that their abundance is comparable to that of more common metals such as Cu, Ni, Zn, Cr, ..., it is difficult to mine and purify them due to their chemical similarity and the fact that they are well dispersed and nowhere occur in very large concentrations. Moreover, the People's Republic of China holds a quasi-monopoly in esteem, resulting into fluctuating prices for raw materials and hence an unstable market [8, 9].

[4] A p-n junction is, as the name tells, a junction of a p-type (anode) and n-type (cathode) semiconductor. An n-type semiconductor is doped by impurity atoms such that the electrons in the conduction band are the majority charge carriers. For a p-type material, the dopant is chosen such that holes in the valence band are the majority charge carriers [11, 12].

[5] William Bradford Shockley, who also invented the semiconductor diode, shared the Nobel prize in 1956 with his colleagues Walter Houser Brattain and John Bardeen of *Bell Telephone Laboratories* for their invention of the semiconductor transistor. Thanks to their work, the cumbersome vacuum tube electronics could be replaced by semiconductor technology.

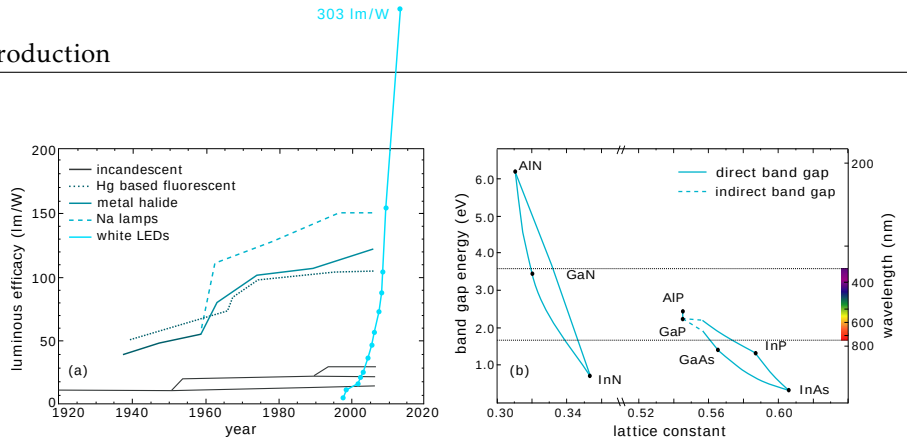

Figure 1.1 – (a) The luminous efficacy of white LEDs, compared to traditional light sources [13, 14]. (b) Band gap energy versus lattice parameter for the most common III-V semiconductors used for LEDs or laser diodes [13, 15].

is equal to the band gap energy of the semiconductor, E_G, a materials property, the photon energy will be $\hbar\omega_k \approx E_G$. For this reason, the light of LEDs is expected to be monochromatic. In reality, multiple effects such as a finite temperature and non-ideal behavior will lead to a significant broadening of the emission spectrum of an LED. Nonetheless, saturated, *i.e.* "pure", colors are found.

In order for a diode to be an efficient LED, the band gap has to be direct. This means that light emission follows the recombination of the charge carriers immediately. In the case of indirect semiconductors, such as silicon or germanium, this is not the case and heat has to be exchanged in addition. This makes silicon diodes poor LEDs. As the initial successes from semiconductor technology pertain mainly to silicon and germanium, the invention of the LED was somewhat delayed until the investigation of direct semiconductors.

In the 1950s, so-called III-V semiconductors were predicted and synthesized by the German physicist Heinrich Welker[6]. This material class does not occur in nature, in contrast to *e.g.* II-VI semiconductors. Gallium arsenide (GaAs) crystals were for the first time grown at a large scale in 1954. This direct semiconductor has a band gap energy which corresponds to infrared (IR) radiation (±870 nm). In the subsequent decades, people succeeded to shift the emission wavelength to the visible wavelength range by constructing GaAs/AlGaAs (red, 1960s) and GaP/GaAsP:N (red, yellow, orange, green, 1960-1970s) structures. The first practical visible light LED was developed in 1962 by Nick Holonyak, Jr.[7], a scientist from General Electric. The LEDs of that time were for multiple reasons limited to applications with low light intensities such as indicator lamps. The first LEDs based on the AlGaInP system were developed in the 1980s. Currently, this materials class is the most used

[6] III-V materials are composed of a cation from the third group (Al, Ga, In) and an anion from the fifth group (N, P, As, Sb) of the periodic table.

[7] Holonyak was a student of John Bardeen and is since his invention known as the godfather of the LED.

semiconductor for efficient LEDs in the red to yellow part of the visible spectrum.

All that time, nobody succeeded in constructing a blue LED. The attempts with GaN led to an extremely poor blue or UV EL and were hence unusable. The main reason for this was the failure to incorporate acceptors in GaN *i.e.* to prepare p-type GaN, which should be accomplished by Mg doping, without generating unwanted deep levels. The first efficient blue LEDs were demonstrated in 1995 by the Japanese scientist Shuji Nakamura of *Nichia Chemical Industries Corporation*. These LEDs, based on GaInN proved to be very efficient, leading to a fast implementation, *e.g.* in lighting. Also the blue GaInN/GaN-based laser diodes are capable to generate high light intensities. Nakamura obtained the Nobel prize in Physics in 2014 for the invention of efficient blue LEDs together with Isamu Akasaki and Hiroshi Amano, two other GaN pioneers.

It is the gallium-indium ratio that determines the emission color of a GaInN device. By adding more indium, the color can be shifted towards the green (see Fig. 1.1(b)). This figure shows that it is possible - in principle - to make LEDs in the full visible wavelength range. This is however not viable in reality as it proves to be impossible to grow good crystals with a high indium content as this main group metal spontaneously evaporates from the growing crystal surface. This complication is the reason why green GaInN LEDs are less efficient than their blue and UV counterparts. For the same reason, efficient green laser diodes cannot be found [8].

1.3.2 Phosphor-converted LEDs

Already in the 1670s, Newton demonstrated that white light is a mixed color, composed from *all colors of the rainbow*, *i.e.* the spectral colors. As LED chips only emit light in a limited wavelength range, white light cannot be directly obtained. Three indirect possibilities however exist:

1. RGB LEDs: In this approach, three p-n junctions with different E_G values, corresponding to the colors red, green and blue, are combined. The mixed color of the three LEDs is white.

2. UV diode + RGB phosphors: Here, an LED with a sufficiently large E_G value, corresponding to UV radiation, is used in combination with three phosphors, a red, green and blue one, to obtain white light.

3. Blue diode + Y/RG phosphors: A blue LED is used to excite a single yellow or a red-green phosphor blend. This is the archetype of a white LED in various applications. The most popular yellow LED phosphor is YAG:Ce^{3+} (see Fig. 1.2), yielding rather *cold-white* LEDs. *Warmer* white light can be obtained by using an additional red phosphor or by using a green-red phosphor blend.

[8] The most efficient green lasers are built from a neodymium-doped yttrium aluminum garnet ($Y_3Al_5O_{12}$) crystal, YAG:Nd^{3+} which emits light at 1064 nm. This IR light is then guided through a nonlinear optical crystal such as potassium hydrogen phosphate (KH_2PO_4), KDP. Due to the nonlinear response, the wavelength of the light is halved to 532 nm, obtaining green laser light indirectly.

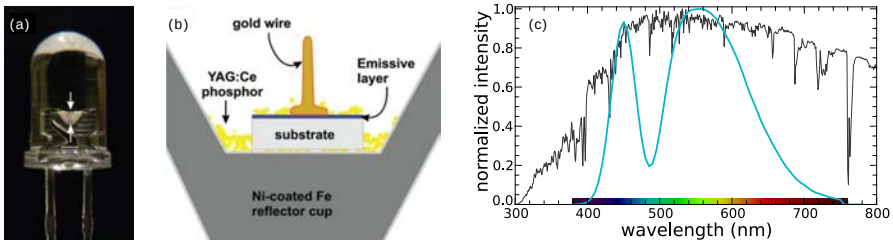

Figure 1.2 – White phosphor-converted LED. (a) 5 mm LED package. (b) Schematic cross-section. (c) Emission spectrum of a white LED, based on a 450 nm InGaN pumping LED and a broadband yellow phosphor (YAG:Ce) (thick blue line), compared to the solar spectrum (thin black line) [13].

The second and third possibility are called phosphor-converted LEDs (pc-LEDs). These pc-LEDs are more appropriate than the RGB LEDs for most applications. The reason is that the latter require more complicated electronics to account for the different aging behavior and temperature response of the different LEDs. Furthermore, a large freedom is available to choose the phosphors in pc-LEDs, allowing to tune the white LEDs to the needs of the envisioned application. To date, improvements are still made, optimizing the composition of the phosphor blend, device geometry etc. It is in this technological context that this work, which focuses on the selection and development of LED phosphors, needs to be placed.

1.3.3 Applications

Obviously, white pc-LEDs find a huge application potential in general lighting. Currently, the market which is primarily based on inefficient incandescent bulbs and polluting fluorescent lamps undergoes a large-scale evolution towards more sustainable LED technology. Depending on the preferences of the consumer, LED lighting with a cold-white or warm-white appearance are available. To meet with the conservativism of many consumers, LED bulbs with the appearance of an incandescent-bulb are nowadays available (see Fig. 1.3b).

While LEDs for lighting already outperform the competing technologies (see Fig. 1.1a), improvements are still possible. A good light source has, among other things, a broad spectrum, allowing for an optimal rendering of colored objects. The spectra of current white LEDs typically show a gap between the blue pumping LED and the green or yellow phosphor, leading to a decreased rendering of objects with blue-green colors (see Fig. 1.3c). It is therefore desirable to fill this gap in some way. This issue is further addressed in chapter 8. Furthermore, the currently used red phosphors all show an emission tail extending into the far red / near IR part of the spectrum. As the human eye sensitivity is very limited in this region, this emission can be considered as superfluous (see Fig. 1.3c). There is hence a need for more narrow-band red phosphors. A possibility to limit these losses is validated in chapter 9.

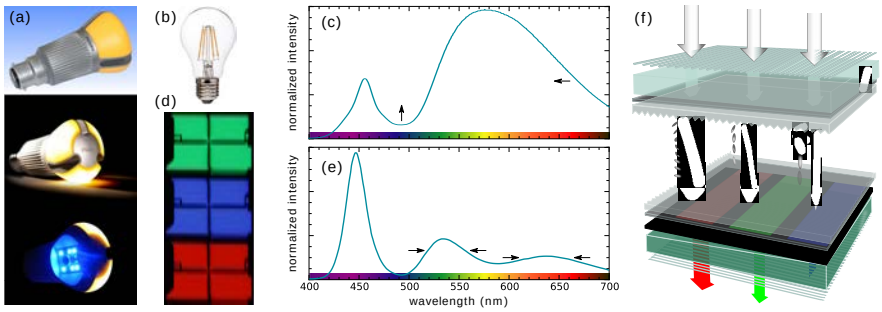

Figure 1.3 – (a) Remote phosphor white pc-LED, pumped with blue LEDs. (b) White pc-LED, designed to resemble an incandescent bulb. (c) Spectrum of a warm-white pc-LED. The black arrows indicate possible improvements to the spectrum. (d) Optical microscope picture of a pixel of a LCD, showing the RGB subpixels. (e) Spectrum of a white pc-LED, used in LCDs. The black arrows indicate possible improvements to the spectrum. (f) Working principle of a pixel of a LCD.

Next to lighting, white LEDs also find an important application in display technology. Current large screens of *e.g.* television sets and computers are mainly liquid crystal displays (LCD). The liquid crystal (LC) part of the display is only responsible for the switching of every (sub)pixel, *i.e.* a separate light source is required. Before the advent of LEDs, cold cathode fluorescent lamps (CCFL) were used for this, however now LED-LCD displays are standard. The color of every pixel is determined by the three primary colors RGB which are mixed in the correct ratios by the three LC cells in the subpixels (see Fig. 1.3f). To obtain a maximal color gamut, the primary colors should be as saturated as possible, *i.e.* corresponding to emission bands which are as narrow as possible. Phosphors used in displays hence feature different spectra as opposed to phosphors used in lighting. As time passed by, the requirements for the saturation of the primary colors got more strict, driven by the demand of the consumer, the corporate willingness to innovate or a combination of both, culminating in the ITU-R Recommendation BT.2020 (Rec. 2020) for ultra high definition television [16]. This recommendation demands emission bands for which the full width at half maximum (FWHM) is limited to a few tens of nm, depending on the emission maximum [17]. Most existing phosphor materials do not achieve these narrow spectra, motivating a systematic search to new, narrow-band phosphors in both the green and red spectral segment (see Fig. 1.3e). This issue is further addressed in chapter 9.

1.4 Phosphor performance

In order to be applicable in white LEDs, phosphors need to fulfill different technological requirements. These are described in detail in [13] and are summarized here:

1. The emission spectrum of the phosphor should be suited for the envisioned application. This differs to a large extent for lighting and displays.
2. The phosphor should be easily excitable by the blue or near-UV light of the pumping diode.
3. The conversion efficiency of the material should be high.
4. The luminescent properties of the material such as the emission color and conversion efficiency should be stable as a function of temperature since elevated temperatures are encountered in devices.
5. The luminescence intensity should show linear behavior as a function of the excitation power, *i.e.* saturation effects are undesired.
6. The material should be chemically stable on the long term. Lifetimes of 50 000 hours are currently specified for white LEDs.

It is important to stress that all these requirements have to be fulfilled simultaneously for a phosphor to be a suitable candidate for applications.

However, using an intelligent device architecture can relax certain requirements to some extent. As an example, requirements 4 and 5 are relaxed in a so-called remote phosphor approach (see Fig. 1.3a). Here, the phosphor is not applied directly onto the semiconductor LED chip, where temperature and excitation fluxes are very stressful, but on a separate phosphor plate at a certain distance from the chip. Here, the conductive heating of the phosphor by the LED chip is completely removed and the excitation flux is spread over a larger surface of phosphor material. An important disadvantage of this remote phosphor approach is that a larger quantity of phosphor powder is needed. Also when used in displays, remote phosphor architectures are possible.

Next to these technological requirements, also economical and environmental requirements can be of importance.

Economical requirements pertain to the cost of the phosphor which is determined by the synthesis procedure and the availability of the starting materials. Due to recent fluctuations of the price of lanthanides, phosphors based on lanthanides are often regarded as economically less interesting. A distinction should however be made between lanthanide-based phosphors where only the activator is a lanthanide and materials where the host compound is lanthanide-based. In the former case, the required amount of lanthanides is rather limited.

Environmental requirements pertain to the impact of the mining and processing of ores to the final product, as well to the recycling of the materials after their lifespan. Especially lanthanides get a bad score for environmental friendliness given their low concentration in ores, difficult separation involving harmful chemicals and the large amount of the radioactive element thorium, which is considered as a waste product, in lanthanide ores. Due to economical and environmental objections, it would be desirable to minimize the amount of lanthanides in phosphors. Nevertheless, the majority of current LED phosphors are lanthanide based. This objection should however be put in a broader context as phosphors are by far not the largest market of lanthanides. Only 8% of the mined lanthanides end up in phosphors. The largest fraction goes into catalysis for chemical and automotive industry, metallurgy and petroleum refinement[9] [18].

In the most rudimentary picture, phosphors are composed of a host compound, doped with metal impurities that activate the luminescence. The luminescence properties of the obtained phosphor depend on the intrinsic properties of both building blocks, *e.g.* on the type of local electronic transition yielding the luminescence (see Tab. 1.1), but also on the details of the interactions between both. Subtle changes in the dopant-host interaction can already have an appreciable influence on the macroscopic physical properties of the phosphor.

Host crystals can have a large variety of chemical composition, ranging from halides, over all kinds of oxides to sulfides or nitrides. Activator ions are typically grouped according to their position in the periodic table. Lanthanides or 4f elements are very popular for various reasons. Furthermore, transition metals, specifically from the 3d series, and so-called s^2 ions, originating from the heavy p block, have regained popularity in the search for lanthanide-free phosphors. Figure 1.4 shows the periodic table of elements with these three regions highlighted.

[9] *"The only way you can avoid the rare earths is to grab your sleeping bag and go into the deep forests or caves in the desert far from civilization without your cell phone or even lighter flints (which are made of iron and cerium-rich rare earths)."* - K. A. Gschneidner, Jr. [18]

Table 1.1 – Overview of localized electronic transitions in defects.

transition	example	
$1s \leftrightarrow 2p$	F-center	electron in vacancy
$ns^2 \leftrightarrow nsnp$	s^2 ions	(*e.g.*: Tl^+, Pb^{2+}, Bi^{3+},...)
$nd^{10} \leftrightarrow nd^9(n+1)s^1$	transition metals	Ag^+, Cu^+, Au^+
$nd^N \leftrightarrow nd^N$	transition metals	(*e.g.*: Mn^{2+}, Cr^{3+}, Co^{2+},...)
$nf^N \leftrightarrow nf^N$	lanthanides and actinides	(*e.g.*: Eu^{3+}, Tb^{3+}, U^{4+},...)
$nf^N \leftrightarrow nf^{N-1}(n+1)d$	lanthanides and actinides	(*e.g.*: Ce^{3+}, Eu^{2+}, Pa^{4+},...)

1.5 Energy levels

A quick consideration learns that an unimaginably large number of combinations between dopants and hosts can be made. Combining the relevant transition metals and lanthanides with the large number of possible binary, ternary, quaternary, ... compounds, possibly existing in different stoichiometries and polymorphs leads indeed to rapidly increasing numbers. Moreover, co-doping can improve the performance of a phosphor in different ways. It is hence practically impossible to experimentally subject all these different materials to the six requirements that are listed above.

The growing demand towards more specialized materials, specified by the above requirements, raises new challenges for science and materials engineering. More than before, a theoretical framework is required to design materials on the drawing board before actual synthesis to prevent getting stuck in an uncreative trial-and-error approach of combining hosts and dopants. So-called energy levels bridge the macroscopic properties of a material with the microscopic physical interactions. In other words, energy level schemes form the key to understand, fine-tune and design new functional materials. A simple example for a Ce^{3+} ion in a certain host material is shown in Fig. 1.5.

The importance of energy level schemes is evident upon inspecting the scientific literature on luminescence, they simply appear in the majority of the published articles. Simultaneously, one would probably notice that there is no agreement on how to use what type of energy level scheme in which situation, even leading to

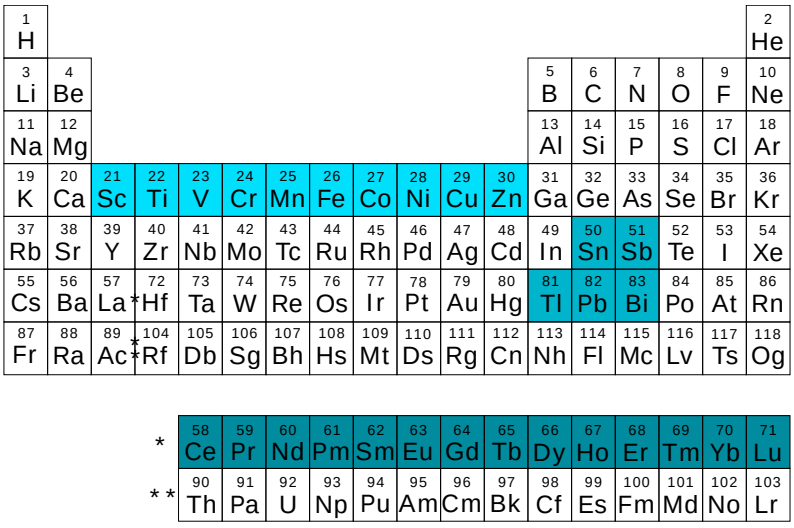

Figure 1.4 – Periodic table showing the three *groups* of elements of which most optical dopants are selected.

energy level schemes with an unclear meaning and interpretations lacking formal grounds [10]. A rationalization of the meaning of the different types of energy level schemes and what they represent under which assumptions is hence essential at this moment. This rationalization is additionally complicated by the multiple theoretical frameworks and computational techniques that are available for every type of energy level scheme ranging from the simplest empirical rules to the most complicated quantum mechanical calculations, requiring a vast amount of computer power.

When theoretical techniques are applied to study or even design luminescent materials, it is very important to grasp the implicit and explicit assumptions of the used model as well as the magnitude of the uncertainties that are associated with it. Knowledge of the assumptions and the uncertainties gives a direct idea of the quality of the predicted properties. If the quality of the prediction is less than required for the application, the model is of little use in designing functional materials. On the other hand, it can be rewarding to investigate the deficiency of simple models, both from the scientific as from the technological point of view because improved models obviously lead to improved predictions and potentially superior materials.

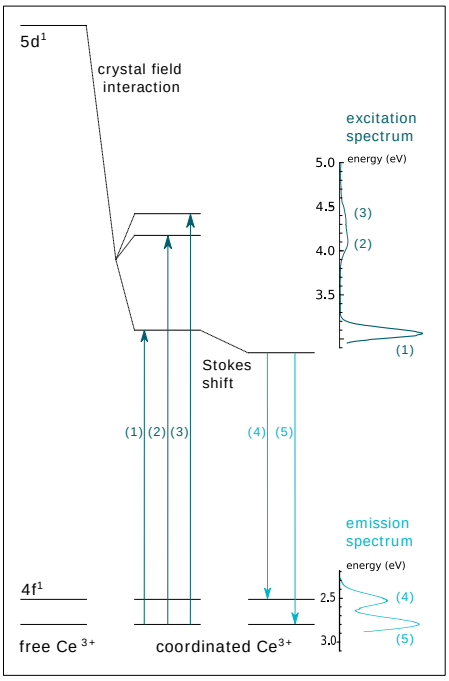

Figure 1.5 – Schematic illustration of the crystal field effects on the energy levels of a Ce^{3+} ion and the corresponding excitation and emission spectra.

1.6 Goal and structure of this text

In the end, it is the target to develop phosphors that are perfectly adapted to their application, in this case white LEDs for either displays or general lighting. Two strategies are applied, *i.e.* the use of energy level models and the mining of existing scientific literature.

As said, different types of energy level schemes and many theories are available to describe luminescent materials. In this text, different techniques are reviewed and exploited to investigate a few selected materials. To meet with the ambiguity pertaining to the different types of energy level schemes, chapters 2, 3, 4 and 5 explain the origin of the different types of energy level schemes. The focus is consciously put on the approximations that are made during the derivation of the models. Furthermore, the theoretical frameworks that are used in the remainder of the text are

[10] *"Das ist nicht nur nicht richtig, es ist nicht einmal falsch!"* - Wolfgang Pauli [19].

regarded from the viewpoint of luminescent materials and some relevant examples are given. Specifically, chapter 2 explains the intimate connection between energy level schemes and spectroscopic properties in general terms. Chapter 3 describes the influence of the dynamics on experimental spectra and offers a microscopic interpretation for key parameters such as thermal quenching and the quantum efficiency of a luminescent material. In chapters 4 and 5, the two major types of energy level schemes are discussed. These are respectively many-body levels or multiplets (chapter 4) and single-particle levels or orbitals (chapter 5). Multiplets are regarded from the atomic point of view in the framework of crystal field theory, while orbital diagrams are regarded from the band point of view in the framework of density functional theory. Alternative computational frameworks are briefly reviewed. Many-body energy level schemes are used to investigate the luminescence properties of the phosphors K_2SiF_6:Mn^{4+} and $SrAl_2O_4$:Eu^{2+}. Appendices A and B provide the necessary mathematical tools to calculate quantum mechanical matrix elements.

In chapter 6, a third approach to obtain energy level schemes, next to crystal field theory and density functional theory, is discussed in detail, *i.e.* empirical band diagrams with impurity levels of lanthanides. The available methodology is critically reviewed and put in the broader context of energy level models. Empirical models are by far the fastest and the easiest to implement, making them the most interesting models from the viewpoint of phosphor development. It is however important to have a good idea of the uncertainties inherent to the model. An error assessment is carried out, not only pertaining to the energy levels itself, but more importantly, to the physical properties that can be calculated, allowing to decide which rules yield sufficiently accurate predictions with respect to the technological requirements and which rules do not (see Fig. 1.6). Furthermore, suggestions are made how existing empirical models can be improved. Empirical band diagrams are exploited to investigate the luminescence of lanthanide-doped $CaGa_2S_4$, $SrGa_2S_4$, $SrAl_2O_4$ and $Sr_2Si_5N_8$. The latter three host compounds are used as examples to demonstrate possible improvements to the empirical rules, inspired by the occurrence of nonequivalent lanthanide defects or charge compensation schemes in the first coordination shell of the lanthanide. The repercussions of the existence of nonequivalent lanthanide defects on the electronic structure and physical properties is discussed. Values of empirical parameters are collected in appendix C.

The second part of this text is more centered around the experimental validation of the above six requirements for a selection of promising phosphors which were selected based on recent literature. In chapter 7, the necessary experimental techniques to achieve this goal are reviewed and put into connection with the six requirements. Special emphasis is put on the construction, calibration and measurement methodology of a setup to obtain absolute quantum efficiencies of powder phosphors, possibly the parameter that is hardest to measure while validating phosphors. Specialized quantities that are used to evaluate the spectra of light sources are reviewed in appendices D and E.

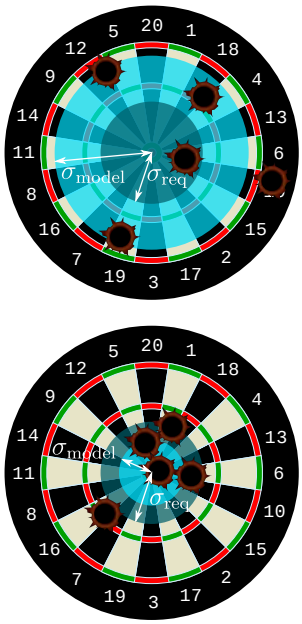

Figure 1.6 – Pictorial representation of two models with predictive possibilities having uncertainties σ_{model} for physical properties. One is able (bottom) and one is unable (top) to obtain sufficiently accurate predictions, dictated by the allowed spread on the technological requirements σ_{req}. This figure represents only the precision of the model. In reality also the accuracy is important which would be represented by the offset of the center of the light blue circle with respect to the bull's-eye [20].

In the subsequent chapters, different phosphors are investigated. Chapter 8 reviews the luminescent properties of Eu^{2+} activated oxonitridosilicates of the form $MSi_2O_2N_2$ (M = Ca, Sr, Ba, Eu) and highlights the results that were obtained for the blue phosphor with M = $Sr_{0.25}Ba_{0.75}$. The blue emission color is rather untypical for the family of europium doped oxonitridosilicates and hence deserves some special attention. Additionally, the sense and nonsense of using blue phosphors in pc-LEDs is discussed based on simulations of LED spectra.

In chapter 9, the luminescent properties of Eu^{2+} activated thiogallates of the form MGa_2S_4 (M = Mg, Zn, Ca, Sr, Ba, Eu) are first reviewed. Subsequently, the performance of the saturated green phosphor $SrGa_2S_4$:Eu^{2+} is discussed. The thermal quenching and concentration quenching of the Eu^{2+} emission are studied in detail and the use of $SrGa_2S_4$:Eu^{2+} as green phosphor for display applications is evaluated. In the second part of this chapter the $ZnGa_2S_4$:Eu^{2+} phosphor is investigated in detail, inspired by positive reports in scientific literature, suggesting LED applications for this material. The incorporation of Eu^{2+} in this remarkable host for lanthanides is studied and the origin of the green emission explained.

Finally, a combined experimental-theoretical study of the red phosphor CaZnOS:Mn^{2+} is conducted in chapter 10. A band diagram, impurity levels and a phonon dispersion relation are obtained with a semi-empirical version of density functional theory and compared to experimental luminescence and absorption spectra. It is settled by the calculation as well as X-ray absorption spectroscopy how the manganese dopant is incorporated in the oxysulfide host. Furthermore, crystal field theory is exploited to reproduce the well-resolved luminescence spectrum of this phosphor. Its use as red phosphor in white LEDs is validated.

Finally, the conclusions of this research work are summarized and some perspectives are formulated.

I

From electronic structure to luminescence

2 A THEORY OF MATTER AND LIGHT

In this chapter, the physical building blocks will be provided that allow a theoretical description of material properties, with a focus on the spectroscopic properties of inorganic luminescent materials. The physical building blocks come in a mathematical form, *i.e.* as the laws of quantum mechanics, permitting to describe the behavior of matter, light and their interaction. The true and complete theory of matter and light is called quantum electrodynamics (QED) and treats light and matter as interacting quantum fields, described by the operators of second quantization. Here, only the light will be considered in field-theoretical disguise, while ordinary quantum mechanics in the form of the many-body Schrödinger equation is used for the matter part. This does not pose severe restrictions to the systems and processes that are studied in this text.

First, the *equation of motion* for matter, the luminescent materials in this case, is treated in a general way. The so-called Born-Oppenheimer approximation is introduced which decouples the motion of nuclei and electrons based on their huge mass difference. This approximation paves the way for a more detailed treatment in further chapters. Subsequently, a quantum mechanical version for the theory of electromagnetism is given, introducing the notion of the photon, the *light particle*. Finally, the interaction between light and matter is studied, yielding a tool to calculate intensities for transitions between ground and excited states of materials upon absorption or emission of light.

2.1 Quantum mechanical description of matter

Crystalline solids are, like all materials, built from atomic nuclei and electrons which behave according to the laws of quantum mechanics. As these laws are exactly known, it is tempting to state that it is possible to predict physical and chemical properties of materials by mere mathematical manipulation of these laws. This is only true in principle and demonstrated for the most simple systems. If one attempts a serious theoretical treatment of experimentally relevant systems, even the most courageous scientist will very soon run into a wall, erected by the limited possibilities of the available mathematical and computational apparatus. The inconceivably large number of particles that makes up a macroscopic amount of matter is clearly responsible for this. In a gram of sand, as an example, one can find $3{\times}10^{22}$

atomic nuclei and $3{\times}10^{23}$ electrons. In the course of the years, multiple shortcuts were disclosed, putting approximate solutions of the quantum mechanical many-body problem within reach. Below, the most relevant approximations for the study of luminescent materials are introduced.

2.1.1 Born-Oppenheimer approximation

As point defects in crystals are considered, a first straightforward approximation can be made by considering only the immediate neighborhood of the defect and forgetting the remainder of the crystal. In this way, one ends up with a molecular defect cluster. The Schrödinger equation for a cluster containing M nuclei with positions $\boldsymbol{R}_\alpha$ and N electrons with positions $\boldsymbol{r}_i$ reads:

$$\begin{aligned}\mathcal{H}_{\text{mat}}\Psi(\boldsymbol{r},\boldsymbol{R}) &= \left[\sum_{\alpha=1}^{M}\left(-\frac{\hbar^2}{2M_\alpha}\nabla_\alpha^2+\sum_{\beta>\alpha}^{M}\frac{Z_\alpha Z_\beta e^2}{4\pi\epsilon_0\left|\boldsymbol{R}_\alpha-\boldsymbol{R}_\beta\right|}\right)\right.\\ &+ \left.\sum_{i=1}^{N}\left(-\frac{\hbar^2}{2m_e}\nabla_i^2-\sum_{\alpha=1}^{M}\frac{Z_\alpha e^2}{4\pi\epsilon_0\left|\boldsymbol{R}_\alpha-\boldsymbol{r}_i\right|}+\sum_{j>i}^{N}\frac{e^2}{4\pi\epsilon_0\left|\boldsymbol{r}_j-\boldsymbol{r}_i\right|}\right)\right]\Psi(\boldsymbol{r}_i,\boldsymbol{R}_\alpha)\\ &= E\Psi(\boldsymbol{r},\boldsymbol{R}),\end{aligned} \tag{2.1}$$

Herein, $\mathcal{H}_{\text{mat}}$ and E denote the total Hamiltonian and total energy of the defect cluster respectively and Ψ the many-body wave function.

An often used simplification of Eq. 2.1, effectively separating electronic and nuclear motion, was found by Robert J Oppenheimer during his stay in Göttingen in 1926-27 under the supervision of Max Born [21]. This approximation is to date standard in most quantum mechanical calculations. It assumes following ansatz for the total wave function:

$$\Psi(\boldsymbol{r},\boldsymbol{R}) = \psi(\boldsymbol{r},\boldsymbol{R})\chi(\boldsymbol{R}). \tag{2.2}$$

ψ and χ respectively denote the electronic and nuclear wave functions. It allows to separate Eq. 2.1 into an electronic and nuclear eigenvalue equation under the condition that the so-called non-adiabatic terms,

$$\mathcal{H}_{\text{n-ad}} = \sum_{\alpha=1}^{M}\frac{-\hbar^2}{2M_\alpha}\Big(2\nabla_\alpha\psi(\boldsymbol{r},\boldsymbol{R})\cdot\nabla_\alpha\chi(\boldsymbol{R})+\chi(\boldsymbol{R})\nabla_\alpha^2\psi(\boldsymbol{r},\boldsymbol{R})\Big), \tag{2.3}$$

can be neglected. This approximation is most often justified due to the large difference between the nuclear and electron masses ($M_\alpha/m_e \approx 10^3 - 10^5$).

The approximate solution of Eq. 2.1 starts by solving the electronic eigenvalue equation,

$$\left[\sum_{i=1}^{N} \left(\frac{-\hbar^2}{2m_e} \nabla_i^2 - \sum_{\alpha=1}^{M} \frac{Z_\alpha e^2}{4\pi\epsilon_0 |\boldsymbol{R}_\alpha - \boldsymbol{r}_i|} + \sum_{j>i}^{N} \frac{e^2}{4\pi\epsilon_0 |\boldsymbol{r}_j - \boldsymbol{r}_i|} \right) + \sum_{\alpha=1}^{M} \sum_{\beta>\alpha}^{M} \frac{Z_\alpha Z_\beta e^2}{4\pi\epsilon_0 |\boldsymbol{R}_\alpha - \boldsymbol{R}_\beta|} \right] \psi_m(\boldsymbol{r}, \boldsymbol{R}) = E_m(\boldsymbol{R})\, \psi_m(\boldsymbol{r}, \boldsymbol{R}), \tag{2.4}$$

for fixed nuclear positions $\boldsymbol{R}$. Different electronic eigenvalues E_m are then obtained. The index m denotes the set of quantum numbers and auxiliary numbers that are required to label the different electronic eigenstates. Depending on the relative size of the different interactions in the electronic Hamiltonian, these can be angular momenta, wave numbers, irreducible representations of crystal symmetry groups or Lie groups. Chapters 4 and 5 are devoted to different solutions of Eq. 2.4 that are relevant for the studied luminescent systems.

Potential energy surfaces $E_m(\boldsymbol{R})$ are obtained by successively solving Eq. 2.4 for different - but always fixed - nuclear coordinates. In this way, the electronic eigenvalues and eigenfunctions depend parametrically on the nuclear coordinates. The $\boldsymbol{R}$ value for which the energy $E_m(\boldsymbol{R})$ reaches a minimal value, $\boldsymbol{R}_{m0}$, corresponds to the equilibrium positions of the nuclei. For the electronic ground state, this corresponds to the experimentally found nuclear geometry. To obtain the complete, however approximate, solution of the total Schrödinger equation 2.1, the nuclear eigenvalue equation has to be solved subsequently:

$$\left(\sum_{\alpha=1}^{M} -\frac{\hbar^2}{2M_\alpha} \nabla_\alpha^2 + E_m(\boldsymbol{R}) \right) \chi_{m\boldsymbol{\mu}}(\boldsymbol{R}) = \epsilon_{m\boldsymbol{\mu}} \chi_{m\boldsymbol{\mu}}(\boldsymbol{R}). \tag{2.5}$$

This equation has to be solved on each potential energy surface (PES) that was found by solving the electronic eigenvalue equation. Equation 2.5 describes the motion of the atomic nuclei in the defect cluster, *i.e.* the vibrations of the nuclei around their equilibrium positions. The index $\boldsymbol{\mu}$ denotes the additional set of quantum numbers that label the different solutions of Eq. 2.5. In chapter 3, approximate analytical solutions are found for Eq. 2.5.

When solutions are found for both eigenvalue equations, 2.4 and 2.5, the general solution of Eq. 2.1 can be constructed from the total wave functions, Eq. 2.2, and energies:

$$E_{m\boldsymbol{\mu}} = E_m(\boldsymbol{R}_{m0}) + \epsilon_{m\boldsymbol{\mu}}. \tag{2.6}$$

These are total energies, *i.e.* the sum of all contributions from all interacting electrons and nuclei, as seen from Schrödinger equation 2.1.

2.1.2 Relativity theory

Schrödinger's equation 2.1 is purely non-relativistic implying that it fails to describe phenomena due to relativistic effects. Rather than striving for a solution of the Dirac

equation (*i.e.* the relativistic invariant wave equation) one typically adds terms to $\mathcal{H}$ to improve the description of physical reality. The theory of relativity explains amongst other things the existence of *spin*, an intrinsic angular momentum that elementary particles possess. This spin angular momentum couples to the orbital angular momentum of bound particles through the so-called spin-orbit interaction, probably the most notable term added to Eq. 2.1. The remaining relativistic effects, related to the mass increase of electrons in high speed orbits are referred to as scalar relativistic effects [22]. These effects become increasingly important for the heavy nuclei found upon descending the periodic table. Relativistic effects are not only required to comprehend the spectra of lanthanide ions, but also to explain daily observations such as why metallic gold has a golden color or mercury is liquid at room temperature. The latter two are direct consequences of the relativistic shrinking of the outer electron orbits [23].

2.2 Quantum mechanical description of light

The most impressive scientific development of the 19^{th} century is doubtlessly the consciousness that electric and magnetic phenomena are two manifestations of one fundamental interaction, *i.e.* electromagnetism. The classical theory of this interaction is built from a few laws that were first written down by James Clerck Maxwell. The modern textbook version of these laws is due to Oliver Heaviside [24]:

$$\nabla \cdot \boldsymbol{E} = \frac{\rho}{\epsilon_0} \qquad \nabla \cdot \boldsymbol{B} = 0 \tag{2.7}$$

$$\nabla \times \boldsymbol{E} = -\frac{\partial \boldsymbol{B}}{\partial t} \qquad \nabla \times \boldsymbol{B} = \epsilon_0 \mu_0 \frac{\partial \boldsymbol{E}}{\partial t} + \mu_0 \boldsymbol{J}, \tag{2.8}$$

where $\boldsymbol{E}$ and $\boldsymbol{B}$ represent the electric and magnetic fields respectively. Although a wave solution of these equations is straightforward to find, the implications are enormous. First of all, it proves the existence of electromagnetic waves. Furthermore, it tells that these waves propagate with a velocity $1/\sqrt{\epsilon_0 \mu_0}$, which can be calculated from the permittivity and permeability of the vacuum, quantities that were known from experiments on electricity and magnetism. Surprisingly -at that time- this velocity was already known as the measured speed of light, *i.e.* $c = 299\ 792$ km/s. Later, more experimental validations of the Maxwell theory followed, for example the famous radio wave experiments of Heinrich Hertz [25].

Although an interaction between light and matter is clearly present in Maxwell's equations through the occurrence of the electric charge density ρ and current density $\boldsymbol{J}$, this classical theory does not succeed to yield a sufficiently profound understanding of how light can interact with matter. For this, light has to be treated on an equal footing as matter was treated in §2.1, *i.e.* quantum mechanically. The classical wave solution will be given upon which the recipe of quantum mechanics will be applied.

2.2.1 Hamiltonian of the radiation field

Rather than working with the electric and magnetic fields $\boldsymbol{E}$ and $\boldsymbol{B}$, it proves to be beneficial to introduce the so-called scalar and vector potentials ϕ and $\boldsymbol{A}$, which yield more clear, though equivalent, equations [26]:

$$\boldsymbol{E} = -\nabla\phi - \frac{\partial \boldsymbol{A}}{\partial t} \qquad \boldsymbol{B} = \nabla \times \boldsymbol{A}. \tag{2.9}$$

As one can see, the fields pertain to changes in the potentials. As such, a constant offset in the latter does not influence the former, physical quantities. More general, it is easy to show that transformations of the type,

$$\boldsymbol{A} \to \boldsymbol{A} + \nabla\chi \qquad \phi \to \phi - \frac{\partial \chi}{\partial t}, \tag{2.10}$$

where χ is an arbitrary function of space and time, does not influence the physical fields and is thus a symmetry, called the gauge symmetry, intrinsic to the theory of electromagnetism [24]. The symmetry 2.10 will be used to find the fastest way towards the physical results that are of our interest. This is done by *fixing* the gauge. When not bothering about relativistic invariant equations, the Coulomb gauge, $\nabla \cdot \boldsymbol{A} = \partial\chi/\partial t = 0$, is an excellent choice [27].

When plugging the expression for $\boldsymbol{A}$ into Maxwell's equations, a wave equation is immediately found,

$$\nabla^2 \boldsymbol{A}(\boldsymbol{r}, t) = \frac{1}{c^2} \frac{\partial^2 \boldsymbol{A}(\boldsymbol{r}, t)}{\partial t^2}, \tag{2.11}$$

for which a general solution can be written as a Fourier series:

$$\boldsymbol{A}(\boldsymbol{r}, t) = \sum_{\boldsymbol{k},\sigma} A_0(k) \boldsymbol{\epsilon}_{\boldsymbol{k}\sigma} \left(a_{\boldsymbol{k}\sigma} \mathrm{e}^{\mathrm{i}\boldsymbol{k}\cdot\boldsymbol{r}} + a^*_{\boldsymbol{k}\sigma} \mathrm{e}^{-\mathrm{i}\boldsymbol{k}\cdot\boldsymbol{r}} \right) \tag{2.12}$$

where discrete normal modes were obtained by imposing Dirichlet boundary conditions at the borders of a box with volume L^3 [1]. The time dependence is absorbed in the coefficients $a_{\boldsymbol{k}\sigma}(t) = a_{\boldsymbol{k}\sigma}(0)\mathrm{e}^{\mathrm{i}\omega_k t}$ and the wave number is related to the frequency by $\omega_k = c\,|\boldsymbol{k}|$. In UV-VIS spectroscopy, the wavelength λ is often used instead of the wavenumber:

$$\hbar\omega_k = \frac{hc}{\lambda}. \tag{2.13}$$

The two polarization vectors, $\epsilon_{\boldsymbol{k}\sigma}$ ($\sigma = 1, 2$) and the wave vector $\boldsymbol{k}$ are mutually perpendicular. Obtaining similar expressions for the physical fields is straightforward in Fourier space as derivatives become algebraic expressions:

$$\boldsymbol{E}(\boldsymbol{r}, t) = \sum_{\boldsymbol{k},\sigma} \underbrace{-\mathrm{i}\omega_k A_0(k) \boldsymbol{\epsilon}_{\boldsymbol{k}\sigma}}_{\boldsymbol{E}_0(\boldsymbol{k}\sigma)} \left(a_{\boldsymbol{k}\sigma} \mathrm{e}^{\mathrm{i}\boldsymbol{k}\cdot\boldsymbol{r}} - a^*_{\boldsymbol{k}\sigma} \mathrm{e}^{-\mathrm{i}\boldsymbol{k}\cdot\boldsymbol{r}} \right) \tag{2.14}$$

$$\boldsymbol{B}(\boldsymbol{r}, t) = \sum_{\boldsymbol{k},\sigma} \underbrace{-\mathrm{i}A_0(k)\, \boldsymbol{k} \times \boldsymbol{\epsilon}_{\boldsymbol{k}\sigma}}_{\boldsymbol{B}_0(\boldsymbol{k}\sigma)} \left(a_{\boldsymbol{k}\sigma} \mathrm{e}^{\mathrm{i}\boldsymbol{k}\cdot\boldsymbol{r}} - a^*_{\boldsymbol{k}\sigma} \mathrm{e}^{-\mathrm{i}\boldsymbol{k}\cdot\boldsymbol{r}} \right) \tag{2.15}$$

[1] This discretization is the consequence of the boundary conditions. The found expression is a solution of Maxwell's equation and thus classical in nature.

The total energy which is present in the electromagnetic field, *i.e.* the classic Hamiltonian, can be obtained from the Fourier series:

$$H_{\text{rad}} = \frac{1}{2}\int_{L^3}\left(\epsilon_0 \boldsymbol{E}^2 + \frac{1}{\mu_0}\boldsymbol{B}^2\right)\mathrm{d}^3\boldsymbol{r} = \sum_{\boldsymbol{k}\sigma} A_0(k)^2 L^3 \epsilon_0 \omega_k^2 \left(a_{\boldsymbol{k}\sigma} a^*_{\boldsymbol{k}\sigma} + a^*_{\boldsymbol{k}\sigma} a_{\boldsymbol{k}\sigma}\right). \tag{2.16}$$

The theory can be canonically quantized according to the recipe of Dirac for many-body systems [28]. Field quantities become operators satisfying certain commutation relations[2]. For the normal modes of the Maxwell field, these are:

$$\left[a_{\boldsymbol{k}\sigma}, a^\dagger_{\boldsymbol{k}'\sigma'}\right] = \delta_{\boldsymbol{k}\boldsymbol{k}'}\delta_{\sigma\sigma'} \qquad [a_{\boldsymbol{k}\sigma}, a_{\boldsymbol{k}'\sigma'}] = \left[a^\dagger_{\boldsymbol{k}\sigma}, a^\dagger_{\boldsymbol{k}'\sigma'}\right] = 0. \tag{2.17}$$

Upon choosing $A_0(k) = \sqrt{\hbar/L^3\epsilon_0\omega_k}$, the quantum mechanical Hamiltonian becomes:

$$\mathcal{H}_{\text{rad}} = \sum_{\boldsymbol{k}\sigma} \hbar\omega_k \left(a^\dagger_{\boldsymbol{k}\sigma} a_{\boldsymbol{k}\sigma} + \frac{1}{2}\right). \tag{2.18}$$

The eigenstates of the radiation field are built from a (large) number of quanta of each mode, $|\ldots, n_{\boldsymbol{k}\sigma}, \ldots, n_{\boldsymbol{k}'\sigma'}\ldots\rangle$, corresponding with eigenenergy $\sum_{\boldsymbol{k}\sigma}\hbar\omega_k\,(n_{\boldsymbol{k}\sigma} + 1/2)$. The operators $a^\dagger_{\boldsymbol{k}\sigma}$ and $a_{\boldsymbol{k}\sigma}$ can be easily shown to raise or lower $n_{\boldsymbol{k}\sigma}$ by one unit, while the operator $n_{\boldsymbol{k}\sigma} = a^\dagger_{\boldsymbol{k}\sigma} a_{\boldsymbol{k}\sigma}$ simply counts the number of quanta with wavenumber $\boldsymbol{k}$ and polarization σ:

$$a_{\boldsymbol{k}\sigma}|\ldots, n_{\boldsymbol{k},\sigma}, \ldots, n_{\boldsymbol{k}',\sigma'}\ldots\rangle = \sqrt{n_{\boldsymbol{k}\sigma}}\,|\ldots, n_{\boldsymbol{k}\sigma} - 1, \ldots, n_{\boldsymbol{k}'\sigma'}\ldots\rangle \tag{2.19}$$

$$a^\dagger_{\boldsymbol{k}\sigma}|\ldots, n_{\boldsymbol{k}\sigma}, \ldots, n_{\boldsymbol{k}'\sigma'}\ldots\rangle = \sqrt{n_{\boldsymbol{k}\sigma} + 1}\,|\ldots, n_{\boldsymbol{k}\sigma} + 1, \ldots, n_{\boldsymbol{k}'\sigma'}\ldots\rangle \tag{2.20}$$

$$n_{\boldsymbol{k}\sigma}|\ldots, n_{\boldsymbol{k}\sigma}, \ldots, n_{\boldsymbol{k}'\sigma'}\ldots\rangle = n_{\boldsymbol{k}\sigma}|\ldots, n_{\boldsymbol{k}\sigma}, \ldots, n_{\boldsymbol{k}'\sigma'}\ldots\rangle \tag{2.21}$$

The quanta of the electromagnetic field are called photons. Their energy and wavelength are given by Eq. 2.13.

2.3 Light-matter interactions

2.3.1 Interaction Hamiltonian

In order to obtain a quantum mechanical Hamiltonian that describes the interaction between light and matter, one can use the same strategy as in §2.2.1 and start from the classical expression for the equations of motion, *i.e.* the Lorentz force, calculate the classical Hamiltonian and perform a canonical quantization. This procedure leads to the so-called minimal coupling substitution,

$$\frac{\partial}{\partial t} \to \frac{\partial}{\partial t} + \frac{\mathrm{i}e}{\hbar}\phi \qquad \nabla \to \nabla - \frac{\mathrm{i}e}{\hbar}\boldsymbol{A}, \tag{2.22}$$

[2] To keep the notation light and because the meaning can be derived from the context, no operator symbols, $\hat{}$, are used.

that has to be implemented in the Schrödinger equation. Interestingly, the same result can be obtained by demanding a *local* U(1) gauge symmetry for the wave function:

$$\Psi \rightarrow \mathrm{e}^{\frac{\mathrm{i}e}{\hbar}\chi}\Psi \tag{2.23}$$

with χ a function of space and time. The Schrödinger equation is only invariant for global U(1) transformations[3], corresponding with constant χ. The symmetry of the Schrödinger equation can be made local by introducing two auxiliary fields, ϕ and $\boldsymbol{A}$ that transform exactly like Eq. 2.10. From §2.2.1 we know that the equations of motion for these fields are the Maxwell equations. Demanding a local gauge symmetry is thus equivalent with introducing an interaction. This deep insight, which is not further explored, is often exploited to find theories for the interactions between elementary particles [29].

When the minimal coupling substitution is performed in the many-particle Hamiltonian, Eq. 2.1, one obtains for the total system, *i.e.* matter and radiation:

$$\mathcal{H} = \mathcal{H}_{\mathrm{mat}} + \mathcal{H}_{\mathrm{rad}} + \mathcal{H}_{\mathrm{int}} \tag{2.24}$$

where the first two terms are given by Eq. 2.1 and 2.18 and the additional term reads:

$$\mathcal{H}'_{\mathrm{int}} + \mathcal{H}''_{\mathrm{int}} = \sum_i \left(-\frac{q_i}{m_i}\boldsymbol{p}_i \cdot \boldsymbol{A} + \frac{q_i^2}{2m_i}\boldsymbol{A}^2 \right). \tag{2.25}$$

Herein, the summation is over all particles, *i.e.* both electrons and nuclei. A term proportional to $\boldsymbol{A}$ and a term proportional to $\boldsymbol{A}^2$ are found. It is instructive to insert the Fourier series Eq. 2.12 into the interaction Hamiltonian:

$$\mathcal{H}'_{\mathrm{int}} = \sum_i \sum_{\boldsymbol{k},\sigma} -\frac{q_i}{m_i}\sqrt{\frac{\hbar}{L^3\epsilon_0\omega_k}}\boldsymbol{p}_i \cdot \boldsymbol{\epsilon}_{\boldsymbol{k}\sigma}\left(a_{\boldsymbol{k}\sigma}\mathrm{e}^{\mathrm{i}\boldsymbol{k}\cdot\boldsymbol{r}} + a^\dagger_{\boldsymbol{k}\sigma}\mathrm{e}^{-\mathrm{i}\boldsymbol{k}\cdot\boldsymbol{r}} \right) \tag{2.26}$$

$$\begin{aligned}\mathcal{H}''_{\mathrm{int}} = \sum_i \sum_{\boldsymbol{k},\sigma} \sum_{\boldsymbol{k}',\sigma'} \frac{\hbar q_i^2}{L^3\epsilon_0\omega_k} \frac{\boldsymbol{\epsilon}_{\boldsymbol{k}\sigma}\cdot\boldsymbol{\epsilon}_{\boldsymbol{k}'\sigma'}}{\sqrt{\omega_k\omega_{k'}}} \Big(& a_{\boldsymbol{k}\sigma}a_{\boldsymbol{k}'\sigma'}\mathrm{e}^{\mathrm{i}(\boldsymbol{k}+\boldsymbol{k}')\cdot\boldsymbol{r}} \\ & + a_{\boldsymbol{k}\sigma}a^\dagger_{\boldsymbol{k}'\sigma'}\mathrm{e}^{\mathrm{i}(\boldsymbol{k}-\boldsymbol{k}')\cdot\boldsymbol{r}} + a^\dagger_{\boldsymbol{k}\sigma}a_{\boldsymbol{k}'\sigma'}\mathrm{e}^{\mathrm{i}(-\boldsymbol{k}+\boldsymbol{k}')\cdot\boldsymbol{r}} + a^\dagger_{\boldsymbol{k}\sigma}a^\dagger_{\boldsymbol{k}'\sigma'}\mathrm{e}^{-\mathrm{i}(\boldsymbol{k}+\boldsymbol{k}')\cdot\boldsymbol{r}} \Big)\end{aligned} \tag{2.27}$$

Hamiltonian $\mathcal{H}'_{\mathrm{int}}$ contains only one creation or annihilation operator in each term and will cause the absorption or emission of a single photon while $\mathcal{H}''_{\mathrm{int}}$ contains two such operators in each term and will therefore be responsible for two-photon processes. Thus far, the spins of the particles were neglected while these give rise to intrinsic magnetic moments[4], and therefore to an additional interaction with the magnetic field component of the radiation field according to $H = -\boldsymbol{m}_s \cdot \boldsymbol{B}$. In Fourier

[3] U(N) is the Lie group of all unitary $N \times N$ matrices, *i.e.* matrices U for which $U^\dagger U = UU^\dagger = I$ with I the unit matrix. For $N = 1$, this boils down to the complex numbers with modulus one. The connection between groups and symmetry transformations is briefly discussed in appendix A.

[4] Magnetic moments are related to spin through $\boldsymbol{m}_s = g\frac{q}{2m}\boldsymbol{s}$. The g-factor is a dimensionless quantity.

space, this Hamiltonian reads

$$\mathcal{H}'''_{\text{int}} = \sum_i \sum_{\boldsymbol{k},\sigma} -\frac{\mathrm{i} g_i q_i}{2m_i} \sqrt{\frac{\hbar}{L^3 \epsilon_0 \omega_k}} \boldsymbol{s}_i \cdot (\boldsymbol{k} \times \boldsymbol{\epsilon}_{\boldsymbol{k}\sigma}) \left(a_{\boldsymbol{k}\sigma} \mathrm{e}^{\mathrm{i}\boldsymbol{k}\cdot\boldsymbol{r}} - a^\dagger_{\boldsymbol{k}\sigma} \mathrm{e}^{-\mathrm{i}\boldsymbol{k}\cdot\boldsymbol{r}} \right) \tag{2.28}$$

and will, like $\mathcal{H}'_{\text{int}}$, give rise to single-photon processes. The complete Hamiltonian for the light-matter interaction is then given by:

$$\mathcal{H}_{\text{int}} = \mathcal{H}'_{\text{int}} + \mathcal{H}''_{\text{int}} + \mathcal{H}'''_{\text{int}} \tag{2.29}$$

The magnitude of $\mathcal{H}_{\text{int}}$ is much smaller than $\mathcal{H}_{\text{mat}}$ or $\mathcal{H}_{\text{rad}}$. Therefore, perturbation theory can be applied with the eigenstates $|\Psi\rangle \otimes |\ldots, n_{\boldsymbol{k},\sigma}, \ldots, n_{\boldsymbol{k}',\sigma'} \ldots\rangle$ of the non-interacting many-particle system $\mathcal{H}_{\text{mat}} + \mathcal{H}_{\text{rad}}$ as starting point.

2.3.2 Transition probabilities

In the following, the general expression for transition probability will be briefly elucidated and subsequently applied to electronic transitions associated with the emission or absorption of photons.

Fermi's golden rule

If the physical system finds itself at a given moment, $t = 0$, in a certain eigenstate of $\mathcal{H}_{\text{mat}} + \mathcal{H}_{\text{rad}}$, denoted by $|i\rangle = |n_0\rangle$[5], the time-dependent[6] perturbation $\mathcal{H}_{\text{int}}$ can effect an evolution as a function of time towards a different state $|f(t)\rangle$:

$$|f(t)\rangle = \sum_n c_n(t) \mathrm{e}^{-\frac{\mathrm{i}}{\hbar} E_{n_0} t} |n_0\rangle. \tag{2.30}$$

Herein, the time evolution of the unperturbed Hamiltonian is given by the time-dependent Schrödinger equation (the factor $\mathrm{e}^{-\frac{\mathrm{i}}{\hbar} E_{n_0} t}$), while $c_n(t)$ is purely due to the perturbation. The probability to find the physical system in state $|n\rangle$ after time t is then given by:

$$P_n(t) = |\langle n | f(t) \rangle|^2 = |c_n(t)|^2 . \tag{2.31}$$

An elegant way to obtain an expression for the coefficients is within the interaction picture[7] where the coefficients are given by matrix elements of the evolution operator, $c_n(t) = \langle n | \mathcal{U}(t) | n_0 \rangle$. From the time-dependent Schrödinger equation, a Dyson series can be found for the evolution operator[8]:

$$\mathcal{U}(t) = \sum_{m=0}^{\infty} \frac{1}{m!} \left(-\frac{\mathrm{i}}{\hbar} \right)^m \int_0^t \mathrm{d}t_1 \ldots \int_0^t \mathrm{d}t_m \, \mathcal{T} \left[\mathcal{H}_{\text{int}}(t_1) \ldots \mathcal{H}_{\text{int}}(t_m) \right]. \tag{2.32}$$

[5] The index n denotes the quantum and occupation numbers needed to specify the eigenstate.

[6] The time-dependence of $\mathcal{H}_{\text{int}}$ is concealed in the coefficients $a_{\boldsymbol{k}\sigma}(t) = a_{\boldsymbol{k}\sigma}(0) \mathrm{e}^{\mathrm{i}\omega_k t}$, see §2.2.1

[7] Up to now, all encountered quantum mechanics was within the Schrödinger picture where all time dependence is absorbed in the state vectors while the operators are time-independent. In the interaction picture, both operators and state vectors take a part of the time dependence, $|\psi(t)\rangle_I = \mathrm{e}^{\mathrm{i}/\hbar H t} |\psi(t)\rangle$ and $O_I(t) = \mathrm{e}^{\mathrm{i}/\hbar H t} O \mathrm{e}^{-\mathrm{i}/\hbar H t}$. The third possibility, where the full time dependence is absorbed in the operators is called the Heisenberg picture.

[8] The time-ordering operation, $\mathcal{T}$, is a shorthand notation to put the operators in the argument according to increasing time.

This equation can be drastically simplified in the case of harmonically oscillating perturbation[9], which happens to be the case for $\mathcal{H}_{\text{int}}$. One rather uses transition probability rates as $P_n(t) \propto t$ for $t \to +\infty$:

$$w_{i\to n} = \lim_{t\to+\infty} \frac{P_n(t)}{t} = \frac{2\pi}{\hbar} |\mathcal{M}_{ni}|^2 \, \delta(E_f - E_i), \tag{2.33}$$

with:

$$\mathcal{M}_{ni} = \langle n|\mathcal{H}_{\text{int}}|i\rangle + \sum_I \frac{\langle n|\mathcal{H}_{\text{int}}|I\rangle\langle I|\mathcal{H}_{\text{int}}|i\rangle}{E_i - E_I + \mathrm{i}\eta} + \ldots. \tag{2.34}$$

The complete set of intermediate states I are sometimes referred to as virtual states. Result Eq. 2.33 which forms the keystone of theoretical spectroscopy is known as Fermi's golden rule.

Photon emission

When a photon with wave vector $\boldsymbol{k}$ and polarization σ is emitted by a many-particle system, this will occur simultaneously with the decay of an excited state Ψ_2 to a lower energy state Ψ_1 while conserving the total energy. Often, the electronic eigenstates are degenerate, denoted by $i_1 = 1 \ldots \mathfrak{g}_1$ and $i_2 = 1 \ldots \mathfrak{g}_2$. The initial and final eigenstates of the light-matter system are:

$$|i\rangle = |\Psi_2\rangle|\ldots n_{\boldsymbol{k}\sigma}\ldots\rangle \qquad |f\rangle = |\Psi_1\rangle|\ldots n_{\boldsymbol{k}\sigma}+1\ldots\rangle. \tag{2.35}$$

The leading order contribution in Eq. 2.33 is due to $\mathcal{H}'_{\text{int}} + \mathcal{H}'''_{\text{int}}$ and can be separated into a radiation factor, which is calculable with Eq. 2.20, and a matter part, yielding:

$$w_{2\to1,\,\boldsymbol{k}\sigma} = \frac{2\pi}{\hbar}\frac{1}{\mathfrak{g}_2}\sum_{i_1 i_2}(n_{\mathrm{k}\sigma}+1)\left|\mathcal{M}^{(1)}_{21,\,\boldsymbol{k}\sigma}\right|^2 \delta(E_1 - E_2 + \hbar\omega_k). \tag{2.36}$$

where the first order transition moment was defined as:

$$\mathcal{M}^{(1)}_{21,\,\boldsymbol{k}\sigma} = \left\langle \Psi_1 \left| \sum_i \sqrt{\frac{\hbar}{L^3\epsilon_0\omega_k}} \frac{q_i}{m_i}\left(\boldsymbol{p}_i\cdot\boldsymbol{\epsilon}_{\boldsymbol{k}\sigma} - \frac{\mathrm{i}g_i}{2}\boldsymbol{s}_i\cdot(\boldsymbol{k}\times\boldsymbol{\epsilon}_{\boldsymbol{k}\sigma})\right)\mathrm{e}^{-\mathrm{i}\boldsymbol{k}\cdot\boldsymbol{r}} \right| \Psi_2 \right\rangle \tag{2.37}$$

and was summed over the final states and averaged over the initial states. The factor $n_{\mathrm{k}\sigma}+1$, which directly originates from Eq. 2.20 splits the transition rate in two terms, one proportional to the number of photons already present in the field with the same wavenumber and polarization as the emitted photon and one term independent of the radiation field. The former term is responsible for stimulated emission, a crucial phenomenon for laser operation, the latter term is responsible for spontaneous emission, the phenomenon of interest for this work.

The number of transitions per unit time is found by multiplying the transition probability rate by the number of available photon states,

$$\mathrm{d}D_\gamma = \left(\frac{L}{2\pi}\right)^3 \mathrm{d}^3\boldsymbol{k} = \left(\frac{L}{2\pi}\right)^3 k^2 \,\mathrm{d}\boldsymbol{k}\,\mathrm{d}^2\Omega_k = \left(\frac{L}{2\pi c}\right)^3 \omega_k^2\,\mathrm{d}\omega_k\,\mathrm{d}^2\Omega_k, \tag{2.38}$$

[9] Of the type $V(t) = V_0 e^{\mathrm{i}\omega t} + V_0^\dagger e^{-\mathrm{i}\omega t}$

to yield

$$\mathrm{d}w_{2\to1} = \frac{L^3}{4\pi^2\hbar c^3 \mathfrak{g}_2} \sum_{i_1 i_2} (n_{\mathrm{k}\sigma}+1) \left| \mathcal{M}^{(1)}_{21,\,\boldsymbol{k}\sigma} \right|^2 \delta(E_2 - E_1 - \hbar\omega_k)\omega_k^2 \,\mathrm{d}\omega_k \,\mathrm{d}^2\Omega_k. \tag{2.39}$$

Integration over the photon energy and wave vector yields:

$$w_{2\to1} = \frac{L^3}{4\pi^2\hbar^2 c^3 \mathfrak{g}_2} \sum_{\sigma=1,2} \omega_k^2 \int_{4\pi} \mathrm{d}^2\Omega_k (n_{\mathrm{k}\sigma}+1) \sum_{i_1 i_2} \left| \mathcal{M}^{(1)}_{21,\,\boldsymbol{k}\sigma} \right|^2, \tag{2.40}$$

with $\hbar\omega_k$ now fixed at the energy difference $E_2 - E_1$ due to the energy conserving delta function. The spectral energy density[10],

$$I(\omega_k) = \frac{\mathrm{d}\Phi}{\mathrm{d}\omega_k} \tag{2.41}$$

$$= \frac{1}{L^3} \sum_{\sigma=1,2} \int_{4\pi} \mathrm{d}^2\Omega_k \frac{\mathrm{d}D_\gamma}{\mathrm{d}\omega_k} n_{\boldsymbol{k}\sigma} \hbar\omega_k \tag{2.42}$$

$$\overset{\text{iso, unpol}}{=} \frac{\hbar\omega_k^3}{\pi^2 c^3} n(\omega_k), \tag{2.43}$$

can be identified in the stimulated emission term. If it is further assumed that the radiation field is isotropic and unpolarized, above expression can be written in terms of the famous Einstein's A and B coefficients:

$$w_{2\to1} = \underbrace{\frac{L^3\omega_k^2}{4\pi^2\hbar^2 c^3 \mathfrak{g}_2} \sum_{\sigma=1,2} \int_{4\pi} \mathrm{d}^2\Omega_k \sum_{i_1 i_2} \left| \mathcal{M}^{(1)}_{21,\,\boldsymbol{k}\sigma} \right|^2}_{A_{2\to1}}$$

$$+ I(\omega_k) \underbrace{\frac{L^3}{4\hbar^3\omega_k \mathfrak{g}_2} \sum_{\sigma=1,2} \int_{4\pi} \mathrm{d}^2\Omega_k \sum_{i_1 i_2} \left| \mathcal{M}^{(1)}_{21,\,\boldsymbol{k}\sigma} \right|^2}_{B_{2\to1}}, \tag{2.44}$$

The ratio of $\hbar\omega_k^3/\pi c^3$ between the coefficients was already derived by Einstein in 1905, based on the empirical assumption of Planck's black-body radiation law. Current derivation makes use of quantum electrodynamics, *i.e.* quantization of Maxwell's equations, and is much more powerful, but unknown to the young Einstein. Elaboration of the QED approach neatly produces Planck's law without further assumptions.

Photon absorption

Conversely to the emission process, photon absorption is now considered, exciting the many-particle system from state Ψ_1 to state Ψ_2 with higher energy. Here, the

[10] Here, the total energy density is given by $\Phi = \int I(\omega_k)\,\mathrm{d}\omega_k$.

initial and final states are:

$$|i\rangle = |\Psi_1\rangle|\dots n_{\boldsymbol{k}\sigma}\dots\rangle \qquad |f\rangle = |\Psi_2\rangle|\dots n_{\boldsymbol{k}\sigma}-1\dots\rangle. \tag{2.45}$$

and the annihilation operator Eq. 2.19 is now used to calculate the matrix element pertaining to the radiation, yielding for the transition probability rate:

$$w_{1\to 2,\,\boldsymbol{k}\sigma} = \frac{2\pi}{\hbar}\frac{1}{\mathfrak{g}_1}\sum_{i_1 i_2} n_{\boldsymbol{k}\sigma}\left|\mathcal{M}^{(1)*}_{21,\,\boldsymbol{k}\sigma}\right|^2 \delta(E_2 - E_1 - \hbar\omega_k), \tag{2.46}$$

and

$$w_{1\to 2} = \frac{L^3}{4\pi^2\hbar^2 c^3 \mathfrak{g}_1}\sum_{\sigma=1,2}\omega_k^2\int_{4\pi}\mathrm{d}^2\Omega_k n_{\mathrm{k}\sigma}\sum_{i_1 i_2}\left|\mathcal{M}^{(1)*}_{21,\,\boldsymbol{k}\sigma}\right|^2 \tag{2.47}$$

$$= I(\omega_k)\underbrace{\frac{L^3}{4\hbar^3\omega_k\mathfrak{g}_1}\sum_{\sigma=1,2}\int_{4\pi}\mathrm{d}^2\Omega_k\sum_{i_1 i_2}\left|\mathcal{M}^{(1)*}_{21,\,\boldsymbol{k}\sigma}\right|^2}_{B_{1\to 2}=\frac{\mathfrak{g}_1}{\mathfrak{g}_2}B_{2\to 1}}, \tag{2.48}$$

for the transition rate.

2.3.3 Transition moments

Before the evaluation of $\mathcal{M}^{(1)}_{21}$, one should realize that the goal is to study systems with typical dimensions of the size of one up to a few atoms, *i.e.* in the range of 0.1-10 nm while the part of the electromagnetic spectrum we are bothered with ranges from the near UV to the near IR, corresponding roughly with wavelengths in the range of 100-1000 nm. The different orders of magnitude for the spatial extension of the matter system and the wavelength of the light allows us to locally approximate the electromagnetic wave according to $\mathrm{e}^{\mathrm{i}\boldsymbol{k}\cdot\boldsymbol{r}} \approx 1 + \mathrm{i}\boldsymbol{k}\cdot\boldsymbol{r}$ as the product $kr \propto r/\lambda$ is a small parameter.

The above approximation allows to rewrite the operator in Eq. 2.37 in such a way that different terms obtain a meaning which is reminiscent of concepts of classical electrodynamics. For this, a few vector identities are applied, together with Heisenberg's equation[11] which relates the linear momentum operator to the position vector. The result reads:

$$\mathcal{M}^{(1)}_{21,\,i} = \left\langle\Psi_1\left|\boldsymbol{D}_i\cdot\boldsymbol{E}_0(\boldsymbol{k}\sigma) + \boldsymbol{m}_i\cdot\boldsymbol{B}_0(\boldsymbol{k}\sigma) + \frac{1}{3}\mathbf{Q}:\nabla\boldsymbol{E}_0(\boldsymbol{k}\sigma)\right|\Psi_2\right\rangle \tag{2.49}$$

where the amplitudes for the electric and magnetic fields, Eq. 2.14 and 2.15, were reintroduced. One clearly recognizes the classical interaction energies of an electric

[11] This equation describes the time evolution of operators in the Heisenberg picture: $\frac{\mathrm{d}O_H}{\mathrm{d}t} = -\frac{\mathrm{i}}{\hbar}[O_H, \mathcal{H}]$.

dipole (E1), magnetic dipole (M1) and electric quadrupole term (E2) in electric and magnetic fields, with the respective multipole moments as the operators [24]:

$$\boldsymbol{D} = \sum_i \boldsymbol{D}_i = \sum_i q_i \boldsymbol{r}_i \tag{2.50}$$

$$\boldsymbol{m} = \sum_i \boldsymbol{m}_i = \sum_i \frac{q_i}{2m_i}(\boldsymbol{\ell}_i + g_i \boldsymbol{s}_i) \tag{2.51}$$

$$\mathsf{Q} = \sum_i \mathsf{Q}_i = \sum_i \frac{3}{2} q_i \left(\boldsymbol{r}_i \boldsymbol{r}_i - r_i^2 \mathbb{1}\right) \tag{2.52}$$

Depending on which transition moment in Eq. 2.37 is dominant for a particular case, one speaks of electric dipole, magnetic dipole or electric quadrupole transitions. The relative transition strengths of the three contributions can be estimated from above expressions, yielding $1{:}10^{-5}{:}10^{-6}$ for E1:M1:E2 [30]. The electric dipole term is dominant upon first sight, however the details of the matter wave functions Ψ are important as specific symmetries can cause matrix elements, such as the E1 matrix element, to vanish and therefore induce changes in the relative importance of the various contributions. Which transitions are dominant in which cases is dictated by the so-called selection rules. These will be discussed in §4.3 after the symmetries of the matter wave functions are discussed.

Electric dipole transitions

The simple expression for the electric dipole moment allows to obtain a simple expression for the transition (probability) rates as well. The transition moment, Eq. 2.37 for E1 transitions is:

$$\mathcal{M}^{\mathrm{E1}}_{21,\boldsymbol{k}\sigma} = -\mathrm{i}\omega_k \sqrt{\frac{\hbar}{L^3 \epsilon_0 \omega_k}} \langle \Psi_1 | \epsilon_{\boldsymbol{k}\sigma} \cdot \boldsymbol{D} | \Psi_2 \rangle. \tag{2.53}$$

The transition rate for emission, Eq. 2.44 is then:

$$w^{\mathrm{E1}}_{2\to 1} = \frac{1}{4\pi^2 c^3 \epsilon \hbar} \frac{1}{\mathfrak{g}_1} \sum_{i_1 i_2} \sum_{\sigma=1,2} \int \mathrm{d}\Omega_k (n_{\boldsymbol{k}\sigma} + 1) |\epsilon_{\boldsymbol{k}\sigma} \cdot \langle \Psi_1 | \boldsymbol{D} | \Psi_2 \rangle|^2. \tag{2.54}$$

When the radiation is emitted uniformly and unpolarized, this becomes:

$$w^{\mathrm{E1}}_{2\to 1} = \frac{[n(\omega_k) + 1]\,\omega_k^3}{3\pi c^3 \epsilon_0 \hbar} \frac{1}{\mathfrak{g}_1} \sum_{i_1 i_2} |\langle \Psi_1 | \boldsymbol{D} | \Psi_2 \rangle|^2, \tag{2.55}$$

or:

$$A^{\mathrm{E1}}_{2\to 1} = \frac{\omega_k^3}{3\pi^3 \epsilon_0 \hbar} \frac{1}{\mathfrak{g}_1} \sum_{i_1 i_2} |\langle \Psi_1 | \boldsymbol{D} | \Psi_2 \rangle|^2 \tag{2.56}$$

$$B^{\mathrm{E1}}_{2\to 1} = \frac{1}{3\epsilon_0 \hbar^2} \frac{1}{\mathfrak{g}_1} \sum_{i_1 i_2} |\langle \Psi_1 | \boldsymbol{D} | \Psi_2 \rangle|^2. \tag{2.57}$$

A similar formula can be found for absorption.

Local field effect

From the above expression for the transition probability in terms of electric or magnetic multipole moments, a factor scaling with the electric or magnetic field strength arises. As the optical transitions that are of our interest do not take place in vacuum, but rather in a dielectric host compound, polarization and possibly magnetization effects should be taken into account, which can change the value of the local fields. For this reason, following correction factors need to be multiplied to the transition probabilities:

$$\left(\frac{E_{\mathrm{loc}}}{E_0}\right)^2 \quad \text{and} \quad \left(\frac{B_{\mathrm{loc}}}{B_0}\right)^2, \tag{2.58}$$

for E1, E2 and M1 transitions respectively. As most host compounds show no strong magnetization ($\mu_r = 1$), no correction is expected for M1 transitions.

Different analytic expressions are available for E_{loc}, but none is exact. The most popular expression is the so-called Lorentz local field which is calculated in classic electrostatic theory by assuming a nearby cubical coordination of electric dipoles and a polarizable continuum further away. The contribution of the former can be shown to vanish while the latter contributes $1/3(\epsilon_r - 1)\boldsymbol{E}_0$ to the local field [24]. Together with the external field, the final expression becomes:

$$\left(\frac{E_{\mathrm{loc}}}{E_0}\right)^2 = \left(\frac{n^2+2}{3}\right)^2, \tag{2.59}$$

with $n = \sqrt{\epsilon_r \mu_r}$ the refractive index of the host compound.

3 VIBRONIC INTERACTIONS

In the previous chapter, a superficial look was cast upon the Schrödinger equation which was symbolically solved in terms of the Born-Oppenheimer approximation. The solutions are energy levels which are tagged by two types of labels, *i.e.* labels associated with the motion of the electrons in the system and labels associated with the motion of the nuclei in the system. The eigenstates factorize in a nuclear and an electronic wave function. In this chapter, the meaning of the nuclear labels is explained by finding approximate solutions of the nuclear eigenvalue equation. Nuclear motion inside a material is nothing more than vibration of the nuclei around their equilibrium position. The quantum mechanical unit for the lattice vibration, *i.e.* the phonon, is introduced. The electron-vibrational (or vibronic) nature of the energy levels has important consequences on the physics of spectroscopy experiments because transitions are not purely electronic, but vibronic in nature, *i.e.* the creation or annihilation of phonons is associated with the emission or absorption of a photon. Broad spectral bands are found instead of sharp lines and the energy of absorbed and emitted photons is different, yielding the desired color conversion for many applications. These effects alter the Einstein theory for transition rates. Furthermore, the interaction between the electronic and nuclear subsystems opens the path for a full non-radiative relaxation which is unwanted in optical materials. The intuitive and often applied configurational coordinate model is derived as a simplification of the more general theory of electron-vibrational interactions, yielding simple expressions for the Stokes shift, band shape and non-radiative decay rate in terms of a single phonon frequency and the Huang-Rhys coupling strength. In this chapter, the electronic eigenstates are treated symbolically. The details of these are discussed in subsequent chapters.

3.1 The harmonic approximation

First, a closer look will be cast on the solutions of the nuclear eigenvalue equation, Eq. 2.5. Consider an electronic eigenstate, m, for which the potential energy surface (PES) is explored:

$$\left(\sum_{\alpha=1}^{M} -\frac{\hbar^2}{2M_\alpha}\nabla_\alpha^2 + E_m(\boldsymbol{R})\right)\chi_{m\boldsymbol{\mu}}(\boldsymbol{R}) = \epsilon_{m\boldsymbol{\mu}}\chi_{m\boldsymbol{\mu}}(\boldsymbol{R}). \tag{3.1}$$

For small deviations from a reference configuration, $\boldsymbol{R}_0$, the PES can be approximated by a Taylor expansion:

$$E_m(\boldsymbol{q}) = E_m(\boldsymbol{q}_0) + \sum_{\alpha=1}^{3M} A_{m,\alpha}\,(q_\alpha - q_{0\alpha}) + \frac{1}{2}\sum_{\alpha=1}^{3M}\sum_{\beta=1}^{3M} \mathcal{K}_{m,\alpha\beta}\,(q_\alpha - q_{0\alpha})(q_\beta - q_{0\beta}) + \mathcal{O}\left(q^3\right) \quad (3.2)$$

where the mass-weighted Cartesian coordinates were introduced[1]: $\boldsymbol{q}_{\alpha'} = \sqrt{M_\alpha}\boldsymbol{R}_{\alpha,i}$ and the expansion coefficients,

$$A_{m,\alpha} = \left(\frac{\partial E_m(\boldsymbol{q})}{\partial q_\alpha}\right)_{\boldsymbol{q}_0} \quad \text{and} \quad \mathcal{K}_{m,\alpha\beta} = \left(\frac{\partial^2 E_m(\boldsymbol{q})}{\partial q_\alpha \partial q_\beta}\right)_{\boldsymbol{q}_0} \quad (3.3)$$

were introduced. $\mathcal{K}_{m,\alpha\beta}$ is a positive definite, symmetric matrix and is called the Hessian matrix or force matrix. For sufficiently small deviations from the reference geometry, the expansion 3.2 can be terminated at second order according to the harmonic approximation. The potential energy surfaces then correspond with multidimensional paraboloids. The second order term corresponds to the force constants of a system of independent oscillators, while the linear term corresponds to the coupling between the luminescent center and the host crystal.

Subsequently, another basis transformation is performed,

$$\boldsymbol{Q}_m = \mathsf{T}_m(\boldsymbol{q} - \boldsymbol{q}_{m,0}), \quad (3.4)$$

which is composed of a translation $\boldsymbol{q}_{m,0}$ and a rotation T_m. The rotation has the goal to diagonalize the Hessian, $\mathcal{K}_m$. The matrix T_m is hence straightforwardly obtained from the eigenvectors of $\mathcal{K}_m$, the eigenvalues are denoted as $K_{m\alpha}$. The translation is such that $Q_{m\alpha} = 0$ for the equilibrium geometry for the eigenstate m, *i.e.* corresponding to the minimum of the paraboloid:

$$q_{m\alpha,0} = -\frac{K_{m\alpha}}{A_{m\alpha}}. \quad (3.5)$$

The new coordinates, $Q_{m\alpha}$ are called the normal coordinates. If these coordinate transformations are filled out in the harmonic approximation for the PES, Eq. 3.2, one obtains:

$$E_m(\boldsymbol{Q}_m) = E_m(\boldsymbol{0}) + \sum_\alpha \frac{1}{2} K_{m\alpha} Q_{m\alpha}^2 - \frac{1}{2}\sum_\alpha \frac{A_{m\alpha}^2}{K_{m\alpha}}. \quad (3.6)$$

A system of independent oscillators is indeed found. The third term, which is a constant term, is usually included in the electronic energy of the state m, along with the first term [31].

[1] In this new notation, the indices $\alpha, \beta, \ldots$ enumerate the complete 3M dimensional space of all nuclear coordinates while $\alpha, \beta, \ldots$ are used to count the M nuclei up to now, which all have three ($i = 1, 2, 3$) degrees of freedom.

The nuclear eigenvalue equation is then obtained from the contributions from the lattice vibrational energy,

$$\sum_{\alpha=1}^{3M}\left(-\frac{\hbar^2}{2}\frac{\partial^2}{\partial Q_{m\alpha}}+\frac{1}{2}K_{m\alpha}Q_{m\alpha}^2\right)\chi_{m\boldsymbol{\mu}}(\boldsymbol{Q}_m)=\epsilon_{m\boldsymbol{\mu}}\chi_{m\boldsymbol{\mu}}(\boldsymbol{Q}_m), \tag{3.7}$$

showing explicitly the decoupling of the solution in $3M$ independent oscillators, the so-called normal modes of the defect cluster in electronic state m. The solution of one quantum harmonic oscillator is given by [2]:

$$\epsilon_{m\alpha\mu_{m\alpha}} = \left(\mu_{m\alpha}+\frac{1}{2}\right)\hbar\omega_{m\alpha} \tag{3.8}$$

$$\chi_{m\alpha\mu_{m\alpha}}(Q_{m\alpha}) = \sqrt{\frac{1}{\mu_{m\alpha}!2^{\mu_{m\alpha}}}\sqrt{\frac{\omega_{m\alpha}}{\pi\hbar}}}\,e^{-\xi_{m\alpha}^2/2}H_{\mu_{m\alpha}}(\xi_{m\alpha}) \tag{3.9}$$

$$\text{with}\qquad \omega_{m\alpha}^2=K_{m\alpha}\quad\text{and}\quad \xi_{m\alpha}(Q_{m\alpha})=\sqrt{\frac{\omega_{m\alpha}}{\hbar}}Q_{m\alpha} \tag{3.10}$$

where $\mu_{m\alpha}=0,\,1,\,2,\,...$ denotes the number of phonons, *i.e.* quanta of vibration, for the mode $\omega_{m\alpha}$. $H_{\mu_{m\alpha}}(\xi)$ are Hermite polynomials [32]. As $H_0(\xi)=1$, the eigenstate corresponding to the zero-point oscillation[2] is a Gaussian function of $Q_{m\alpha}$. The $3M$ normal modes do not all correspond to vibrations of the defect cluster. Explicit calculation of the $Q_{m\alpha}$ as a function of R_α shows that three normal modes correspond to mutually perpendicular translations and another three with independent rotations. In both cases, the shape of the defect cluster does not change. Furthermore, the cluster is embedded in a crystal, prohibiting these movements to occur. In the end, one remains with $3M-6$ independent vibrational modes[3]. The vibrational modes can be labeled by the irreducible representations (IR) of the point group of the defect cluster, $\alpha=a\Gamma\gamma$, with a the branching multiplicity label and γ the partner of the IR Γ (see appendix A). The total nuclear wave function and energy corresponding to electronic state m, solution of Eq. 3.1, is given by:

$$\epsilon_{m\boldsymbol{\mu}_m} = E_m(\boldsymbol{q}_{m,0})-\frac{1}{2}\sum_\alpha\frac{A_{m\alpha}^2}{\omega_{m\alpha}^2}+\sum_\alpha\epsilon_{m\alpha\mu_\alpha} \tag{3.11}$$

$$\chi_{m\boldsymbol{\mu}_m}(\boldsymbol{R}) = \prod_\alpha\chi_{m\alpha\mu_\alpha}(Q_{m\alpha}) \tag{3.12}$$

with occupation numbers $\boldsymbol{\mu}_m=(\mu_{m\alpha}),\ \alpha=1...3M-6$.

[2]The lowest vibrational eigenvalue is not zero, but $\epsilon_{m\alpha0}=1/2\hbar\omega_{m\alpha}$. This is referred to as the zero-point oscillation.

[3]In the case of linear defect clusters, the axial rotation is not prohibited and $3M-5$ modes remain. Examples of linear defects are dichalcogenide ions such as O_2^- and S_2^- and actinyl ions such as UO_2^{2+} and NpO_2^{2+}. Even in these cases, the axial symmetry is broken by the surrounding crystal. Irrespective of their interesting luminescent and structural properties, these ions are not encountered in this work.

To summarize, for every PES, corresponding to an electronic energy level m, multiple vibrational energy levels $\boldsymbol{\mu}_m$ are associated. The normal coordinates and frequencies are in general different for every electronic eigenstate. Duschinsky proposed a linear relationship to relate the normal coordinates of two different electronic eigenstates, $m = 1$ and $m = 2$ [33]:

$$\boldsymbol{Q}_1 = \mathsf{J}\boldsymbol{Q}_2 + \boldsymbol{K}, \tag{3.13}$$

with J the Duschinsky matrix and $\boldsymbol{K}$ the shift vector. These can be simply calculated from the transformation, Eq. 3.4,

$$\mathsf{J} = \mathsf{T}_1\mathsf{T}_2^{-1} \quad \text{and} \quad \boldsymbol{K} = \mathsf{T}_1(\boldsymbol{q}_{2,0} - \boldsymbol{q}_{1,0}). \tag{3.14}$$

This is a good approximation if the geometrical differences between both electronic states are limited [34].

3.2 Vibronic transitions

Now that we have expressions at our disposal for both the electronic and nuclear wave functions, as well as for the electromagnetic transition rates, we can finally put the pieces of the puzzle together and obtain the spectrum of our phosphor, *i.e.* calculate the line shape of the transitions involving the metal ion which is incorporated in a vibrating host crystal.

3.2.1 Franck-Condon approximation

According to Fermi's golden rule, the rate of an absorption or spontaneous emission transition is determined by the evaluation of matrix elements of a certain transition moment (Eq. 2.36, 2.46), which is denoted as $\boldsymbol{\mu}$ in general. These transition moments are calculated by simply summing the contributions of all particles. At the atomic level only two types of particles are found, *i.e.* nuclei and electrons, which are treated on a completely different footing in the adiabatic approximation. For this reason, the transition moment is decomposed in an electronic and a nuclear part:

$$\boldsymbol{\mu} = \underbrace{\sum_{i=1}^{N} \boldsymbol{\mu}_{\mathrm{e},i}}_{\boldsymbol{\mu}_\mathrm{e}} + \underbrace{\sum_{\alpha=1}^{M} \boldsymbol{\mu}_{\mathrm{n},\alpha}}_{\boldsymbol{\mu}_\mathrm{n}}. \tag{3.15}$$

In the Born-Oppenheimer approximation, the total wave function was factorized in an electronic and nuclear part, Eq. 2.2. Filling out this ansatz for a transition from state "1" to state "2" yields:

$$\langle \Psi_2 | \boldsymbol{\mu} | \Psi_1 \rangle = \underbrace{\langle \chi_{2\mu_2} | \langle \psi_2 | \boldsymbol{\mu}_\mathrm{e} | \psi_1 \rangle | \chi_{1\mu_1} \rangle}_{\langle \chi_{2\mu_2} | \boldsymbol{\mu}_{21} | \chi_{1\mu_1} \rangle} + \underbrace{\langle \psi_2 | \psi_1 \rangle}_{0} \langle \chi_{2\mu_2} | \boldsymbol{\mu}_\mathrm{n} | \chi_{1\mu_1} \rangle. \tag{3.16}$$

The second term of the right hand side vanishes because of the orthogonality of the electronic eigenstates. For this reason, only the electronic part of the transition moment is needed for the evaluation of transition rates.

The electronic transition moment depends, analogously to the PES, on the nuclear positions. For this reason, $\boldsymbol{\mu}_{12}$ will in general not be constant during an electronic transition. Still, in the same philosophy as the adiabatic approximation, it can be assumed that the electronic transition occurs much faster than the induced nuclear reorganization. Then, $\boldsymbol{\mu}_{12}$ can be Taylor expanded around the initial state's equilibrium geometry:

$$\boldsymbol{\mu}_{21}(\boldsymbol{Q}_1) = \boldsymbol{\mu}_{21}(\mathbf{0}) + \sum_{\alpha} \left(\frac{\partial \boldsymbol{\mu}_{21}}{\partial Q_{1\alpha}} \right)_{\mathbf{0}} Q_{1\alpha} + \frac{1}{2} \sum_{\alpha} \sum_{\beta} \left(\frac{\partial^2 \boldsymbol{\mu}_{21}}{\partial Q_{1\alpha} \partial Q_{1\beta}} \right)_{\mathbf{0}} Q_{1\alpha} Q_{1\beta} + \mathcal{O}(\boldsymbol{Q}_1^3), \quad (3.17)$$

where the normal coordinates of the initial electronic state, $\boldsymbol{Q}_1$, were used instead of the Cartesian coordinates $\boldsymbol{R}$. The lowest order approximation corresponds to a static electronic transition moment and is widely known as the Franck-Condon (FC) approximation, named after James Franck and Edward Condon, the two pioneers who first formulated this principle [35, 36]. Higher order terms in above series expansion can be safely neglected for fully allowed transitions (see chapter 4), while the linear term can have important contributions in the case of weakly allowed or electric dipole-forbidden transitions, *i.e.* when the FC term is small or vanishes. Herzberg and Teller were the first to apply this, giving their name to this next level of approximation.

3.2.2 Band shapes

In this paragraph, the shape of a spectral band, corresponding to a single electronic transition, will be derived. It is solely determined by the nuclear motion according to the FC principle.

Only one electronic transition is considered and no information is required for the electronic eigenstates as the electronic transition moment is after all merely a proportionality constant, *i.e.* $\boldsymbol{\mu}_{21}(\mathbf{0})$. This constant is added to the other factors that occur in the formula for the relevant transition probability (see §2.3.2), denoted as F_0[4]. It is then clear that the shape of the spectrum is determined by the square of the Frank-Condon integrals $\langle \chi_{2\boldsymbol{\mu}_2} | \chi_{1\boldsymbol{\mu}_1} \rangle$. One has to sum over all possible final and initial states, while the initial states are weighted by their temperature-dependent occupation number. As vibrational quanta are bosons, the Bose-Einstein distribution is used for this. When this is all considered, the shape function for the transition

[4] These additional factors can have a frequency dependence. See *e.g.* the Einstein A coefficient for E1 transitions, which has a factor ω_k^3 in front (Eq. 2.56).

$\Psi_1 \to \Psi_2$ becomes:

$$F(\omega_0-\omega) = F_0(\omega_0-\omega)\times \sum_{\mu'_1=-\infty}^{\infty}\cdots\sum_{\mu'_{3M-6}=-\infty}^{\infty}\sum_{\mu_1=-\infty}^{\infty}\cdots\sum_{\mu_{3M-6}=-\infty}^{\infty}\prod_{\alpha'=0}^{3M-6}\prod_{\alpha=0}^{3M-6} \left|\left\langle \chi_{2\alpha'\mu'_{\alpha'}}(Q_{2\alpha'})|\chi_{1\alpha\mu_\alpha}(Q_{1\alpha})\right\rangle\right|^2 \frac{\delta[\epsilon_{2\alpha'\mu'_{\alpha'}}-\epsilon_{1\alpha\mu_\alpha}-\hbar(\omega_0-\omega)]}{\mathrm{e}^{\epsilon_{1\alpha\mu_\alpha}/k_BT}-1}, \quad (3.18)$$

where $\hbar\omega_0$ is the energy of the zero-phonon line (ZPL), *i.e.* the purely electronic transition where no vibrational quanta are created or annihilated. The vibrational modes and quantum numbers that correspond to the final state, '2' were denoted with a prime. At finite temperature, phonons can also be annihilated in the transition which is then referred to as an anti-Stokes line. Evaluation of the Frank-Condon integrals additionally requires the Duschinsky transformation, Eq. 3.13 to be performed. Calculating $F(\omega_0-\omega)$ is clearly not a trivial problem, therefore many limiting cases that reduce the complexity of Eq. 3.18 are available. The most popular simplification is the configurational coordinate model which is elaborated in §3.4.

3.3 Non-radiative transitions

The coupling between electronic and vibrational states can give rise to non-radiative transitions. The interaction Hamiltonian which is then used in Fermi's golden rule, Eq. 2.33, is not the electron-light interaction but the electron-vibration interaction. The non-adiabatic terms that were neglected in the Born-Oppenheimer approximation can be held responsible:

$$\mathcal{H}_{\mathrm{n-ad}}\psi_m\chi_{m\boldsymbol{\mu}} = -\sum_{\alpha=1}^{3M}\left(\hbar^2\frac{\partial\psi_m}{\partial Q_\alpha}\frac{\partial\chi_{m\boldsymbol{\mu}}}{\partial Q_\alpha}+\frac{1}{2}\chi_{m\boldsymbol{\mu}}\frac{\partial^2\psi_m}{\partial Q_\alpha^2}\right), \quad (3.19)$$

giving rise to a transition probability, similar to Eq. 3.18:

$$w_{2\to1}^{\mathrm{n-rad}} = \frac{2\pi}{\hbar}\sum_{\mu'_1=-\infty}^{\infty}\cdots\sum_{\mu'_{3M-6}=-\infty}^{\infty}\sum_{\mu_1=-\infty}^{\infty}\cdots\sum_{\mu_{3M-6}=-\infty}^{\infty}\prod_{\alpha'=0}^{3M-6}\prod_{\alpha=0}^{3M-6} \left|\left\langle\psi_1\chi_{1\alpha\mu_\alpha}|\mathcal{H}_{\mathrm{n-ad}}|\psi_2\chi_{2\alpha\mu_\alpha}\right\rangle\right|^2 \frac{\delta(\epsilon_{2\alpha'\mu'_{\alpha'}}-\epsilon_{1\alpha\mu_\alpha})}{\mathrm{e}^{\epsilon_{2\alpha\mu_\alpha}/k_BT}-1}. \quad (3.20)$$

Again a bulky formula which will be simplified for the comprehensive configurational coordinate model.

Non-radiative decay of excited activators is typically an unwanted phenomenon. For applications, the energy that was used to excite the phosphor should obviously be utilized to create light in an as efficient as possible way. Nonetheless, the above formula demonstrates that non-radiative processes always compete with the radiative decay. The quantum efficiency is a parameter which is used to indicate to which

extent non-radiative pathways dominate the decay of the luminescence activator. If N_{inc} is the number of photons that is incident on the luminescent material, one has:

$$N_{\text{inc}} = N_{\text{refl}} + N_{\text{abs}} \tag{3.21}$$
$$= N_{\text{refl}} + N_{\text{rad}} + N_{\text{n-rad}}, \tag{3.22}$$

where N_{refl} and N_{abs} are respectively the number of reflected and absorbed photons while N_{rad} and $N_{\text{n-rad}}$ are the number of absorbed photons that give rise to respectively a radiative and a non-radiative decay. The internal quantum efficiency is defined as [13]:

$$\text{QE}_{\text{i}} = \frac{N_{\text{rad}}}{N_{\text{abs}}} = \frac{N_{\text{rad}}}{N_{\text{inc}} - N_{\text{refl}}}. \tag{3.23}$$

Additionally, one has the external quantum efficiency,

$$\text{QE}_{\text{e}} = \frac{N_{\text{rad}}}{N_{\text{inc}}}, \tag{3.24}$$

which is a useful parameter in the light of applications (see chapter 7). The decay dynamics of the considered excited state is described by:

$$\left(\frac{\mathrm{d}N^*(t)}{\mathrm{d}t}\right)_{\text{r + n-r}} = -\left(\frac{1}{\tau_{\text{rad}}} + \frac{1}{\tau_{\text{n-rad}}}\right)N^*(t) \tag{3.25}$$

with $\tau_{\text{rad}}^{-1} = \sum w_{2\to1}$, and $\tau_{\text{n-rad}}^{-1} = \sum w_{2\to1}^{\text{n-rad}}$ summed over all possible radiative and non-radiative decay channels. The quantum efficiency can hence be obtained indirectly when the decay rates are known:

$$\text{QE}_{\text{i}} = \frac{\tau_{\text{rad}}}{\tau_{\text{rad}} + \tau_{\text{n-rad}}} = \frac{1}{1 + \frac{\tau_{\text{n-rad}}}{\tau_{\text{rad}}}} \tag{3.26}$$

Even when a material has a high quantum - or conversion - efficiency, the energy efficiency is limited by the Stokes shift (see chapter 7).

Upon increasing temperature, non-radiative decay channels can become more important, driven by the population of higher-lying vibrational levels according to the Bose-Einstein distribution in Eq. 3.20. This phenomenon is referred to as thermal quenching (TQ) and offers an experimental tool to obtain information on the electronic structure of the luminescent defect cluster (see §3.4.4, 6.2.7). Regarding applications of luminescent materials, TQ should be avoided as a high conversion efficiency is required irrespective of the working temperature (see §1.4).

3.4 Configurational coordinate model

The first occurrence of a configurational coordinate diagram dates from the 1930's and is due to the physicist Arthur von Hippel who worked under the supervision of James Franck and Robert Pohl in Göttingen. He applied the model to the study of

electric conduction in insulators [37, 38]. Frederick Seitz was the first to use a similar intuitive argument to explain some features in the luminescence spectra of thallium activated salts [39]. As Sir Nevill Francis Mott used this model to explain the temperature-dependent behavior of the luminescence of point defects, the configurational coordinate model is also referred to as the Mott-Seitz model [40]. Strangely enough, it lasted until 1950 before the model was quantitatively elaborated in order to get analytical expressions describing spectral band shapes or the temperature dependence of luminescence efficiency. This thorough theoretical treatment was done by Kun Huang and Avril Rhys who gave name to the most important parameter of this model, S. [31]. Rather surprisingly, the Mott-Seitz model succeeds to give a qualitative, and sometimes even quantitative understanding of different phenomena associated with the luminescence of isolated defects.

3.4.1 Energy levels

In the configurational coordinate model, only one vibrational mode is considered. In most textbooks the totally symmetric or *breathing* mode is chosen. For allowed electronic transitions one can always be sure that the creation of totally symmetric phonons is allowed (see §3.2). This simplification has another important advantage, next to the simplification of Eq. 3.18 as it allows to depict the PES in a simple two-dimensional sketch as the electronic energies E_m are only function of one normal coordinate, Q, referred to as *the* configurational coordinate in this model (see Fig. 3.1).

The two electronic energy levels that are depicted in Fig. 3.1 can be described in the harmonic approximation for the configurational coordinate as:

$$E_1(Q) = E_1(0) + A_1 Q + \frac{1}{2} K_1 Q^2 \tag{3.27}$$

for the ground state "1" and

$$E_2(Q) = E_2(0) + A_2 Q + \frac{1}{2} K_2 Q^2 \tag{3.28}$$

for the excited state "2". The minimum of the ground state parabola is typically chosen as the energy reference:

$$Q_1 = -\frac{A_1}{K_1} \qquad Q_2 = -\frac{A_2}{K_2} \tag{3.29}$$

$$E_1(0) = \frac{A_1^2}{2K_1} \qquad E_2(0) = \Delta E + \frac{A_2^2}{2K_2}. \tag{3.30}$$

The numbers $\Delta Q = Q_2 - Q_1$ and ΔE give the offset of the excited state level with respect to the ground state and are obtained by solving the electronic eigenvalue equation, Eq. 2.4. The equidistant eigenvalues of the nuclear eigenvalue equation are displayed for both electronic states (see Eqs. 3.7-3.8).

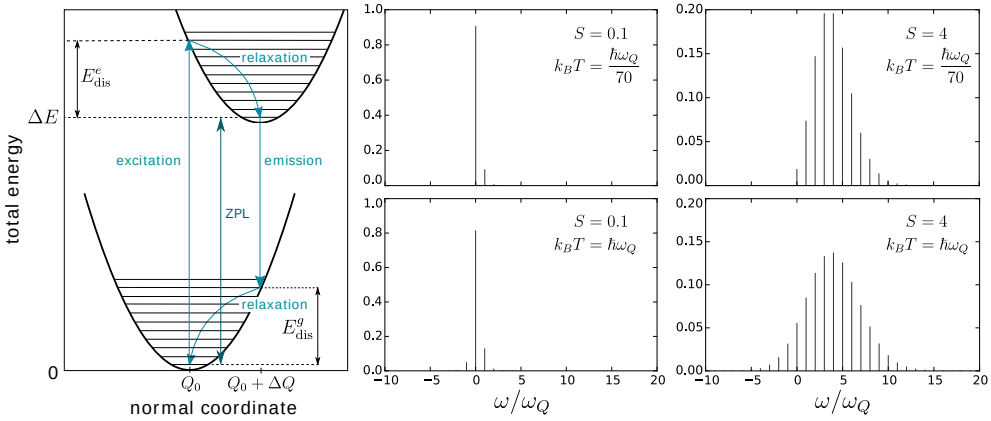

Figure 3.1 – Two-energy-level system as a function of the single configurational coordinate. Band shapes for different electron-phonon coupling S and temperature T.

3.4.2 Stokes shift

According to the FC approximation, electronic transitions occur *vertically*, leaving the nuclear coordinates unchanged. For the excitation from the electronic ground state to the excited state, this is shown by arrow (1) in Fig. 3.1. It is assumed that temperature is sufficiently low such that the starting point is the lowest vibrational level. Due to the nonzero ΔQ, the excited state that is created does not correspond to the vibrational ground state. Therefore, the electronic transition is followed by a spatial relaxation towards the lowest vibrational level of the electronic excited state. During this non-radiative transition, vibrational quanta, *i.e.* phonons are created. Subsequently[5], the electronic excited state will decay to a non-equilibrium nuclear geometry for the electronic ground state where a similar relaxation occurs.

From this description and Fig. 3.1, it is clear that there is an energy difference between the absorbed and emitted photon,

$$\Delta S = E_{\rm exc} - E_{\rm em} > 0. \tag{3.31}$$

This energy difference is called the Stokes shift, named after Sir George Stokes who was the first to establish this phenomenon in 1852, in the early years of spectroscopy [1]. The Stokes shift, ΔS can be easily found as a function of ΔQ within the configurational coordinate model. For this, it is typically assumed that both parabola have

[5]The reason why we can assume this fixed sequence of excitation-relaxation-decay-relaxation is because of the large discrepancies between the time scales of these phenomena, $\tau_{\rm relaxation} \ll \tau_{\rm decay}$, where the latter is the lifetime of the electronic excited state.

the same curvature, $K_1 = K_2 = K$. This yields:

$$\begin{aligned} E_{\text{exc}} &= E_2(Q_1) - \left[E_1(Q_1) + \frac{1}{2}\hbar\omega_Q\right] \\ &= \Delta E + \frac{A_2^2}{2K} - \frac{A_1 A_2}{K} + \frac{A_1^2}{2K} - \frac{1}{2}\hbar\omega_Q \qquad (3.32) \\ E_{\text{em}} &= \left[E_2(Q_2) + \frac{1}{2}\hbar\omega_Q\right] - E_1(Q_2) \\ &= \Delta E - \frac{A_1^2}{2K} + \frac{A_1 A_2}{K} - \frac{A_2^2}{2K} + \frac{1}{2}\hbar\omega_Q \qquad (3.33) \end{aligned}$$

with $\Delta E = \hbar\omega_0$ and where the zero-point energy, was taken into account. The Stokes shift is then found:

$$\begin{aligned} \Delta S &= E_{\text{exc}} - E_{\text{em}} \\ &= \frac{1}{K}(A_2 - A_1)^2 - \hbar\omega_Q \\ &= K\Delta Q^2 - \hbar\omega_Q \qquad (3.34) \end{aligned}$$

Conventionally, the Huang-Rhys parameter is introduced:

$$S = \frac{E_{\text{dis}}}{\hbar\omega_Q} = \frac{K}{2\hbar\omega_Q}(Q_2 - Q_1)^2 - \frac{1}{2}, \qquad (3.35)$$

with $\frac{E_{\text{dis}}}{}$ the dissipated energy during one transition (see Fig. 3.1). This yields:

$$\Delta S = 2S\hbar\omega_Q. \qquad (3.36)$$

The Huang-Rhys parameter signifies the average number of created phonons per electronic transition.

3.4.3 Band shape

Under the approximations of the configurational coordinate model, Eq. 3.18 simplifies significantly. Only one vibrational mode is considered, Q, which is the same for the ground and excited electronic level:

$$F(\omega_0 - \omega) = F_0(\omega_0 - \omega) \sum_{\mu=-\infty}^{\infty} \sum_{\mu'=-\infty}^{\infty} \left|\left\langle \chi_{2\mu'}(Q) | \chi_{1\mu}(Q)\right\rangle\right|^2 \frac{\delta[\epsilon_{2\mu'} - \epsilon_{1\mu} - \hbar(\omega_0 - \omega)]}{e^{\epsilon_{1\mu}/k_B T} - 1}. \qquad (3.37)$$

The FC integral can be calculated by using some identities for the Hermite polynomials. The result is [41]:

$$\left\langle \chi_{2\mu'}(Q) | \chi_{1\mu}(Q)\right\rangle = \sqrt{\frac{\mu!}{\mu'!}}(-S)^{\mu'-\mu} e^{-S/2} L_\mu^{\mu'-\mu}(S). \qquad (3.38)$$

Here, $L_n^k(x)$ are the associated Laguerre polynomials [32]. By using another identity relating different classes of special functions, the general formula for the band shape in the configurational coordinate model is obtained:

$$F(\omega_0-\omega) = F_0(\omega_0-\omega)\sum_{\mu'=-\infty}^{\infty}\exp\left[\frac{\mu'\hbar\omega_Q}{2k_BT}-S\coth\frac{\hbar\omega_Q}{2k_BT}\right]I_{\mu'}\left[S\,\mathrm{csch}\left(\frac{\hbar\omega_Q}{2k_BT}\right)\right] \times\delta\left(\mu'\hbar\omega_Q-\hbar\omega\right), \tag{3.39}$$

where $I_\nu(x)$ are the modified Bessel functions [32]. This band shape function was first derived by Huang and Rhys and is therefore often referred to as the Huang-Rhys band shape [31]. Fig 3.1 shows some examples of band shapes for transitions with a low ($S = 0.1$) and intermediate ($S = 4$) electron-phonon interaction, yielding respectively line and broadband spectra, for different temperatures.

It is clear that spectra broaden when the temperature increases. The integrated intensity remains however unchanged. It can be shown that the bandwidth varies as

$$\Gamma(T)\approx\Gamma(0)\sqrt{\coth\frac{\hbar\omega_Q}{2k_BT}} \tag{3.40}$$

with temperature. At sufficiently low temperature, the thermal averaging can be avoided as then only the vibrational ground state will be occupied ($\mu = 0$). This simplifies the calculation of the FC integral to a trivial problem, yielding,

$$F(\omega_0-\omega)=F_0(\omega_0-\omega)\sum_{\mu'=0}^{\infty}\frac{\mathrm{e}^{-S}S^{\mu'}}{\mu'!}\,\delta(\mu'\hbar\omega_Q-\hbar\omega). \tag{3.41}$$

The band shape is hence approximated by a Poisson distribution, which is often referred to as a Pekarian or Huang-Rhys-Pekar shape function.

3.4.4 Non-radiative decay

For the configurational coordinate model, Eq. 3.20 reduces to:

$$w_{2\to1}^{\mathrm{n-rad}}=\frac{2\pi}{\hbar}\sum_{\mu=-\infty}^{\infty}\left|\left\langle\psi_1\chi_{1(\mu_0+\mu)}(Q)\middle|\mathcal{H}_{\mathrm{n-ad}}\middle|\psi_2\chi_{2\mu}(Q)\right\rangle\right|^2\frac{\delta(\epsilon_{1(\mu_0+\mu)}-\epsilon_{2\mu})}{\mathrm{e}^{\epsilon_{2\mu}/k_BT}-1}. \tag{3.42}$$

with $\mu_0 = {}^{\omega_0}\!/_{\omega_Q}$. The eigenfunctions of the harmonic oscillator fulfill the identity,

$$\frac{\partial\chi_{m\alpha\mu_\alpha}}{\partial Q_\alpha}=\sqrt{\frac{K_{m\alpha}}{2\hbar\omega_{m\alpha}}}\left(\sqrt{\mu}\chi_{m\alpha(\mu_\alpha-1)}-\sqrt{\mu+1}\chi_{m\alpha(\mu_\alpha+1)}\right), \tag{3.43}$$

allowing for a re-summation, yielding:

$$\begin{aligned} w_{2\to1}^{\mathrm{n-rad}} &= \frac{2\pi}{\hbar}\sum_{\mu=-\infty}^{\infty}\left|\langle\psi_1|\hbar^2\sqrt{\frac{K}{2\hbar\omega_Q}}(\sqrt{\mu+1}-\sqrt{\mu})\frac{\partial}{\partial Q}+\frac{1}{2}\frac{\partial^2}{\partial Q^2}|\psi_2\rangle\right|^2 \\ &\qquad\times\left|\langle\chi_{1(\mu_0+\mu)}(Q)|\chi_{2\mu}(Q)\rangle\right|^2\frac{\delta(\epsilon_{1(\mu_0+\mu)}-\epsilon_{2\mu})}{\mathrm{e}^{\epsilon_{2\mu}/k_BT}-1} \\ &\approx w_0^{\mathrm{n-rad}}\sum_{\mu=-\infty}^{\infty}\left|\langle\chi_{1(\mu_0+\mu)}(Q)|\chi_{2\mu}(Q)\rangle\right|^2\frac{\delta(\epsilon_{1(\mu_0+\mu)}-\epsilon_{2\mu})}{\mathrm{e}^{\epsilon_{2\mu}/k_BT}-1} \end{aligned} \tag{3.44}$$

where in the last step, the Condon approximation for the matrix elements of $\partial/\partial Q$ was applied. This simplifies the calculation appreciably while the end-result remains very close to the exact solution [42]. All the electronic contributions are collected in the constant $w_0^{\mathrm{n-rad}}$, which is in physical situations of the order 10^{12}-10^{14} s^{-1}. Eq. 3.44 can be elaborated with Eq. 3.38, or more practically thanks to the recursion formulas of Manneback which even allow a different curvature of the two PES. Charles W. Struck and William H. Fonger worked this out for different types of luminescence spectra in the 1970's [42–46].

Here, Eq. 3.44 is applied to two insightful examples. Important quantities that can be compared to experimental data are the quantum efficiency and the thermal quenching. These are evaluated within the Condon approximation for two typical non-radiative decay channels, outside crossover (Fig. 3.2a) and small-offset multiphonon emission (Fig. 3.2b). The quantum efficiency was evaluated according to Eq. 3.44 as a function of temperature, yielding the thermal quenching which is displayed in Fig. 3.2c for both cases. Fig. 3.2d displays the contribution to the rate $w_{1\to2}^{\mathrm{n-rad}}$ of a multiphonon transition with μ phonons in the initial state at a temperature of 300 K.

In the case of outside crossover, it is clear that the non-radiative decay rate is highly temperature-dependent, giving rise to a TQ profile strongly resembling experimental profiles. While the average number of initial state phonons, μ, increases with temperature, it is remarkably lower than the number of phonons that is required to cross the energy barrier, formed by the point of intersection of the two parabola, which lies $14\hbar\omega_Q$ above ϵ_{20} in this case. This has an important consequence when a TQ profile is fitted by an empirical Mott prescription,

$$w_{1\to2}^{\mathrm{n-rad}} = w_0^{\mathrm{n-rad}}\mathrm{e}^{-E_{\mathrm{Mott}}/k_BT} \tag{3.45}$$

which yields TQ profiles according to:

$$I(T) = \frac{I_0}{1+\frac{w_0^{\mathrm{n-rad}}}{w_{1\to2}^{\mathrm{rad}}}\mathrm{e}^{-E_{\mathrm{Mott}}/k_BT}}. \tag{3.46}$$

If the TQ profile of the outside crossover in Fig 3.2c is fitted by Eq. 3.46, one is fated to obtain a severe underestimation of the energy of the PES intersection point.

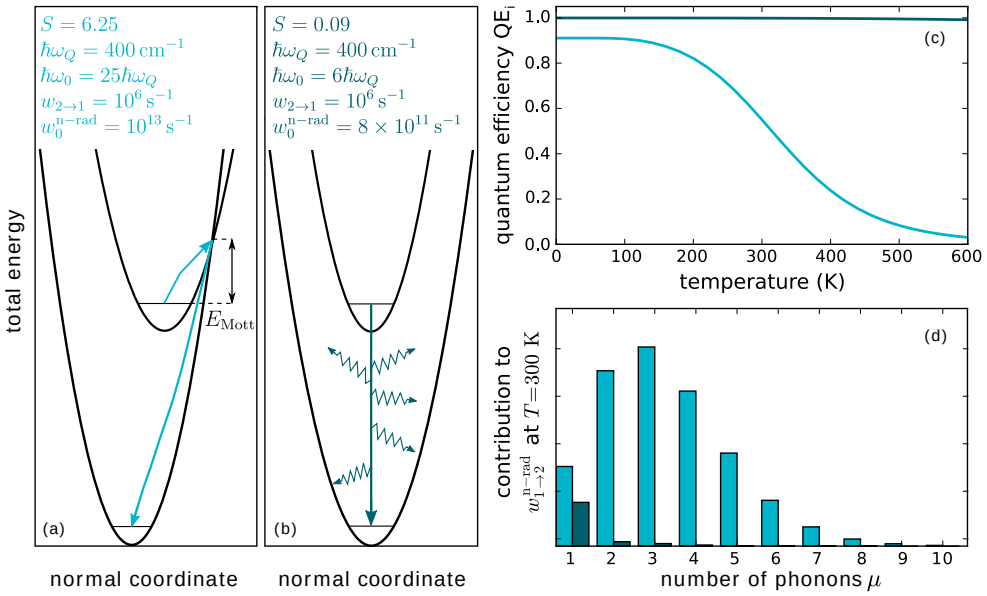

Figure 3.2 – (a), (b) Two different non-radiative decay channels, respectively outside crossover and small-offset multiphonon emission. (c) Calculated TQ profiles for the parameters shown in (a) and (b). (d) Relative contributions for the different terms, corresponding with the number of emitted phonons, in the total non-radiative decay rate.

Furthermore, if the expected values of $w_0^{\mathrm{n-rad}}$ and $w_{1\to2}^{\mathrm{rad}}$ are used, the drop in the TQ profile is much sharper, going from a maximal to a minimal QE in a region of ± 200 K, while this takes a region of ± 500 K for the exact calculation. Unphysical values for the rates are hence often used. The closer the point of intersection is to the bottom of the higher parabola, the higher the overlap between the vibrational wave functions will be and the higher the non-radiative decay rate. This can be represented by the Mott energy barrier which becomes smaller. When the non-radiative decay rate is as high such that the luminescence is also quenched at low temperature, it is called a fast bottom crossover.

Multiphonon relaxation (MPR) is typically found for energy levels with a small offset between the PES. Here, a crossover point is not available and the vibrational wave function overlap is only appreciable for small μ. This is clear from Fig. 3.2d where only the terms up to three or four created phonons participate in the transition probability. For this reason, MPR will only play an appreciable role for electronic energy levels that are reasonably close, up to $3-4\hbar\omega_Q$. This is evidenced in Fig. 3.2c, where the QE is high due to the large ZPL energy of $6\hbar\omega_Q$.

3.5 Breakdown of the adiabatic approximation

Within the Born-Oppenheimer approximation, it was assumed that the total wave function could be neatly separated in an electronic and a nuclear part that are treated independently. For this to hold, the non-adiabatic part of the many-body Hamiltonian, $\mathcal{H}_{\text{n-ad}}$ was neglected. This Hamiltonian can however become important for some physical phenomena. In §3.3 it was shown that it plays a crucial role to explain non-radiative decay of a luminescent center. Here, different PES were found to intersect or to lie near each other.

In general, it can be shown that the adiabatic approximation breaks down when the condition

$$\hbar\omega_{m_1\alpha} \ll \left|E_{m_1}(\boldsymbol{q}) - E_{m_2}(\boldsymbol{q})\right| \tag{3.47}$$

is no longer valid [47], *i.e.* when the difference between the electronic energy levels becomes comparable to the difference between the vibrational energy levels. This has repercussions on the eigenstates and eigenvalues of the many-body problem. A notable consequence is the lifting of degeneracies. These are after all the extreme cases where the above condition is not fulfilled. The lifting of degeneracies by vibronic interactions was formalized by Hermann A. Jahn and Edward Teller in two papers in 1937-38 [48, 49]. They used group theoretical arguments to show that the only remaining degeneracy that can be left is the so-called twofold Kramers degeneracy[6]. Thanks to their pioneering work, this effect is now known as the Jahn-Teller effect. It has consequences on multiple physical observables such as optical spectra, decay behavior, thermal quenching and so on [47]. Often the effects are rather small, hidden by other mechanisms that also induce the splitting of energy levels. It is in particular a popular aid to explain the spectroscopic behavior of s^2 ions such as Pb^{2+}, Bi^{3+}, ... where crystal field splitting is absent for sufficiently high symmetries (see §4.2).

A semantic confusion might arise in this context. In specialized literature pertaining to the Jahn-Teller effect, "vibronic interactions" specifically refer to the effects of $\mathcal{H}_{\text{n-ad}}$, while in the broader luminescence literature, the designation "vibronic interaction" is often used in the context of the Stokes shift, vibrational band broadening and related phenomena for systems that satisfy the adiabatic approximation.

[6] In the original work of Jahn and Teller, the non-adiabatic Hamiltonian was linearized in q. For this approximation, linear nuclear geometries can keep a higher degeneracy which is however lifted upon inclusion of higher-order terms, *e.g.* by the quadratic Jahn-Teller effect (also known as the Renner-Teller effect) [47].

4 Atomic picture

A deep understanding of the electronic structure of free ions offers a good starting point to understand the electronic structure of the defect centers, formed by these ions when they are introduced as impurities in solids. Therefore, the first part of this chapter is devoted to explain how the ground and excited states of atoms come about. Many famous scientists have racked their brain during the previous century in their attempt to describe the atomic states formed by incompletely filled d and f shells of respectively transition metal and lanthanide/actinide ions. These ions are different from the atoms in the s and p blocks of the periodic table in the sense that the usage of the standard techniques in atomic physics due to Slater, Condon and Shortley becomes extraordinary involved. In the 1940s, Giulio Racah revolutionized physics by applying group theoretical techniques to this problem. This launched the penetration of group theory in physics where it soon became indispensable. Racah was the first to make the distinction between *simple* and *complex* spectra, the latter originating from d^N or f^N configurations ($N \geq 3$) where the Russell-Saunders quantum numbers $LSJM$ are insufficient to obtain an unambiguous labeling of states. Later, in the 1990s Brian Judd continued the masterpiece of atomic shell theory by fully exploiting the machinery of Lie groups to devise the quark theory for the atomic f shell. This treatment, which is based on the diagonalization of Hamiltonian matrices starts from an independent particle model, the so-called central field approximation, of which the solutions are electron configurations. Subsequently, the most important corrections to this model are discussed, *i.e.* the non-spherical part of the interelectronic repulsion and the spin-orbit coupling. Expressions to calculate matrix elements are derived and appropriate labels for the electronic eigenstates are found. Further smaller corrections, originating from interactions between different configurations are discussed.

It is a dramatic event for an atom to be inserted as an impurity in a solid. The alien environment strongly alters its electronic structure. Atomic states can undergo relative shifts and will split due to the lowering of the symmetry of its environment. Furthermore, the electrons of the impurity atom will interact with the electrons and nuclei in the solid and *vice versa*. In crystal field theory (CFT), a third term is added to the Hamiltonian which already contained the interelectronic repulsion and spin-orbit coupling, allowing to describe the splitting of atomic states. The foundations for this theory were laid by the Nobel laureates Hans Bethe and John Van Vleck in

the late 1920s/early 1930s. Since then, the interpretation of the crystal field effect has largely changed, although the general principles of the theory hold and yield an accurate and simple interpretation of many experiments. The second part of this chapter gives an overview of crystal field theory and applies this to the important cases of transition metal and lanthanide ions in solid hosts, yielding the highly popular Tanabe-Sugano and Dieke diagrams respectively. The excited $4f^{N-1}5d^1$ configuration, which is important in spectra of *e.g.* Eu^{2+} and Ce^{3+}, is discussed in the context of CFT and contemporary luminescence literature. It is highlighted how the parameters of CFT can be obtained by quantum mechanical calculations from *first principles*. Finally, this theory is applied to shed a light on some spectroscopic dubieties concerning the red LED phosphor K_2SiF_6:Mn^{4+} and the green afterglow phosphor $SrAl_2O_4$:Eu^{2+}.

4.1 Free ions

A free ion is a conceptually simple system consisting of a positively charged nucleus around which negatively charged electrons orbit. In secondary school chemistry courses, it is already taught that the electrons organize themselves in shells, causing periodicity upon adding electrons to atoms. The concept of electron shells enables the existence of the periodic table, one of the flagships of science for already more than 150 years. The ordering of electrons in shells lies also at the foundation of atomic spectroscopy as will be discussed in this paragraph. The story does not end here, and important refinements of the shell model are discussed subsequently.

4.1.1 The central field

The Hamiltonian of the electronic eigenvalue equation, Eq. 2.4, reads[1]

$$\mathcal{H}_{\mathrm{e}} = \sum_{i=1}^{N} -\frac{\hbar^2}{2m_e}\nabla_i^2 - \sum_{i=1}^{N}\frac{Ze^2}{4\pi\epsilon_0 r_i} + \frac{1}{2}\sum_{i,j=1}^{N}\frac{e^2}{4\pi\epsilon_0\left|\boldsymbol{r}_i-\boldsymbol{r}_j\right|} \tag{4.1}$$

for the atomic case with N electrons in the field of a nucleus with charge Ze. Unless we have only one electron, this Schrödinger equation has no simple analytical solution. The reason for this is the occurrence of the third term, breaking spherical symmetry as it contains a factor $1/\left|\boldsymbol{r_i}-\boldsymbol{r_j}\right|$. In a first approximation, one can split this term into two parts, an as large as possible central field and the remaining problematic part, called the Russell-Saunders (RS) Hamiltonian:

$$U_{\text{centr.field}}(r_1,\ldots,r_N) = \sum_{i=1}^{N} U_i(\boldsymbol{r}_i) = -\sum_{i=1}^{N}\frac{Ze^2}{4\pi\epsilon_0 r_i} + \left\langle\frac{1}{2}\sum_{i,j=1}^{N}\frac{e^2}{4\pi\epsilon_0\left|\boldsymbol{r}_i-\boldsymbol{r}_j\right|}\right\rangle \tag{4.2}$$

$$\mathcal{H}_{\mathrm{RS}}(\boldsymbol{r}_1,\ldots,\boldsymbol{r}_N) = \frac{1}{2}\sum_{i,j=1}^{N}\frac{e^2}{4\pi\epsilon_0\left|\boldsymbol{r}_i-\boldsymbol{r}_j\right|} - \left\langle\frac{1}{2}\sum_{i,j=1}^{N}\frac{e^2}{4\pi\epsilon_0\left|\boldsymbol{r}_i-\boldsymbol{r}_j\right|}\right\rangle \tag{4.3}$$

[1] We work in the Born-Oppenheimer approximation (see §2.1.1) and omit the constant nucleus-nucleus repulsion.

The central field is necessarily a single-particle (sp) potential and signifies the averaged interaction an electron feels in the field of the other electrons. When neglecting the RS Hamiltonian, an independent particle model (IPM) is obtained,

$$\mathcal{H}_{\text{centr.field}} = \sum_{i=1}^{N} \mathcal{H}_{\text{centr.field}}(i) = \sum_{i=1}^{N} \left(-\frac{\hbar^2}{2m_e}\nabla_i^2 - \frac{Ze^2}{4\pi\epsilon_0 r_i} + U_i(r_i) \right). \tag{4.4}$$

In this case, the total wave function can be written as a product of sp wave functions (*orbitals*) and the total energy is the sum of the sp energies (*binding energies*). Subsequently, realizing that the solution of a particle in a central potential can always be written as a product of a radial wave function and a spherical harmonic (see appendix A). This yields finally:

$$\begin{aligned} \Psi_{\text{centr.field}}(x_1, \ldots, x_N) &= \prod_{i=1}^{N} \psi_{n_i \ell_i m_{\ell i} s_i m_{si}}(x_i) \\ \psi_{n_i \ell_i m_{\ell i} s_i m_{si}}(x_i) &= R_{n_i \ell_i}(r_i) Y_{\ell_i m_{\ell i}}(\Omega_i) \chi_{s_i m_{si}}(i) \\ E_{\text{centr.field}} &= \sum_{i=1}^{N} \epsilon_{n_i \ell_i m_{\ell i} s_i m_{si}} \end{aligned} \tag{4.5}$$

where the additional spin degree of freedom was included ($x_i = (\boldsymbol{r}_i, m_{s_i})$). Here, the atomic shell model already emerges if the allowed values for the quantum numbers are inspected:

$$\begin{aligned} n &= 1, 2, 3 \ldots \\ \ell &= 0, 1, \ldots, n-1 \\ m_\ell &= -\ell, -\ell+1, \ldots, \ell-1, \ell \\ s &= 1/2 \\ m_s &= -1/2, 1/2 \end{aligned} \tag{4.6}$$

for which every unique combination corresponds to a sp orbital. Anti-symmetrization of the sp solution yields the well-known Slater determinants. The physical meaning of the principle quantum number n is related to the sp energy of the orbital, while ℓ and m_ℓ pertain to the size and projection of the electrons' orbital angular momentum[2]. The spherical symmetry of the central potential conserves angular momentum and does not affect spin, resulting into a $(2\ell+1)(2s+1) = 4\ell+2$ -fold degeneracy of the sp energies. The total energy, *i.e.* the eigenvalues, can therefore be labeled by the occupation numbers, N_i, for every shell, quantified by the sp quantum numbers n and ℓ. The many-particle (mp) solutions therefore correspond to so-called electron configurations, $n_1\ell_1^{N_1} \ldots n_r\ell_r^{N_r}$, with $N_1 + \ldots + N_r = N$. The degeneracy of these mp states is obviously obtained by combining the available sp orbitals

[2]The algebra $\hat{\ell}^2 |n\ell m_\ell\rangle = \hbar^2 \ell(\ell+1)|n\ell m_\ell\rangle$ and $\hat{\ell}_z |n\ell m_\ell\rangle = \hbar m_\ell |n\ell m_\ell\rangle$ applies (see appendix A). Spectroscopic notation is common, where the quantum number ℓ is denoted by s ($\ell = 0$), p ($\ell = 1$), d ($\ell = 2$), f ($\ell = 3$), ...

with the occupation numbers:

$$\prod_{i=1}^{r}\binom{4\ell_i+2}{N_i} = \prod_{i=1}^{r}\frac{(4\ell_i+2)!}{N_i!(4\ell_i+2-N_i)!}. \tag{4.7}$$

In the most simple case of a one-electron atom, the central field corresponds exactly to the Coulomb potential of the nucleus which has a $1/r$ behavior[3]. Potentials with this inverse distance proportionality exhibit an additional internal symmetry, corresponding to the Lie group SO(4) which gives rise to a higher n^2-fold degeneracy of the energy eigenvalues. The additional conserved quantity is the Laplace-Runge-Lenz vector, which is well-known from the classical Kepler problem. The existence of electron spin increases the degeneracy by a factor $2s+1=2$ [50].

In a many-electron atom, the potential does not show a $1/r$ proportionality anymore, breaking the SO(4) symmetry. Another practical consequence is that an analytical expression for the potential cannot be found anymore, nor an analytic solution to the radial Schrödinger equation. Obtaining the radial wave functions therefore requires numerical techniques. Hartree found a straightforward method to determine this function and the central field potential in a self-consistent way in 1927. Later, Fock and Slater independently added the Pauli exclusion principle to the theory, resulting in what is now widely known as Hartree-Fock (HF). It can be shown that HF is the mean field theory for an electron gas, *i.e.* it corresponds to the lowest order term (Feynman diagram) in the many-body perturbation series in the two-particle (tp) interaction [51].

The obtained energy level schemes are very simple, the example of a Na atom is given in Fig. 4.1. The excited state landscape of this IPM is generated by all the particle-hole excitations, the energies of which are obtained by subtracting the binding energies of the individual orbitals. The excited states can be displayed in a total energy diagram which contains exactly the same information as the sp scheme for an IPM. In the case of Na, this description is already close to reality because it contains only one s valence electron. For more complex cases, elements containing more than one valence electron in highly degenerate d or f shells, this approximation obviously fails to describe the excited states and the RS interaction needs to be included in the description. It will result in a splitting of the degenerate central field energy levels.

In most treatises, including this one, the central field approximation is assumed to be a good lowest order approximation to the energy spectrum. Additional interactions, such as the RS Hamiltonian, are subsequently treated in first order perturbation theory. This means that the notion of an electron configuration, defined by the sp occupation numbers holds. In the cases when this is not compatible with reality, configuration mixing can be allowed, meaning that the physical eigenstates can

[3] This $1/r$ feature is generally not present for a central field of a many-electron atom because of nuclear shielding by electrons.

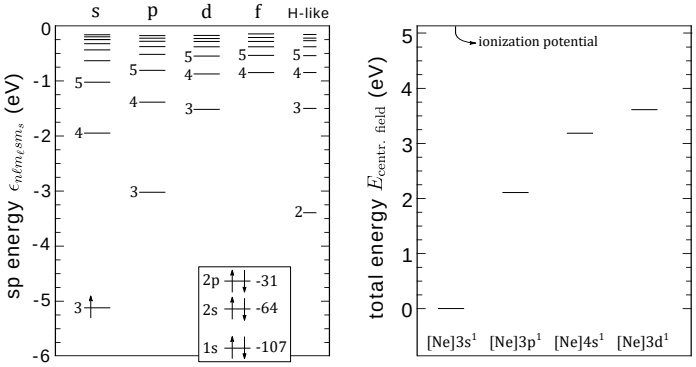

Figure 4.1 – Result of a central field calculation for the Na atom. The single-particle (sp) diagram compares the solutions of the central field with the exactly solvable $1/r$ central field of the H-atom. The many-particle (mp) diagram shows the total energy of the system, which is simply the sum of the sp energies within the central field approximation. The ground state is put at zero total energy. Adapted from [51].

have character of more than one electron configuration. This is for example required to explain the transition probabilities for intraconfigurational $4f^N$ transitions in the lanthanides, which is briefly discussed in §4.3. One can also include the effect of configuration interaction (CI) in an effective way, while keeping the *active space* restricted to initial configuration in second order perturbation theory (see §4.1.6).

In the following, matrix elements have to be calculated for the different corrections to the central field. The way this is done always boils down to the same procedure. Quantum numbers can be found by searching operators that commute with the total electronic Hamiltonian. In reality, when all interactions are taken into account, this is seldomly possible and one rather speaks of labels of basis vectors into which the eigenstates of the Hamiltonian are expressed. If a basis is chosen, matrix elements have to be calculated. Typically, matrix elements are factorized into an angular part and a radial part. The angular part can be analytically calculated by algebraic methods, which are due to G. Racah. These methods essentially consist of two ingredients, irreducible tensor operators and expansion into coefficients of fractional parentage (CFP). Appendix B gives a rather detailed account on how these concepts are used for the calculation of matrix elements. Below, the results of this appendix are applied to calculate the matrix elements of the interactions which are of interest for the luminescent systems under study.

4.1.2 Russell-Saunders interaction - equivalent electrons

It can be checked that the individual angular momenta ℓ_i do not commute with $1/\left|\boldsymbol{r}_i - \boldsymbol{r}_j\right|$. The sp labels can therefore not be used for the eigenstates when $\mathcal{H}_{\mathrm{RS}}$ is added to the description. Other labels are required and the operators L^2 and S^2,

with the total angular momenta defined as

$$\boldsymbol{L} = \sum_{i=1}^{N} \boldsymbol{\ell}_i \qquad \boldsymbol{S} = \sum_{i=1}^{N} \boldsymbol{s}_i, \tag{4.8}$$

can be shown to commute with $1/\left|\boldsymbol{r}_i - \boldsymbol{r}_j\right|$. The associated eigenvalues L and S can thus be regarded as good quantum numbers upon inclusion of RS. It will be demonstrated for a configuration featuring N equivalent electrons, *i.e.* electrons with the same n and ℓ quantum numbers, how eigenstates and energies are obtained.

Shell of N equivalent electrons, ℓ^N

The allowed $|\ell^N\, LS\rangle$ basis states, often referred to as terms, can be found by reducing the direct products of SO(3) irreducible representations (irreps):

$$\bigotimes_{i=1}^{N} \mathcal{D}^{(\ell_i)} = \bigoplus_{L} \mathcal{D}^{(L)} \quad \text{and} \quad \bigotimes_{i=1}^{N} \mathcal{D}^{(s_i=1/2)} = \bigoplus_{S} \mathcal{D}^{(S)}, \tag{4.9}$$

under particle exchange antisymmetry restrictions. This group theoretical viewpoint thus allows to predict the occurrence of term splitting and the residual degeneracies without calculating any matrix element. This demonstrates the power and usefulness of group theory in spectroscopy. Similar symmetry arguments will be applied in the study of the crystal field (see further, §4.2.1).

Group theory allows for a quick counting of spectral lines, however quantitative information can only be obtained upon calculation of matrix elements and subsequent diagonalization of the Hamiltonian. As the operators L^2, L_z, S^2 and S_z all commute with $1/\left|\boldsymbol{r}_i - \boldsymbol{r}_j\right|$, the inter-electronic repulsion Hamiltonian will be diagonal in the proposed basis. So, in the following, only diagonal matrix elements will be considered.

It is insightful to re-include the inter-electronic repulsion Hamiltonian completely, and re-separate the spherically symmetric part afterwards. Matrix elements are calculated by expanding the Coulomb potential in a multipole expansion[4]:

$$\begin{aligned}\langle n\ell^N\, LS| \sum_{i<j=1}^{N} \frac{e^2}{4\pi\epsilon_0 \left|\boldsymbol{r}_i - \boldsymbol{r}_j\right|} |n\ell^N\, LS\rangle = \underbrace{\sum_{k=0}^{\infty} \frac{4\pi}{2k+1} \langle n\ell^N\, LS| \sum_{i<j=1}^{N} Y^{(k)}(i) \cdot Y^{(k)}(j) |n\ell^N\, LS\rangle}_{f_k(\ell^N\, LS)} \\ \times \underbrace{\frac{e^2}{4\pi\epsilon_0} \int_0^\infty \mathrm{d}r_i r_i^2 \int_0^\infty \mathrm{d}r_j r_j^2 R_{n\ell}^2(r_i) \frac{r_<^k}{r_>^{k+1}} R_{n\ell}^2(r_j)}_{F^k(n\ell,n\ell)}.\end{aligned} \tag{4.10}$$

[4]Here, $r_<$ and $r_>$ denote respectively the smaller and larger distance of r_i and r_j.

The projections M_L and M_S are left out of the equations for notational simplicity and the definition of the scalar product of two spherical harmonics was used (Eq. B.23). Furthermore, the Slater-Condon parameters $F^k(n\ell, n\ell)$ are introduced. Although these are symbolically rather simple-looking, they cannot be analytically evaluated as the radial wave functions $R_{n\ell}(r)$ depend on the details of the central field (see §4.1.1). They are however equal for all terms of the same configuration. Furthermore, it is important to note that the spherical harmonics in the above expression are regarded as operators. Their particular symmetry properties allow to use Racah's toolbox to crack the angular integrals. In particular, the unit tensor is introduced according to Eq. B.21:

$$\begin{aligned}
&\langle n\ell^N\, LS| \sum_{i<j=1}^{N} Y^{(k)}(i)\cdot Y^{(k)}(j)|n\ell^N\, LS\rangle \\
&\qquad = \langle \ell\|\, Y^{(k)}\,\|\ell\rangle^2 \langle n\ell^N\, LS| \sum_{i<j=1}^{N} u^{(k)}(i)\cdot u^{(k)}(j)|n\ell^N\, LS\rangle \\
&\qquad = \frac{1}{2}\langle \ell\|\, Y^{(k)}\,\|\ell\rangle^2 \Big(\langle n\ell^N\, LS|\, U^{(k)}\cdot U^{(k)}|n\ell^N\, LS\rangle \\
&\qquad\qquad -\langle n\ell^N\, LS| \sum_i u^{(k)}(i)\cdot u^{(k)}(i)|n\ell^N\, LS\rangle\Big) \qquad (4.11)
\end{aligned}$$

The first term in Eq. 4.11 is of the form B.24 and reads

$$\frac{1}{2L+1}\sum_{L'}(-1)^{L-L'}\left|\langle n\ell^N\, LS\|\, U^{(k)}\,\|n\ell^N\, L'S\rangle\right|^2, \qquad (4.12)$$

while the second term in Eq. 4.11 needs an additional step. Using the Wigner-Eckart theorem and the fact that the scalar product $\sum_{i=1}^{N} u^{(k)}(i)\cdot u^{(k)}(i)$ can be considered as a rank-0 tensor yields:

$$\begin{aligned}
&\langle n\ell^N\, LSM_LM_S| \sum_{i=1}^{N} u^{(k)}(i)\cdot u^{(k)}(i)^{(0)}_0|n\ell^N\, LSM_LM_S\rangle \\
&\qquad = (-1)^{L-M_L}\begin{pmatrix} L & 0 & L \\ -M_L & 0 & M_L\end{pmatrix}\langle LS\|\sum_{i=1}^{N} u^{(k)}(i)\cdot u^{(k)}(i)^{(0)}\,\|L'S\rangle \\
&\qquad = N\sqrt{\frac{1}{2\ell+1}}\langle \ell\|\, u^{(k)}\cdot u^{(k)}\,\|\ell\rangle \\
&\qquad = \frac{N}{2\ell+1}, \qquad (4.13)
\end{aligned}$$

where Eq. B.47 and Eq. B.24 were used consecutively. Finally, combining the above, and using Eq. B.13 yields:

$$f_k(\ell^N\, LS) = \frac{1}{2}(2\ell+1)^2\begin{pmatrix}\ell & k & \ell\\ 0 & 0 & 0\end{pmatrix}^2\left(\frac{1}{2L+1}\sum_{L'}(-1)^{L-L'}\left|\langle LS\|\, U^{(k)}\,\|L'S\rangle\right|^2 - \frac{N}{2\ell+1}\right). \qquad (4.14)$$

From this expression, it is clear that the range of k is limited by $k \leq 2\ell$ because of the selection rules of the Wigner-3j symbol. Furthermore, as the lowest three entries are zero, the sum of the upper three, $2\ell + k$, must be even, implying that k must be even.

Furthermore, evaluation of the $k = 0$ coefficient yields

$$f_0(\ell^N\, LS) = \frac{N(N+1)}{2}, \tag{4.15}$$

which is equal for all terms. In other words, $f_0 F^0$ shifts all energy levels of the configuration by an equal amount and corresponds to the spherical symmetric part of the inter-electronic repulsion Hamiltonian which is added to the central field (§4.1.1). Optical spectra originate often from transitions between terms of the same configuration. In that case, the value of the F^0 parameter is unimportant.

Summarized, for the d^N and f^N configurations which are of importance for this work, respectively two (F^2 and F^4) and three (F^2, F^4 and F^6) Slater-Condon parameters are required to parametrize the RS Hamiltonian.

As the f_k's contain a common denominator irrespective of N, it is often absorbed in the Slater-Condon parameters, which are then denoted with subscript k and referred to as the normalized Slater-Condon parameters to avoid confusion:

$$\begin{array}{ll} \ell = 2: & \ell = 3: \\ & \\ F_0 = F^0 & F_0 = F^0 \\ F_2 = \frac{1}{49} F^2 & F_2 = \frac{1}{225} F^2 \\ F_4 = \frac{1}{441} F^4 & F_4 = \frac{1}{1089} F^4 \\ & F_6 = \frac{1}{184041} F^6. \end{array} \tag{4.16}$$

The inadequacy of SO(3): Racah's parentage groups

Unambiguous labeling of terms by L and S is possible, provided that every irrep found in Eq. 4.9 is unique. It can be checked that this is always the case for incompletely filled shells of s and p electrons. For d^N and f^N configurations, on the other hand, multiply occurring LS terms emerge when $N \geq 3$ and an additional label, α, is introduced which can be interpreted as a branching multiplicity label. Nevertheless, the interpretation of α is not clear at first sight as supergroups for SO(3) are required in order to be able to use the notion of branching multiplicity. Furthermore, a recipe is required to obtain the matrix elements for these different states. It was again Racah who found an elegant way to resolve this issue. As α is implicitly present in Eq. 4.14 and other matrix elements for other interactions, unambiguous labeling of states is of importance and the solution of Racah is discussed here briefly.

The current point of discussion is about the labeling of RS terms corresponding to irreps of the product group SO(3)⊗SU(2), the former pertaining to L, the latter to S.

This discussion however started from Slater determinants, *i.e.* the anti-symmetrized solutions for the central field, which correspond to $4\ell+2$ spin orbitals that form a basis for an anti-symmetrical representation of SU($4\ell+2$). The mp eigenstates form an alternative basis for this anti-symmetrical representation and in principle the row indices of this irrep, Ξ, can be used to distinguish the RS states. It will however prove to pay off when intermediate groups are traced.

Separating the spin degrees of freedom corresponds to limiting SU($4\ell+2$) to its subgroup SU($2\ell+1$)$\otimes$SU(2), where the label S emerges for the irreps of SU(2). Unambiguous labeling can be achieved by using the row index of the relevant irrep of SU($2\ell+1$), Δ, in addition. Intermediate Lie groups still exist, but these are different for $\ell = 2$ and $\ell = 3$.

For d electrons, one arrives ultimately at the group chain[5]:

$$\mathrm{SU}(10) \quad \supset \quad [\mathrm{SU}(5) \quad \supset \quad \mathrm{SO}(5) \quad \supset \quad \mathrm{SO}(3)] \quad \otimes \quad \mathrm{SU}(2), \tag{4.17}$$

corresponding to the mp labels:

$$|\mathrm{d}^N\ \Xi\rangle \quad \rightarrow \quad |\mathrm{d}^N\ \Delta S M_S\rangle \quad \rightarrow \quad |\mathrm{d}^N\ \upsilon S M_S\rangle \quad \rightarrow \quad |\mathrm{d}^N\ \upsilon L M_L S M_S\rangle. \tag{4.18}$$

So the orthogonal group SO(5) is found in addition. While all mp eigenstates used belong to the same irrep of SU(5), reducing this irrep to SO(5) will cause a breakup into the irreps of SO(5) which are characterized by $\ell = 2$ numbers, $W = (w_1, w_2)$, which can be used to label the eigenstates.

Before adhering to this group theoretical method, Racah obtained a consistent labeling of the d^N states from inspecting the RS terms across the d^N series for varying N. He noticed that the terms of d^N recur for d^{N+2} and used this to introduce the seniority number υ, denoted as ${}^{2S+1}_{\upsilon}L$, which represents the N value for which ${}^{2S+1}L$ occurs for the first time. A two-particle operator was introduced, which is now referred to as Racah's seniority operator[6],

$$\mathcal{Q} = \sum_{i<j=1}^{N} q_{ij} \quad \text{for which} \quad \langle \ell^2 L M_L | q_{ij} | \ell^2 L M_L \rangle = (2\ell+1)\delta_{L0}. \tag{4.19}$$

with eigenvalues that yield exactly the *ad hoc* introduced seniority number:

$$Q(N,\upsilon) = \frac{(N-\upsilon)(4\ell+4-N-\upsilon)}{4}, \tag{4.20}$$

proving that υ (or Q) is a good label. Further analysis of the branching of irreps from SU($2\ell+1$) to SO($2\ell+1$) reveals that the seniority operator is directly related to

[5] An alternative, but less common group chain contains the symplectic group Sp($4\ell+2$).

[6] In the field of atomic spectroscopy, this seniority operator does not have a pronounced physical meaning and is solely used to distinguish nonequivalent eigenstates. In nuclear physics however, the seniority operator, which signifies a pairing force, gives a good first approximation for the strong interaction between identical nucleons [52].

$\mathcal{G}[\mathrm{SO}(2\ell+1)]$, the Casimir operator of $\mathrm{SO}(2\ell+1)$:

$$\mathcal{Q} = \frac{N(4\ell+4-N)}{4} - \mathcal{G}[\mathrm{SU}(2)] - (2\ell+1)\,\mathcal{G}[\mathrm{SO}(2\ell+1)]. \tag{4.21}$$

Both viewpoints are thus equivalent, *i.e.* a one-to-one correspondence exists between (v, S) and $W = (w_1, w_2)$, and v can be used as an additional label for the eigenstates.

The above reasoning about the seniority number can be extended to f^N configurations. It can however be shown that already for $N = 3$, multiple terms with identical vLS labels emerge upon reducing the irreps $W = (w_1, w_2, w_3)$ of SO(7) into SO(3). Consequently, additional measures have to be taken. It happens that $\ell = 3$ is a special case as an additional Lie group appears in the chain[7]:

$$\mathrm{SU}(14) \supset [\mathrm{SU}(7) \supset \mathrm{SO}(7) \supset \mathrm{G}_2 \supset \mathrm{SO}(3)] \otimes \mathrm{SU}(2), \tag{4.22}$$

corresponding with mp labels:

$$|\mathrm{f}^N\ \Xi\rangle \to |\mathrm{f}^N\ \Delta S M_S\rangle \to |\mathrm{f}^N\ W S M_S\rangle \to |\mathrm{f}^N\ W U S M_S\rangle \to |\mathrm{f}^N\ W U L M_L S M_S\rangle. \tag{4.23}$$

G_2 is one of the five exceptional simple Lie groups, first described by Wilhelm Killing. It is a rank-2 group, so its irreps are labeled by two numbers, $U = (u_1, u_2)$. In analogy with the seniority operator, a two-particle operator can be devised, which distinguishes the different irreps of G_2. In the reduction of all possible W's of SO(7) to U's of G_2, no multiplicities higher than one are found. However, for the reduction of G_2's U's into SO(3)'s $\mathcal{D}^{(L)}$'s, ambiguity remains for the irreps $U = (31)$ and $U = (40)$, which occur for $N \geq 5$. In principle, this can be fully resolved by including the irreps of SO(4) as an intermediate step. This is in practice not done because of the severe mathematical complication this involves and an arbitrary branching multiplicity label, τ, is used when required.

An important remark regarding the above argumentation is that it is a strange result that (almost) unambiguous labeling can be achieved with the used Lie groups. After all, except for SO(3), these are no symmetry groups for the atomic Hamiltonian, *i.e.* the generators of these groups do not commute with $\mathcal{H}_\mathrm{e}$. Labels such as v, W or U can therefore not be regarded as good quantum numbers.

The greatest advantage of the group theoretical approach is revealed when matrix elements are calculated. If the operator can be formulated in terms of the irreps of the complete Lie group chain, the Wigner-Eckart theorem can be applied for these supergroups. This allowed Racah to achieve his *tour de force*, to calculate the matrix elements for the Coulomb interaction in all d^N and f^N configurations [54]. For this, the $Y^{(k)}(i) \cdot Y^{(k)}(j)$ terms are re-summed by projecting them on the irreps of $\mathrm{SO}(2\ell+1)$ (and G_2 for $\ell = 3$) to obtain well-behaving tensor operators. This leads to a reformulation of the f^k's in terms of $a(\mathrm{d}^N\ vLS)$, $b(\mathrm{d}^N\ vLS)$ and $c(\mathrm{d}^N\ vLS)$ for $\ell = 2$ and $e_0(\mathrm{f}^N\ WULS)$, $e_1(\mathrm{f}^N\ WULS)$, $e_2(\mathrm{f}^N\ WULS)$, $e_3(\mathrm{f}^N\ WULS)$ for $\ell = 3$. The

[7] According to Brian R. Judd this is merely ´´*an extraordinary stroke of good fortune*´´ [53].

radial integrals that correspond to these coefficients are linear combinations of the Slater-Condon parameters and referred to as Racah parameters:

$$\begin{array}{ll} \ell = 2: & \ell = 3: \\ A = F_0 - 49F_4 & E^0 = F_0 - 10F_2 - 33F_4 - 286F_6 \\ B = F_2 - 5F_4 & E^1 = \frac{1}{9}(70F_2 + 231F_4 + 20020F_6) \\ C = 35F_4 & E^2 = \frac{1}{9}(F_2 - 3F_4 + 7F_6) \\ & E^3 = \frac{1}{3}(5F_2 + 6F_4 - 91F_6) \end{array} \tag{4.24}$$

This is the background why Racah's parameters are found in literature rather than Slater-Condon parameters.

4.1.3 Russell-Saunders interaction - nonequivalent electrons

Often, one encounters configurations in which more than one incompletely filled shell is found. Examples are the $n\mathrm{f}^{N-1}(n+1)\mathrm{d}^1$ and $n\mathrm{f}^{N-1}(n+2)\mathrm{s}^1$ configurations that are found in lanthanides ($n = 4$) and actinides ($n = 5$) or the $n\mathrm{s}^1 n\mathrm{p}^1$ configuration that is found upon exciting s^2 ions such as Tl^+, Pb^{2+}, Bi^{3+}. For spectroscopy of metal impurities, the most common configurations of nonequivalent electrons feature an incompletely filled shell $n_1\ell_1^{N-1}$, coupled to a single electron in a different shell, $n_2\ell_2^1$. This is an important observation as it drastically simplifies increasingly complicated formulas for matrix elements.

For the general case of a two shell configuration, $\ell_1^{N_1}\ell_2^{N_2}$, there are different possibilities to couple the angular momenta of the shells (see §4.1.5). Here, we proceed as before (Eq. 4.8) and consider the total momenta of the separate shells, L_1, S_1 and L_2, S_2 and subsequently the total momenta of the complete electronic system, L and S. This gives rise to basis kets $|\psi\rangle = |n_1\ell_1^{N_1}\,\alpha_1 L_1 S_1, n_2\ell_2^{N_2}\,\alpha_2 L_2 S_2; LS\rangle$. A similar argument as before learns that the Coulomb interaction will be diagonal with respect to L and S. As this Hamiltonian only has positional dependence and no spin dependence, it will also be diagonal with respect to S_1 and S_2.

In the case of a two shell configuration, $\ell_1^{N_1}\ell_2^{N_2}$, the Hamiltonian is rewritten:

$$\sum_{i<j=1}^{N_1+N_2} \frac{e^2}{4\pi\epsilon_0 |\boldsymbol{r}_i - \boldsymbol{r}_j|} = \frac{e^2}{4\pi\epsilon_0}\left(\sum_{i<j=1}^{N_1} \frac{1}{|\boldsymbol{r}_i - \boldsymbol{r}_j|} + \sum_{i<j=1}^{N_2} \frac{1}{|\boldsymbol{r}_i - \boldsymbol{r}_j|} + \sum_{i=1}^{N_1}\sum_{j=1}^{N_2} \frac{1}{|\boldsymbol{r}_i - \boldsymbol{r}_j|}\right) \tag{4.25}$$

The first term acts only on the first shell and is therefore diagonal with respect to the quantum numbers of the second shell. Its matrix elements can be calculated with the above derived expression for equivalent electrons. A similar argument applies to the second term. The third term is different and describes the Coulomb interaction

between the nonequivalent electrons. Multipole expansion of the last term leads to a similar expression as Eq. 4.10:

$$\begin{aligned}\langle\psi|\sum_{i=1}^{N_1}\sum_{j=1}^{N_2}\frac{e^2}{4\pi\epsilon_0\left|\boldsymbol{r}_i-\boldsymbol{r}_j\right|}|\psi'\rangle \quad &= \quad \underbrace{\sum_{k=0}^{\infty}\frac{4\pi}{2k+1}\langle\psi|\sum_{i=1}^{N_1}\sum_{j=1}^{N_2}Y^{(k)}(i)\cdot Y^{(k)}(j)|\psi'\rangle}_{f_k\left(n_1\ell_1^{N_1}\,\alpha_1L_1L_1'S_1,n_2\ell_2^{N_2}\,\alpha_2L_2L_2'S_2;LS\right)} \\ &\times\underbrace{\frac{e^2}{4\pi\epsilon_0}\int_0^\infty \mathrm{d}r_i\,r_i^2\int_0^\infty \mathrm{d}r_j\,r_j^2R_{n\ell}^2(r_i)\frac{r_<^k}{r_>^{k+1}}R_{n\ell}^2(r_j)}_{F^k(n_1\ell_1,n_2\ell_2)} \\ &+\underbrace{\sum_{k=0}^{\infty}\frac{4\pi}{2k+1}\langle\psi|\sum_{i=1}^{N_1}\sum_{j=1}^{N_2}Y^{(k)}(i)\cdot Y^{(k)}(j)|\psi'\rangle_{\mathrm{ex}}}_{g_k\left(n_1\ell_1^{N_1}\,\alpha_1L_1L_1'S_1,n_2\ell_2^{N_2}\,\alpha_2L_2L_2'S_2;LS\right)} \\ &\times\underbrace{\frac{e^2}{4\pi\epsilon_0}\int_0^\infty \mathrm{d}r_i\,r_i^2\int_0^\infty \mathrm{d}r_j\,r_j^2R_{n_1\ell_1}(r_i)R_{n_2\ell_2}(r_j)\frac{r_<^k}{r_>^{k+1}}R_{n_1\ell_1}(r_j)R_{n_2\ell_2}(r_i)}_{G^k(n_1\ell_1,n_2\ell_2)}.\end{aligned} \tag{4.26}$$

where the subscript "ex" denotes the exchange matrix element. Both terms ask for a slightly different elaboration.

Direct part

The angular matrix element is simply calculable with the tensor methods. Upon substituting the unit tensor (Eq. B.21), one obtains:

$$\begin{aligned}&\langle\psi|\sum_{i=1}^{N_1}\sum_{j=1}^{N_2}Y^{(k)}(i)\cdot Y^{(k)}(j)|\psi'\rangle \\ &\qquad=\langle\ell_1\|\,Y^{(k)}\,\|\ell_1\rangle\langle\ell_2\|\,Y^{(k)}\,\|\ell_2\rangle\langle\psi_1|\,U^{(k)}(1)\cdot U^{(k)}(2)|\psi'\rangle \\ &\qquad\overset{N_2=1}{=}\langle\ell_1\|\,Y^{(k)}\,\|\ell_1\rangle\langle\ell_2\|\,Y^{(k)}\,\|\ell_2\rangle(-1)^{L_1'+\ell_2+L}\delta_{LL'}\delta_{M_LM_L'}\begin{Bmatrix}L_1' & \ell_2 & L\\ \ell_2 & L_1 & k\end{Bmatrix}, \\ &\qquad\times\langle\ell_1^{N_1}\;L_1S_1\|\,U^{(k)}\,\|\ell_1^{N_1}\;L_1S_1\rangle\end{aligned} \tag{4.27}$$

where $U^{(k)}(1)$ and $U^{(k)}(2)$ sum over the electrons in shell ℓ_1 and ℓ_2 respectively. In the last step, $N_2 = 1$ was assumed to simplify the derivation and because only this

special case is of interest to the spectroscopic experiments that follow. $U^{(k)}(2)$ becomes $u^{(k)}(2)$ and Eq. B.32 was used. From the above and Eq. B.13, one obtains:

$$f_k\left(n_1\ell_1^{N_1}\,\alpha_1 L_1 L_1' S_1, n_2\ell_2^1\right) = (-1)^{L_1'+\ell_2+L}\begin{pmatrix}\ell_1 & k & \ell_1\\ 0 & 0 & 0\end{pmatrix}\begin{pmatrix}\ell_2 & k & \ell_2\\ 0 & 0 & 0\end{pmatrix}\begin{Bmatrix}L_1' & \ell_2 & L\\ \ell_2 & L_1 & k\end{Bmatrix} \times(2\ell_1+1)(2\ell_2+1)\langle\ell_1^{N_1}\ L_1S_1\|\,U^{(k)}\,\|\ell_1^{N_1}\ L_1S_1\rangle. \quad (4.28)$$

Exchange part

Exchange matrix elements are troublesome because the Wigner-Racah algebra does not apply to them. For this reason, g_k is first rewritten as a direct matrix element of a different operator. Upon application of the CFP formalism, the evaluation of a two-particle operator for a many-particle system boils down to the calculation of matrix elements for the two electrons that relate the grandparent terms to the granddaughter terms (see appendix B):

$$\begin{aligned}&\langle\ell_1 s(i),\ \ell_2 s(j);\ LS|\,Y^{(k)}(i)\cdot Y^{(k)}(j)|\ell_1 s(j),\ \ell_2 s(i);\ LS\rangle\\ &\quad=(-1)^{\ell_1+\ell_2-L'+S'}\langle\ell_1 s(i),\ \ell_2 s(j);\ LS|\,Y^{(k)}(i)\cdot Y^{(k)}(j)|\ell_2 s(i),\ \ell_1 s(j);\ LS\rangle\\ &\quad=\delta_{SS'}\delta_{LL'}(-1)^{\ell_1+\ell_2+S+k}\begin{Bmatrix}\ell_2 & \ell_1 & L\\ \ell_2 & \ell_1 & k\end{Bmatrix}\left|\langle\ell_1\|\,Y^{(k)}\,\|\ell_2\rangle\right|^2, \end{aligned} \quad (4.29)$$

where the factor (-1) in the first step originates from the antisymmetrized two-electron basis states as derived in any standard quantum mechanics handbook[8]. In the second step, the scalar product was decoupled in factors working on electron i and j respectively. Racah's sum rule (Eq. B.5) is applied to the Wigner-6j symbol, yielding:

$$\begin{aligned}&=\delta_{SS'}\delta_{LL'}(-1)^{S+L+\ell_1+\ell_2}\left|\langle\ell_1\|\,Y^{(k)}\,\|\ell_2\rangle\right|^2\\ &\qquad\times\sum_r(-1)^r(2r+1)\begin{Bmatrix}\ell_2 & \ell_1 & L\\ \ell_1 & \ell_2 & r\end{Bmatrix}\begin{Bmatrix}\ell_2 & \ell_1 & k\\ \ell_1 & \ell_2 & r\end{Bmatrix}\\ &=\delta_{SS'}\delta_{LL'}(-1)^{S}\left|\langle\ell_1\|\,Y^{(k)}\,\|\ell_2\rangle\right|^2\sum_r(-1)^r(2r+1)\begin{Bmatrix}\ell_2 & \ell_1 & k\\ \ell_1 & \ell_2 & r\end{Bmatrix}\\ &\qquad\times\langle\ell_1 s(i),\ \ell_2 s(j);\ LS|\,u^{(r)}(i)\cdot u^{(r)}(j)|\ell_1 s(i),\ \ell_2 s(j);\ LS\rangle. \end{aligned} \quad (4.30)$$

where in the first step it was used that $\ell_1+\ell_2+k$ is even (due to the $\langle\ell_1\|\,Y^{(k)}\,\|\ell_2\rangle$ factors) to simplify the exponent of (-1). Then, Eq. 4.27 was used for $N_1=1$ and inspection of Eq. 4.30, reveals that the exchange matrix element was indeed rewritten

[8] Two electron can form either a spin singlet, for which the spin part is antisymmetric and the orbital part symmetric: $|^1LM_LM_S\rangle = 1/\sqrt{2}\ |00\rangle_S\left(|\ell_1(i)\ell_2(j)LM_L\rangle+(-1)^{\ell_1+\ell_2-L}|\ell_2(i)\ell_1(j)LM_L\rangle\right)$, or a spin triplet, for which the spin part is symmetric and the orbital part antisymmetric: $|^3LM_LM_S\rangle = 1/\sqrt{2}\ |1M_S\rangle_S\left(|\ell_1(i)\ell_2(j)LM_L\rangle-(-1)^{\ell_1+\ell_2-L}|\ell_2(i)\ell_1(j)LM_L\rangle\right)$

in a direct matrix element. The factor $(-1)^S$ originated from the two-particle antisymmetrized wave function and is only valid for the two-electron case where S can be 0 or 1. A generalization is thus required. From angular momentum algebra it is simple to show that

$$\langle\psi|-\frac{1}{2}-2\sum_{i=1}^{N_1}\sum_{j=1}^{N_2}\boldsymbol{s}(i)\cdot\boldsymbol{s}(j)|\psi'\rangle=1-S(S+1), \tag{4.31}$$

which indeed boils down to $(-1)^S$ for $N_1=N_2=1$. This allows to rewrite Eq. 4.29 in its final form:

$$\begin{aligned}&\langle\ell_1 s(i),\,\ell_2 s(j);\,LS|\,Y^{(k)}(i)\cdot Y^{(k)}(j)|\ell_1 s(j),\,\ell_2 s(i);\,LS\rangle \\ &\quad=-\frac{1}{2}\delta_{SS'}\delta_{LL'}\left|\langle\ell_1\|\,Y^{(k)}\,\|\ell_2\rangle\right|^2\sum_r(-1)^r(2r+1)\begin{Bmatrix}\ell_2 & \ell_1 & k\\ \ell_1 & \ell_2 & r\end{Bmatrix} \\ &\quad\times\langle\ell_1 s(i),\,\ell_2 s(j);\,LS|\,u^{(r)}(i)\cdot u^{(r)}(j)+4v^{(r1)}(i)\cdot v^{(r1)}(j)|\ell_1 s(i),\,\ell_2 s(j);\,LS\rangle\end{aligned} \tag{4.32}$$

upon introduction of the direct product B.22. From the CFP algebra (see appendix B), this expression can be easily generalized to the general case. As before, only the case $N_2=1$, which is of particular interest for this work, is further explored:

$$\begin{aligned}\langle\psi|\sum_{i=1}^{N_1}\sum_{j=1}^{N_2}Y^{(k)}(i)\cdot Y^{(k)}(j)|\psi'\rangle_{\text{ex}} &= -\frac{1}{2}\left|\langle\ell_1\|\,Y^{(k)}\,\|\ell_2\rangle\right|^2\sum_r(-1)^r(2r+1)\begin{Bmatrix}\ell_2 & \ell_1 & k\\ \ell_1 & \ell_2 & r\end{Bmatrix} \\ &\quad\times\langle\psi|\,U^{(r)}(1)\cdot u^{(r)}(2)+4V^{(r1)}(1)\cdot v^{(r1)}(2)|\psi'\rangle\end{aligned} \tag{4.33}$$

The first term of this expression is identical to the operator in Eq. 4.27, so this expression can be copied. The second term contains a scalar product of two direct products of irreducible tensor operators. To work this out, Eq. B.38 can be used. When the reduced matrix elements (Eqs. B.13, B.20 and B.22) are filled in, one finally obtains:

$$\begin{aligned}g_k\left(n_1\ell_1^{N_1}\,\alpha_1 L_1 L_1' S_1,\,n_2\ell_2^1\right) &= -\frac{1}{2}(2\ell_1+1)(2\ell_2+1)\begin{pmatrix}\ell_1 & k & \ell_2\\ 0 & 0 & 0\end{pmatrix}^2 \\ &\times\sum_r(-1)^r(2r+1)\begin{Bmatrix}\ell_2 & \ell_1 & k\\ \ell_1 & \ell_2 & r\end{Bmatrix}\Bigg[(-1)^{L_1'+L+\ell_2+L}\begin{Bmatrix}L_1' & \ell_2 & L\\ \ell_2 & L_1 & r\end{Bmatrix}\langle\ell_1^{N_1}\;L_1S_1\|\,U^{(r)}\,\|\ell_1^{N_1}\;L_1S_1\rangle \\ &+2\sqrt{6}(-1)^{L_1'+\ell_2+L+S_1'+1/2+S}\begin{Bmatrix}L_1' & \ell_2 & L\\ \ell_2 & L_1 & r\end{Bmatrix}\begin{Bmatrix}S_1' & 1/2 & S\\ 1/2 & S_1 & 1\end{Bmatrix}\langle\ell_1^{N_1}\;L_1S_1\|\,V^{(r1)}\,\|\ell_1^{N_1}\;L_1S_1\rangle\Bigg]\end{aligned} \tag{4.34}$$

4.1.4 Spin-orbit interaction

As already explained in §2.1.2, relativistic effects are not accounted for in the Schrödinger equation, possibly leading to incorrect results if no appropriate measures are taken. An important correction term, which can be derived from the Dirac equation, is the spin-orbit coupling, described by the Hamiltonian:

$$\mathcal{H}_{\mathrm{so}} = \sum_{i=1}^{N} \xi(r_i)\boldsymbol{\ell}_i \cdot \boldsymbol{s}_i. \tag{4.35}$$

It is a single-particle interaction, simplifying the calculation of matrix elements. In the case nonequivalent electrons are present, the Hamiltonian can be evaluated for each shell separately, and the results added. On the other hand, the calculation becomes more involved because the tensor operator is non-scalar. The expression for the function $\xi(r_i)$ follows from Dirac's equation. It contains the gradient of the scalar potential, ϕ (see §2.2.1) and it is implicitly assumed that ϕ depends only on r.

It can be verified that the commutators of $\mathcal{H}_{\mathrm{so}}$ with L^2, L_z, S^2 and S_z are nonzero. For this reason, L, S, M_L and M_S cease to be good quantum numbers when $\mathcal{H}_{\mathrm{so}}$ is taken into account. It is easily shown that both $\mathcal{H}_{\mathrm{so}}$ and the other terms in the atomic Hamiltonian commute with J^2 and J_z, where J corresponds to the total angular moment $\boldsymbol{J} = \boldsymbol{L} + \boldsymbol{S}$ [9]. For this reason, the label J (and M_J) are added to the mp basis states. $\mathcal{H}_{\mathrm{so}}$ is evidently diagonal with respect to these quantum numbers.

For a shell $n\ell^N$, the matrix elements of $\mathcal{H}_{\mathrm{so}}$ are evaluated as follows:

$$\langle n\ell^N\, LSJ| \sum_{i=1}^{N} \xi(r_i)\boldsymbol{\ell}_i\cdot\boldsymbol{s}_i |n\ell^N\, L'S'J\rangle = \underbrace{\langle n\ell^N\, LSJ| \sum_{i=1}^{N} \boldsymbol{\ell}_i \cdot \boldsymbol{s}_i |n\ell^N\, L'S'J\rangle}_{A_{\mathrm{so}}(\ell^N\, LL'SS'J)} \underbrace{\int_0^\infty \mathrm{d}r\, r^2 R_{n\ell}^2(r)\xi(r)}_{\zeta_{n\ell}}, \tag{4.36}$$

again separating angular and radial contributions. The angular integral can be calculated analytically when the tensor character of the operator is recognized. $\boldsymbol{\ell}_i \cdot \boldsymbol{s}_i$ can be considered as a scalar product of two rank-1 tensor operators, working on different Hilbert spaces (see appendix B).

The Wigner-Eckart theorem can be used to decouple L and S according to Eq. B.32:

$$\begin{aligned} A_{\mathrm{so}}(\ell^N\, LL'SS'J) &= (-1)^{L'+S+J} \begin{Bmatrix} L' & S' & J \\ S & L & 1 \end{Bmatrix} \\ &\quad \times \sum_{\alpha''} \langle \ell^N\, \alpha L \| \boldsymbol{\ell}^{(1)} \| \ell^N\, \alpha'' L' \rangle \langle \ell^N\, \alpha'' S \| \boldsymbol{s}^{(1)} \| \ell^N\, \alpha' S' \rangle, \end{aligned} \tag{4.37}$$

[9] Angular momentum algebra applies, so $J = |L-S|, \ldots, L+S$ and $M_J = -J, \ldots, J$.

where the definition of the direct product $V^{(11)}$, Eq. B.22, can be recognized, up to a factor $\langle \ell \| \boldsymbol{\ell} \| \ell \rangle$ (Eq. B.17). The result is then immediately found:

$$A_{\mathrm{so}}(\ell^N\ LL'SS'J) = (-1)^{L'+S+J}\sqrt{(2\ell+1)(\ell+1)\ell} \times \begin{Bmatrix} L' & S' & J \\ S & L & 1 \end{Bmatrix} \langle n\ell^N\ \alpha LS \| V^{(11)} \| n\ell^N\ \alpha' L'S' \rangle \tag{4.39}$$

and shows clearly that spin-orbit interaction can mix basis states with different S and L.

4.1.5 Coupling schemes

At this point, the two most important corrections to the central field model were discussed. The relative size of the Russell-Saunders interaction and the spin-orbit coupling changes from atom to atom. For the radial wave functions of a one-electron atom, it is possible to derive a Z^4 dependence of $\zeta_{n\ell}$, indicating that the magnitude of the spin-orbit coupling shows an increase upon proceeding through the periodic table.

In the case of two interactions, three different coupling schemes are possible. In the Russell-Saunders coupling case, first $\mathcal{H}_{\mathrm{RS}}$ is diagonalized, *i.e.* by working in the RS basis, $|\ell^N\ \alpha LS\rangle$ as explained above. Subsequently, $\mathcal{H}_{\mathrm{so}}$ is evaluated in the separate eigenspaces of $\mathcal{H}_{\mathrm{RS}}$, leading to an additional splitting with respect to J, *i.e.* one obtains the kets $|\ell^N\ \alpha LSJ\rangle$ as solutions.

Alternatively, in the so-called jj coupling case, $\mathcal{H}_{\mathrm{so}}$ is first diagonalized. In this regime, the single-electron labels m_ℓ and m_s do not have a proper meaning, but the individual total momenta and projections, corresponding to $\boldsymbol{j}_i = \boldsymbol{\ell}_i + \boldsymbol{s}_i$, do. As $s = 1/2$, two subshells are found for every ℓ^N shell, $j_+ = \ell + 1/2$ and $j_- = \ell - 1/2$. The jj terms are then labeled by $|\ell^N\ \alpha_+ j_+^{N_+},\ \alpha_- j_-^{N_-}\rangle$ with $N_+ + N_- = N$. Similar as in the RS states, additional labels are required to obtain unambiguous labeling of the coupled subshells. These are included in the α's and represent a seniority label v, and one additional label, often denoted as Nr. Upon inclusion of $\mathcal{H}_{\mathrm{RS}}$, the individual j^2 cease to commute with the Hamiltonian and additional multiplet splitting for every jj configuration is caused according to the total momentum J. The kets $|\ell^N\ \alpha_+ j_+^{N_+} J_+,\ \alpha_- j_-^{N_-} J_-;\ J\rangle$ are then found as solutions.

The disadvantage of both coupling schemes is that the second Hamiltonian is evaluated in the eigenspaces of the first Hamiltonian, allowing no interaction between the different eigenspaces. This approximation is only valid if the ratio of the magnitudes of the matrix elements is very small. Two reasons are thinkable why this approach is nevertheless sometimes followed. First, the expressions for the diagonal matrix elements are often simpler than for the non-diagonal matrix elements. Second, the computational cost is reduced as the diagonalization of a large matrix is avoided.

Both reasons do not apply for our case as computational cost is almost no longer an issue and we have general formulas at our disposal (*e.g.* Eq. 4.14 and Eq. 4.39). Therefore, the complete Hamiltonian is evaluated and diagonalized according to the intermediate coupling scheme. Two choices for basis states are possible, *i.e.* the RS or jj states. As the RS basis states are closer to reality for most atoms, they are a natural choice. The kets $|\ell^N\ \alpha LSJ\rangle$ are thus no longer regarded as physical eigenstates, but as the basis vectors into which the physical eigenstates are expanded. Often, the basis state with the highest expansion coefficient is used to label a state in energy level diagrams, increasing readability. If jj labels are required, a matrix of basis transformation can be obtained by means of Racah algebra.

Figure 4.2 shows intermediate coupling calculations for a $n\mathrm{p}^3$ configuration, illustrating that the RS coupling is well reproduced for the light elements N, P and As ($n = 2, 3, 4$), while intermediate coupling is required to have a good description of the heavier element Sb ($n = 5$). For Bi ($n = 6$), jj coupling can give a reasonably good description. The color of the curves illustrates the breakdown of S as a good quantum number.

In the pure jj coupling case, an IPM is again obtained as the two-particle interaction vanishes. The IPM is characterized by equidistant energy levels in a total energy diagram, corresponding to the binding energy difference between the orbitals. The sp energy level scheme is shown for the ground state and different excited states (Fig. 4.2).

4.1.6 Additional interactions

If the atomic Hamiltonian correcting the central field solution is restricted to the Russell-Saunders and spin-orbit interactions, a suboptimal description of experimental spectra is obtained, indicating that something is overlooked. Over time, multiple additional terms were added to the Hamiltonian in order to improve the correspondence with experimental spectra.

The first correction term to the atomic Hamiltonian was phenomenologically found by Richard E. Trees in 1951 [55, 56]. Based on the observation for $3\mathrm{d}^N$ configurations that the error decreased upon increasing N, he found that adding a term proportional to $L(L+1)$ could decrease the overall error by a factor of 2 to 8 [55]. Ten years later, Racah found that including a second additional term, proportional to the seniority operator, Q, could improve the description by another 20% [57].

A physical interpretation of these terms was found later by Rajnak and Wybourne [58]. They calculated the effect of configuration interaction, emerging in second order perturbation theory with respect to the central field solutions (see §4.1.1):

$$\Delta E(\psi a) = \sum_{\psi'} \sum_{a} \frac{\left|\langle \psi' a' | \mathcal{H}_{\mathrm{RS}} + \mathcal{H}_{\mathrm{so}} | \psi a \rangle\right|^2}{E_\psi - E_{\psi'}}. \tag{4.40}$$

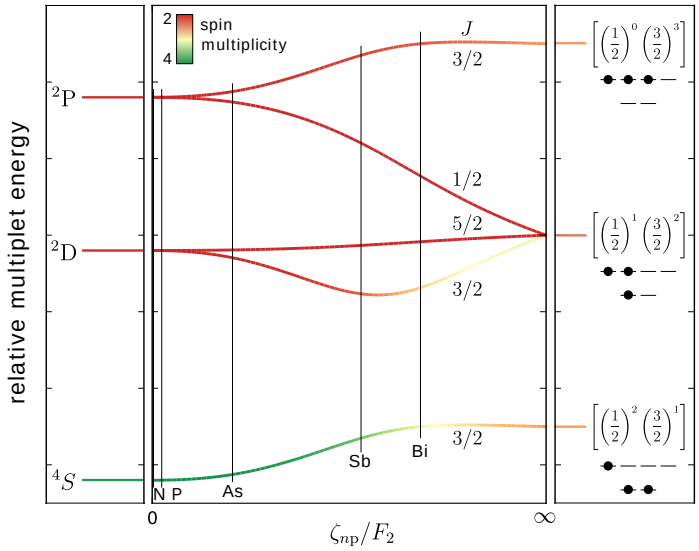

Figure 4.2 – Intermediate coupling calculations for an np^3 configuration. The color of the lines encodes the content of spin-doublet ($S = 1/2$) and spin-quartet ($S = 3/2$) character in the eigenstates, illustrating the breakdown of Russell-Saunders coupling for heavier elements. The vertical lines represent the experimental parameter ratio. The single-particle energy level schemes for the different excited states in the jj extreme case are shown in the right box where a black dot represents an occupied orbital.

Here, the notation ψ signifies configurations, *e.g.* ℓ^N, and $|a\rangle$ the states, found from first order perturbation theory, *e.g.* $|\alpha LSJ\rangle$. The primed symbols pertain to the configurations that interact with the configuration under study, with unprimed symbols. Elaborating this expression yields different contributions:

$$\Delta E(\psi a)_1 = \sum_{\psi'} \sum_{a} \frac{\langle \psi a | \mathcal{H}_{\mathrm{RS}} | \psi' a' \rangle \langle \psi' a' | \mathcal{H}_{\mathrm{RS}} | \psi a \rangle}{E_\psi - E_{\psi'}} \tag{4.41}$$

$$\Delta E(\psi a)_2 = 2 \sum_{\psi'} \sum_{a} \frac{\langle \psi a | \mathcal{H}_{\mathrm{RS}} | \psi' a' \rangle \langle \psi' a' | \mathcal{H}_{\mathrm{so}} | \psi a \rangle}{E_\psi - E_{\psi'}} \tag{4.42}$$

$$\Delta E(\psi a)_3 = \sum_{\psi'} \sum_{a} \frac{\langle \psi a | \mathcal{H}_{\mathrm{so}} | \psi' a' \rangle \langle \psi' a' | \mathcal{H}_{\mathrm{so}} | \psi a \rangle}{E_\psi - E_{\psi'}} \tag{4.43}$$

In the Russell-Saunders coupling regime, $\Delta E(\psi a)_1$ is expected to give the largest contribution. It was calculated by Rajnak and Wybourne for the ℓ^N configuration, interacting with multiple other configurations. They were able to show that a large part of $\Delta E(\psi a)_1$ can be described by a linear combination of the two-particle tensor operators $\sum_{i<j=1}^{N} u^{(k)}(i) \cdot u^{(k)}(j)$. The terms with even k produce exactly the same form as the RS interaction (see §4.1.2) , while the tensor operators in the terms with odd k were not yet encountered. By rearranging the odd operators according to the parentage groups, Rajnak and Wybourne retrieved the following matrix elements [58]:

$$\begin{aligned}
\langle \mathrm{d}^N\ \alpha LS | \mathcal{H}_{\mathrm{ci-2}} | \mathrm{d}^N\ \alpha' L' S' \rangle &= \delta_{\alpha\alpha'} \delta_{LL'} \delta_{SS'} \Big(\alpha\ \langle \mathrm{d}^N\ \alpha LS |\ \mathcal{G}[\mathrm{SO}_L(3)]\ | \mathrm{d}^N\ \alpha LS \rangle \\
&\qquad + \beta\ \langle \mathrm{d}^N\ \alpha LS |\ \mathcal{G}[\mathrm{SO}(5)]\ | \mathrm{d}^N\ \alpha' L' S' \rangle \Big) \\
\langle \mathrm{f}^N\ \alpha LS | \mathcal{H}_{\mathrm{ci-2}} | \mathrm{f}^N\ \alpha' L' S' \rangle &= \delta_{\alpha\alpha'} \delta_{LL'} \delta_{SS'} \Big(\alpha\ \langle \mathrm{f}^N\ \alpha LS |\ \mathcal{G}[\mathrm{SO}_L(3)]\ | \mathrm{f}^N\ \alpha LS \rangle \\
&\qquad + \beta\ \langle \mathrm{f}^N\ \alpha LS |\ \mathcal{G}[\mathrm{G}_2]\ | \mathrm{f}^N\ \alpha' L' S' \rangle \\
&\qquad + \gamma\ \langle \mathrm{f}^N\ \alpha LS |\ \mathcal{G}[\mathrm{SO}(7)]\ | \mathrm{f}^N\ \alpha' L' S' \rangle \Big).
\end{aligned} \tag{4.44}$$

The first and second term indeed correspond to the phenomenological $L(L+1)$ (see Eq. A.30) and $\mathcal{Q}$ (see Eq. 4.21) corrections of Trees and Racah. An additional term is found for f^N configurations. The radial integrals, α, β and γ are now known as Trees' parameters.

In their work on Coulomb CI, $\Delta E(\psi a)_1$, Rajnak and Wybourne found that for specific configurations, interacting with the ℓ^N configuration under study, terms of the form $\sum_{i\neq j\neq h}^{N} [[u^{(k_1)}(i) u^{(k_2)}(j)]^{(k)} u^{(k)}(h)]^{(0)}$, *i.e.* including the coordinates of three electrons, emerge [58]. This was formalized by Judd, using the parentage groups, who found that six or two additional terms are needed for f^N or d^N configurations, respectively

[59][10]:

$$\langle \ell^N\ \alpha LS|\mathcal{H}_{\mathrm{ci-3}}|\ell^N\ \alpha' L'S'\rangle = \sum_i T^i\ \langle \ell^N\ \alpha LS|t_i|\ell^N\ \alpha' L'S'\rangle, \tag{4.45}$$

where T^i are the radial integrals. Of course, $\mathcal{H}_{\mathrm{ci-3}}$ does only yield nontrivial contributions for $N \geq 3$.

A smaller, but measurable effect is expected from $\Delta E(\psi a)_2$, which is referred to as the electrostatically correlated spin-orbit interaction, while the CI effect, purely from spin-orbit coupling is expected to be several orders of magnitude smaller in situations close to Russell-Saunders coupling [60]. The effect of $\Delta E(\psi a)_2$ is expected to be of comparable magnitude to higher order magnetic interactions, treated at first order perturbation theory [61].

These magnetic interactions have the same origin as spin-orbit coupling, *i.e.* from relativistic quantum mechanics as described by the Dirac equation. Many different interactions emerge simultaneously in the non-relativistic limit when inspecting Breit's equation, a many-body equation, derived from Dirac's equation [62]. Retardation of the Coulomb interaction, magnetic orbit-orbit interaction and the contact interaction between electron spins yield tensor operators which are already covered by other interactions, discussed above. Only the spin-spin and the spin-other-orbit interactions have an operator form which is fundamentally different. Their expressions were already calculated by Marvin in 1947 [63]. It lasted until 1968 before they got embodied into lanthanide spectroscopy [61]. The matrix elements factorize according to:

$$\langle \ell^N\ \alpha LS|\mathcal{H}_{\mathrm{ss+soo}}|\ell^N\ \alpha' L'S'\rangle = \sum_{i=0,2,4} M^i\ \langle \ell^N\ \alpha LS|m_i|\ell^N\ \alpha' L'S'\rangle. \tag{4.46}$$

The radial integrals, M^i are referred to as the Marvin parameters.

A large part of $\Delta E(\psi a)_2$ contains the same tensor operators as Eq. 4.46 [61]. The remaining contributions are collected in three new operators:

$$\langle \ell^N\ \alpha LS|\mathcal{H}_{\mathrm{ecso}}|\ell^N\ \alpha' L'S'\rangle = \sum_{i=2,4,6} P^i\ \langle \ell^N\ \alpha LS|p_i|\ell^N\ \alpha' L'S'\rangle, \tag{4.47}$$

which concludes the long list of interaction Hamiltonians used to describe the electronic structure of ℓ^N shells.

In practical applications, the Trees correction is typically the only additional term in the Hamiltonian for d^N configurations. However in the case of f^N configurations, for which more transition energies can typically be resolved from the spectra, more additional terms are usually taken into account.

[10] Strangely, this interaction term is in literature often referred to as a three-body interaction, although it originates from interelectronic Coulomb repulsion, a two-body interaction. Up to four electron coordinates can however occur in matrix elements of two-body operators.

4.1.7 Summary and interpretation

When all contributions that were discussed in previous sections are gathered together, the free ion Hamiltonian for a general configuration $\ell_1^{N_1}\ldots\ell_r^{N_r}$ is obtained[11]:

$$\mathcal{H}_0(\ell_1^{N_1}\ldots\ell_r^{N_r}) = \sum_{i=1}^{r}\mathcal{H}_0(\ell_i^{N_i}) + \sum_{i<j=1}^{r}\left(\sum_k f_k(\ell_i,\ell_j)F^k(\ell_i,\ell_j) + \sum_k g_k(\ell_i,\ell_j)G^k(\ell_i,\ell_j)\right), \tag{4.48}$$

with

$$\mathcal{H}_0(\mathrm{d}^N) \quad = \quad E_{\text{centr. field}}(\mathrm{d}^N) + \sum_{k=2,4} f_k F^k + \zeta_{n\mathrm{d}} A_{\mathrm{so}} + \alpha L(L+1) + \beta\mathcal{Q}, \tag{4.49}$$

or

$$\begin{aligned}\mathcal{H}_0(\mathrm{f}^N) \quad = \quad & E_{\text{centr. field}}(\mathrm{f}^N) + \sum_{k=2,4,6} f_k F^k + \zeta_{n\mathrm{f}} A_{\mathrm{so}} + \alpha L(L+1) + \beta\mathcal{G}[\mathrm{G}_2] \\ & + \gamma\mathcal{G}[\mathrm{SO}(7)] + \sum_i t_i T^i + \sum_{i=0,2,4} m_i M^i + \sum_{i=2,4,6} p_i P^i,\end{aligned} \tag{4.50}$$

for each shell of equivalent electrons. Every term is composed of two factors, an angular integral for which an analytical expression is available, and a radial integral which has to be obtained in another way. Most commonly, radial integrals are treated as empirical parameters and fitted to experimental spectra. Different theoretical frameworks exist, allowing to calculate radial integrals from more fundamental principles. This is elaborated in §4.2.4.

Remarkably, the treatment of higher order interactions in §4.1.6 brings to light that parts of these additional terms have the same functional dependence as the RS and spin-orbit interactions. This has some important consequences. When radial integrals are obtained by fitting a Hamiltonian to experimental spectra, these need to be interpreted as *effective* parameters, not necessarily only quantifying the *primary suspect* interaction, but equally containing contributions of other interactions with (partially) the same transformation behavior. If radial integrals are calculated within some theoretical framework, it is for this reason of importance to know exactly which interactions are included in order to be able to compare calculated with empirical parameters.

It is in this context that the notion of an effective Hamiltonian can be explained, which is defined as a Hamiltonian which acts in a finite subspace of the Hilbert space, called model space and which gives rise to the same eigenvalues as the exact Hamiltonian in the full Hilbert space. The effective Hamiltonian's eigenfunctions are referred to as the model eigenfunctions [64]. $\mathcal{H}_0$ is considered as an effective Hamiltonian as its *active space* is limited to a single configuration of the N valence

[11] In these expressions, the use of a diversifying notation for operators, matrix elements and eigenvalues as was persevered up to now, was abandoned in imitation of most scientific literature.

electrons.

Now that the theory for the atomic states is well developed, it should - according to the atomic picture - be possible to understand the electronic structure and optical spectra of these metal atoms as impurities in crystals with only a small additional effort. This small additional effort is called crystal field theory and adds - maybe unsurprisingly at this point - another set of terms to the effective Hamiltonian.

4.2 Crystal field theory

The basic ideas of crystal field theory (CFT) were devised in the 1930s by Hans Bethe and John Hasbrouck Van Vleck. This theory allowed them to qualitatively understand the colors and magnetic properties of transition metal salts. To appreciate the innovative aspect of their work, one should realize that representation theory of point groups was not yet available at that time, necessitating Bethe to develop this tool. Also the notion of a double group (see appendix A) is due to him.

The original theory was characterized by two major lines of reasoning. First, group theoretical arguments were used to predict the splitting of degenerate states due to the symmetry lowering in crystals. These arguments are explained for different coupling schemes in §4.2.1. Second, splitting energies could be calculated by the parametrization of the crystal field interaction by a point charge electrostatic model (PCEM) where the atoms of the host crystal, or more specifically the anions in the first coordination shell, are envisaged as point charges with charge equal to their oxidation state, localized on their lattice site.

As the PCEM model is not well suited to describe reality, improvements to the model have been proposed throughout the years. In particular ligand field theory (LFT) is worth mentioning. Here, molecular orbital theory is applied to the chemical bonding between the metal atom and its neighbors, so-called ligands. The result is a molecular orbital diagram containing single-particle levels which are filled by valence electrons of both the metal and the ligands. Many-electron states can be obtained by suitable linear combinations of the obtained Slater determinants.

In fact, CFT can be perfectly formulated from symmetry arguments without deciding how the crystal field should be parametrized, be it by a PCEM, or a more advanced model taking wave function overlap, ligand polarization and other effects into account. For this reason, the distinction between CFT and LFT can be considered as a historical artifact and the designation CFT will be used in the remainder.

A very persistent notation that modern research has inherited from the old PCEM model and which might lead to confusion, is $10Dq$. It emerges if the crystal field splitting in the PCEM is calculated for a single d electron in the field of point charges, positioned in an octahedron while neglecting spin-orbit coupling or any other additional interaction. For the octahedral symmetry, the fivefold degenerate sp level of

the d electron splits into two levels with remaining twofold and threefold degeneracy. Within the PCEM, the splitting energy between the sp levels reads:

$$\Delta\epsilon = 10 \times \underbrace{\frac{35Ze^2}{16\pi\epsilon_0 d^5}}_{D} \times \underbrace{\frac{2}{105}\int_0^\infty \mathrm{d}r r^2\, R_{n\mathrm{d}}(r)\, r^4\, R_{n\mathrm{d}}(r)}_{q}. \tag{4.51}$$

Although $10Dq$ is also used to quantify ´´crystal field splitting´´ for many-electron systems, one should be aware that this designation is purely phenomenological since a larger number of splitting mp levels are present and sp levels are in general terms meaningless for the correlated many-electron systems.

4.2.1 Coupling schemes

The interaction of the valence electrons of the metal ion with the host crystal can be described by an effective Hamiltonian, $\mathcal{H}_{\mathrm{cf}}$, which can be added to Eq. 4.48. Before we discuss the details of this Hamiltonian and how matrix elements can be calculated, a general discussion about the symmetry of this Hamiltonian and the magnitude of its matrix elements with respect to those of other Hamiltonians, in particular $\mathcal{H}_{\mathrm{RS}}$ and $\mathcal{H}_{\mathrm{so}}$, can offer interesting physical insights.

Symmetry operations for the metal atom in a crystal are very much restricted with respect to the atom in a free state. Under the assumption of a perfect incorporation in the host crystal[12], the symmetry operations are those of the point group of the lattice site, *i.e.* $\mathcal{H}_{\mathrm{cf}}$ commutes with these symmetry operations. $\mathcal{H}_0$ obviously commutes as well with these operations as the point group is a subgroup of the rotation group. On the other hand, $\mathcal{H}_{\mathrm{cf}}$ does not commute with all operations of SO(3). Therefore, angular momentum labels cease to be good labels and the irreps of the point group have to be used to label the eigenstates of $\mathcal{H}_0 + \mathcal{H}_{\mathrm{cf}}$. However, similar as explained in §4.1.5, it is sometimes a good approximation to treat the Hamiltonians consecutively, leading to solutions where the angular momentum labels can still have a meaning. If we assume RS coupling, three possible CF coupling schemes are thinkable:

- weak crystal field: $\langle\mathcal{H}_{\mathrm{cf}}\rangle \ll \langle\mathcal{H}_{\mathrm{so}}\rangle \ll \langle\mathcal{H}_{\mathrm{RS}}\rangle$,
- intermediate crystal field: $\langle\mathcal{H}_{\mathrm{so}}\rangle \ll \langle\mathcal{H}_{\mathrm{cf}}\rangle \ll \langle\mathcal{H}_{\mathrm{RS}}\rangle$,
- strong crystal field: $\langle\mathcal{H}_{\mathrm{so}}\rangle \ll \langle\mathcal{H}_{\mathrm{RS}}\rangle \ll \langle\mathcal{H}_{\mathrm{cf}}\rangle$.

The orders of magnitude of these three interactions for the different types of valence electrons are summarized in Tab. 4.1. In this table, the increase of the strength of the spin-orbit coupling with the atomic number is evident. Furthermore, it is striking that the crystal field strength is much smaller for $n\mathrm{f}^N$ configurations than for the other configurations. This can be explained when the electron density is studied as

[12] By this, it is meant that only the translation symmetry of the host crystal is broken, *i.e.* the point group remains the same. This assumption can be incorrect if the doping causes strain in the crystal or when the metal defect favors other defects in its close environment.

Table 4.1 – Typical order of magnitude for the matrix elements of different Hamiltonians for d block and f block electron configurations. All values in eV.

	$\mathcal{H}_{\mathrm{RS}}$	$\mathcal{H}_{\mathrm{so}}$	$\mathcal{H}_{\mathrm{cf}}$
$3d^N$	1-10	0.1	1.0
$4d^N$	1-10	0.1-1	1.0
$5d^N$	1-10	1.0	1.0
$4f^N$	1-10	0.1-1	0.01
$5f^N$	1-10	1.0	0.01-0.1

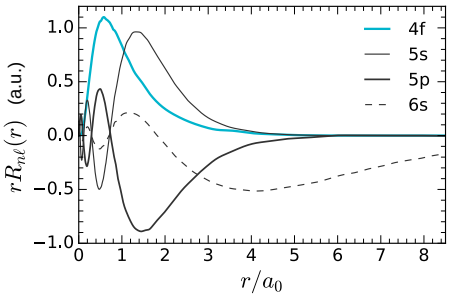

Figure 4.3 – Radial wave functions $rR_{n\ell}(r)$ for a europium atom, obtained by a Hartree-Fock calculation [65]. While the 6s electrons are removed upon formation of the Eu^{2+} and Eu^{3+} ions, the filled 5s and 5p shells are unaffected and screen the 4f valence electrons from the crystal environment.

a function of radial distance for the different shells (see Fig. 4.3). It happens that the 4f valence electrons of the lanthanides and the 5f valence electrons of the heavy actinides are well shielded from the crystal field by filled 5s, 5p and 6s, 6p shells, respectively[13].

In the following paragraph, the electronic states originating from the three perturbation schemes are discussed. This discussion is limited to a single shell of equivalent electrons, ℓ^N. In the case of a configuration with more shells, other coupling schemes exist. In §4.5.3, this is demonstrated for a particular example, $4f^{N-1}5d^1$ configurations, which are of importance for the spectroscopy of lanthanides. The results of the representation theory of point groups required to support this discussion are summarized in appendix A.

Weak crystal field

In the weak field perturbation scheme, the crystal field can be seen as a perturbation on the free ion's multiplets. This is the case of nf^N configurations. The r crystal field levels can be simply found upon reducing according to the label J, which can be regarded as a good quantum number in this limiting case:

$$\mathcal{D}^{(J)} = \bigoplus_{i=1}^{r} a_i \Gamma^{(i)}. \tag{4.52}$$

As J is half integer for an odd number of electrons, the reduction is generally performed for the double group (see §A.4.2). The labels of the crystal field levels are

[13] This effect is less pronounced for the lighter actinides [66].

$|\ell^N\ \alpha LSJ\ a\Gamma\rangle$ where a is the branching multiplicity and Γ denotes the irrep. If some degeneracy remains, the different partners of the irreps can be labeled by an additional row index γ. These symmetry adapted linear combinations (SALCs) can be obtained from,

$$|\ell^N\ \alpha LS\ Ja\Gamma\gamma\rangle = \sum_{M=-J}^{J} \langle JM|Ja\Gamma\gamma\rangle |\ell^N\ \alpha LSJM\rangle, \tag{4.53}$$

upon calculation of the reduction coefficients.

Intermediate crystal field

In the case of an intermediate crystal field, term splitting according to $\mathcal{H}_{\mathrm{RS}}$ is dominant. Therefore, the terms $|\ell^N\ \alpha LS\rangle$ are the starting point. The crystal field is spin-independent and acts therefore only on the orbital angular momentum:

$$\mathcal{D}^{(L)} = \bigoplus_{i=1}^{r} a_i \Gamma_L^{(i)}. \tag{4.54}$$

While L ceases to be a good quantum number at this point, S is unaffected and the resulting levels are $(2S+1)d_\Gamma$ degenerate, with d_Γ the dimension of irrep Γ, and labeled by $|\ell^N\ \alpha L\Gamma\ S\rangle$, or shorter ${}^{2S+1}\Gamma$.

In the double group, $\mathcal{D}^{(S)}$ shows following reduction:

$$\mathcal{D}^{(S)} = \bigoplus_{j=1}^{s} a_j \Gamma_S^{(j)}. \tag{4.55}$$

The ${}^{2S+1}\Gamma$ levels will show additional splitting due to the (weak) spin-orbit coupling according to:

$$\begin{aligned} {}^{2S+1}\Gamma_L^{(i)} \quad \rightarrow \quad \Gamma_L^{(i)} \otimes \mathcal{D}^{(S)} \quad &= \quad \bigoplus_{j=1}^{s} a_j \left(\Gamma_L^{(i)} \otimes \Gamma_S^{(j)} \right) \\ &= \quad \bigoplus_{j=1}^{s} a_j \bigoplus_{k=1}^{t} a_k \Gamma^{(k)} \end{aligned} \tag{4.56}$$

where the irreps belong to the double group. The associated kets can be obtained if the Clebsch-Gordan (or coupling) coefficients of the (double) point group are known in addition to the reduction coefficients:

$$\begin{aligned} |\ell^N\ \alpha(La_L\Gamma_L,\ Sa_S\Gamma_S)\ a\Gamma\gamma\rangle \quad = \quad \sum_{M_L M_S \gamma_L \gamma_S} & \langle LM_L|La_L\Gamma_L\gamma_L\rangle \langle SM_S|Sa_S\Gamma_S\gamma_S\rangle \\ & \times \langle \Gamma_L\gamma_L\Gamma_S a_S|a\Gamma\gamma\rangle |\ell^N\ \alpha LM_L SM_S\rangle. \end{aligned} \tag{4.57}$$

The intermediate crystal field terms are common in the literature on the electronic structure of transition metal $n\mathrm{d}^N$ shells.

Strong crystal field

In this coupling scheme, the crystal field is the dominant interaction. If we assume that the crystal field is described by a single-particle Hamiltonian, it will accordingly act on the individual orbital angular momenta:

$$\mathcal{D}^{(\ell)} = \bigoplus_{i=1}^{r} a_i \gamma^{(i)}. \tag{4.58}$$

Here, we copy the notation used in the atomic case that sp labels are small characters and those for coupled states capital symbols. The sp label for the irrep, $\gamma^{(i)}$ should not be confused with the symbol of partners.

If there are N valence electrons, these can be used to fill the crystal field orbitals according to an *aufbau* principle, $(a_1\gamma_1)^{n_1}(a_2\gamma_2)^{n_2}\ldots(a_r\gamma_r)^{n_r}$ with $n_1+n_2+\ldots+n_r = N$. In this context, the designation *configuration* is also used. Excited states are obviously found as particle-hole excitations. The energy spectrum will hence be the one of an IPM, characterized by sets of equidistant lines, depending on the remaining degeneracies and number of electrons, N. It is found by simply adding the sp energies:

$$E[(a_1\gamma_1)^{n_1}(a_2\gamma_2)^{n_2}\ldots(a_r\gamma_r)^{n_r}] = \sum_{i=1}^{r} n_i \epsilon_{a_i\gamma_i}. \tag{4.59}$$

Interelectronic Coulomb repulsion subsequently couples the orbitals to multiplets:

$$\bigotimes_{i=1}^{r} (\gamma^{(i)})^{n_i} = \bigoplus_{j=1}^{s} a_j \Gamma_L^{(j)}. \tag{4.60}$$

Spin labels are added while taking care of the required antisymmetry of the mp wave function and the result of spin-orbit coupling can finally be accounted for in a similar way as in Eq. 4.56. The strong field states are found from some more extensive, but straightforward algebra with recoupling and Clebsch-Gordan coefficients:

$$|\ell^N\ \alpha\,[((a_1\gamma_1)^{n_1}(a_2\gamma_2)^{n_2}\ldots(a_r\gamma_r)^{n_r})\ a_L\Gamma_L,\ a_S\Gamma_S]\ a\Gamma\gamma\rangle. \tag{4.61}$$

Single-particle crystal field models, as described by Eq. 4.58 and 4.59 are abundant in handbooks and scientific literature. This is undoubtedly due to its conceptual simplicity. However, it offers seldom a good description of reality if more than one valence electron is present. The d^N and f^N configurations are highly correlated and the many-particle effects can almost never be neglected. The closest agreement is found for transition metal complexes with CN^- or CO ligands [67].

4.2.2 One-electron crystal field hamiltonian

Crystal field potential

The most common crystal field Hamiltonian originates from the interaction of the metal's valence electrons with an external potential,

$$\mathcal{H}_{\mathrm{cf}} = -e \sum_{i=1}^{N} V(\boldsymbol{r}_i). \tag{4.62}$$

Here, $\mathcal{H}_{\mathrm{cf}}$ is a single-particle Hamiltonian. In the spirit of Bethe and Van Vleck, we tentatively parameterize the potential $V(\boldsymbol{r})$ as an electrostatic one:

$$V(\boldsymbol{r}_i) = \int \mathrm{d}^3\boldsymbol{r} \frac{\rho(\boldsymbol{r})}{4\pi\epsilon_0 |\boldsymbol{r} - \boldsymbol{r}_i|}, \tag{4.63}$$

where a general charge distribution $\rho(\boldsymbol{r})$ was chosen[14]. Later, it will become clear that the exact nature of the potential does not matter and the shortcomings of the electrostatic model can be easily overcome. Thanks to the factor $1/|\boldsymbol{r} - \boldsymbol{r}_i|$, a multipole expansion can be applied, analogously as in §4.1.2. It is assumed that the electrons are spatially separated from the charge density, *i.e.* $r > r_i$ and some manipulations on the spherical harmonics are performed:

$$\begin{aligned}
V(\boldsymbol{r}_i) &= \int \mathrm{d}^3\boldsymbol{r}\, \frac{\rho(\boldsymbol{r})}{4\pi\epsilon_0} \sum_{k=0}^{\infty} \frac{r_i^k}{r^{k+1}} \frac{4\pi}{2k+1} \sum_{q=-k}^{k} (-1)^q Y_{-q}^{(k)}(\Omega) Y_q^{(k)}(\Omega_i) \qquad (4.64)\\
&= \int \mathrm{d}^3\boldsymbol{r}\, \frac{\rho(\boldsymbol{r})}{4\pi\epsilon_0} \sum_{k=0}^{\infty} \frac{r_i^k}{r^{k+1}} \frac{4\pi}{2k+1} \\
&\qquad \times \left[Y_0^{(k)}(\Omega) Y_0^{(k)}(\Omega_i) + \sum_{q=1}^{k} (-1)^q \left(Y_{-q}^{(k)}(\Omega) Y_q^{(k)}(\Omega_i) + Y_q^{(k)}(\Omega) Y_{-q}^{(k)}(\Omega_i) \right) \right] \\
&= \int \mathrm{d}^3\boldsymbol{r}\, \frac{\rho(\boldsymbol{r})}{4\pi\epsilon_0} \sum_{k=0}^{\infty} \frac{r_i^k}{r^{k+1}} \frac{4\pi}{2k+1} \Bigg[Y_0^{(k)}(\Omega) Y_0^{(k)}(\Omega_i) \\
&\qquad + \sum_{q=1}^{k} \frac{1}{2} \left(\left(Y_{-q}^{(k)}(\Omega) + (-1)^q Y_q^{(k)}(\Omega) \right) \left(Y_{-q}^{(k)}(\Omega_i) + (-1)^q Y_q^{(k)}(\Omega_i) \right) \right) \\
&\qquad - \frac{1}{2} \left(\left(Y_{-q}^{(k)}(\Omega) - (-1)^q Y_q^{(k)}(\Omega) \right) \left(Y_{-q}^{(k)}(\Omega_i) - (-1)^q Y_q^{(k)}(\Omega_i) \right) \right) \Bigg].
\end{aligned}$$

[14] In the original CFT model, $\rho(\boldsymbol{r}) = \sum_{i=1}^{\mathrm{CN}} Q_i \delta(\boldsymbol{r} - \boldsymbol{r}_i)$, where CN is the coordination number, *i.e.* the number of nearest neighbors/ligands.

Upon introduction of the crystal field coefficients:

$$\mathcal{B}_{k0}(r_i) = \sqrt{\frac{4\pi}{2k+1}}\, r_i^k \int \mathrm{d}^3\, \boldsymbol{r}\rho(\boldsymbol{r})\, \frac{1}{r^{k+1}}\, Y_0^{(k)}(\Omega), \tag{4.65}$$

$$\mathcal{B}_{kq}(r_i) = \sqrt{\frac{4\pi}{2k+1}}\, r_i^k \int \mathrm{d}^3\, \boldsymbol{r}\rho(\boldsymbol{r})\, \frac{1}{r^{k+1}}\, \frac{1}{2}\left(Y_{-q}^{(k)}(\Omega) + (-1)^q Y_q^{(k)}(\Omega)\right), \tag{4.66}$$

$$\mathcal{B}'_{kq}(r_i) = \sqrt{\frac{4\pi}{2k+1}}\, r_i^k \int \mathrm{d}^3\, \boldsymbol{r}\rho(\boldsymbol{r})\, \frac{1}{r^{k+1}}\, \frac{\mathrm{i}}{2}\left(Y_{-q}^{(k)}(\Omega) - (-1)^q Y_q^{(k)}(\Omega)\right), \tag{4.67}$$

which depend only on the radial coordinate of the electrons and contain the details of the crystal field, the expression for the potential assumes a simpler form:

$$V(\boldsymbol{r}_i) = \sum_{k=0}^{\infty}\Bigg[\mathcal{B}_{k0}(r_i)C_0^{(k)}(\Omega_i) + \sum_{q=1}^{k}\mathcal{B}_{kq}(r_i)\left(C_{-q}^{(k)}(\Omega_i) + (-1)^q C_q^{(k)}(\Omega_i)\right) + \mathrm{i}\mathcal{B}'_{kq}(r_i)\left(C_{-q}^{(k)}(\Omega_i) - (-1)^q C_q^{(k)}(\Omega_i)\right)\Bigg]. \tag{4.68}$$

The normalized spherical harmonics were introduced:

$$C_q^{(k)}(\Omega_i) = \sqrt{\frac{4\pi}{2k+1}}\, Y_q^{(k)}(\Omega_i). \tag{4.69}$$

Matrix elements

The CF coefficients facilitate the calculation of matrix elements as a factorization in a radial and angular part is again possible. The radial part is obtained from the CF coefficients and defines the so-called crystal field parameters:

$$B_{k0} = -e\int_0^{\infty}\mathrm{d}r_i\; r_i^2 R_{n\ell}^2(r_i)\mathcal{B}_{k0}(r_i), \tag{4.70}$$

$$B_{kq} = -e\int_0^{\infty}\mathrm{d}r_i\; r_i^2 R_{n\ell}^2(r_i)\mathcal{B}_{kq}(r_i), \tag{4.71}$$

$$B'_{kq} = -e\int_0^{\infty}\mathrm{d}r_i\; r_i^2 R_{n\ell}^2(r_i)\mathcal{B}'_{kq}(r_i). \tag{4.72}$$

The angular part consists of combinations of the normalized spherical harmonics, $\sum_{i=1}^{N} C_q^{(k)}(\Omega_i)$. An analytic expression can be derived by means of Racah algebra. In

the RS basis, $|\ell^N\ \alpha LSJM\rangle$,

$$\begin{aligned}
&\langle \ell^N\ \alpha LSJM| \sum_{i=1}^{N} C_q^{(k)}(i) |\ell^N\ \alpha' L'S'J'M'\rangle \\
&\qquad = (-1)^{J-M} \begin{pmatrix} J & k & J' \\ -M & q & M' \end{pmatrix} N\, \langle \ell^N\ \alpha LSJ \| C^{(k)} \| \ell^N\ \alpha' L'S'J' \rangle \\
&\qquad = \delta_{SS'}\, (-1)^{2J-M+S+L'+k}\, N\, \sqrt{(2J+1)(2J'+1)} \begin{pmatrix} J & k & J' \\ -M & q & M' \end{pmatrix} \begin{Bmatrix} J & k & J' \\ L' & S & L \end{Bmatrix} \\
&\qquad\qquad \times \langle \ell^N\ \alpha LS \| C^{(k)} \| \ell^N\ \alpha' L'S \rangle \\
&\qquad = \delta_{SS'}\, (-1)^{2J-M+S+L'+k+\ell} \begin{pmatrix} \ell & k & \ell \\ 0 & 0 & 0 \end{pmatrix} \begin{pmatrix} J & k & J' \\ -M & q & M' \end{pmatrix} \begin{Bmatrix} J & k & J' \\ L' & S & L \end{Bmatrix} \\
&\qquad\qquad \times (2\ell+1)\, \sqrt{(2J+1)(2J'+1)}\, \langle \ell^N\ \alpha LS \| U^{(k)} \| \ell^N\ \alpha' L'S \rangle, \qquad (4.73)
\end{aligned}$$

where the Wigner-Eckart theorem was first applied, Eq. B.11, followed by a decoupling of L and S, Eq. B.33, while keeping in mind that the operator does not affect S. In the last step, the unit tensor, Eq. B.20, was introduced and Eq. B.13 applied.

The first Wigner-3j symbol in Eq. 4.73 also occurs in the matrix elements of $\mathcal{H}_{\text{RS}}$ for ℓ^N configurations, Eq. 4.14. Hence, the possible ranks of CF parameters are restricted to the same values as the ranks of Slater-Condon parameters, *i.e.* $k = 2, 4$ for d electrons while $k = 2, 4, 6$ for f electrons.

The matrix elements were calculated in the basis $|\ell^N\ \alpha LSJM\rangle$ which is straightforwardly available for all electron configurations. If $\mathcal{H}_{\text{cf}}$ is required in other bases, the matrix element can be calculated directly in the other basis or a suitable transformation of the matrix can achieve the same, *e.g.* Eq. 4.53 or Eq. 4.58.

Now that the exact formula for matrix elements is available for all interactions discussed in §4.2.1, calculations can be performed without making any assumptions on the coupling scheme by the exact diagonalization of the total Hamiltonian. This is similar to the intermediate coupling scheme for free ions, §4.1.5[15].

The B_{kq}/B'_{kq} parametrization of the crystal field is due to Brian G. Wybourne, one of the pioneers of lanthanide spectroscopy [68]. Other equivalent parametrization schemes are possible and can be found in literature, together with translation tables that relate the different schemes. Recalling from §4.2.1, $\mathcal{H}_{\text{cf}}$ should show the point group symmetry of the defect cluster. This puts additional restrictions on the number of $C_q^{(k)}$'s that will be present in the expansion. The higher the symmetry, the less terms are needed. Table 4.2 summarizes this number for the different point groups

[15] The designation intermediate coupling scheme asks for some cautiousness as it can pertain to the full diagonalization of the atomic Hamiltonian (§4.1.5), an approximate perturbation sequence for the crystal field (§4.2.1) or the full diagonalization of the total Hamiltonian as discussed here.

Table 4.2 – Number of one-electron crystal field parameters required for energy level calculations.

$\ell = 2$		$\ell = 3$	
# B_{kq}	groups	# B_{kq}	groups
14	C_i, C_1	27	C_i, C_1
8	C_2h, C_2, C_S	15	C_2h, C_2, C_S
5	D_2h, D_2, C_2v	12	C_3
4	C_3, S_6, C_4h, C_4, S_4	9	D_2h, D_2, C_2v, C_3, S_6
3	D_3d, D_3, C_3v, D_4h, D_2d,	7	C_4h, C_4, S_4
	D_4, C_4v	6	D_3d, D_3, C_3v
2	C_3h, C_5h, C_6h, C_5, C_6,	5	D_4h, D_2d, D_4, C_4v, C_3h, C_5h, C_6h,
	D_3h, D_6h, D_5d, D_5,		C_5, C_6
	D_6, C_5v, C_6v, D_5h, $D_{\infty\mathrm{h}}$,	4	D_3h, D_6h, D_5d, D_5, D_6, C_5v, C_6v
	D_4d, D_6d, $C_{\infty\mathrm{v}}$, S_8	3	D_5h, $D_{\infty\mathrm{h}}$, D_4d, D_6d, $C_{\infty\mathrm{v}}$, S_8
1	O_h, T_d	2	O_h, T_d
0	I_h	1	I_h

for d and f electrons.

The expansion of $\mathcal{H}_\mathrm{cf}$ in terms of spherical harmonics can be seen as a *general* single-electron Hamiltonian with the symmetry of the defect cluster. In other words, this Hamiltonian can be used without the need to restrict oneself to the electrostatic model that was used to derive it. Spherical harmonics form a special class of tensor operators as they form a complete set of orthogonal operators[16] [69,71]. The importance of operator orthogonality was stressed by Brian R. Judd, another pioneer of lanthanide spectroscopy, as a third criterion to select operators for effective Hamiltonians next to their physical interpretation and the availability of group theoretical methods to calculate matrix elements [71,72].

4.2.3 Correlation crystal field

Up to now, the crystal field effect was limited to a single-particle potential and one could wonder whether the two-particle interaction is well described for metal ions in a crystal field by the same method as for the free metal ion. It was found that the conventional crystal field description showed some remarkable discrepancies with the experiments for a few particular multiplets. This aberration could not be resolved by adding terms to the free ion Hamiltonian or tweaking its parameters. Therefore, it appeared that a generalization of the conventional CF model was necessary, paving the way for Bishton and Newman to propose an anisotropic two-particle interaction [73]. Judd and Read worked out the possible orthogonal tp operators by means of Racah's parentage groups, yielding the modern version of the correlation crystal

[16] Two operators, $\mathcal{O}_1$ and $\mathcal{O}_2$ are orthogonal if $\mathrm{Tr}(\mathcal{O}_1\mathcal{O}_2) = 0$ [69,70].

field (CCF) [74,75]:

$$\mathcal{H}_{\mathrm{CCF}} = \sum_{iKQ} g_{iQ}^{(K)} G_{iQ}^{K}. \tag{4.74}$$

The $g_{iQ}^{(K)}$ are combinations of direct products of unit tensors, $[U^{k_1}(i)U^{k_2}(j)]_Q^{(K)}$. The disadvantage of this model is that a great number of parameters is added, complicating or precluding the comparison with experimental spectra. Without symmetry constraints, 637 CCF parameters are required for f electrons while still 41 CCF parameters are required for octahedrally coordinated f systems [70]. Fortunately, prescriptions are available that introduce an important part of the CCF effect while keeping the number of added parameters limited. A particularly successful model is the so-called spin-correlated crystal field.

Spin-correlated crystal field

The spin-correlated crystal field (SCCF) was devised by Judd as an alternative with less parameters, compared to the more general CCF. It was inspired by the phenomenological finding for the $4f^N$ spectra of lanthanides that sp CF parameters, able to reproduce CF levels of multiplets with a certain S value, failed notably when predicting the CF levels of a multiplet with a different S [70,76]. The form of the SCCF Hamiltonian was inspired by the spin-dependent Coulomb exchange interactions and is obtained with the substitution,

$$C_q^{(k)}(\Omega_i) \quad \rightarrow \quad (1 + c_k\, \boldsymbol{s}_i \cdot \boldsymbol{S})\; C_q^{(k)}(\Omega_i) \qquad (k = 2,4,6) \tag{4.75}$$

in the CF Hamiltonian, yielding:

$$\begin{aligned} \mathcal{H}_{\mathrm{sccf}} \;=\; \sum_k \Bigg[& \mathcal{B}_{k0}(r_i) C_0^{(k)}(\Omega_i) + \sum_{q=1}^{k} c_k \mathcal{B}_{kq}(r_i) \boldsymbol{s}_i \cdot \boldsymbol{S} \left(C_{-q}^{(k)}(\Omega_i) + (-1)^q C_q^{(k)}(\Omega_i) \right) \\ & + \mathrm{i} c_k \mathcal{B}'_{kq}(r_i) \boldsymbol{s}_i \cdot \boldsymbol{S} \left(C_{-q}^{(k)}(\Omega_i) - (-1)^q C_q^{(k)}(\Omega_i) \right) \Bigg]. \end{aligned} \tag{4.76}$$

which leads to a better agreement with experiment if added to the total Hamiltonian. The parameters c_k can be written as linear combination of a few CCF parameters [70].

4.2.4 Meaning and calculation of radial parameters

Up to now, only the general formalism of crystal field theory was explained. The short summary is that all relevant interactions are collected as different terms in an effective Hamiltonian. Each term of this Hamiltonian can be written as a product of an angular integral and a radial integral. The former are exactly calculable by means of the Wigner-Racah algebra, while for the latter analytical expressions cannot be obtained. The radial integrals can either be obtained from experimental spectra by a fitting procedure (see §4.4) or can be calculated numerically within a

theoretical framework of choice. Most of the theoretical methods available in literature do however use empirical input, although some authors have succeeded well in hiding this nuance. Still these models decrease the number of empirical parameters needed, which is especially interesting for low-symmetry complexes (see Tab. 4.2). In this paragraph, the most popular techniques to calculate radial integrals are briefly enumerated.

The parameterization which appeared historically as first is the point charge electrostatic model (PCEM) [77, 78]. Here, the nearest neighbors of the optically active metal ion are treated as fixed point charges, effecting a Stark splitting on the electron configuration of interest. A PCEM is intuitively simple and can explain certain observations in a qualitative fashion. Despite its didactic value, quantitative predictions are however far from reality as a consequence of the simplistic assumptions. In modern applications, the role of the PCEM is therefore limited to an initial guess for fitting procedures.

The superposition model (SM), which was developed by Newman and his coworkers in the 1960s decreases the number of empirical parameters of the general CF model by assuming that the contribution to the CF of every ligand can be superposed [70, 79, 80]. For every ligand, an axially symmetric crystal field ($C_{\infty v}$) is calculated, characterized by B_{k0}, which is then rotated and summed to construct the crystal field Hamiltonian for the first coordination shell. The atomic positions are assumed to be known for this procedure. In addition to this model, intrinsic parameters, $\overline{B}_k$ are introduced for every type of ligand, which can be transferred to other materials. To compensate for remaining discrepancies, an empirically determined factor depending on the binding distance is introduced.

In parallel with the development of the SM, Schäfer and Jørgenson developed what is called the angular overlap model (AOM) [70, 80–82]. This model assumes a superposable nature for the contributions of the different ligands, similar to the SM. The AOM parametrizes the matrix elements of the sp crystal field Hamiltonian directly, rather than yielding coefficients for an expansion in irreducible tensor operators. The formulation of the AOM parameters is inspired by molecular orbital theory, where σ-, π- or δ- molecular orbitals are found, centered at the metal site. For this reason, the AOM can be interpreted as a quantitative formulation of LFT.

The exchange charge model (ECM), invented by B. Malkin in the 1970s, extends the PCEM model with wavefunction overlap directly at the level of CF parameters [83–85]. The PCEM parameters are supplemented by a term which contains overlap integrals that are calculated by a wave function-based quantum mechanical technique, typically Hartree-Fock. Moreover, this term contains an empirical factor which is calculated from the first absorption band.

The above models all have as disadvantage that they give no information on how the atomic parameters, most notably those describing the Coulomb interaction, are altered in the crystal field. However, it is empirically known that these can change

appreciably. As an example, the decrease of the free ion Racah parameters upon the formation of chemical bonds has obtained a dedicated name, *i.e.* the nephelauxetic effect [67, 86]. Models describing these effects are as a rule computationally more demanding than the simple models described above. Nonetheless, increasing computer power enables these models to be applied to systems that are studied experimentally.

Ligand field density functional theory (LFDFT) has been demonstrated to yield a satisfying description of the excited states of transition metal and lanthanide ions. This method, which was developed by M. Atanasov, C. Daul and C. Rauzy, can be regarded as a modern version of the SM or AOM [87–89]. First, an optimized geometry and electronic structure is obtained by density functional theory (DFT) calculations[17]. Although DFT is by definition not suited to describe excited states, a cunning procedure, where the single-particle states are combined into many-particle states, allows the user to distill Racah and CF parameters from the DFT calculation and hence obtain excitation energies in an indirect way.

A complementary method to obtain some information on excited states from *ordinary* DFT is upon forcing the system into a non-equilibrium orbital occupation. The difference in total energy can then be used to estimate the vertical excitation energy, while it is also possible to relax the geometry for the excited state to estimate the energy of the zero-phonon line. The limitation of this technique is that it can only be used to obtain energy differences for interconfigurational transitions. This use of DFT is further elaborated in §5.3 as it is more commonly applied within the band picture. Term- and multiplet splitting hamper a straightforward extension of this technique to interconfigurational transitions [90–94]. For the latter, LFDFT offers an alternative.

To meet with the restriction of DFT being a ground-state method, Runge and Gross developed a time-dependent variant of DFT (TD-DFT). By determining the connection between the time-dependent density and external potential via linear response theory, the excitation energies of the system can be found as the poles of the response function [95, 96]. While TD-DFT was able to prove its use in the description of excited states of organic systems, its successful application to d or f shell systems is limited, although its popularity is considerable given the relatively small threshold for users due to the limited required computer power and black-box behavior [97]. Reasons for the limited success can be found in the multiconfigurational nature of the systems and high degeneracies of open-shell configurations [97].

The multiconfigurational nature of the excited state landscape of the systems under study suggests the use of multiconfigurational quantum mechanical techniques such as CASSCF [97, 98]. Dynamic correlation can be included in perturbation theory, *cfr.* CASSCF/CASPT2 [97, 98]. While these and related techniques are by far the most involved of this list, concerning both required computer resources as

[17] For details on DFT, the reader is referred to §5.3 where this formalism is applied to other aspects of luminescent materials.

user-experience, they have resulted in accurate and above-all insightful results concerning the spectroscopy of d- and f-block elements, including information on the electron-vibrational coupling, in contrast to most of the above techniques [98–102]. To date, these calculations can therefore be regarded as the theoretical benchmark.

4.3 Electric dipole transitions

In the previous paragraphs, it was explained how the energy eigenvalues of the Hamiltonian are obtained. The energy differences between these eigenvalues yield the energies that can appear in experimental spectra. So far, it was however not yet discussed which transitions are allowed and what intensities to expect. In §2.3 it was shown that matrix elements of a transition moment have to be calculated. Under the assumption of the Born-Oppenheimer approximation and the Frank-Condon principle (see §3.2.1), only the electronic part, *i.e.* the intensity of the ZPL needs to be calculated. Here, we will restrict ourselves to electric dipole radiation[18].

Here, line strengths are inspected, defined as:

$$\mathcal{S}(\alpha LSJ, \alpha' L'S'J') = \sum_{MM'} \left| \langle \alpha LSJM | \boldsymbol{D} | \alpha' L'S'J'M' \rangle \right|^2, \tag{4.77}$$

for pure Russell-Saunders states. For intermediate coupling eigenstates, the appropriate linear combinations of Eq. 4.77 have to be made. Line strengths can be related to emission, excitation and absorption spectra in a straightforward way (see §2.3.2). Care should however be taken as the Einstein relations between the A and B coefficients are not necessarily found in real materials which are no two level systems. After absorption of a photon, a fast non-radiative relaxation can occur, dissipating part of the energy and messing up the detailed balance of Einstein. Nonetheless, the individual expressions for the coefficients can still be applied, provided the correct wave functions are used.

In spectroscopy, selection rules are of great interest. These rules tell when matrix elements such as Eq. 4.77 vanish. These rules can be found by direct calculation, or more interestingly by group theory. In the latter case, the irreps of a symmetry group of the system have to be identified for both wave functions and the operator. Generally written as

$$\left\langle f_\Gamma \middle| O_{\Gamma_1} \middle| g_{\Gamma_2} \right\rangle, \tag{4.78}$$

the matrix element will only be nonzero if the totally symmetric irrep is found in the reduction of the direct product $\Gamma \otimes \Gamma_1 \otimes \Gamma_2$ or similarly, when Γ is found in the reduction of $\Gamma_1 \otimes \Gamma_2$ (see appendix A).

[18] Here, M1 and E2 transitions are not considered although these can be indicative for certain spectroscopic studies.

Laporte rule

When the system contains a symmetry center, the irreps of the wave functions have a well-defined parity label, *i.e.* even or odd. Parity is defined as the eigenvalue of the parity operator, $\mathcal{P}$ which transforms $\boldsymbol{r}$ to $-\boldsymbol{r}$. The parity of an electron configuration is given by:

$$(-1)^{\sum_{i=1}^{N}\ell_i} \tag{4.79}$$

and does not depend on any other quantum number, *i.e.* parity is the same for every term or multiplet of the same configuration. As the parity of the electric dipole operator is odd, the parity of the initial and final wave function should be opposite for E1 transitions to be allowed. This is clearly not the case for intraconfigurational transitions such as $n\mathrm{d}^N \leftrightarrow n\mathrm{d}^N$ and $n\mathrm{f}^N \leftrightarrow n\mathrm{f}^N$ transitions. If the point group of the defect center is non-centrosymmetric, the Laporte rule does not strictly hold and a relaxation of the parity selection rule can be expected.

Matrix element

First, the dipole moment of the electrons is recast in irreducible tensor form:

$$D_q^{(1)} = -e\sum_{i=1}^{N} r_i C_q^{(1)}(\Omega_i). \tag{4.80}$$

Selection rules for the electric dipole transitions are found by applying the Wigner-Eckart theorem to the angular part,

$$\left\langle \alpha LSJM \left| C_q^{(1)} \right| \alpha' L'S'J'M' \right\rangle = (-1)^{J-M} \begin{pmatrix} J & 1 & J' \\ -M & q & M' \end{pmatrix} \langle \alpha LSJ \| C^{(1)} \| \alpha' L'S'J' \rangle. \tag{4.81}$$

The Wigner-3j symbol vanishes unless (see B.1):

$$\Delta J = 0, \pm 1 \qquad \text{except} \qquad J = J' = 0 \quad \text{is not allowed.} \tag{4.82}$$

These are the selection rules for E1 transitions. Additional selection rules can be found by decoupling J, Eq. B.33:

$$\langle \alpha LSJ \| C^{(1)} \| \alpha' L'S'J' \rangle = (-1)^{L+S+J'+1} \sqrt{(2J+1)(2J'+1)} \begin{Bmatrix} J & 1 & J' \\ L' & S & L \end{Bmatrix} \langle \alpha L \| C^{(1)} \| \alpha' L' \rangle. \tag{4.83}$$

yielding

$$\Delta S = 0 \qquad \text{and} \qquad \Delta L = 0, \pm 1. \tag{4.84}$$

In the intermediate coupling scheme, these rules get relaxed as spin-orbit coupling mixes states with different L and S (see §4.1.5).

The parity-allowed E1 transitions that are of relevance for phosphors are of the type $\ell^N \leftrightarrow \ell^{N-1}\ell'$ such as the $4\mathrm{f}^N \leftrightarrow 4\mathrm{f}^{N-1}5d^1$ transitions in lanthanides or the $n\mathrm{s}^2 \leftrightarrow$

ns^1np^1 transitions in s^2 ions. Their line strength can be obtained by elaborating the above matrix element, yielding [68]:

$$\begin{aligned}\mathcal{S}(n\ell^N\alpha LSJ,\, n\ell^{N-1}\alpha_1 L_1 S_1, n'\ell'; S'L'J') &= \delta_{SS'}N\ell'(2J+1)(2J'+1)(2L+1)(2L'+1)\\ &\times\begin{Bmatrix} J & 1 & J' \\ L' & S & L\end{Bmatrix}^2\begin{Bmatrix} L & 1 & L' \\ \ell' & L_1 & \ell\end{Bmatrix}^2\left|\langle \ell^{N-1}\ \alpha_1\ L_1\ S_1;\ \ell|\}\ \ell^N\,\alpha LS\rangle\right|^2\\ &\times\underbrace{\left[(-e)\int_0^\infty R_{n'\ell'}(r)r^3R_{n\ell}(r)\mathrm{d}r\right]^2}_{[s(n\ell,n'\ell')]^2}.\end{aligned} \tag{4.85}$$

Breaking the selection rules

It is an experimental fact that $n\mathrm{d}^N \leftrightarrow n\mathrm{d}^N$ and $n\mathrm{f}^N \leftrightarrow n\mathrm{f}^N$ transitions occur. Their spectra can only be partially explained by higher order transition moments, indicating that the above-derived selection rules can be avoided. Multiple mechanisms are held responsible.

Of historical importance in the understanding of lanthanide spectroscopy is the Judd-Ofelt mechanism, proposed independently by Brian R. Judd and George S. Ofelt in 1962 [103, 104]. They explained the intensities of intraconfigurational 4f transitions by mixing of the $4\mathrm{f}^N$ configuration with higher-lying configurations of different parity through the odd components of the one-electron crystal field Hamiltonian and hence quantified the breaking of the Laporte rule.

The configuration mixing was treated at second order perturbation theory, starting from the wave functions, calculated in the intermediate coupling scheme (§4.1.5). After extensive rewriting of the matrix element for these induced electric dipole transition while adding multiple assumptions concerning the degeneracies in the higher-lying configurations, they arrive at a condensed expression for the line strength, requiring three radial integrals. In the modern version, the line strength for induced E1 transitions reads [105, 106]:

$$\mathcal{S}(n\ell^N\alpha LSJ,\, n\ell^N\alpha'L'S'J') = \sum_{\lambda=2,4,6}\Omega_\lambda\left|\langle\ell^N\alpha LSJ\|\,U^{(\lambda)}\|\ell^N\alpha'L'S'J'\rangle\right|^2, \tag{4.86}$$

where the Judd-Ofelt parameters conceal the odd crystal field coefficients (see §10.2.2) [107]:

$$\Omega_\lambda = (2\lambda+1)\sum_{k=1,3,5}\sum_{q=-k}^{k}\frac{\Xi^2(kq,\lambda)}{2k+1} \tag{4.87}$$

with

$$\Xi(kq,\lambda) = 2\sum_{n'\ell'}\frac{(-1)^{\ell+\ell'}(2\ell+1)(2\ell'+1)}{E(n\ell)-E(n'\ell')}\begin{Bmatrix}1 & \lambda & k\\ \ell & \ell' & \ell\end{Bmatrix}\begin{pmatrix}\ell & 1 & \ell'\\ 0 & 0 & 0\end{pmatrix}\begin{pmatrix}\ell' & k & \ell\\ 0 & 0 & 0\end{pmatrix} \times\int_0^\infty R_{n\ell}(r)rR_{n'\ell'}(r)r^2\mathrm{d}r\int_0^\infty R_{n\ell}(r)\mathcal{B}_{kq}(r)R_{n'\ell'}(r)r^2\mathrm{d}r. \quad (4.88)$$

The reduced matrix elements in Eq. 4.86 are proportional to the Wigner-6j symbol

$$\begin{Bmatrix}L & \lambda & L'\\ J' & S & J\end{Bmatrix} \quad (4.89)$$

according to Eq. B.33, yielding the following selection rules for induced E1 transitions:

$$|\Delta J|\leq\lambda\leq J+J' \qquad \text{and} \qquad \Delta J \text{ even} \quad (4.90)$$

while

$$\Delta S=0 \qquad \text{and} \qquad |\Delta L|\leq\lambda\leq L+L' \quad (4.91)$$

are relaxed by the spin-orbit interaction.

In reality, the Ω_λ parameters are obtained by fitting expression Eq. 4.86 to an experimental spectrum rather than being calculated from first principles. From the parameters, a theoretical lifetime can be obtained for every excited state. Comparing these values with experimentally determined lifetimes gives a rough idea of the quantum efficiency of the luminescence (see §3.3). Given the drastic approximations that were made during the derivation of Eq. 4.86, the Judd-Ofelt parameters should be regarded as phenomenological parameters, not necessarily yielding additional in-depth information of the physical system which is modeled [106].

In Judd-Ofelt theory, the configuration interaction is regarded as a perturbative, *i.e.* a small, effect. For appreciable CI, the approximation breaks down and one should consider the mixed configuration explicitly. In this case, the mixing matrix elements are evaluated, requiring values for the odd CF parameters. It was shown that this approach is necessary to yield a good description for the transition intensities of Pr^{3+} and U^{4+}, using the extended bases $|4f^2\alpha_1 L_1 S_1 J_1 M_1\rangle\oplus|4f^1 5d^1\alpha_2 L_2 S_2 J_2 M_2\rangle$ and $|5f^3\alpha_1 L_1 S_1 J_1 M_1\rangle\oplus|5f^2 6d^1\alpha_2 L_2 S_2 J_2 M_2\rangle$ respectively [108, 109][19].

In addition to the static mechanism that breaks the E1 selection rules, also dynamical effects, *i.e.* the coupling of odd vibrational modes to the electronic eigenfunctions can yield the same result [107].

[19] Along the same line of reasoning, explicitly accounting CI mixing through even CF parameters can improve the transition energies themselves, *e.g.* by adding a third configuration to describe the spectra of Pr^{3+}: $|4f^2\alpha_1 L_1 S_1 J_1 M_1\rangle\oplus|4f^1 5d^1\alpha_2 L_2 S_2 J_2 M_2\rangle\oplus|4f^1 6p^1\alpha_3 L_3 S_3 J_3 M_3\rangle$ [108]

4.4 Numerical implementation

4.4.1 General overview

A Python [110] program was developed which implements the effective Hamiltonian formalism that was described above. The CFP tables of Nielson and Koster, as well as Racah's tables for the calculation of the e_i matrix elements were used as input [111, 112]. This program allows to construct and diagonalize matrices for the electron configurations which are most common in luminescence research such as $n\mathrm{d}^N$, $n\mathrm{d}^{N-1}(n+1)\mathrm{s}^1$, $n\mathrm{f}^N$, $n\mathrm{f}^{N-1}(n+1)d^1$ or $n\mathrm{s}^1 np^1$. The program offers the utility to optimize radial integrals in order to minimize the deviation from experimental transition energies, defined as:

$$\sigma_{\mathrm{CF}} = \sqrt{\frac{\sum_{i=1}^{N}(E_i^{\mathrm{exp}} - E_i^{\mathrm{calc}})^2}{N-P}}, \tag{4.92}$$

for N levels of a manifold, using P empirical parameters. The optimization is performed by a downhill-simplex algorithm [113].

Besides the calculation of transition energies, the wave functions which are optimized simultaneously can be used to calculate line strengths for E1 allowed transitions or induced E1 transitions in the case of f↔f transitions when Ω_k parameters are available. Along the same line, the Ω_k parameters can be obtained empirically from experimental spectra. In principle, it is possible to obtain other physical properties from the optimized wave functions, such as the magnetic susceptibility of the metal defect.

Furthermore, point group representation theoretical manipulations are included in the program. As an example, the automated calculation of supergroup-subgroup relations for both single and double point groups is of importance to obtain the correct symmetry of crystal field states.

4.4.2 Choice of basis

It was chosen to calculate matrix elements of operators in a basis where the implementation is as simple as possible, additionally avoiding the use of symmetry adapted bases. This leads to a complication on another point, *i.e.* when Hamiltonians have to be summed, they have to be transformed to the same basis first. For this, a module is provided that calculates matrices of basis transformation such as:

$$|\alpha LSJ\rangle \leftrightarrow |\alpha_- j_-^{N_-},\ \alpha_+ j_+^{N_+};\ J\rangle \tag{4.93}$$

for a single-shell configuration $n\ell^N$ and

$$\begin{aligned} &|\alpha_1 L_1 S_1,\ \alpha_2 L_2 S_2,;\ LSJ\rangle \\ &\qquad \leftrightarrow |\alpha_1 L_1 S_1 J_1,\ \alpha_2 L_2 S_2 J_2;\ J\rangle \\ &\qquad \leftrightarrow \left|\left[\left(\left(\alpha_{1-} j_{1-}^{N_{1-}} J_{1-},\ \alpha_{1+} j_{1+}^{N_{1+}} J_{1+}\right) J_1,\ \alpha_{2-} j_{2-}^{N_{2-}} J_{2-}\right) J'_{12},\ \alpha_{2+} j_{2+}^{N_{2+}} J_{2+}\right] J\right\rangle \end{aligned} \tag{4.94}$$

for a two-shell configuration $n_1\ell_1^{N_1} n_2\ell_2^{N_2}$. It is clear that more possibilities are found in the second case as the additional choice of coupled and uncoupled representations (concerning M_L, M_S and M) can be made.

In general, these basis transformations boil down to a suitable (re-/de-)coupling of angular momenta, which can be performed using the algebra of the Wigner $3j$-, $6j$- and $9j$- symbols (see appendix B). Transformation between LS and jj coupling becomes however rather complicated but for a few simple textbook examples. Fortunately, the algebra of so-called quasi-spin, applied by Kerman and Helmers to nuclear shell theory, simplifies the manipulations [114–117]. Briefly, quasispin, Q, obeys angular momentum algebra whereby the advantages of the Wigner-Eckart theorem are applicable [118]. While the quasispin itself is directly related to seniority, its projection M_Q, on the other hand, is directly related to the occupation number of the subshell. Therefore, the quasi-spin formalism is not restricted to a fixed particle number, but yields a simultaneous description for all allowed occupation numbers. For this reason, it is not very surprising that the fermion creation and annihilation operators of second quantization can be cast as quasi-spin tensors [118, 119].

4.5 Representative examples

4.5.1 Transition metals - Tanabe-Sugano diagrams

The breakthrough of crystal field theory in the study of transition metal (TM) spectra was reinforced by the Japanese researchers Yukito Tanabe and Satoru Sugano in a series of four papers in the 1950's [120–123]. They combined Bethe's and Van Vlecks' crystal field theory with Racah's tensor and CFP techniques, as sketched above, to obtain the splitting of a shell of N equivalent d electrons. Their approach was different, yet equivalent to the one sketched above in the sense that they worked in a strong field basis, Eq. 4.61, rather than in the atomic basis $|\ell^N\ LSJM\rangle$ that was used in §10.2.2.

Tanabe and Sugano considered the case of an octahedral or cubic crystal field, corresponding to O_h symmetry. For d electron systems, only one crystal field parameter is required (see Table 4.2). Although only one parameter is required, three matrix elements (Eq. 4.73) are nonzero. It depends on the choice of reference frame which ones are nonzero. In the case one chooses the z-axis along a fourfold symmetry axis, the crystal field Hamiltonian reads:

$$\mathcal{H}_{\text{cf}}^{(4)} = \sum_{i=1}^{N} B_{40}^{(4)} \left[C_{40}(i) + \sqrt{\frac{5}{14}} \Big(C_{44}(i) + C_{4\,-4}(i) \Big) \right] \tag{4.95}$$

and the cubic symmetry of the Hamiltonian fixes B_{44}/B_{40} at the *cubic ratio* of $\sqrt{5/14}$. The superscript (4) denotes the reference system and is added to avoid confusion. Alternatively, the crystal field Hamiltonian can be written with respect to a reference

system where the z-axis is put along the threefold rotation axis:

$$\mathcal{H}_{\mathrm{cf}}^{(3)} = \sum_{i=1}^{N} B_{40}^{(3)} \left[C_{40}(i) + \sqrt{\frac{10}{7}} \Big(C_{43}(i) - C_{4\ -3}(i) \Big) \right]. \tag{4.96}$$

In this case one is left with the B_{40} and B_{43} parameters which are mutually connected by the cubic ratio $\sqrt{10/7}$. When the same physical system is described, one has the following relationship:

$$B_{40}^{(3)} = -\frac{2}{3} B_{40}^{(4)}. \tag{4.97}$$

To start with, consider the case of a single d electron, $N = 1$, while neglecting spin-orbit interaction. Upon reducing $\mathcal{D}^{(\ell)}$ in the O_h point group (Eq. 4.58), two irreps are found for $\ell = 2$:

$$\mathcal{D}^{(\ell)} = t_{2g} \oplus e_g, \tag{4.98}$$

corresponding to respectively threefold and twofold degenerate single-particle states. Upon diagonalization of $\mathcal{H}_{\mathrm{cf}}$ indeed two levels are found, for which the crystal field splitting is

$$\epsilon_{\mathrm{cfs}} = \left| \epsilon_{t_{2g}} - \epsilon_{e_g} \right| = 10Dq = \frac{10}{21} B_{40}^{(4)}. \tag{4.99}$$

Here, the notation $10Dq$ reappears, although no PCEM is mentioned. In the remainder, Eq. 4.99 is regarded as the definition of $10Dq$. For this reason, $10Dq$ can also appear in discussions for which $N > 1$, although the interpretation of sp crystal field splitting is only valid in the strong field limit.

For $N > 1$, a nonzero $\mathcal{H}_{\mathrm{RS}}$ (and possibly other terms) unavoidably enters the total Hamiltonian, complicating the spectrum. Tanabe and Sugano calculated diagrams where the crystal field multiplets, *i.e.* the mp states, are shown as a function of the crystal field strength, quantified by B_{40} (or alternatively $10Dq$). They did this for all possible N, here the diagram is calculated and discussed for $N = 3$.

The conventional Tanabe-Sugano diagrams show a linearly increasing $10Dq$ for fixed Racah parameters B and C (see Fig. 4.4a). These are omnipresent in literature and show the free ion terms (^{2S+1}L) splitting according to the intermediate crystal field regime into CF multiplets ($^{2S+1}\Gamma$).

The luminescence spectrum of d^3 ions can be explained with this diagram. In the excitation and absorption spectra, the spin allowed transitions for the $^4\mathrm{F}(^4A_{2g})$ ground state to the excited spin quartets, $^4\mathrm{F}(^4T_{2g})$, $^4\mathrm{F}(^4T_{1g})$ and $^4\mathrm{P}(^4T_{2g})$ dominate. Broad bands are expected based on the observation that a significant portion of the eigenstate will change its character with respect to the strong field configuration, *i.e.* while the ground state corresponds to a large extent to a t_{2g}^3 configuration, the excited spin-quartets have a larger amount of $t_{2g}^2 e_g^1$ and $t_{2g}^1 e_g^2$ character (see Fig. 4.4c). A relatively large electron-phonon coupling, featured by broad bands, is hence expected.

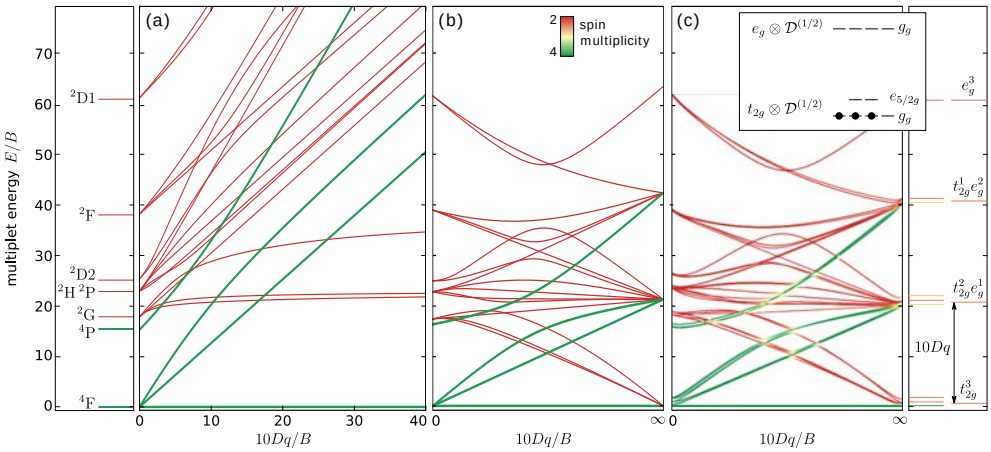

Figure 4.4 – Excited state landscape of a d^3 configuration. The color of the curves encodes the amount of spin multiplicity. (a) shows the Tanabe-Sugano diagram where the RS terms of a free atom, ^{2S+1}L, are split into crystal field multiplets, $^{2S+1}\Gamma$ according to the intermediate coupling scheme, as a function of $10Dq$ (in units of B) for fixed B and C. (b) shows a modified diagram where both $10Dq$ and B are varied to obtain the IPM of the strong field limit. (c) includes spin-orbit coupling, yielding again an IPM in the strong field limit, but with decreased degeneracies. The inset shows the associated sp energy level scheme with the ground state occupation.

After excitation, multiphonon relaxation ensures that the emission occurs from the first excited state, which can be the $^4\mathrm{F}(^4T_{2g})$ level for relatively low crystal fields, giving rise to broad bands, or the $^2\mathrm{G}(^2E_g)$ level for higher crystal fields, when the crossing point around $10Dq \approx 15B$ in Fig. 4.4 is passed, giving rise to a spin forbidden transition and sharp lines due to the small electron-phonon coupling of this transition where the CF configuration remains essentially unchanged.

A modification of the Tanabe-Sugano diagram can be obtained by varying B and C along with $10Dq$. The example is given for the d^3 configuration in Fig. 4.4b. Here, the transition is shown from the intermediate coupling scheme to the strong coupling scheme. In the latter limiting case, an IPM is again obtained as indicated in the figure. During the calculation a fixed ratio of $C/B = 4$ was taken.

As explained in §10.2.2, a full diagonalization allows to include all interaction without making assumptions on any coupling scheme. As such, spin-orbit coupling can be added to the Tanabe-Sugano diagram. An example is shown in Fig. 4.4c, which was calculated with the same settings as 4.4b, but with $\mathcal{H}_{\mathrm{so}}$ added where the $\zeta_{3\mathrm{d}}$ value was kept fixed. On the right hand side, where the limit of a vanishing tp interaction is found, an IPM exhibiting CF splitting as well as spin-orbit coupling is now obtained. Although this limit is not found as a physical reality (except for the trivial $N = 1$ case), a similar picture can be encountered if quasi-particles are used to model the luminescent ion (see §5.3).

Luminescence of K_2SiF_6:Mn^{4+}

Finally, crystal field theory is applied to give an explanation for the peculiar decay behavior of the red LED phosphor K_2SiF_6:Mn^{4+}. This material was synthesized and investigated in the context of the Ph.D. work of Heleen Sijbom[20].

The results of this work were published in:

> **Luminescent behavior of the K_2SiF_6:Mn^{4+} red phosphor at high fluxes and at the microscopic level**
>
> Heleen F. Sijbom, Jonas J. Joos, Lisa I. D. J. Martin, Koen Van den Eeckhout, Dirk Poelman, Philippe F. Smet
>
> *ECS Journal of Solid State Science and Technology*, **5** (1) R3040-R3048 (2016).

K_2SiF_6 forms cubic crystals with the K_2PtCl_6 structure (space group $Fm\bar{3}m$) [124]. Upon activation with Mn^{4+}, occupying the octahedral Si sites, a saturated red luminescence emerges. For this reason, K_2SiF_6:Mn^{4+} has been multiply proposed as LED

[20] Details on the synthesis and characterization of luminescent powders is given in chapter 7.

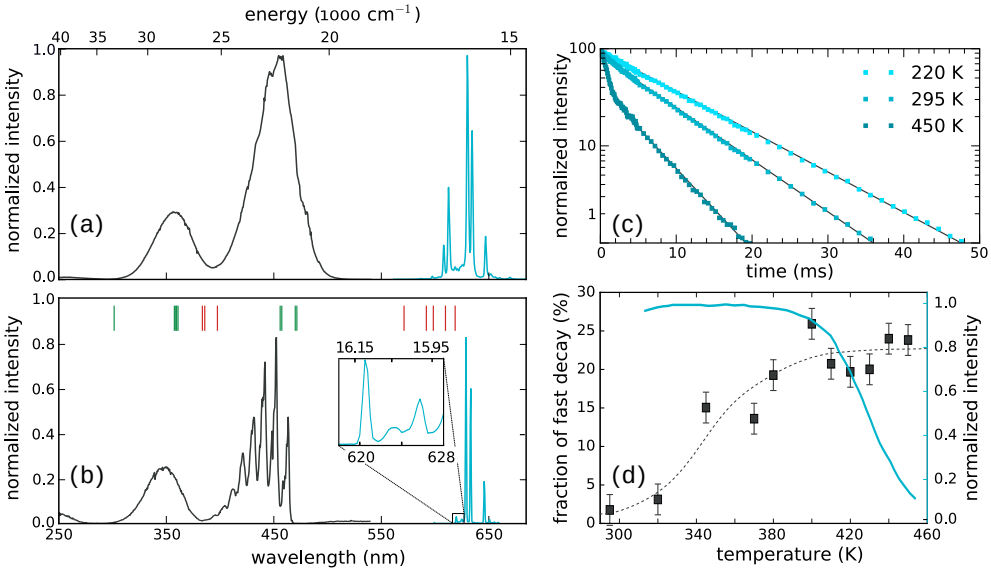

Figure 4.5 – (a) and (b) Photoluminescence excitation (upon monitoring emission at 630 nm) and emission (upon excitation at 455 nm) spectra of K_2SiF_6:Mn^{4+} measured at room temperature (a) and at 10 K (b). (c) Measured luminescence decay profiles (dots) and fits (lines) at 450 K, 295 K and 220 K. (d) Integrated emission intensity of K_2SiF_6:Mn^{4+} as a function of temperature (blue) and the fraction of the fast decay component, as obtained from the fits (grey). The dashed line is a guide to the eye.

phosphor [125–128].

The photoluminescence (PL) emission and excitation spectrum of K_2SiF_6:Mn^{4+} are shown in Fig. 4.5(a-b), measured at room temperature and at 10 K.

Tetravalent manganese features three valence 3d electrons, implying that the above-discussed Tanabe-Sugano diagrams are applicable. The room-temperature PL emission spectrum shows narrow emission bands due to the $^2E_g \rightarrow {}^4A_{2g}$ spin-forbidden transitions of Mn^{4+}. Two broad excitation bands are present corresponding to the $^4A_{2g} \rightarrow {}^4T_{2g}$ and $^4A_{2g} \rightarrow {}^4T_{1g}$ spin-allowed transitions.

In the low temperature PL spectra, the vibronic fine structure is clearly visible in the case of the $^2E_g \rightarrow {}^4A_{2g}$ and $^4A_{2g} \rightarrow {}^4T_{2g}$ transitions. For the $^2E_g \rightarrow {}^4A_{2g}$ transition, the zero phonon line (ZPL) is located at 620.5 nm. The location of the ZPL is hard to determine in case of the $^4A_{2g} \rightarrow {}^4T_{2g}$ transition because in addition to the occurrence of the different phonon-assisted transitions, the $^4T_{2g}$ electronic energy level is expected to be split due to low-symmetry crystal field components and the spin-orbit interaction (see further).

The luminescent-lifetime measurements in Fig. 4.5(c) show a mono-exponential decay at 220 K with a decay time τ_1 = 10.5 ms. With increasing temperature (in the 295-450 K range), a bi-exponential decay is required since a second, faster decay component emerges. The time constant of the slow component decreases with increasing temperature, reaching τ_1 = 8.1 ms at room temperature and τ_1 = 4.9 ms at 450 K. This behavior is consistent with the drop in the overall decay time from 15 to 7 ms in the 20-300 K temperature range that was reported earlier [129]. These results show that the drop in decay time continues further with increasing temperature, although thermal quenching only starts above 400 K.

The second, faster component, has a decay time between 0.63 and 1.0 ms in the 295-450 K range. The fraction of the total emission assigned to the fast component increases from 2-3% in the 295-320 K temperature range to 15% at 345 K and 24% at 450 K (see Fig. 4.5(d)). The largest fraction of the emission, 76% at 450 K, takes place following the slower, spin-forbidden $^2E_g \rightarrow {}^4A_{2g}$ transition and no extra peaks are observed in the emission spectrum with increasing temperature.

From the particular shape of the decay curves, it is plausible to assume that a certain minority of the Mn^{4+} centers show different emission dynamics, provided that sufficient thermal energy is available. This energy allows the defect center to be thermally excited to an electronic eigenstate, characterized by a slightly higher total energy and a higher probability for radiative decay. In the case of perfectly octahedral MnF_6^{2-} defect clusters, the degeneracy of the emitting ^2E_g level is maintained, even with the inclusion of spin-orbit coupling. In that case, the emitting level transforms according to the four-dimensional irrep G of the double group O_h^* . This is visualized in the modified Tanabe-Sugano diagram, displayed in Fig. 4.6(a). Therefore, the question boils down to what the origin is of such a faster-decaying, higher-lying

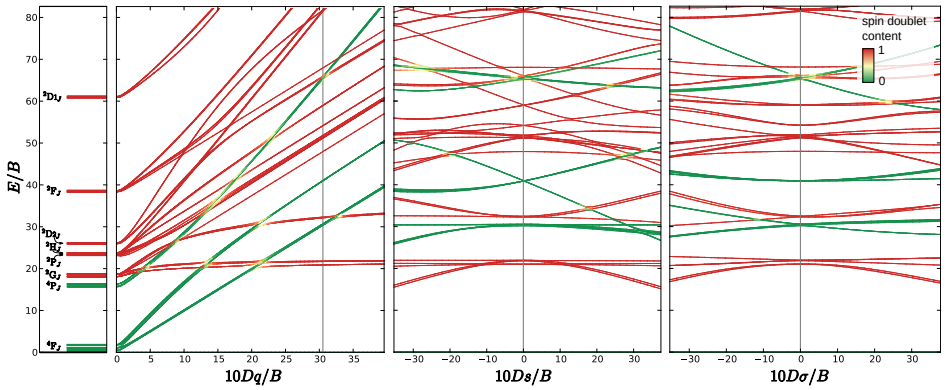

Figure 4.6 – (a) Tanabe-Sugano diagram of a d^3 configuration in octahedral symmetry. Spin-orbit coupling is included ($\zeta_{3d} = 47\,\text{meV}$). (b) The effect of tetrahedral deformation of the octahedral Mn^{4+} defect ($O_h \rightarrow D_{4h}$) on the multiplet energies for a constant $10Dq = 30.2B$ and $Dt = 0$. (c) The effect of trigonal deformation of the octahedral Mn^{4+} defect ($O_h \rightarrow D_{3d}$) on the multiplet energies for a constant $10Dq = 30.2B$ and $D\tau = 0$.

multiplet. In the following, it is examined through crystal field theory whether this can be the result of a small deformation of the octahedral complex, for example by nearby lattice defects or other Mn^{4+} ions.

Two straightforward ways exist to lower the octahedral symmetry, either tetragonally by prolonging or shortening the body diagonal along a fourfold rotation axis or trigonally by altering the length of the body diagonal along a threefold rotation axis. Consequently, one ends up with respective point symmetries D_{4h} and D_{3d}, which require three instead of one parameter to quantify the one-electron crystal field. The Ballhausen parametrization of the CF parameters is applied [130].

In the case of D_{4h} symmetry, one has according to Wybourne's parametrization:

$$\mathcal{H}_{cf} = \sum_{i=1}^{N} \left[B_{20} C_0^{(2)}(i) + B_{40} C_0^{(4)}(i) + B_{4\,-4} \left(C_4^{(4)}(i) + C_{-4}^{(4)}(i) \right) \right]. \tag{4.100}$$

The parameters are related to the Ballhausen parameters according to:

$$B_{20} = -7Ds \tag{4.101}$$

$$B_{40} = 21(Dq - Dt) \tag{4.102}$$

$$B_{44} = 21\sqrt{\frac{5}{14}}Dq \tag{4.103}$$

Ds is related to the extra parameter that emerges from the descent of symmetry while Dt describes the deviation from the cubic ratio. Only when $Dt = 0$, the relationship between B_{40}, B_{44} and Dq is the same as in the case of octahedral symmetry (Eq. 4.95).

For D_{3d} symmetry, the crystal field Hamiltonian becomes:

$$\mathcal{H}_{cf} = \sum_{i=1}^{N} \left[B_{20} C_0^{(2)}(i) + B_{40} C_0^{(4)}(i) + B_{43} \left(C_3^{(4)}(i) + C_{-3}^{(4)}(i) \right) \right]. \tag{4.104}$$

A similar alternative parametrization is again available:

$$B_{20} = -7Ds \tag{4.105}$$
$$B_{40} = -14Dq - 21D\tau \tag{4.106}$$
$$B_{43} = -2\sqrt{70}Dq \tag{4.107}$$

When $D\tau = 0$, the relationship between B_{40}, B_{43} and Dq is the same as in the case of octahedral symmetry when referred to the threefold axis (Eq. 4.96).

In Figures 4.6(b) and (c), the effect of the deformation on the multiplets is given as a function of the Ballhausen $10Ds$ and $10D\sigma$ parameters, quantifying the deformations. In both cases, it is assumed that the cubic ratios of the crystal field parameters in octahedral symmetry are maintained during the deformation.

In the case of a tetragonal deformation, the emitting ^2E_g multiplet splits into two singlets, transforming as the $^2A_{1g}$ and $^2B_{1g}$ irreps of D_{4h}, corresponding to the Kramers doublets $E_{1/2g}$ and $E_{5/2g}$. The ground-state multiplet $^4A_{2g}$ of O_h corresponds to the $^4B_{1g}$ irrep of D_{4h}. Due to the spin-orbit interaction, this level is split in two Kramers doublets, $E_{1/2g}$ and $E_{5/2g}$. If the selection rules for electric dipole transitions in D_{4h} symmetry are considered, every transition is forbidden due to the presence of an inversion center and Laporte's rule. If this parity selection rule is relaxed, or in other words, after a further descent of symmetry towards C_{4v}, one finds that the $B_1 \rightarrow B_1$ transition is electric-dipole allowed in this reduced symmetry, that is the direct product $B_1 \otimes A_1 \otimes B_1$ transforms according to the total symmetric representation A_1 in C_{4v} symmetry. In this case, the z component of the electric dipole moment has symmetry label A_1. The $A_1 \rightarrow B_1$ transition remains symmetry forbidden at the electric dipole level as $A_1 \otimes A_1 \otimes B_1$, for polarization along the z axis, and $A_1 \otimes E \otimes B_1$, for polarizations perpendicular to the z axis, do not contain A_1 in their reduction. If the B_1 multiplet has a slightly higher energy than the A_1 multiplet, the particular decay behavior can be explained. This corresponds to negative Ds values. If the crystal field is parametrized in terms of a point charge model, negative Ds and Dt values signify a shortening of the body diagonal of the coordination polyhedron. Tetragonal deformation can be expected in the K_2SiF_6 crystal from a nearby fluorine vacancy or interstitial atom. Interstitials might occupy the octahedral voids in the crystal structure (Wyckoff site 4*b*) and are indeed expected to compress the coordination polyhedron in the direction of the fourfold rotation axis.

In the case of a trigonal deformation, the ^2E_g multiplet does not split due to symmetry breaking, but rather transforms as the irrep ^2E_g of D_{3d}. However, unlike the octahedral case, this multiplet splits in two Kramers doublets, $E_{1/2g}$ and $E_{3/2g}$ due to

O_h	D_{4h}	calc. (cm^{-1})	exp. (cm^{-1})
$^4A_{2g}$	$^4B_{1g}$	0.00	0.00
		0.16	0.00
^2E_g	$^2A_{1g}$	16166	16117
	$^2B_{1g}$	16406	≈ 16360
$^2T_{1g}$	^2E_g	16685	
		16837	
	$^2A_{2g}$	17456	
$^4T_{2g}$	^4E_g	21166	21553
		21167	
		21186	
		21234	
	$^4B_{2g}$	21827	
		21888	
$^2T_{2g}$	$^2B_{2g}$	25118	
	^2E_g	25882	
		26012	
$^4T_{1g}$	^4E_g	27671	27300
		27758	
		27828	
		27919	
	$^4A_{2g}$	33052	
		33082	

Table 4.3 – Calculated multiplet energies of K_2SiF_6:Mn^{4+}, obtained from a crystal field calculation, compared to the experimental energies, obtained from low temperature PL spectroscopy.

parameter	value (cm^{-1})	ref.
B	770	[131]
C	3470	[131]
ζ_{3d}	380	[132]
α	91	[132,133]
$10Dq$	21791	
$10Ds$	-1118	
$10Dt$	0	

Table 4.4 – Parameters used in the crystal field calculation for K_2SiF_6:Mn^{4+}.

spin-orbit interaction. In the case of positive $10Dσ$ values, the higher-lying Kramers doublet features a slightly higher $S = 3/2$ content than the lower-lying one, ensuring a faster decay due to a relaxation of the spin selection rule. However, the weak spin-orbit interaction for 3d ions mixes spin multiplicity only in a limited way. Typically 0.2-0.5% of quartet character is present in the relevant eigenstates. This is also clear from Fig. 4.6. Only where energy levels are sufficiently close to interact, substantial spin mixing is visible. For this reason, it is more likely that the observed decay behavior originates from tetragonal deformation rather than from trigonal deformation. Electron paramagnetic resonance (EPR) offers a way to distinguish one case from the other. Trigonal deformation is induced when two Mn^{4+} ions are sitting on neighboring Si^{4+} sites in the crystal or from an adjacent potassium vacancy.

From symmetry arguments, it is most likely that the observed decay dynamics originate from a tetragonal compression of the coordination polyhedron. For this reason, the crystal field Hamiltonian for D_{4h} symmetry was fit to the experimental low temperature photoluminescence spectrum. Racah, spin-orbit and Trees parameters were kept fixed at literature values that were obtained for similar Mn^{4+} systems [131–133]. The crystal field $10Dq$ and $10Ds$ values were varied in order to reproduce the experimental transition energies as well as possible. The location of the ZPLs of the ${}^4A_{2g} \rightarrow {}^4T_{2g}$ and ${}^4A_{2g} \rightarrow {}^4T_{1g}$ transitions were assigned to the low energy side of the respective excitation bands. The crystal field splitting between the ${}^2B_{1g}$ and ${}^2A_{1g}$ multiplets was estimated in the order of $kT \approx 250$ cm^{-1} from the activation temperature of the fast decay component. The fixed and optimized parameters are summarized in Table 4.3, the optimized energies are tabulated in Table 4.4. The root-mean-square deviation of the fit is 270 cm^{-1} which is reasonable given the limited number of experimentally available energies.

4.5.2 Lanthanides - The Dieke diagram

The $4f^N$ configurations show unique properties due to the effective shielding by the 5s and 5p electrons, leading to a limited crystal field interaction and associated level splittings of maximum a few hundreds of meV (see Tab. 4.1 and Fig. 4.3). For the same reason, the electron-phonon coupling for intraconfigurational $4f^N$ transitions is very limited and line spectra are found. This allows spectroscopists to experimentally determine the locations of the large number of multiplets of the $4f^N$ manifolds very accurately not only from gaseous discharges, but also from solid state samples. The spectra of the different lanthanides were extensively studied in the 1950s-1960s by multiple laboratories, using gas discharges as well as lanthanide doped crystals as sample, culminating in 1968 in a summarizing monograph by Gerhard H. Dieke [134]. This monograph featured an energy level scheme for all trivalent lanthanides, which is known as the Dieke diagram ever since.

The energy scale of the original Dieke diagram was limited to ±5 eV by the experimental and computational limitations of the 1960s. Decades later, the diagram could be completed thanks to VUV spectroscopy and increased computer power. For this, Peijzel *et al.* used samples of LaF_3 inspired by the important work of William T.

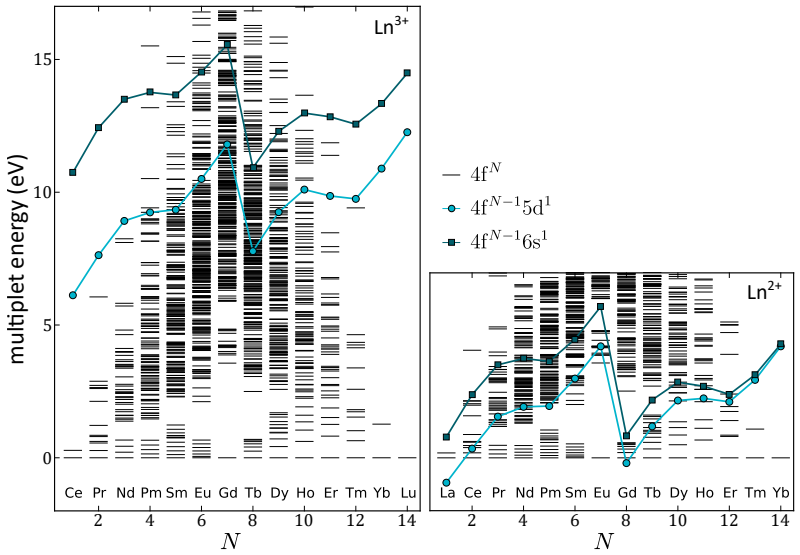

Figure 4.7 – Extended Dieke diagram of the Ln^{3+} and Ln^{2+} ions. The lowest spin allowed (with respect to the $4f^N$ ground state) $4f^{N-1}5d^1$ and $4f^{N-1}6s^1$ levels are indicated by the zig-zag lines.

(*a.k.a.* Bill) Carnall from 1989 [135,136].

The modern version of the Dieke diagram is shown in Fig. 4.7, along with a similar diagram for the divalent lanthanide ions. This diagram is fundamental to interpret $4f^N$-$4f^N$ spectra, but not limited to this. Also in the study of $4f^N$-$4f^{N-1}5d^1$ spectra, approximate models use the Dieke diagram as input (see §4.5.3). For completeness, the locations of the lowest multiplet for the nearby $4f^{N-1}5d^1$ and $4f^{N-1}6s^1$ configurations are shown in the diagram. Upon connecting these multiplets for the different lanthanides, the -almost symbolic- zig-zag curves emerge.

4.5.3 Lanthanides - Cracking the $4f^{N-1}5d^1$ configuration

In the case of transition metal ions, the only intra-atomic transitions that are found in the visual range are within the d^N configuration, implying that this is the only configuration of our interest. Lanthanides on the other hand often feature low-lying $4f^{N-1}5d^1$ and $4f^{N-1}6s^1$ configurations that can be found in the visible or near-UV spectral ranges. Therefore, these configurations are worthwhile to investigate in addition to the $4f^N$ manifold. This paragraph is devoted to $4f^{N-1}5d^1$ configurations, which are accessible by E1 transitions and are hence most common in literature. The $4f^{N-1}6s^1$ configurations can be treated analogously.

Crystal field theory

Although crystal field theory has already a long history and has been applied to d^N and f^N configurations for decades, the description of the $4f^{N-1}5d^1$ manifold is rather novel and largely due to Michael F. Reid and coworkers [137–147]. Different reasons are possible to explain this. Next to the computational cost which is larger, it is experimentally often impossible to obtain well-resolved $4f^{N-1}5d^1$ structures due to vibronic broadening, a high density of energy levels and high energies required to assess a lot of the excited $4f^{N-1}5d^1$ configurations.

The effective Hamiltonian can be symbolically written as:

$$\mathcal{H} = \mathcal{H}_{\text{centr. field}}(\text{fd}) + \mathcal{H}_{\text{RS}}(\text{ff}) + \mathcal{H}_{\text{RS}}(\text{fd}) + \mathcal{H}_{\text{cf}}(\text{f}) + \mathcal{H}_{\text{cf}}(\text{d}) + \mathcal{H}_{\text{so}}(\text{f}) + \mathcal{H}_{\text{so}}(\text{d}), \quad (4.108)$$

where the additional correction terms (see §4.1.6 and §4.2.3) were left out for simplicity. For $4f^{N-1}5d^1$ configurations, the selection rules for the Coulomb matrix elements, Eqs. 4.14, 4.28 and 4.34 learn that nontrivial $F^2(4f,4f)$, $F^4(4f,4f)$, $F^6(4f,4f)$, $F^2(4f,5d)$, $F^4(4f,5d)$, $G^1(4f,5d)$, $G^3(4f,5d)$ and $G^5(4f,5d)$ Slater-Condon parameters can be expected.

In general, all Hamiltonians can be simultaneously evaluated and $\mathcal{H}$ fully diagonalized, yielding solutions which do not depend on a predetermined perturbation sequence. Possible basis states for $4f^{N-1}5d^1$ manifolds were listed by C.-G. Ma *et al.* and make extensive use of the point group irreps and SALCs [144]. These bases correspond to different coupling schemes. Of particular interest is the following perturbation sequence:

$$\langle \mathcal{H}_{\text{RS}}(\text{ff}) + \mathcal{H}_{\text{so}}(\text{f}) \rangle, \langle \mathcal{H}_{\text{cf}}(\text{d}) \rangle \gg \langle \mathcal{H}_{\text{RS}}(\text{fd}) \rangle \gg \langle \mathcal{H}_{\text{so}}(\text{d}) \rangle \gg \langle \mathcal{H}_{\text{cf}}(\text{f}) \rangle. \quad (4.109)$$

which is called the decoupled scheme if only the first step of the sequence is applied. It is decoupled in the sense that the $4f^{N-1}$ core and the 5d electron do not interact. The basis is formed by the direct product of the bases for both parts, *i.e.* $|4f^{N-1}\ \alpha LSJ\rangle|5d^1\ a\Gamma\gamma\rangle$ and the Hamiltonian is block diagonal. Typically, only the lowest $4f^{N-1}$ $(^{2S+1}L_J)$ multiplet is taken into account, resulting in a very simple picture with a limited number of energy levels. This model can of course only be used to describe the low energy tail of the $4f^{N-1}5d^1$ manifold.

In a variant of this coupling scheme, the evaluation of the spin-orbit coupling of the f^{N-1} core is postponed and a simplified Hamiltonian replaces $\mathcal{H}_{\text{RS}}(\text{fd})$ [141]:

$$\langle \mathcal{H}_{\text{RS}}(\text{ff}) \rangle, \langle \mathcal{H}_{\text{cf}}(\text{d}) \rangle \gg \langle \mathcal{H}_{\text{ex}}(\text{fd}) \rangle \gg \mathcal{H}_{\text{so}}(\text{f}), \langle \mathcal{H}_{\text{so}}(\text{d}) \rangle \gg \langle \mathcal{H}_{\text{cf}}(\text{f}) \rangle. \quad (4.110)$$

The isotropic exchange Hamiltonian, $\mathcal{H}_{\text{ex}}(\text{fd})$, is the part of $\mathcal{H}_{\text{RS}}(\text{fd})$ which is responsible for a splitting of the configuration in a high spin (HS) and a low spin (LS) part. It is given by [141]:

$$\mathcal{H}_{\text{ex}}(\text{fd}) = -J_{\text{ex}} \boldsymbol{S}_{\text{f}} \cdot \boldsymbol{s}_{\text{d}}. \quad (4.111)$$

The value of the interaction strength J_{ex} is calculated from the average exchange interaction strength, *i.e.* from the G^k parameters [141].

A typical example where the decoupled scheme is applied, is the $4f^6 5d^1$ excited manifold of the Eu^{2+} ion where the $4f^6$ core is modeled by the ${}^7F_{J_f}$ multiplets of the Eu^{3+} ion. This picture was first described by Freiser, Methfess and Holtzber in 1968 and is shown in Fig. 4.8(a) [148]. The validity of this approach is often justified by the occurrence of a so-called staircase structure that can be resolved in certain low temperature Eu^{2+} spectra [149–152]. The occurrence of a staircase structure does however not necessarily mean that the Coulombic exchange can be neglected and decoupled energy level labels are correct. This is demonstrated in Fig. 4.8(b) where $\mathcal{H}_{\text{RS}}(\text{fd})$ is switched on and its strength increased while keeping the ratios of the Slater-Condon parameters at the free ion values [141,153–155]. The vertical line estimates the value of the interaction strenght in the case of Eu^{2+} in CaF_2 according to Weakliem [153]. A separation of the excited state landscape in a HS and LS part due to $\mathcal{H}_{\text{RS}}(\text{fd})$ is visible, demonstrating the ability of the exchange interaction, Eq. 4.111 to approximate the f-d Coulomb interaction.

When $4f^N \leftrightarrow 4f^{N-1}5d^1$ transitions are studied, a second effective Hamiltonian is required in addition to Eq. 4.108 to describe the $4f^N$ ground state configuration (see §4.5.2). The energy difference between both configurations is given by:

$$\Delta_{\text{fd}} = \left\langle \mathcal{H}_{\text{centr. field}}(f^{N-1}d^1) \right\rangle - \left\langle \mathcal{H}_{\text{centr. field}}(f^N) \right\rangle. \tag{4.112}$$

In the case of Eu^{2+}, this is a rather trivial extension because the $4f^7$ ground state has almost pure ${}^8S_{7/2}$ character. Other multiplets of the $4f^7$ configuration lie at relatively high energies and are mostly obscured by the lower-lying $4f^6 5d^1$ configuration. In Fig. 4.8(c), a calculated E1 excitation spectrum is shown from the Eu^{2+} $4f^7({}^8S_{7/2})$ ground state towards the $4f^6 5d^1$ manifold corresponding to the vertical line in Fig. 4.8(b). Here, electron-phonon coupling was not taken into account, however every transition was broadened by means of a Lorentzian shape function (FWHM of 800 cm^{-1}). It is clear that the spin-allowed transitions to the HS states dominate the spectrum. This example shows that even when J_f ceases to be a good quantum number, a staircase structure can still be found if a good experimental resolution is obtained, *e.g.* by measuring at low temperature. When the symmetry of the crystal field is lower, more $5d(a\gamma)$ levels with smaller separations are expected. Then, the combined effect of $\mathcal{H}_{\text{so}}(\text{f})$ and $\mathcal{H}_{\text{RS}}(\text{fd})$ in addition to $\mathcal{H}_{\text{cf}}(\text{d})$ causes the excitation spectrum to become broad and featureless, a description that is indeed often used in Eu^{2+} spectroscopy.

Alternative quantities

In experimental studies of $4f^N \leftrightarrow 4f^{N-1}5d^1$ transitions, the parameters that occur in the effective Hamiltonians are not always directly obtainable, nor are spectra sufficiently resolved to start fitting the spectrum with the Hamiltonian. For this reason,

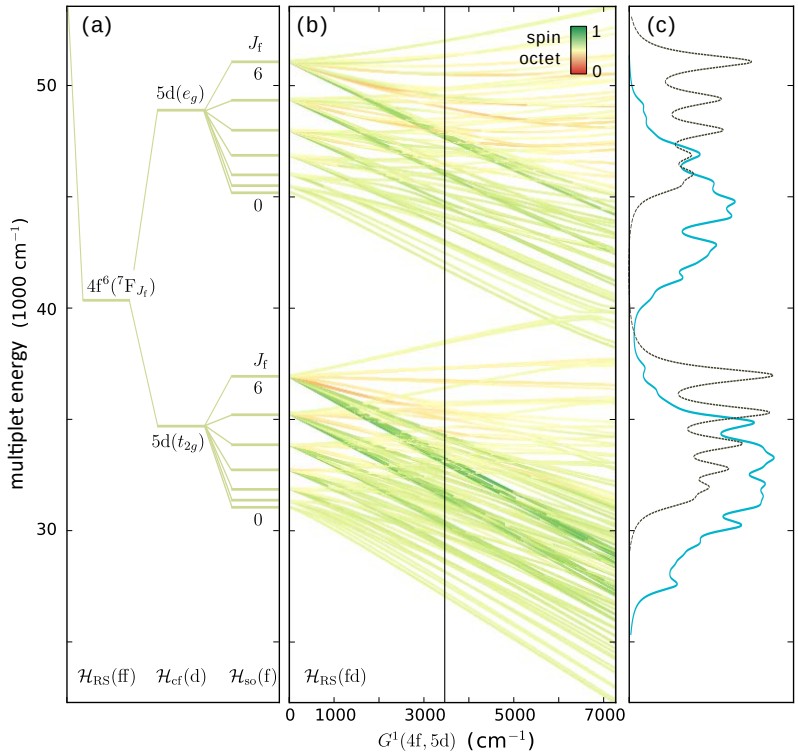

Figure 4.8 – Crystal field calculation for the low energy part of the $4f^6 5d^1$ configuration of Eu^{2+} in an octahedral crystal field, calculated in the 490 dimensional $|4f^6(^7F_{J_f}), 5d_{j_d}; JM\rangle$ basis, approximating the 30030 dimensional basis for the full configuration. (a) Decoupled scheme. (b) Showing the influence of $\mathcal{H}_{RS}(fd)$ on the energy levels. (c) Calculated low energy part of the $4f^7$-$4f^6 5d^1$ spectrum with ($G^1 = 3500$ cm^{-1}, solid blue line) and without (grey dashed line) 4f-5d interaction.

an experimentally inspired nomenclature has evolved. The most important quantities are enumerated.

The redshift of a $4f^N \rightarrow 4f^{N-1}5d^1$ transition is defined as the energy decrease for the transition between the lowest levels of both configurations for the free and incorporated ion,

$$D(Ln^{Q+}, A) = E^{fd}(Ln^{Q+}, \text{free}) - E^{fd}_{abs}(Ln^{Q+}, A), \tag{4.113}$$

where Ln denotes the lanthanide ion, Q its oxidation state and A the host material. Ideally, it would be calculated from the location of the zero phonon line (ZPL). However, this is not always possible, and often the maxima of the different bands in absorption or excitation spectra are used, unavoidably adding some contributions of vibronic effects into $D(Ln^{Q+}, A)$.

The electronic contribution to $D(Ln^{Q+}, A)$ can be envisaged as originating from two different sources. First, the environmental dependence on the difference in the central fields for both configurations gives rise to a relative shifting of the barycenters of the configurations, which is denoted as the centroid shift, $\epsilon_c(Ln^{Q+}, A) = \Delta_{fd}(\text{free}) - \Delta_{fd}(A)$. The other differences in $\mathcal{H}_0$ between the free and incorporated ion and the crystal field Hamiltonians for the incorporated ion will lead to level splittings which are different in both configurations, giving rise to a second contribution to $D(Ln^{Q+}, A)$.

When a perturbation sequence is assumed in which $\mathcal{H}_{cf}(d)$ is evaluated first, such as the decoupled scheme, the second contribution to $D(Ln^{Q+}, A)$ is separated in a part which originates from $\mathcal{H}_{cf}(d)$, referred to as the crystal field splitting, $\epsilon_{cfs}(Ln^{Q+}, A)/r(Ln^{Q+}, A)$, where ϵ_{cfs} is the total one-particle crystal field splitting and $1/r$ the fraction contributing to the redshift. The remaining differences in splittings of the configuration, originating *e.g.* from different Slater-Condon parameters for the free and incorporated ion, are collected in a term $\Delta\epsilon_{cfs}(Ln^{Q+}, A)$. Collecting all contributions yields:

$$D(Ln^{Q+}, A) = \epsilon_c(Ln^{Q+}, A) - \Delta\epsilon_c(Ln^{Q+}, \text{free}) + \frac{\epsilon_{cfs}(Ln^{Q+}, A)}{r(Ln^{Q+}, A)} + \Delta\epsilon_{cfs}(Ln^{Q+}, A) \tag{4.114}$$

the term $\Delta\epsilon_c(Ln^{Q+}, A)$ is the energy difference between the barycenter and the lowest level of the $4f^{N-1}5d^1$ configuration of the free ion. These concepts are further clarified through the example in the next paragraph.

The attainable $4f^N \leftrightarrow 4f^{N-1}5d^1$ energies for varying chemical environment depend on the lanthanide ion under consideration. Often, these energies are in the UV region (typically for trivalent lanthanides) or in the IR region (typically for divalent lanthanides). However, few ions such as Ce^{3+} ($N = 1$), Eu^{2+} ($N = 7$) and Yb^{2+} ($N = 14$) have their $4f^{N-1}5d^1$ manifold desirably within reach of the visible spectral range. Especially Eu^{2+} is well-known for its extreme color tunability upon incorporation in various host crystals (see Fig. 4.9).

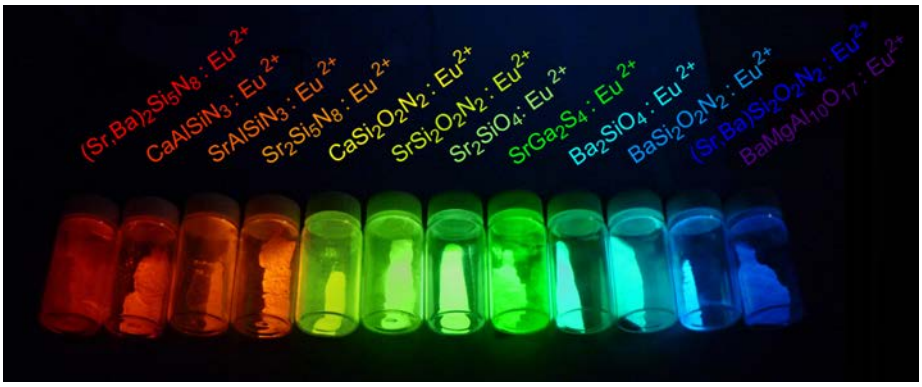

Figure 4.9 – Series of Eu^{2+} phosphors excited by a UV lamp, exposing the extreme color tunability of the Eu^{2+} $4f^6 5d^1 \rightarrow 4f^7$ emission upon changing the chemical environment.

Luminescence of $SrAl_2O_4$:Eu^{2+} - an empirical approach

$SrAl_2O_4$:Eu^{2+} is a well-known afterglow material. This means that light emission can still be observed a long time after the excitation has ceased. Although this phenomenon is already known since the Age of Enlightenment and omnipresent in daily life in the form of safety signalization or glow-in-the-dark gadgets, an in-depth scientific explanation for the phenomenon is still lacking, notwithstanding substantial progress that was achieved in the last years [156–162]. It has been shown that charge carriers escape from the activator, in this case the Eu^{2+} ion, during the energy storage. Open questions pertain to the nature of the defects where these charge carriers are trapped, the reason why co-doping with Dy^{3+} can prolong the afterglow time significantly and by which mechanism the charge carriers are released from the activator during charging and from the trap during afterglow.

Next to the above questions, which mainly pertain to the dynamics of the phenomenon, the interpretation of the steady-state PL spectra of the compound has proven to be problematic. Next to the well-known green emission, a second, blue emission band emerges when the material is cooled below room temperature (see Fig. 4.10). Different hypotheses to explain the occurrence of the two bands can be found in literature. Given that there are two nonequivalent strontium sites in the $SrAl_2O_4$ crystal structure (see Fig. 4.11), it seems straightforward to assign the occurrence of both emission bands to the substitution of Eu on these two lattice sites. Different coordination for both sites is then expected to sufficiently change the electronic structure to arrive at the observed spectral differences. Nevertheless, several authors discarded this hypothesis because both sites are too similar to explain the large en-

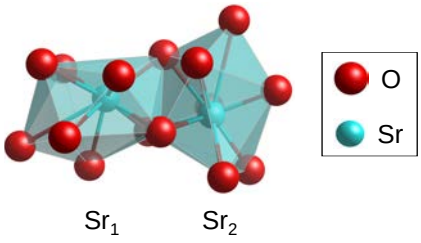

Figure 4.11 – Coordination environment for the two Sr sites in $SrAl_2O_4$ [163].

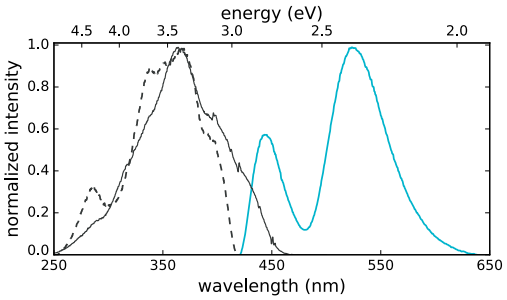

Figure 4.10 – Photoluminescence emission (upon excitation at 370 nm, blue line) and excitation spectra (upon monitoring at 445 nm, dashed grey line and upon monitoring at 520 nm, solid grey line) of $SrAl_2O_4$:Eu^{2+} at 10 K.

	green	blue
$E_{em}^{fd}(Eu^{2+}, A)$	2.37	2.79
FWHM	0.27	0.21
$D(Eu^{2+}, A)$	1.42	1.22
$\epsilon_{cfs}(Eu^{2+}, A)$	1.10	1.13
$\epsilon_c(Eu^{2+}, A)$	1.65	1.44
$\Delta S(Eu^{2+}, A)$	0.43	0.21

Table 4.5 – Properties of the emission and excitation spectra of $SrAl_2O_4$:Eu^{2+}, measured at 10 K. All values in eV.

ergy difference when judging on the emission bands. As an alternative explanation, Poort et al. [164] suggested that the two emission bands result from a possible preferential orientation of the d orbitals of Eu^{2+} on Sr sites that appear to line up. Clabau et al. proposed that the blue emission band arises from the charge transfer from the fundamental level of the $4f^7$ configuration of Eu^{2+} to the valence band and is associated to a hole detrapping mechanism (interatomic processes are discussed in more detail in chapter 5) [165]. Hölsä et al. considered the blue emission band as anomalous low-temperature luminescence and proposed that it originates from a higher Eu^{2+} 5d state that may be observed due to the absence of high energy lattice vibrations at low temperatures [166].

In order to ascertain whether the incorporation of the europium activator on the two similar, but nonequivalent Sr sites can give rise to different luminescent properties and can explain the occurrence of the blue and green emission bands in $SrAl_2O_4$:Eu, empirical rules are exploited that relate structural properties to the excited $4f^6 5d^1$ manifold of Eu^{2+}.

This investigation was performed in the broader context of the Ph.D. work of Dr. Jonas Botterman. The results of this work were published in:

Trapping and detrapping in $SrAl_2O_4$:Eu,Dy persistent phosphors: influence of excitation wavelength and temperature

Jonas Botterman, Jonas J. Joos, Philippe F. Smet

Physical Review B, **90** 085147 (2014).

The decoupled perturbation scheme for the $4f^6 5d^1$ excited configuration of the Eu^{2+} ion is applied to distill the different parameters in Eq. 4.114 from the experimental

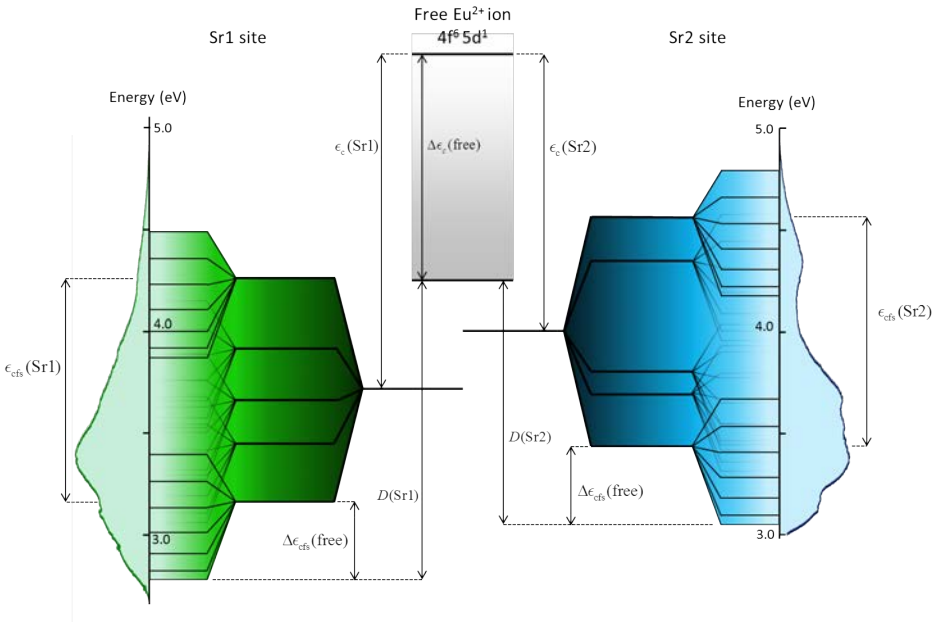

Figure 4.12 – Energy level scheme showing the multplets of the $4f^6 5d^1$ manifold of Eu^{2+} within a very simplified model (see text) on the Sr1 (yielding green emission) and on the Sr2 (yielding blue emission) sites in monoclinic $SrAl_2O_4$. The meaning of the different quantities and the connection with the excitation spectra is displayed.

excitation spectra (Fig. 4.10). Only the lowest term of the $4f^6$ core is considered, *i.e.* ^7F, yielding a very simplified picture (displayed in Fig. 4.12).

The redshift values of both excitation spectra were determined by taking the point where the intensity equals 20% of the first maximum of the overlapping staircase structure which originates from the splitting of the underlying $4f^6(^7F)$ term. This yields a good estimate of the location of the lowest $4f^6(^7F_0)$ level [167, 168].

Obtaining accurate experimental values for the 5d crystal field splitting of Eu^{2+} is a tedious occupation for low coordination symmetries. In this particular case, the $4f^6 5d^1$ level is split by the crystal field into five bands which strongly overlap due to the energy level structure of the remaining $4f^6$ configuration. Hence, a broad and relatively featureless band is obtained, which is, for instance, in contrast to the case of Ce^{3+}, having only a single 4f electron in the ground state [169]. In the case of $SrAl_2O_4$:Eu^{2+}, an estimate of the crystal field splitting can nevertheless be made since fundamental absorption only becomes significant above 6.50 eV and therefore does not appear in the part of the excitation spectrum that is related to $4f^7 \rightarrow 4f^6 5d^1$ absorption due to the Eu^{2+} impurities [170]. In analogy with the low energy side, the point where the intensity is 20% of the maximum of the staircase structure is selected to pin the highest $4f^6(^7F_6)$ level. By subtracting both values, an energy dif-

ference is obtained which equals the crystal field splitting combined with the total splitting energy of one $4f^6(^7F)$ term. This can be approximated by using the splitting energy of the $4f^6(^7F)$ term in Eu^{3+}, being 0.62 eV [167,171]. The obtained values are shown in Table 4.5.

Once the experimental redshift and crystal field splitting are determined, the experimental centroid shifts can also be calculated with Eq. 4.114. A value of $\Delta\epsilon_c(Eu^{2+}, \text{free}) = 1.12$ eV was used, based on the energy scheme constructed by Sugar and Spector [172, 173]. It can be assumed that $r(Eu^{2+}, A)$ is equal for both lattice sites. A point charge model was applied to verify this [78]. $r(Eu^{2+}, A) = 1/0.45$ was obtained for both Sr sites within this model. The experimental values for $\epsilon_c(Eu^{2+}, A)$ are included in Table 4.5 The experimental ratios are:

$$\frac{\epsilon_{cfs}(\text{green})}{\epsilon_{cfs}(\text{blue})} = 0.97 \qquad \text{and} \qquad \frac{\epsilon_c(\text{green})}{\epsilon_c(\text{blue})} = 1.14. \tag{4.115}$$

Both the centroid shift and the crystal field splitting can be related to the size and nature of the coordination polyhedra by empirical formulas:

$$\frac{\epsilon_c}{\text{CN}} = \frac{\alpha_{sp} e^2}{4\pi\epsilon_0 d_{\text{eff}}^6}\left(\left\langle r^2\right\rangle_{5d} - \left\langle r^2\right\rangle_{4f}\right) \tag{4.116}$$

$$\epsilon_{cfs} = \frac{\beta_{\text{poly}}^Q}{d_{\text{av}}^2}. \tag{4.117}$$

In these expressions, α_{sp} and β_{poly}^Q are empirical parameters, introduced by Dorenbos [174,175]. Equation 4.116 was originally introduced for Ce^{3+}, but the theoretical basis for this empirical relation is more generally valid for $4f^{N-1}5d^1$ configurations as was derived by Morrison, based on a suggestion of Judd [175, 176]. The average and effective bond lengths are defined as:

$$\frac{1}{d_{\text{eff}}^6} = \frac{1}{\text{CN}}\sum_{i=1}^{\text{CN}} \frac{1}{\left[d_i - f(R_{Sr^{2+}} - R_{Eu^{2+}})\right]^6} \tag{4.118}$$

$$d_{\text{av}} = \langle d\rangle - f(R_{Sr^{2+}} - R_{Eu^{2+}}). \tag{4.119}$$

These distances give a measure for the size of the coordination polyhedron, adapted for the relaxation which originates from the substitution of a lanthanide ion on the site of a metal ion with a different crystal radius, R. $\langle d\rangle$ is the arithmetic average of the bond lengths in the undoped crystal. The constant f measures the strength of the lattice relaxation and is empirically chosen in the range of 0.5-0.7. These distances can be calculated from the crystal structure of $SrAl_2O_4$. The monoclinic structure of $SrAl_2O_4$ was first described by Schulze and Müller-Buschbaum in 1981 [163]. As said, the structure contains two nonequivalent Sr sites, both completely lacking symmetry. Bond lengths range from 2.5 to 3.5 Å for both sites [163] . Furthermore, $f = 0.6$ was taken, and $Sr^{2+} = 1.32$ Å and $Eu^{2+} = 1.31$ Å were used [177].

From the crystallographic data of $SrAl_2O_4$ and the above algebra, it can now be verified whether it is plausible that the two different redshifts originate from incorporation of Eu^{2+} on the Sr1 and Sr2 sites. For this, the assumption is made that α_{sp}, β^Q_{poly}, and the expectation values $\left\langle r^2 \right\rangle_{n\ell}$ are equal for both lattice sites and the difference in redshift is thus the mere consequence of the difference in bond length. This yields:

$$\frac{\epsilon_{cfs}(Sr1)}{\epsilon_{cfs}(Sr2)} = \frac{d^2_{av}(Sr2)}{d^2_{av}(Sr1)} = 0.90 \qquad \text{and} \qquad \frac{\epsilon_c(Sr1)}{\epsilon_c(Sr2)} = \frac{d^6_{eff}(Sr2)}{d^6_{eff}(Sr1)} = 1.21. \tag{4.120}$$

Regardless of the simplicity of the model, these calculated ratios are in good correspondence (deviations of only 0.07 and 0.06) with the experimental ratios for the green and blue emission bands. Therefore, it is certainly plausible that the different spectral features are the consequence of the small but significant difference between the two lattice sites. The green emission band is attributed to the Sr1 site, and the blue emission to the Sr2 site within this simple model. The obtained energy level scheme is displayed in Fig. 4.12. Herein, the relative locations of the five $4f^6 5d^1$ levels after crystal field splitting were estimated with a point charge model [78]. A good qualitative correspondence with the experimental spectrum is observed, when adding all the different sub-levels. Represented in this way, it is also clear that upon excitation towards higher excited levels, the multitude of sub-levels leads to a quick non-radiative relaxation to the lowest excited state, even at low temperature. Hence, the hypothesis that the blue emission originates from emission starting at higher excited states can be discarded. In addition, the clear differences on the high energy side of the excitation spectrum point at a different origin of both emission bands as well.

The above results led to an interesting discussion in scientific literature. Hagemann, Bierwagen and coworkers found very similar results concerning the energy storage processes in $SrAl_2O_4$ [178, 179]. Wavelength dependence of the different processes and the increase of energy transfer for increasing doping concentrations indicate the correctness of the model with the two nonequivalent Eu defects.

Next to these investigations of dynamics, some more studies on the incorporation of Eu^{2+} in $SrAl_2O_4$ appeared. In particular, Nazarov *et al.* performed VUV spectroscopy on this phosphor and ECM calculations for both nonequivalent Eu^{2+} ions [180]. Interestingly, the VUV spectroscopy revealed additional spectral features above 5 eV. These were all attributed to transitions towards the excited $4f^6 5d^1$ configurations except for intese band slightly below 7 eV which is most likely due to fundamental absorption of the $SrAl_2O_4$ host crystal (see also §5.4). As the calculation of Slater-Condon parameters is not possible within the ECM, the authors assumed a simple effective Hamiltonian containing only the $\mathcal{H}_{cf}(d)$ term. They obtained 5d crystal field splittings of 3.15 eV and 2.73 eV for Eu^{2+} at the Sr1 and Sr2 site respectively, spanning the full violet-VUV region of their measurements. These are remarkably high values, compared to typical values that are found in literature [173]. Furthermore, given the low symmetry of the compound it is expected that the five

different *sets* of energy levels will interact severely, *i.e.* contributions of $\mathcal{H}_{\mathrm{so}}(\mathrm{f})$ and $\mathcal{H}_{\mathrm{RS}}(\mathrm{fd})$ cannot be neglected here, devaluating the meaning of the five discrete 5d levels. In addition, it is expected that effects from $\mathcal{H}_{\mathrm{RS}}(\mathrm{ff})$ will be important as well when crystal field splittings of 2-3 eV are considered. After all, the first excited multiplet of the $4f^6$, *i.e.* $^5\mathrm{D}3_{J_\mathrm{f}}$ lies only 2.1 eV above the $^7\mathrm{F}_0$ ground state [171][21]. Probably, the VUV spectral features originate at least partially from transitions to energy levels corresponding to $|4f^6(^5D3_{J_\mathrm{f}}), 5d_{j_d}; JM\rangle$ states.

Anyway, the qualitative empirical study arguing that the observed spectral and dynamical differences are due to two nonequivalent Eu^{2+} ions holds. Reliably assessing which ion gives rise to which spectral feature is obviously out of the scope of both above empirical study and the oversimplified ECM calculation by Nazarov *et al.* This issue is further elaborated in §6.5.

[21] The ´´3´´ in ^{5}D3 denotes the ^{5}D term with $v = 6$, $W = (2,1,0)$ and $U = (2,1)$ (see §4.1.2).

5 BAND PICTURE

The band theory of solids was first written down by Alan H. Wilson and Felix Bloch in the late 1920s - early 1930s. Despite its simplicity, this theory was able to revolutionize physics and to provide the theoretical keystone of the new discipline of solid state physics, which quickly expanded the successes of semiconductor science and technology. It describes the electronic structure of crystalline solids in terms of single-particle orbitals, the bands. In the case of insulators and semiconductors, a forbidden band, called the band gap, separates the occupied from the empty bands. Impurities or other defects in the crystal give rise to levels that lie in the band gap. In the case of transition metal or lanthanide impurities, multiple charge states can be found and many-electron effects cannot be neglected hence giving rise to complications with the single-electron band picture. In order to hold on to the notion of occupied and empty bands, charge-state transition levels are used, describing the stabilities of the charge states of the impurities in terms of total energies, while maintaining the band picture for the host crystal. Charge-state transition levels can be numerically calculated with density functional theory, using a defective supercell and periodic boundary conditions.

5.1 Perfect crystals

Crystals are highly symmetric structures. Translation symmetry allows to find a primitive unit cell which can be copied along the basis vectors a, b and c to generate the full crystal, which is assumed to be infinitely large. As in the atomic case, group theoretical techniques can simplify the description of the electronic structure for crystals. The symmetry group of a crystal is called a space group and is composed of the familiar point group operations, supplemented with translations, $\boldsymbol{T}$, along the crystallographic directions a, b and c. For non-symmorphic space groups, glide planes and screw axes are found in addition. The space group operations commute with the Hamiltonian and provide good quantum numbers to label the electronic eigenstates (see appendix A).

Band theory offers an approximate solution to the Schrödinger equation for a crystalline solid. Next to the assumption of perfect crystallinity, it is additionally assumed that the electrons behave independently. This means that band theory is a single-particle theory where the total wave function can be written as the product of

single-electron wave functions, ψ and the Hamiltonian is the sum of sp Hamiltonians:

$$\mathcal{H}_0(i) = -\frac{\hbar^2}{2m_e}\nabla_i^2 + V(\boldsymbol{r}_i). \tag{5.1}$$

The electron's potential energy will show periodicity, dictated by the crystal symmetry. In terms of the translation operators one has:

$$T(\boldsymbol{R}_i)V(\boldsymbol{r}) \equiv V(\boldsymbol{r}+\boldsymbol{R}_i) = V(\boldsymbol{r}), \tag{5.2}$$

where $\boldsymbol{R}_i$ are the lattice vectors[1]. The eigenfunctions of the Hamiltonian are simultaneously supposed to be eigenfunctions of the translation operators (see appendix A):

$$T(\boldsymbol{R}_i)\psi(\boldsymbol{r}) = \psi(\boldsymbol{r}+\boldsymbol{R}_i) = \lambda_i\psi(\boldsymbol{r}). \tag{5.3}$$

The electron density necessarily has the same periodicity as the potential, implying that the eigenvalues λ_i are limited to a phase factor $\lambda_i = \mathrm{e}^{\mathrm{i}\phi_i}$. When translation operations are performed consecutively, the eigenvalues get multiplied, yielding that $\phi_i = \boldsymbol{k}\cdot\boldsymbol{R}_i$, with $\boldsymbol{k}$ an arbitrary vector which is the same for all operations. This $\boldsymbol{k}$ vector can be used to label the eigenfunction:

$$\psi_{\boldsymbol{k}}(\boldsymbol{r}+\boldsymbol{R_i}) = e^{\mathrm{i}\boldsymbol{k}\cdot\boldsymbol{R}_i}\psi_{\boldsymbol{k}}(\boldsymbol{r}). \tag{5.4}$$

This result is known as Bloch's theorem and is central to the study of the electronic structure of crystals. Typically, a function $u_{\boldsymbol{k}}(\boldsymbol{r})$ is introduced as,

$$\psi_{\boldsymbol{k}}(\boldsymbol{r}) = \mathrm{e}^{\mathrm{i}\boldsymbol{k}\cdot\boldsymbol{r}}u_{\boldsymbol{k}}(\boldsymbol{r}), \tag{5.5}$$

and thus has by definition the same periodicity as the crystal potential. The wave vector serves as a quantum number for the Hamiltonian and simultaneously as label for the eigenstates of the translation operator.

Local physical properties have the same periodicity as the crystal, suggesting a description in terms of (discrete) Fourier transforms. For the electron density, ρ, one has for instance:

$$\rho(\boldsymbol{r}) = \sum_{\boldsymbol{G}}\rho(\boldsymbol{G})\mathrm{e}^{\mathrm{i}\boldsymbol{r}\cdot\boldsymbol{G}}. \tag{5.6}$$

As ρ needs to be invariant for the space group operations, most notably the translations, this puts restrictions on the allowed values for the vectors $\boldsymbol{G}$. It can be shown that the $\boldsymbol{G}$ vectors form a lattice, the so-called reciprocal lattice, defined by its basis vectors $\boldsymbol{b}_i$ for which $\boldsymbol{b}_i\cdot\boldsymbol{a}_j = 2\pi\delta_{ij}$. As for the crystal lattice, a primitive unit cell can also be found for the reciprocal lattice, which is referred to as the first Brillouin zone. The reciprocal lattice vectors have the same unit as the $\boldsymbol{k}$ vector, which hence *live* in reciprocal space. A general wave vector $\boldsymbol{k}$ can be translated to the first Brillouin zone by a suitable reciprocal lattice vector $\boldsymbol{G}$:

$$\boldsymbol{k}' = \boldsymbol{k} - \boldsymbol{G}. \tag{5.7}$$

[1] A lattice vector can correspond to one or more atomic positions. In the latter case, the atomic unit is referred to as the motif. The motif is repeated at every lattice point $\boldsymbol{R}$.

The Bloch function of this vector outside the first Brillouin zone reads:

$$\psi_{\boldsymbol{k}}(\boldsymbol{r}) = \underbrace{u_{\boldsymbol{k}}(\boldsymbol{r})\mathrm{e}^{\mathrm{i}\boldsymbol{G}\cdot\boldsymbol{r}}}_{u'_{\boldsymbol{k}}(\boldsymbol{r})}\mathrm{e}^{\mathrm{i}\boldsymbol{k}'\cdot\boldsymbol{r}}. \tag{5.8}$$

The factor $\mathrm{e}^{\mathrm{i}\boldsymbol{G}\cdot\boldsymbol{r}}$ has the same periodicity and can therefore be absorbed in $u_{\boldsymbol{k}}(\boldsymbol{r})$. This can be done for all wave vectors outside the first Brillouin zone and hence an additional quantum number is required. This is called the band index n. We finally obtain the general expression

$$\psi_{n\boldsymbol{k}}(\boldsymbol{r}) = u_{n\boldsymbol{k}}(\boldsymbol{r})\mathrm{e}^{\mathrm{i}\boldsymbol{k}\cdot\boldsymbol{r}} \tag{5.9}$$

for the sp solutions for electrons of a perfect crystal corresponding to sp energy $\epsilon_n(\boldsymbol{k})$. When the Fourier transform of the periodic function $u_{n\boldsymbol{k}}(\boldsymbol{r})$ is introduced, the sp states can be written alternatively as:

$$\psi_{n\boldsymbol{k}}(\boldsymbol{r}) = \sum_{\boldsymbol{G}} c_{n\boldsymbol{k}}(\boldsymbol{G})\mathrm{e}^{\mathrm{i}(\boldsymbol{k}+\boldsymbol{G})\cdot\boldsymbol{r}}, \tag{5.10}$$

with $\boldsymbol{G}$ a reciprocal lattice vector.

Very similar to the central field solution for atoms, Eq. 4.5, the Bloch states $\psi_{\boldsymbol{k}}(\boldsymbol{r})$ and the sp potential $V(\boldsymbol{r})$ can be regarded as the mean field (or Hartree-Fock) solution of the electronic structure problem. Electron correlation can be added at a higher level of approximation. As an example, Fig. 5.1 shows the single-particle energy level structure of $SrZrO_3$. In the left part of the figure (5.1(a)), the dispersion of the energy eigenvalues is shown as a function of the $\boldsymbol{k}$ vector. The capital letters denote points of high symmetry in the Brillouin zone of the compound, as shown Fig. 5.1(d). This figure illustrates that continuous energy bands are formed, separated by gaps where no electronic states occur.

The single-electron states are filled according to the Fermi-Dirac distribution,

$$f(E) = \frac{1}{\mathrm{e}^{(E-\mu(T))/k_BT}+1}, \tag{5.11}$$

where $\mu(T)$ represents the chemical potential of the system, *i.e.* the energy cost or gain upon adding or removing an electron to the system. The Fermi level, E_F, is defined as the electron chemical potential at absolute zero. If the Fermi level is inside a band, one obtains a metal, while a semiconductor or insulator[2] is obtained when the Fermi level lies inside a forbidden band. This forbidden band is then referred to as *the* band gap and its width as the band gap energy, E_G. The highest filled band is the valence band (VB), the lowest unfilled band the conduction band (CB). As metals are poor host materials for luminescent ions, only semiconductors and insulators are

[2]The distinction between semiconductors and insulators is rather ambiguous and very *craft dependent*. Anyway, insulators have the larger band gap energies.

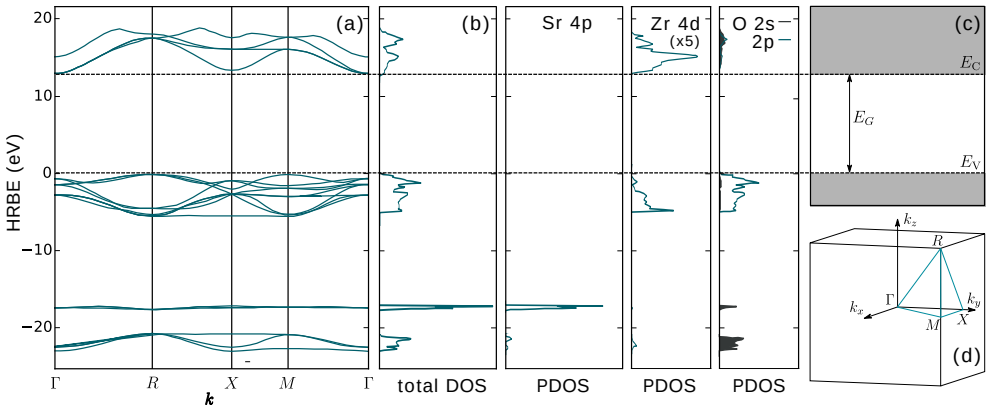

Figure 5.1 – (a) Single-particle band structure of a $SrZrO_3$ crystal (space group $Pm\bar{3}m$) shown along a line in the Brillouin zone, connecting some points of high symmetry. (b) Total and projected density of states of the band structure. (c) Band diagram. (d) Path in the Brillouin zone along Γ $(0,0,0)$, R $(1/2,1/2,1/2)$, X $(0,1/2,0)$ and M $(1/2,1/2,0)$. Adapted from [181, 182].

considered from here. For crystals where the curvature[3] of the valence band top and the conduction band bottom with respect to the $\boldsymbol{k}$ vector is equal, E_F lies exactly in the middle of the band gap.

Furthermore, the so-called density of states (DOS) is shown in Fig. 5.1(b). This property is calculated by counting the number of available sp states in the energy interval $[E, E + dE]$ and can be interpreted as a condensed version of the full band structure. The DOS can also be *projected* on the different atomic orbitals[4] or on the different *orbitals* to obtain the projected DOS (PDOS). This is in practice done by calculating overlap integrals between the Bloch solutions and atomic orbitals, centered onto the nuclear positions.

An even more simplified representation of the compound's sp electronic structure is shown in Fig. 5.1(c). Here, only two parameters are left, *i.e.* the locations of the valence band top, E_V and the conduction band bottom, E_C. The band gap energy is obviously found by the difference, $E_G = E_C - E_V$. This ultimately condensed representation is referred to as the band diagram in the following. These band diagrams are often found in qualitative analyses and empirical models (see also chapter 6).

[3] These are the so-called effective masses of electrons and holes, $m_{ij}^{*-1} = \frac{\partial^2 \epsilon(\boldsymbol{k})}{\partial k_i \partial k_j}\Big|_{\boldsymbol{k}=\boldsymbol{k}_0}$ for the sp eigenvalue $\epsilon(\boldsymbol{k})$, evaluated at the extremal point $\boldsymbol{k}_0$.

[4] Formally spoken, the concept of an atom is lost within a molecule or solid, which should be rather regarded as a collection of nuclei and electrons. Nonetheless, atomic cores can unambiguously be found and only for the valence electrons it becomes problematic to assign them to an *atom*. This covalency is clearly visible in the overlapping PDOS.

5.2 Imperfect crystals

In the derivation of the Bloch sp states for the crystal, it was explicitly assumed that the crystal is perfect, showing the long range order as described by the space group. This means that no *defects* are present in the crystals. Real materials however always contain defects, either intrinsically present or extrinsically applied [183]. Depending on their extent, defects are divided into point or extended defects such as line and planar defects. This work is restricted to point defects. Intrinsic point defects are either vacancies (V_M) or interstitials (M_i), representing a missing and a surplus of atomic species M respectively. Extrinsic defects are impurity atoms (X) that can be incorporated substitutionally (X_M) or interstitially (X_i). Defect clusters often occur, *e.g.* an antisite defect ($M_{1M_2} + M_{2M_1}$), a Frenkel defect ($V_M + M_i$) or a Schottky defect where vacancies cluster in a stoichiometric fashion. Here, the Kröger-Vink notation was used to label the different types of defects. Typically, the Kröger-Vink charge is also given, defined as the difference between the oxidation state of the defect and the oxidation state of the pristine lattice site. It is denoted by $'$, $^\times$ or $^\bullet$ for negatively, neutral (or isovalent) and positively charged defects respectively [183].

The presence of a point defect breaks the translation symmetry of the crystal and possibly also the point group symmetry. The pristine band structure will be altered through the occurrence of impurity levels, *i.e.* sp states that occur at energies that were forbidden for electrons in the pristine crystal. Furthermore, the defect can scatter electrons in Bloch states, changing the density of states of the allowed bands [184]. It has been experienced that a general treatment of the electronic structure is not simple. In the following, the most remarkable results are briefly reviewed in order to get a better understanding of energy levels of defects in the band picture [185].

5.2.1 Shallow levels

The so-called effective mass theory for impurities was devised by Joaquin M. Luttinger and Walter Kohn in 1955 [186, 187]. It is valid for substitutional impurities which differ by only one atomic number with the atom they replace. In this case, the impurity has one excess or one deficient valence electron with respect to the pristine material. Luttinger and Kohn proposed a sp Schrödinger equation for the excess electron or hole, which interacts by a Coulomb-like $1/r$ potential with the remainder of the impurity. In other words, a hydrogen-like eigenvalue equation is obtained. Instead of taking the vacuum level as energy reference as in the atomic case, here the CB bottom, E_C or VB top, E_V is taken for electrons and holes respectively, as this point corresponds to exempting the charge carrier from the impurity. Consequently, the sp electronic structure of this Luttinger-Kohn defect shows hydrogen-like orbitals reaching towards the associated band. When the effective mass impurity is ionized, this corresponds to a neutral Kröger-Vink charge. When not ionized, a single negative or positive Kröger-Vink charge is found for electron donors or acceptors respectively. The energy to ionize the defect exactly corresponds to the energy difference between the 1s ground state and E_C or E_V. Two possible charge-states are

hence found for effective mass defects.

The substitutional defects that can be described by effective mass theory give rise to shallow impurity levels. This means that the occupation of the defect can be altered by varying the temperature. For higher temperatures, the defects will be ionized, while for low temperature, the charge carrier is frozen at the defect. The location of the Fermi level is found upon evaluation of the condition for charge neutrality. It is found that the Fermi level lies between the impurity level and the closest energy band at low temperature, when the charge carrier is trapped at the defect, while it converges towards the middle of the band gap for higher temperatures. When the Fermi level crosses the impurity level, the charge carriers get massively delocalized.

The Luttinger-Kohn model assumes a charged defect which exhibits a rather long-range Coulomb-like perturbation on the excess charge-carrier. Obviously, these assumptions are not valid for all point defect which are often neutral, showing a short-range perturbation potential, mainly originating from the different core potentials. In this sense, the notion of deep levels is introduced as opposed to shallow levels, where the difference is not necessarily the depth of the impurity level with respect to the CB or VB, but rather whether effective mass theory offers a successful description or not.

5.2.2 Deep levels

Simultaneously with the development of the Luttinger-Kohn model, George F. Koster and John C. Slater came with the first theory for deep levels [188,189]. In this model, Wannier functions are used as sp basis states rather than Bloch functions[5]. It is assumed that only the Wannier functions centered at the impurity contribute to the deep level. Green's function techniques were applied to the study of defects for the first time. Additionally, Slater and Koster initially assumed that only one sp level was perturbed by the defect. This band is then pulled into the band gap and pinned there. Depending on the sign of the matrix element of the perturbing Hamiltonian, the level has a different origin. For a negative potential, the perturbed eigenvalue is smaller than the original eigenvalue, implying that the impurity level has CB character and stays relatively close to the CB if the perturbation is small. Similarly, for a positive potential, an impurity level with VB character is found. If the magnitude of the perturbation increases, the impurity level will go further into the band gap and is expected to obtain character of both VB and CB, requiring a description in terms of more than one sp level, which can be effectuated in the model.

The Koster-Slater model assumes that the Bloch electrons get scattered at the impurity by its different core potential, yielding impurity levels with s or p character. In the case of transition metals, the Bloch electrons get however mainly scattered by the d electrons, yielding impurity levels with d character. This requires a dif-

[5]Wannier functions are the Fourier transform of Bloch functions. Given the extended nature of the Bloch states in coordinate space, Wannier functions are localized, which is advantageous in the description of defects.

ferent model. In 1976, F. Duncan Haldane and Philip W. Anderson extended the Anderson impurity model for metals to the case of semiconductors [190]. Their research was mainly motivated by the remarkable discrepancy between the energy differences between the different charge states for free metal atoms and the occurrence of many different charge states as defects in semiconductors, *e.g.* Au^{3-} and Au^{+} can be formed in germanium, irrespective of its small band gap energy. In the Haldane-Anderson model, the localized d or f electrons are explicitly considered in addition to the itinerant electrons which are mixed, *hybridized*, by a single-particle interaction, parametrized by V, which is included in the model Hamiltonian:

$$\begin{aligned}\mathcal{H} &= \epsilon_\ell \sum_{m_\ell m_s} c^\dagger_{m_\ell m_s} c_{m_\ell m_s} + \sum_{\boldsymbol{k} m_s} \epsilon_{\boldsymbol{k}} c^\dagger_{\boldsymbol{k} m_s} c_{\boldsymbol{k} m_s} + V \sum_{m_\ell \boldsymbol{k} m_s} \left(c^\dagger_{m_\ell m_s} c_{\boldsymbol{k} m_s} + c^\dagger_{\boldsymbol{k} m_s} c_{m_\ell m_s} \right) \\ &\quad + \frac{1}{2} U \sum_{m_\ell m_s \neq m'_\ell m'_s} c^\dagger_{m_\ell m_s} c^\dagger_{m'_\ell m'_s} c_{m_\ell m_s} c_{m'_\ell m'_s}. \end{aligned} \tag{5.12}$$

The localized electrons mutually interact by a Hubbard-like U term[6]. The Hamiltonian was solved within the Hartree-Fock approximation with the band gap, location of the d level with respect to the band gap, tp interaction strength and the hybridization strength as tunable parameters. The result of this investigation was the confirmation that, when the hybridization is sufficiently large with respect to the tp interaction, multiple charge states of the defect can be stable. When the number of electrons in a d orbital is increased, the hybridization ensures that the increased electron density close to the metal ion is compensated by a decrease of the density coming from VB electrons. This charge self regulating mechanism is the key to understand the occurrence of multiple charge states of metal ions doped in semiconductors or insulators. This mechanism is also directly responsible for the breakdown of Koopmans' theorem, *i.e.* the binding energy of the localized electrons is only identical to the highest occupied mean field level when the sp wave functions are not altered upon adding an electron, which is indeed not the case due to the hybridization. This means that the sp level schemes depend on the number of localized electrons and that in reality a sp level scheme is required for all relevant charge states.

While the Haldane-Anderson model gives a qualitative account on how the impurity levels of metal defects can be interpreted, it evades the inclusion of correlation effects as the Hubbard term is treated in a mean field approximation. Therefore, a multiplet picture, as required to understand the excited state landscape, does not occur. The link between the two viewpoints was elaborated in 1979 by the Soviet physicists K. A. Kikoin and V. N. Fleurov by an approach which can be regarded as a hybrid form of the original work of Tanabe and Sugano and the Haldane-Anderson model [191]. They refer to this calculation scheme as the *impurity pseudoion*. In a first step, an Anderson Hamiltonian is solved by a mean field calculation, using

[6] It describes the two-particle Coulomb interaction in an effective fashion, neglecting the details of the term splitting (see §4.1.2) by restricting the number of parameters to one instead of two (for $\ell = 1$), three (for $\ell = 2$) or four (for $\ell = 3$). See also §5.3.3.

a basis containing both Bloch functions as well as suitable linear combinations of impurity centered d functions, adapted to the symmetry of the defect cluster. The hybridization causes both types of basis functions to mix, altering the radial wave function associated with the localized electrons, which obtains a symmetry label $R_{n\ell\gamma}(r)$. This calculation is referred to as covalent renormalization. Subsequently, the obtained sp radial wave functions are used to calculate Slater-Condon parameters. In contrast to conventional CFT, more radial parameters, $F^k(\gamma_1, \gamma_2, \gamma_3, \gamma_4)$ (see *e.g.* Eq. 4.10), are found as each sp function has its own symmetry label, *e.g.* one obtains 18 parameters instead of 3 for a d shell in a cubic environment. Multiplets can be constructed by suitably combining the d-like functions, requiring recoupling and Clebsch-Gordan coefficients of the point group (see §4.2.1). Although similarities can be found, this approach is fundamentally different from ordinary CFT, *e.g.* no sp CF parameters exist in the theory of the pseudoion. Calculations within the framework of the impurity pseudoion are in practice not straightforward and the choice of realistic parameters is difficult. Nonetheless, this model offers the unique feature to combine the single-particle band picture and the many-particle atomic picture within the same formal framework, yielding interesting insights into the meaning of both types of energy level schemes.

5.2.3 Charge-state transition levels

From the above overview it is clear that a sp band picture containing impurity levels cannot be easily related to real materials. The main reasons are the multiplet effects and the occupation dependence of the sp spectrum with its associated geometric reorganization, *i.e.* the violation of Koopmans' theorem. To obtain a full picture of a real system, one needs a sp energy level scheme for every charge-state of the defect, while the mp energy level scheme should accommodate the different configurations. In order to retain the concept of impurity levels, a generalization of the impurity levels as they occur in the Luttinger-Kohn or Slater-Koster model was introduced by Schockley and Last in 1957 for defects that adopt multiple charge states [192]. *Energy levels* of a charged defect were pragmatically defined as the Fermi level locations at which the defect changes its charge to minimize the total free energy of the system. It was argued that the total energy of a defect cluster is a linear function of the Fermi level location, *i.e.* the chemical potential of the electron reservoir. Later, Zhang and Northrup found that the defect energy additionally depends on the chemical potentials of the atoms that are relevant for the defect, which are bound in a restricted range determined by the formation of unwanted impurity phases [193].

The formation energy for a defect X in a host compound A is calculated as:

$$E^f(A:X^Q) = E_{\text{tot}}(A:X^Q) - E_{\text{tot}}(A) - \sum_i n_i \mu_i + Q E_{\text{F}}. \tag{5.13}$$

Herein, Q denotes the Kröger-Vink charge of the defect and E_{tot} represents the total energy of the pristine crystal and a crystal with one defect. The integer n_i indicates the number of atoms of type i that have been added ($n_i > 0$) or removed ($n_i < 0$)

to form the defect and μ_i are the atomic chemical potentials. The Fermi level is referred with respect to the VB maximum, $E_V = 0$. The impurity levels are found as the so-called charge-state transition levels, *i.e.* the Fermi level locations at which two charge states of the defect have the same formation energy:

$$\epsilon(Q/Q') = \frac{1}{Q-Q'}\left(E^f(A:X^{Q'})\big|_{E_F=E_V} - E^f(A:X^{Q})\big|_{E_F=E_V} \right) \tag{5.14}$$

These levels correspond to the experimental impurity levels which can be assessed through various techniques such as deep-level transient spectroscopy (DLTS) or charge-transfer (CT) luminescence [94].

One should keep in mind that these impurity levels cannot be identified with energy levels in the sense that these are no solutions of an eigenvalue equation. Charge-state transition levels are thermodynamic concepts, indicating the relative stability of the different charge states of defects. The underlying electronic structure is in general more complex as explained in §5.2.1-5.2.2.

Figure 5.2 shows a schematic illustration of the defect formation energies as a function of the Fermi level location for a certain defect. The linear relation with the Kröger-Vink charge as proportionality factor is immediately clear. This figure shows how the impurity levels can be found as the point where the straight lines cross.

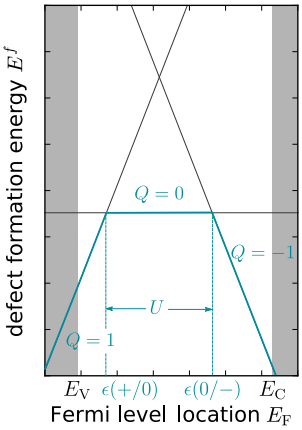

Figure 5.2 – Illustration of the formation energy E^f versus Fermi level E_F for a defect that can take three charge states, $Q = -1, 0, 1$. Two charge-state transition levels are found, a deep donor level $\epsilon(+/0)$ and a deep acceptor level $\epsilon(0/-)$. The thick line indicates the energetically favored charge state for a given Fermi level. Adapted from [94].

Often, a so-called U parameter or Coulomb correlation parameter is introduced for defects that can take multiple charge states. It gives a measure for the electron-electron repulsion at the defect, which is larger for highly localized states and for host compounds with a small electronic screening. In the case of two successive impurity levels:

$$\begin{aligned} U &= \epsilon(Q/Q-1) - \epsilon(Q+1/Q) \\ &= E^f(A:X^{Q+1}) + E^f(A:X^{Q-1}) - 2E^f(A:X^{Q}) \\ &= E_{tot}(A:X^{Q+1}) + E_{tot}(A:X^{Q-1}) - 2E_{tot}(A:X^{Q}). \end{aligned} \tag{5.15}$$

The notation and definition of this parameter is reminiscent of the Coulomb correlation parameter in the Anderson model[7]. In these models, the U parameters described the full electron correlation, while in the realistic case of d or f shells Coulomb correlation requires a description in terms of Slater-Condon or Racah parameters

[7] If the hybridization is switched off in the Haldane-Anderson Hamiltonian ($V = 0$), one immediately finds that the energy for a shell containing N electrons equals $E_N = N\epsilon_\ell + \frac{N(N+1)}{2}U$, yielding indeed $U = E_{N+1} + E_{N-1} - 2E_N$.

(see 4.1.2). For this reason, knowledge of U through experiments or the calculation of charge-state transition levels is not sufficient to generate the excited state landscape of the impurity.

Charge-state transition levels can be calculated within a theoretical framework of choice that yields total energies. In §5.3 it will be shown how density functional theory can be employed for this.

5.3 DFT description of point defects

Density functional theory (DFT) is a popular tool to study the incorporation, chemical bonding and electronic structure of defects in crystalline solids. A recent tutorial review of Freysoldt *et al.* is available on how to calculate defect formation energies by means of DFT for defects in supercells, imposed to periodic boundary conditions, offering an in-depth overview of many aspects concerning the interpretation of results and the practical implementation on how to obtain them [94]. Here, the most important aspects of the DFT formalism and its application to the study of luminescent defects is summarized. The calculations in this work are performed with the Vienna Ab Initio Simulation Package (VASP) [194–196].

5.3.1 Density functional theory

The special feature that distinguishes DFT from other electronic structure methods is that it does not search for solutions in terms of the many-electron wave function, a complex-valued function of the $(3+1)N$ electronic degrees of freedom of the N electron system, but it searches for the *ground state* electron density, a real function of only the three spatial dimensions.

According to quantum mechanics, knowledge of the external potential $v(\boldsymbol{r})$, defined as the system-dependent part of the electronic Hamiltonian[8]:

$$\mathcal{H}_e = \underbrace{\sum_{i=1}^{N}\left(-\frac{\hbar^2}{2m_e}\nabla_i^2 + \sum_{j>i}^{N}\frac{e^2}{4\pi\epsilon_0\left|\boldsymbol{r}_j-\boldsymbol{r}_i\right|}\right)}_{\substack{\text{system independent}\\ F}} \underbrace{-\sum_{i=1}^{N}\sum_{\alpha=1}^{M}\frac{Z_\alpha e^2}{4\pi\epsilon_0\left|\boldsymbol{R}_\alpha-\boldsymbol{r}_i\right|}}_{\substack{\text{system dependent}\\ +\sum_{i=1}^{N} v(\boldsymbol{r}_i)}}, \tag{5.16}$$

yields the total wave function ψ as solution of the Schrödinger equation. Subsequently, the electron density ρ can be obtained by integrating $\left|\psi\right|^2$ over the $3N$ spatial coordinates of the electrons. One thus arrives at the *"ordinary"* sequence:

$$v(\boldsymbol{r}) \Rightarrow \psi(\boldsymbol{r}_1 \ldots \boldsymbol{r}_N) \Rightarrow \rho(\boldsymbol{r}). \tag{5.17}$$

[8] We work in the Born-Oppenheimer approximation (see §2.1.1) and omit the constant nucleus-nucleus repulsion.

The development of the DFT formalism dates back to the 1960s and is largely due to Pierre Hohenberg, Walter Kohn and Lu Jeu Sham. The at first sight surprising fact that the electron density contains all the information which is also hidden in the total wave function is essential to understand DFT. This is governed by the first Hohenberg-Kohn theorem which states that $v(\boldsymbol{r})$ can be determined from the ground state density, implying bijectivity of previous relation:

$$v(\boldsymbol{r}) \Leftrightarrow \psi(\boldsymbol{r}_1 \dots \boldsymbol{r}_N) \Leftrightarrow \rho(\boldsymbol{r}). \tag{5.18}$$

Thanks to this relation, it can be easily seen that the total energy -and any other physical property- will be a functional of the electron density, $E[\rho(\boldsymbol{r})]$. It is typically separated in its purely electronic and external contributions, $E[\rho] = F[\rho] + V_{\text{ext}}[\rho]$ with $F[\rho]$ the universal or Hohenberg-Kohn potential and

$$V_{\text{ext}}[\rho] = \int \rho(\boldsymbol{r}) v[\rho, \boldsymbol{r}] \mathrm{d}^3\boldsymbol{r}. \tag{5.19}$$

If an expression for $F[\rho]$ can be found, DFT would be an exact solution method. This is unfortunately not the case and an approximate functional needs to be used.

The second Hohenberg-Kohn theorem offers a means to find the true ground state density for a given external potential. It states that the energy of an arbitrary density is always larger than the energy of the true ground state density. A minimization algorithm can then be used to find $\rho(\boldsymbol{r})$.

In practice, it is however difficult to find an expression for the kinetic energy as a functional of the density, $T[\rho]$, making it laborious and inaccurate to directly work with the density. To accommodate this difficulty, Kohn and Sham introduced a system of fictitious independent particles that give rise to the same density as the physical electrons. For the IPM, the kinetic energy can be simply calculated from the Kohn-Sham (KS) orbitals and is denoted as $T_s[\rho]$. The universal functional is separated as:

$$F[\rho] = T_s[\rho] + J[\rho] + E_{\text{xc}}[\rho], \tag{5.20}$$

with

$$E_{\text{xc}}[\rho] = T[\rho] - T_s[\rho] + V_{\text{ee}}[\rho] - J[\rho], \tag{5.21}$$

the exchange-correlation energy and $J[\rho]$ the direct part of the mean field of the inter-electronic repulsion[9], $V_{\text{ee}}[\rho]$ for the ground state density. The sp KS equations read

$$\left(\frac{-\hbar^2}{2m_e}\nabla_i^2 + v_{\text{eff}}(\boldsymbol{r}_i)\right)\phi_i^{\text{KS}}(\boldsymbol{r}_i) = \epsilon_i^{\text{KS}}\phi_i^{\text{KS}}(\boldsymbol{r}_i). \tag{5.22}$$

The sp effective potential is obtained by claiming that the density, calculated from the KS orbitals is the same as the density of the physical interacting electrons:[10]

$$v_{\text{eff}}(\boldsymbol{r}) = v(\boldsymbol{r}_i) + \frac{\delta J[\rho]}{\delta\rho(\boldsymbol{r})} + \frac{\delta E_{\text{xc}}[\rho]}{\delta\rho(\boldsymbol{r})} = v(\boldsymbol{r}_i) + \int \frac{\rho(\boldsymbol{r}')}{|\boldsymbol{r}-\boldsymbol{r}'|}\mathrm{d}^3\boldsymbol{r}' + v_{\text{xc}}(\boldsymbol{r}), \tag{5.23}$$

[9] $J[\rho] = \frac{1}{2}\iint \frac{\rho(\boldsymbol{r})\rho(\boldsymbol{r}')}{|\boldsymbol{r}-\boldsymbol{r}'|.}\mathrm{d}^3\boldsymbol{r}\mathrm{d}^3\boldsymbol{r}'$

[10] The definition of functional derivative is used here: $\delta F[f(x)] = F[f+\delta f] - F[f] = \int \delta f(x)\frac{\delta F[f]}{\delta f(x)}\mathrm{d}x$.

where $v_{xc}(\boldsymbol{r})$ is the exchange-correlation potential. The KS equations are solved in a self-consistent iteration scheme, reminiscent of Hartree-Fock theory, minimizing total energy:

$$E[\rho] = \sum_{i=1}^{N} \epsilon_i^{\mathrm{KS}} - J[\rho] + E_{\mathrm{xc}}[\rho] - \int v_{\mathrm{xc}}(\boldsymbol{r})\rho(\mathrm{r})\mathrm{d}^3\boldsymbol{r}. \tag{5.24}$$

DFT is exact in principle, in contrast to *e.g.* Hartree-Fock which is approximate by definition. This of course requires an expression for the exact exchange-correlation functional, an expression which unfortunately does not exist. In reality, many different approximations to this functional are used. The most important classes are:

- Local density approximation (LDA): Here, the functional depends solely on the value of the electron density at each point in space, *e.g.* no derivatives occur. The expression for the functional is often based on the equations for a homogeneous electron gas.
- Generalized gradient approximation (GGA): In addition to LDA, here the functional depends also on the gradient of the density, $\nabla\rho$, improving the description for non-homogeneous systems. If the functional depends in addition on the kinetic energy of the electrons, it is referred to as a meta-GGA functional.
- Hybrid functionals: Here, the GGA or meta-GGA functional is extended with a certain fraction of "exact exchange", meaning that a Coulomb exchange integral is calculated for the KS orbitals. These functionals require significantly more computational labor because of the occurrence of four-center integrals.

The above enumeration of functionals was called Jacob's ladder by DFT pioneer John Perdew in 2000. Here, every rung represents an increasingly sophisticated functional, ultimately reaching the *heaven of chemical accuracy*. The exact formulation of exchange-correlation functionals is outside the scope of this text and a specialization in its own. It should however be remarked that this is the point where empiricism sneaks into DFT. Most functionals contain parameters which are tuned such that well-chosen experimental data sets are reproduced by the DFT calculation. Although this devalues in a certain sense the philosophical superiority of those who want to predict properties of materials *from first principles*, a pragmatic point of view intrudes where DFT is one of the possible tools, including experiments, that are combined to obtain a better understanding of functional materials, finally leading to new applications or improvements of existing applications. In the meantime, the quest for the exact exchange-correlation functional, and the eternal glory for those to reach the heaven of chemical accuracy, continues unabated [197].

5.3.2 Physical interpretation of the Kohn-Sham eigenvalues

The KS wave functions were introduced as a mathematical trick to find the ground state density of the physical system. Therefore, there is no *a priori* reason to attach a physical meaning to the KS orbitals and eigenvalues. This is in stark contrast with what can be found in scientific literature. More than often, KS eigenvalues, mostly

in their disguise as a density of states (DOS) are used to explain physical properties. In particular, defect-projected PDOS are often interpreted as impurity levels. This is possibly in part motivated by the lower computational cost of a DOS calculation compared to calculating the full defect formation energy as sketched in §5.2.3 and §5.3.4. In the following, it is reviewed under which constraints this association is valid.

Related to that, the KS eigenvalues show a band gap which is typically compared to experimentally determined band gaps of solids. It is well-known in the materials science community that DFT has some issues with predicting the values of band gaps, discouraging many outsiders to apply DFT to their research as band gaps are important parameters for fundamental investigations as well as for technological applications of functional materials. In this paragraph, the origin of this bothersome shortcoming is briefly discussed. In §5.3.3 it is shown how this issue is circumvented in this work.

Quasiparticles

A popular interpretation of the KS orbitals and energies is that they originate from so-called quasiparticles. These objects can be envisaged as the relics of the sp excitations when the interaction is turned on [198]. Quasiparticles obey different equations of motion than free particles, although their properties are modeled as those of free particles. In this treatment, effective parameters are then introduced, reminiscent of the free particle parameters, but with different values. A conduction band electron in band theory is an excellent example. Its $E(k)$ dispersion relation close to the CB minimum is modeled as that of a free electron,

$$E(k) = \frac{\hbar^2 k^2}{2m_e^*}, \tag{5.25}$$

however with an effective mass which is different than m_e.

Analysis of the quasiparticle concept by means of many-body physics learns that quasiparticles have a well-defined meaning for sp near the Fermi level. Further away from the Fermi level, the quasiparticle states acquire a width and lose their single-particle or single-hole meaning. This implies that, even when KS eigenstates can really be interpreted as quasiparticles, only those near the Fermi level have an experimental meaning.

Janak's theorem

In contrast to Hartree-Fock theory, KS-DFT does not feature a handy property such as Koopmans' theorem to relate excitation energies to the sp eigenvalues. However, by taking a small detour, another argument can be used to relate the KS eigenvalues close to the Fermi level to an addition (electron affinity) or removal (ionization potential) energy.

The theory of KS-DFT can be formally extended to accommodate fractional occupation numbers n_i ($0 \leq n_i \leq 1,\ 0 \leq i \leq N$). Janak showed that in this case the equality

$$\frac{\partial E[\rho]}{\partial n_i} = \epsilon_i^{\mathrm{KS}}, \tag{5.26}$$

holds, irrespective of which functional is used. Upon integration, this formula offers indeed a prescription for addition or removal energies, *e.g.*

$$I = E(N-1) - E(N) = -\int_0^1 \epsilon_N^{\mathrm{KS}}(n_N)\mathrm{d}n_N, \tag{5.27}$$

for the ionization potential. If this integral is rudimentarily approximated by using the trapezoidal rule[11], or in other words by assuming that $\epsilon_N^{\mathrm{KS}}(n_N)$ is a linear function, one obtains:

$$I = -\frac{1}{2}\left[\epsilon_N^{\mathrm{KS}}(0) + \epsilon_N^{\mathrm{KS}}(1)\right]. \tag{5.28}$$

Often, it is further assumed that $\epsilon_N^{\mathrm{KS}}(0) = \epsilon_N^{\mathrm{KS}}(1)$ so that the highest occupied KS eigenvalue is directly used to yield the ionization potential. The latter approximation is then justified by the argument that the electron density of the system containing many electrons is not altered significantly by removing one electron. This sounds reasonable for infinite systems, but is highly doubtful in the case of the localized d or f states of transition metal or lanthanide impurities in insulators. In contrast, it has been shown that Kohn-Sham levels can give qualitative insights into the occupation of defects and defect clusters in their charge-neutral state [199].

Delocalization error

The band gap of a system with N electrons is given by the difference between the ionization potential, I, and the electron affinity, A:

$$E_G = [E(N-1) - E(N)] - [E(N+1) - E(N)] = I - A. \tag{5.29}$$

Hence to obtain a good value for E_G, the behavior of the energy as a function of the particle number has to be well-described. A few years after Janak's paper, Perdew, Parr, Levy and Balduz showed with a thermodynamic argument that the exact $E(N)$ is a continuous piece-wise linear function with a discontinuous slope at integer N values (see Fig. 5.3) [200]. The chemical potential μ, *i.e.* the derivative of the total energy with respect to the particle number will be constant for non-integer N and shows discrete jumps at every integer N. This yields an alternative way to express the band gap as:

$$E_G^{\mathrm{deriv}} = \lim_{\substack{\delta\to 0\\ >}} \frac{\partial E}{\partial N} - \lim_{\substack{\delta\to 0\\ <}} \frac{\partial E}{\partial N}. \tag{5.30}$$

And it is clear that when the total energy shows the correct piece-wise linear behavior, Eq. 5.30 is equivalent to Eq. 5.29, *i.e.* $I - A$.

[11] $\int_a^b f(x)\mathrm{d}x = \frac{1}{2}(b-a)[f(a) + f(b)]$.

It can be shown that

$$\mu = \frac{\partial E}{\partial N} = \frac{\partial E}{\partial n_f}, \tag{5.31}$$

for the optimized ground state where n_f is the occupation number of a frontier orbital, *i.e.* the highest occupied (HOMO) or lowest unoccupied (LUMO) KS state. Upon application of this equality and the Janak theorem, Eq. 5.26, we obtain:

$$E_G^{\text{deriv}} = \epsilon_{\text{LUMO}}^{\text{KS}} - \epsilon_{\text{HOMO}}^{\text{KS}}. \tag{5.32}$$

From the above, it is thus found that when the total energy shows the correct piecewise linear behavior:

$$E_G = I - A = \epsilon_{\text{LUMO}}^{\text{KS}} - \epsilon_{\text{HOMO}}^{\text{KS}}. \tag{5.33}$$

In other words, the assumptions at the end of §5.3.2 boil down to a correct description of the total energy as a function of the fractional occupation numbers. Hence, the accuracy by which the frontier KS eigenvalues yield a correct band gap depends on how well the used functional satisfies the linearity condition [197].

It turns out that the approximate functionals that are used in real calculations show a convex behavior, meaning that a too low energy is found for fractional charges (see Fig. 5.3). This implies that the calculated charge density will show a higher delocalization than the physical charge density. This is the definition of the delocalization or self-interaction error of DFT which lies at the origin of the systematically underestimated band gap values.

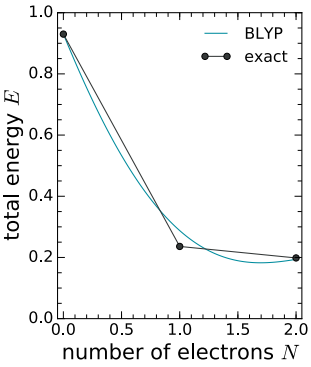

Figure 5.3 – E versus N for an external potential composed of a single proton. Comparison between the exact behavior and the GGA functional BLYP. The missing of discontinuous behavior is the hallmark of the failures of DFT for strong correlation. Adapted from [197].

5.3.3 On-site Coulomb interaction

Different possibilities exist to correct for the delocalization error of DFT of which some are very sophisticated. A possibility that is computationally rather cheap and which has proven its success, is inspired by the Anderson model (Eq. 5.12) and separates the system in localized and delocalized electrons. An explicit Coulomb interaction is added to the localized electrons, typically d and f electrons. Of course, the unaltered functional already took electron-electron interactions into account, so a part of the Hubbard term has to be subtracted again to avoid double counting. For the latter, the mean field approximation is usually taken. One then arrives at the total energy that is written as [201]:

$$E[\rho] = E_0[\rho] + \sum_I \left(E_{\text{Hubb}}^I[\rho] - E_{\text{dc}}^I[\rho] \right), \tag{5.34}$$

where $E_0[\rho]$ represents the uncorrected energy and $E_{\text{dc}}^I[\rho]$ is the term that avoids the double counting of interactions. The corrections are summed over all contributing

atomic sites I.

In the general formulation of Liechtenstein *et al.*, the expressions for the correction terms are [201, 202]:

$$E^I_{\text{Hubb}}[\rho] = \frac{1}{2}\sum_{m_\ell m'_\ell m''_\ell m'''_\ell}\sum_{m_s m'_s}\Big(\langle m_\ell m''_\ell|\,V_{\text{ee}}\,|m'_\ell m'''_\ell\rangle - \delta_{m_s m'_s}\langle m_\ell m''_\ell|\,V_{\text{ee}}\,|m'''_\ell m'_\ell\rangle\Big) c^\dagger_{m_\ell m_s} c^\dagger_{m''_\ell m'_s} c_{m'_\ell m_s} c_{m'''_\ell m'_s}, \tag{5.35}$$

$$E^I_{\text{dc}}[\rho] = \frac{U}{2}n(n+1) - \frac{J}{2}\Big[n^\uparrow(n^\uparrow-1) + n^\downarrow(n^\downarrow-1)\Big], \tag{5.36}$$

where the Hubbard and Stoner U and J parameters were introduced. n, $n^\uparrow$ and $n_\downarrow$ represent the total number and the number of spin-up and spin-down electrons in the shell to which the interaction is added. The atomic-like m_ℓ states are obtained by projecting the KS orbitals on the states of a localized basis set and the mean field double-counting term is obtained in the fully-localized limit, *i.e.* with the occupation numbers of every atomic orbital equal to 0 or 1. The matrix elements of V_{ee} are related to the Slater-Condon parameters (see §4.1.2) and provide the interpretation of the U and J terms in of the F^k's via the mean field term:

$$U = \frac{1}{(2\ell+1)^2}\sum_{m_\ell m'_\ell}\langle m_\ell m'_\ell|\,V_{ee}\,|m_\ell m'_\ell\rangle = F^0, \tag{5.37}$$

$$J = \frac{1}{2\ell(2\ell+1)}\sum_{m\neq m'}\langle m_\ell m'_\ell|\,V_{ee}\,|m'_\ell m_\ell\rangle = \begin{cases} \frac{F^2+F^4}{14} & (\ell=2) \\ \frac{286F^2+195F^4+250F^6}{6435} & (\ell=3). \end{cases} \tag{5.38}$$

Three implementations of this additional interaction are encountered in literature:

- Only the lowest order Slater-Condon parameter $F^0 = U$ is retained and $F^2 = F^4 = F^6 = J = 0$.

- Both U and J are retained. J is required to correctly describe atoms which have a net magnetic moment.

- U and J are combined in an effective parameter $U_{\text{eff}} = U - J$. This is known as Dudarev's scheme [203, 204].

The parameters U, J or U_{eff} are specified as input for the calculation. These parameters can themselves be obtained by self-consistent calculations at different levels of theory, or empirically chosen to reproduce experimental data such as band gaps. Because of the conspicuousness of the Hubbard U parameter in these correction schemes, these techniques are referred to as LDA+U, GGA+U or in general DFT+U.

5.3.4 Practical issues

In this section, some practical issues pertaining to DFT calculations of defect formation energies (Eq. 5.13) are summarized.

Plane-wave basis sets

To solve the KS equations, it is customary to expand the orbitals in a basis set, b_μ. Eq. 5.22 can then be rewritten as a matrix equation,

$$HC = SCE, \tag{5.39}$$

with

$$\begin{aligned} H_{\mu\nu} &= \langle b_\mu | -\frac{-\hbar^2}{2m_e}\nabla^2 + v_{\text{eff}} | b_\nu \rangle && (5.40)\\ C_{\nu i} &= \langle b_\mu | \phi_i \rangle && (5.41)\\ S_{\mu\nu} &= \langle b_\mu | b_\nu \rangle && (5.42)\\ E_{ij} &= \epsilon_i \delta_{ij}, && (5.43) \end{aligned}$$

where the indices i, j run to N, the number of KS orbitals and μ, ν to M, the dimension of the basis set. Many possible basis sets are available depending on the nature of the system under study. In this work, crystalline solids are investigated, suggesting the use of plane waves as basis sets. The use of plane waves comes with two advantages. First, the overlap integrals $S_{\mu\nu}$ automatically vanish. Second, the KS equations can be rephrased in reciprocal space (see §5.1) which implies a simplification of the equations [204, 205]. A discrete grid is typically chosen in $\boldsymbol{k}$ space. Fast Fourier transforms (FFT) are used to switch between $\boldsymbol{r}$ and $\boldsymbol{k}$ spaces (see also Eq. 5.6).

In reality, one cannot use the infinitely large plane wave basis set, but one needs to introduce a cut-off. The larger the vector $\boldsymbol{k} + \boldsymbol{G}$ becomes in the expansion Eq. 5.10, the smaller the associated wavelength, and hence the smaller the details that can be described by the plane wave. The resolution can be limited by introducing an upper bound for $\boldsymbol{k} + \boldsymbol{G}$, $\boldsymbol{G}_{\text{max}}$. In calculations, this is specified as a cut-off energy which can be calculated according to

$$E_{\text{cut-off}} = \frac{\hbar^2 G_{\text{max}}^2}{2m_e}. \tag{5.44}$$

Near atomic nuclei, the electron density typically oscillates very rapidly, requiring a high resolution and hence a very large number of plane waves to obtain a reasonable description. Often, space is separated in so-called muffin-tin spheres to accommodate this problem. Inside the spheres, atomic sp orbitals are used which are solutions of the radial Schrödinger equation for a pseudopotential while plane waves are used outside these spheres. The projector augmented wave (PAW) method is slightly different from the pseudopotential method. Here, the rapidly oscillating part of the wave functions is projected onto smooth wave functions that are easily expanded in terms of plane waves [195, 204, 206].

Charged supercells

The performed DFT calculations are subject to periodic boundary conditions and plane waves (see §5.3.4) are used to describe the KS orbitals. This means that a unit cell is defined which is copied infinite times in the three crystallographic directions. This is highly convenient for perfect crystals, but requires some thinking when defects are modeled. In reality, defects only occur at low concentrations, requiring large supercells to simulate their diluted occurrence. This size of the supercell is chosen such that the interaction between neighboring defects is nullified, requiring some pre-analysis using different cell sizes. The total energies that are required to calculate defect formation energies (see Eq. 5.13) are then calculated for pristine and defective supercells.

Simulating charged defects requires an additional measure to be taken into account. A net charge cannot be plainly put into the supercell as then the net charge of the infinite crystal would diverge. To guarantee charge neutrality, a homogeneously distributed background charge is added to the supercell. Furthermore, a term has to be added to Eq. 5.13 to correct for the interaction between the defect with its periodic images [94, 207, 208]. The monopole-monopole correction was applied, scaled by the macroscopic dielectric constant of the host material. The latter was calculated within the framework of density functional perturbation theory [209, 210].

Extrapolation scheme for transition levels

In §5.3.3 it was discussed that the DFT band gap can be widened further by adding an on-site Coulomb interaction, characterized by the parameters U and J or U_{eff}. It is clear that this interaction will affect not only the band gap energy, but also the location of charge-state transition levels. To handle both the inaccuracy of the band gap energy determined by DFT+U as well as the dependence of the band gap energy and impurity level locations on the U and J or U_{eff} parameters, an extrapolation scheme was proposed by Janotti and Van de Walle for the LDA+U functional [211]. This scheme can likewise be applied to a GGA+U functional.

Physical impurity level locations are obtained by shifting formation energies according to the differences between the PBE (Perdew-Burke-Ernzerhof, an often-used GGA functional) and PBE+U band gap on one hand and the experimental band gap and the PBE+U band gap on the other hand [211]:

$$E^f(A:X^Q) = E^{f,\text{GGA}+U}(A:X^Q) + \frac{E_\text{G}^\text{exp} - E_\text{G}^{\text{GGA}+U}}{E_\text{G}^{\text{GGA}+U} - E_\text{G}^\text{GGA}} n\Delta\bar{\epsilon}. \tag{5.45}$$

Here, n is the single-particle occupation number of the defect states in the band gap for charge state Q and $\Delta\bar{\epsilon}$ is the difference for the $\epsilon(Q/Q')$ values, calculated with GGA+U and GGA, averaged over the available charges Q'. A good correspondence between these extrapolated impurity levels and the experimental levels has been shown for multiple examples [94, 211, 212].

5.4 Charge transfer states

As shown in the previous paragraphs, a d block or f block defect can show different charge states. In reality, only one charge state will be stable at ambient conditions for most materials. However, through disturbing the equilibrium conditions, *e.g.* by illuminating the material with light, non-equilibrium charge states can be created during a short time span. In spectroscopy, these so-called charge transfer (CT) transitions have special characteristics and can be an important information source when constructing energy level schemes.

5.4.1 Mobile excitations

The most straightforward CT transitions do not involve defects, but are *simply* the fundamental interband transitions of the pristine host compound. In the IPM offered by band theory, these excitations correspond with particle-hole excitations, implying that these are found at an energy which is exactly the band gap energy. Unfortunately, or interestingly depending on one's point of view, interband excitations are poorly described by an IPM. The constituents of the formed *electron-hole* pair can interact strongly, entailing a strong correlation and hence the breakdown of the sp picture. The collective excitation which is formed is referred to as an exciton.

The most important experimental feature of this many-body effect is that excitation energies can be found in the region which was forbidden in the IPM. The energy difference between the lowest energy excitation and the sp band gap is often referred to as the exciton binding energy. It can be visualized that the individual particles are separated upon adding this energy to the system. Higher excited versions of the exciton can be found, not surprisingly similar to the spectrum of the hydrogen atom, or more appropriately positronium. In experimental contexts, the sp gap is often referred to as the electronic band gap, while the optical band gap is what is found in absorption experiments, *i.e.* the energy to create an exciton. Furthermore, many different types of excitons can be specified, depending on the binding energy, the spatial extent of the excitation, or even the scientific sub-discipline [12]. These distinctions fall outside the scope of this text.

5.4.2 Local excitations

A ligand to metal charge transfer (LMCT) can be found for most metal dopants, hence it is often referred to as charge-transfer without further specification. In a LMCT, an electron is transferred from the host compound to the impurity. In terms of the sp particle picture, this transition again corresponds with a particle-hole excitation, *i.e.* a transition from the VB maximum to an empty sp state of the impurity which is localized in the band gap. Also in this case, it is thinkable that many-body effects cannot be neglected, *i.e.* the full details of the multiplets of the d or f shell need to be taken into account in the initial and final states. A straightforward ex-

tension of the CFT formalism is imposed, so-called charge-transfer multiplet (CTM) theory, where configuration interaction with CT states is included. The latter are denoted as $|n\ell^{N+1}\underline{L}\rangle$, where $\underline{L}$ denotes a hole in the ligand shell L. The configuration interaction with the $|n\ell^{\overline{N}}\rangle$ states occurs through a Haldane-Anderson-like hybridization interaction (see Eq. 5.12) [213]. As this is a sp interaction, no Coulomb correlation between the ligand and metal electrons is accounted for, while this can be of importance to describe excitonic effects. In this case, the exciton is not mobile as in §5.4.1, but is fixed to the impurity by the electron. This is then referred as an impurity trapped exciton (ITE).

Interestingly, the distance between a $(Q/Q-1)$ charge-state transition level as defined by Eq. 5.14 and the VB maximum equals the energy of a LMCT by definition:

$$\epsilon(Q/Q-1) = E_{\text{tot}}(A:X^{Q-1}) - E_{\text{tot}}(A:X^{Q}) = E^{\text{CT}}(A:X^{Q}). \tag{5.46}$$

Here, total energies are used which include correlation effects. This shows that charge-state transition levels resolve the deficiencies of the sp model, while maintaining its simple interpretation and accounting for the complex mp interactions. It should be remarked that the total energies can be calculated for the relaxed atomic geometries for both charge states, corresponding to the thermodynamic charge-state transition level. For optical transitions, it can however be more meaningful to use the geometry of the initial state for both total energy calculations given the Frank-Condon principle (see §3.2.1). This yields the so-called optical charge-state transition level [94].

When an electron is transferred from the activator ion to another transition metal or lanthanide ion of the host compound, the transfer is referred to as a metal to metal charge transfer (MMCT). In both cases, the hole is fixed to the activator and the excitations can be regarded as ITE in the mp point of view.

A special case of a MMCT is when the partners that exchange an electron have the same atomic number. This can only occur for metals which can take two charge states that are relatively close in energy. A homonuclear MMCT is referred to as an intervalence charge transfer (IVCT)[12].

Often ITEs and CTs are regarded as different types of excitations. It is probably more correct to state that these are respectively the many-particle and single-particle pictures of the same kind of excitation.

[12] In luminescence literature, the vocabulary MMCT and IVCT are sometimes falsely interchanged [101, 214]. The definitions given here agree with the IUPAC prescriptions [215].

6 Impurity levels of lanthanides: empirical rules

In the previous chapters it was shown that an extensive choice of theoretical frameworks is available to understand and predict the properties of luminescent materials starting from a combination of a host and an activator. In general terms, a greater level of detail is achieved upon increasing the computational effort, considering hardware, software as well as user experience. On the other hand, a back-of-the-envelope calculation learns that an incredible number of host-dopant combinations are possible, preventing the large scale application of sufficiently accurate theoretical techniques.

A straightforward alternative is the use of empirical rules. These rules lack the formal theoretical basis of *ab initio* techniques, but allow for fast and computationally simple predictions of optical properties. Empirical relationships and rules of thumb pertaining to lanthanide materials have been reported during the last 40 years by multiple authors. Progressive was the PhD work of Charles Thiel, who constructed empirical band schemes, containing charge-state transition levels for all lanthanides based on photoelectron spectroscopy. During the last 20 years, Pieter Dorenbos excavated many of these relationships and observations from literature and tested them to a vast amount of experimental data, both confirming the correctness of existing models and rules, as well as uncovering new relationships [216]. Thiels' energy level schemes were refined by Dorenbos, who contrived a straightforward way to construct them from few simple-to-obtain optical spectra, immensely popularizing empirical modeling in the field of luminescent materials.

Rather than being rooted in a strong physical description, these models are empirical in nature, as they are constructed from a large amount of experimental data or parameters and subsequent fitting. Models are thus statistical in nature and predictions about yet to be performed experiments are essentially an extrapolation of existing data. However, interpretation of the empirical laws in terms of more fundamental physical laws is sometimes possible, but even then it usually remains necessary to introduce empirical parameters.

If a theory or a model allows to predict observable quantities, it should also be possible to get a grasp of the error margins associated with the model and consequently of the accuracy of the calculated parameters. This chapter aims to give an overview

of the errors, which are statistical in nature, of electronic and optical properties calculated by the conventional empirical relationships.

These empirical relationships are further explored to construct energy level schemes of lanthanide doped $CaGa_2S_4$ phosphors. This ternary sulfide is well known as host crystal for efficient lanthanide luminescence. It is therefore a suitable test case based on the detailed description in literature [5, 217–220]. An empirical band diagram for the lanthanide impurities was already constructed in 2005, although some radical simplifications were made at that time [220]. Relevant quantities, describing the optical and electronic properties of $CaGa_2S_4$:Ln^{Q+} materials are calculated and the error margins assessed, based on the prior error analysis.

Many of the common empirical rules are constructed in a most pragmatic way, neglecting as much crystallographic detail as possible. For instance, it is seldom considered that lanthanide ions can form multiple nonequivalent defects in certain host materials. Moreover, it is typically assumed that all lanthanide ions, which can be divalent or trivalent[1] incorporate in an identical fashion. Although this is often true due to the chemical similarity across the series, exceptions occur. In the second part of this chapter, it is assessed in which way these *nonidealities* affect the constructed energy level schemes and even corrupt the uncertainties associated with the empirical rules.

The findings in this chapter are published as:

Energy level modeling of lanthanide materials: review and uncertainty analysis

Jonas J. Joos, Dirk Poelman, Philippe F. Smet

Physical Chemistry Chemical Physics, **17** 19058-19078 (2015).

Nonequivalent lanthanide defects: Energy level modeling

Jonas J. Joos, Dirk Poelman, Philippe F. Smet

Optical Materials, **61** 50-58 (2016).

6.1 Nomenclature and roadmap

The energy level schemes that are constructed in this chapter belong to the *band picture*. The impurity levels that are discussed correspond to the charge-state transition levels (see §5.2.3) which signify the point that the electronic chemical potential needs to cross in order for the trivalent lanthanide ions to get reduced or oxidized, *i.e.* $\epsilon(Ln^{2+}/Ln^{3+})$ and $\epsilon(Ln^{3+}/Ln^{4+})$ using spectroscopic notation. In the following,

[1] Tetravalent lanthanide ions are not explicitly accounted for in these models.

the notation by Dorenbos is used:

$$E_{4f}(Ln^{2+}) \quad \leftrightarrow \quad \epsilon(Ln^{2+}/Ln^{3+}), \tag{6.1}$$
$$E_{4f}(Ln^{3+}) \quad \leftrightarrow \quad \epsilon(Ln^{3+}/Ln^{4+}), \tag{6.2}$$

which highlights the interpretation that the concepts of impurity levels and many-electron multiplets can be united. As this usage has not been theoretically substantiated to date, this text chooses not to take part in this movement and sticks to the distinction between single-electron and many-electron pictures as in traditional quantum mechanics and quantum field theory. The popularity of miscellaneous band diagrams in current literature is the motivation to use this notation nonetheless.

When vacuum referred energy level schemes are constructed, the chemical shift, $E_{4f}^{chem}(Ln^{Q+}, A)$, is the first parameter to be determined. The chemical shift refers to the similar meaning of a charge-state transition level for a lanthanide as defect and the ionization potential of the free lanthanide ion. It is hence defined as the energy difference between the impurity level and the free ion's corresponding ionization potential (denoted here as $E_{4f}(Ln^{Q+}, free)$):

$$E_{4f}(Ln^{Q+}, A) = E_{4f}(Ln^{Q+}, free) + E_{4f}^{chem}(Ln^{Q+}, A). \tag{6.3}$$

The symbol A refers to the host material, or more specifically to the crystallographic location where the lanthanide defect is situated.

The notion of chemical shift was first introduced by Pauling in 1929 for alkali halides [221]. It was revived by Pedrini *et al.* in 1978 to describe the photoconductivity threshold of divalent lanthanide impurities in alkaline earth fluorides [222–224]. In 2001, Thiel constructed a complete vacuum referred lanthanide energy level scheme by adding a parameter to the model used by Pedrini and experimental input from photoemission spectroscopy (PES) [225–228]. Later, Dorenbos elaborated on the chemical shift in the optical spectroscopy of lanthanides [216, 229]. For a detailed historical survey on the chemical shift and the various effects influencing it, we refer to chapter 5 of [227].

The parametrization of the chemical shift by Thiel and Dorenbos and the equivalence of both approaches are elucidated in §6.3. Despite the simplifying rationale of the model, it can explain some features of lanthanide spectra without cherishing the ambition to serve as a microscopic theory describing the electronic structure of lanthanide compounds, as this requires a framework of quantum mechanical many-body theory. In practice it is recommended to use the model only as a set of empirical rules yielding energy level schemes that are able to describe certain electronic and optical properties.

A semantic confusion might arise about the term chemical shift. As defined in Eq. 6.3, the chemical shift is a physical observable which can be calculated in multiple theoretical frameworks. The designation *chemical shift model* as introduced by

Dorenbos pertains to the parametrization of $E_{4f}^{chem}(Ln^{Q+}, A)$ in terms of a Coulomb potential (Eq. 6.22) and is thus one of all possible parametrizations.

The approach to obtain full vacuum referred binding energy (VRBE) and host referred binding energy (HRBE) level schemes is sketched in the following. Furthermore, in every step of the energy level roadmap (Fig. 6.1), the induced error is assessed in order to obtain a reliable error margin for every quantity calculated in this way. For averaged values, a single standard deviation was used for the error, *i.e.* 68% of the values lie within the error margin[2]. Similar for fitted trends, prediction limits of 68% were used, containing the accumulated effect of the uncertainty of the fit based on the available data - the confidence limits - and the scatter of the data around the fitted curve.

All steps of the calculation are summarized in Fig. 6.1, serving as a guide during reading or as a flow scheme when energy level diagrams for lanthanides inside a given host matrix are to be constructed. Additionally, the result of the error analysis is displayed. Figure 6.4 shows explicitly how energy level schemes are drawn from the calculated parameters. The model requires multiple parameters which are fixed. These are summarized in appendix C.

The empirical rules discussed in the remainder of this chapter contain only those relationships that are directly used to construct band diagrams with lanthanide impurity levels. Other relationships exist, such as those between the crystal structure of host compounds and the spectroscopic properties of lanthanide dopants, *i.e.* the multiplet energies [174, 175, 230, 231]. Some of these were applied in §4.5.3, but are left out of this discussion for consistency.

6.2 Review and uncertainty analysis

6.2.1 Vacuum referred impurity level, the chemical shift

The 4f-4f Coulomb repulsion energy of europium, $U(Eu, A)$, takes a prominent place in the empirical models. This parameter represents the difference in 4f binding energy of the Eu^{3+} and Eu^{2+} ion (see Eq. 5.16):

$$U(Eu, A) = E_{4f}(Eu^{2+}, A) - E_{4f}(Eu^{3+}, A). \tag{6.4}$$

For europium ions in free space, the Coulomb repulsion energy amounts to $U(Eu, free) = 18.05$ eV [229].

Europium is usually selected as lanthanide of reference because it is the divalent lanthanide on which most experimental data can be found. Two reasons can be devised for this. First, it is the lanthanide which can be stabilized in the divalent charge state most easily. Second, the Eu^{2+} ion is the most interesting lanthanide for designing

[2] A normal distribution is assumed.

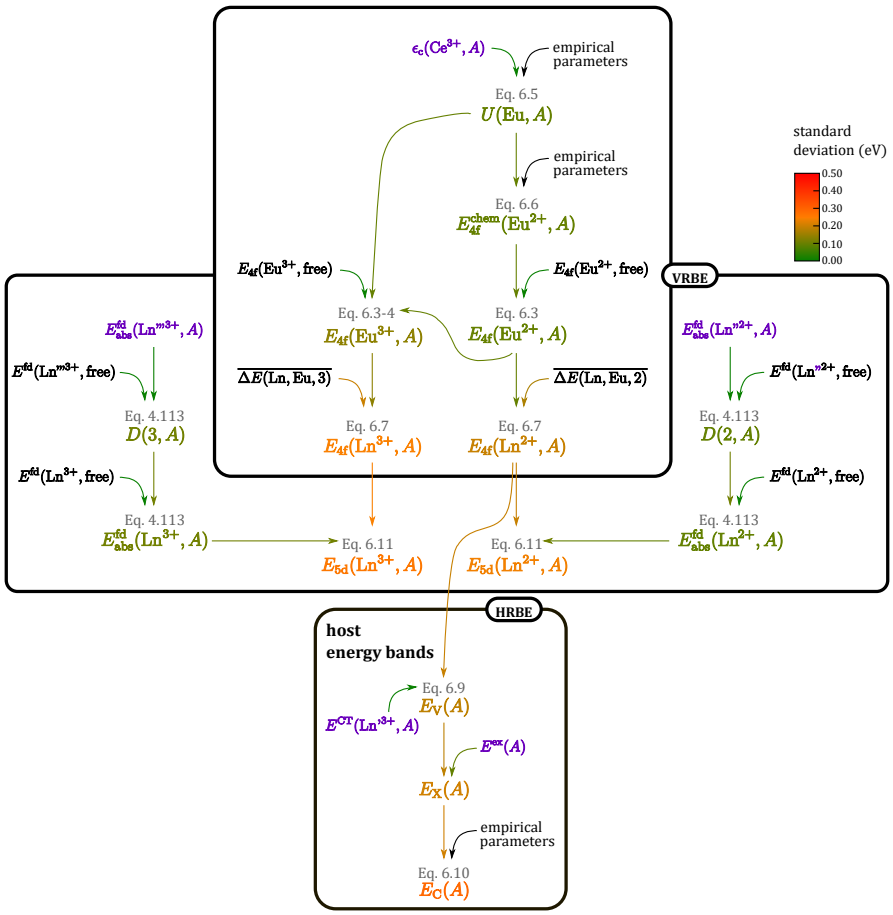

Figure 6.1 – Lanthanide energy level scheme roadmap. This flow diagram illustrates how VRBE and HRBE level schemes are obtained and which errors are accumulated. Empirical parameters are displayed in black, experimental parameters in purple and the color of calculated quantities maps their standard deviation. Ln', Ln'' and Ln''' denote specific lanthanide ions from which input is needed, such as the experimental charge transfer and 4f-5d transition energies (for divalent and trivalent lanthanides).

applicable materials due to its highly tunable emission color across the full visible spectrum (see 4.5.3).

$U(\mathrm{Eu}, A)$ can be acquired from an empirical relationship which relates this parameter with the centroid shift of the Ce^{3+} ion, $\epsilon_c(Ce^{3+}, A)$, *i.e.* the shift of the barycenter of the $5d^1$ manifold upon incorporation (see §4.5.3) on the lattice site A under study [232, 233]:

$$U(\mathrm{Eu}, A) = 5.44 + 2.834\, e^{-\epsilon_c(Ce^{3+}, A)/2.2}, \tag{6.5}$$

The obtained value for $U(\mathrm{Eu}, A)$ is expected to be less susceptible to random errors compared to the value one could obtain with the aid of a common host referred binding energy level scheme [233]. However, uncertainty originating from the nonlinear least square fitting procedure has to be taken into account.

The 68% prediction limits amount to 100 meV for $U(\mathrm{Eu}, A)$ when $\epsilon_c(Ce^{3+}, A)$ is in the range of 1.0-3.0 eV, which are typical values for Ce^{3+} doped dielectrics. The experimental error on $\epsilon_c(Ce^{3+}, A)$ is sufficiently small to be ignored as this can directly be obtained from luminescence spectroscopy. The data, fit and associated prediction band, yielding Eq. 6.5 are displayed in Fig. 6.2(a).

One could also calculate $\epsilon_c(Ce^{3+}, A)$ from crystallographic information of the host compounds, *i.e.* from the binding distance of the Ce^{3+} ion and its nearest neighbors and electronegativity values of the atomic species contained in the host compound [216, 234]. This is not explored in this overview to prevent the introduction of supplementary errors and the relatively straightforward way to obtain $\epsilon_c(Ce^{3+}, A)$ from experiment.

Subsequently, the chemical shift (in eV) of the Eu^{2+} ion is obtained from the empirical formula [216, 229]:

$$E_{4f}^{\mathrm{chem}}(Eu^{2+}, A) = \frac{U(\mathrm{Eu}, \mathrm{free}) - U(\mathrm{Eu}, A)}{0.777 - 0.0353\, U(\mathrm{Eu}, A)}, \tag{6.6}$$

The numbers in this formula were chosen to yield reliable chemical shifts for lanthanides in LaF_3, aqueous solution and lanthanide metals [229]. It is therefore rather difficult to estimate the error on $E_{4f}^{\mathrm{chem}}(Eu^{2+}, A)$ as calculated by Eq. 6.6. If a standard deviation of two units in the last digit of the numbers is taken into account, standard deviations for $E_{4f}^{\mathrm{chem}}(Eu^{2+}, A)$ in the range of 100-110 meV are obtained through propagation. Now $U(\mathrm{Eu}, A)$ and $E_{4f}^{\mathrm{chem}}(Eu^{2+}, A)$ are known, the VRBE of the Eu^{2+} and Eu^{3+} ions can be calculated from Eq. 6.3 and 6.4 with associated standard deviations of 100 meV and 150 meV respectively. The impurity levels for the Eu atom can then be added to the energy level scheme (Fig. 6.4-a,b).

6.2.2 Shape of the 4f zig-zag curves

Now that the impurity levels corresponding to Eu^{2+} and Eu^{3+} are localized with respect to the vacuum level, the zig-zag curves connecting the 4f levels of the different lanthanides can be constructed (Fig. 6.4-c). Zig-zag refers to the particular shape of this curve emerging from the gradual filling of the 4f shell across the lanthanide series. The 4f electrons are more tightly bound when the shell is completely or half filled, *i.e.* when 14 or 7 f electrons are present. This is reflected in the ionization energies of the free lanthanide ions [235]. Since the same trend is observed for the $4f^N$-$4f^{N-1}5d^1$ transition energies (see §4.5.3), the binding energies of the 5d electrons is approximately equal for all lanthanide ions with the same charge state (see §6.2.5).

The 4f zig-zag curves are defined by the difference in binding energy between the lanthanide ions and the europium ion:

$$\Delta E(\mathrm{Ln}, \mathrm{Eu}, Q, A) = E_{4f}(\mathrm{Ln}^{Q+}, A) - E_{4f}(\mathrm{Eu}^{Q+}, A). \tag{6.7}$$

In the lowest order of approximation, one could assume that the shape of these curves is unchanged when lanthanide ions are brought from the vacuum into the host lattice. This is however a poor approximation as the 4f curves are subject to *a rotation* (with the Eu ion as pivoting point) attributed to the slightly different crystal field experienced by the different ions due to their unequal ionic radii (see 6.3) [225, 226, 229]. There are two ways to account for this rotation.

The first possibility, which is most commonly used, is to utilize averaged ΔE parameters, $\overline{\Delta E(\mathrm{Ln}, \mathrm{Eu}, Q)}$. These were determined by averaging the shape of the zig-zag curves over a large number of host materials and are thus host independent [216].

The second possibility is to calculate a host specific version of ΔE by taking the degree of rotation into account in an empirical way. To acquire this, the contraction tilt parameter $\alpha(Q, A)$ is utilized (see §6.3):

$$E_{4f}(\mathrm{Ln}^{Q+}, A) = E_{4f}(\mathrm{Ln}^{Q+}, \mathrm{free}) + E_{4f}^{\mathrm{chem}}(\mathrm{Eu}^{Q+}, A) + \alpha(Q, A)\left[R(\mathrm{Ln}^{Q+}) - R(\mathrm{Eu}^{Q+})\right] \tag{6.8}$$

The contraction tilt can be calculated from Eq. 6.28 (see §6.3). In Eq. 6.28, f takes the lattice relaxation around the lanthanide impurity into account, R is the ionic radius [177]. In this work, f is taken to be 0.6 [216]. The real value of f depends however on the elastic properties of the host crystal and can only be assessed by advanced experimental techniques such as X-ray absorption spectroscopy (XAS) or calculation from first principles. Although Eq. 6.28 has some *theoretical* justification, it is not expected that the chemical shift model can really account for all the details of the interactions between metal ions and their crystalline environment. If correct values are used for the quantities in the right hand side of Eq. 6.28, one can calculate $\Delta E(\mathrm{Ln}, \mathrm{Eu}, Q, A)$ values which are as close to $\overline{\Delta E(\mathrm{Ln}, \mathrm{Eu}, Q)}$ as 50-150 meV. In any case, the similar values for $E_{4f}^{\mathrm{chem}}(\mathrm{Eu}^{Q+}, A)$ regardless of A indicate that only

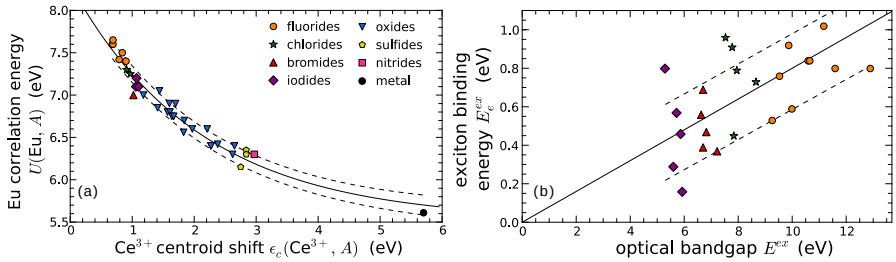

Figure 6.2 – (a) Experimental Ce^{3+} centroid shifts versus Eu Coulomb correlation energy values for different materials. The solid black line represents the empirical rule, Eq. 6.5. Data from [233]. (b) Experimental exciton binding energies versus optical band gap values for halide wide band gap semiconductors. The solid black line represents the $E^{ex}_{e-h}(A) = 0.08E^{ex}(A)$ rule. Data from [239]. In both cases, the dashed lines display the 68% prediction interval for the fit.

small variations in $\alpha(Q, A)$ are expected and the $\overline{\Delta E(\mathrm{Ln}, \mathrm{Eu}, Q)}$ values should be sufficiently accurate.

For the Ln^{2+} ions, the average $\overline{\Delta E(\mathrm{Ln}, \mathrm{Eu}, 2)}$ values were determined by Dorenbos from Ln^{3+} charge transfer (CT) energies ($E^{\mathrm{CT}}(\mathrm{Ln}^{3+}, A)$, see §6.2.3). For Sm^{3+}, Tm^{3+} and Yb^{3+}, a sufficient amount of data was available to reliably pin the $\overline{\Delta E(\mathrm{Ln}, \mathrm{Eu}, 2)}$ values within a standard deviation of typically 150 meV [236, 237]. For Pr^{3+}, Nd^{3+}, Dy^{3+}, Ho^{3+} and Er^{3+} only a few or even one CT data point was available to calculate the average [236]. For these ions, we estimate a standard deviation of 200 meV.

For the Ln^{3+} ions, initially, the rule of thumb $\overline{\Delta E(\mathrm{Ln}, \mathrm{Ce}, 3)} = 1.2\ \overline{\Delta E(\mathrm{Ln}, \mathrm{Ce}, 2)}$ was used together with the known values of $\Delta E(\mathrm{Ln}, \mathrm{Eu}, Q, \mathrm{free})$ for the shape of the free Ln^{3+} ions 4f curve [236]. A first improvement of this model was introduced by estimating binding energies of Ln^{3+} by pinning thermally quenched 5d levels close to or in the conduction band [236] . Recently, more accurate parameters were obtained from the MMCT energies of Pr^{3+} and Tb^{3+} in transition metal containing compounds [231, 238]. Since these transitions were only investigated for these two ions, more uncertainty is presumed for the shape of the Ln^{3+} 4f curve. In analogy with the Ln^{2+} 4f curve, a standard deviation of 200 meV is adapted.

When the standard deviation for $E^{\mathrm{chem}}_{4f}(\mathrm{Eu}^{Q+}, A)$ is propagated through Eq. 6.28, standard deviations of 1-2 meV/pm are obtained for $\alpha(Q, A)$, yielding standard deviations of 150 meV for $\Delta E(\mathrm{Ln}, \mathrm{Eu}, Q, A)$.

Hence, using the average shape of the zig-zag curves ($\overline{\Delta E(\mathrm{Ln}, \mathrm{Eu}, Q)}$) or a host compound specific one ($\Delta E(\mathrm{Ln}, \mathrm{Eu}, Q, A)$ through calculation of $\alpha(Q, A)$) gives rise to a similar accuracy.

6.2.3 Fixing the valence band

Now the vacuum referred binding energies (VRBE) of the lowest 4f levels are determined. They should be positioned with respect to the energy bands of the host compound (HRBE). Charge transfer (CT) energies of trivalent lanthanides are used to probe the distance between the top of the host's valence band (VB) and the $E_{4f}(Ln^{2+},A)$ ($\epsilon(Ln^{2+}/Ln^{3+})$) impurity level (see Eq. 5.46) [236]. In this way, the valence band of the host is added to the energy level scheme (Fig. 6.4-d).

The thermodynamic charge-state transfer energy was used to define the *impurity levels* of the lanthanide ions. As explained in §5.4.2, optical absorption experiments yield an energy value which is larger than the thermodynamic one due to a relaxation of the nuclear positions. Within this empirical framework, the distinction between the thermodynamic and optical charge-state transition energies is neglected, giving rise to intrinsic errors.

Since errors were already taken into account for the shape of the 4f curves, no additional error is induced in pinning the valence band with respect to the 4f curves. The experimental error on the charge transfer energy depends on the exact features of the spectrum. Typically, the maximum of the excitation band, corresponding to the CT is chosen as input for the energy level scheme. Frequently, this energy can be simply read from the spectrum with a small experimental error. It is however not uncommon that multiple CT transitions are present in the spectrum, possibly obscured by $4f^N$-$4f^{N-1}5d^1$ or $4f^N$-$4f^N$ absorption bands. In this case, resolving the desired energy value can be more challenging and a larger experimental error is expected. For current error assessment, the best case scenario, corresponding to an experimental error of 10 meV is adapted since the accuracy of the empirical models is the main topic of this work.

The vacuum referred binding energy of valence band electrons, *i.e.* the photoelectric threshold, $E_{PE}(A)$, is calculated as:

$$\begin{aligned} E_V(A) = -E_{PE}(A) \quad &= \quad E_{4f}(Eu^{2+},\text{free}) + E_{4f}^{\text{chem}}(Eu^{2+},A) \\ &\quad + \overline{\Delta E(Ln,Eu,2)} - E^{CT}(Ln^{3+},A) \end{aligned} \tag{6.9}$$

The uncertainty on $E_{PE}(A)$ is obtained from the uncertainties on all terms in Eq. 6.9, yielding standard deviations in the range of 150-200 meV. The most reliable value for $E_{PE}(A)$ is thus obtained if the CT energy of the Eu^{3+} ion is used, as in this case the third term in Eq. 6.9 vanishes (Ln = Eu). This quantity is experimentally accessible through X-ray or Ultraviolet Photoelectron Spectroscopy (XPS or UPS) [240]. Since these are surface techniques, the experimental value of E_{PE} is highly dependent on which surface of the crystal is probed and on possible surface reconstruction and passivation [240]. In the case of metals, the work function - defined as the energy difference between the vacuum level and the chemical potential of the electrons - is identical to the photoelectric threshold [240]. It is sometimes overlooked that this

is not true in the case of insulators or semiconductors where the chemical potential lies inside the forbidden band [240].

6.2.4 Self-trapped excitons and the conduction band

The conduction band (CB) can be added to the energy level scheme if the electronic band gap energy ($E_G(A)$) is known. This can be obtained by adding the exciton binding energy ($E^{ex}_{e-h}(A)$) to the optical band gap ($E^{ex}(A)$) as displayed in Fig. 6.4-e,f. Although a horizontal line is typically added to the band diagrams below the CB to indicate the exciton binding energy, this does not correspond to an energy level. As explained in §5.4.1, excitons are many-body effects which cannot be represented in a single-particle orbital diagram.

The optical band gap value is typically determined from absorption spectroscopy or diffuse reflection spectroscopy on powders, combined with Kubelka-Munk (KM) fitting of the absorption coefficient (see §7.2.1). The rather inaccurate nature of this technique in the case of powder reflection spectroscopy does not allow to neglect the error on this experimental parameter. One standard deviation is estimated to be 100 meV.

To obtain the electronic band gap, one needs the excitonic binding energy in addition. Unfortunately, this quantity is hard to determine. To meet this difficulty, a rule of thumb was introduced in [241] to relate the electronic and optical band gap values:

$$E_G(A) = 1.08E^{ex}(A) \tag{6.10}$$

The 1.08 proportionality factor was determined as the average of the limited available data.

The error on the location of the conduction band depends on the accuracy of the *1.08-rule of thumb*. In Fig. 6.2(b), the underlying data to obtain this rule are displayed. The proportionality between the optical band gap energy and the exciton binding energy of a compound is not so clear. Furthermore, the used data set is biased towards halides and does not consider oxides, nitrides, ... However, thanks to the small binding energies of (self-trapped) excitons compared to the band gap of the considered material classes, the large relative error for $E^{ex}_{e-h}(A)$ (in the order of 20-100%) reduces to a moderate relative error for $E_G(A)$, corresponding to a standard deviation of typically 250 meV if both the experimental uncertainty on $E^{ex}(A)$ and the limited accuracy of Eq. 6.10 are taken into account.

If needed, the electron affinity, $A(A) = -E_C(A)$, can be obtained by subtracting $E_G(A)$ from $E_{PE}(A)$, yielding standard deviations in the range of 250-350 meV [240]. With this kind of modeling, the electron affinity of a semiconductor or insulator can easily be obtained from lanthanide spectroscopy [232, 233, 240, 242].

The valence stability of the divalent ions in a particular host can be estimated from the location of the lowest Ln^{2+} 4f level with respect to the host's energy bands. This is true by definition of the charge-state transition levels (see §5.2.3). Dorenbos confirmed the validity of the empirically found 4f levels as charge-state transition levels for multiple compounds [243]. The location of the electronic chemical potential is assumed to be halfway the band gap. This is only formally true at absolute zero and in the case when the effective masses of electrons and holes are equal [11]. Furthermore, the location of the chemical potential of the electrons is supposed to be unaltered upon introduction of the dopants. The energy difference between the center of the band gap and the relevant Ln^{2+} $4f^N$ level can be calculated with a standard deviation of 250 meV for Eu^{2+} and 300 meV for Sm^{2+}, Tm^{2+} and Yb^{2+}. Of course, the occurrence of shallow donor or acceptor defects can shift the chemical potential away from the center of the band gap (see §5.2.1). These defects can be intrinsically present, be a consequence of charge compensation schemes or induced via intentionally or unintentionally co-doping or treatment in specific gas atmospheres [243]. The specific shape of the 4f zig-zag curve which is to a large extent host-compound independent explains why Eu^{2+} is the most abundant divalent lanthanide, followed by Yb^{2+}, Sm^{2+} and Tm^{2+}. The most abundant tetravalent lanthanide ions are Ce^{4+}, Pr^{4+} and Tb^{4+}.

6.2.5 Interconfigurational 4f-5d transitions

In lanthanide spectroscopy, $4f^{N-1}5d^1$ configurations play often a crucial role. Adding a 5d level to the band diagram does not pose an additional difficulty. The significance of this level as a charge-state transition level is clear. When the chemical potential as well as the thermodynamic 4f charge-state transition level are higher than the 5d level, a $4f^{N-1}5d^1$ ground state is to be expected rather than a $4f^N$ ground state. This can be the case for certain divalent lanthanides [244, 245].

Typically, it is assumed that the spectroscopic redshifts ($D(Ln^{Q+}, A)$), *i.e.* the decrease in $4f^N$-$4f^{N-1}5d^1$ absorption energy from the free to the incorporated ion (see Eq. 4.113) are equal for all lanthanide ions having the same charge, regardless of their differing ionic radii [216]. The spectroscopic redshift was first introduced by Dorenbos in his large-scale investigation of reported transition energies [246]. However, the idea that the $4f^N$-$4f^{N-1}5d^1$ transition energies of the lanthanide ions are related is much older [247–249].

The energy of the $4f^N$-$4f^{N-1}5d^1$ transition was first investigated in great detail for the trivalent ions, mainly based on data for Ce^{3+}, Pr^{3+} and Tb^{3+}, confirming the known trend within a standard deviation of 100-115 meV. More data, underpinning this rule, was gathered during the last 20 years.

For the divalent lanthanides, similar data mining was performed, mainly based on electronic spectra of the Eu^{2+}, Yb^{2+} and Sm^{2+} ions [167]. The associated standard deviations amount to 50-100 meV. Other divalent lanthanides are very difficult or impossible to stabilize in compounds (see §6.2.4) leading to a lack of available data

for the redshifts.

These standard deviations pertain to the $4f^N$-$4f^{N-1}5d^1$ absorption energies. For the VRBE of the 5d level, the uncertainty on the location of the 4f level has to be added

$$\begin{aligned} E_{5d}(Ln^{Q+},A) &= E_{4f}(Eu^{Q+},\text{free}) + E_{4f}^{chem}(Eu^{Q+},A) + \overline{\Delta E(Ln,Eu,Q)} \\ &\quad + E^{fd}(Ln^{Q+},\text{free}) - D(Q,A), \end{aligned} \tag{6.11}$$

leading to standard deviations of 250-300 meV. If the location of the 5d level with respect to the host's valence band is required, one obtains:

$$\begin{aligned} E_{5d}(Ln^{Q+},A) - E_V(A) &= E^{fd}(Ln^{Q+},\text{free}) - D(Q,A) - \delta_{Q,3}U(Eu,A) \\ &\quad + \overline{\Delta E(Ln,Eu,Q)} - \overline{\Delta E(Ln',Eu,2)} + E^{CT}(Ln'^{3+},A), \end{aligned} \tag{6.12}$$

where Ln'^{3+} is the lanthanide ion for which the CT energy was used to pin the valence band. For the Kronecker delta, $\delta_{Q_1,Q_2} = 1$ if $Q_1 = Q_2$ and $\delta_{Q_1,Q_2} = 0$ if $Q_1 \neq Q_2$. If Ln = Ln' and $Q = 2$, this relationship simplifies to the often used formula:

$$E_{5d}(Ln^{2+},A) - E_V(A) = E_{abs}^{fd}(Ln^{2+},A) + E^{CT}(Ln^{3+},A). \tag{6.13}$$

In this case, the uncertainty is the experimental accuracy for probing both parameters on the right hand side of Eq. 6.13. In the more general case, a higher uncertainty is obtained, coming from the $\overline{\Delta E}$ terms. If the energy difference between the 5d level and the exciton binding energy or the CB bottom is needed, additional contributions to the standard deviation have to be considered.

In 2003, a linear relationship was proposed between the redshifts of the divalent and trivalent lanthanide ions, based on data from Ce^{3+} and Eu^{2+} spectra:

$$D(Eu^{2+},A) = 0.64D(Ce^{3+},A) - 0.233 \text{ eV}. \tag{6.14}$$

The data underlying this empirical rule is shown in Fig. 6.3, where error margins are given, corresponding to the 68% prediction interval, amounting to 250 meV.

By spectroscopic measurement of one $4f^N$-$4f^{N-1}5d^1$ energy for each valence state (or for one valence state, supplemented with formula 6.14), one can add the locations of the 5d levels for all ions to the energy level scheme (Fig 6.4-g,h).

6.2.6 Vibronic interactions

Up to now only static interactions between the luminescent ion and the host crystal have been considered. No attention has been paid to vibronic interactions resulting from the coupling of electronic states and vibrational modes of the defect cluster. However, this interaction has a strong influence on the spectroscopic properties of the compound. Vibronic broadening of emission and excitation bands and the Stokes

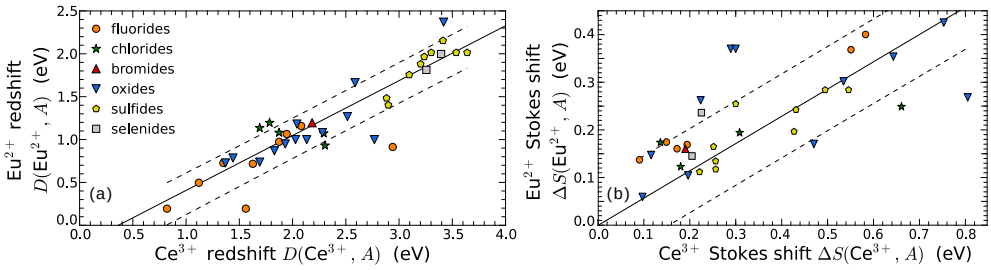

Figure 6.3 – (a) Spectroscopic redshifts of Ce^{3+} versus those of Eu^{2+} on the same lattice site. The solid black line represents the empirical rule, given by Eq. 6.14. The dashed lines display the 68% prediction interval for the linear fit. (b) Similar figure for the Stokes shifts and the empirical rule given by Eq. 6.16. Data from [168, 250].

shift are direct consequences of this interaction (see chapter 3).

The Stokes shift, ΔS, is defined as the energy difference between the absorbed and emitted photons originating from transitions between the lowest ground state (in this case the lowest $4f^N$ multiplet) and excited state (in this case the lowest $4f^{N-1}5d^1$ multiplet):

$$\Delta S(Ln^{Q+}, A) = E^{fd}_{abs}(Ln^{Q+}, A) - E^{fd}_{em}(Ln^{Q+}, A). \tag{6.15}$$

Similar to the redshift, it has been proposed that the Stokes shifts of Ln^{Q+} $4f^N$-$4f^{N-1}5d^1$ transitions are the same for all ions with the same charge in the same host crystal [167, 246, 250]. This was first substantiated for trivalent lanthanides, based on data from UV and VUV spectroscopy of Ce^{3+}, Pr^{3+}, Nd^{3+}, Er^{3+} and Tm^{3+} ions. The trend holds within a standard deviation of 15 meV. For divalent lanthanides, a similar trend has been shown for Sm^{2+}, Eu^{2+}, Tm^{2+} and Yb^{2+} within a standard deviation of 30 meV.

Stokes shifts for the $4f^N$-$4f^{N-1}5d^1$ intraconfigurational transitions of the Eu^{2+} and Ce^{3+} ions were compared in [173]. A positive correlation is clearly present and the values were connected through a linear fit,

$$\Delta S(Eu^{2+}, A) = 0.61 \Delta S(Ce^{3+}, A). \tag{6.16}$$

This fit is displayed in Fig. 6.3. Prediction intervals are situated at about 100 meV above and below the fitted value for $\Delta S(Eu^{2+}, A)$, corresponding to relative errors in the range of 20-80%. If the energy of Eu^{2+} emission in a certain host is to be estimated from spectroscopy of the Ce^{3+} ion, one needs to apply Eq. 6.14 and Eq. 6.16 consecutively yielding standard deviations of 270 meV. For example, if the lowest energy 4f-5d absorption band of Ce^{3+} is situated at 400 nm and shows a Stokes shift of 0.25 eV, the emission of the Eu^{2+} ion in the same host is predicted at 525 nm using Eq. 4.113, 6.14, 6.15 and 6.16. However, the uncertainty interval corresponding to a single standard deviation of 270 meV ranges from 470 nm to 595 nm, spanning a

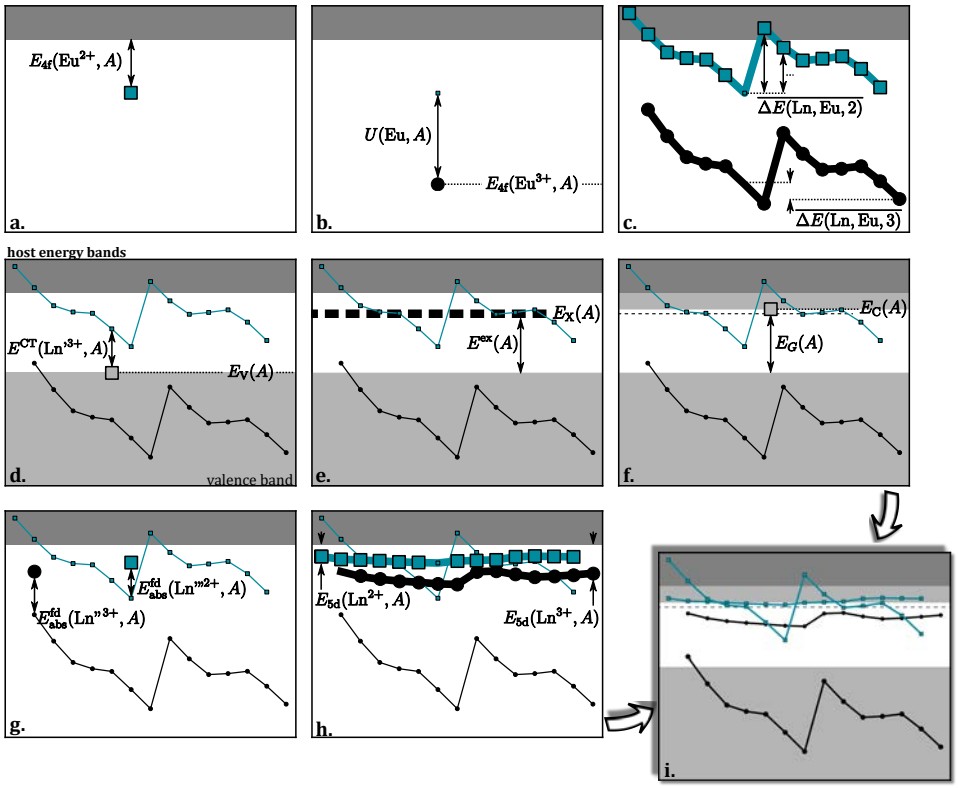

Figure 6.4 – Illustrative cartoon on how to obtain a lanthanide band diagram from the calculated quantities, summarizing §6.2.1-6.2.5. It shows how the impurity levels for Eu are positioned with respect to the vacuum level from knowledge of $U(\mathrm{Eu}, A)$ (a,b). The recurring shape of the 4f zig-zag curves is used to locate the impurity levels of the other lanthanides (c). Subsequently, the VB top is positioned from a LMCT energy (d) and the CB minimum from the optical band gap energy (e,f). A $4f^N$-$4f^{N-1}5d^1$ transition energy allows to localize the 5d levels (g,h), yielding the complete lanthanide impurity level scheme for host compound A (i).

significant fraction of the visible spectrum, ranging from blue to orange light emission. For this reason, these kinds of relationships have limited use for designing LED phosphors where specifications for emission peak wavelengths have a typical tolerance of a few to 10 nm (see chapter 1).

Furthermore, the width of the emission band cannot be assessed from these empirical relations while this is of major importance for the emission color of the phosphor. This can deviate strongly from host to host for the same luminescent ion, for example $Ba_{0.8}Sr_{0.2}SiO_4:Eu^{2+}$ shows an emission band full width at half maximum (FWHM) of 84 nm while for $SrGa_2S_4:Eu^{2+}$, the FWHM is only 52 nm. Emission bands of both

materials are nevertheless located in the same wavelength range [251, 252]. Within a configurational coordinate model, the emission band width can be expressed in terms of the Stokes shift and a phonon frequency, related to the host (see §3.4). Dorenbos applied this on a large number of Eu^{2+} activated crystals [168]. This model is however not sufficiently accurate to be used for practical applications [168].

The effects of vibronic interactions are hence not very well described by the empirical models. An important remark regarding the empirical energy level schemes is that all excited states (including CT transitions to fix the position of the top of the valence band) were derived from excitation spectra (or alternatively absorption spectra). Though this is the most straightforward way to assess the excited state landscape, one should not forget that in this way one does not consider the excited state in its relaxed form, *i.e.* the lowest vibrational energy level as illustrated in Fig. 3.1.

During excitation, a vertical transition occurs, corresponding to the energy of the absorbed photon. This is the energy which is used for constructing the energy level schemes. However, almost immediately after the photon absorption, a relaxation of the excited state occurs towards the lowest vibrational state of the excited state potential energy surface (at absolute zero temperature). It would be more appropriate to display this energy (*i.e.* the energy of the zero phonon line, ZPL) in purely electronic energy level schemes. Zych and coworkers have succeeded in obtaining more accurate $\overline{\Delta E(\mathrm{Ln},\mathrm{Ce},3)}$ values from measurement of the ZPL of Ln^{3+} $4f^N$-$4f^{N-1}5d^1$ transitions in four different hosts [253]. The applicability of this approach is however limited since ZPLs are most often obscured in spectra of 4f-5d transitions. Additionally, in designing materials for a specific application, the emission band maximum and FWHM are more important parameters than the location of the ZPL, both requiring a more detailed knowledge of the specific nature of vibronic interactions.

6.2.7 Thermal quenching of luminescence

Luminescent materials show a particular response as a function of temperature. Most often, the photoluminescence quantum efficiency drops when temperature rises above a certain critical temperature. Observationally, an energy barrier, E_{Mott} is often associated with thermal quenching in imitation of the Mott model (see §3.4.4). Then, the thermal quenching (TQ) profile of the material is described by:

$$I(T) = I_0\left(1 + \frac{\tau^{\mathrm{rad}}_{1\to 2}}{\tau^{\mathrm{n-rad}}_0}\mathrm{e}^{-E_{\mathrm{Mott}}/k_BT}\right)^{-1}, \tag{6.17}$$

where $\tau^{\mathrm{rad}}_{1\to 2} = 1/w^{\mathrm{rad}}_{1\to 2}$ is the intrinsic radiative decay constant of the ion and $\tau^{\mathrm{n-rad}}_0 = 1/w^{\mathrm{n-rad}}_0$ is the decay constant for the non-radiative decay path, responsible for TQ.

According to Blasse, this empirically determined energy barrier corresponds to the energy difference between the emitting excited state and the conduction band of

the host material in the case of the $4f^1$-$5d^1$ transition of Ce^{3+} [254]. This idea was extended to other $4f^N$-$4f^{N-1}5d^1$ transitions by multiple authors through the comparison of energy level schemes and TQ experiments [255–258]. Within this theoretical framework, one can calculate the TQ behavior from the constructed energy level scheme. It is however not very clear whether the CB bottom, the *exciton level* or some intermediate value has to be used. Note that in transition metal host compounds, TQ can proceed via an MMCT state. The confusion that arises when applying Eq. 6.17 has several origins which will be enumerated below.

E_{Mott} can be obtained from TQ measurements using two methods: one can fit Eq. 6.17 to the experimental quenching profile, or one can take $T_{0.5}$, *i.e.* the temperature where the intensity reaches 50% of the intensity at low temperature, as sole experimental parameter. This is then related to E_{Mott} by:

$$T_{0.5} = \frac{E_{\text{Mott}}}{k_B \ln \frac{\tau^{\text{rad}}_{1\to 2}}{\tau^{\text{n-rad}}_{0}}}, \tag{6.18}$$

as obtained from Eq. 6.17. Recently, Dorenbos and Rogers studied the Tb^{3+} $^5D_4$ and $^5D_3$ emissions and the Pr^{3+} $^3P_0$ emission in more detail for transition metal oxide host compounds, allowing a determination of the accuracy of this method [259]. In this work, the thermal quenching of the interconfigurational 4f transitions is ascribed to the presence of a MMCT state. The available data is displayed in Fig. 6.5.

Though one would expect a unit slope straight line through the origin, the fitted line intersects the horizontal axis around 70 K. This is attributed to the exact geometry of the potential energy surfaces (approximated as 1D parabola) in nuclear coordinate space in [259]. Since our interest is oriented towards the deviations from the trend line, neither the nonzero intercept nor the exact nature of the thermal quenching are of interest at this moment.

From the 68% prediction intervals, displayed in Fig. 6.5, the accuracy in determining $T_{0.5}$ from an energy level scheme is limited to 115 K for the Tb^{3+} and Pr^{3+} ions. A substantial fraction of the inaccuracy is coming from the E_{Mott} value. If one uses the self-trapped exciton lowest energy level as

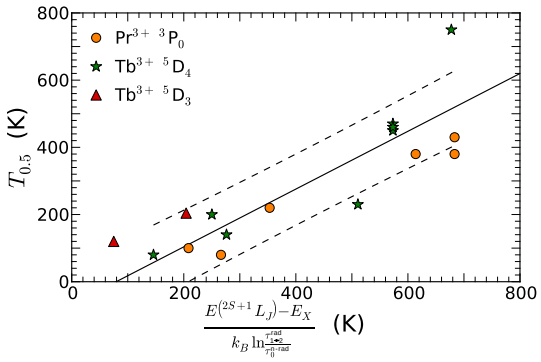

Figure 6.5 – Experimental versus calculated $T_{0.5}$ for Pr^{3+} $^3P_0$ emission and Tb^{3+} $^5D_4$ and $^5D_3$ emission. E_X represents the VRBE of a self-trapped exciton, $E(^{2S+1}L_J)$ of the emitting $4f^N$ level. $\tau^{\text{rad}}_{1\to 2}$ was taken to be 1 ms, 0.5 ms and 0.1 ms for $^5D_4$, $^5D_3$ and $^3P_0$ emission, respectively. A straight line is fit (slope 0.86, intercept -68 K) and the 68% prediction interval is shown. Data from [259]. Datapoints where only an upper or lower boundary was given, were omitted.

"end point" for the thermal quenching process, E_{Mott} is obtained from

$$\begin{aligned} E_{\text{Mott}}(\text{Ln}^{Q+}, A) &= E_X(A) - E_{\text{emitting level}}(\text{Ln}^{Q+}, A) \\ &= E^{ex}(A) - E^{\text{CT}}(\text{Ln}'^{3+}, A) - E_{\text{abs}}^{\text{transition}}(\text{Ln}^{Q+}, A) \\ &\quad + \delta_{Q,3} U(\text{Eu}, A) + \overline{\Delta E(\text{Ln}', \text{Eu}, 2)} - \overline{\Delta E(\text{Ln}, \text{Eu}, Q)}, \end{aligned} \tag{6.19}$$

inducing standard deviations in the range of 300-350 meV. If these standard deviations are propagated through Eq. 6.18, standard deviations for $T_{0.5}$ in the range of 160 K, 220 K and 280 K are obtained for Tb^{3+} $4f^8(^5D_4)$, Eu^{2+} $4f^6 5d^1$ and Ce^{3+} $5d^1$ emission respectively. These values are obtained without taking any additional error for $\tau_{1\to 2}^{\text{rad}}$ and $\tau_0^{\text{n-rad}}$ into account. It is seen that, while trends are usually able to predict transition energies and absolute level positions with sufficient accuracy, this type of model fails for the determination of TQ, since the standard deviations on the quenching temperature become excessive.

The accuracy of the method can be improved by using reliable values for the parameters $\tau_{1\to 2}^{\text{rad}}$ and $\tau_0^{\text{n-rad}}$ in Eq. 6.17. The lifetime of the excited state can be obtained from time-resolved luminescence spectroscopy (see §7.2.5). It is in general not sufficient to utilize a predetermined value for $\tau_{1\to 2}^{\text{rad}}$ as the radiative decay probability of an ion is sensitive to the embedding host (see §2.3.3) [260, 261]. $\tau_0^{\text{n-rad}}$ has the meaning of a frequency factor or attempt rate. The period of the main vibrational mode at the defect site is taken for $\tau_0^{\text{n-rad}}$ which is around $0.5-1 \times 10^{-13}$ s [258,259].

In the common reasoning which was sketched above, the calculation of the energy barrier height uses the location of the excited state as obtained from absorption or excitation spectroscopy. Again, the role of geometrical relaxation after photon absorption is not included. Thermal ionization of the defect is governed through the thermodynamic charge-state transition level, rather than the optical counterpart which was used to construct the energy level scheme. Nonetheless, the error margins are too large for accurate prediction of the thermal quenching temperature $T_{0.5}$. Furthermore, in §3.4.4, it was shown by explicitly calculating the overlap integrals between the vibrational wave functions and the temperature-dependent occupation of the vibrational energy levels that thermal quenching cannot be reliably described by a Mott-like expression such as Eq. 6.17 and that the details of the potential energy surfaces are required.

In addition, multiple competing (non-radiative) decay mechanisms exist, all having a different temperature response or nonequivalent luminescent centers might exist. For these reasons, thermal quenching (and decay dynamics) are very complex phenomena for which a simple model as Eq. 6.17 is inappropriate to grasp the details. In summary, a correct description of thermal ionization requires more details of the energy landscape which are harder to obtain from spectroscopic experiments.

Thermal quenching is not the only phenomenon for which conduction band states are thought to be involved. Anomalous luminescence, *i.e.* a luminescence phenomenon featuring a too low emission energy and a too large Stokes shift according to empirical experience, is often attributed to the radiative decay of an impurity trapped exciton. Furthermore, electrons or holes can sometimes be released from the activator ion, possibly leading to charge storage and delayed luminescence [156, 262–265]. Due to above mentioned reasons, quantitative predictions of these phenomena are not straightforward and in reality, empirical energy level schemes need to be considered as a qualitative aid in understanding experimental results rather than a way to predict experimental results [266,267]. First principles calculations can additionally be of great help to understand individual cases [268,269].

6.3 Parameterization of the chemical shift

C. W. Thiel parametrized the chemical shift as originating from the electrostatic, *i.e.* Madelung, interaction of the ions of the host crystal with the dopant ion, complemented with a term, correcting for the relaxation (α) of the lattice due to the non-equal ionic radii (R) of the lanthanide dopant (Ln^{Q+}) and the metal ion ($M^{Q'+}$) for which it substitutes [225–228]:

$$E_{4f}^{chem}(Ln^{Q+},A) = \frac{Qe^2}{4\pi\epsilon_0 d(A)} M(A) + \alpha(Q,A)\Delta R(Ln^{Q+},A). \tag{6.20}$$

Herein, $M(A)$ is the Madelung constant corresponding to the crystal lattice site on which the lanthanide incorporates and d the bond length to the nearest neighbors in the undoped crystal. ΔR is the difference in ionic radii between the dopant and the metal ion that is substituted by the dopant:

$$\Delta R(Ln^{Q+},A) = R(Ln^{Q+}) - R(M^{Q'+}). \tag{6.21}$$

In Dorenbos' model, the chemical shift is rationalized as the energy resulting from an electrostatic interaction between a single 4f electron and a charge at a certain *screening distance* ($R_Q(Ln^{Q+},A)$) described by a Coulomb-like law [229]:

$$\begin{aligned} E_{4f}^{chem}(Ln^{Q+},A) &= \frac{Qe^2}{4\pi\epsilon_0 R_Q(Ln^{Q+},A)} \\ &= \frac{Qe^2}{4\pi\epsilon_0 R_Q(Eu^{Q+},A)} \\ &\quad + \alpha(Q,A)\Big[\Delta R(Ln^{Q+},A) - \Delta R(Eu^{Q+},A)\Big] + \dots \end{aligned} \tag{6.22}$$

where a series expansion was applied around the case of the europium ion and a linear relationship utilized for the screening distance across the lanthanide series:

$$R_Q(Ln^{Q+},A) = R_Q(Eu^{Q+},A) - f\Big[R(Ln^{Q+}) - R(Eu^{Q+})\Big]. \tag{6.23}$$

Herein, f represents the extent of mechanical lattice deformation upon incorporation of impurity ions. It is assumed to be independent of both host lattice and dopant ion [229].

As one can see from Eqs. 6.20 and 6.22, both models are equivalent up to linear order in series expansion of Eq. 6.22, the former without a lanthanide as reference, the latter with europium as the lanthanide of reference (*i.e.* the last line of Eq. 6.22 vanishes for Ln=Eu).

The equivalence of the α parameters in the chemical shift models of Thiel and Dorenbos can be shown by explicitly writing the chemical shift for Eu^{Q+}:

$$E_{4f}^{\text{chem,T.}}(Eu^{Q+},A) = \frac{Qe^2}{4\pi\epsilon_0 d(A)}M(A) + \alpha_T(Q,A)\Delta R(Eu^{Q+},A) \tag{6.24}$$

$$E_{4f}^{\text{chem,D.}}(Eu^{Q+},A) = \frac{Qe^2}{4\pi\epsilon_0 R_Q(Eu^{Q+},A)} \tag{6.25}$$

Where T and D denote Thiel and Dorenbos respectively. If Eq. 6.24 and 6.25 are respectively subtracted from 6.20 and 6.22, one obtains $E_{4f}^{\text{chem}}(Ln^{Q+},A)$–$E_{4f}^{\text{chem}}(Eu^{Q+},A)$ for both models. These ought to be equal:

$$\begin{aligned}\alpha_T(Q,A)\Big[R(Ln^{Q+}) - R(M^{Q'+})\Big] - \alpha_T(Q,A)\Big[R(Eu^{Q+}) - R(M^{Q'+})\Big] \\ = \alpha_D(Q,A)\Big[R(Ln^{Q+}) - R(Eu^{Q+})\Big],\end{aligned} \tag{6.26}$$

indeed yielding $\alpha_T(Q,A) = \alpha_D(Q,A)$. The subscripts T and D can thus be omitted.

The screening distance $R_Q(Eu^{Q+},A)$, introduced by Dorenbos, is then related to the Madelung constant:

$$\frac{1}{R_Q(Eu^{Q+},A)} = \frac{M(A)}{d(A)} + \frac{4\pi\epsilon_0\alpha(Q,A)}{Qe^2}\Delta R(Eu^{Q+},A). \tag{6.27}$$

The binding energy shift per unit change in ionic radius, α, is named the contraction tilt parameter by Dorenbos, referring to the lanthanide contraction, *i.e.* the decrease in ionic radius for increasing atomic number for the lanthanides [229].

Both authors state that the chemical shift model should be approached in an empirical way, *i.e.* by making abstraction of an exact meaning of the M (or R_Q) and α parameters, but rather regard them as effective parameters. In this way the model can describe more complex interactions than purely the electrostatic one. Thiel considered M and α as two independent parameters which can be fitted to experimental photoelectron spectroscopy (PES) spectra. Dorenbos considers Eq. 6.20 as an approximation of Eq. 6.22, restricting the number of independent parameters to one. In this case, α can be calculated as:

$$\alpha(Q,A) = \frac{Qe^2 f}{4\pi\epsilon_0 R_Q^2(Eu^{Q+},A)} = \frac{4\pi\epsilon_0 f}{Qe^2}\Big[E_{4f}^{\text{chem}}(Eu^{Q+},A)\Big]^2 \tag{6.28}$$

In reality, the choice to use one or two parameters in the chemical shift model is of no relevance because the chemical shift is usually determined from another, purely empirical relationship (Eq. 6.6, see §6.2.1).

6.4 Example: $CaGa_2S_4$:Ln^{Q+}

In this part, the energy level modeling and error analysis is explicitly applied to lanthanide doped calcium thiogallate $CaGa_2S_4$. This will allow assessing to which extent these models can be used for predicting spectroscopic properties. Sulfides form an interesting class of host materials for energy level modeling due to their small band gap energy, allowing to measure charge transfer and fundamental absorption bands within the limits of standard experimental equipment, *i.e.* without the need for VUV spectroscopy.

The $CaGa_2S_4$ polymorph with the orthorhombic crystal structure, corresponding to space group Fddd, is considered [270]. Although three nonequivalent alkaline earth metal sites are present on which the lanthanide dopants can incorporate, their shapes and sizes differ barely such that it can be safely assumed that only one alkaline earth metal site is present. This is underpinned by the narrow emission band of the Eu^{2+} ion (see §6.4.1). The D_2 (or C_2) site symmetry can be approximated by a (non-crystallographic) D_{4d} point symmetry since the coordination polyhedra deviate only minimally from an idealized square antiprism [270]. In the strong-field coupling scheme, a single d electron with a fivefold degenerate energy level is expected to split in a singlet and two doublets:

$$\mathcal{D}^{(2)} = a_1 \oplus e_2 \oplus e_3. \tag{6.29}$$

6.4.1 Experimental spectra

Fig. 6.6 shows the emission and excitation spectra of Eu^{2+}, Ce^{3+} and Tm^{3+} in the described host material. The details on the spectroscopic experiments that were performed to obtain these spectra can be found in chapter 7. The numerical values of the parameters that can be obtained from these measurements are summarized in Table 1. For band maxima, an experimental error of 20 meV was taken into account. To obtain the transition energy from the $4f^7(^8S_{7/2})$ ground state to the lowest $4f^6(^7F_0)5d^1$ state of Eu^{2+}, the point where the excitation band is 20% of its maximum value is usually taken (see §4.5.3). For this procedure, an experimental error of 50 meV is adopted. The error on empirical parameters that are regarded as constants, such as $E^{fd}(Ln^{Q+}, \text{free})$ is taken to be 10 meV.

The Eu^{2+} and Ce^{3+} spectra are characterized by broadband luminescence in the visual range, coming from the intraconfigurational 5d-4f transition. Tm^{3+} shows line emission, originating from interconfigurational $4f^{12}$ transitions. The emission can be efficiently excited by a charge transfer transition, yielding a broad band in the

UV range of the excitation spectrum. In the $CaGa_2S_4$:Tm^{3+} excitation spectrum, an additional band peaking at 4.43 eV is visible. A similar band was also reported elsewhere and ascribed to fundamental absorption in the host material, sensitizing the Tm^{3+} emission [220]. Comparison of the Tm^{3+} excitation spectrum of a sample prepared in forming gas atmosphere (N_2 /H_2), with a similar sample, though prepared in hydrogen sulfide (H_2S) atmosphere, shows that the relative intensity of the Tm-S charge transfer peak increases in the latter case. This suggests that the additional band can as well originate from sulfur defects, unavoidably present in the prepared materials.

6.4.2 Energy level scheme, construction and discussion

The complete lanthanide energy level scheme for $CaGa_2S_4$ is displayed in Fig. 6.7. In this figure, error margins are indicated, based on the error analysis in the previous paragraph, corresponding to single standard deviations and 68% prediction limits.

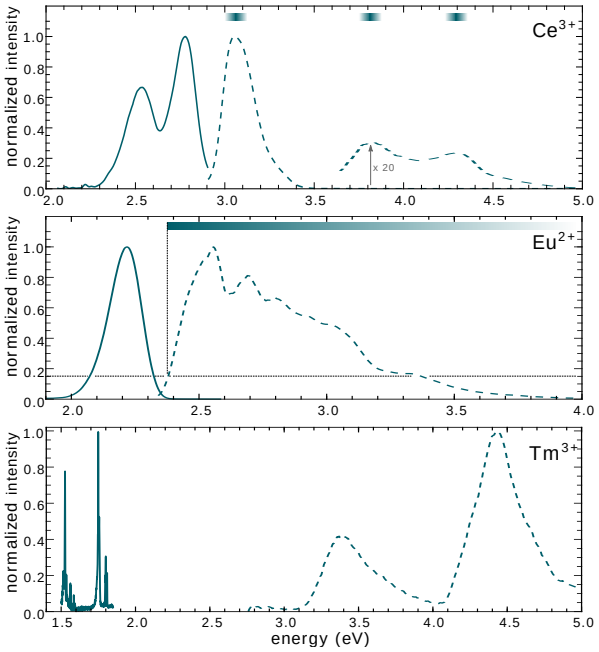

Figure 6.6 – Emission (solid lines) and excitation spectra (dashed lines) of lanthanide doped $CaGa_2S_4$, measured at 75 K. Top: Ce^{3+} doped, emission spectrum upon 410 nm (3.02 eV) excitation, excitation spectrum for 445 nm (2.79 eV) emission. Middle: Eu^{2+} doped, emission spectrum upon 450 nm (2.76 eV) excitation, excitation spectrum for 560 nm (2.21 eV) emission. Bottom: Tm^{3+} doped, emission spectrum upon 370 nm (3.35 eV) excitation, excitation spectrum for 810 nm (1.53 eV) emission. The colored bands indicate the locations of the $4f^N5d^1$ multiplets with respect to the $4f^N$ ground state.

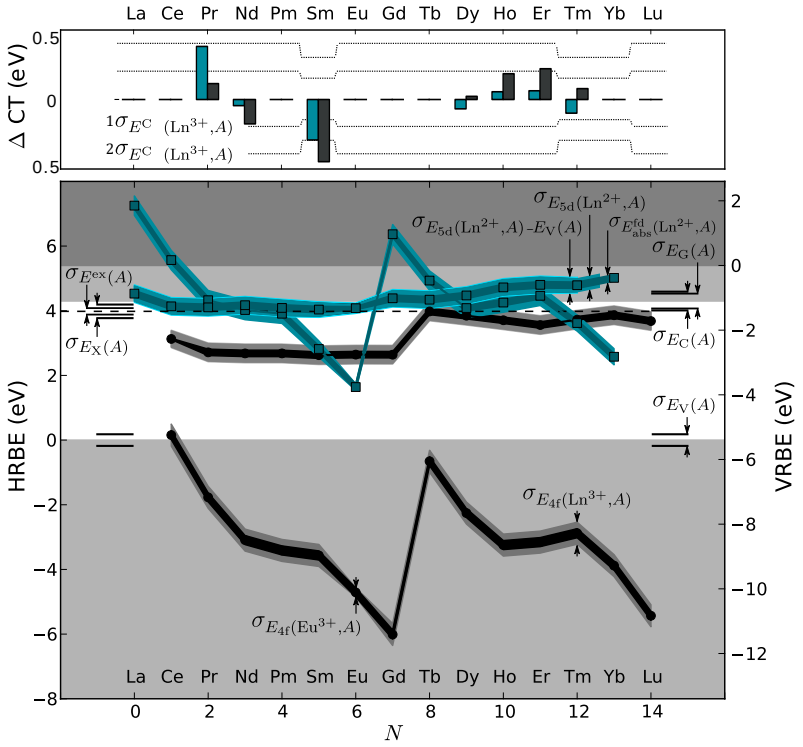

Figure 6.7 – Lanthanide impurity energy level scheme for the $CaGa_2S_4$ ($A = CaGa_2S_4$) host, calculated with the $\overline{\Delta E}$ parameters. The saw tooth shaped (zig-zag) curves represent the lowest 4f charge-state transition level of the ion, the more or less horizontal lines the lowest 5d level. Blue squares for divalent lanthanide ions ($\epsilon(\mathrm{Ln}^{2+}/\mathrm{Ln}^{3+})$), black circles for trivalent lanthanide ions ($\epsilon(\mathrm{Ln}^{3+}/\mathrm{Ln}^{4+})$). The single standard deviations, σ, for the impurity levels are represented by the thickness of the lines, the errors on the location of the host's VB, CB and exciton binding energy are indicated at the left and right sides of the figure. The symbol of the quantity of which the standard deviation is shown, is denoted in the subscript. The differences between the calculated and experimentally determined CT energies (ΔCT) are represented in the bar diagram on top. Blue for CT energies calculated from the averaged $\overline{\Delta E}$s, black for CT energies, calculated from the contraction tilt parameters α. When multiple experimental energies were available, the average was calculated. The dotted lines represent the calculated $\sigma_{E^C(Ln}3+,A)$ and $2\sigma_{E^C(Ln}3+,A)$ values [219, 220].

Table 6.1 – Optical properties of Ce^{3+}, Eu^{2+} and Tm^{3+} ions in the MGa_2S_4 (M = Ca, Sr) hosts. These parameters serve as input for the calculation of the lanthanide energy level schemes. d_1, d_2 and d_3 denote the positions of the three 4f-5d excitation bands of Ce^{3+}, f_1 and f_2 denote the positions of the two 5d-4f emission bands of Ce^{3+}. The spectra of $SrGa_2S_4$, their interpretation and the discussion of the energy level schemes can be found in §6.5.2. All values in eV.

		$A = SrGa_2S_4$	$A = CaGa_2S_4$
	Optical band gap $E^{ex}(A)$	4.16 ± 0.10	3.98 ± 0.10
$\mathbf{Ce^{3+}}$	Absorption $E_{abs}^{fd_1}(Ce^{3+}, A)$	3.03 ± 0.02	3.05 ± 0.02
	Absorption $E_{abs}^{fd_2}(Ce^{3+}, A)$	4.04 ± 0.02	3.81 ± 0.02
	Absorption $E_{abs}^{fd_3}(Ce^{3+}, A)$	4.32 ± 0.02	4.29 ± 0.02
	Redshift $D(Ce^{3+}, A)$	3.09 ± 0.03	3.07 ± 0.03
	Centroid shift $\epsilon_c(Ce^{3+}, A)$	2.40 ± 0.02	2.50 ± 0.02
	Crystal field splitting $\epsilon_{cfs}(Ce^{3+}, A)$	1.29 ± 0.03	1.24 ± 0.03
	Emission $E_{em}^{f_1 d}(Ce^{3+}, A)$	2.54 ± 0.02	2.54 ± 0.02
	Emission $E_{em}^{f_2 d}(Ce^{3+}, A)$	2.80 ± 0.02	2.78 ± 0.02
	Stokes shift $\Delta S(Ce^{3+}, A)$	0.23 ± 0.03	0.27 ± 0.03
$\mathbf{Eu^{2+}}$	Redshift $D(Eu^{2+}, A)$	1.76 ± 0.05	1.83 ± 0.05
	Stokes shift $\Delta S(Eu^{2+}, A)$	0.16 ± 0.06	0.17 ± 0.06
$\mathbf{Tm^{3+}}$	Charge transfer $E^{CT}(Tm^{3+}, A)$	3.32 ± 0.02	3.37 ± 0.02

In Fig. 6.7, the deviations between the calculated and measured CT energy are displayed in a bar diagram for both types of calculations, *i.e.* from $\overline{\Delta E}$ parameters and from the contraction tilt parameters ($\alpha(2, CaGa_2S_4) = 0.109$ eV/pm and $\alpha(3, CaGa_2S_4) = 0.175$ eV/pm). The typical error lies within 0.5 eV, corresponding to twice the calculated standard deviation. A better correspondence was found for the CT energies when the average $\overline{\Delta E}$ parameters were used. The difference in CT energies between these two approaches amounts up to a few 100 meV.

From the point of view of error analysis, no larger deviation is *a priori* expected for the CT energies obtained from the contraction tilt than those obtained from the $\overline{\Delta E}$s. Nevertheless, it appears to be the case. A possible reason for this is the inability to describe the detailed interactions in the lanthanide defect cluster with the main premise of the chemical shift model, namely the Coulomb potential, Eq. 6.22. In this case, Eq. 6.28 does not furnish the correct relation between $\alpha(Q, A)$ and $E_{4f}^{chem}(Eu^{Q+}, A)$. Alternatively, a simple rotation as described by Eq. 6.8 - which remains valid for a more general class of models than the chemical shift model - might be insufficient to describe the change of shape of the 4f curves upon incorporation. After all, the 4f curves obtained with $\overline{\Delta E}(Ln, Eu, Q)$ cannot be obtained by simple rotation of $\Delta E(Ln, Eu, Q, \text{free})$, the optimal contraction tilt parameters of $\alpha(2, \overline{A}) = 0.097$eV/pm and $\alpha(3, \overline{A}) = 0.156$eV/pm yield some deviations.

If the energy level scheme (Fig. 6.7) is compared with the one available in literature, a few differences show up [220]. In Fig. 6.7, most Ln^{2+} 5d levels are within the conduction band while they are below in [220]. This can be attributed to the different E^{ex} values used in both calculations. Bessière *et al.* used the maximum of a host related excitation band in the spectrum of Ce^{3+} [220]. It is however not sure whether the maximum of the broad excitation band corresponds to self-trapped exciton creation. Furthermore, the Coulomb correlation energy in [220] is rather low (around 5.5 eV according to their Fig. 5), corresponding to the value for Eu metal, recorded by Dorenbos (Fig. 6.2 and [233]). This results in a Ln^{3+} 4f curve which is too loosely bound with respect to the vacuum, having the Tb^{3+} 4f state in the band gap while in Fig. 6.7 it lies in the VB. This deviation can be related to the less extended energy level model used 10 years ago. On the other hand, if one considers realistic errors on all calculated quantities, the differences between both energy level schemes are limited and the scheme of Bessière *et al.* can be used as well. From the energy level scheme, electronic and optical properties of $CaGa_2S_4$:Ln^{Q+} are predicted.

From the locations of the $4f^N$ levels, it is inferred that the europium ion will be divalently incorporated, matching observation. All other lanthanides except for ytterbium are expected to be trivalent. Ytterbium is a more difficult case as the Yb^{2+} $4f^N$ ground state is very close to the center of the band gap. Comparison with other sulfide hosts suggests that ytterbium will most likely be incorporated as Yb^{2+} [267].

Afterglow of a few seconds has been reported in $CaGa_2S_4$:Eu^{2+} when this phosphor is co-doped with another lanthanide ion [271–273]. The locations of the Ln^{2+} 4f states with respect to the host's conduction band are of particular interest since it has been suggested that Ln^{3+} ions behave as electron acceptors, trapping auto-ionized electrons from the light emitting ion [156]. This has been successfully demonstrated for YPO_4:Ce^{3+}, Ln^{3+}, where trap depths between 0.5 eV and 3.2 eV were found from the analysis of thermoluminescence glow curves [264] . In the case of $CaGa_2S_4$ however, the 4f levels of Pr^{2+}, Nd^{2+}, Gd^{2+}, Dy^{2+}, Ho^{2+} and Er^{2+} lie very close or inside the conduction band of $CaGa_2S_4$. For this reason, all these lanthanides are expected to be poor trapping centers and no meaningful trend is expected as a function of N. This is also reflected in Figure 7 of [273] where three trap levels were fitted to TL glow peaks. The observed traps might be rather coming from defect levels, other than those associated with the 4f electrons of the codopant, nonetheless potentially caused by the incorporation of the codopant. For Sm^{3+} and Tm^{3+} as codopant, no light emission was observed which is in accordance with the calculated trap depths of 1.48 ± 0.31 eV and 0.68 ± 0.23 eV respectively, calculated with respect to the conduction band bottom. In these cases, the afterglow will be obscured by the deep traps from the Tm^{3+} and Sm^{3+} acceptor ions, which cannot be emptied at room temperature within a reasonable time. If the trap depths are calculated with respect to the self-trapped exciton binding energy, one obtains 1.16 ± 0.24 eV and 0.36 ± 0.10 eV for Sm^{3+} and Tm^{3+}. The error on the trap depth for Tm^{3+} is smaller thanks to the fact that the Tm^{3+} CT was used to position the VB. The predictive power of these trap depths is limited due to the large error margin and the neglect of vibrational effects. Concerning the large errors, a trap of depth 0.68 ± 0.23 eV can be too shallow

for efficient charge storage, perfect for gradual charge release to construct persistent luminescent materials or too deep to be emptied at room temperature.

6.5 Nonequivalent defects

Up to now, the described empirical rules and techniques for constructing charge-state transition level schemes have been applied to many host materials [267, 274–280]. This can be unambiguously done for host materials in which all lanthanides act identically in chemical and crystallographic terms. One can expect that often this is true because of their similar ionic radii and chemical behavior. However examples are known where this is not the case. Furthermore, there is a one-to-one correspondence between the number of nonequivalent defects in a certain host and the number of charge-state transition levels for a dopant. If multiple defect geometries for the same foreign atom are possible, multiple energy level schemes are necessary for a correct description. Both these subtleties are often neglected or simply forgotten.

Below, the empirical energy level models are applied to lanthanide-doped materials with more challenging host compounds, featuring multiple nonequivalent lattice sites on which the lanthanides can incorporate. $SrAl_2O_4$ and $Sr_2Si_5N_8$ are presented as case studies. Site-selective spectroscopy can offer a tidy opportunity to separate the spectral features and construct energy level schemes for the different defect geometries. Remaining difficulties such as correlating the spectral features to the defects are discussed.

Subsequently, spectra of the lanthanide doped ternary sulfide $SrGa_2S_4$ are presented. It is known that the first coordination shell is severely altered when Ce^{3+} is incorporated [281], yielding a completely different situation than for Eu^{2+} doping. In this case, the use of empirical rules that relate spectral properties of different lanthanides becomes severely restricted. The repercussions on the construction of charge-state transition level schemes are discussed in detail.

6.5.1 Multiple nonequivalent lanthanide defects

In this paragraph, two examples of host compounds ($SrAl_2O_4$ and $Sr_2Si_5N_8$) are discussed which feature two nonequivalent substitutional defects upon lanthanide doping. This poses additional difficulties when the electronic structure is empirically assessed as both lanthanide defects require a separate energy level scheme. Examples are included for which the occurrence of the nonequivalent defects is clear from the optical spectra, *i.e.* site-selective spectroscopy can be performed. This is preferably done on low-concentrated systems, avoiding interactions between nonequivalent defect centers. Interactions between centers result in energy transfer which can obscure the optical spectra.

Site-selective spectroscopy of the Ce^{3+} ion is an important first step as it allows to construct vacuum referred binding energy level schemes for the 4f levels. This is thanks to empirical rule Eq. 6.5. Next, the host compound's valence and conduction band need to be added. From photoluminescence excitation spectroscopy of a trivalent lanthanide, the anion to lanthanide CT energy can be obtained, approximately probing the 2+/3+ charge-state transition level (see §5.4.2, §6.2.3). The binding energy difference between two nonequivalent Ln^{3+} defects is significantly smaller than the typical width of a charge-transfer spectral band [236]. As the ionization potentials for both defects were already calculated, deconvolution of the CT band poses no additional problems.

$SrAl_2O_4$

Doped with divalent europium, strontium aluminate ($SrAl_2O_4$) features an extensively studied green afterglow which can be intensified upon codoping with trivalent dysprosium [158, 159, 282]. Interestingly, when this material is cooled below 250 K, a second emission band emerges in the blue spectral region [266]. The origin of this band has been the debated since it was first found. Although an explanation in terms of incorporation of Eu^{2+} on the two nonequivalent lattice sites seems the most simple one, it was pleaded that the minor geometrical differences between the Sr1 and Sr2 sites cannot account for the differences between the two spectral features [164–166, 283]. Alternatively, more exotic explanations such as alignment of Eu ions, hole release or even emission from a higher $4f^6 5d^1$ multiplet were contrived [164–166].

In §4.5.3, empirical rules, relating the bond lengths of the undistorted lattice sites to the multiplet structure of the excited $4f^6 5d^1$ configuration were applied, showing that the order of magnitude of the spectral differences between the excitation bands of the blue and green emission can be perfectly explained by the structural differences between both lattice sites, discarding the more exotic explanations for the occurrence of two emission bands.

Also upon Ce^{3+} doping, it was spectroscopically shown that two different defects are present [284]. Based on this data, which is summarized in Table 6.2, charge-state transition level schemes can be constructed. The 2+/3+ levels for all the lanthanides, *i.e.* the *divalent 4f curves*, are shown in Fig. 6.8.

$Sr_2Si_5N_8$

Strontium nitridosilicate, $Sr_2Si_5N_8$, has been frequently reported as a chemically stable host material for lanthanides. In particular, upon doping with divalent europium, an efficient red phosphor is formed which is applied in phosphor-converted white light-emitting diodes (LEDs) [288–293].

Spectroscopy of Ce^{3+} in $Sr_2Si_5N_8$ was performed by Li *et al.* They clearly found the effect of two nonequivalent cerium defects in their spectra of which different crystal

Table 6.2 – Experimental spectroscopic parameters for lanthanides incorporated on the nonequivalent Sr sites in $SrAl_2O_4$ and $Sr_2Si_5N_8$. ϵ_{cfs}, ϵ_c and D denote respectively the crystal field splitting, centroid shift and redshift of the $4f^{N-1}5d^1$ manifolds. ΔS denotes the Stokes shift of the $4f^N$-$4f^{N-1}5d^1$ luminescence. All values in eV.

		$SrAl_2O_4$		$Sr_2Si_5N_8$		ref.
		low energy	high energy	low energy	high energy	
Ce^{3+}	ϵ_{cfs}	0.85	1.14	1.91	1.61	[266, 285, 286]
	ϵ_c	2.65	2.23	2.73	2.41	[266, 285, 286]
	D	2.85	2.47	3.24	3.02	[266, 285, 286]
	ΔS	0.25	0.31	0.33	0.87	[266, 285, 286]
Eu^{2+}	D	1.42	1.22	2.05	2.02	[266, 287]
	ΔS	0.43	0.21	0.32	0.23	[266, 287]

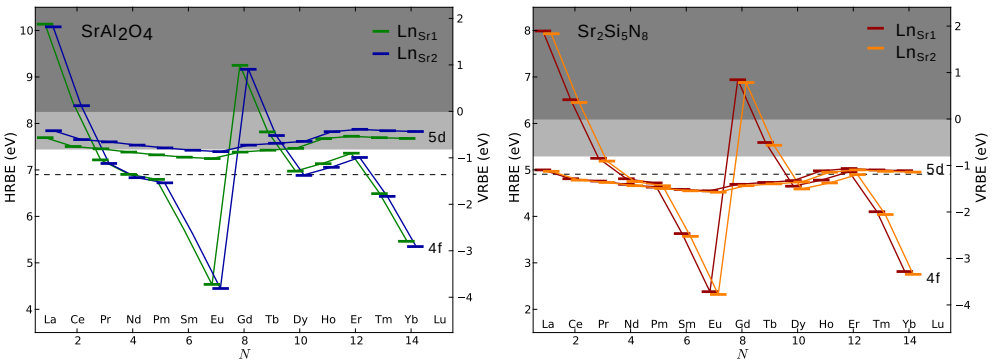

Figure 6.8 – Diagrams with the 2+/3+ charge-state transition levels for the Ln_{Sr1} and Ln_{Sr2} defects in $SrAl_2O_4$ and $Sr_2Si_5N_8$. Assignation for $Sr_2Si_5N_8$ according to [286] and [287].

field splitting energies could be extracted [286]. Based on their data, the centroid shifts of the cerium $5d^1$ configuration for both cerium defects were estimated. The data is summarized in Table 6.2.

More recently, Lazarowska *et al.* performed a detailed site-selective spectroscopy study of the Eu^{2+} ion in $Sr_2Si_5N_8$ [287]. From the $4f^7$-$4f^6 5d^1$ excitation spectra, it was concluded that the spectroscopic redshift for both europium defects are very similar. The difference in emission energy is therefore almost completely due to a different electron-vibrational interaction. Empirical total energy level schemes within the single configurational coordinate approximation were provided.

Based on site-selective spectroscopy on Ce^{3+} and Eu^{2+} and the charge transfer energy of Sm^{3+} [294], charge-state transition level schemes were constructed for both defect geometries (see Fig. 6.8).

An empirical charge-state transition level scheme for lanthanide defects in $Sr_2Si_5N_8$ was first constructed in 2013 by ten Kate *et al.* [294]. Only the charge-state transition levels for the low energy site were calculated. Though not represented in the energy level scheme, the $4f^N$-$4f^{N-1}5d^1$ transition energies for lanthanides were compared for both defect configurations. Interestingly, for the Tb^{3+} ion only one $4f^8$-$4f^7 5d^1$ excitation band was found. By extrapolating the 4f-5d energies of the cerium defects according to the empirical finding that all Ln^{3+} ions feature the same 4f-5d spectroscopic redshift, the excitation band was attributed to the Sr1 site. This means that the Tb^{3+} ion occupies preferentially the smaller Sr1 site while no preference was found for the slightly larger Ce^{3+} ion [294].

Inspection of the diagram in Fig. 6.8 learns that the binding energies for both defect sites are very close. How can this be compatible with the undeniable spectral differences between both types of defects? This is a direct consequence of the fact that charge-state transition level schemes do not directly display spectroscopic information, but have a thermodynamic meaning (see §5.2.3) . In the case of Ce^{3+}, there is a clear difference in the details of the 5d manifold for both defects. This is dictated by the exact details of the crystal field interaction, which is not described by the charge-state transition levels. In the case of Eu^{2+}, the spectral difference is a direct consequence of a different local electron-vibration interaction. To correctly describe the dynamics, details of the potential energy surfaces, such as curvatures, equilibrium coordinates and relevant normal modes are indispensable. No empirical rules to obtain these quantities are available to date.

In [287], it was argued that the preferential incorporation of Eu on the site yielding the higher-energy emission is due to the *4f level* of this defect being more strongly bound than for the alternative defect. This is however an incorrect interpretation of the charge-state transition levels. It is true, by definition of the charge-state transfer energies, that the Eu_{Sr2} defect requires slightly more energy in order to oxidize. On the other hand, preferential occupation of certain lattice sites is governed by the defect formation energy which is calculated in terms of total energies (see §5.2.3).

Furthermore, if the difference in defect formation energies would be the same as the difference in charge-state transition levels, it would be too small to yield an observable difference in site occupation given the high temperature at which the materials are synthesized.

Relating crystal sites to spectra

The remaining challenge is linking the separate spectral features to the different defect geometries. It is often assumed that a smaller lattice site corresponds to a lower 4f-5d energy. The reasoning is that the crystal field strength, and implicitly the spectroscopic redshift of the 5d level, increases upon decreasing bond lengths. The validity of this assumption is doubtful for lattice sites for which the geometry does not differ too much. Moreover, the crystal lattice will locally relax to a different equilibrium geometry, adapted to the specific lanthanide atom in an unknown way.

As the different lanthanide ions behave very similar in chemical terms, it is likely that high- and low-energy sites can be correlated for the different lanthanides, allowing to construct empirical charge-state transition diagrams for both defects. Exceptions to this rule of thumb are discussed in §6.5.2.

$SrAl_2O_4$ forms monoclinic crystals (space group $P2_1$) in which two nonequivalent Sr sites occur, both on Wyckoff position 2a. $Sr_2Si_5N_8$ forms orthorhombic crystals (space group $Pmn2_1$) [295] in which likewise two nonequivalent Sr sites occur, both corresponding to Wyckoff site 2a [295].

In $Sr_2Si_5N_8$, the Sr1 site has a lower coordination number and features a smaller polyhedron than the Sr2 site [295]. Specifying the coordination number, *i.e.* the number of neighboring atoms is somewhat arbitrary in these cases. This is illustrated in literature where different coordination numbers are reported for the same compound [286, 287, 294].

The reason for the ambiguity is demonstrated in Fig. 6.9 where the number of anions lying inside a sphere, centered at the Sr atom is given as a function of the radius of the sphere. This figure shows that coordination shells cannot be identified in a straightforward fashion, neither for $SrAl_2O_4$ nor $Sr_2Si_5N_8$. In the case of $SrGa_2S_4$, a higher symmetry is present and well-defined coordination shells can be identified.

To straighten out this ambiguity, Rudolf Hoppe introduced the effective coordination number in 1979 in which a weighing of the different bond lengths is carried out [296]. This quantity turns out to be simply the ordinary coordination number in the case of compounds with a high symmetry and well-defined coordination shells, while it yields a rational number in other cases. The effective coordination numbers for the Sr1 and Sr2 sites of $Sr_2Si_5N_8$ are respectively 5.98 and 6.88. The coordination polyhedra of the first 6 and 7 neighbors for the Sr1 and Sr2 sites of $Sr_2Si_5N_8$ are approximate pentagonal and hexagonal pyramids respectively [295].

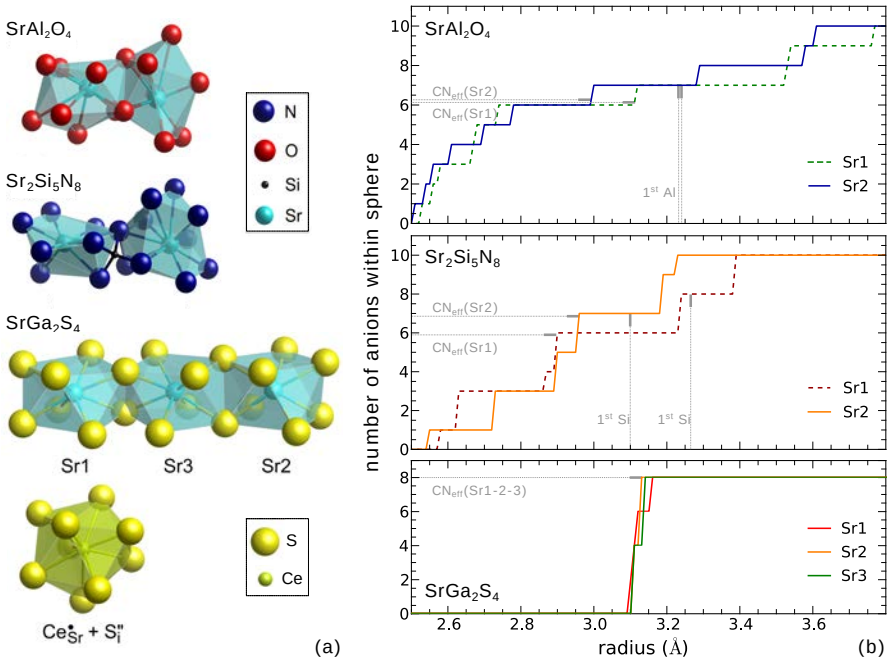

Figure 6.9 – (a) Coordination environments for the different Sr sites in $Sr_2Si_5N_8$, $SrAl_2O_4$ and $SrGa_2S_4$. Crystal data from [163, 295, 296]. (b) Illustration of the number of anions (O, N or S) contained inside a sphere centered at the cationic (Sr) sites as a function of the radius of the sphere for $SrAl_2O_4$, $Sr_2Si_5N_8$ and $SrGa_2S_4$. The effective coordination number, as defined by R. Hoppe, is given for each site [296]. Furthermore, the location of the closest cation (Al, Si) is given. The smallest Sr-Ga distance in $SrGa_2S_4$ is 3.86 Å.

Several assignments of the spectral bands of $SrAl_2O_4$:Ln^{Q+} are available in literature. Jia *et al.* showed that the high energy band in $SrAl_2O_4$:Ce^{3+} has an emission intensity which is 10 times higher than the intensity for the low energy band at room temperature [284]. From this result, it was concluded that the high energy emission originates from Ce incorporated on the larger Sr1 site as this provides more space for the suggested charge compensation [284]. This is however a somewhat arbitrary argument because the intensity of an emission band is not necessarily related to a preferential site occupation and can as well be the result of a different thermal quenching behavior.

The empirical structure-property rules, used in §4.5.3, showed that the high energy emission is most likely attributed to the smaller Sr2 site.

More recently, vacuum UV spectroscopy of $Sr_{0.75}Ce_{0.125}Na_{0.125}Al_2O_4$ was combined with quantum mechanical calculations to gain a better understanding of the connection between defect geometry and spectral properties [100]. The sodium atoms were added for charge-compensating the $Ce^{\bullet}_{Sr}$ defects and located on the nearest or

next-nearest Sr site for the calculations. The multireference calculations confirmed that the two spectral features originate from incorporation on the different Sr sites. The allocation of the $Ce^{\bullet}_{Sr1}$ and $Ce^{\bullet}_{Sr2}$ defects to respectively the low and high energy emission bands was however reversed by the calculation. It still remains a question why the 4f-5d transition of Ce^{3+} on the larger Sr site would correspond to the highest energy. Additionally, the influence of the nearby Na'_{Sr} defect on the multiplets of the Ce^{3+} ion is unclear as the Coulomb interactions between the different defects can have a rather long range [183].

In the case of $Sr_2Si_5N_8$:Eu^{2+}, the lowest energy emission was attributed to the smallest undistorted Sr site according to the typical rule of thumb [286, 287]. It was found that the Eu^{2+} ion occupies both Sr sites, although it has a preference for the larger Sr2 site because it is the only occupied site for low doping concentrations. In the article of Lazarowka *et al.*, the labeling of the Sr1 and Sr2 sites was exchanged with respect to the assignation by Schlieper *et al.* [295] which is used in this text, following the convention of Yeh *et al.* [297].

From these examples, it is clear that the subtle differences in defect geometry can result in appreciable spectral changes which are very difficult to predict.

6.5.2 Structural distortions across the Ln series: $SrGa_2S_4$

Previous examples, $SrAl_2O_4$ and $Sr_2Si_5N_8$, were challenging host compounds for constructing empirical charge-state transition level schemes in the sense that two nonequivalent lanthanide defects occurred and formally, two different schemes are required. Yet, because site selective spectroscopy allows to separate the different spectral features, the two schemes can be constructed almost independently.

A more complex situation occurs if not all lanthanides behave in the same way with respect to incorporation. If this is the case, the systematics which is normally exploited in the construction of the charge-state transition level schemes breaks down and it should be carefully considered which empirical rules are still usable. $SrGa_2S_4$ is an example of such a host compound.

Crystal structure

Strontium thiogallate ($SrGa_2S_4$) is isostructural to calcium thiogallate (see §6.4). Similarly as for the Ca-compound, the existence of only one nonequivalent Sr site of effective D_{4d} symmetry is assumed because all three Sr sites differ only very slightly as demonstrated in Fig. 6.9. Eu^{2+} doping is expected to deform the coordination polyhedron only minimally due to the comparable ionic radii of Eu^{2+} and Sr^{2+} and given that $EuGa_2S_4$ is isostructural with $SrGa_2S_4$ [177, 298, 299]. Doped with Eu^{2+} or Ce^{3+}, this compound has been thoroughly described in view of multiple applications such as electroluminescent displays, field-emissive devices and more recently

LED phosphors (see also chapter 9) [251, 300–304].

Although this compound effectively features only one Sr site and might therefore be considered as a straightforward case upon lanthanide doping, a discontinuity across the lanthanide series occurs. Warren *et al.* have shown by electron paramagnetic resonance (EPR) spectroscopy that the $Ce^{\bullet}_{Sr}$ defect induces a sulfur interstitial S_i in the first coordination shell to compensate the excess positive charge [281]. The deformed coordination polyhedron for the Ce^{3+} dopant features approximate C_{3h} point symmetry and a coordination number of 9 (see Fig. 6.9).

The geometrical deviation for the $Ce^{\bullet}_{Sr}$ defect is expected to have an influence on the luminescence properties. It is self-evident that this has to be taken into account when constructing charge-state transition level schemes. In the following, the optical spectra and electronic structure of $SrGa_2S_4$:Ln^{Q+} will be compared to the previously discussed $CaGa_2S_4$:Ln^{Q+}. It has been shown by EPR that for the isostructural $CaGa_2S_4$:Ln^{Q+} the pristine symmetry and coordination number of the Sr site is maintained upon Ce^{3+} doping. This might be due to the similar ionic radii of Ce^{3+} and Ca^{2+} [305]. For this reason, $CaGa_2S_4$:Ln^{Q+} is a good choice as a well-behaving reference.

Photoluminescence

Fig. 6.10(a-b-c) shows the emission and excitation spectra of Eu^{2+}, Ce^{3+} and Tm^{3+} in $SrGa_2S_4$, compared to the spectra of the same lanthanides in $CaGa_2S_4$. The spectra of these three defects can be used as input to construct the empirical charge-state transition level schemes. This was done for $CaGa_2S_4$ in §6.4. The numerical values of the parameters that can be obtained from these measurements are summarized in Table 6.1.

The spectra for $SrGa_2S_4$:Ln^{Q+} are -at first sight- very similar to the spectra of $CaGa_2S_4$:Ln^{Q+}, with broadband $4f^N$-$4f^{N-1}5d$ luminescence for Eu^{2+} and Ce^{3+} and $4f^{12}$-$4f^{12}$ line emission for Tm^{3+} with a CT band and an additional unassigned band in the excitation spectrum. The latter is significantly less intense for the Sr-compound than for the Ca-compound.

If the excitation spectra of Ce^{3+} and Eu^{2+} are more closely compared for both host materials, a deviation from the idealized situation, described by Eq. 6.14, occurs. The Eu^{2+} band is red-shifted for $CaGa_2S_4$ with respect to $SrGa_2S_4$, in agreement with the observed yellow and green emission respectively. This is understood to be due to the increased crystal field strength, *i.e.* the accumulated effect of the centroid shift and crystal field splitting, due to the decreased bond length in the case of the Ca-compound. In the case of Ce^{3+}, however, both excitation spectra approximately coincide at the low energy side (Fig. 6.10).

Although this behavior lies fully within the expected uncertainties, it is still remarkable if an isomorphous coordination polyhedron would be expected. However, from

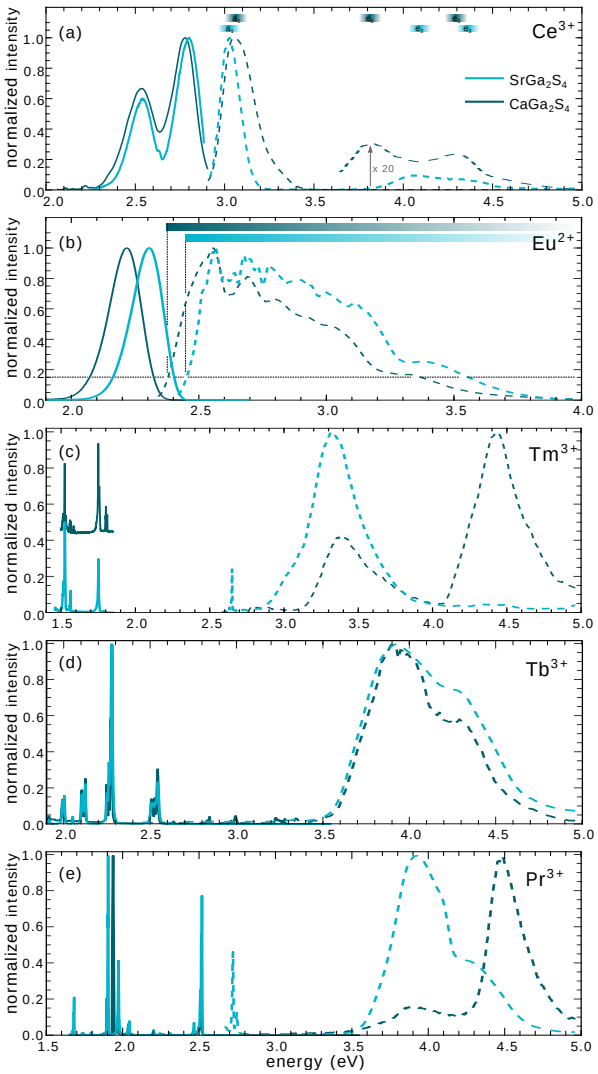

Figure 6.10 – Emission (solid lines) and excitation spectra (dashed lines) of lanthanide doped $SrGa_2S_4$ (light blue lines) and $CaGa_2S_4$ (dark blue lines), measured at 75 K. (a) Ce^{3+} doped, emission spectrum upon 410 nm (3.02 eV) excitation, excitation spectrum for 445 nm (2.79 eV) emission. (b) Eu^{2+} doped, emission spectrum upon 450 nm (2.76 eV) excitation, excitation spectrum for 535 nm (2.32 eV) (560 nm (2.21 eV)) emission for $SrGa_2S_4$ ($CaGa_2S_4$). (c) Tm^{3+} doped, emission spectrum upon 370 nm (3.35 eV) excitation, excitation spectrum for 810 nm (1.53 eV) emission. (d) Tb^{3+} doped, emission spectrum upon 302 nm (4.11 eV) (320 nm (3.88 eV)) excitation, excitation spectrum for 544 nm (2.28 eV) emission for $SrGa_2S_4$ ($CaGa_2S_4$). (e) Pr^{3+} doped, emission spectrum upon 320 nm (3.87 eV) excitation, excitation spectrum for 651 nm (1.90 eV) (640 nm (1.94 eV)) emission for $SrGa_2S_4$ ($CaGa_2S_4$). The colored bands indicate the locations of the $4f^N5d^1$ multiplets with respect to the $4f^N$ ground state.

the EPR study of Warren *et al.* (see §6.5.2) [281], it is known that the situation is locally completely different for $SrGa_2S_4$:Ce^{3+} which can explain this anti-correlation between the calcium and strontium thiogallates.

Typical green Tb^{3+} $^5D_4$ emission is often excited by $4f^8$-$4f^7 5d^1$ absorption in the UV range. Remarkably, the excitation spectra of Tb^{3+}, displayed in Fig. 6.10(d), coincide for doping in $CaGa_2S_4$ and $SrGa_2S_4$, which indicates that $Tb^{\bullet}_{Sr}$ is likely to be charge-compensated in the same way as $Ce^{\bullet}_{Sr}$. Assuming an equal spectroscopic redshift for both lanthanides, the $SrGa_2S_4$:Tb^{3+} spin-allowed and spin-forbidden absorption bands are predicted at respectively 4.68 eV and 3.98 eV [262]. The experimental excitation spectrum (Fig. 6.10) shows this feature around 3.91 eV, most likely corresponding to the spin-forbidden transition. The spin-allowed transition is therefore believed to be obscured by fundamental absorption by the host crystals.

The Pr^{3+}-S^{2-} charge transfer is expected at 4.47 eV ± 0.20 eV and the $4f^2$-$4f^1 5d^1$ absorption band is expected at 4.54 ± 0.12 eV in $SrGa_2S_4$ assuming isostructural $Pr^{\bullet}_{Sr}$ and $Ce^{\bullet}_{Sr}$ defects. Experimentally, broadband excitation peaks are found at lower energy, peaking around at 3.92 eV and 4.32 eV (Fig. 6.10(e)). If the lowest energy band is assigned to the charge-transfer band and the higher energy band to the $4f^2$-$4f^1 5d^1$ transition, the mismatch between prediction and experiment is respectively $2.7\sigma_{CT}$ and $1.8\sigma_{fd}$, with the σ-values as obtained above. These are rather large deviations, suggesting that possibly a different mechanism causes the origin of the excitation bands. Yet another distorted coordination polyhedron is a possible alternative explanation.

In 2004, Iwamaru *et al.* studied the cathodoluminescence of $SrGa_2S_4$:Sm [306]. They found a broad red emission band about 700 nm (1.77 eV) which was attributed to $4f^5 5d^1$-$4f^6$ emission of Sm^{2+}. From the Eu^{2+} spectra, the absorption threshold of Sm^{2+} in $SrGa_2S_4$ is estimated at 1.25 eV and the emission at 1.09 eV. Therefore, it is unlikely that the observed emission band is due to Sm^{2+}. From the approximate location of the 2+/3+ charge-state transition level of Sm (see Fig. 6.11), it is moreover expected that Sm will be preferentially incorporated in a trivalent state, assuming that the electronic chemical potential lies in the middle of the band gap [243, 307].

Energy level schemes

Because of the deviating Ce incorporation, the charge-state transition level scheme for $SrGa_2S_4$ cannot be simply constructed based on $E^{ex}(A)$, $E^{fd_1}_{abs}(Ce^{3+}, A)$, $E^{fd}_{abs}(Eu^{2+}, A)$ and $E^{CT}(Tm^{3+}, A)$, as was done for $CaGa_2S_4$ in §6.4.

The Coulomb 4f correlation parameter for Eu, $U(Eu, A)$, which is a key parameter for constructing vacuum referred binding energy level schemes, is assessed from the Ce^{3+} centroid shift according to Eq. 6.5. This relationship cannot be used in this case because of the different defect geometries for Ce and Eu. Since this and other equations are completely empirical, it is unknown to which extent different charge compensating effects or other imperfections are present in the data used to obtain

these equations. It is more specifically possible that this kind of effects is readily accounted for in the empirical routine without the users knowledge. Inspection of the data used for deriving Eq. 6.5 learns for instance that $SrGa_2S_4$ was used as a data point [232].

Concerning this question, it can also be of interest to take a look at the uncertainties, associated with the empirical rules. Eq. 6.5 allows to calculate $U(\mathrm{Eu}, A)$ with a 68% uncertainty interval of 100 meV. This is of the same order of magnitude as the deviations between $U(\mathrm{Eu}, A)$ for two different defect sites in the same host, based on the above examples. As the occurrence of multiple nonequivalent defects nor discontinuous behavior such as different charge-compensation schemes were systematically taken into account in devising the set of empirical rules, the uncertainties on these empirical rules, as calculated above, are larger than differences between possible nonequivalent defects.

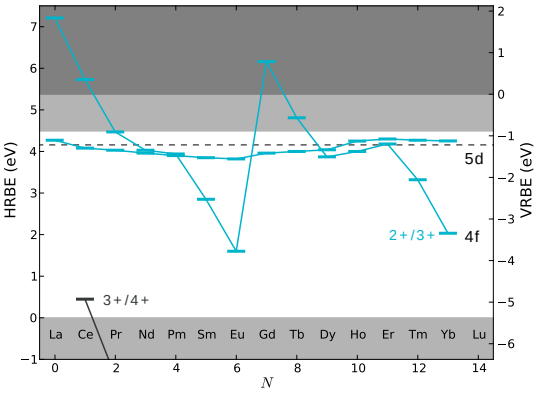

Figure 6.11 – Diagram with the 2+/3+ and 3+/4+ charge-state transition levels for the Ln_{Sr} defects which are isostructural to the $Ce^{\bullet}_{Sr}$ defect in $SrGa_2S_4$.

Of course, applying the empirical rules in a thoughtful way by making the distinction between different defect geometries will yield more information about the relative positions of the charge-state transition levels for each nonequivalent defect, allowing a comparison between the different physical observables associated with them.

Assuming that the $Ce^{\bullet}_{Sr}$ and $Tm^{\bullet}_{Sr}$ defects are isostructural in $SrGa_2S_4$, host referred and vacuum referred binding energy level schemes for the defect with nearby sulfur interstitial can be constructed according to the usual routine. The result is displayed in Fig. 6.11.

Obtaining a charge-state transition level scheme for the 8-fold coordinated lanthanide defects in $SrGa_2S_4$ such as the Eu_{Sr} defect is not straightforward as neither the Ce^{3+} centroid shift can be used to obtain vacuum referred binding energies nor a charge-transfer energy of a trivalent lanthanide to probe host referred binding energies. Both rely on spectroscopy of trivalent lanthanides which form different defect geometries. Remaining possibilities are core-hole spectroscopic techniques such as photo-electron spectroscopy or photoconductivity measurements.

6.6 Prospects

This chapter featured an extensive discussion on the empirical modeling of luminescent lanthanide materials. The fundamental relationships of the model were devised by multiple authors during the last 40 years and extensively reviewed and fine-tuned by Dorenbos during the last 20 years through data mining and revisiting of scientific literature on lanthanide materials.

The different empirical relationships of the model were reviewed as well as the necessary steps to build an energy level scheme from spectroscopic measurements. A profound analysis was performed on the accumulated errors. The errors are not only determined for the energy level scheme itself, but also for the commonly derived physical observables.

The error analysis revealed that a different accuracy is obtained when the energy level locations are calculated with respect to the vacuum or to the host's valence or conduction bands. The 4f and 5d charge-state transition levels of the divalent and trivalent lanthanide ions can be probed with a standard deviation of respectively 100-150 meV and 250-300 meV with respect to the vacuum level. If referred to the valence band, the standard deviations are typically 50 meV higher.

The conduction band bottom can only be positioned within a standard deviation of 300 meV. Not only can the optical band gap be determined in a rather approximate way from diffuse reflection spectroscopy, but also the empirical relationship for calculating the self-trapped exciton binding energy proves to be inaccurate, yielding relative errors up to 100% for materials with a small band gap energy. This has its repercussions on the accuracy of quantities describing phenomena in which conduction band states are reckoned to be involved such as thermal quenching, electron transfer or anomalous luminescence. The model does not allow to quantitatively describe these phenomena. Nevertheless, correlations which are revealed by the model remain valid and allow for qualitative interpretation of experiments.

As example of an ideally behaving host compound, an energy level scheme was devised for $CaGa_2S_4$ based on optical spectroscopy of Ce^{3+}, Eu^{2+} and Tm^{3+}. The comparison between calculated and measured quantities is in accordance with the prior error analysis and the energy level schemes allowed for a better understanding of new and already reported results on these materials.

Furthermore, possible refinements of the set of empirical rules used to construct charge-state transition level schemes for lanthanide materials have been discussed. More specifically, it was investigated to what extent the occurrence of multiple nonequivalent defects within the lanthanide series alters the level schemes.

Following reports in literature containing energy level schemes, it is commonly assumed that only one nonequivalent defect is present in a certain host which is isostructural for each lanthanide dopant, whatever its formal charge. The validity

of this assumption is doubtful, however a painstaking task to confirm experimentally. This involves doping with a large number of lanthanide ions and possibly specialized analytical techniques such as electron paramagnetic resonance or X-ray absorption spectroscopy. In this chapter, a few cases were discussed where the above assumption is known to be invalid. A distinction between two situations was made.

First, host compounds were considered in which multiple nonequivalent substitutional defects occur. $SrAl_2O_4$ and $Sr_2Si_5N_8$ are examples for which the lanthanide ions spontaneously occupy both Sr sites. In these cases, clear spectroscopic differences are visible and site-selective spectroscopy allows to construct independent charge-state transition level schemes for each defect geometry. From these examples, it is clear that very limited structural differences of coordination environment can give rise to important deviations in the optical spectra.

Second, host compounds were considered for which different lanthanide ions show a different behavior with respect to the local coordination. $SrGa_2S_4$ is an example in which Ce^{3+} and Eu^{2+} form very different defect geometries. If this is the case, a discontinuity across the lanthanide series exists and the empirical rules exploiting the systematic behavior for the different ions cannot be used to construct charge-state transition level schemes. Therefore, only partial schemes can be made.

The energy differences between the charge-state transition levels and energy levels belonging to the same lanthanide in a different defect geometry were compared with the typical uncertainties of the empirical models. It is concluded that both are of the same order of magnitude. This could imply that some of the data used to derive the empirical rules are compromised, if multiple nonequivalent defects occur or if structural distortions across the lanthanide series were not identified. Consequently, the error margins related to the present empirical rules might potentially be reduced if the underlying input data is scrutinized.

II

The quest for LED phosphors

7 PHOSPHORS FOR WHITE LEDS: SYNTHESIS AND EVALUATION

The development of (novel) luminescent materials for use in LEDs can be summarized in a few steps. First, a candidate-material is selected for investigation. This is often based on promising reports of specific properties, the result from a selection based on theoretical models, possibly empirical ones or a trial-and-error approach. The last option is clearly the least desirable strategy. Secondly, the selected material is synthesized. Different techniques can be used, the most effective typically depending on the chemical composition of the host compound. The solid state synthesis is often most popular as it requires a minimum number of processing steps and a limited amount of chemical dedication. This technique is explained in §7.1. If the purity of the synthesized sample is of sufficient quality, the actual evaluation of the six technological requirements (see chapter 1) can commence. The various luminescence techniques that are employed for this are reviewed in §7.2. In the third step, the obtained results are interpreted in terms of physical models, not seldomly energy level models. This is of importance to understand the physical limitations of the studied material, often allowing to separate fundamental deficiencies from deficiencies that can be resolved by a well-performed optimization of the material. This optimization, with the envisioned application in mind, is the final step of the phosphor design.

7.1 Synthesis of phosphors

Below it is described how the powder phosphors are produced by solid state synthesis. Subsequently, the techniques used to verify the structural and chemical compositions of the powders are explained.

7.1.1 Solid state synthesis

For a solid state synthesis, inorganic salts or oxides are typically used as starting materials. Stoichiometric amounts of every precursor are weighed, mixed and ground in an agate mortar. Subsequently, the mixed powders are put into alumina (Al_2O_3) or zirconia (ZrO_2) crucibles.

The mixtures are sintered at high temperature for a certain time span in a gas atmosphere of choice. For the syntheses in this text, tube furnaces are used. The

temperature of the heat treatment is chosen such that it is below the melting point of the precursors and the envisioned end product. While at high temperature, the atoms in the powder mixture gain a higher mobility and can diffuse into neighboring grains, ultimately forming crystals with a different chemical composition, which is in the most ideal case uniform over the complete contents of the crucible.

After the synthesis, the obtained powders are typically slightly ground before characterization.

7.1.2 X-ray diffraction

X-ray diffraction (XRD) is an analytical technique from which information on the crystal structure of materials can be obtained. For this, monochromatic X-rays are elastically scattered from the sample, which in this case is a powder (PXRD). Every electron in the solid scatters X-rays and can hence be regarded as a secondary source, emitting a spherical wave. A given crystal structure will then give rise to specific directions into which the monochromatic X-rays will interfere constructively, corresponding to the different planes in the crystal lattice.

Suppose that a plane wave of X-rays, $e^{i\boldsymbol{k}\cdot\boldsymbol{r}}$ impinges the sample. Far away, the scattered X-ray will be a plane wave as well, $e^{i\boldsymbol{k}'\cdot\boldsymbol{r}}$. Then, it is assumed that the amplitude of the scattered wave is proportional to the electron density, yielding a scattering amplitude:

$$F = \int \rho(\boldsymbol{r}) e^{-i\Delta\boldsymbol{k}\cdot\boldsymbol{r}} d^3\boldsymbol{r}, \tag{7.1}$$

where the scattering vector $\Delta\boldsymbol{k} = \boldsymbol{k}' - \boldsymbol{k}$ was introduced. Using the Fourier transform of the electron density, Eq. 5.6, this becomes:

$$\begin{aligned} F &= \sum_{\boldsymbol{G}} \rho(\boldsymbol{G}) \int e^{i(\boldsymbol{G}-\Delta\boldsymbol{k})\cdot\boldsymbol{r}} d^3\boldsymbol{r} && (7.2)\\ &= 2\pi \sum_{\boldsymbol{G}} \rho(\boldsymbol{G}) \delta(\boldsymbol{G} - \Delta\boldsymbol{k}). && (7.3) \end{aligned}$$

This expression shows that discrete diffraction peaks, *reflections*, emerge where the condition for incoming and outgoing waves,

$$\boldsymbol{G} = \Delta\boldsymbol{k}, \tag{7.4}$$

is fulfilled, *i.e.* when their difference in wave vector corresponds exactly to a reciprocal lattice point. In XRD, only elastically scattered X-rays are considered, having $|\boldsymbol{k}| = |\boldsymbol{k}'| = k$, yielding for the condition:

$$2\boldsymbol{k}\cdot\boldsymbol{G} = G^2, \tag{7.5}$$

which is the vectorial form of the famous Laue conditions. The reciprocal lattice vectors $\boldsymbol{G} = h\boldsymbol{b}_1 + k\boldsymbol{b}_2 + l\boldsymbol{b}_3$ are perpendicular to the crystal lattice plane with Miller

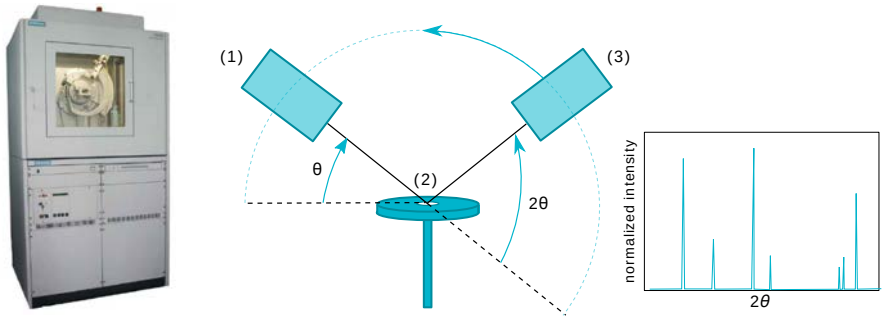

Figure 7.1 – Left: Siemens D5000 diffractometer. Middle: Schematic image of a Bragg-Brentano diffractometer. The meaning of the numbers is elucidated in the text Right: Typical XRD pattern.

indices (hkl) and the spacing between these planes is $d_{hkl} = 2n\pi/|\boldsymbol{G}|$ with n a natural number, allowing to rewrite the Laue condition as

$$2d_{hkl}\sin\theta = n\lambda, \tag{7.6}$$

the well-known Bragg condition for diffraction which is equivalent to the Laue condition. Here, θ is the angle between the incoming X-ray and the crystal lattice plane (hkl) [308].

From Bragg's law, Eq. 7.6, it is clear that a peak will only be found for specific combinations of d_{hkl}, θ and λ. For powder samples, all θ values occur simultaneously[1], yielding a cone of reflections around the incoming beam for every lattice plane.

Nowadays, PXRD patterns are collected by Bragg-Brentano diffractometers as illustrated in Fig. 7.1. Here, the X-ray source (1) is in a static position while the table holding the sample (2) rotates, specified by the angle θ. The X-ray detector (3) moves around the sample on a circle, specified by the angle 2θ (see Fig. 7.1). The diffraction peaks are then obtained as a function of 2θ while their intensities are determined by Eq. 7.3. For this work, a Siemens D5000 diffractometer was used, equipped with an X-ray tube (40 kV, 40 mA), producing Cu Kα_1 radiation ($\lambda = 0.15418$ nm).

7.1.3 Scanning electron microscopy

Optical microscopy can only resolve structures which are not smaller than approximately half of the wavelength of the used light. From the Rayleigh criterion[2] it follows that a minimal resolution around 175 nm can be obtained for optical microscopy with 400 nm violet light. From quantum mechanics, it is also known that electrons have a wave character. This important principle was first formulated by

[1] At least in the absence of texture, *i.e.* preferential alignment of the powder grains.

[2] This criterion gives the minimal angle between two point sources in the far field for which the diffraction patterns can be distinct.

Louis-Victor de Broglie in 1924. The wavelength of an electron is inversely proportional to its momentum, p:

$$\lambda = \frac{h}{p}. \tag{7.7}$$

In a scanning electron microscope (SEM) electrons are accelerated to energies of the order of 10 keV, corresponding to wavelengths in the range of 0.01 nm, allowing atomic resolution in principle. The practical resolution is determined by the width of the electron beam and is about 1-3 nm [309].

SEM allows to study the morphology of materials, but is not limited to it. When the correct peripherals are present, the chemical composition (EDX) as well as possible cathodoluminescence (CL) of the sample can be studied.

SEM

For the SEM measurements in this work, a Hitachi S-3400N SEM was used (see Fig. 7.2). The free electrons are created at the top of the device by a tungsten hairpin through thermionic emission (1). These electrons are accelerated in the direction of the sample by the anode (2) and focused by a condenser lens (3). The deflection coil (4) bends the electron beam such that the sample is scanned in a row-by-row fashion, reminiscent of a cathode ray tube (CRT). A last lens (5) finally focuses the beam onto the sample (6) [309].

The interaction of the electrons with the sample results in the emission of various secondary particles or photons with different energies. While the sample surface is scanned, the secondary particles are detected, yielding different *images* of the sample, encoded in the secondary particle flux.

Every type of particle is released from a different part of the sample (Fig. 7.2) and carries specific information [309]:

1. Secondary electrons (SE) have a fairly low energy (10 to 50 eV) and are ejected near the spot where the beam strikes the sample. Due to their low energy, their trajectories can be easily bent by an anode, leading the electrons towards the SE detector (7). The number of detected SE depends primarily on the topography of the sample. As only the SE that are created close to the surface make it out of the sample, SE yield the best resolution.
2. Backscattered electrons (BSE) are those electrons which are elastically scattered by the atoms in the sample. As they have a high kinetic energy, they are not deflected by the electric field of the SE detector. The BSE detector (8) is placed above the sample, around the incident electron beam. As the scattering cross section increases for heavier atoms, the BSE intensity gives an idea about the chemical composition of the sample, *i.e.* Z contrast.

The information which is obtained from SE (topography) and BSE (chemistry) is hence complementary.

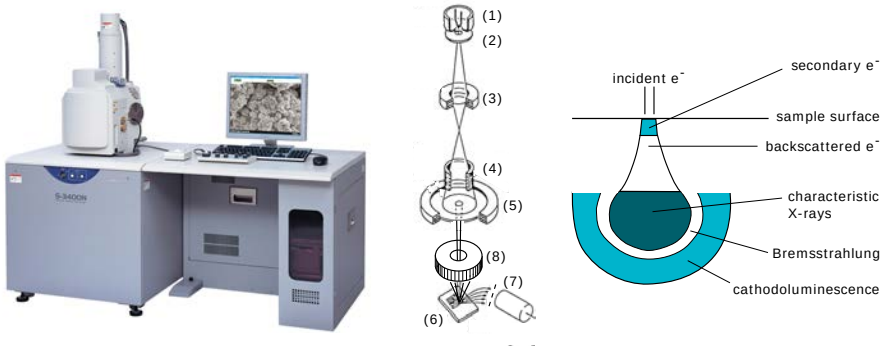

Figure 7.2 – Left: Hitachi S-3400N SEM. Middle: Schematic image of the most important parts of a SEM. The meaning of the numbers is elucidated in the text. Right: Interaction volume of an electron beam with a sample. The different spatial resolutions for the detection of the different types of secondary particles and radiation is indicated.

EDX

The incident electrons have a sufficiently high energy to excite a core electron in the atoms of the specimen. The core-hole can then be rapidly filled by a valence electron, creating a characteristic X-ray. Energy-dispersive X-ray spectroscopy (EDX) resolves the different energies of the X-rays and hence allows to obtain detailed information about the chemical composition throughout the sample [309].

Cathodoluminescence

The electron beam can also cause the excitation of valence electrons, yielding so-called cathodoluminescence (CL). For materials which are also photoluminescent, both spectra are typically very similar. The CL light can be collected by an optical fiber and analyzed by a detector (Princeton Instruments ProEM 1600^2) which is equipped by a monochromator (Princeton Instruments Acton SP2300). By mapping the CL together with the EDX, variations in chemical composition can be correlated to variations in the luminescence spectrum. This proves to be a very useful combination in the study of luminescent materials [310, 311].

7.1.4 X-ray absorption spectroscopy

X-ray absorption spectroscopy (XAS) is used to study the local structure around a selected element. Next to information on the first coordination shells, XAS can also assess the charge-state of transition metal and lanthanide ions.

During a XAS measurement, a deeply bound electron is excited by selecting the correct characteristic X-ray energy and a core-hole is formed. Upon excitation near the absorption edge (X-ray absorption near edge structure, XANES), the excited electron can occupy the lowest unoccupied orbitals of the excited atom. The energy at which these are found yields information on the charge-state of the ion. For higher X-ray

energies (extended X-ray absorption fine structure, EXAFS), the excited electron gets ionized and behaves as a photo-electron in the vicinity of the absorbing center. The fine structure that can be found in this range of the X-ray absorption spectrum is due to the scattering of the photo-electron in the compound. Analysis of the spectrum therefore yields information on the coordination of the absorbing atom [213]. For this, a self-consistent real space multiple scattering code called FEFF[3] is used [312].

X-ray spectra can be measured in transmission, or in fluorescence. In the latter case, the total X-ray fluorescence, which gives a good measure of the absorbed fraction, is followed as a function of incident photon energy. The X-ray spectra in this work were measured in fluorescence mode at the Dubble beamline (BM26A) at the ESRF synchrotron facility in Grenoble (France).

The analysis of the data was performed by Dr. Katleen Korthout [312, 313].

7.2 Evaluation of phosphor properties

When the purity of the synthesized powders has been checked, their luminescence and optical properties can be experimentally obtained.

7.2.1 Diffuse reflection spectroscopy

For specular or *mirror-like* reflection, the angle of incidence, *i.e.* the angle between the incoming light ray and the sample, equals the angle of reflection. In contrast, diffuse reflection accounts for all possible angles of reflection. In the case that powders are studied, the latter quantity is more meaningful.

Diffuse reflection is measured in an integrating sphere, where indeed all the reflected light is collected and *integrated* (see also §7.2.3). This technique is used to *e.g.* quantify the colors of powders. In this work, it is used to obtain an estimate of the (optical) band gaps of the phosphor hosts. The measurements are performed with a Varian Cary 500 spectrophotometer, equipped with an internal integrating sphere, using $BaSO_4$ as a reference.

As the optical band gap is a quantity solely related to the host, it is recommended that undoped host materials are used to obtain the band gap rather than doped samples where absorption bands related to the dopant can obscure the measurement. The Kubelka-Munk function,

$$F[R(E)] = \frac{K(E)}{S(E)} = \frac{[1 - R(E)]^2}{2R(E)}, \tag{7.8}$$

relates the reflectance of a layer of material, R, to the absorption and scattering coefficients, K and S [314, 315]. This relationship carries the assumption that the layer

[3] The name FEFF is derived from f_{eff}, the effective curved wave scattering amplitude in the EXAFS equation [312]

is sufficiently thick such that the reflectance does not change upon layer thickness increase. If $F(R)$ is quantitatively used as an absorption spectrum, it is assumed that the scattering coefficient is independent of the photon energy in the measurement range. This is often a tedious restriction as it is only fulfilled when grain sizes are significantly larger than the wavelength of measurement. On the other hand, when the grains are exceedingly coarse, the dynamical range of the fundamental jump in the absorption spectrum is lowered due to increased specular reflection [315].

When an absorption spectrum is available, the optical band gap E^{ex} can be estimated by fitting of the absorption coefficient:

$$F[R(E)] \propto (E - E^{ex})^p \,. \tag{7.9}$$

This relationship can be derived using elementary quantum mechanics [316]. The value of the exponent p depends on the nature of the fundamental absorption transition. For direct band gaps, $p = 1/2$ or $p = 3/2$ for allowed and forbidden transitions respectively. For indirect band gaps, $p = 2$ or $p = 3$ for allowed and forbidden transitions respectively [316]. This method to determine the band gap of semiconductors is attributed to Jan Tauc [317]. The nature of the band gap and the electronic transition are often unknown making the value of p in the ansatz Eq. 7.9 essentially unknown. Ideally, the type of band gap can be determined from choosing the best fit among the different possible equations, but this requires a very good experimental data set, which is seldom obtained.

Given the approximate character of both Eq. 7.8 and 7.9, a standard deviation of at least 100 meV has to be considered when the optical band gap of powders is assessed from diffuse reflectance spectroscopy.

7.2.2 Photoluminescence spectroscopy

To determine the photoluminescent properties of a phosphor, two types of spectra are typically recorded:

1. Emission spectrum: The material is excited at a fixed wavelength while the spectrum of the emitted light is collected. According to Stokes' law, the wavelength of the emitted light is longer than the chosen wavelength for the excitation. The first requirement can be validated from the phosphor's emission spectrum (see §1.4).

2. Excitation spectrum: The emission intensity at a fixed wavelength is probed as a function of the excitation wavelength. In this way, it is established which wavelengths can be used to effectively excite the phosphor material, allowing to validate the second requirement (see §1.4).

Both types of spectra can be obtained with the same apparatus, *i.e.* a photoluminescence spectrometer. Here the FS920 of Edinburgh Instruments, which is used in this

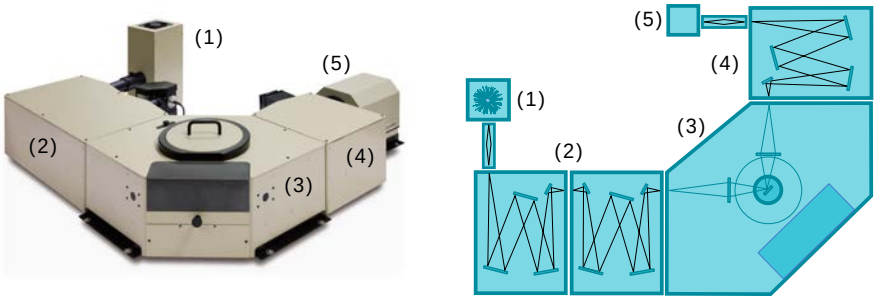

Figure 7.3 – Left: Edinburgh FS920 photoluminescence spectrometer. Right: Schematic image of the most important parts of the spectrometer. The meaning of the numbers is elucidated in the text.

text, is described (Fig. 7.3).

A high pressure xenon arc lamp of 450 W is used as light source (1). The light is generated by a so-called arc discharge, a self-sustaining DC gas discharge, characterized by a low voltage drop. Electrons are emitted from the cathode through both thermionic and field emission. These are accelerated in the plasma, colliding with Xe ions or evaporated electrode material (tungsten, W) which get excited due to the collision. The ions can decay radiatively, emitting characteristic photons. Thanks to the high pressure, of the order of 10 atm, the density of the plasma is high such that high efficiencies can be obtained [318].

The excitation wavelength is selected through a double excitation monochromator (2). These are constructed from a diffraction grating and some mirrors to guide the light in the desired direction. The diffraction grating consists of a plate upon which parallel lines are etched. The spacing of these lines should be of the same order of magnitude as the wavelength of the incident light. The lines which are not etched reflect the light, forming a diffraction pattern (Fraunhofer diffraction) which has an angle-dependent light distribution showing different maxima (diffraction orders). As the diffraction angles for the maxima are wavelength-dependent, the grating gives rise to dispersion, *i.e.* the light beam is decomposed into its constituting wavelengths. By rotating the grating, a particular wavelength can be selected to coincide with the exit slit. The second excitation monochromator is added not only to improve the wavelength resolution, but more important to remove as much stray light as possible [319, 320]. This illumination system is able to excite samples in the wavelength range of 250 nm to 900 nm.

Subsequently, the monochromated light enters the sample compartment (3). Here, a semi-transparent mirror reflects a small part of this light, the reference beam, onto a photodiode. The majority of the light is focused by a lens onto the sample. The light which is emitted by the luminescent sample is imaged, by another lens, into

the emission monochromator (4) which is tuned to select a wavelength of choice.

Finally, the monochromated emission light strikes a point detector (5). Depending on the wavelength range of the phosphor's emission, different detectors are available. For the spectral range up to 800 nm, a photomultiplier tube (PMT) is used (Hamamatsu 928). When hit by a photon, the photocathode of the PMT emits an electron according to the photoelectric effect. This electron is accelerated by an electrode, called the dynode, into which the electron smashes, creating multiple secondary electrons. Different dynodes with increasing voltages succeed, creating an electron avalanche which can be electrically detected when the anode is finally reached. An amplification factor of 10^6 is common. To improve the signal-to-noise ratio, the PMT is cooled to -20°C by a Peltier element [321]. For near IR emission, a germanium detector is available.

7.2.3 Quantum efficiency

The quantum efficiency (QE) is an important quantity to assess the application potential of a luminescent material (requirement 3, §1.4). It is hence important to be able to measure it in a reproducible way. Two techniques are commonly used to measure the QE of a luminescent material, *i.e.* absolute and relative measurements. In the latter case, a reference sample with a well-known QE is required which has similar absorption, emission and reflection characteristics as the sample under consideration. As the availability of stable reference samples for different spectral characteristics is questionable, unknown systematic errors are likely to occur and an absolute measurement approach is favored. To this means, a set-up containing an integrating sphere was constructed, calibrated and extensively tested in an inter-laboratory validation. This validation, together with a detailed description of how quantum efficiency values can be reliably obtained was published within the framework of the Ph.D. work of Dr. Sven Leyre as:

Absolute determination of photoluminescence quantum efficiency using an integrating sphere setup

Sven Leyre, Eduardo Coutino-Gonzales, Jonas J. Joos, Jana Ryckaert, Youri Meuret, Dirk Poelman, Philippe F. Smet, Guy Durinck, Johan Hofkens, Geert Deconinck, Peter Hanselaer

Review of Scientific Instruments, **85** 123115 (2014).

A 152 mm diameter, Spectralon-coated integrating sphere (Labsphere) was purchased and mounted on a stand (see Fig. 7.4). Three ports are provided to perform a measurement. The optical in- and outcoupling is furnished by SMA connections, allowing for a fast and playable setup with optical fibers. The excitation light, which originates from an illumination system built of a xenon arc lamp with monochromator or a 5 mm LED, enters the sphere from the top (1) and is focused on the powder sample (2), which can be mounted into the sphere from the bottom. The reflected excitation light and the luminescence from the sample are scattered in all directions

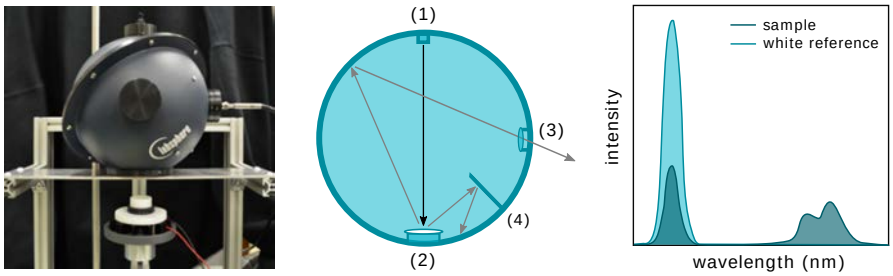

Figure 7.4 – Left: Integrating sphere setup that can be equipped for various types of measurements. Middle: Schematic image of the integrating sphere, equipped to determine QEs of powders. The meaning of the numbers is elucidated in the text. Right: Typical spectra, obtained for a luminescent powder and a white reference powder.

from the powder sample. Thanks to the use of an integrating sphere all emitted and reflected light scatters multiple times from the diffusive reflecting coating in the sphere, allowing for an *integration* both in terms of the emitted direction and emission time. The integrated light can couple out of the sphere through the third port, which is covered by a diffuser, towards the detector (3), which is the same detector that is used for SEM-CL measurements (see §7.1.3). A baffle (4) prevents that light gets detected without reflecting at least once from the inside wall of the sphere.

Before QEs can be measured, the complete setup, *i.e.* the sphere, optical fiber between the sphere and the detection system and the detection system itself, have to be intensity calibrated. This intensity calibration accounts for wavelength-dependent absorptions and the spectral response of the detector. For this means, calibrated lamps with a well-known emission spectrum are used, a deuterium lamp for the spectral range from 200 nm to 400 nm and a halogen lamp for the longer wavelengths. The spectral signal measured by the detector, $S_L(\lambda)$, is related to the spectral radiant flux, $\Phi_L(\lambda)$ that is coupled into the sphere through[4]:

$$S_L(\lambda) = R(\lambda)\Phi_L(\lambda), \tag{7.10}$$

where the index L denotes the calibrated lamp and $R(\lambda)$ is the spectral response of the full setup, including the so-called sphere factor, and the sensitivity of the CCD. When the signal of an unknown light source is now measured, $S(\lambda)$, the spectral response corrected signal can be obtained by:

$$I(\lambda) = S(\lambda)\frac{\Phi_L(\lambda)}{S_L(\lambda)} \tag{7.11}$$

To calculate quantum efficiencies, photon fluxes are required instead of irradiances, requiring an additional division by the photon energy for every wavelength (Eq. 2.13):

$$n(\lambda) = S(\lambda)\frac{\Phi_L(\lambda)}{S_L(\lambda)}\frac{\lambda}{hc}. \tag{7.12}$$

[4]For an overview of radiometric and photometric units see appendix D).

When the setup is properly calibrated, actual measurements can be performed. For this, two different approaches are available, the three measurement approach and the two measurement approach. In both cases, measurements are performed when the excitation beam hits a white reference sample and the luminescent sample. In the three measurement approach, an additional spectrum is collected where the luminescent sample is in the sphere, but when the excitation beam hits the sphere wall instead of the sample. Leyre *et al.* were able to show by means of the integrating sphere theory that both approaches are equivalent [322]. Hence, the two measurement approach is applied in this work. Three parameters are obtained from the two measurements by calculating suitable integrals of the spectrum, *i.e.* the reflection of excitation light of the white reference, $N_{\mathrm{ex}}^{\mathrm{w}}$, the reflection of the excitation light of the luminescent sample, N_{ex}, and the luminescent emission in the latter case, N_{em} (see Fig. 7.4). In general, the transmission, absorption and reflection of excitation light by the luminescent sample add to one,

$$T + A + R = 1. \tag{7.13}$$

Here, it is assumed that $T = 0$ by piling the sample sufficiently thick. Additionally, $A = 0$ for the white reference, yielding finally for the internal and external QE (for their definitions, see §3.3):

$$\mathrm{QE_i} = \frac{N_{\mathrm{em}}}{N_{\mathrm{ex}}^{\mathrm{w}} - N_{\mathrm{ex}}} \qquad \mathrm{QE_e} = \frac{N_{\mathrm{em}}}{N_{\mathrm{ex}}^{\mathrm{w}}} \qquad A = \frac{N_{\mathrm{ex}}^{\mathrm{w}} - N_{\mathrm{ex}}}{N_{\mathrm{ex}}^{\mathrm{w}}} \tag{7.14}$$

The use of this setup is not restricted to the determination of QEs of powder phosphors. The powder cup at the bottom port of the sphere can be removed and replaced by a high-power pumping LED, mounted in a white light mixing cup. On top of this cup, phosphor plates can be put, effectively constructing a remote phosphor pc-LED. The spectrum, and more importantly, the efficiency of the constructed pc-LEDs can then be accurately studied thanks to this setup.

Furthermore, the integrating sphere setup has a fourth access port that allows to measure cuvettes with fluorescent dyes or colloidal quantum dots. In this case, the light enters the sphere from the front side while the cuvette hangs in the middle of the sphere from the top port. A baffle is mounted on the cuvette holder, again preventing the direct detection of luminescent light.

Finally, this setup was also used to determine the upconversion effiency of powder samples[5]. In this case, an IR pump laser was used in combination with grey filters, allowing to measure as a function of excitation power, for illumination, while a calibrated radiometer (ILT 1700, International Light Technologies) was used for the light detection. As this is a point detector, a cut-off filter was used to decouple the excitation and upconverted light.

[5]Upconversion is a nonlinear phenomenon, typically involving multiple optical centers which transfer energy, finally leading to *e.g.* the emission of a visible light photon upon the absorption of two IR photons.

Figure 7.5 – Left: T-TL setup, used to measure thermal quenching [323]. Middle: Cryostat, used for low temperature experiments. Right: ICCD and schematic overview of the experimental determination of decay profiles. The meaning of the numbers is elucidated in the text.

7.2.4 Temperature-dependence

It proves useful to measure luminescent properties also as function of temperature. From the application point of view, the properties of luminescent materials should be stable up to their working temperatures (requirement 4, §1.4) while from the more fundamental point of view, spectra at low temperature are better resolved, allowing a more accurate identification of the different electronic and vibrational levels.

For measuring thermal quenching (TQ), *i.e.* the variation of the external quantum efficiency upon increasing temperature, an in-house built vacuum chamber is available (Fig. 7.5) [323]. Samples in powder or pressed pellet form are mounted on a heating stage inside a vacuum chamber. The stage can be heated up to temperatures of 500 K by a resistive element and cooled to 210 K by a flow of liquid nitrogen. Excitation and measurement of the samples is performed by the same optical-fiber-based illumination and detection system as the QE measurements, allowing to collect complete spectra. This λT-TL setup can also be used to measure thermoluminescence profiles.

For low temperature experiments, from 4 K or 75 K depending on the cooling liquid, He or N_2, which is used, to 475 K, an Oxford Instruments OptistatCF cryostat is available (Fig. 7.5). This cryostat is equipped with transparent windows, allowing spectroscopic measurements.

7.2.5 Time-resolved photoluminescence

Studying the decay dynamics is desirable from both the application-oriented as the fundamental point of view. First, it allows to validate requirement 4 (see §1.4) as the luminescent lifetime of the emitting level can be obtained. Secondly, decay profiles cast a unique view upon the dynamics by which the absorbed energy is dissipated or transferred between centers inside the luminescent material.

The decay dynamics of a luminescent center happen in a time span of the excited state's lifetime after the excitation, *i.e.* it ranges from milliseconds to nanoseconds depending on the dominant mechanisms. In order to measure the emitted light intensity for these short time scales, a dedicated setup is required. The most important part is an intensified CCD (ICCD), Andor Technology DH720 (Fig. 7.5).

An ICCD is built from a conventional CCD chip (charge-coupled device), a phosphor, a micro channel plate (MCP) and a photocathode. These three additional parts amplify the original light signal and can be steered as a fast switching shutter. When a photon strikes the photocathode, an electron is released, which is then accelerated towards the MCP where it is *multiplied* in a similar fashion as in a PMT. In contrast to a PMT, a MCP is constructed from a large number of channels, conserving the spatial information, *i.e.* the position where each photon hits the detector. The *multiplied* electrons excite a CL phosphor of which the emitted light is in turn detected by the CCD. As the ICCD can be considered as a line detector, a monochromator is positioned in front of the entrance slit, resulting in the collection of a full spectrum for every time step. The fast switching is obtained by changing the polarity of the voltage between the photocathode and the MCP, deflecting the photoelectrons and effectively closing the shutter.

Reading out the ICCD (1) takes longer than the luminescent decay of the excited sample (2), implying that a full decay profile cannot be measured in one shot. To achieve a sufficiently dense sampling, a pulsed excitation source (3) is used, along with a variable delay between the excitation pulse and the opening of the shutter of the ICCD. This strategy can result in a decay profile with nanosecond resolution. A nitrogen laser (337 nm) or a pulsed LED can be used as excitation source. The excitation source and ICCD are synchronized by a photodiode (4), triggered by the laser beam (using a beam splitter (5)) in the case of the nitrogen laser or an electronic trigger signal in the case of the pulsed LED.

7.2.6 Chemical stability

Up to now, experimental techniques were reviewed that allow to validate the first five technological requirements (see §1.4) for LED phosphors. The sixth requirement, *i.e.* long-term chemical stability of the phosphor powder is the last requirement to by checked. Phosphors can degrade during their operation as a consequence of being exposed to air or water, or as a consequence of the stressful irradiation by blue or near-UV pumping light, *i.e.* photodegradation.

Degradation is potentially a slow process, requiring an accelerated aging test. This is typically performed inside a climate chamber (Memmert HCP 108) where a constant temperature and relative humidity of, for example, 75°C and 75% are retained. The degradation can be probed by structural characterization of the powders, or by following the variation of the quantum efficiency. Various lasers are available to study photodegradation. Here, the degradation can be most conveniently followed *in situ*

through probing of the luminescence signal.

Even when materials suffer from degradation through contact with ambient air or water, a proper encapsulation can protect them, offering a means to at least partially circumvent the sixth technological requirement [324].

8 Blue luminescence from Eu^{2+} in oxonitridosilicates

Blue phosphors are relatively underrepresented in luminescence literature because the pumping LED typically covers the blue spectral region in phosphor-converted white LEDs. Still, some authors claim that LEDs with improved properties are obtained when a UV pump LED is combined with RGB phosphors. This idea is elaborated in this chapter with the blue oxonitridosilicate phosphor $Sr_{0.25}Ba_{0.75}Si_2O_2N_2:Eu^{2+}$ as guidance. First, the class of the alkaline earth oxonitridosilicates is briefly described in terms of their crystal structure and luminescence properties upon activation by divalent europium. Subsequently, the luminescence properties of the protagonist phosphor are studied and discussed in greater detail, including a microscopic investigation where inhomogeneities in the emission spectrum are addressed. Finally, white LEDs with a UV pump LED and RGB conversion phosphors, including the blue emitting oxonitridosilicate, are simulated in order to assess their performance in terms of color quality and overall energy efficiency.

8.1 Overview of oxonitridosilicates

The $MSi_2O_2N_2:Eu^{2+}$ (M = Ca, Sr, Ba) system has already been the subject of extensive and detailed studies [292, 325–331]. All three basic compounds (*i.e.* with only one type of alkaline earth metal) exhibit strong $4f^6 5d^1 \rightarrow 4f^7$ luminescence upon doping with divalent europium. While $BaSi_2O_2N_2:Eu^{2+}$ features a greenish-blue narrow banded emission, $SrSi_2O_2N_2:Eu^{2+}$ and $CaSi_2O_2N_2:Eu^{2+}$ are characterized by significantly broader yellowish-green and yellow emission bands, respectively.

Structurally, the class of $MSi_2O_2N_2$ oxonitridosilicates is built from alternating layers of metal ions and layers of $SiON_3$ tetrahedra in which the nitrogen atoms connect the silicon atoms, forming a structure with so-called *dreier Ringe*. Although this layered structure is similar for all members of the $MSi_2O_2N_2$ family, the basic compounds possess significantly different crystal structures, for example the orientation of the O atoms in the $SiON_3$ tetrahedra. For more details about the crystal structures of the $MSi_2O_2N_2$ oxonitridosilicates, we refer to [332–334]. The structural differences between the basic compounds implicate that forming a solid solution by mixing of the metal ions is only possible up to a certain limit, above which a second phase will be formed during the synthesis [325]. Generally, a precise determination of the crystal structure is often difficult for these layered materials. Here, the already

known luminescent properties of the $MSi_2O_2N_2:Eu^{2+}$ family are shortly reviewed. Key structural and luminescent quantities are summarized in Tab. 8.1.

$BaSi_2O_2N_2:Eu^{2+}$ is an efficient phosphor, even though it has the lowest quantum efficiency of the basic compounds (Tab. 8.1). It features a narrow emission band peaking at 495 nm (full width at half maximum (FWHM) of 32 nm). Depending on the synthesis conditions, an appreciable afterglow and strong mechanoluminescence are observed, making it suitable for use as pressure sensor [327, 335, 336].

$SrSi_2O_2N_2:Eu^{2+}$ is a very efficient phosphor with a reported internal quantum efficiency of up to 90% [328]. It also exhibits afterglow upon UV excitation [327]. The superior thermal properties make this phosphor a primary candidate as green-yellow conversion phosphor in white phosphor converted LEDs. Up to 50% of Sr^{2+} can be replaced by Ca^{2+} to gently shift the emission color from yellow-green to yellow while keeping a single crystal phase [325]. Finally, $CaSi_2O_2N_2:Eu^{2+}$ is characterized by a much worse thermal quenching behavior [325].

In Bachmann *et al.*, the $Sr_{1-x}Ba_xSi_2O_2N_2:Eu^{2+}$ solid solution is investigated for x up to 0.75 [325]. By replacing Sr^{2+} by Ba^{2+} in the $SrSi_2O_2N_2:Eu^{2+}$ phosphor, the color is surprisingly red-shifted. This was explained by Eu^{2+} preferentially occupying Sr^{2+} sites in the lattice, while further substitution of Sr^{2+} by Ba^{2+} enlarges the experienced crystal field strength, due to compression of the coordination sphere of the remaining Sr sites. It is impossible to synthesize solid solutions between the yellow (x = 0.75) and blue-green (x = 1) phosphor [325, 329].

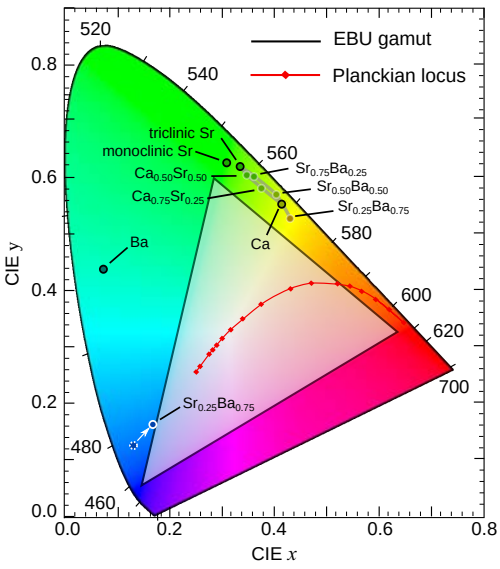

Figure 8.1 – CIE 1931 chromaticity diagram with the color points of the $MSi_2O_2N_2:Eu^{2+}$ family members. The white arrow indicates the color shift of the saturated blue $Sr_{1-x}Ba_xSi_2O_2N_2:Eu^{2+}$ phosphor to the white due to the yellow emitting impurity phase. Color points of other phosphors from [325].

In 2012, Seibald *et al.* reported the remarkably blue luminescence of a $Sr_{0.25}Ba_{0.75}Si_2O_2N_2:Eu^{2+}$ phosphor and its crystal structure [337]. From single-crystal diffraction, the averaged crystal structure was determined to be orthorhombic, while a more detailed investigation with HRTEM allowed to resolve the local cation ordering, resulting in a triclinic structure [337]. This is in contrast to the yellow phosphor with the same stoichiometry, which resembles the triclinic $SrSi_2O_2N_2$ crystal structure. The host material of this blue emitting ma-

Table 8.1 – Structural and luminescence properties of europium doped $MSi_2O_2N_2$ phosphors. All properties are given at room temperature. (o), (m) and (t) stand for the orthorombic, monoclinic and triclinic phase respectively.

M	space group	# M sites	λ_{max} (nm)	FWHM (nm)	QE int/ext	τ (μs)	$T_{0.5}$ (K)	Refs.
Ca	$P2_1$	6	555	106	76/-	1.00	440	[325, 332]
Sr (t)	P1	4	538	76	91/-	1.15	600	[325, 328, 333]
Sr (m)	$P2_1$	4	532	75	-/-	-	-	[338]
$Sr_{0.25}Ba_{0.75}$ (t)	P1	4	564	95	66/-	-	-	[325]
$Sr_{0.25}Ba_{0.75}$ (o)	$Pna2_1$	1	467	41	41/30	0.35	545	[337], this work
Ba	$Cmc2_1$	1	495	32	71/-	0.47	600	[325, 334, 335]
Eu	P_1	4	568	120	-/-	-	-	[339, 340]

terial turned out to be composed of a $BaSi_2O_2N_2$ like structure. However, for this particular composition, the metal layers are corrugated, yielding different luminescent properties than $BaSi_2O_2N_2$:Eu^{2+} where the metal layers are parallel [337].

In another paper, in 2013, Seibald *et al.* reported the occurrence of an additional monoclinic $SrSi_2O_2N_2$ phase [338]. A single crystal could be isolated and structurally analyzed. The emission signal is slightly blue-shifted compared with the common triclinic $SrSi_2O_2N_2$ phase. The structural difference between the two phases is the relative orientation of consecutive silicate layers. It was questioned whether it would be possible to synthesize a pure $SrSi_2O_2N_2$ phase without formation of the other one [338].

In this chapter, a more thorough luminescence study is conducted on the blue oxonitridosilicate phosphor $Sr_{0.25}Ba_{0.75}Si_2O_2N_2$:$Eu^{2+}$, which was reported in 2012 but not yet fully characterized until this moment. Possible applications for this phosphor are evaluated, after which the discussion is generalized to evaluate the usefulness of blue phosphors in LED lighting technology. The findings that are collected in this chapter were published as:

Evaluating the use of blue phosphors in white LEDs: the case of $Sr_{0.25}Ba_{0.75}Si_2O_2N_2$:$Eu^{2+}$

Jonas J. Joos, Jonas Botterman, Philippe F. Smet

Journal of Solid State Lighting, **1** (6) (2014).

8.2 Microscopic investigation of $Sr_{0.25}Ba_{0.75}Si_2O_2N_2:Eu^{2+}$

8.2.1 Synthesis and phase purity

$Sr_{0.25}Ba_{0.75}Si_2O_2N_2:Eu^{2+}$ (with an europium concentration of 1 molar %) luminescent powders were synthesized by a solid state reaction in a tube furnace at high temperature. During all heat treatments, the powder mixtures were kept in a controlled atmosphere of forming gas (90% N_2, 10% H_2 mixture) and put inside zirconia crucibles. Two different synthesis methods were carried out:

1. In one step, with $SrCO_3$ (Alfa Aesar, 99.99%), $BaCO_3$ (Alfa Aesar, 99.95%), Si_3N_4 (-phase, Alfa Aesar, 99.9%) and EuF_3 (Alfa Aesar, 99.5%) as starting materials. After dry ball mixing, the powder mixture was heat treated at 1400°C for 4 hours (heating rate of 4.7°C/min).

2. In two steps. First $(Sr_{0.25}Ba_{0.75})_2SiO_4$:Eu is prepared from $SrCO_3$, $BaCO_3$, SiO2 (Alfa Aesar, 99.9%) and EuF_3 at 1250°C for 3 hours (heating rate of 4.7°C/min). Second, Si_3N_4 was dry ball mixed with the obtained orthosilicate and heat treated at 1400°C for 4 hours (heating rate of 4.7°C/min). This is the synthesis recipe described in [337].

After the heat treatments, the powders were allowed to cool naturally and were lightly ground.

For the synthesis of the blue emitting $Sr_{0.25}Ba_{0.75}Si_2O_2N_2:Eu^{2+}$ phosphor, Seibald *et al.* used a dual step solid state synthesis based on the orthosilicate $(Sr_{0.25}Ba_{0.75})_2SiO_4:Eu^{2+}$ phosphor as intermediate product [337, 341]. In this work, it could be confirmed that this synthesis method indeed yields the described blue phosphor. However, the same phosphor could also be synthesized in a faster one-step way, similar to the method described in [325]:

$$3\,MCO_3 + 2\,Si_3N_4 \quad \rightarrow \quad 3\,MSi_2O_2N_2 + N_2 + 3\,CO. \tag{8.1}$$

After the heat treatment, visual inspection under UV illumination learns that the bulk of the obtained phosphor powder has the desired blue color. On top of the blue powder, a thin, green emitting layer is formed. For further investigation, this green emitting top layer was removed and kept apart. This green emitting layer was also formed during the dual step synthesis. X-ray diffraction (XRD) and photoluminescence (PL) measurements (see further) were addressed to verify that the result of both syntheses are indeed identical. The powder prepared with the one step synthesis was selected for further investigation.

It was reported that the addition of small amounts of NH_4Cl as fluxing agent during the temperature treatment improves the formation and crystallization of the $SrSi_2O_2N_2:Eu^{2+}$ phosphor [342]. The influence of NH_4Cl (2 weight% of the final mass) on the formation of the blue phosphor was investigated. It turns out that the fluxing agent rather stimulates the formation of an undesired yellow emission band

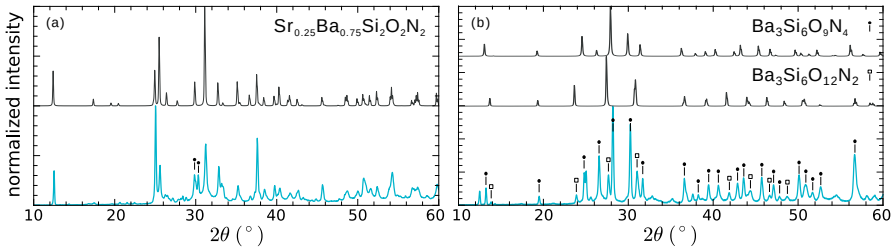

Figure 8.2 – XRD measurements (blue) compared with simulated patterns (black). (a) The prepared $Sr_{1-x}Ba_xSi_2O_2N_2$:Eu^{2+} powder (bottom), compared with the calculated pattern for $Sr_{1-x}Ba_xSi_2O_2N_2$ (top) [337]. The black circles indicate reflections, possibly originating from $BaSi_6N_8O$ [343]. (b) The prepared green emitting top layer (bottom), compared with the calculated pattern for $Ba_3Si_6O_{12}N_2$ (middle) and $Ba_3Si_6O_9N_4$ (top) [344, 345].

next to the blue emission band. Therefore, NH_4Cl was omitted from further syntheses.

To specify the composition of the powders, X-ray diffraction (XRD) measurements were performed. The results are summarized in Fig. 8.2. The XRD pattern for the blue emitting bulk powder (Fig. 8.2(a)) shows a reasonably good comparison with the calculated one from the structure reported in [337]. The XRD measurement indicates that texture effects are present. However, the locations of the reflections are in correspondence with those of the reference pattern, indicating that the desired $Sr_{0.25}Ba_{0.75}Si_2O_2N_2$:$Eu^{2+}$ phosphor is obtained. Additionally, some extra reflections appear around $2\theta = 30°$. These might be originating from small amounts of $BaSi_6N_8O$ that formed during the high temperature synthesis. Since $BaSi_6N_8O$:Eu^{2+} is reported to show fluorescence in the blue-green spectral region (emission band peaking at 503 nm, FWHM of 102 nm [346]), this might compromise the characterization of the $Sr_{0.25}Ba_{0.75}Si_2O_2N_2$:$Eu^{2+}$ phosphor.

From the XRD measurement of the green emitting top layer, it can be derived that it is mainly composed of $Ba_3Si_6O_9N_4$:Eu^{2+} (filled circles, Fig. 8.2(b)) and $Ba_3Si_6O_{12}N_2$:Eu^{2+} (open squares, Fig. 8.2(b)). The locations of the experimental reflections are slightly shifted to higher 2θ values, which is explained by the incorporation of some Sr^{2+} in the crystal structure, decreasing the effective lattice parameters. $Ba_3Si_6O_{12}N_2$:Eu^{2+} is known to give green emission, explaining the green color of the top layer under UV excitation [344, 347]. The blue luminescence of $Ba_3Si_6O_9N_4$:Eu^{2+} is thermally quenched at room temperature [347]. Note that both impurities have the same (Sr,Ba):Si ratio of 1:2, as in the intended stoichiometry. The main difference is the larger oxygen to nitrogen ratio, which is probably due to oxygen traces during the synthesis process.

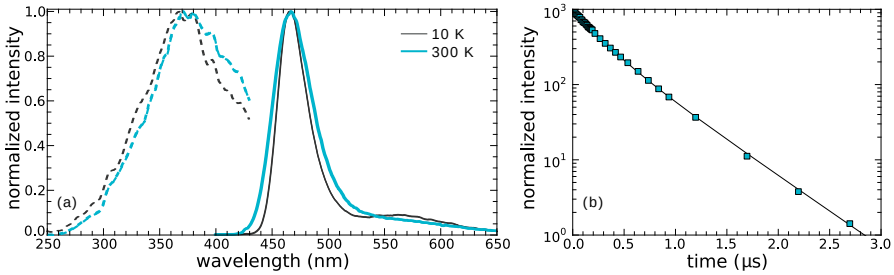

Figure 8.3 – (a) Photoluminescence emission (excitation at 370 nm, solid lines) and excitation (emission at 466 nm, dashed lines) spectra of $Sr_{0.25}Ba_{0.75}Si_2O_2N_2:Eu^{2+}$, measured at room temperature and at 10 K. (b) Decay profile of the blue emission band at 300 K. Measured with a 337 nm pulsed laser as excitation source (blue diamonds). Fit with the sum of two exponential functions (black line).

8.2.2 Luminescence at the macroscale

The photoluminescence of the $Sr_{0.25}Ba_{0.75}Si_2O_2N_2:Eu^{2+}$ phosphor features broadband emission and excitation spectra (see Fig. 8.3(a)), characteristic for the $4f^7$ - $4f^65d^1$ transitions within the Eu^{2+}ion. The emission spectrum peaks at room temperature at 467 nm and has a full width at half maximum (FWHM) of 41 nm.

In the emission spectrum, a second contribution in the yellow range around 560 nm, is clearly visible. The origin of this second emission band might be the occurrence of a $Sr_{1-x}Ba_xSi_2O_2N_2:Eu^{2+}$ phase with a different structure than the intended blue phosphor, which has averaged an orthorhombic structure. In their paper, Bachmann *et al.* report a $Sr_{0.25}Ba_{0.75}Si_2O_2N_2:Eu^{2+}$ phase with the triclinic $SrSi_2O_2N_2$ structure, emitting a broadband spectrum, peaking at 564 nm [325,348]. It is not unlikely that this is the phase responsible for the weak yellow emission band. If this impurity phase indeed has the $SrSi_2O_2N_2$ structure, it is not surprising that the addition of NH_4Cl flux during the heat treatment stimulates the formation of it [342]. This yellow emission band also occurred in the spectrum from the original paper reporting the blue phosphor [337].

Since the XRD measurements suggest the occurrence of small quantities of $BaSi_6N_8O:Eu^{2+}$, it is important to verify whether this has an influence on the photoluminescence of the powders. The emission spectrum of $BaSi_6N_8O:Eu^{2+}$ features a broad band (FWHM = 102 nm), centered at 503 nm and can be excited between 200 nm and 400 nm [346], although no values for the QE have been reported. To verify the occurrence of this blue-green phosphor, two emission scans of the prepared powder were compared, one at 310 nm excitation and one at 410 nm excitation, the former chosen in the maximum of the excitation band of $BaSi_6N_8O:Eu^{2+}$, the latter chosen outside the excitation band of $BaSi_6N_8O:Eu^{2+}$. Since no observable differences between the two scans were noticed, it can be concluded that the light-emitting $BaSi_6N_8O:Eu^{2+}$ phase, as described by R.-J. Xie *et al.*, is not observed in the prepared powder. This has therefore no influence on the characterization of the lu-

minescence of the $Sr_{0.25}Ba_{0.75}Si_2O_2N_2:Eu^{2+}$ powders apart from a possibly negative influence on the overall quantum efficiency of the phosphor.

The color point (CIE x, CIE y) of the complete emission spectrum (*i.e.* blue and yellow band) at room temperature is (0.165, 0.165). If the blue component would be the only feature of the emission spectrum, the color point is estimated at (0.129, 0.067). Clearly, a small amount of the impurity phase shifts the color point towards the white region of the chromaticity diagram (see Figure 8.1).

The internal and external quantum efficiency (QE) of the photoluminescence were measured upon excitation with a 370 nm LED. For the $Sr_{0.25}Ba_{0.75}Si_2O_2N_2:Eu^{2+}$ phosphor, values of QE_{ext} = 30% and QE_{int} = 41% were obtained. This is significantly lower than the internal quantum efficiencies of benchmark phosphors (typically $QE_{int} \approx 90\%$ [169, 328]). The grey shade in the body color of the powder already hinted towards an insufficient QE. If impurity phases which do not emit light (potentially $BaSi_6N_8O$) are present in the powders, the measured QE will be lower than the intrinsic QE of the $Sr_{0.25}Ba_{0.75}Si_2O_2N_2:Eu^{2+}$ phosphor. However, a sound optimization of the synthesis process (*e.g.* finding a suitable fluxing agent) might improve the quantum efficiency considerably because there does not seem to be a fundamental reason why the $Sr_{0.25}Ba_{0.75}Si_2O_2N_2:Eu^{2+}$ phosphor should have a lower QE than comparable phosphors such as $BaSi_2O_2N_2:Eu^{2+}$ or $SrSi_2O_2N_2:Eu^{2+}$.

8.2.3 Luminescence at the microscale

From the photoluminescence measurements, it is clear that not a phase pure material is obtained. Combining cathodoluminescence (CL) and energy dispersive X-ray spectroscopy (EDX) inside a scanning electron microscope (SEM) should help to get a better grasp of the different phases that occur in the phosphor powder and their luminescence [349].

The morphology of the prepared powders consists of agglomerated, rod to plate-like particles, typically 10 to 20 μm in length (Fig. 8.4). This rather uncommon morphology seems not incompatible with the layered crystal structure of the host material. The EDX maps reveal a rather homogeneous composition, taking the influence of the sample morphology on the X ray detection efficiency for the different elements into account.

At a few places, a higher than average silicon content could be found, although it could not be linked to a specific chemical composition, nor was it reflected in the CL spectra. These Si rich areas are possibly related to the $BaSi_6N_8O$ phase which might be present in the powder. SEM-CL confirms the result from the PL measurement that there is no light emission originating from this phase. No results from thermal quenching or quantum efficiency measurements of the $BaSi_6N_8O:Eu^{2+}$ phosphor are reported in literature. Furthermore, given the peculiarly high Stokes shift of this material (1.14 eV or 9200 cm^{-1}) and width of the emission band (estimated about 0.5 eV or 4033 cm^{-1}), one can doubt whether the reported luminescence is originating

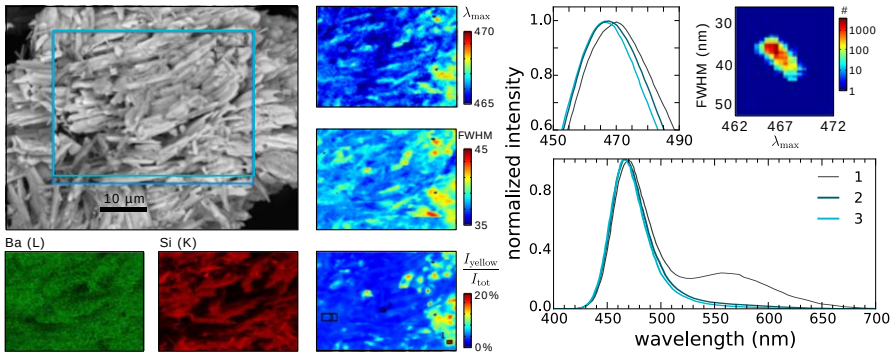

Figure 8.4 – (left) Backscattered electron image (top) of the $Sr_{0.25}Ba_{0.75}Si_2O_2N_2$:$Eu^{2+}$ powder, along with EDX maps for barium and silicon (bottom). (middle) Maps for the peak emission wavelength (λ_{max}, in nm), the FWHM (also in nm) and the emission intensity in the wavelength range (550-650 nm), relative to the total emission intensity. (right) Correlation between peak wavelength and FWHM (top right) and emission spectra (bottom) for the three selected areas indicated in the CL map. All maps (EDX and CL) are corresponding to the area indicated by the blue rectangle on the backscattered electron image. All data obtained at a sample temperature of 255 K.

from a "normal" Eu^{2+} activated phosphor [168, 262, 346].

The studied area, indicated by the blue rectangle in Fig. 8.4, was divided into 256 by 192 pixels and in each pixel a full cathodoluminescence (E = 15 keV) emission spectrum was recorded. Then for each spectrum, key luminescence parameters, such as the band width (FWHM) and the peak emission wavelength (λ_{max}) were determined. Fig. 8.4 clearly shows that all studied particles have an emission peaking between 465 and 468 nm, while the FWHM ranges between 37 and 43 nm. This effect is larger than the mere consequence of the use of wavelength units. Averaging out over all pixels, a CL emission spectrum is obtained which is similar to the PL emission spectrum. Although the emission is very homogeneous over the studied area, there appears to be some correlation between λ_{max} and the FWHM, as longer peak emission wavelengths tend to coincide with wider emission bands (Fig. 8.4), which could be due to local variations in composition (*e.g.* Eu concentration or Sr:Ba ratio).

The SEM-CL study also allows to probe the origin of the yellow emission band, peaking at 558 nm, when preparing $Sr_{0.25}Ba_{0.75}Si_2O_2N_2$:$Eu^{2+}$. Note that this emission band is found both in [337] and in this work. The yellow emission amounts to no more than 20% of the total emission intensity, and certainly no areas with pure yellow emission (*i.e.* in the absence of the blue emission band) could be found, which would be the case for a separately formed impurity phase. For these areas with a larger fraction of long wavelength emission, no deviation in stoichiometry could be found by means of SEM-EDX. This is no surprise since it was shown by Seibald *et al.* by a combination of TEM/HRTEM/TEM-EDX that a domain structure is present at a

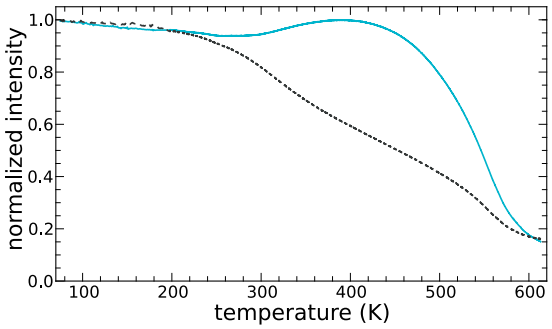

Figure 8.5 – Integrated emission intensity of the blue (blue, solid line) and yellow (grey, dotted line) emission band as a function of temperature. Measured upon excitation with a 370 nm LED.

nanometer length scale, impossible to resolve with SEM-EDX. The yellow emission is originating from domains with a Sr-richer content, composed of the $SrSi_2O_2N_2$ structure [331, 337].

The SEM-CL study shows that yellow emission is always accompanied by the blue emission, within the same phosphor particles, supporting the conclusion by Seibald *et al.* that the yellow emission is due to intergrowth on the nanoscale. Nevertheless, the main fraction of the studied phosphor particles shows only the blue emission band, which offers the promise to prepare a purely blue emitting phosphor, without the additional yellow emission band from the Sr-rich domains. Regardless the impossibility of a SEM to resolve the nanoscopic domain structure, this clearly illustrates that the majority of the micrometer sized grains exhibit only the blue luminescence. Therefore, the submicron resolution of CL in a SEM offers a fast and elegant way to probe the luminescence behavior at the single grain level, by being complementary to the aforementioned TEM study at the nanoscale [350].

8.2.4 Thermal quenching

In Fig. 8.5, the integrated emission intensity is displayed as a function of temperature. Thermal quenching is starting around 450 K and the temperature where the emission intensity is halved with respect to low temperature ($T_{0.5}$) is 545 K. This means that this phosphor can safely be used in typical lighting applications, where the phosphors temperature will remain below 450 K. The thermal quenching behavior of the yellow component ($T_{0.5}$ = 454 K) is worse though. In Tab. 8.2, some parameters describing the emission of $Sr_{0.25}Ba_{0.75}Si_2O_2N_2$:$Eu^{2+}$ are given as a function of temperature. Not only the intensity of the blue luminescence stays constant in the relevant temperature range, also the color point remains stable, which is important from an application point of view. This is due to two opposite effects, namely the slightly broadening of the blue emission band and the quenching of the yellow one, which tend to cancel out to a large extent when the color point is calculated.

Table 8.2 – Features of the emission spectrum of $Sr_{1-x}Ba_xSi_2O_2N_2$:Eu^{2+} as a function of temperature, maximum (λ_{max}) and FWHM of the emission band, relative intensity of the blue emission band with respect to 300 K, color point of the complete emission spectrum (blue and yellow component) and corresponding color shift in CIE Luv color space.

T (K)	λ_{max}	FWHM	$\frac{I(T)}{I(300K)}$	(CIE x, CIE y)	$d_{u'v'}(T, 300K)$
300 K	467.4	41	1.00	(0.165, 0.165)	0.0000
350 K	467.0	43	1.04	(0.164, 0.164)	0.0002
400 K	466.6	49	1.06	(0.164, 0.165)	0.0008

8.2.5 Decay of luminescence

The decay of the blue emission band was measured at room temperature. The decay profile is displayed in Figure 8.3(b). This profile could be fitted with a sum of two exponential functions:

$$I(t) = I_1 e^{-t/\tau_1} + I_2 e^{-t/\tau_2}. \tag{8.2}$$

The obtained decay times are 461 ns and 219 ns, with contributions of 66% and 34%, respectively, to the total decay. The fractions were calculated as:

$$f_i = \frac{\int I_i e^{-t/\tau_i} dt}{\int I(t) dt} = \frac{I_i \tau_i}{I_1 \tau_1 + I_2 \tau_2} \qquad (i = 1, 2). \tag{8.3}$$

Both components are in the expected range for lifetimes of the $4f^6 5d^1$ excited state in the case of blue emission. This is slightly faster than the luminescent lifetime of Eu^{2+} in $BaSi_2O_2N_2$ (Tab. 8.1). It is within expectations because the luminescence lifetime shortens when the emission color is blue-shifted on condition that the refractive index does not change (see §2.3.2). The origin of the faster decay component, presumably related to a non-radiative decay path, could not yet be clarified.

Because of the fast decay of the $4f^6 5d^1$ excited state of Eu^{2+} in this host lattice, it is expected that high excitation fluxes can be used without sublinear response, as is the case in some applications [351].

8.2.6 Chemical stability

The chemical stability of the oxonitridosilicate phosphor was inspected by monitoring the *in-situ* photoluminescence (excitation with a 370 nm LED) during an accelerated aging test inside a humidity chamber (75°C, 75% relative humidity). In a timescale of 200 hours, no significant decrease of the luminescence could be measured for both the blue and yellow components (not shown).

8.3 Blue phosphors for increased color rendering?

Almost all current white pc-LEDs are composed of a blue pumping LED (peaking typically at 455 to 460 nm and 20 nm FWHM) and a yellow phosphor or green-red phosphor blend. As it was suggested that the blue phosphor under study can be applied in pc-LEDs with high color rendering index (CRI) [337], a simulation is conducted in order to estimate the increase in color rendering that can be achieved by using an additional blue phosphor [352].

In the simulations, a white LED with a correlated color temperature (CCT) of 4000 K is intended. For lower CCT, the blue spectral region will only have a minor influence on the color rendering. To account for the green and red spectral region, standard broadband phosphors were selected for this: $SrSi_2O_2N_2$:Eu^{2+} and $Sr_2Si_5N_8$:Eu^{2+}, a typical combination which is known to yield white light of good color quality and color rendering when combined with a blue pumping diode [13, 353].

For the blue component, a gaussian spectral shape was taken, serving as an approximation to the spectrum of a blue phosphor in a UV-pumped pc-LED or a blue LED in a blue-pumped pc-LED. To examine the influence on the color quality scale (CQS) and luminous efficacy of the radiation (LER), the peak wavelength and width (FWHM) of the blue component were varied. It was opted to study the CQS instead of the CRI, since the former was designed to account for the defects inherent to the definition of the latter.

The relative contributions of the red and green phosphors in the simulated LED were adapted such that a constant CCT of 4000 K and a limited deviation of the Planck locus ($|D_{uv}| < 0.001$) are obtained for all variants of the blue component. The result of this simulation is displayed in Fig. 8.6(a-b). In this figure, the approximate locations of a three-band LED with the $Sr_{0.25}Ba_{0.75}Si_2O_2N_2$:$Eu^{2+}$ blue phosphor and a traditional blue diode pumped white LED are indicated. Also the location of a three-band LED with the well-known $BaMgAl_{10}O_{17}$:Eu^{2+} blue phosphor is indicated. This phosphor is characterized by an emission maximum at 450 nm, a FWHM of 55 nm, internal QE of 90% and can be efficiently excited between 220 nm and 380 nm [354, 355].

It can be seen that it is possible to improve the color quality (CQS) by replacing the blue pumping LED by a UV pumping LED and a blue phosphor. However, the improvement is rather limited because good color quality can already be achieved in the traditional way with a pumping LED of 455 nm. The increase in CQS (from a value of 87 to 89), is at the expense of a decrease in luminous efficacy (315 lm/W instead of 331 lm/W). Higher color qualities can be achieved if blue phosphors with a broader emission spectrum are used (CQS up to 95 for a phosphor with FWHM $\geq$ 60 nm).

To illustrate this, the spectra of three simulated white LEDs are displayed in Figure 8.6(c). As one can see, the cyan gap between the blue pumping LED and the green

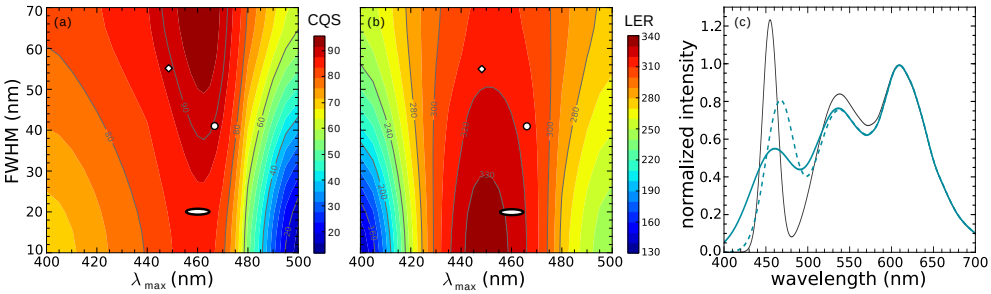

Figure 8.6 – Influence on color quality scale (CQS, a) and luminous efficacy of radiation (LER, b) of the spectral shape of the blue component in a three-band LED. The approximate location of the $Sr_{0.25}Ba_{0.75}Si_2O_2N_2$:$Eu^{2+}$ phosphor is indicated by a circle, the location of the standard blue phosphor $BaMgAl_{10}O_{17}$:Eu^{2+} is indicated by a diamond and the locations of blue pumping LEDs are indicated by the oval. (c) White LED spectra from simulations. Blue LED pumped (455 nm peak wavelength, grey solid line), UV pumped with a narrow band blue phosphor (467 nm peak wavelength, 40 nm FWHM, blue dotted line) and UV pumped with a broad band blue phosphor (460 nm peak wavelength, 65 nm FWHM, blue solid line).

phosphor can be bridged by using a blue phosphor instead of a blue pumping LED. The highest CQS can be achieved by using a blue phosphor which is significantly broader (FWHM of 65 nm, peaking at 460 nm) than the described $Sr_{0.25}Ba_{0.75}Si_2O_2N_2$:$Eu^{2+}$ phosphor. In this case, a CQS of 96 can be achieved. The LER is 314 lm/W, which is comparable with the LER of the white LED when the narrow blue phosphor is used.

However, if a blue phosphor is used instead of a blue pumping LED, the phosphor mix needs to be pumped by a UV LED. Because of this, the Stokes shifts will be significantly higher, especially for the red and green phosphors. This will have a severe impact on the overall electrical to optical power conversion efficiency (η_{e-o}), the so-called wall-plug efficiency [13, 15]:

$$\eta_{e-o} = \frac{P_{opt}}{P_{el}} = \eta_{LED}\,\eta_{extr}\left(f_0 + \sum_{i=1}^{N} f_i \mathrm{QE}_{int}\frac{\int I_i(E)E\mathrm{d}E / \int I_I(E)\mathrm{d}E}{\int I_{LED}(E)E\mathrm{d}E / \int I_{LED}(E)\mathrm{d}E}\right). \tag{8.4}$$

In this formula, η_{LED} and η_{extr} represent the electrical to optical power conversion efficiency of the pumping LED and the extraction efficiency of the LED package respectively. N phosphors are used with relative weights f_i ($\sum_{i=1}^{N} f_i = 1$), internal quantum efficiencies QE_{int} and spectra $I_i(E)$. f_0 is the fraction of the spectrum of the pumping LED which is not absorbed by the phosphors. For UV pumping LEDs, f_0 is ideally 0. The ratios in the right-hand side of Eq. 8.4 are called the quantum deficits, originating from the Stokes shifts of the phosphors.

The term between brackets can be calculated for the spectra of the simulated LEDs. Internal quantum efficiencies of 90% were assumed for all phosphors. This yields a

wall-plug efficiency of

$$\eta_{e-o} = 0.83\,\eta_{LED}\,\eta_{extr}, \tag{8.5}$$

for the traditional blue pumped white LED and

$$\eta_{e-o} = 0.66\,\eta_{LED}\,\eta_{extr}, \tag{8.6}$$

for a 400 nm pumped white LED with three phosphors. If the pumping LED has a peak wavelength of 370 nm, this becomes:

$$\eta_{e-o} = 0.61\,\eta_{LED}\,\eta_{extr}. \tag{8.7}$$

Given the similar external quantum efficiencies of $In_{1-x}Ga_xN$ LEDs (η_{LED}) in the blue and UV spectral region, there is no possibility to overcome the efficiency difference of at least 20% between blue and UV LED pumped white LEDs [356].

Because of the decrease in luminous efficacy and wall-plug efficiency while the color quality improves only slightly, it is very unlikely that relatively narrow band blue phosphors will be used in future high color quality LEDs for lighting. For devices with high color quality, whether expressed in CQS or CRI, much broader emission bands are to some extent beneficial.

For certain display or projection applications, based on violet laser excitation, blue phosphors with a narrow emission spectrum such as $Sr_{0.25}Ba_{0.75}Si_2O_2N_2:Eu^{2+}$ are interesting. In this case, color rendering is irrelevant and saturated colors, corresponding with narrow emission bands are compulsory to achieve a large color gamut for the display [357].

8.4 Conclusions

In this chapter, a complete characterization of the luminescence of a recently reported phosphor in the oxonitridosilicate family was given. The blue emitting material with stoichiometry $Sr_{0.25}Ba_{0.75}Si_2O_2N_2:Eu^{2+}$ is characterized by broadband emission peaking at 467 nm at room temperature and a good thermal stability of both the emission intensity and color. An additional weak yellow emission band was observed. The currently obtained internal quantum efficiency of 41% is too low to allow this phosphor to be used in applications. Nevertheless, this might be improved by an optimization of the synthesis procedure. The phosphor was found to be chemically stable. As a conclusion of this feasibility study, this blue oxonitridosilicate can be suitable for the use in applications if the quantum efficiency can be improved.

Additionally, the microscopic structure of this phosphor was studied. It turned out that no grains with a pure yellow emission could be found, the blue emission is everywhere dominant. The majority of the powder particles do however only emit blue light.

Finally, the potential of blue phosphors to improve the color quality of white LEDs for lighting was investigated because this is often quoted as motivation to study blue phosphors. It was found that only a minor improvement of color quality can be achieved by using a saturated blue phosphor such as the oxonitridosilicate which was subject of this study, or the $BaMgAl_{10}O_{17}:Eu^{2+}$ phosphor. This increase in color quality is at the expense of a decrease in luminous efficacy and overall electrical-to-optical conversion efficiency of the LED, leading to the conclusion that only the use of blue phosphors with a significant broader emission band (FWHM $\geq$ 60) is justifiable to produce LEDs with very high color quality (CQS > 90). Narrow band phosphors with a saturated blue color are however useful in case of projection or display applications based on conversion of near-UV light, *e.g.* in the case of laser diode excitation.

9 GREEN LUMINESCENCE FROM Eu^{2+} IN THIOGALLATES

Alkaline earth thiogallates are ternary sulfides which are well-known for their efficient and color-pure luminescence upon activation by divalent europium. In this chapter, the green emitting phosphors of this family are investigated in detail. This is especially motivated by the increasingly stringent recommendations for backlights in liquid crystal displays, requiring extremely saturated colors. After a general overview of the Eu^{2+} activated thiogallates and the similar thioaluminates, the solid solution series $Sr_{1-x}Eu_xGa_2S_4$ is studied. The luminescence properties are optimized and the phosphor is applied in white LEDs in combination with red emitting quantum dots. Finally, the structural and luminescence properties of $Zn_{1-x}Eu_xGa_2S_4$ are studied in order to resolve the fog around the luminescence mechanism of this apostate member of the thiogallate family.

9.1 Overview of thiogallates and thioaluminates

The europium doped alkaline earth thiogallates and thioaluminates offer a very interesting set of luminescent materials, both from the application point of view, thanks to their color tunability and color purity, as well as from the fundamental point of view (see chapter 6). All compounds of this set, and most of the solid solutions, exhibit efficient broadband $4f^6 5d^1 \rightarrow 4f^7$ luminescence upon activation by the Eu^{2+} ion. These materials were already known before the quest for LED phosphors exploded, in particular as EL phosphors for electroluminescent thin film displays or CL phosphors for field emission displays upon activation by divalent europium or trivalent cerium [5, 303, 358–362]. The basic structural and luminescence properties of this family of compounds are briefly discussed. The key parameters are summarized in Tab. 9.1 and the color points shown in Fig. 9.1.

The alkaline earth thiogallates and thioaluminates crystallize into only two different structures. The calcium and strontium compounds form orthorhombic crystals with three nonequivalent alkaline earth sites which resemble to a large extent (see also §6.4) square antiprisms (Fig. 9.2(a)) [270, 302]. The fully concentrated materials $EuGa_2S_4$ and $EuAl_2S_4$ form the same crystal structure, implying that there are no restrictions on the europium concentration in the Ca and Sr compounds.

The Ca and Sr thioaluminates feature a remarkably saturated bluish-green emission upon activation by Eu^{2+} [150, 359]. The similar thiogallates yield a yellowish and green emission which is still saturated, however somewhat broader than in the case of the thioaluminates [302, 361, 363, 364]. For these four compounds, only the emission band of $SrGa_2S_4$:Eu^{2+} is ideally located to be used in white LED applications. A similar color point can be obtained by the solid solution of $CaAl_2S_4$:Eu^{2+} and $CaGa_2S_4$:Eu^{2+}, although slightly less saturated [365]. By adding some Ba to $SrGa_2S_4$:Eu^{2+}, the emission spectrum can be shifted slightly to shorter wavelengths [366]. Yu *et al.* were able to show that by using appropriate Ca:Sr and Al:Ga ratios, a large part of the green and green-bluish area of color space can be covered [365].

Remarkably, both fully concentrated Eu compounds still feature photoluminescence at room temperature [367–369].

The barium compounds crystallize into structures with a cubic unit cell where two Ba sites are found (Fig. 9.2(b))[1]. In contrast to the structure of the Ca and Ba compounds, the two Ba sites are completely different. The Ba1 site is twelvefold coordinated by sulfur and can be approximated by a icosahedron, while the Ba2 site is sixfold coordinated, approximating an octahedron. Jabbarov *et al.* hypothesize that the Eu ion will occupy both Ba sites in $BaGa_2S_4$ and even attribute different features in the excitation spectrum to the different Eu coordination, based on rather hand waving arguments [362]. $BaAl_2S_4$:Eu^{2+} features a saturated blue emission, explaining the attention it got in the context of EL displays [5, 370, 371]. $BaGa_2S_4$:Eu^{2+} shows a broader bluish-green emission which was attributed to a larger electron-phonon coupling [218].

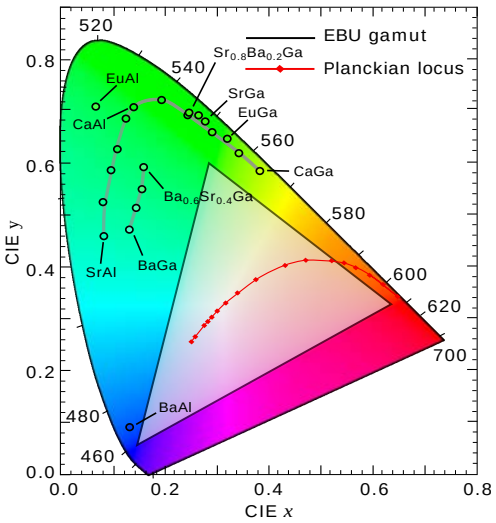

Figure 9.1 – CIE 1931 chromaticity diagram with the color points of the $MGa_{1-y}Al_yS_4$:Eu^{2+} family members (M = Ca, Sr, Ba).

Due to its different crystal structure, solid solutions with Ba and another alkaline earth metal will not be stable over the full concentration range. Upon adding Sr to $BaGa_2S_4$:Eu^{2+}, a redshift towards the green is found before phase segregation occurs at 40% of Sr [366]. When Ba is added to $SrGa_2S_4$:Eu^{2+}, a blueshift is found up to the

[1] $BaAl_2S_4$ shows a less common orthorhombic phase in addition. This phase is isostructural to the Ca and Sr thioaluminates [370].

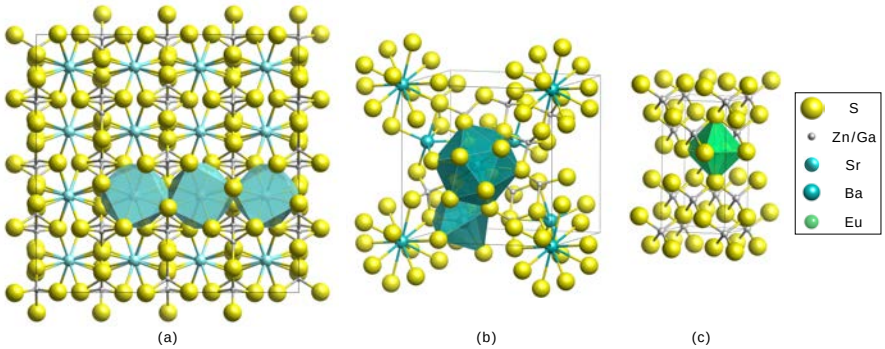

Figure 9.2 – Crystal structures of the alkaline earth thiogallates and thioaluminates and zinc thiogallate. (a) Orthorhombic Fddd structure of *e.g.* $CaGa_2S_4$ and $SrGa_2S_4$. The three nonequivalent metal sites are accentuated. An enlarged figure is shown in Fig. 6.9 [270]. (b) Cubic $Pa\overline{3}$ structure of $BaAl_2S_4$ and $BaGa_2S_4$, the two nonequivalent Ba-sites, with coordination numbers of 6 and 12, are accentuated [217]. (c) The defect stannite structure, $I\overline{4}2m$, of $ZnGa_2S_4$ with an Eu^{2+} occupying an octahedral void as proposed by Wickleder *et al.* [372, 373]

maximal Ba concentration of 20% [366].

The thioindates were deliberately left out of this overview. Although $SrIn_2S_4$ and $BaIn_2S_4$ crystallize in the recurring orthorhombic structure, no conclusive studies on the luminescence of Eu^{2+} dopants are available [270, 374, 375]. A few available literature reports describe very broad and redshifted emission bands which doubtfully originate from $4f^6 5d^1 \rightarrow 4f^7$ transitions in Eu^{2+} [376,377]. This might be related to the small band gaps of the thioindates and hampers applications for these materials [5].

Next to the *classical* Ca, Sr and Ba compounds, the zinc and magnesium thiogallates are added to this overview as saturated green luminescence of Eu^{2+} in these compounds was claimed. It is however unconventional that Eu^{2+} substitutes for Mg^{2+} or Zn^{2+} given the large discrepancy in ionic radius. Wickleder *et al.* proposed a model for $ZnGa_2S_4$:Eu^{2+} where the dopant occupies octahedral voids in the defect stannite host compound (see Fig. 9.2). These compounds are investigated in detail in §9.3.

As described in §1.3.3, efficient phosphors with a saturated green color are required to achieve the modern standards for display applications. From the above literature overview, it seems that especially $SrGa_2S_4$:Eu^{2+}, $ZnGa_2S_4$:Eu^{2+} and $MgGa_2S_4$:Eu^{2+} have a potentially interesting color point. For this reason, these materials are highlighted and further investigated in the following.

$SrGa_2S_4$:Eu^{2+} is investigated while varying the europium concentration. Increasing the dopant concentrations can help to optimize the external quantum efficiency of the phosphor. One should however keep an eye on possible non-radiative decay

Table 9.1 – Structural and luminescence properties of europium doped thiogallate and thioaluminate phosphors. All properties are given at room temperature. $ZnGa_2S_4$ and $MgGa_2S_4$ are shown in blue as their luminescence is most likely not due to Eu^{2+} defects in these hosts (see §9.3).

	space group	# M sites	λ_{max} (nm)	FWHM (nm)	QE int/ext	τ (μs)	$T_{0.5}$ (K)	Refs.
$CaAl_2S_4$	Fddd	3	516	39	0.10/-	0.400	> 350	[150, 270]
$SrAl_2S_4$	Fddd	3	496	38	0.20/0.15		400	[270, 359]
$BaAl_2S_4$	$Pa\bar{3}$	2	470	43	0.62/0.54	0.345	> 300	[359, 370]
$EuAl_2S_4$	Fddd	3	506	26		0.064		[369]
$CaGa_2S_4$	Fddd	3	565	50	0.30/-	0.610	350	[270, 361, 363]*
$SrGa_2S_4$	Fddd	3	536	50	0.71/0.50	0.445	475	[270, 302, 364]*
$BaGa_2S_4$	$Pa\bar{3}$	2	493	60		0.290	420	[217, 362]
$EuGa_2S_4$	Fddd	3	544	45	0.21/-	0.116	204	[367, 368]*
$MgGa_2S_4$	C12/c1	3	538	49		0.149		[369, 378]
$ZnGa_2S_4$	$I\bar{4}2m$	1	542	50	0.13/0.06	0.127	240	[373]*

* this work

channels and a proper distribution of the dopant inside the host compound. The first part of this chapter is therefore dedicated to a study of the thermal quenching and the decay dynamics of this compound. The result of this investigation was published as:

Thermal quenching and luminescence lifetime of saturated green $Sr_{1-x}Eu_xGa_2S_4$ phosphors

Jonas J. Joos, Katrien W. Meert, Anthony B. Parmentier, Dirk Poelman, Philippe F. Smet

Optical Materials, **34** (2012), 1902-1907.

Subsequently, optimized $SrGa_2S_4$:Eu^{2+} powders were applied to manufacture white pc-LEDs, suitable for display applications, with a remote phosphor architecture (see §1.3.3). As the red component, CdSe/CdS quantum dots were used as these show a highly tunable and efficient saturated red emission. This work, which was largely performed within the framework of the Ph.D. work of Dr. Sofie Abé, was published as:

Hybrid remote quantum dot / powder phosphor layers for display backlights

Sofie Abe, Jonas J. Joos, Lisa I. D. J. Martin, Zeger Hens, Philippe F. Smet

Light: Science & Applications, **6** (2017), e16271.

In the case of $ZnGa_2S_4$:Eu^{2+}, it was up to now unclear how the Eu ion gets incorporated in the unconventional host compound. The final part of this chapter aspires to answer this question. Furthermore, the phosphor is evaluated for the use in white LEDs. This work is published in following form:

Origin of saturated green emission from europium in zinc thiogallate

Jonas J. Joos, Katleen Korthout, Sergey Nikitenko, Dirk Poelman, Philippe F. Smet

Optical Materials Express, **3** (2013), 1338-1350.

9.2 Thermal quenching and luminescent lifetime of Eu^{2+} in $SrGa_2S_4$

9.2.1 Synthesis

$Sr_{1-x}Eu_xGa_2S_4$ powders with x = 0.01, 0.02, 0.03, 0.04, 0.05, 0.07, 0.10, 0.15, 0.20 and 0.30 were prepared by solid state synthesis. Appropriate amounts of SrS (Alfa Aesar, 99.9%), Ga_2S_3 (Alfa Aesar, 99.99%) and EuF_3 (Alfa Aesar, 99.5%) were weighed, mixed in an agate mortar and put into an alumina crucible. Then the powders were heat treated under a flow of H_2S at 900°C for 2h. Powders were allowed to cool naturally. After recuperation they were lightly ground.

From the X-ray diffraction patterns of the synthesized $Sr_{1-x}Eu_xGa_2S_4$ phosphors, it was observed that crystalline powders were obtained, without the presence of impurity phases.
Although the powders that were investigated in this work were prepared by a synthesis in H_2S, it was validated that powders with very similar behavior can be obtained by performing the same synthesis in forming gas, which is more promising when considering working safety and environmental friendliness.

9.2.2 Steady-state luminescence

The PL emission and excitation spectra for $Sr_{1-x}Eu_xGa_2S_4$ at room temperature are shown in Fig. 9.3(a). Both the width and the position of the emission spectrum (Tab. 9.2) are stable over the entire studied range ($0.01 \leq x \leq 0.30$). The excitation spectrum is similar for all dopant concentrations, except for an increasing excitation efficiency at lower energies upon increasing dopant concentration, corresponding to the observations of Hidaka and Takizawa [364].

Figure 9.3(b) shows the internal and external QE of the $Sr_{1-x}Eu_xGa_2S_4$ phosphors. QE_i peaks at 71% for a dopant concentration of 4%, and drops off slowly for higher dopant concentration. For instance, it equals 39% for x = 0.20. Iida *et al.* reported a QE of 21% for the fully substituted $EuGa_2S_4$ [367]. The external QE, which takes

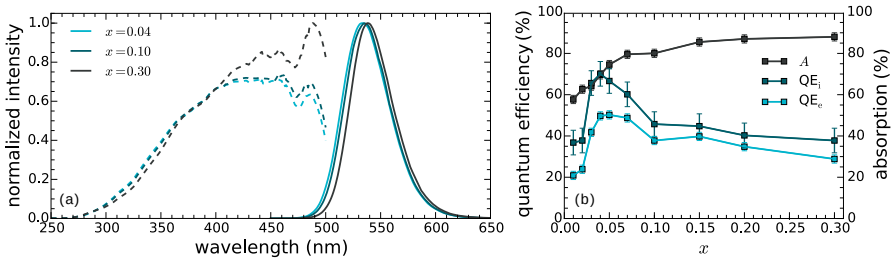

Figure 9.3 – (a) PL emission (at 400 nm excitation, solid lines) and excitation (at 532 nm emission, dashed lines) spectra for different $Sr_{1-x}Eu_xGa_2S_4$ powders at room temperature. The dip in the excitation spectra around 470 nm is an experimental artifact. (b) Absorption, internal and external QE (as defined in §3.3 and 7.2.3) for $Sr_{1-x}Eu_xGa_2S_4$ at room temperature, measured at 460 nm excitation.

into account the absorption of the excitation light, is stable at around 50% for a dopant concentration range from 4% to 7%. This is due to the steady increase of the absorption in the blue region for increasing dopant concentration and is also reflected in the body color of the phosphors which is yellowish-green. The internal QE of 71% is in line with the (indirectly obtained) value reported by Hidaka and Takizawa [364].

The relatively low values of QE_i for $Sr_{0.99}Eu_{0.01}Ga_2S_4$ and $Sr_{0.98}Eu_{0.02}Ga_2S_4$ are rather surprising, as one expects similarly high internal QE as for $Sr_{0.96}Eu_{0.04}Ga_2S_4$. The two phosphors with the lowest dopant concentration (1% and 2%) appear greyish-yellow under white light illumination, in contrast to the other phosphors, which show a much brighter body color. This was quantified by looking at the reflection on the phosphors surface of the emission from an orange-red LED. In this region of the visible spectrum, one does not have absorption from the Eu^{2+} luminescence centers. For the higher dopant concentrations, about 85-95% of the light is reflected compared to a white reference standard. For the lower concentrations ($x \leq 0.02$), this reflection drops to about 65-70%, which is in line with the visual observation of the greyish body color. These absorptions obviously lower the internal QE, due to an increased fraction of the absorbed (blue) excitation light which does not lead to excitation of Eu^{2+} centers. It also reduces the fraction of emitted light which reaches the phosphor surface. Consequently, the (calculated) internal QE will be lower. An explanation of the lower optical quality of the powders with low dopant concentration might be related to the use of EuF_3 as dopant precursor. Fluorides are known to act as flux material, enhancing synthesis and promoting grain growth. Obviously, for higher dopant concentrations, a higher degree of fluxing can be expected.

9.2.3 Decay behavior and thermal quenching

The luminescence decay profiles of $Sr_{1-x}Eu_xGa_2S_4$ at room temperature are shown in Fig. 9.4(a). For low dopant concentrations ($x \leq 0.04$), the decay profile can be fitted with a single exponential with a decay constant of 445 ns (±5 ns), which is

Table 9.2 – Influence of dopant concentration and temperature on the emission properties of $Sr_{1-x}Eu_xGa_2S_4$. λ_{em} is the (fitted) wavelength of the emission peak, $T_{0.5}$ is the temperature for which the emission intensity is half of the intensity at low temperature (100 K), $I(T)$ is the integrated emission intensity at temperature T. (*) denotes extrapolated value.

x	λ_{em} (nm)		FWHM (nm)		$T_{0.5}$ (K)	I(400 K)/I(300 K)
	300 K	400 K	300 K	400 K		
0.01	535.8	533.8	52	59	475 (*)	0.90
0.03	536.4	535.2	51	57	460	0.92
0.07	536.8	536.0	50	56	445	0.83
0.15	539.2	539.7	48	53	435	0.78
0.30	539.7	540.0	49	54	385	0.69

only slightly smaller than the value of 480 ns reported by Chartier *et al.* for the radiative decay time of $Sr_{0.999}Eu_{0.001}Ga_2S_4$ [302]. For dopant concentrations of 7% and higher, a deviation from the single exponential decay is observed with the emergence of a faster decay component. The 445 ns component is still preserved, as seen in the similar steepness in the second half of the decay profiles.

To quantify this aspect, the decay profiles were fitted with two exponentially decaying components according to Eqs. 8.2 and 8.3. For the entire studied concentration range, it turns out that the decay profiles can be fitted with two components having decay constants of τ_1 = 445 ns and τ_2 = 220 ns. While for the lower concentrations ($x \leq 0.04$), the decay is purely monoexponential, for higher concentrations the fraction f_2 steadily increases (inset of Fig. 9.4(a)). For x = 30%, both decay components contribute almost equally. These observations nicely correlate with the behavior of the internal QE (Fig. 9.3(b)). For concentrations of 5% and higher, the internal QE starts to decrease, which can be related to the emergence of non-radiative decay. This is in correspondence with the observed fast decay component. Also, the fact that the decay profile is described by only one component of 445 ns for the low dopant concentrations ($x \leq 0.02$) shows that the observed lower internal QE (Fig. 9.3(b)) is entirely related to the body color of the phosphor, and not due to additional non-radiative decay paths at these low dopant concentrations.

From the decay measurements, it appears that there exist two types of Eu centers in $Sr_{1-x}Eu_xGa_2S_4$. At low concentration ($x < 5\%$), the majority of the dopant ions can be considered as isolated centers, and the decay profile is described by a single exponential decay. For higher dopant concentrations, a second type of configuration is formed for which the lifetime is considerably shorter, presumably due to energy transfer between nearby Eu centers, and locally approaching the situation in $EuGa_2S_4$. This assumption will be further substantiated when the influence of temperature on the decay profiles is discussed.

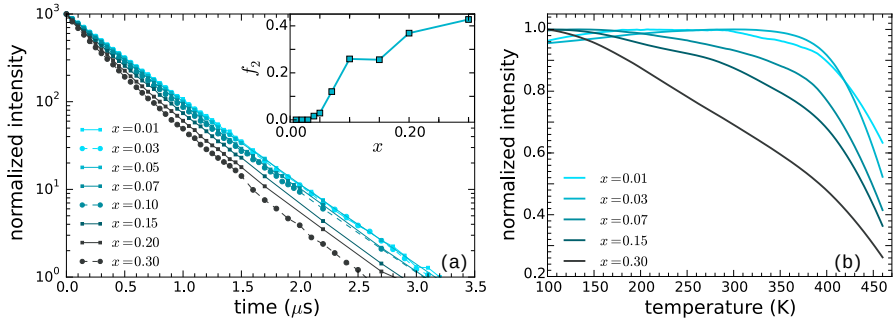

Figure 9.4 – (a) Decay profiles of the green emission of $Sr_{1-x}Eu_xGa_2S_4$, measured at room temperature with a 337 nm pulsed laser as excitation source. The inset shows the fitted fraction of the fast decay component, f_2 (Eq. 8.3). (b) Integrated emission intensity of $Sr_{1-x}Eu_xGa_2S_4$ powders upon excitation with 400 nm as a function of temperature.

For most phosphors the optimum dopant concentration is relatively low (typically 0.5%), with the luminescence emission intensity dropping fast for elevated dopant concentrations. Similar to for instance Eu_2SiS_4 [379], the stoichiometric phosphor $EuGa_2S_4$ is still luminescent with an emission peak at 549 nm at room temperature [367, 380]. However, the high dopant concentration leads to a strong thermal quenching, with $T_{0.5}$ being reported at 150-200 K [367, 381]. For low dopant concentrations, the emission intensity is almost constant up to about 400 K (Fig. 9.4(b)). At this temperature, the emission intensity is still more than 90% of this at room temperature (Tab. 9.2). Therefore, this phosphor is suitable for color conversion purposes. For higher temperatures, the emission intensity drops steeply. This is a typical thermal quenching behavior, and the observed intensity profiles are in line with those reported by Chartier *et al.* on $Sr_{0.999}Eu_{0.001}Ga_2S_4$ [303]. The thermal quenching temperature $T_{0.5}$ is 460 K for $Sr_{0.97}Eu_{0.03}Ga_2S_4$ (Tab. 9.2). For higher dopant concentrations ($x > 5\%$), the behavior is somewhat more complex, with two components. First, the steep decay setting in at 400 K is clearly visible. In addition, the emission intensity decreases steadily between 100 K and 400 K, with the steepness of the decrease directly related to the concentration. This behavior is closely

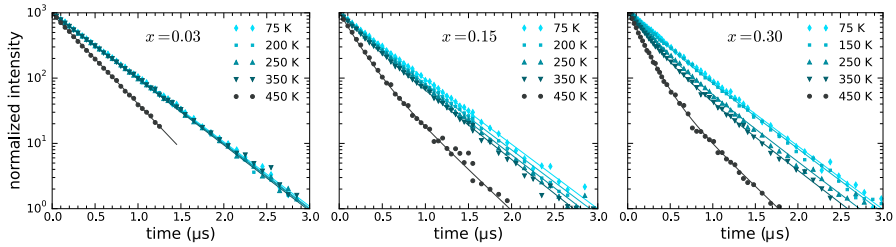

Figure 9.5 – Decay profiles of the green emission of $Sr_{1-x}Eu_xGa_2S_4$ as a function of temperature. The profiles were fitted with one or the sum of two exponential functions (see text for details).

related to the internal QE at room temperature, which starts to drop for dopant concentrations above 5%.

During the thermal quenching study, emission spectra were collected, allowing to calculate the influence of the temperature on the emission color. As shown in Tab. 9.2, heating from room temperature to 400 K hardly changes the position of the emission peak ($\Delta\lambda < 2$ nm), while the FWHM only slightly increases by about 10%. Consequently, the emission color of all studied $Sr_{1-x}Eu_xGa_2S_4$ phosphors is stable. The CIE (x, y) chromaticity diagram (Fig. 9.1) shows the location of the saturated green emission which is well above the green color point of the EBU gamut, without the need for filtering of the spectrum. In the case when the newest Rec. 2020 standards are pursued, a minimal amount of green light needs to be filtered.

To get a better grasp of the influence of the dopant concentration on the thermal quenching behavior, luminescence decay profiles were recorded for selected phosphors at different temperatures (Fig. 9.5).

For the phosphor with the lowest dopant concentration ($x = 0.03$), the decay profile can be fitted with a single exponential decay component. The decay constant τ is stable at 440 ns (±5 ns) up to 375 K, after which it starts to drop quickly. Nevertheless, a single exponential decay is maintained up to 475 K (not shown). These results are in line with the report of Chartier *et al.* on $Sr_{0.999}Eu_{0.001}Ga_2S_4$ [303]. For higher dopant concentrations, the situation is more complicated. At low temperature (75 K), a single exponential decay is obtained with a radiative decay time close to 440 ns. Increasing the temperature leads to the emergence of a second component. One component is showing the same behavior as in lightly doped phosphors (*i.e.* a constant decay time of about 440 ns, which starts to decrease beyond 375 K). The second component shows a different dependency of temperature, *e.g.* about 230 ns around 150 K and steadily reducing to about 150 ns at 450 K. This type of behavior is rather similar to the decay profiles shown for $EuGa_2S_4$ by Barthou *et al.* [381]. Increasing the dopant concentration from 15% to 30% (Fig. 9.5) leads to basically the same two decay components, albeit with a different relative contribution. The decay behavior shows large similarities with the thermal quenching profiles. For low dopant concentrations, the emission intensity is stable (reflected in a constant value for τ), to drop off quickly beyond 400 K. For higher dopant concentrations, there are two components in the thermal quenching profile: the first, steady decrease in emission intensity ($T < 400$ K) is related to the steady shortening of the fast decay component. Second, for higher temperatures, the intensity falls off quickly, related to the shortening of the slow decay component. From these observations, we can conclude that presumably there exist two types of environments in $Sr_{1-x}Eu_xGa_2S_4$ phosphors. The first one, predominant at low doping concentrations, is related to Eu ions with relatively little interaction with other Eu ions. In this way excitation energy is not able to migrate over the lattice and will therefore in general not reach defects. The second type is characterized by luminescence properties in terms of thermal quenching and lifetime behavior which are in correspondence with those of $EuGa_2S_4$. It corresponds to an environment where several neighboring Sr ions

are replaced by Eu ions. In that case, energy transfer between Eu ions can occur, and non-radiative decay at defects is more likely to take place, thus resulting in a shorter lifetime. The lower thermal quenching temperature can be explained by a (locally) smaller energy separation between the excited 5d state and the conduction band, which bears more resemblance to $EuGa_2S_4$ than to $SrGa_2S_4$. For moderate Eu concentrations, we clearly observe a mix of both types of environments, which leads us to the conclusion that the Eu ions do not distribute homogeneously over the $SrGa_2S_4$ lattice, but that local concentration variations can occur. Given the similar ionic radii of Sr^{2+} and Eu^{2+}, this is not unlikely. By means of X-ray absorption spectroscopy, or other analytical techniques able to probe the local environment, this hypothesis could be verified, and will be the subject of further research.

9.2.4 Chemical stability

Most sulfide materials suffer from irreversible degradation upon exposure to moist air, due to hydrolysis. $SrGa_2S_4$:Eu is relatively stable, especially when compared to thioaluminates (like the green emitting $CaAl_2S_4$:Eu [150]) or most thiosilicates [5, 382]. $EuGa_2S_4$ is reported to be stable against hydrolysis [381]. We evaluated the stability of unprotected $Sr_{0.96}Eu_{0.04}Ga_2S_4$ phosphor powder by means of an accelerated aging test in a controlled atmosphere (air, 80°C, 80% relative humidity) and continuous monitoring of the PL intensity. After 100h, the PL intensity was reduced to 81% of the initial value. The phosphor emission intensity degraded to about 95% of the initial value within 1h of exposure, after which the degradation slowed down. This behavior is considerably better than this for micron-sized CaS:Eu particles [324, 383]. For these alkaline earth sulphides, Avci *et al.* reported efficient encapsulation methods which considerably improved the stability under accelerated aging conditions [324,383]. Therefore, it is believed that the potential stability problems of $Sr_{1-x}Eu_xGa_2S_4$ phosphors can be circumvented.

9.2.5 Application potential

We can now evaluate the $Sr_{1-x}Eu_xGa_2S_4$ phosphors against the six requirements for conversion phosphors, as outlined in §1.4:

- The saturated green emission color is ideally suited for display applications. A large color gamut can be obtained based on this green phosphor, without the need for filtering, thus optimizing conversion efficiency.
- The phosphors can be excited efficiently by both blue, violet or near ultraviolet light sources. The excitation spectrum is broad and relatively featureless, so that the emission intensity is not influenced by slight variations in the emission spectrum of the pumping light source.
- The quantum efficiency is reasonably high (QE_i of 71%), in combination with a strong absorption, for a wide concentration range. Considering that little filtering is required due to the saturated color, this quantum efficiency is suitable for most display applications.

- The decay times are sufficiently short to avoid saturation under high excitation fluxes. Furthermore, the dopant concentration can be relatively high before concentration quenching sets in, which is also beneficial to avoid saturation.
- Both the emission color and the conversion efficiency are stable up to 400 K, which is sufficient for a wide range of applications.
- In this work the chemical stability was not assessed in detail, although the $Sr_{1-x}Eu_xGa_2S_4$ phosphors appear considerably more stable than other sulfide phosphors. Encapsulation of phosphor particles appears a prerequisite though for long term stability, as required for solid state lighting and backlighting.

In conclusion, we can state that $Sr_{1-x}Eu_xGa_2S_4$ phosphors are an interesting option to provide saturated green emission in color conversion applications, given that they fulfill the critical requirements mentioned above.

9.2.6 White pc-LEDs for display applications with *hybrid* phosphor layers

Materials and strategy

Given the suitable properties of $SrGa_2S_4$:Eu^{2+}, an optimized white light-emitting diode will be constructed where this phosphor covers the green component. Due to its narrow emission band, a white LED for display applications is aimed for. As in contrast to the previous, more fundamental investigation, the efficiency of the device is of primordial importance for this proof-of-concept, a fully optimized $SrGa_2S_4$:Eu^{2+} phosphor was obtained from a commercial collaborator. This powder features an absorption, internal and external quantum efficiency of respectively 80%, 95% and 75% upon illumination with a blue LED, emitting at 450 nm. The emission peaks at 535 nm (FWHM of 51 nm).

For the red component, multiple possibilities are available within the realm of traditional metal-activated inorganic crystals (see §10.2.4). Here, a more multidisciplinary approach is chosen. Colloidal quantum dots (QD) are semiconductor crystals with dimensions in the nanometer range. Due to their particular size, which is of the same order of magnitude as the exciton radius of the semiconductor, quantum mechanical confinement effects become important, resulting in size-dependent physical properties [384]. The property that is exploited here is the luminescence of the QDs which features superior narrow emission bands in the case of CdSe QDs and a high quantum efficiency upon excitation with blue light. The QDs that are used here were synthesized by Dr. Sofie Abé and are composed of CdSe cores (typical diameter of 2.77 nm), around which a CdS shell is grown (with a typical thickness of 3.3 nm), improving the above-mentioned optical properties [17, 385]. Their emission peaks at 629 nm (FWHM of 39 nm) and they have an internal QE of 79% when measured as a diluted dispersion.

Luminescent layers of the individual components or a mixture of the green and red components were prepared by mixing the luminescent materials with a dissolved

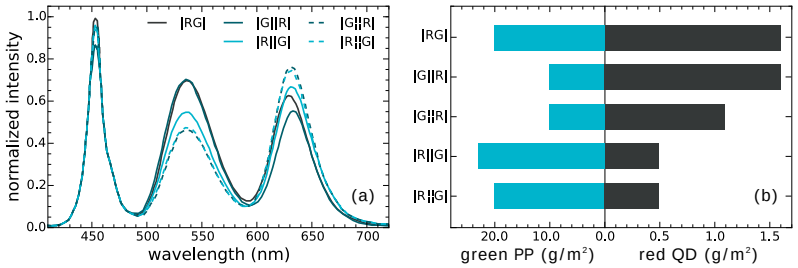

Figure 9.6 – (a) White pc-LED spectra, with a CCT of 6500-7000 K for all configurations (see Tab. 9.3). (b) Loading of green powder phosphor (PP) and red QDs in the layers shown in (a).

polymer, Kraton FG1901X in toluene and methyl ethyl ketone. The mixture was applied onto circular glass substrates, obtaining the homogeneous luminescent layers after evaporation of the solvent. These layers are used in combination with a high-power blue LED (Royal-Blue LUXEON Rebel ES with emission maximum at 454 nm) in the remote phosphor LED configuration as shown in §7.2.3, allowing for a quantitative study with the integrating sphere setup. In the following, optimized white LEDs are shown, indicating the advantages of the approach where microcrystalline phosphor particles are combined with QDs in so-called *hybrid* phosphor layers. The key idea of this strategy is that the large phosphor crystals scatter the light and hence improve outcoupling in contrast to a full-QD phosphor layer as QDs are too small to effectively scatter visible light, leading to an optical trapping of down-converted light due to total internal reflection, resulting in a suboptimal device efficiency.

Result and design rules

Five different conversion layers were optimized according to the above-described procedure:

- |RG |: The green phosphor powder and the red QDs are combined in the same polymer layer.
- |G||R|: Two separate layers, a green and a red, are stacked, leaving an air gap between the layers, with the green layer facing the blue pump LED.
- |R||G|: Two separate layers, a green and a red, are stacked, leaving an air gap between the layers, with the red layer facing the blue pump LED.
- |G‖R |: The two separate layers are *connected* by an index-matched liquid (ethylene glycol) with the green layer facing the blue pump LED.
- |R‖G |: The two separate layers are *connected* by an index-matched liquid (ethylene glycol) with the red layer facing the blue pump LED.

The optimized white LEDs were fully characterized to assess their performance as well as to understand the differences between the different stacking geometries in

terms of a simple physical picture. Their spectra are shown in Fig. 9.6(a) while the most important quantitative measures are given in Tab. 9.3. The required amount of powders phosphor and quantum dots for every geometry are indicated in Fig. 9.6(b).

Given the data, all five geometries yield state-of-the art white LEDs, tuned to fit the transmission characteristic of color filters in LCDs [357]. Prior to color filtering, the three primary components already cover 86% of the NTSC display standard in CIE (u', v') space (see appendix E). Relatively high color temperatures and LER values are obtained as required in LCD backlights. The electrical-to-optical power efficiency of the blue LED is reflected in the LE-value.

When both phosphors are incorporated in the same layer, the measurements show that the absorption of the blue pump light exceeds that of green emitted and red emitted light by a factor of 15 and 78, respectively. As this will translate into a proportionally longer path length for green and red light, it is expected that undesired reabsorption - where a QD is excited by a red photon emitted by another QD or a green instead of a blue photon - will be relatively limited with these CdSe/CdS QDs. Moreover, the 5 nm redshift of the QD emission maximum in the red layer relative to the QD dispersion is reduced to less than 1 nm in |RG|, substantiating a significant reduction of the QD self-absorption, due to the enhanced outcoupling of the red light through scattering by the STG microcrystals. When the degree of scattering is too high, multiple scattering events will increase the path length of the QD emission and hence also reabsorption, leading to efficiency losses and a redshifted emission. This is not the case in the present green layers, as the scattering is just sufficient to redirect trapped (red) light that did not immediately leave the film. Nonetheless, a certain amount of green light is reabsorbed by the QDs. This secondary excitation has very little effect on the QE of the mixed hybrid remote phosphor layer given the internal QE of the green phosphor which is close to unity. This is evidenced by the internal QE of the |RG | film (80%) which lies between the internal QEs of individual red (71%) and green (93%) layers with the same loading. Although the properties of this, most simple, geometry are already very favorable, it will prove to be more cost-efficient when adhering to an alternative stacking geometry, minimizing either the used quantity of green powder phosphor or red QDs, conform the prizes of raw materials.

In the case of the |G||R| and |R||G| layers, the emission spectrum of each configuration depends on the interplay between the relative absorption of the blue pump light by both color convertors, the scattering of light by the powder phosphor, and reabsorption of green and red emission by the QDs [386–389]. As the lowest layer is exposed to the highest blue intensity, its emission is proportionally more dominant with respect to the emission of the upper layer. To achieve a similar color point as in the |RG| case, a reduced amount of red or green color convertor is required for the |R||G| and |G||R|geometries respectively. The disadvantage of this approach is that the conversion efficiency of the red QD layer is reduced due to optical trapping and reabsorption of the red light as a consequence of the absence of light scattering. This is evidenced by the redshift of the QD emission (see Fig. 9.6(a)). Although these

Table 9.3 – Internal quantum efficiency, correlated color temperature (CCT), luminous efficacy of the radiation (LER), electrical-to-optical luminous efficacy (LE) and CIE (x, y) color point of the white LEDs that were made of the optimized phosphor layers.

layer	QE_i (%)	CCT (K)	LER (lm/W)	LE (lm/W)	CIE (x, y)
|RG |	80	7082	314	58	(0.299, 0.345)
|G||R|	77	7288	326	56	(0.290, 0.365)
|R||G|	75	7097	284	48	(0.304, 0.320)
|G‖R |	77	6488	265	45	(0.317, 0.299)
|R‖G |	77	6536	266	45	(0.316, 0.300)

configurations suffer from self-absorption of red light by the QDs and are prone to reabsorption of green light by the QDs, an internal QE of 77% can still be obtained for the |G||R| configuration. Hence, with the highly efficient $SrGa_2S_4$:Eu^{2+}phosphor and the CdSe/CdS QDs designed to show little self-absorption, reabsorption losses are not a major issue in this hybrid remote phosphor.

Hybrid layers where the two separate films are optically *connected* by applying an index-matching liquid are investigated subsequently. This liquid obviously prevents the optical trapping of the converted red light by bringing the scattering green luminescent crystals within reach for the red light, while preserving the important advantage of stacked layers, *i.e.* the reduced loading for the lowest color component. Given that in this configuration, a larger part of the green light will be available for reabsorption by the QDs, leading to a QD loading which is further reduced by one-third in the |G‖R \| geometry while high efficiencies are maintained thanks to the high internal QE of the green phosphor.

A remote phosphor for display applications is expected to provide the highest performance at the lowest cost. Performance is assessed by considering the properties of the eventual white LED emission spectra and the internal QE of the entire color conversion. The proposed hybrid remote QD/powder phosphor combination, with CdSe/CdS QDs and $SrGa_2S_4$:Eu^{2+} microcrystals, meets state-of-the-art spectral specifications for display applications, with an internal QE of 75-80% for all assessed configurations - the latter affected mainly by the somewhat lower internal QE of the QDs. The cost, on the other hand, can be reasonably assumed to be determined primarily by the cost of the color-convertor materials, implying that the loading of both components (see Fig. 9.6(b)) gives an immediate idea of the remote phosphor layer cost if the unit prize for every component is known. Depending on the economical situation, a grounded choice can be made for either the |G‖R \| or the |R‖G \| geometry, based on the above design rules.

9.3 Origin of the green emission of $ZnGa_2S_4$:Eu^{2+}

9.3.1 Motivation

Europium doped zinc thiogallate, $ZnGa_2S_4$:Eu^{2+} is, like most Eu^{2+} activated phosphors, expected to be a broadband emitter due to the $4f^6 5d \rightarrow 4f^7$ transition that is responsible for the luminescence. The emission band of this material has been reported to be rather narrow, yielding a saturated green color [390–394]. In this paragraph, it is investigated whether $ZnGa_2S_4$:Eu^{2+} has the same advantageous properties as the chemically similar $SrGa_2S_4$:Eu^{2+} (Tab. 9.1). The particular motivation for this work is the contradiction between a number of reports which are published on $ZnGa_2S_4$:Eu^{2+} phosphors.

The photoluminescence of $ZnGa_2S_4$:Eu^{2+} was first described by Yuta and White reporting broadband emission at 535 nm and a Stokes shift of 0.78 eV [390]. Kim and Kim elaborated on the photoluminescence (PL) and cathodoluminescence (CL) of $ZnGa_2S_4$:Eu^{2+} and (Ca,Zn)Ga_2S_4:Eu^{2+} mixtures [391, 395]. The synthesis parameters of the solid-state reaction yielding the powders were optimized and a saturated green emission at 540 nm was reported. The lack of efficient CL was ascribed to the small particle size of the phosphor powders. By adding only a small amount of calcium to the mixture, the emission band at 540 nm disappeared abruptly and a new emission band was formed at longer wavelengths (> 550 nm). Recently, Yu *et al.* reported the thermal properties of $ZnGa_2S_4$:Eu^{2+}. Herein, it was found that this material has a relatively low thermal quenching temperature, but it remains a potential candidate for LED applications because of the favorable excitation spectrum [393]. Reported key parameters about $ZnGa_2S_4$:Eu^{2+} (at room temperature) are an emission band at 540 nm (FWHM of 50 nm), a luminescence lifetime ranging from 126 to 79 ns, depending on the europium concentration and a quenching temperature $T_{0.5}$ of 407 K. $T_{0.5}$ was defined as the temperature where the emission intensity dropped to half the intensity value at 300 K, which is somewhat in contrast to the common approach to comparing the intensity to the value at low temperature, where no thermal quenching is noticeable. In [394], luminescence in ZnS-$ZnGa_2S_4$:Eu^{2+} mixed compounds was explained by energy transfer from ZnS:Eu^{2+} to $ZnGa_2S_4$:Eu^{2+}. In contrast to the above reports, an anomalously broad emission at 565nm has been reported in [396]. Up to now, no value of the quantum efficiency of $ZnGa_2S_4$:Eu^{2+} has been reported.

Additionally, there is still discussion about the position of the Eu^{2+} ions in the zinc thiogallate lattice. Due to the size mismatch between the Eu^{2+} and Zn^{2+} ions, one can expect a difficult incorporation of the europium ions in the zinc-based host material. The ions could (1) substitute for the zinc ions, (2) occupy the tetrahedral vacancy sites in the lattice, or (3) substitute at octahedral voids of the host lattice. Yuta and White proposed an energy level scheme for Eu^{2+} in $ZnGa_2S_4$, based on tetrahedral coordination [390]. The difficult incorporation of Eu^{2+} on small tetrahedral coordinated sites is already drawn to attention by Wickleder *et al.* [372]. They argued that the octahedral voids are favored, based on the $4f^6 5d \rightarrow 4f^7$ transition energy

and the observation that no europium doped compounds exist where the doping ion is fourfold coordinated as would be the case on the zinc or vacancy sites. However, no direct proof for any of the europium positions has been given yet [372, 397].

The hypothesis which is explored here is that the observed luminescence originates from small amounts of unintentionally formed $EuGa_2S_4$. This stoichiometric phosphor is known to exhibit efficient green luminescence, centered around 545 nm [367]. This is surprisingly similar to the reported values for the $ZnGa_2S_4$:Eu^{2+} phosphors. In $EuGa_2S_4$, the europium ions are eightfold coordinated by sulfur ions. The internal and external quantum efficiencies and the other vital properties of the luminescence of $ZnGa_2S_4$:Eu^{2+} are characterized and discussed, to complement the previously published data on this phosphor. Next, the suitability of $ZnGa_2S_4$:Eu^{2+} as a conversion phosphor for lighting and display applications is evaluated. Emphasis is put on the microscopic structure of the phosphor, both at the level of individual phosphor particles and at the atomic level, to get a thorough understanding of the doping of Eu^{2+} into $ZnGa_2S_4$.

9.3.2 Synthesis

$Zn_{1-x}Eu_xGa_2S_4$ powders with europium concentrations of $x = 0.01$, 0.02, 0.03, 0.04, 0.06, 0.08 and 0.10 were synthesized by a solid state reaction between ZnS (Alfa Products, 99.9%), Ga_2S_3 (Alfa Aesar, 99.99%) and EuF_3 (Alfa Aesar, 99.5%). Stoichiometric quantities of these starting materials were mixed and heat treated at 1000°C for 2 hours in alumina crucibles under a H_2S flux. After the heat treatment, the powders cooled naturally and were lightly ground. Pure $EuGa_2S_4$ was synthesized in a similar fashion, however using EuS instead of EuF_3 and without ZnS.

9.3.3 Steady-state luminescence and reflection spectra

The photoluminescence emission and excitation spectra of the powders with dopant concentrations up to $x = 0.10$ were measured at room temperature. Both the position of the maximum (at about 542 nm) and the full width at half maximum (FWHM, about 50 nm) of the emission peak show no significant dependence on the europium concentration. The spectra of $Zn_{0.99}Eu_{0.01}Ga_2S_4$, which are also representative for all other doping concentrations, are shown in Fig. 9.7(b). The absolute intensity of the emission bands is discussed further on. The emission band of the phosphor corresponds with a saturated green color (CIE $(x, y) = (0.31, 0.66)$), exceeding the green color point of the EBU gamut.

Both the emission and excitation spectra of the powders are very similar to the spectra of the stoichiometric phosphor $EuGa_2S_4$ which are also included in the figure. This is surprising given the very different structure of the $ZnGa_2S_4$ and $EuGa_2S_4$ host crystals. The difference in the excitation spectra below 420 nm can be explained in terms of interband absorption in $ZnGa_2S_4$. The absorbed energy is not transferred to Eu^{2+} ions and is dissipated non-radiatively. Diffuse reflectance spectra are displayed in Fig. 9.7(a) for $Zn_{0.99}Eu_{0.01}Ga_2S_4$, $EuGa_2S_4$ and undoped $ZnGa_2S_4$. The

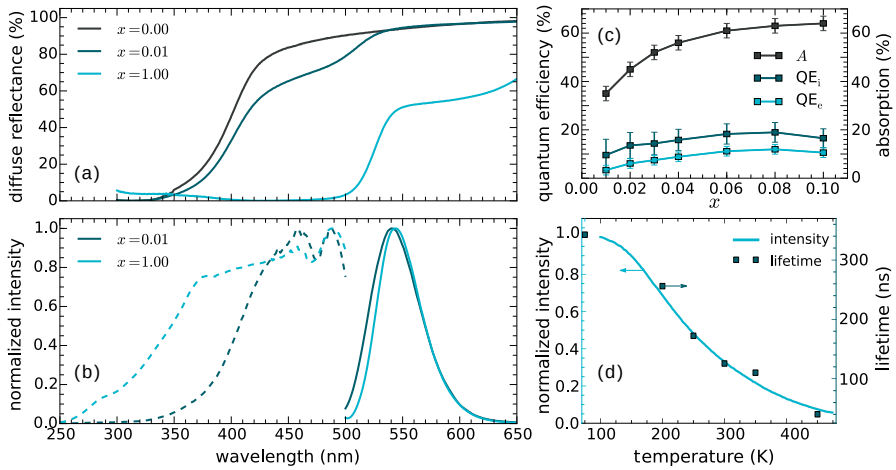

Figure 9.7 – (a) Diffuse reflection spectra for $ZnGa_2S_4$ ($x = 0.00$), $Zn_{0.99}Eu_{0.01}Ga_2S_4$ ($x = 0.01$) and $EuGa_2S_4$ ($x = 1.00$) at room temperature. (b) PL emission (at 450 nm excitation solid lines) and excitation (at 540 nm emission, dashed lines) spectra for $Zn_{0.99}Eu_{0.01}Ga_2S_4$ ($x = 0.01$) and $EuGa_2S_4$ ($x = 1.00$) at room temperature. The dip in the excitation spectra around 470 nm is an experimental artifact. (c) Absorption, internal and external QE (as defined in §3.3 and 7.2.3) for $Zn_{1-x}Eu_xGa_2S_4$ at room temperature, measured at 460 nm excitation. (d) Normalized PL intensity and luminescent lifetime as function of temperature for $Zn_{0.94}Eu_{0.06}Ga_2S_4$ upon excitation at 400 nm.

steep increase in the $ZnGa_2S_4$ absorption around 400 nm is due to interband absorption of the host material. The bandgap of $ZnGa_2S_4$, 3.4 eV, was obtained from a fit to the Kubelka-Munk spectrum, calculated from the reflection spectrum (see §7.2.1). This is in correspondence with the reported value of 3.22 eV [372]. $EuGa_2S_4$ starts to absorb light from 520 nm due to electronic excitation towards the 5d levels of Eu^{2+}.

The internal and external quantum efficiencies of the $Zn_{1-x}Eu_xGa_2S_4$ powders are depicted in Fig. 9.7(c). The internal quantum efficiency remains essentially constant as a function of Eu-concentration at a value of about 18%. This is striking since concentration quenching is expected to occur because of the increasing probability for energy transfer between two adjacent Eu^{2+} ions when they are closer together. Still, some small changes as a function of doping concentration can be observed. If one assumes that small grains of luminescent $EuGa_2S_4$ are mixed in $ZnGa_2S_4$ powder (this assumption will be substantiated in the remainder of this section), these changes can be attributed to scattering effects, the nonzero absorption of $ZnGa_2S_4$ (at low x-values, see Fig. 9.7(a)) and reabsorption of converted light by other $EuGa_2S_4$ grains (at higher x-values). In any case, the low conversion efficiency of this phosphor hampers the possibilities for technological applications.

9.3.4 Decay and thermal quenching

The decay profiles of the samples were measured at different temperatures with the pulsed excitation from an LED emitting at 400 nm. A luminescent lifetime was determined by fitting the initial decay with a single exponential function. The lifetime of 127 ± 24 ns did not change as a function of the europium concentration. This is a remarkably short luminescent lifetime for $4f^6 5d \rightarrow 4f^7$ transitions in Eu^{2+}. In comparison, the luminescent lifetime of other europium doped thiogallate and thioaluminate phosphors are given in Tab. 9.1. Emission maxima are also displayed because of the intrinsic dependence of the lifetime on the emission color, shorter wavelengths corresponding with shorter lifetimes (if the refractive indices are assumed to be similar, see §2.3.3). At low temperature (77 K), the lifetime increased to 350 ns. The other, more efficient thioaluminate and thiogallate phosphors do not show a change in lifetime as a function of temperature unless thermal quenching sets in [362].

The integrated emission intensity of the $Zn_{1-x}Eu_xGa_2S_4$ powders was monitored as a function of temperature (Fig. 9.7(d)). It is notable that the emission intensity does not show a stable region as a function of temperature as most conventional phosphors (see §3.4.4), but decreases over the entire temperature range. This is, in contrary, a common behavior for stoichiometric phosphors [30, 368]. The quenching temperature, defined as the temperature where the emission intensity is half of the intensity at low temperature (here, 100 K), is about 240 K for $x = 0.06$. The obtained result is in accordance with the quenching temperature of 407 K as reported in [393], taking into account that the reference level was then taken at 300 K. No significant influence of the doping concentration on the decay or thermal quenching behavior was observed. From these measurements, we can state that the luminescence of these phosphor powders is essentially quenched over the whole studied temperature range, and is characterized by an unusual short luminescent lifetime.

The temperature dependence of the corresponding time constant is very similar to that of the non-radiative decay path, as identified in $SrGa_2S_4:Eu^{2+}$ (see §9.2). For the latter phosphor, this decay path is only relevant at high doping concentrations or temperatures above 400 K. It was found that in this phosphor, which in contrast to $ZnGa_2S_4$ is isostructural to $EuGa_2S_4$, the environment of Eu locally resembles that of $EuGa_2S_4$ due to clustering of europium. The luminescent lifetime for $EuGa_2S_4$ was evaluated to be 116 ns (at 300 K). Within the error range, this is the same as the decay time of the $ZnGa_2S_4:Eu^{2+}$ powders. The thermal quenching profile of $EuGa_2S_4$ was measured by Iida *et al.* [367]. Their result is very similar to the profiles we obtained for $ZnGa_2S_4:Eu^{2+}$. This luminescence characterization of $Zn_{1-x}Eu_xGa_2S_4$ powders indicates that the light emission most likely originates from $EuGa_2S_4$ impurities. The PL emission and excitation spectra, quantum efficiency, thermal behavior and decay dynamics can be explained with this conjecture. In the next part, structural analysis will be applied to confirm this finding.

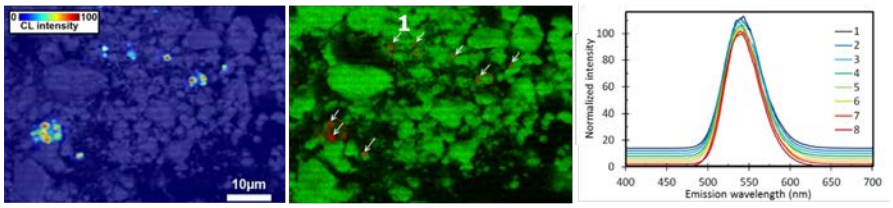

Figure 9.8 – SEM-CL-EDX mapping of $Zn_{0.99}Eu_{0.01}Ga_2S_4$ powder, obtained at 250 K. Left: Phosphor morphology, obtained by a BSE image. The integrated CL emission intensity is shown as an overlay in false colors. Middle: Elemental distribution by EDX, where the colors are determined by color coding with green for Zn and red for Eu. Simultaneous detection would lead to a yellow color. Right: CL emission spectra for the points indicated in the middle figure, obtained in clockwise direction.

9.3.5 Microscopic investigation

By the combined mapping of cathodoluminescence and characteristic X-rays in a scanning electron microscope setup, local variations in the chemical composition of a powder sample can be related to differences in luminescent properties (see 7.1.3). In Fig. 9.8, a SEM-CL-EDX mapping of the $Zn_{0.99}Eu_{0.01}Ga_2S_4$ powder is displayed. In the EDX map, the areas which are colored red (green) are the result from the mapping on Eu (Zn). One can clearly discern $EuGa_2S_4$ grains, where no Zn is detected, among the majority of $ZnGa_2S_4$ grains, where no Eu is detected. The CL map shows that the characteristic green luminescence is indeed originating from the $EuGa_2S_4$ grains, due to the perfect correlation between the CL and the EDX maps. No light output is detected from the $ZnGa_2S_4$ phase.

There are two possible reasons for the absence of luminescence in the $ZnGa_2S_4$ grains. First, it is possible that no europium is incorporated in the $ZnGa_2S_4$ lattice at all. This is plausible due to the size mismatch between the Zn^{2+} and Eu^{2+} ions (88 pm versus 131 pm for sixfold coordination [177]). Secondly, incorporation of europium ions in the host lattice does not necessarily cause light emission [258]. It would not be surprising if Eu in $ZnGa_2S_4$:Eu^{2+} is not luminescent. When $ZnGa_2S_4$ doped with europium would coincidentally have a very similar emission spectrum as $EuGa_2S_4$, then the absorption energy is estimated to be 2.4 eV, for the transition between the $4f^7$ ground state and the lowest $4f^6 5d^1$ excited state of europium. This absorption energy is the value where the PL excitation spectrum amounts to 20% of its maximum value [168]. Given the small band gap of this host material (3.2-3.4 eV), the excited states will probably overlap with or be in close distance to exciton states of the $ZnGa_2S_4$ host, totally quenching any europium activated luminescence. One could also argue that the absence of CL does not automatically imply the absence of PL. Although there can be a noticeable difference between the efficiency of CL and PL, a complete absence of cathodoluminescence for a lanthanide doped inorganic crystal is not expected [398].

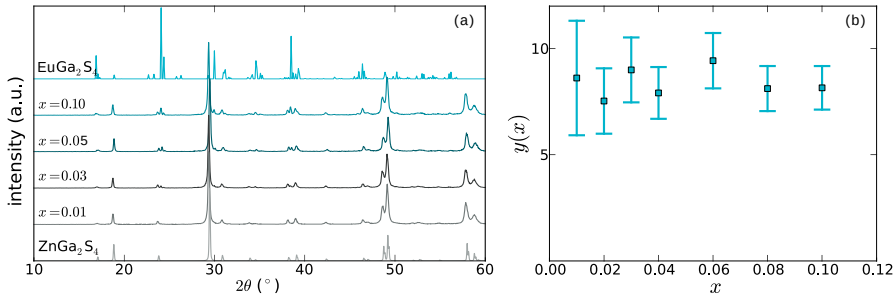

Figure 9.9 – (a) X-ray diffraction patterns for $Zn_{1-x}Eu_xGa_2S_4$ powders, compared to reference patterns for $ZnGa_2S_4$ (ICSD 69542) and $EuGa_2S_4$ (ICSD 8053) [298, 373]. (b) $y(x)$ as defined by Eq. 9.1.

9.3.6 X-ray diffraction

The XRD patterns show that crystalline powders are obtained, corresponding with the defect-stannite structure of $ZnGa_2S_4$ (Fig. 9.9) [373, 399]. However, only a limited amount of europium can apparently be dissolved in the $ZnGa_2S_4$ lattice without clustering, as diffraction peaks originating from a $EuGa_2S_4$, having a different crystal structure, are observed. Careful inspection of earlier reports on XRD patterns of $ZnGa_2S_4$:Eu^{2+}, also suggests the presence of $EuGa_2S_4$ as an impurity phase [298, 391, 394].

The emerging of the $EuGa_2S_4$ (4 4 2) peak at 24.1° is studied, together with the $ZnGa_2S_4$ (1 1 0) peak at 23.8° to estimate the dependence of the $ZnGa_2S_4$: $EuGa_2S_4$ fractional content on the doping concentration. The separate peak intensities, I, were calculated by a fitting procedure in the 2θ range from 23° to 25° with three pseudo-Voigt peak shapes. The third peak is the less intense $EuGa_2S_4$ (4 4 0) peak at 24.4°. The pseudovoigt profile is calculated as a linear combination of a Gaussian and a Lorentzian peak shape [400].

In Fig. 9.9(b), the values of

$$y(x) = \frac{I_{EuGa_2S_4}}{I_{ZnGa_2S_4}} \frac{1-x}{x} \tag{9.1}$$

are displayed. Herein, I are the integrated areas of the XRD peaks for the $EuGa_2S_4$ (4 4 2) and $ZnGa_2S_4$ (1 1 0) peaks. One can expect a constant y as function of x when no europium is incorporated in $ZnGa_2S_4$ or zinc in $EuGa_2S_4$. However, when a reasonable amount of Eu is incorporated in $ZnGa_2S_4$, one expects a disproportionately low amount of $EuGa_2S_4$ in the powders with small x-values, resulting in a smaller y-value. Since there does not seem to be a variation of y for different europium concentrations, no incorporation of europium in $ZnGa_2S_4$ is discerned within the accuracy of the XRD measurements and fitting procedure. Therefore, if any europium is incorporated, it is restricted to a small fraction, unlike the case of conventional phosphor materials. This is underpinned by the constant XRD peak locations upon

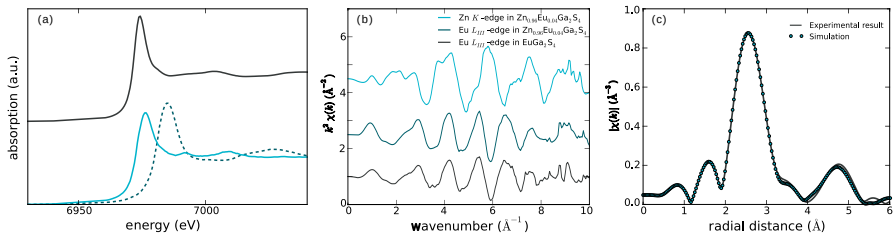

Figure 9.10 – (a) Eu L_{III} XANES spectrum of (top) $Zn_{0.96}Eu_{0.04}Ga_2S_4$, compared to the spectra of reference compounds for Eu^{2+} and Eu^{3+} (bottom), EuS (solid line) and Eu_2O_3 (dashed line). (b) Top: Zn K edge extracted EXAFS spectrum, Middle: Eu L_{III} edge extracted EXAFS spectrum, both in $Zn_{0.96}Eu_{0.04}Ga_2S_4$. Bottom: Eu L_{III} edge extracted EXAFS spectrum in $EuGa_2S_4$. (c) Fourier transform of $k^2\chi(k)$ to radial distance space for a $Zn_{0.92}Eu_{0.08}Ga_2S_4$ powder (solid line) and the result of the simulation, based on the structure of $EuGa_2S_4$ and the europium ions occupying the octahedral voids (circles).

changing the doping concentration. To measure the incorporation with a better accuracy, different experimental techniques have to be addressed.

9.3.7 X-ray absorption spectroscopy

X-ray absorption spectroscopy is ideally suited to study both the valence state and dopant incorporation in polycrystalline inorganic materials (see §7.1.4). The analysis of the XAS data was performed by Dr. Katleen Korthout. Figure 9.10(a) shows the Eu L_{III} edge XANES spectrum of $Zn_{0.96}Eu_{0.04}Ga_2S_4$ compared to those of Eu_2O_3 and EuS, measured as reference compounds for Eu^{3+} and Eu^{2+}, respectively. The shape of the spectrum of $Zn_{0.96}Eu_{0.04}Ga_2S_4$ is almost the same as that for EuS having a sharp single peak at 6972 eV and different from that for Eu_2O_3 having a single peak 8 eV higher in energy. This result shows that most of Eu atoms in $Zn_{0.96}Eu_{0.04}Ga_2S_4$ are divalent. This implies that the europium, which is doped in a trivalent state through EuF_3 is effectively reduced during the heat treatment in the H_2S atmosphere. The extracted EXAFS spectra, $k^2\chi(k)$ of the Eu L_{III} edge and the Zn K edge in $ZnGa_2S_4$:Eu^{2+} (4%) are shown in Fig. 9.10(b). This figure already suggests that the Eu ions do not occupy the Zn^{2+} sites in the lattice, but are more likely to be present in the powders as $EuGa_2S_4$.

To investigate the structure around dopant ions in detail, FEFF simulations were carried out (see §7.1.4). In the first step, the $EuGa_2S_4$ powder was fitted using the known crystallographic structure [298]. In this way the Debye-Waller parameters were determined. First, a simulation with only $EuGa_2S_4$ was performed. The correspondence with the experimental spectrum was already very good. This indicates that the true composition of the powders does not deviate far from this model and the majority of the europium occurs as $EuGa_2S_4$, as already established with SEM-CL-EDX and XRD.

Secondly, the simulation where a small amount of the Eu^{2+} ions substitute on the tetrahedral coordinated zinc sites showed a bigger deviation from the experimental spectrum. This is not surprising considering the limited volume of the Zn first coordination sphere and the size mismatch between Zn^{2+} and Eu^{2+}. This clearly confirms the hypothesis by Wickleder *et al.* that Eu^{2+} is not substituting for Zn^{2+} [372].

Thirdly, a simulation with a small amount of the Eu on the octahedral voids in $ZnGa_2S_4$ and the majority in the form of $EuGa_2S_4$, was performed. The simulated Fourier transforms of Eu L_{III} edge EXAFS are shown in Fig. 9.10(c), compared to experimental data. In this case, the Fourier transforms were performed in the k range of 2.1 $Å^{-1}$ - 7.8 $Å^{-1}$.

As can be seen in the figure, there is a very good correspondence between the two. The volume of the octahedral voids in the $ZnGa_2S_4$ structure is ≈24 $Å^3$, being much larger than the volume of the coordination tetrahedron of the Zn site, but still significantly smaller than the volume of the coordination octahedron of other sulfide hosts for Eu^{2+} (≈ 31 $Å^3$ for CaS, ≈ 36 $Å^3$ for SrS [401]). The simulation also showed that the closest zinc neighbor of the incorporated europium ions disappears. This observation can be explained by charge compensation, the europium ions are divalent as well as the zinc ions. Furthermore it is observed that some of the sulfur atoms move away from the dopants. This effect can be caused by the vacancy that occurs at the cationic position in the lattice. A crystal model of this simulation is displayed in Fig. 9.2(c).

Although the analysis was not explicitly performed, it seems very credible that the case of $MgGa_2S_4$:Eu^{2+} is completely analogous. The luminescent properties of this compound are also identical to those of $EuGa_2S_4$ (see Tab. 9.1) while also for this host, the site where the Eu^{2+} ion would sit, *i.e.* the Mg site, is remarkably small (23 $Å^3$ for the largest Mg site).

9.4 Conclusions

In this chapter, first a general overview of the europium doped thioaluminates MAl_2S_4 and thiogallates MGa_2S_4 (M = Ba, Sr, Ca, Mg, Zn) was given. From this overview, those phosphors with the most promising properties regarding white LED applications, *i.e.* $SrGa_2S_4$:Eu^{2+} and $ZnGa_2S_4$:Eu^{2+}, were selected for further investigation.

The luminescent properties of the solid solution series $Sr_{1-x}Eu_xGa_2S_4$ were studied in detail, with a focus on the luminescence decay behavior and the thermal quenching. This investigation yielded insight into the clustering of Eu centers for increasing doping concentration. The highest internal quantum efficiency was found for a doping concentration of $x = 0.04$, corresponding with a relatively high absorption for blue light which is beneficial for applications.

Furthermore, a fully optimized $SrGa_2S_4$:Eu^{2+} phosphor was combined with red CdSe/CdS quantum dots to prepare remote phosphor layers for blue pumped white LEDs that can be used for display backlights. A detailed quantitative investigation of the luminescent layers helped to compose design rules for different stacking geometries of remote phosphor layers, minimizing the cost as a function of the economical reality while maintaining state-of-the art color quality and device efficiencies.

Finally, $Zn_{1-x}Eu_xGa_2S_4$ phosphors were investigated. The luminescent properties and the distribution and incorporation of europium in the powders was investigated. Due to their excessive thermal quenching and low quantum efficiency, these materials should be discarded from applications, despite earlier reports. The structural characterization revealed that only a limited amount of europium - if any - can be incorporated into the $ZnGa_2S_4$ lattice. If these ions are incorporated, they occupy octahedral voids instead of the smaller zinc or vacancy sites with tetrahedral coordination. The majority of the europium ions form the $EuGa_2S_4$ phase which gives rise to the measured luminescent properties. It is believed that the same conclusions can be drawn for the $MgGa_2S_4$:Eu^{2+} phosphors which have been reported in literature.

10 Red luminescence from Mn^{2+} in CaZnOS

Divalent manganese, Mn^{2+}, is an activator ion that gained popularity in phosphors in cathode ray tubes (CRT) or fluorescence lamps [7, 402–405]. With the breakthrough of LED technology for both lighting and displays, lanthanide ions such as Ce^{3+} and Eu^{2+} became the dopants of choice due to their superior performance for these applications. This is because Mn^{2+}, although it can be very efficiently excited by cathode rays or UVC radiation (100-280 nm), has a very low absorption strength for blue light, as required for LED applications. This is caused by the symmetry- and spin-forbidden nature of the intraconfigurational $3d^5$ transitions exciting the luminescence (see §4.3) [70, 85]. Very recently, however, Mn-based materials have again gained increased attention in the context of rare-earth-free LED phosphors. CaZnOS:Mn^{2+} was proposed as red phosphor because the absorption strength of the $3d^5$ transitions appears to be unusually high compared to other Mn^{2+} based phosphors. [406].

Calcium zinc oxysulfide (CaZnOS) can be considered as an atypical host compound for optical dopants. First, not many host materials are known with a mixed anion coordination polyhedron for the luminescent ion. Secondly, CaZnOS crystallizes in polar crystals, which allow a nonzero internal electric field [407]. As an effect, upon incorporation of luminescent impurities, non-centrosymmetric compounds can show mechanoluminescence (ML) [408, 409]. For this to occur, energy has to be stored in the material first, presumably by trapping photo-ionized charge carriers. They can be released through the pressure-induced change of the internal electric field, eventually recombining radiatively at the ionized activator [408–411]. ML has been demonstrated in undoped CaZnOS and is ameliorated upon doping it with Mn or Cu [274, 412–415]. The ML can be generated by different types of mechanical stresses such as ultrasound and compressive stress [274, 412–415].

In a series of two papers, B. Huang studied Mn and Cu impurities and intrinsic defects in CaZnOS by means of DFT+U calculations [416, 417]. This approach is expected to yield important insights, especially with respect to the impurity level locations of intrinsic and extrinsic defects as these are experimentally hard to determine, while they are of utmost importance for the functional behavior of luminescent materials, *e.g.* the ML in the considered case. The impurity level locations that were found for a large number of intrinsic defects form important pieces to

solve the puzzle of the ML in CaZnOS. The orange emission in CaZnOS:Mn^{2+} is explained from energy differences between Kohn-Sham single particle energy levels, referred to as *3d fine levels*, of different defects. This interpretation of Kohn-Sham levels yields results which contrast with the common interpretation of spectroscopic transitions as differences in total energy between multiplets of the Mn ion. In particular, the energy difference between a single-particle level of a Schottky defect V'_{ZnO} with a singly negative Kröger-Vink charge and a single-particle level of $Mn^{\bullet\bullet}_{Zn}$ with a doubly positive Kröger-Vink charge is 2.1 eV and hence labeled as the reason for the orange emission band in CaZnOS:Mn. Notice that the doubly positive Kröger-Vink charge corresponds here to a Mn^{4+} ion in spectroscopic notation. This point of view asks for a solid investigation towards the charge state and spectroscopy of Mn defects in CaZnOS.

This chapter contains a fundamental study of the incorporation of Mn^{2+} in CaZnOS and the electronic structure of the resulting luminescent material. Both single- and many-particle schemes, *i.e.* band diagrams and multiplet schemes, are calculated and compared with experimental photoluminescence spectra. This phosphor is evaluated as a rare-earth free alternative as red LED phosphor. Finally, the ML behavior of this material is studied as a function of temperature and compared to thermoluminescence glow curves.

The results in this chapter are published as:

Charge transfer induced energy storage in CaZnOS:Mn - insight from experimental and computational spectroscopy

Jonas J. Joos, Kurt Lejaeghere, Katleen Korthout, Ang Feng, Dirk Poelman, Philippe F. Smet

Physical Chemistry Chemical Physics, ***19*** *9075-9085 (2017).*

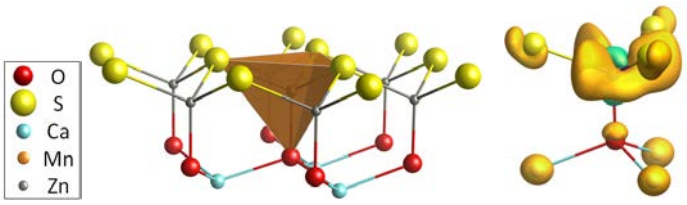

Figure 10.1 – Left: Coordination environment for the Mn_{Zn} defect in CaZnOS. In this figure, the layered Zn-S/Ca-O structure of the oxysulfide host is clearly visible. Right: Difference in electron density for the Mn_{Zn} defect, before and after the LMCT, calculated with PBE+U. The orange and green isosurfaces correspond to charge density differences of 0.0019 eÅ^{-3} and -0.0019 eÅ^{-3} respectively.

10.1 Synthesis

CaZnOS powders were prepared by a solid state reaction, starting from $CaCO_3$ (Alfa Aesar, 99.95%) and ZnS (Alfa Aesar, 99.99%). The mixed precursors were heated to 1000°C in nitrogen atmosphere and kept there for 12h. Afterward, the samples were allowed to cool naturally, before slight grinding. Manganese doping was achieved by adding a small amount of $MnCO_3$ (Alfa Aesar, 99.9%) or MnS (Cerac, 99.9%) to the mixture. The phase purity of the materials was checked using powder X-ray diffraction. The described experiments were performed on powders with a nominal Mn molar concentration of 0.5%.

10.2 Crystal structure and incorporation of Mn in CaZnOS

CaZnOS forms hexagonal crystals consisting of alternating layers of Zn-S and Ca-O and belongs to the non-centrosymmetric space group $P6_3mc$ [407, 418]. The zinc atoms are coordinated by one oxygen and three sulfur atoms in a deformed tetrahedron of symmetry C_{3v}, while the calcium atoms are coordinated by three sulfur and three oxygen atoms in a deformed octahedron of symmetry C_{3v} [407]. Density functional calculations at the PBE and PBE+U level were performed to optimize the unit cell of CaZnOS. A good correspondence was achieved between the experimental and calculated geometries (see Tab. 10.1).

It is known that the quaternary compound CaZnOS is unstable at high temperature. The competitive reaction $ZnS + CaO \rightleftharpoons CaS + Zn + 0.5\,O_2$, which is the principle to recycle Zn in industry, is unavoidable, especially in a reducing atmosphere. This results in impurities, mainly of the binary compounds ZnS, CaS and CaO [419, 420]. This finding is reflected in the formation energy of the compound which was calculated with respect to the experimental precursors ZnS and CaO. While PBE yields a positive value of 39 meV per formula unit, corresponding with an unstable CaZnOS phase, PBE+U yields a negative value of -16 meV per formula unit. These small numbers support the empirical finding of most experimental studies -including this one- that it is hard to obtain phase-pure CaZnOS. Small contaminations of binary by-products are always found in PXRD patterns before post-treatments. Nevertheless, the stability of synthesized CaZnOS was positively validated at room temperature through PXRD and luminescence spectroscopy of doped samples over time.

There are two straightforward possibilities for the manganese dopant to incorporate in the oxysulfide structure, by substituting for a zinc or calcium cation, forming a Mn_{Zn} or a Mn_{Ca} defect, respectively. Duan *et al.* presumed the former case to be most plausible due to the similar ionic radii of Zn^{2+} (60 pm) and Mn^{2+} (66 pm), compared to Ca^{2+} (100 pm) [177, 406]. The defect formation energies can be calculated by considering that μ_{Mn} equals the energy of Mn in a reference state, *i.e.* the *manganese reservoir* [94]. Given the above-described physical reality of the crystal structure, MnS was chosen as the reference state to calculate the formation energy of the Mn_{Zn} defect. Analogously, ZnS was chosen as reference state for Zn. Con-

versely, MnO and CaO were chosen as reference compounds regarding the Mn_{Ca} defect.

Our DFT calculations confirm the assumption of Duan *et al.* that the Mn dopants are found on the Zn site. The Mn_{Zn} defect has a slightly lower defect formation energy for all possible Fermi level locations (see further). Upon incorporation, the volume of the MOS_3 coordination polyhedron is slightly increased, in correspondence with the higher ionic radius of Mn^{2+} [177]. The shape and dimensions of the polyhedron are shown in Fig. 10.1 and Table 10.2. EXAFS was used to probe the details on the geometry of the nearby environment of the probed element. The analysis of the Mn K edge EXAFS spectrum was used as an experimental verification of the calculated preference for incorporation of the Mn ion. The analysis of the XAS data was performed by Dr. Katleen Korthout.

Figure 10.2 shows the Fourier transform of the EXAFS spectrum compared to the fitted profile, based on the deformed tetrahedral coordination of Mn_{Zn}. A similar profile, based on the deformed octahedral coordination of Mn_{Ca} was not able to reproduce the experimental data (not shown). Linearly combining both models showed indeed that tetrahedrally coordinated Mn dominates the spectrum and that the component originating from octahedrally coordinated Mn can be safely neglected. The parameters of the tetrahedral model were subsequently optimized in order to reproduce the experimental spectrum. Bond lengths could be estimated from the fit, which was restricted to the first two coordination shells as indicated by the window in Fig. 10.2. These are shown in Tab. 10.2 and are in good agreement with the DFT values. The presence of the pre-edge peak in the XAS spectrum (see inset Fig. 10.2) also hints towards tetrahedral coordination [421].

Even though the DFT calculations and the EXAFS experiments show that the Mn dopants are incorporated on the Zn site for the low doping concentration of 0.5 molar %, it cannot be excluded that some Mn will incorporate on the Ca site when the doping concentration is increased. Huang et al. used this argument to explain the redshift of the emission spectrum for increasing Mn concentration [417]. This is a plausible explanation to understand the redshift for increasing Mn concentration as a higher coordination number gives rise to a higher crystal field strength and hence a redshift in the case of Mn^{2+} (see also the discussion on the Tanabe-Sugano diagram in §4.3.) [7, 422]. An alternative reason for the redshift upon increasing the concentration is the interaction between neighboring Mn ions, as proposed by Zhang et al. for CaZnOS:Mn^{2+} [415]. This effect was also found to be responsible for the redshift of the Mn^{2+} emission in Zn_2SiO_4 [423, 424].

10.2.1 Electronic properties

The intention is to construct a complete energy level scheme of the excited state landscape of the CaZnOS:Mn^{2+} phosphor. The first important parameter pertains to the undoped host crystal, *i.e.* the band gap determines the absorption spectrum of this material in the visible and near UV spectral region. This parameter can be

Table 10.1 – Comparison between experimental and calculated unit cell parameters and band gap. Experimental data obtained at room temperature.

	a (Å)	c (Å)	E_G (eV)
exp.	3.757 [407]	11.401 [407]	4.27*
PBE*	3.792	11.450	2.10
PBE+U*	3.758	11.380	3.12
PBE+U [416]	3.76	11.52	3.895

* this work

Table 10.2 – Comparison between MOS_3 polyhedra. $d_{(O/S)}$ denotes the Mn-(O/S) and Zn-(O/S) bond lengths, while d_{av} denotes the arithmetic average. Results from the PBE+U optimization and EXAFS analysis.

	$ZnOS_3$ (DFT)	$ZnOS_3$ (PXRD [407])	$MnOS_3$ (DFT)	$MnOS_3$ (EXAFS)
volume (Å^3)	5.678	5.826	6.380	
d_{av} (Å)	2.234	2.254	2.322	2.325 ± 0.009
d_O (Å))	1.865	1.900	1.968	2.001 ± 0.019
d_S (Å)	2.357	2.372	2.440	2.445 ± 0.006
$\widehat{O\text{-}M\text{-}S}$ (°)	113.83	113.85	112.83	
$\widehat{S\text{-}M\text{-}S}$ (°)	105.92	104.76	105.92	

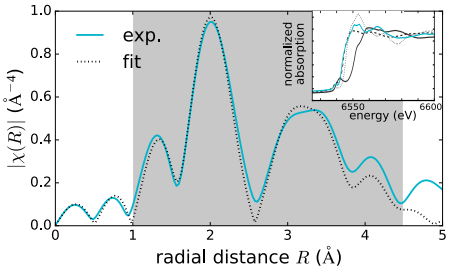

Figure 10.2 – Fourier transform of the Mn K-edge EXAFS spectrum of CaZnOS:Mn (blue, solid line), compared to the fit, based on a tetrahedral Mn_{Zn} defect model (black, dotted line). The grey window indicates where the deviations between the two curves was minimized. The inset shows the XAS spectra in the Mn K-edge XANES region of CaZnOS:Mn (blue, solid line), compared to the Mn(II) salts MnF_2 (black, dotted line) and $MnCO_3$ (black, dashed line) and to the Mn(IV) oxide MnO_2 (black, solid line).

determined using UV-VIS spectroscopy as well as calculated with DFT.

Upon doping with transition metal ions such as Mn, impurity levels are formed in the band gap. The locations of these impurity levels are calculable with DFT and are closely connected to the energy of charge transfer bands that can occur in optical spectra (see §5.4.2).

Band gap of CaZnOS

Based on diffuse reflectance measurements, followed by a Kubelka-Munk analysis, experimental values of 3.7 eV [407], 3.88 eV [274, 419], 4.0 eV [406] and 4.16 eV [415] can be found in literature for the optical band gap of CaZnOS. A similar measurement on our undoped CaZnOS samples revealed an even higher value of 4.27 eV, where a model for allowed transitions across a direct band gap was used. The scatter on these values might be explained by the unintended occurrence of intrinsic or extrinsic defects, giving rise to an apparently lower band gap. These uncertainties are accounted for in an estimated error margin of 100 meV on the value of the optical band gap (see 7.2.1).

Both PBE and PBE+U calculations give rise to a Kohn-Sham band gap which is too low compared to the experimental value (see Tab. 10.1). This is however within expectations given the well-known self-interaction error of DFT (see 5.3.2). To account for this underestimation and, more importantly, to predict in which sense this affects the locations of the calculated impurity levels, the extrapolation scheme of Janotti and Van de Walle [94, 211, 212] (see §5.3.4) was applied in the following. Assigning additional Hubbard U parameters to the np electrons of sulfur and oxygen can open the calculated band gap even further [416].

Mn impurity levels

The charged supercell formalism was used to calculate the impurity levels of both the Mn_{Zn} and Mn_{Ca} defects. Electrons were added or removed from the Mn defect to simulate the different occupation numbers. In order to maintain a charge-neutral system, a homogeneously distributed background charge was added, compensating for the added or removed electrons. A monopole-monopole correction term was taken into account to correct the total energies for unphysical interaction between the defect and its periodic images, using the macroscopic dielectric constant of the host material calculated with density functional perturbation theory.

Figure 10.3 shows the defect formation energies as a function of Fermi level location for different charge states of the defect in a host referred (HRBE) and a vacuum referred binding energy (VRBE) diagram. The Kröger-Vink notation (see §5.2) was used. As Ca and Zn are both divalent ions, an uncharged $Mn_{Zn}^{\times}$ or $Mn_{Ca}^{\times}$ defect corresponds to a Mn^{2+} ion according to spectroscopic notation. It is apparent from the figure that the Mn_{Zn} defect has the lowest defect formation energy for most Fermi level locations and is hence expected to be the Mn defect found in reality. This is in line with expectations given the similar ionic radii of Zn^{2+} and Mn^{2+}. Only for high chemical potentials for the electrons, *i.e.* when the Fermi level approaches the conduction band bottom, it can be energetically favorable to form negatively charged Mn_{Ca} defects.

For both defects, the lowest charge-state transition level within the band gap is the $\epsilon(0/-1)$ (or Mn^{2+}/Mn^{+}) level, lying 3.32 eV and 2.99 eV above the valence band maximum for Mn_{Zn} and Mn_{Ca}, respectively. The physical significance of this level is that when the electron chemical potential is below $\epsilon(0/-1)$, manganese will be stable in the Mn^{2+} ($Mn_{Zn}^{\times}$) charge state, while the defect will be stabilized in the Mn^{+} ($Mn_{Zn}^{\prime}$) charge state when the chemical potential is above the impurity level. The experimental charge state of the Mn dopant could be obtained from the XANES spectrum. The inset of Fig. 10.2 shows the measured Mn K-edge XANES spectrum of CaZnOS, compared to the Mn(II) salts MnF_2 and $MnCO_3$ and the Mn(IV) compound MnO_2. For the former, a good correspondence with the K-edge location is found, while this is not the case for the latter, implying a predominant occurrence of Mn in the divalent state in CaZnOS.

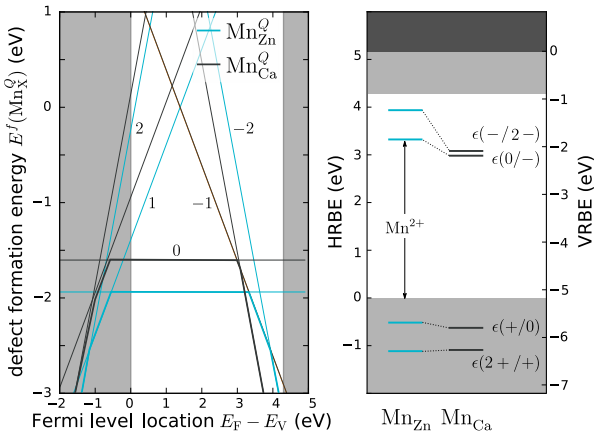

Figure 10.3 – Defect formation energies for Mn_{Zn}^Q and Mn_{Ca}^Q (the value of Q is indicated in the figure) as a function of the Fermi level location in CaZnOS (left). The secants of the straight lines correspond with the physical impurity levels, *i.e.* charge-state transition levels. The obtained impurity levels are shown in a conventional band diagram, representing host referred and vacuum referred binding energies, HRBE and VRBE (right). The results were obtained from PBE+U calculations which were extrapolated according to the scheme by Janotti and Van de Walle [94, 211, 212].

The impurity levels are thermodynamic transition levels, meaning that they were calculated for optimized geometries in both charge states. These levels are therefore involved in *slow processes*, *i.e.* where the system has time to adapt itself to the external factors. An examples is the path towards chemical equilibrium during the synthesis of the material, eventually by oxidizing or reducing the impurity. In the case of optical charge transfer transitions, a thermodynamic transition level corresponds to the energy of the ZPL (see §5.2.3 and §5.4.2). An absorption band due to a ligand-to-metal charge transfer is thus expected above 3.32 eV for CaZnOS:Mn_{Zn}, based on the supercell calculations. The optical charge-state transition level, where the geometry was not allowed to reorganize, was calculated at 3.44 eV. The absolute location of the impurity level is roughly in accordance with the universal trend, observed for Mn in II-VI compounds, as identified by Caldas *et al.* [425].

Figure 10.1 shows the difference in electron density between both charge states, *i.e.* the shift in electron density during the optical absorption. It is clear that the additional charge is spatially spread out around the Mn defect. This is in accordance with the prediction of Haldane and Anderson of self-regulating behavior which states that the effective charge of a transition metal remains close to neutrality whatever its valence due to the hybridization with valence band states, allowing the additional charge to be localized further away from the transition metal (see §5.2) [190, 426–428].

It should be emphasized that the calculated charge-state transition levels do not coincide with Kohn-Sham eigenvalues (density of states, DOS) in the forbidden band

for the defect of neutral charge. More elaboration on the meaning of KS levels can be found in §5.3.2.

10.2.2 Spectroscopic properties

Up to now, only ground state properties of the neutral and charged CaZnOS:Mn^{2+} phosphor were addressed. To understand the physical processes behind the luminescence behavior, knowledge on the excited states of the $3d^5$ configuration of Mn^{2+} is required. DFT can only describe those states that correspond to the lowest energy state for different symmetry classes. Examples are the calculation of the ZPL energy of the emitting transition of Mn^{4+}, or the energy of the lowest $4f^N$-$4f^{N-1}5d^1$ transition in some lanthanide-based scintillators by forcing the system into an orbital occupation which does not correspond to the lowest energy [90, 93, 429]. Here, all the multiplets originating from the $3d^5$ configuration are however required and for this reason, the focus is changed towards crystal field theory (CFT), which can describe all excited states of a certain electron configuration. Electron-phonon coupling is taken into account to discuss the CFT results in a rational way. The coupling is quantified based on the vibronic fine structure of the emission spectrum and the phonon density of states, obtained from DFT.

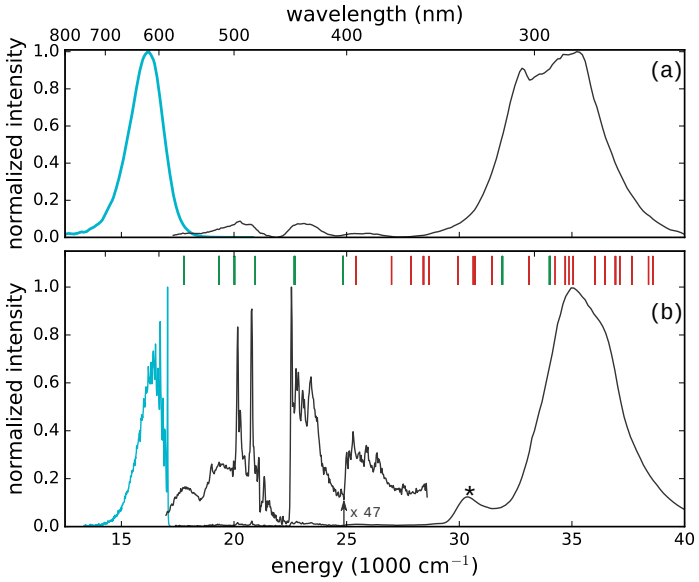

Figure 10.4 – Photoluminescence emission (upon excitation at 280 nm, blue lines) and excitation spectra (when monitoring the emission at 610 nm, black lines) of CaZnOS:Mn^{2+}, measured at room temperature (a) and at 4.5 K (b). The vertical lines indicate the locations of the excited multiplets for the ground state geometry of the defect cluster, as obtained from the CFT optimization. The green and red color denote a total spin of $S = 3/2$ and $S = 1/2$ respectively. The charge transfer transition is indicated by $*$.

Photoluminescence of the Mn^{2+} ion

The experimental room temperature photoluminescence (PL) excitation and emission spectra of CaZnOS:Mn are shown in Fig. 10.4a. The emission spectrum is in correspondence with literature, reporting an emission peaking around 610 nm and originating from the spin-forbidden transition from the first excited $3d^5$ multiplet to the $3d^5(^6S_{5/2})$ ground state [406, 415]. The excitation spectrum shows characteristic $3d^5$-$3d^5$ transitions on the low-energy side, *i.e.* between 350 nm and 600 nm. On the high-energy side, a more intense broad excitation band is found, due to transitions related to the host material.

The high-energy band below 315 nm originates most probably from fundamental absorption in the CaZnOS host with subsequent energy transfer to the Mn defect. This band has a shoulder at 338 nm, which is clearly resolved at low temperature. It is reasonable to assign this band to the ligand-to-metal charge transfer that was predicted from the DFT calculations. The thermodynamic charge-state transition level lies 3.32 eV above the valence band top, while the maximum of the excitation band is found at 3.78 eV. The energy difference of 0.43 eV is perfectly consistent with half of the typical values for the Stokes shift associated with CT transitions [236]. While the thermodynamic charge-state transition level found after extrapolating the PBE+U results seems to be in accordance with experiment, the calculated difference with the optical charge-state transition level of 0.12 eV is too low. This discrepancy is most likely due to higher-order phenomena, such as excitonic effects, which are not included in the DFT calculations.

The low temperature PL spectra are shown in Fig. 10.4b, where fine structure emerges in both the emission and excitation spectra. In the emission spectrum, the zero phonon line at 17051 cm^{-1} (586.5 nm) stands out and comes with a detailed vibrational fine structure, clearly containing multiple active modes. The Stokes shift amounts to 1550 cm^{-1} (0.19 eV). In the excitation spectrum, the transitions from the $3d^5(^6S_{5/2})$ ground state towards the different excited $3d^5$ multiplets are well-resolved along with some vibrational progressions. The fine details of the low temperature spectrum allow to fit a crystal field Hamiltonian to the experimental transition energies (see further).

The thermal quenching of the emission upon excitation in the different excitation bands was measured (not shown). While the intraconfigurational $3d^5$ transitions remain stable between low temperature and room temperature, the broad excitation bands at higher energy show severe thermal quenching, resulting in the relative intensity difference between both spectra in Fig. 10.4. This suggests the existence of a non-radiative decay channel near the higher-lying excited states, requiring only a small amount of thermal energy to reach.

Crystal field parameterization

Optical spectra of fourfold coordinated Mn^{2+} are typically labeled with irreducible representations of the tetrahedral point group T_d. In this case, the two broad excitation bands in the region of 17300-19800 cm^{-1} correspond to transitions from the $^6A_1$ ground state to the $^4T_1$ and $^4T_2$ crystal field states originating from the ^4G Russell-Saunders term. Because excitation to the $^4T_1$ and $^4T_2$ states induces geometric relaxation of the nuclear positions in the Mn defect cluster, the maximum values of the excitation bands are used to fit crystal field parameters rather than the ZPL in order to obtain a more reliable result for the ground state situation.

Other crystal field states originating from the ^4G term are $^4A_1$ and ^4E which are accidentally degenerate in T_d and O_h symmetries. In contrast with the former two excitations, the latter two transitions correspond with a sharp peak. This can be intuitively interpreted in terms of the independent particle configurations in the high crystal field limit. No electron changes *orbital* for $^6A_1 \rightarrow (^4A_1, {}^4E)$ transitions as both initial and final state originate from the $e^2t_2^3$ configuration while an electron is transferred from a t_2 orbital to an e orbital in the case of excitation to the $^4T_1$ or

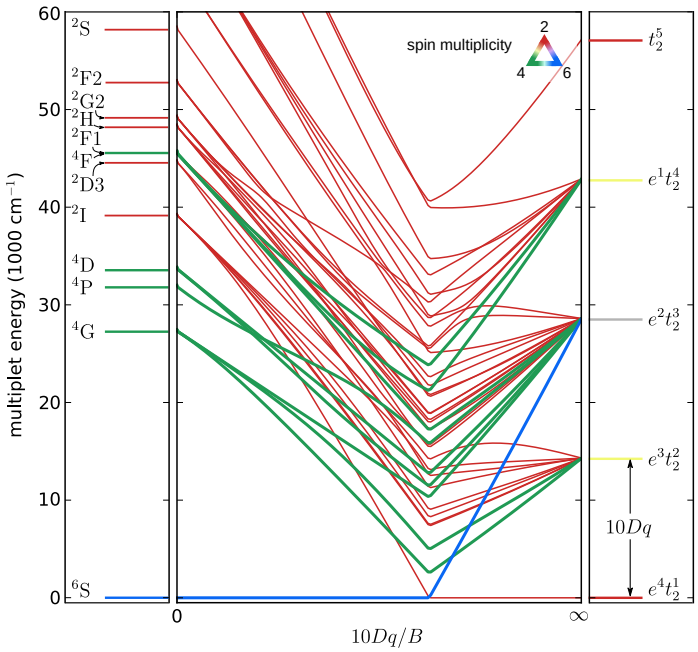

Figure 10.5 – Tanabe-Sugano diagram for a nd^5 configuration, showing the variation of the multiplets from the weak-field limit (labeled by the atomic term symbols) to the strong-field limit (labeled by the single-electron occupation numbers of the crystal field orbitals) limits. The color of the lines represents the spin doublet (S = 1/2, red), quartet (S = 3/2, green) or sextet (S = 5/2, blue) character of the states. The energy scale was chosen to correspond with the correct values in the free ion limit.

$^4T_1$ state which originate from the $e^3t_2^2$ configuration. This argument can be derived from the modified Tanabe-Sugano diagram in Fig. 10.5. In this figure, the popular convention is adapted to use $10Dq$, the single-particle crystal field splitting. It is related to the Wybourne parameter $B_{40} = -14/10\ 10Dq$ for T_d fields [130].

Higher lying excited states visible in the excitation spectrum are the $^4T_2$ and ^4E states originating from the ^{4}D term. In the same energy region, crystal field states originating from the ^{2}I term can be found. These are however not visible in the excitation spectrum because of the larger difference in spin quantum number S with respect to the ground state.

The coordination polyhedron for Mn^{2+}, when incorporated on a Zn site is not perfectly T_d symmetric, but the mixed anionic nature of the compound results in a lower C_{3v} symmetry. This has two repercussions on the crystal field (CF) parameterization, *i.e.* the tetrahedral ratio between B_{40} and B_{43} ceases to hold and another nonzero parameter, B_{20}, emerges, yielding a total of three independent CF parameters. Often, an alternative parameterization due to Ballhausen is used in this case [130]:

$$\begin{aligned} B_{20} &= -7D\sigma \\ B_{40} &= -14Dq - 21D\tau \\ B_{43} &= -2\sqrt{70}Dq. \end{aligned} \tag{10.1}$$

When using this notation, the lowering of symmetry is stressed through the deviation of the tetrahedral ratio ($D\tau \neq 0$) and the emergence of the additional term in the Hamiltonian ($D\sigma \neq 0$).

The additional terms in the CF Hamiltonian cause further splitting of the crystal field levels, *i.e.* the orbital triplets split in a doublet and a singlet, while the orbital doublets and singlets maintain their degeneracy. As the ^{4}G(T_1/T_2) terms feature broad excitation bands, their splitting is not visible. Different lines are resolved from excitation to the ^{4}D(T_2) term, but it is not possible to derive the splitting due to the symmetry lowering as the lines can also originate from vibronic side bands. At first sight, it therefore seems difficult to quantify the symmetry lowering in terms of crystal field parameters.

A straightforward explanation for the lifting of the accidental degeneracy of the $^4A_1$ and ^4E levels would be to attribute it to the symmetry lowering, offering a means to quantify $D\sigma$ and $D\tau$. Figure 10.6 compares the effect of the two additional crystal field parameters on the energy difference between $^4A_1$ and ^4E, denoted as $\Delta E(^4\Gamma)$, and on the energy of the lowest excited state, $E(^4T_1)$. As one can see from this figure, symmetry lowering alone cannot account for the degeneracy lifting as it requires unrealistically high values of $|10D\sigma|$ in the range of $25B$, compared to typical $|10Dq|$ values in the range of $5-10B$ for tetrahedral Mn^{2+} complexes [430–433].

The accidental degeneracy of the $^4A_1$ and ^4E levels and its lifting - even in fields of T_d or O_h symmetry - has been the subject of long debate [433–435]. Koide and Pryce

modeled this phenomenon by proposing non-equal Racah parameters for electrons in the e and t_2 orbitals, which they attributed to *covalency*. Ng and Newman showed that the assumptions of this so-called epsilon or renormalization model are in contradiction with two-electron integrals, calculated through a configuration interaction technique [436, 437]. Subsequently, the same authors showed that an improved description of experimental spectra of octahedral Mn^{2+} ions in halides, corresponding with σ_{CF} values in the range of 290-770 meV, could be obtained by adding the spin-correlated crystal field, already known from lanthanide spectroscopy, Eq. 4.76, to the effective Hamiltonian [435].

In the high-symmetry case of T_d, only one additional parameter, c_4, is required. Upon lowering symmetry to C_{3v}, a second nonzero parameter, c_2, emerges. As crystal field studies have shown that the importance of c_k parameters increases with k, c_2 can be neglected at leading order, along with $D\sigma$ and $D\tau$ [76]. In Fig. 10.6, it is shown that the experimental $^4A_1$ - ^4E splitting can be obtained together with a realistic value for the lowest excited state. Therefore, the spin-correlated crystal field term is used to describe the experimental spectrum. To reduce the number of fitting parameters, T_d symmetry is assumed, which is an acceptable simplification.

Furthermore, the ratio of Racah parameters is kept fixed at the conventional value $C/B = 4$ and the experimental Trees parameters for the free Mn^{2+} ion are used for the calculation. A remarkably good correspondence between calculated and experimental transition energies is obtained as shown in Fig. 10.4 and Tab. 10.3, with a standard deviation σ_{CF} of 198 cm^{-1}. The optimal parameters for the effective Hamiltonian are summarized in Tab. 10.4.

Table 10.3 – Calculated multiplet energies, obtained from a spin-correlated crystal field calculation, compared to the experimental energies, obtained from low-temperature PL spectroscopy.

term	T_d	C_{3v}	calc. (cm^{-1})	exp. (cm^{-1})
^{6}S	$^6A_1$	$^6A_1$	0	0
^{4}G	$^4T_1$	$^4A_2 \oplus {}^4E$	17774	17826
				(ZPL: 17051)
	$^4T_2$	$^4A_1 \oplus {}^4E$	19342	19456
	^4E	^4E	20019	20061
	$^4A_1$	$^4A_1$	20939	20705
^{4}D	$^4T_2$	$^4A_1 \oplus {}^4E$	22688	22549
	^{4}E	^4E	24839	25002
^{4}P	$^4T_2$	$^4A_1 \oplus {}^4E$	24840	

Table 10.4 – Parameters used in the spin-correlated crystal field calculation.

parameter	value (cm^{-1})	reference
B	636	this work
C	2544	this work
α	65	[433]
β	-128	[433]
$10Dq$	3983	this work
c_4B_{40}	1570	this work

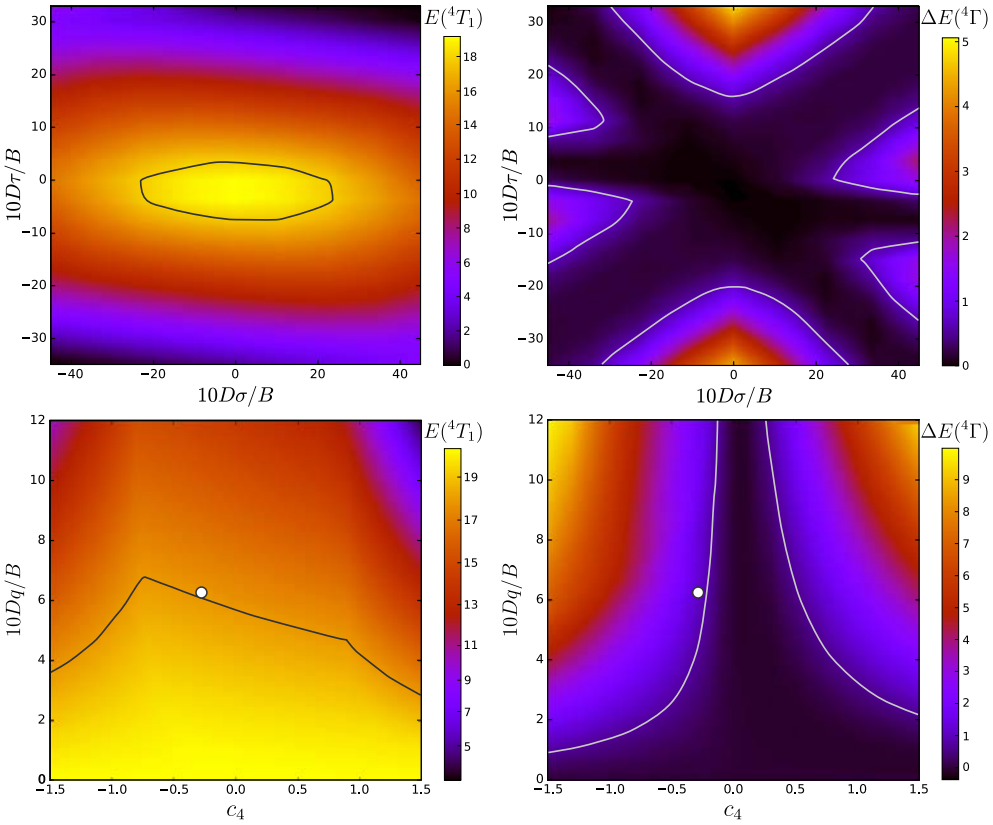

Figure 10.6 – Energy of the emitting level, $E(^4T_1)$ (left) and the lifting of the accidental degeneracy, $\Delta E(^4\Gamma) = E(^4A_1) - E(^4E)$ (right), as a function of symmetry lowering, $10D\sigma$ and $10D\tau$ (top) and as a function of the spin-correlated crystal field, c_4 (bottom). The parameter values at which the experimental values for the displayed quantities are found, are marked by the black and white lines, the optimized parameter values by the white dot. All energy values in 1000 cm^{-1}.

Electron-phonon coupling

Although intraconfigurational 3d transitions have a small transition probability, it is nonzero in the case of CaZnOS:Mn_{Zn}. The tetrahedral coordination of the Mn ion does not possess a symmetry center whereby the Laporte parity selection rule does not hold and the intraconfigurational 3d transition can become symmetry allowed if the E1 selection rules $\Delta L = 1$, $\Delta S = 0$ are fulfilled. This seems not to be the case at first sight. However, the crystal field can mix some ^{4}P character in the ^{4}G eigenstate, relaxing the $\Delta L = 1$ rule. Furthermore, the $\Delta S = 0$ rule is relaxed by the spin-orbit interaction. The electronic transition moment $\left\langle {}^6S(A_1)|\boldsymbol{D}|{}^4G(E)\right\rangle$ can then be nonzero for the point group C_{3v}, evidenced by the occurrence of the totally symmetric irreducible representation (irrep) A_1 in the reduction of the direct product $A_1 \otimes E \otimes E$, considering that the electric dipole moment transforms according to

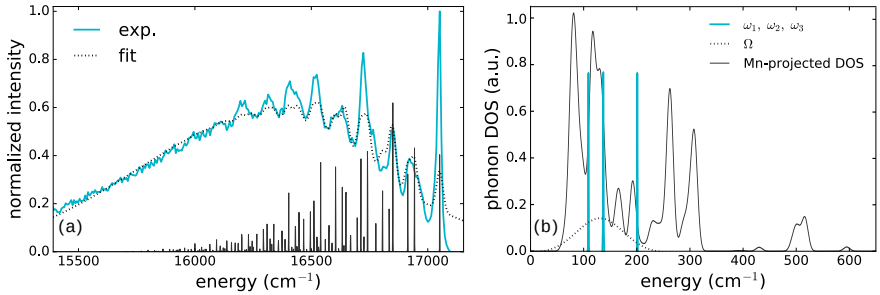

Figure 10.7 – (a) Low temperature (4.5 K) emission spectrum (excitation at 280 nm (35700 cm^{-1})) of CaZnOS:Mn. The dotted line shows the calculated multiphonon vibronic spectrum corresponding to the unbroadened harmonic and frequency mixed lines as shown. (b) PBE+U phonon density of states, projected on the Mn_{Zn} defect in CaZnOS, compared to the experimentally obtained phonon energies. The uncertainties on the experimental energies were used as bandwidth in this plot.

the irrep E for light which is polarized perpendicular to the threefold rotation axis. Additional contributions can originate from mixing with higher-lying excited states through the odd part of the crystal field (see §4.3).

The shape of an emission or excitation band is given by 3.18. It shows how many quanta, *i.e.* phonons of every vibrational mode, are created or annihilated during the transition. The vibrational fine structure was well-resolved in the low temperature emission spectrum in Fig. 10.4. The different phonon lines are not equidistant, implying that the spectrum is multiphononic in nature (Fig. 10.7(a)). For this reason, the standard Huang-Rhys theory for vibronic transitions involving one vibrational mode in the harmonic approximation is not directly applicable. Liu *et al.* have proposed an extension of the low temperature limit of this theory for multiphonon vibronic spectra [438] inspired by the observation by Bron and Wagner that both local and lattice modes can couple to electronic transitions [439–441]. The spectral shape of an emission band is then given by the sum of two contributions:

$$
\begin{aligned}
I(E) \;=\; & I_{0,\mathrm{loc}} \sum_{N_k} \cdots \sum_{N_1} \left(\prod_{i=1}^{k} \mathrm{e}^{-S_i} \frac{S_i^{N_i}}{N_i!} \right) \\
& \times \left(\frac{E_0 - \sum_{i=1}^{k} N_i \hbar\omega_i}{E_0} \right)^4 f\left(E; E_0 - \sum_{i=1}^{k} N_i \hbar\omega_i; \sigma \right) \\
& + I_{0,\mathrm{lat}} \sum_{N_k} \cdots \sum_{N_1} \sum_{N_\Omega} \left(\prod_{i=1}^{k} \mathrm{e}^{-S_i} \frac{S_i^{N_i}}{N_i!} \right) \left(\mathrm{e}^{-S_\Omega} \frac{S_\Omega^{N_\Omega}}{N_\Omega!} \right) \\
& \times \left(\frac{E_0 - \sum_{i=1}^{k} N_i \hbar\omega_i}{E_0} \right)^4 f\left(E; E_0 - N_\Omega \hbar\Omega - \sum_{i=1}^{k} N_i \hbar\omega_i; \sigma_\Omega \right).
\end{aligned}
\tag{10.2}
$$

Table 10.5 – Optimized parameters for the vibronic line shape function for the emission spectrum of CaZnOS:Mn.

mode	frequency (cm^{-1})	S	σ (cm^{-1})
ω_1	108.5 ± 0.4	0.96 ± 0.03	13.9 ± 0.3
ω_2	137.2 ± 0.5	0.71 ± 0.03	13.9 ± 0.3
ω_3	201.4 ± 0.2	1.33 ± 0.02	13.9 ± 0.3
Ω	131 ± 44	1.6 ± 0.6	500 ± 197

The first term reflects the low-temperature limit of Eq. 3.18 in the absence of Duschinsky effects and contains the contributions of the k different local modes with suitable symmetry labels, characterized by frequency ω_i and electron-phonon coupling S_i (see §3.1, 3.2.2 and 3.4.3). This term contains harmonic lines as well as lines originating from frequency mixing between the different modes. The lines are broadened by a Gaussian shape function $f(E;\mu;\sigma)$, centered at μ and having a width σ. E_0 denotes the energy of the ZPL. The second term originates from the coupling of Frank-Condon allowed modes to lattice acoustic modes [438]. This is modeled by a single average lattice phonon frequency Ω, coupled to all allowed local modes with an effective Huang-Rhys parameter S_Ω and a broad density of phonon modes, yielding $\sigma_\Omega \gg \sigma$ [438]. The second term ensures a good fit of the broad band underlying the fine structure.

It was possible to get a reasonable fit when three vibrational modes were taken into account in the first term of Eq. 10.2. The result is shown in Fig. 10.7(a) and the obtained phonon energies summarized in table 10.5. Statistical analysis of the performed fit reveals a strong correlation between the parameters belonging to the *average* mode Ω, S_Ω and σ_Ω, which corrupts an accurate determination of these parameters. On the other hand, the parameters belonging to the local vibrational modes can be determined with a good accuracy (Tab. 10.5).

As a means of comparison, the phonon density of states was calculated for the PBE+U optimized supercell in the Γ-point to identify the modes corresponding to an isolated Mn defect. Upon projecting this phonon DOS on the Mn defect, Fig. 10.7(b) is obtained. In this figure, the experimental phonon energies from the Mn^{2+} emission spectrum (Tab. 10.5) are added. This comparison shows that the three experimental modes indeed correspond to peaks in the phonon DOS with less than 10 cm^{-1} deviation, which is in line with previously documented accuracy of Γ-point phonon frequency predictions [442–444]. The modes corresponding to the other peaks in the phonon DOS might contribute to the luminescence spectrum as well, but extracting them from the fit, Eq. 10.2, is impossible without overparameterization.

10.2.3 Energy level scheme

Figure 10.8 summarizes the results of the above sections. It represents the total energy of the complete system, *i.e.* the 3d valence electrons of the Mn dopant, as well as all the nuclei and electrons that make up the host material and interact with the optical dopant. The complementarity of DFT (yielding the transition energy and geometric relaxation of a charge-transfer), CFT (yielding the excitation energies of the intraconfigurational $3d^5$ transitions), and the analysis of the electron-phonon coupling (yielding different equilibrium geometries for the different eigenstates), is demonstrated. The curvatures of the potential energy surfaces were obtained from the phonon energies, while the relative offsets were determined from the experimental Stokes shifts. One should be aware that this figure is a simplified representation of reality. This was proven by the quantitative analysis of the vibronic structure of the emission spectrum, indicating at least three and possibly more involved phonon modes of the defect cluster, and thus requiring a higher-dimensional energy diagram. Furthermore, only the location of the lowest energy LMCT state is indicated. In reality, this excited configuration features numerous multiplets, similar to any other electron configuration. The energy level scheme was projected on two normal modes, Q_1 and Q_2, the former dominant for intraconfigurational $3d^5$ transitions, the latter dominant for the LMCT. Both normal modes are not necessarily linearly independent and possibly feature different curvatures of the PES. The grey band indicates the creation of an electron-hole pair in the CaZnOS host itself. It is assumed that this excitation does not interact with the Mn impurity, allowing to

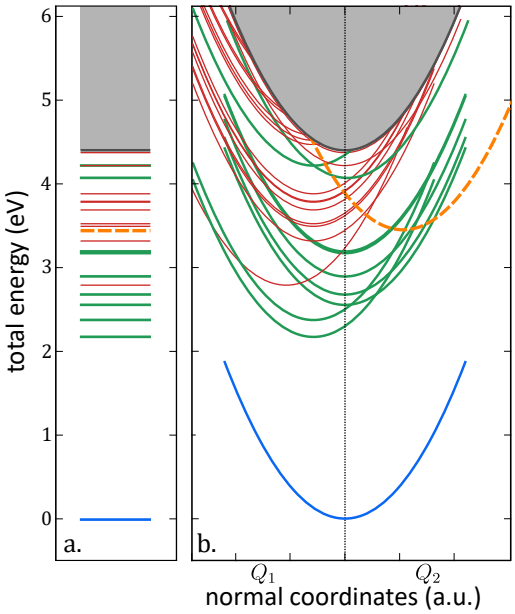

Figure 10.8 – Complete energy level scheme, combining the results obtained with the different theories. The blue, green and red lines represent the potential energy surfaces involving localized excitations of the $3d^5$ manifold with respectively $S = 5/2$, $S = 3/2$ and $S = 1/2$, while the dashed orange line is the lowest energy level belonging to the ligand-to-metal charge transfer, *i.e.* by adding a valence electron of the host's anions to the Mn defect, and the grey line represents the continuum of excitations across the host's band gap, forming an electron-hole pair without affecting the local structure of the Mn defect.

simply copy the ground state parabola to the energy for exciton creation[1].

As this diagram is obtained by a combination of experimental and computed parameters, it should be regarded as a semi-quantitative tool for the interpretation of experiments. A fully quantitative version of the diagram, including all possible vibrational modes can be obtained from multireference calculations such as CASSCF/CASPT2. The assets of these theoretical techniques were demonstrated by multiple authors, yielding a deeper understanding of specific materials [98–102]. Yet, a lot of user-experience is required for these techniques, provisionally hampering a large-scale in-depth analysis of functional materials [97]. The semi-empirical configurational coordinate diagram in Fig. 10.8 was constructed in an attempt to offer a more attainable alternative. It was recently shown by multireference calculations that empirical configurational coordinate diagrams are reliable tools to describe intervalence charge transfers (IVCT) in particular compounds [445].

Although simplified, this sole many-particle picture explains all the physics that was discussed in detail in the above sections, without the need for ambiguous diagrams displaying both single-particle and multiplet levels. Furthermore, it explains additional physics which is not covered by separate band diagrams or $3d^5$ multiplets. Figure 10.8 shows why no emission is to be expected from the CT level. If the system is excited to this level by absorbing a photon of suitable energy, it is immediately followed by a non-radiative cascade of energy via the ^{4}G multiplets towards the emitting $^4G(^4T_1)$ level because of the potential energy surfaces crossing (see §3.4.4). No additional thermal energy is required for this, excluding CT emission also at low temperature. In general, the excited state landscape is crowded, implying that non-radiative multiphonon emission towards the emitting level is to be expected, regardless which level of the $3d^5$ manifold is reached by photon absorption. The energy level scheme allows to estimate activation temperatures of thermally assisted processes as potential barrier heights can be extracted. The latter possibility is of great importance in the study of phenomena where energy is stored in the material such as mechanoluminescence. The relative location of energy levels can indicate the channels through which the system can rearrange its charge carriers. Specifically, an overlap between localized excited states of the activator and mobile excited states such as excitons have to be looked for. The diagram shows that the energy surface of the $3d^5$ ^{4}F multiplets around 4.0 eV show overlap with the energy surfaces of the excited states of the host compound. This indicates that mechanoluminescence will only be caused upon excitation with light of sufficient high energy, reaching these particular levels.

[1] In literature, this grey band is sometimes referred to as the conduction band. This is however a confusing designation as the grey band in Fig. 10.8 features many-body states while the conduction band is a notion from single-particle band theory, *i.e.* the collection of empty orbitals (see chapter 5).

10.2.4 Red LED phosphor

Recent cost, environmental and supply issues for the rare earth elements have triggered a tendency to develop LED phosphors which are rare-earth free. In this context, it makes sense to evaluate CaZnOS:Mn^{2+} for an application as red LED phosphor. Duan *et al.* have suggested this possibility based on the relatively intense intraconfigurational $3d^5$ transitions in the excitation spectrum at room temperature (see Fig. 10.4(a)) [406]. Here, we compare the performance of the CaZnOS:Mn^{2+} phosphor with that of different alternative red-emitting materials with respect to the necessary conditions that were outlined in §1.4.

As a benchmark, the commercially available, europium based nitrides $Sr_2Si_5N_8$:Eu^{2+} [288, 289, 291] and $CaAlSiN_3$:Eu^{2+} [446] are used. Here, the broadband emission originates from parity allowed, interconfigurational $4f^6 5d^1 \rightarrow 4f^7$ electric dipole transitions. As rare earth free alternative, we select the manganese based phosphor K_2SiF_6:Mn^{4+}, which is frequently discussed in literature [126, 128]. In this material, the intraconfigurational $3d^3$ transitions of the Mn^{4+} ion are responsible for the luminescence, yielding narrow line emission, rather than the broadband emission of the $3d^5$ configuration of Mn^{2+} (see also §4.5.1). For completeness, a phosphor based on the Eu^{3+} ion, showing intraconfigurational $4f^6$ transitions is added as Eu^{3+} based phosphors are often suggested for LED applications, despite their difficult excitation with near-UV to blue light [447]. To evaluate CaZnOS:Mn^{2+}, a powder with a doping concentration of 4% was selected, as the highest quantum efficiency upon direct excitation of the $3d^5$ manifold was reported for this concentration [415]. The internal quantum efficiency of the materials is not used in this comparison as this depends largely on the synthesis conditions and it can be safely assumed that there are no fundamental restrictions for any of these materials at room temperature, as deduced from the high temperatures at which thermal quenching sets in (see §1.4).

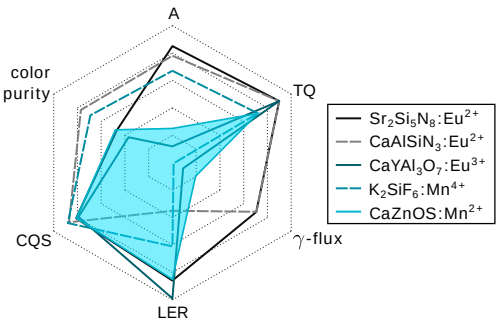

Figure 10.9 – Performance of CaZnOS:Mn^{2+} as LED phosphor for lighting or displays, compared with the benchmarks $Sr_2Si_5N_8$:Eu^{2+} and $CaAlSiN_3$:Eu^{2+}, the rare-earth free phosphor K_2SiF_6:Mn^{4+} and line-emitter $CaYAl_3O_7$:Eu^{3+}. The indication "A" scales with the absorptance of blue light while "TQ" scales with the maximum temperature up to which the external quantum efficiency of the phosphor stays constant. γ-flux gives a measure for the maximum excitation intensity where no saturation effects occur. "LER" and "CQS" scale with the luminous efficacy of the radiation of the phosphor's emission and the color quality scale of a white LED based on this phosphor (combined with a blue pump LED and the yellow phosphor YAG:Ce^{3+}). Finally, the indication "color purity" scales with the transmission of the phosphor's emitted light through display color filters, tuned to the recent Rec. 2020 recommendation [16].

Fig. 10.9 shows the performance of the selected phosphors on the enumerated points. It is immediately clear that the absorption strength of blue light (A) is still too low for CaZnOS:Mn^{2+}, even for the relatively high doping concentration of 4%, compared to the Eu^{2+} based benchmark materials. This is the same problem which also Eu^{3+} based phosphors are known to suffer. If this problem could be overcome, for instance by codoping with a suitable sensitizer, the color point of CaZnOS:Mn^{2+} is ideal for using it in addition to $Y_3Al_5O_{12}$:Ce^{3+} to create warm-white LEDs with high color rendering, quantified by the color quality scale (CQS) [352], while keeping the luminous efficacy of the radiation (LER) at an acceptable level. The emission spectrum of CaZnOS:Mn^{2+} is less suitable for display applications as too much color filtering is necessary to achieve the Rec. 2020 standard for the red primary color [16]. Mn^{4+} based phosphors are more suited for this purpose, provided that their absorption strength can also be increased. The phosphors based on Mn^{2+}, Mn^{4+} and Eu^{3+} suffer from saturation effects at moderate photon fluxes, given their slow decay due to the forbidden intraconfigurational transitions. Applying a remote phosphor LED design can circumvent this problem to a certain extent.

10.2.5 Thermoluminescence and mechanoluminescence

Thermoluminescence (TL) is a valuable tool to evaluate the density and depth of the traps involved in energy storage processes. Quite often, a TL study is performed after illumination with a single wavelength or with a broad spectral distribution (e.g. from a Xe discharge lamp). Studying the wavelength dependency of the trap filling can however provide relevant information on the trapping routes [266, 448, 449].

Here, TL glow curves were obtained after exciting the CaZnOS:Mn phosphor in its various excitation bands. The results are shown in Fig. 10.10 and correspond to excitation by intraconfigurational $3d^5$ transitions (at 500 nm and 440 nm to the crystal field levels of the ^4G and ^4D terms respectively), the ligand-to-metal charge transfer (at 328 nm) and fundamental absorption in the CaZnOS host (at 280 nm). The four TL profiles were rescaled in order to make the high-temperature tail coincide. The absolute intensities of the different profiles differ over three orders of magnitude and are shown in the inset.

Upon inspection of the TL results, some features immediately stand out. The nature of the traps that can be reached upon nonlocal or local excitation is clearly different, as evidenced by the different TL profiles after fundamental absorption (280 nm) on the one hand and after local excitation of the Mn_{Zn} defect, be it through the LMCT (328 nm) or $3d^5$-$3d^5$ transitions (440 nm and 500 nm), on the other hand. Traps that are in the near vicinity of the Mn_{Zn} defect give rise to rather narrow TL bands, peaking around 240 K, 350 K while more shallow traps can be adressed after fundamental absorption, corresponding to a TL band peaking at 125 K and two broader TL bands that span the full temperature range.

Furthermore, the trapping efficiency differs significantly between the different routes, corresponding roughly to a factor of 40 between nonlocal traps and local traps that

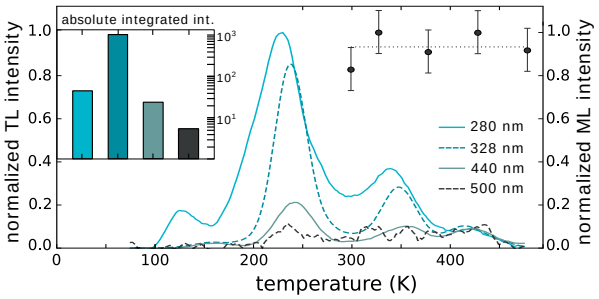

Figure 10.10 – Thermoluminescence (TL) profiles of CaZnOS:Mn upon excitation with various wavelengths at 75 K, obtained by heating the phosphor at 10 °C/min. The TL profiles were normalized such that the high-temperature tails coincided. The absolute intensities of the integrated TL profiles are shown on a logarithmic scale in the bar diagram in the inset. The data points display the mechanoluminescence intensity as a function of the temperature of the thermal cleaning of the CaZnOS:Mn sample before applying pressure, indicating up to which level traps are emptied. The horizontal line serves as a guide to the eye.

are reached after LMCT absorption (see inset of Fig. 10.10). As it was ensured that the phosphor was saturated after the charging, the effects of the different excitation fluxes and excitation efficiencies at the different wavelengths are not expected to account for the observed intensity difference. This indicates that the traps which are significant for the TL behavior are found close to the Mn_{Zn} defect and that charging is most effectively done through charge transfer excitation. This also implies that when the electronic structure of the traps which are responsible for TL are studied, one ideally has to consider defect clusters, accounting the Mn_{Zn} defect as well as the nearby intrinsic (or extrinsic) defect in the same computation. Defect clusters after all yield a different local electronic structure than individual defects as evidenced by the different TL curves in Fig. 10.10 and various computational and experimental studies [100, 199, 450, 451].

In order to investigate whether the same (local) traps are responsible for the thermoluminescence and the mechanoluminescence (ML), the intensity of the latter was recorded as a function of the temperature of a thermal cleaning in between the charging (by a Hg lamp) and the application of pressure. During the thermal cleaning, the sample is heated to a specified temperature, emptying occupied traps up to an associated depth. In this way it is possible to study the connection between the traps involved in ML and those in TL. For this, the CaZnOS powder was fixated in a silicon resin. These measurements were performed by scratching the films and simultaneously collecting the emitted light. The reproducibility of this measurement procedure was validated and the associated uncertainty estimated at 10% of the measured intensity.

The result is shown by the data points in Fig. 10.10. Within the experimental accuracy, the ML intensity remains constant in the available temperature range, i.e. a

bright mechanoluminescence is still observed after the CaZnOS:Mn phosphor was kept at 470 K for a significant time. This implies that the traps which are responsible for the ML in CaZnOS:Mn have a different nature than the traps that are responsible for the TL or that the ML mechanism itself is different, in contrast to previous assumptions [274, 417, 452]. Extending current experiment to higher temperatures might reveal the true origin of the mechanoluminescence.

The ML emission spectrum was found to be identical to the PL emission spectrum. This implies that the ML emission is the result of the $3d^5\ {}^4G({}^4T_1) \rightarrow 3d^5\ {}^6S({}^6A_1)$ transition as described in §10.2.2 and is opposed to the finding in [417] that the emission is due to an electron transfer from an isolated V'_{ZnO} Schottky defect to an isolated $Mn^{\bullet\bullet}_{Zn}$ defect.

Its resistance to high working temperatures is a unique feature of CaZnOS:Mn^{2+} which is absent for alternative ML phosphors such as $BaSi_2O_2N_2$:Eu^{2+} or $SrAl_2O_4$:Eu^{2+}, Dy^{3+}, unlocking potential technological applications for CaZnOS:Mn under circumstances where the more traditional ML phosphors cease to work.

10.3 Conclusions

This chapter featured a combined experimental-theoretical investigation of the insulating material CaZnOS and the luminescent material CaZnOS:Mn^{2+}. A single-particle band diagram and a many-particle multiplet energy level scheme of the Mn defect were constructed and discussed.

CaZnOS shows a rather low formation energy of 39 meV and -16 meV, calculated with respect to the experimental precursors ZnS and CaO, for PBE and PBE+U respectively, confirming the experimental finding that it is hard to prepare phase-pure CaZnOS powders.

The optical band gap of 4.27 eV makes CaZnOS a suitable compound to host optical dopants. DFT calculations and XAS measurements were used to show that manganese occupies a zinc site in the inorganic host, forming a neutral $Mn^{\times}_{Zn}$ defect. Band diagrams and the associated impurity levels were obtained from defect formation energies, calculated for large supercells. The thermodynamic impurity level (0/−) is formed in the forbidden band of CaZnOS, predicting a charge transfer transition, which was spectroscopically verified in the expected energy range.

The experimental low-temperature photoluminescence spectrum was well-resolved, allowing a precise determination of the multiplet energies of the $3d^5$ electron configuration. An effective crystal field Hamiltonian was fitted to the experimental spectrum yielding a small deviation of only 198 cm^{-1} upon inclusion of the spin-correlated crystal field.

Three local phonon energies could be accurately extracted from the low temperature emission spectrum, which were reproduced by the PBE+U calculation within 10 cm^{-1}.

A critical feasibility analysis of the potential of CaZnOS:Mn^{2+} for the use as red phosphor in white LEDs was performed. As red LED phosphor, this materials cannot achieve the high standards set by the red-emitting Eu^{2+} doped nitrides. Especially the low absorption strength, intrinsic to the forbidden nature of the luminescence transition, is an important issue.

Thermoluminescence glow curves were obtained upon charging through the different features in the excitation spectrum. This shows that different types of traps are addressed when exciting the host itself or locally at the activator site. Furthermore, the excitation band which was attributed to the ligand-to-metal charge transfer by the DFT study turns out to be a very efficient route for trapping and subsequent thermoluminescence.

Given that a thermal treatment up to 473 K does not influence the ML response, it is concluded that the underlying mechanism is different from the mechanism underlying the TL behavior, rejecting the prior assumption that the same traps are responsible for ML as for the TL peaks around 400 K. The ML is hence governed by deeper traps, which can be local or nonlocal, or by a completely different mechanism that is yet to be resolved.

This case study demonstrated that a correct interpretation of different types of energy level schemes can improve current understanding of luminescent materials and processes, paving the way for discovering new functional materials through thoughtful engineering.

Summary

Conclusions

This dissertation features an investigation of inorganic luminescent materials, activated by transition metal or lanthanide impurities. These materials, which are in this context referred to as phosphors, form a key building block of white LEDs, a technology that has already revolutionized, and will continue to revolutionize, electric lighting in terms of functionality, design and consumption. LED technology is not limited to lighting, it improves display technology in terms of color gamut, contrast and user experience. In this work, phosphors are developed, investigated and optimized for either lighting or display applications, the former requiring broadband emission, guaranteeing a pleasant light source providing a good color rendering, the latter requiring narrow emission, allowing displays with a superior color range. Next to this spectral condition, five other requirements have to be fulfilled simultaneously before a material can be considered as a good candidate for applications. These are described in chapter 1.

Given the different requirements that have to be validated for every candidate-material and the huge number of possible combinations between the available activator ions and thinkable host materials, an urge has originated for a thoughtful engineering of materials. Two different strategies are explored in this dissertation, *i.e.* computational methods, calculating properties of luminescent materials in different mathematical formalisms and rules, and the mining of scientific literature in the hope to excavate the luminescent material one was searching for. Both strategies require few or no experimental input.

Computational methods can be rooted in a strong theoretical framework, being constructed by the careful inspection of empirically found trends and correlations or find itself into the spacious gray zone in between both extremes. No matter which computational technique is applied, it is of great importance to know exactly which assumptions are made, implicit or explicit, their impact on the predicted physical properties and the uncertainties or systematic errors that are to be expected. Energy level schemes are the computational tools that stand out to describe luminescent properties and happen to be intrinsic quantum mechanical concepts. For this reason, it is endeavored in the first chapters of this work to give a detailed description of how different luminescence phenomena, be them desirable or undesirable for ap-

plications, can be understood in terms of quantum mechanical theory. Chapter 2 offers the theoretical basis by illuminating those aspects of the theory of light, matter and their interaction to understand spectroscopic experiments with phosphors. Chapter 3 builds on this by focusing on the matter part. Very useful approximations are introduced, allowing to consider the nuclear and electronic motion separately to a certain extent. The nuclear motion governs the microscopic dynamics that are associated with luminescent properties such as spectral shapes, Stokes shifts, temperature-dependence and non-radiative decay of excited states, while the electronic motion is responsible for the luminescent transitions themselves.

To describe the electronic motion which is associated with luminescent transitions, two different types of energy level schemes exist, *i.e.* single-particle and many-particle schemes. Whatever theoretical framework or computational technique one uses, the resulting energy level scheme will always be one of these two. Chapters 4 and 5 discuss respectively the relevance of many-particle and single-particle energy level schemes in the study of luminescent materials.

Crystal field theory is used to explain the use of many-particle or multiplet schemes in chapter 4. In simplified terms, this theory starts from the atomic states of the activator ion and regards the host crystal as a perturbation. A Python program was developed, allowing crystal field calculations for the electron configuration that are relevant in the study of phosphors. This chapter is rather extensive, allowing to cast a look under the hood of the Python code and appreciating the assumptions and limitations of crystal field theory. The theory is illustrated and the developed program validated by applying it to the emblematic Dieke diagram and the Tanabe-Sugano diagrams for lanthanide and transition metal ions respectively. Both diagrams can be considered as historical landmarks. Of more recent relevance are the excited $4f^{N-1}5d^1$ configurations of lanthanide ions which are essential in many LED phosphors. Many-particle schemes are constructed for the currently relevant LED phosphor K_2SiF_6:Mn^{4+}, explaining its peculiar decay behavior and to the well-known afterglow material $SrAl_2O_4$:Eu^{2+}, explaining the origin of a somewhat mysterious blue emission which is only present at low temperatures.

In chapter 5, band theory is explained as an example of a single-particle theory. It is addressed how defects alter the properties in a perfect crystal structure by introducing discrete levels into the band gap of the host material. For certain types of impurities, these impurity single-particle levels give a good idea of the luminescence properties, while for the activators that are of interest in this work, the single-particle description intrinsically fails due to electron correlation. In order to stick to the single-electron picture, a generalization of impurity levels, called charge-state transition levels, is introduced, attaching meaning to impurity levels of highly correlated activators. Density functional theory is discussed with the goal to calculate charge-state transition levels, while illuminating the limitations of the technique and focusing on the meaning of the obtained results. Finally, luminescent transitions involving single-particle states of both the host and activator ion are discussed.

During the last 40 years, several empirical methods and relationships were devised for constructing single-particle schemes, containing the charge-state transition levels of lanthanide defects in wide band gap solids. Chapter 6 reviews these empirical rules and explains the notable systematic in lanthanide spectroscopy. Up to now, an unbiased assessment of the accuracy of the obtained values of the calculated parameters is still lacking to a large extent. To address this issue, error margins for calculated electronic and optical properties are deduced. It is found that optical transitions can be predicted within an acceptable error margin, while the description of phenomena involving conduction band states is limited to qualitative interpretation. This is due to the large error margins for physical observables, such as thermal quenching temperature, corresponding to standard deviations in the range 0.3-0.5 eV for the relevant energy differences. As an example, the electronic structure of $CaGa_2S_4$:Ln^{Q+} is determined, taking the experimental spectra of Ln^{Q+} = Ce^{3+}, Eu^{2+} and Tm^{3+} as input. Two different approaches to obtain the shape of the zig-zag curves connecting the 4f levels of the different lanthanides are explored and compared. When these empirical rules are applied, it is implicitly assumed that all lanthanide ions form isostructural defects. However, in practice, multiple nonequivalent defects related to the same lanthanide can occur or different lanthanides can even incorporate in different ways. The consequences of these complications on the impurity energy levels are discussed. It seems that small structural differences around the lanthanide dopant can give rise to important spectral differences in its emission. These are not always clearly reproduced by the charge-state transition level schemes. Improvements to the existing procedure are suggested, potentially decreasing the uncertainties, which are then applied to the lanthanide ions in the host crystals $SrAl_2O_4$, $Sr_2Si_5N_8$ and $SrGa_2S_4$.

In the second part of this dissertation, multiple phosphors are selected based on reports in scientific literature describing promising luminescent properties. In these chapters, it is described how the phosphors are prepared and it is validated to which extent the technological requirements are fulfilled. To investigate the quantum efficiency of the phosphors in a quantitative way, next to the more traditional experimental techniques, a setup with an integrating sphere was designed, purchased and characterized (see chapter 7).

The luminescence properties of the blue emitting phosphor $Sr_{0.25}Ba_{0.75}Si_2O_2N_2$:$Eu^{2+}$ are extensively investigated and compared to other members of the europium doped $MSi_2O_2N_2$ oxonitridosilicates in chapter 8. This phosphor features strong $4f^65d^1 \leftrightarrow 4f^7$ luminescence originating from the Eu^{2+} ion, with a narrow emission band peaking at 467 nm and a full width at half maximum (FWHM) of only 41 nm. Thermal quenching of the blue luminescence only sets in above 450 K, making this material an interesting candidate as LED conversion phosphor. The fast decay of the luminescence prevents the phosphor to be susceptible to saturation effects at high excitation fluxes. Furthermore it is proven to be chemically stable against moisture. The only drawback is the relatively low quantum efficiency of the synthesized powder, provisionally preventing this material to be used in applications. In addition, the phosphor features a weak yellow emission band, originating from small domains

featuring a different crystal structure. It is shown that the majority of the powder grains only exhibit blue emission. Finally, the spectrum of a white LED, based on a UV pumping LED and three (oxo)nitridosilicate phosphors is simulated in order to assess the usefulness of blue phosphors in LEDs for lighting. Only a marginal improvement in terms of color quality can be achieved with a narrow banded phosphor, at the expense of a decrease in luminous efficacy and overall electrical to optical power efficiency.

Subsequently, in chapter 9, the interesting class of thiogallate and thioaluminate host materials is considered. From the general overview of their properties upon doping with divalent europium, two thiogallates, $SrGa_2S_4$ and $ZnGa_2S_4$ are selected for further investigation. The luminescent properties of $Sr_{1-x}Eu_xGa_2S_4$ phosphors are studied over a wide dopant concentration range (x = 0.01-0.3) as function of temperature. The phosphors show a saturated green emission over the entire studied range, with a typical peak wavelength around 536 nm and a FWHM of 50 nm. The internal quantum efficiency is 71% for x = 0.04. For this concentration, the emission intensity at 400 K is still 90% of the intensity at room temperature. By measuring both decay and thermal quenching profiles as a function of europium concentration, the emission properties can be explained on the basis of the local environment of the europium ions in the lattice. As $SrGa_2S_4$:Eu^{2+} achieves a very good score with respect to the technological requirements, a fully optimized powder is used to deliver a proof-of-concept remote phosphor white LED, suitable for display applications. The red component is provided by CdSe/CdS quantum dots and different remote *hybrid* phosphor layers are prepared, featuring different stacking geometries of the green and red components. The optimized white LEDs show favorable properties such as internal quantum efficiencies in the 75-80% range, high luminous efficacies and saturated primary colors. The different stacking geometries provide a means to select the most cost-efficient layer design given the relative cost of the green powder and red quantum dot components.

The second europium doped thiogallate which is studied is $ZnGa_2S_4$:Eu^{2+}. This material has been reported as a saturated green emitting phosphor, suitable as conversion phosphor in white LEDs for lighting or displays. No direct proof for the incorporation of Eu^{2+} in $ZnGa_2S_4$ has however been given. Here, X-ray diffraction (XRD), cathodoluminescence in electron microscopy (SEM-CL) and X-ray absorption spectroscopy (XAS) are combined to study the incorporation of the europium ions in the host material. The previously reported green luminescence was found to originate from small amounts of unintentionally formed $EuGa_2S_4$, and not from europium ions incorporated into $ZnGa_2S_4$. $EuGa_2S_4$ has a low quantum efficiency (< 20%) and shows strong thermal quenching, already below room temperature. The XAS data analysis suggests that a certain amount of europium might occupy octahedral voids inside the zinc thiogallate lattice in a divalent state. The zinc ion next to these interstitial dopants is then removed for charge compensation. Notwithstanding the possible, but limited, incorporation of Eu^{2+} in $ZnGa_2S_4$, these ions do not activate any luminescence as was shown with SEM-CL.

The final chapter, chapter 10, features a combined experimental-theoretical study of the luminescent material CaZnOS:Mn^{2+}. This compound features orange broadband luminescence, peaking at 612 nm, originating from intraconfigurational $3d^5$ transitions within the Mn^{2+} ion. DFT calculations at PBE+U level and X-ray absorption spectroscopy indicate that the Mn impurity is incorporated on the Zn site in a divalent charge state. The electronic structure of the Mn_{Zn} defects is obtained by two complementary techniques. On the one hand, impurity levels in the band diagram, *i.e.* the single-particle energy level scheme, are obtained from defect formation energies calculated with PBE+U. On the other hand, the excited state landscape of the Mn^{2+} $3d^5$ electron configuration is assessed through the spin-correlated crystal field, yielding the multiplets, *i.e.* the many-particle energy level scheme, of the optical dopant. Experimental photoluminescence spectra at room and low temperature are analyzed in detail and a good correspondence is found between the calculated energy levels and the experimental transition energies. The electron-phonon interaction is investigated from the luminescence spectra showing that at least three different vibrational modes are active in the transition. These are also found in the Mn-projected phonon density of states. This case study demonstrates how physical information can be extracted from the two complementary, but different types of energy level schemes. The CaZnOS:Mn^{2+} phosphor is finally evaluated for the use as red phosphor in white LEDs. Despite its favorable emission spectrum, the forbidden nature of the intraconfigurational $3d^5$ transitions yield a much too low external quantum efficiency.

Perspectives

It is clear that white LEDs, and the conversion phosphors being an essential part of it, will remain relevant technologies in the future and will continue to consolidate their increasing market share in lighting and display markets. Although an incredible advantage has already been achieved on the phosphor point-of-view, going from cold white YAG:Ce^{3+}-based LEDs towards two- or three-phosphor LEDs with a well-balanced color, incremental improvements can still be expected in the future.

In this work, phosphors based on different types of activator ions were investigated, largely inspired by the unstable prices of lanthanides precursors. Straightforward alternatives for the dipole allowed $4f^N \leftrightarrow 4f^{N-1}5d^1$ transitions of Ce^{3+} and Eu^{2+} are the dipole forbidden intraconfigurational $4f^N$ or $3d^N$ transitions of respectively lanthanides and transition metals. A huge drawback of both transitions is their forbidden nature, prohibiting an efficient excitation with blue pump light, making it difficult to achieve the required values for the absorption around 80%. The external quantum efficiency is hence limited by the selection rules. Sensitizing these ions by another absorbing ion is a straightforward solution, potentially showing high internal *and* external quantum efficiency, at least in theory. Up to now, no convincing lanthanide-free system exploiting this strategy can be found. An alternative from this series which is possibly viable is the tetravalent Mn ion, Mn^{4+}. Recent reports indicate that this ion seems to suffer less from a low external quantum efficiency than its fellow 3d ions. Future research, and specifically critical feasibility studies,

have to be performed to unambiguously assess whether this small ion can dethrone the dominant lanthanide ions. Until then, the ultimately color-tunable divalent europium ion, Eu^{2+} is still the king.

Regarding energy level modeling, novel empirical rules can be expected, complementing the existing empirical rules for lanthanide, transition metal or s^2 ions. These rules might relate properties of ions of different groups or limit the required experimental input even further. Despite that, a rational footnote should however be made that the most obvious empirical rules have probably already been found. Critically scrutinizing the data used to construct the existing rules might decrease the uncertainty of predictions to some extent, although no wonders can be expected from this angle.

From the quantum mechanical side, progress is to be expected especially from the high-level-of-theory side. The limitations pertaining to computational resources become less problematic due to rapidly increasing computer power. A large-scale computational screening of dopant-host combinations can hence be expected in the near to mid-long term. A fundamental restriction of density functional theory remains however the inability to describe excited states. Possibly more important, the most complete computational techniques, such as multireference calculations, will become more standard to interpret spectroscopic experiments, potentially leading to new insights into functional materials.

In general, despite what is often claimed, designing novel functional materials with well-defined properties, solely from the computational drawing board is currently still far away. The reason for this is not only the barrier of computational cost, but also the error margins of computational results which are still largely exceeding the stringent restrictions by technological requirements. This pertains to essentially all computational techniques with predictive potential. The distance in energy between blue and red light is after all only 850 meV, a tiny energy interval which contains all colors of the rainbow!

SAMENVATTING

Conclusies

Deze verhandeling bestaat uit een onderzoek naar anorganische lichtgevende of luminescente materialen die geactiveerd worden door transitiemetaal- of lanthanide-onzuiverheden. Deze materialen, die in deze context vaak fosforen genoemd worden, zijn een belangrijk onderdeel van witte leds, een technologie die revolutionair is gebleken voor elektrische verlichting op het vlak van functionaliteit, ontwerp en verbruik. De technologie van witte leds is echter niet beperkt tot verlichting, maar behelst ook beeldschermtechnologie waar belangrijke verbetering op het vlak van kleurgamma, contrast en gebruikservaring werden geboekt. In dit werk worden fosforen ontwikkeld, onderzocht en geoptimaliseerd voor het gebruik in verlichting of beeldschermen. Verlichting noodzaakt brede emissiebanden opdat het licht als aangenaam wordt ervaren en de kleuren van belichte objecten correct worden weergegeven. Beeldschermen vereisen daarentegen smalle emissiebanden teneinde een superieur kleurengamma te verkrijgen. Naast deze spectrale voorwaarden, kunnen nog vijf andere voorwaarden opgesteld worden waaraan een fosfor tegelijkertijd moet voldoen vooraleer in aanmerking te komen voor toepassingen. Specifiek moet de fosfor een hoge absorptie hebben voor het blauwe of nabij-UV pomplicht, getuigen van een hoge conversie-efficiëntie die stabiel blijft bij hogere temperaturen, een voldoende snel luminescent verval vertonen opdat sublineare gedrag bij verhoogde excitatie-intensiteiten vermeden wordt en chemisch stabiel zijn over lange tijdspannes. Deze voorwaarden worden beschreven in hoofdstuk 1.

Gegeven deze zes noodzakelijke voorwaarden en het enorme aantal dopant-gastmateriaalcombinaties dat moet worden gevalideerd, bestaat er een zekere noodzaak voor een voor een bedachtzaam ontwerp van deze functionele materialen. Twee verschillende aanpakken worden gebruikt in deze thesis, namelijk computationele technieken waarbij eigenschappen van fosforen berekend worden in verschillende formalismes en regels en het ontginnen van de talrijke wetenschappelijke literatuur in de hoop het luminescente materiaal met de perfecte eigenschappen te vinden. Het voordeel van beide technieken is dat ze weinig experimentele inbreng vergen.

Computationele technieken kunnen wortelen in een sterke theoretische basis, maar evengoed ontworpen zijn door met veel zin voor detail te zoeken naar empirische trends in een groot aantal experimentele studies. De grijze zone tussen deze ex-

tremen puilt bovendien uit van de beschikbare technieken. Ongeacht welke computationele techniek men verkiest, is het belangrijk om exact te weten welke aannames - die zowel impliciet als expliciet kunnen zijn - gemaakt worden, wat hun weerslag is op de fysische eigenschappen die voorspeld worden en met welke onzekerheden en systematische fouten deze voorspellingen gemaakt worden. Energieniveauschema's zijn de computationele hulpmiddelen bij uitstek voor de studie van luminescente materialen. Aangezien energieniveauschema's intrinsiek kwantummechanische concepten zijn, wordt in de eerste hoofdstukken gepoogd om een gedetailleerde beschrijving te geven van hoe de verschillende luminescente fenomenen, zowel de wenselijke als de te vermijden fenomenen, kunnen begrepen worden vanuit de kwantummechanica. Hoofstuk 2 geeft een theoretische basis door de aspecten die relevant zijn voor spectroscopische experimenten uit de theorie van licht en materie te belichten. Hoofdstuk 3 bouwt hierop verder door de nadruk te leggen op het materie aspect. Nuttige benaderingen worden ingevoerd die toelaten om de nucleaire en elektronische bewegingen tot op zekere hoogte apart te behandelen. De beweging van de atoomkernen geeft aanleiding tot de microscopische dynamica die wordt geassocieerd met luminescente eigenschappen zoals spectrale vormen, de Stokesverschuiving, temperatuursafhankelijkheid en het niet-radiatief verval van aangeslagen toestanden. De beweging van de elektronen worden daarentegen verantwoordelijk geacht voor de luminescente transities zelf en wordt verder besproken in de volgende hoofdstukken.

Om de elektronische beweging te beschrijven bestaan er twee soorten energieniveauschema's, namelijk ééndeeltjes- en veeldeeltjesenergieschema's. Ongeacht welk theoretisch kader of welke computationele techniek men gebruikt, het resulterende energieniveauschema zal steeds tot één van beide categorieën behoren. Hoofdstukken 4 en 5 bespreken de relevantie van respectievelijk veeldeeltjes- en ééndeeltjesenergieschema's in de studie van luminescente materialen.

Kristalveldtheorie wordt gebruikt om het gebruik van veeldeeltjesenergieschema's of multipletschema's toe te lichten in hoofdstuk 4. Eenvoudig gesteld gaat deze theorie uit van de atomaire toestanden van het activatorion en beschouwt ze het gastkristal als verstoring van deze toestanden. Een Pythonprogramma werd ontwikkeld dat kristalveldberekeningen kan uitvoeren voor de elektronconfiguraties die voorkomen in luminescente materialen. Dit hoofdstuk is redelijk uitgebreid met als dubbel doel een blik te werpen onder de motorkap van het Pythonprogramma en een beter idee te krijgen van de aannames en beperkingen van kristalveldtheorie. De theorie wordt geïllustreerd en het computerprogramma gevalideerd aan de hand van het symbolische Dieke diagram en de Tanabe-Suganodiagrammen, beide historische mijlpalen in het onderzoek naar lanthaniden en transitiemetalen. Van meer recent belang zijn de aangeslagen $4f^{N-1}5d^1$ configuraties van lanthanide-ionen die essentieel zijn voor de werking van veel ledfosforen. Veeldeeltjesschema's worden opgesteld voor de ledfosfor K_2SiF_6:Mn^{4+} en helpen om het afwijkende vervalgedrag van deze fosfor te verklaren. Energieschema's worden eveneens opgesteld voor de bekende nalichtfosfor $SrAl_2O_4$:Eu^{2+} om de oorsprong van een mysterieuze blauwe emissie, die enkel

zichtbaar is op lage temperatuur, te achterhalen.

In hoofdstuk 5 wordt de theorie van energiebanden uiteengezet als voorbeeld van een ééndeeltjestheorie. Er wordt geïllustreerd hoe defecten de eigenschappen van perfecte kristallen kunnen beïnvloeden door discrete energieniveaus in de verboden zone van het gastmateriaal te genereren. Voor bepaalde types van onzuiverheden geven de ééndeeltjesonzuiverheidsniveaus een goede beschrijving van de luminescente eigenschappen, terwijl dit niet het geval is voor de activatoren die in dit werk onderzocht worden. Hierbij faalt de ééndeeltjesbeschrijving fundamenteel door de manifeste elektroncorrelatie. Om het ééndeeltjesmodel toch niet helemaal af te danken, wordt er een veralgemening van onzuiverheidsniveau geïntroduceerd, met name de ladingstoestandtransitieniveaus, die ook betekenis hebben voor de sterk gecorreleerde metaalonzuiverheden. Dichtheidsfunctionaaltheorie wordt besproken met als doel om ladingstoestandtransitieniveaus te berekenen. De beperkingen van de techniek worden besproken en de nadruk wordt gelegd op de betekenis van de oplossingen van deze theorie. Tenslotte worden luminescente transities besproken waarbij zowel ééndeeltjestoestanden van de activator als het gastmateriaal betrokken zijn.

Tijdens de laatste 40 jaar werden verschillende empirische methodes en relaties vooropgesteld die toelaten om ééndeeltjesenergieschema's met ladingstoestandtransitieniveaus voor lanthanidedefecten in gastmaterialen te construeren. Hoofdstuk 6 geeft een overzicht van deze empirische regels en gaat verder in op de opmerkelijke systematiek die teruggevonden wordt in de optische spectra van lanthaniden. Tot dusver ontbrak het aan een objectieve onzekerheidsanalyse van de fysische grootheden die berekend worden met deze empirische regels. Om hieraan tegemoet te komen, worden foutenmarges afgeleid voor de berekende elektrische en optische eigenschappen. Er wordt bevonden dat optische transities met een aanvaardbare foutenmarge kunnen worden voorspeld terwijl de beschrijving van fenomenen waarbij conductiebandtoestanden betrokken zijn beperkt wordt tot kwalitatieve interpretaties door de grote foutenmarges in de fysische grootheden. Zo worden bijvoorbeeld temperaturen voor thermische uitdoving voorspeld met een foutenmarge van 0.3-0.5 eV in de geassocieerde energiebarrière. Ter illustratie van de empirische regels wordt de elektronische structuur van $CaGa_2S_4$:Ln^{Q+} bepaald, gebruik makende van de experimentele spectra van Ln^{Q+} = Ce^{3+}, Eu^{2+} en Tm^{3+}. Twee verschillende aanpakken om de vorm van de zig-zagcurves die de 4f ladingstoestandtransitieniveaus verbinden worden vergeleken. Bij het toepassen van deze empirische regels wordt het impliciet verondersteld dat de lanthanide-ionen isostructurele defecten vormen. In de praktijk is het echter al gebleken dat hier niet altijd aan voldaan wordt en dat verschillende niet-equivalente defecten horend bij hetzelfde lanthanide kunnen voorkomen of dat zelfs verschillende lanthaniden zich verschillend gedragen met betrekking tot incorporatie in de kristalstructuur. De gevolgen van de complicaties op de onzuiverheidsniveaus worden besproken. Het blijkt zo te zijn dat kleine structurele verschillen rond de dopant aanleiding kunnen geven tot belangrijke spectrale verschillen, voornamelijk in het emissiespectrum. Deze verschillen worden vaak niet duidelijk teruggevonden in de ladingstoestandtransitieniveaus. Verbeteringen

in de bestaande procedure worden voorgesteld en toegepast op de gastmaterialen $SrAl_2O_4$, $Sr_2Si_5N_8$ en $SrGa_2S_4$. De voorgestelde aanpassingen kunnen mogelijks een verkleining van de onzekerheden op de empirische regels tot gevolg hebben.

In het tweede deel van deze thesis worden verschillende fosforen geselecteerd op basis van de wetenschappelijke literatuur waarin beloftevolle luminescente eigenschappen worden beschreven. In deze hoofstukken wordt beschreven hoe deze materialen worden gesynthetiseerd en in welke mate zij voldoen aan de technologische voorwaarden. Om naast de standaard experimentele technieken ook de kwantumefficiënties van fosforen kwantiatief te bestuderen, werd een opstelling met een integrerende sfeer ontworpen, aangeschaft en gekarakteriseerd (zie hoofstuk 7).

De luminescente eigenschappen van de blauw emitterende fosfor $Sr_{0.25}Ba_{0.75}Si_2O_2N_2:Eu^{2+}$ wordt uitgebreid onderzocht en vergeleken met de andere leden van de europium gedoteerde $MSi_2O_2N_2$ oxonitridosilicaten in hoofdstuk 8. Deze fosfor vertoont sterke $4f^6 5d^1 \leftrightarrow 4f^7$ luminescentie door het Eu^{2+} ion met een smalle emissieband die piekt bij 467 nm en een piekbreedte (FWHM) van slechts 41 nm heeft. Thermische uitdoving van de blauwe emissie start pas boven 450 K wat dit materiaal een interessante kandidaat-ledfosfor maakt. Het snelle verval van de luminescentie voorkomt dat verzadigdingseffecten zullen optreden bij hoge excitatie-intensiteiten. Bovendien is dit materiaal chemisch stabiel in een vochtige omgeving. Het enige bezwaar tegen dit materiaal is de relatief lage kwantumefficiëntie van het gesynthetiseerde poeder. Dit verhindert voorlopig de toepassing. Bovendien vertoont dit materiaal een bijkomende, evenwel zwakke, gele emissieband. Deze vindt zijn oorsprong in kleine domeinen met een andere kristalstructuur. Niettemin vertonen de meeste poederdeeltjes uitsluitend blauwe emissie. Tenslotte wordt het spectrum van een witte led, gebaseerd op een UV pompled en drie (oxo)nitridosilicaatfosforen gesimuleerd om de zin of onzin van blauwe fosforen in leds voor verlichting te valideren. Enkel een marginale verbetering in kleurkwaliteit kan bereikt worden met een smalbandige blauwe fosfor en dit ten koste van een afname in visueel rendement en elektro-optische efficiëntie.

Vervolgens wordt in hoofdstuk 9 de interessante klasse van de thiogallaat en thioaluminaat gastmaterialen beschouwd. Uit het algemene overzicht van hun eigenschappen bij europiumdotering worden twee gastmaterialen, $SrGa_2S_4$ en $ZnGa_2S_4$ uitgekozen voor een verder studie. De luminescente eigenschappen van de $Sr_{1-x}Eu_xGa_2S_4$ fosforen worden bestudeerd voor een breed interval van dopantconcentraties (x = 0.01-0.3) in functie van de temperatuur. De fosforen vertonen een verzadigde groene emissie voor alle concentraties met een typische piekgolflengte van 536 nm en een FWHM van 50 nm. De interne kwantumefficiëntie is 71% voor x = 0.04. Bij deze europiumconcentratie is de intensiteit bij 400 K nog steeds 90% van de intensiteit bij kamertemperatuur. Door zowel het vervalgedrag als de thermische uitdoving te meten als functie van de europiumconcentratie kunnen de emissie-eigenschappen uitgelegd worden op basis van de lokale omgeving van de europiumionen in het kristalrooster. Vermits $SrGa_2S_4:Eu^{2+}$ een goede score haalt op de technologische voorwaarden, wordt een volledige geoptimaliseerd poeder ge-

bruikt om een experimenteel ontwerp van een witte led voor beeldschermen te maken waarbij de fosforen op een zekere afstand van de blauwe ledchip zitten. Als rode component worden CdSe/CdS kwantumstippen gebruikt. Hiermee worden verschillende *hybride* fosforlagen gemaakt met een verschillende stapeling van groen en rood. De geoptimaliseerde leds vertonen gunstige eigenschappen zoals een interne kwantumefficienties van 75-80%, een hoog visueel rendement en verzadigde primaire kleuren. De verschillende stapelingen laten toe om een kostenefficiënt ontwerp van de luminescente laag te kiezen, ingegeven door de huidige prijzen van de groene poederfosfor en de rode kwantumstippen.

Het tweede europium gedoteerd thiogallaat dat bestudeerd wordt is $ZnGa_2S_4$:Eu^{2+}. Dit materiaal is gerapporteerd als een verzadigd groene fosfor en geschikt als conversiefosfor voor witte leds in beeldschermen en verlichting. Rechtstreeks bewijs voor de incorporatie van Eu^{2+} in $ZnGa_2S_4$ is evenwel niet beschikbaar. In dit werk worden X-straaldiffractie (XRD), kathodeluminescentie in een rasterelektronenmicroscoop (SEM-CL) en X-straalabsorptiespectroscopie (XAS) gecombineerd om de incorporatie van het europium te bestuderen. Er wordt gevonden dat de eerder gerapporteerde groene emissie het gevolg is van kleine hoeveelheden ongewenst $EuGa_2S_4$ dat gevormd wordt en niet van europiumionen in $ZnGa_2S_4$. $EuGa_2S_4$ heeft een lage kwantumefficiëntie (< 20%) en vertoont een sterke thermische uitdoving die al actief is onder kamertemperatuur. De analyse van de XAS data suggereert dat een zeer kleine hoeveelheid Eu^{2+} mogelijks octaëdrische holten in de $ZnGa_2S_4$ structuur opvult. Een zinkion verdwijnt dan in de buurt van het interstitieel omwille van de ladingscompensatie. Niettegenstaande de mogelijke, doch beperkte incorporatie van Eu^{2+} in $ZnGa_2S_4$, activeren deze ionen geen enkele luminescentie zoals werd aangetoond met SEM-CL.

In het laatste hoofdstuk, hoofdstuk 10 wordt een gecombineerd experimentele-theoretische studie toegelicht naar het luminescente materiaal CaZnOS:Mn^{2+}. Dit materiaal vertoont een oranje breedbandemissie die piekt bij 612 nm en die afkomstig is van intraconfigurationele $3d^5$ transities binnenin het mangaanion. DFT-berekeningen op PBE+U niveau en X-straalabsorptiespectroscopie tonen aan dat de Mn-onzuiverheid inbouwt op een Zn-site in een divalente ladingstoestand. De elektronische structuur van het Mn_{Zn} defect wordt beschreven aan de hand van twee complementaire technieken. Enerzijds worden ladingstoestandtransitieniveaus in de verboden zone berekend, dus een ééndeeltjesenergieschema opgesteld met PBE+U. Anderzijds wordt het landschap van geëxciteerde multipletten van de Mn^{2+} $3d^5$ configuratie bestudeerd via het spin-gecorreleerde kristalveld waardoor een veeldeeltjesenergieschema bekomen wordt. Experimentele fotoluminescentiespectra bij kamer- en lage temperatuur worden in detail geanalyseerd en een goede overeenkomst tussen de berekende en experimentele energieniveaus wordt bekomen. De elektron-fononkoppeling wordt bestudeerd aan de hand van de luminescentiespectra en minstens drie verschillende vibrationele modes die actief zijn tijdens de transitie worden gedestilleerd. Dezelfde vibrationele modes worden ook gevonden in de Mn-geprojecteerde fonontoestandsdichtheid. Deze studie toont aan hoe fysische informatie kan worden verkregen uit de twee complementaire, maar verschillende types

energieschema's. CaZnOS:Mn^{2+} wordt uiteindelijk geëvalueerd als rode fosfor in witte leds. Ondanks het gunstige emissiespectrum verhindert de lage externe kwantumefficiëntie van de intraconfigurationele $3d^5$ transities de toepassing van dit materiaal in witte leds.

Perspectieven

Het is duidelijk dat witte leds, en de conversiefosforen die hier een essentieel deel van uitmaken, een relevante technologie zullen blijven en een groeiende aandeel van de verlichtings- en beeldschermmarkten zullen consolideren. Hoewel er reeds een ongeloofelijke vooruitgang werd geboekt vanuit het fosforstandpunt, waarbij koudwitte YAG:Ce^{3+}-gebaseerde leds vervangen werden door twee- of driefosforleds met een goed gebalanceerde kleur, kunnen er nog incrementale verbeteringen verwacht worden in de toekomst.

In dit werk werden fosforen die gebaseerd zijn op verschillende types activatorionen onderzocht, voornamelijk ingegeven door de onstabiele prijzen van de lanthaniden. Voor de hand liggende alternatieven voor de dipool-toegelaten $4f^N \leftrightarrow 4f^{N-1}5d^1$ transities van Ce^{3+} en Eu^{2+} zijn de dipool-verboden intraconfigurationele $4f^N$ en $3d^N$ transities van respectievelijk lanthaniden en transitiemetalen. Een groot nadeel van deze beide transities is hun verboden karakter dat een hoge excitatie-efficiëntie met blauw licht, overeenkomstig met gewenste absorpties rond 80%, verhindert. De externe kwantumefficiëntie wordt dus beperkt door de selectieregels. Een voor de hand liggende oplossing is het sensiteren van deze ionen door het toevoegen van een bijkomend, absorberend ion. Op die manier worden potentieel hoge interne *en* externe kwantumefficiënties gehaald, ten minste in theorie. Vooralsnog bestaat er geen overtuigend lanthanide-vrij systeem dat deze strategie toepast. Een alternatief uit deze reeks dat mogelijks haalbaar is, is het tetravalente Mn-ion, Mn^{4+}. Recente rapporten suggereren dat dit ion minder last lijkt te hebben van een lage externe kwantumefficiëntie dan de andere 3d ionen. Kritische haalbaarheidsstudies moeten ondubbelzinnig kunnen aantonen of dit kleine ion de dominante lanthanide-ionen van de troon kan stoten. Tot dan blijft het Eu^{2+} ion, met zijn uniek kleurenpalet, koning.

Aangaande energieniveaumodellering kunnen nieuwe empirische regels nog verwacht worden die de bestaande regels voor lanthaniden, transitiemetalen en s^2 ionen aanvullen. Deze regels zullen mogelijks eigenschappen van ionen uit verschillende reeksen relateren of de benodigde experimentele invoer verder beperken. Naast deze stelling moet echter een rationele voetnoot geplaatst worden, namelijk dat het redelijk is om aan te nemen dat de meest toegankelijke empirische regels al gevonden zijn. Het kritisch onder de loep nemen van de bestaande data kan mogelijks de bestaande regels enigszins verfijnen en dus de onzekerheden van voorspellingen verkleinen. Hiervan mogen echter ook geen wonderen verwacht worden.

Vanuit kwantummechanische zijde kan nog enige vooruitgang verwacht worden, meer specifiek van de dieper gewortelde theoretische kaders die aanleiding geven

tot complexere berekeningen, met dank aan de toenemende rekenkracht. Een grootschalige computationele doorlichting van grote aantallen dopant-gastrooster combinaties kan bovendien ook verwacht worden op de korte tot middellange termijn. Een fundamentele beperking van dichtheidsfunctionaaltheorie blijft wel het onvermogen om aangeslagen toestanden correct te beschrijven. Wat misschien interessanter is, is dat de meest complete computationele technieken zoals multireferentieberekeningen meer standaard zullen worden en dat hierdoor de interpretatie van spectroscopische experimenten gefaciliteerd kan worden en vermoedelijk aanleiding kan geven tot frisse, nieuwe inzichten.

In het algemeen, en in tegenstelling tot wat vaak beweerd wordt, ligt het computationeel ontwerpen van nieuwe functionele materialen met vooraf gedefinieerde eigenschappen nog niet binnen handbereik. De reden hiervoor is niet enkel de barrière van de computationele kost, maar voornamelijk de strenge restricties die de technologische voorwaarden vooropstellen. De afstand in energie tussen blauw en rood licht is immers maar 850 meV, een zeer klein energie-interval dat alle kleuren van de regenboog bevat!

List of abbreviations

AOM	angular overlap model
BLYP	Becke-Lee-Yang-Parr
BSE	backscattered electrons
CASSCF	complete active space self-consistent field
CASPTn	complete active space perturbation theory (n^{th} order)
CB	conduction band
CCD	charge-coupled device
CCF	correlation crystal field
CCFL	cold cathode fluorescent lamp
CF	crystal field
CFP	coefficient of fractional parentage
CFS	crystal field splitting
CFT	crystal field theory
CI	configuration interaction
CIE	*Comité Internationale de l'Eclairage*
CL	cathodoluminescence
CN	coordination number
CRT	cathode ray tube
CT	charge transfer
CTM	charge transfer multiplet
DFT	density functional theory
E1	electric dipole (transition)
E2	electric quadrupole (transition)
EBU	European Broadcasting Union
ECSO	electrostatically correlated spin-orbit
ECM	exchange charge model
EDX	energy-dispersive X-ray spectroscopy

EL	electroluminescence
EPR	electron paramagnetic resonance
EXAFS	extended X-ray absorption fine structure
FC	Franck-Condon
FFT	fast Fourier transform
FWHM	full width at half maximum
GGA	generalized gradient approximation
HF	Hartree-Fock
HRBE	host referred binding energy
HRTEM	high resolution TEM
HS	high spin
ICCD	intensified CCD
ICSD	inorganic crystal structure database
IPM	independent particle model
IR	infrared
irrep	irreducible representation
ITE	impurity trapped exciton
IUPAC	International Union of Pure and Applied Chemistry
IVCT	intervalence charge transfer
KS	Kohn-Sham
LC	liquid crystal
LCD	liquid crystal display
LDA	local density approximation
LED	light-emitting diode
LFDFT	ligand field DFT
LFT	ligand field theory
LMCT	ligand to metal charge transfer
LS	low spin
M1	magnetic dipole (transition)
ML	mechanoluminescence
MLCT	metal to ligand charge transfer
MMCT	metal to metal charge transfer
mp	many-particle
NTSC	National Television Standards Committee

PAW	projector-augmented wave
PBE	Perdew-Burke-Ernzerhof
PCEM	point charge electrostatic model
pc-LED	phosphor-converted LED
PES	potential energy surface
PL	photoluminescence
PXRD	powder X-ray diffraction
RGB	red-green-blue
SALC	symmetry adapted linear combination
SCCF	spin-correlated crystal field
SE	secondary electrons
SEM	scanning electron microscopy
SM	superposition model
SO	spin-orbit
SOO	spin-other-orbit
sp	single-particle
SS	spin-spin
TDDFT	time-dependent DFT
TEM	transmission electron microscopy
TL	thermoluminescence
TM	transition metal
tp	two-particle
UV	ultraviolet
VASP	Vienna Ab Initio Simulation Package
VB	valence band
VIS	visual
VRBE	vacuum referred binding energy
VUV	vacuum UV ($\lambda < 200$ nm)
XAS	X-ray absorption spectroscopy
XANES	X-ray absorption near edge structure
XRD	X-ray diffraction
YAG	yttrium aluminium garnet
ZPL	zero-phonon line

Examination committee

Chairman

Prof. Dr. Toon Verstraelen	-	Department of Physics and astronomy, Ghent University

Supervisors

Prof. Dr. Philippe Smet	-	Department of Solid state sciences, Ghent University
Prof. Dr. Dirk Poelman	-	Department of Solid state sciences, Ghent University

Other members of the examination committee

Prof. Dr. Luis Seijo	-	Department of Chemistry, Universidad Autónoma de Madrid
Prof. Dr. Rik Van Deun	-	Department of Inorganic and physical chemistry, Ghent University
Prof. Dr. Johan Lauwaert	-	Department of Electronics and information systems, Ghent University
Prof. Dr. Ir. Henk Vrielinck	-	Department of Solid state sciences, Ghent University
Dr. Ir. Kurt Lejaeghere	-	Department of Applied physics, Ghent University
Dr. Katleen Korthout	-	Department of Solid state sciences, Ghent University

PUBLICATION LIST

Papers in international, peer-reviewed journals

- **Charge transfer induced energy storage in CaZnOS:Mn - insight from experimental and computational spectroscopy**
  Jonas J. Joos, Kurt Lejaeghere, Katleen Korthout, Ang Feng, Dirk Poelman, Philippe F. Smet
  Physical Chemistry Chemical Physics, **19** 9075-9085 (2017).

- **Hybrid remote quantum dot / powder phosphor layers for display backlights**
  Sofie Abe, Jonas J. Joos, Lisa I. D. J. Martin, Zeger Hens, Philippe F. Smet
  Light: Science & Applications, **6** e16271 (2017).

- **Nonequivalent lanthanide defects: Energy level modeling**
  Jonas J. Joos, Dirk Poelman, Philippe F. Smet
  Optical Materials, **61** 50-58 (2016).

- **Investigation of the quenching mechanisms of Tb^{3+} doped scheelites**
  Katrien W. Meert, Jonas J. Joos, Dirk Poelman, Philippe F. Smet
  Journal of Luminescence, **173** 263-273 (2016).

- **First-principles study of antisite defect configurations in $ZnGa_2S_4$:Cr persistent phosphors**
  Arthur De Vos, Kurt Lejaeghere, Danny E. P. Van Poucke, Jonas J. Joos, Philippe F. Smet, Karen Hemelsoet
  Inorganic Chemistry, **55** (5) 2402-2412 (2016).

- **Luminescent behavior of the K_2SiF_6:Mn^{4+} red phosphor at high fluxes and at the microscopic level**
  Heleen F. Sijbom, Jonas J. Joos, Lisa I. D. J. Martin, Koen Van den Eeckhout, Dirk Poelman, Philippe F. Smet
  ECS Journal of Solid State Science and Technology, **5** (1) R3040-R3048 (2016).

- **Energy level modeling of lanthanide materials: review and uncertainty analysis**

  Jonas J. Joos, Dirk Poelman, Philippe F. Smet

  Physical Chemistry Chemical Physics, **17** 19058-19078 (2015).

- **Evaluating the use of blue phosphors in white LEDs: the case of $Sr_{0.25}Ba_{0.75}Si_2O_2N_2$:$Eu^{2+}$**

  Jonas J. Joos, Jonas Botterman, Philippe F. Smet

  Journal of Solid State Lighting, **1** (6) (2014).

- **Absolute determination of photoluminescence quantum efficiency using an integrating sphere setup**

  Sven Leyre, Eduardo Coutino-Gonzales, Jonas J. Joos, Jana Ryckaert, Youri Meuret, Dirk Poelman, Philippe F. Smet, Guy Durinck, Johan Hofkens, Geert Deconinck, Peter Hanselaer

  Review of Scientific Instruments, **85** 123115 (2014).

- **Luminescence of ytterbium in CaS and SrS**

  Anthony B. Parmentier, Jonas J. Joos, Philippe F. Smet, Dirk Poelman

  Journal of Luminescence, **154** 445-451 (2014).

- **Trapping and detrapping in $SrAl_2O_4$:Eu,Dy persistent phosphors: influence of excitation wavelength and temperature**

  Jonas Botterman, Jonas J. Joos, Philippe F. Smet

  Physical Review B, **90** 085147 (2014).

- **Origin of saturated green emission from europium in zinc thiogallate**

  Jonas J. Joos, Katleen Korthout, Sergey Nikitenko, Dirk Poelman, Philippe F. Smet

  Optical Materials Express, **3** (2013), 1338-1350.

- **Thermal quenching and luminescence lifetime of saturated green $Sr_{1-x}Eu_xGa_2S_4$ phosphors**

  Jonas J. Joos, Katrien W. Meert, Anthony B. Parmentier, Dirk Poelman, Philippe F. Smet

  Optical Materials, **34** (2012), 1902-1907.

Papers in national journals

- **Designing phosphors for brighter LEDs**

  Jonas J. Joos, Dirk Poelman, Philippe F. Smet

  BPHY, Belgian Physical Society Magazine, **1** (2014), 10-15.

Contribution at international conferences

- **Mn impurities in CaZnOS: insight from luminescence spectroscopy and density functional theory**

  Jonas J. Joos, Kurt Lejaeghere, Katleen Korthout, Ang Feng, Dirk Poelman, Philippe F. Smet

  Workshop on Charge Trapping Defects in Semiconductors and Insulators, York, United Kingdom, 20/03/2017-21/03/2017.

- **Electronic structure and applications of CaZnOS:Mn phosphors**

  Jonas J. Joos, Kurt Lejaeghere, Ang Feng, Karen Hemelsoet, Philippe F. Smet

  6^{th} *International Conference on Excited States of Transition Elements (ESTE2016)*, Polanica Zdrój, Poland, 21/08/2016-26/08/2016.

- **Luminescence of Mn in CaZnOS: from energy levels to applications**

  Jonas J. Joos, Ang Feng, Kurt Lejaeghere, Karen Hemelsoet, Philippe F. Smet

  2016 International Conference on Defects in Insulating Materials (ICDIM2016), Lyon, France, 10/07/2016-15/07/2016.

- **Connecting crystal structure and luminescence: the case of $SrAl_2O_4$**

  Jonas J. Joos, Jonas Botterman, Dirk Poelman, Philippe F. Smet

  2016 International Conference on Defects in Insulating Materials (ICDIM2016), Lyon, France, 10/07/2016-15/07/2016.

- **Optically and mechanically stimulated detrapping in persistent phosphors**

  Philippe F. Smet, Claude Tydtgat, Katrien W. Meert, Jonas Botterman, Katleen Korthout, Koen Van den Eeckhout, Dirk Poelman, Mathias Kersemas, Simon Michels, Jonas J. Joos

  PRE'16: 6^{th} international workshop on photoluminescence in rare earths : photonic materials and devices, Greenville, SC, USA, , 08/06/2016-10/06/2016.

- **Rare earths for phosphor development: the final frontier?**

  Dirk Poelman, Olivier Q. De Clercq, Jesse Bouman, Heleen F. Sijbom, Jonas J. Joos, Katleen Korthout, Kevin Braeckmans, Philippe F. Smet

  Rare Earths 2016, Sapporon, Japan, 05/06/2016-10/06/2016.

- **Temperature-dependent cathodoluminescence: quantifying thermal quenching at the microscopic level**

  Lisa I. D. J. Martin, Jonas J. Joos, Dirk Poelman, Philippe F. Smet

  Beam Injection Assessment of Microstructures in Semiconductors (BIAMS), 13th International conference, Versailles, France, 05/06/2016-09/06/2016.

- **Empirical energy level modeling of lanthanide defects in $CaGa_2S_4$ and $SrGa_2S_4$: uncertainty analysis and unexpected behavior**

  Jonas J. Joos, Dirk Poelman, Philippe F. Smet

*The 4*th *international conference on the physics of optical materials and devices (ICOM 2015)*, Budva, Montenegro, 31/08/2015-04/09/2015.

- **Investigation of the quenching mechanisms of Tb^{3+} doped scheelites**

  Katrien W. Meert, Jonas J. Joos, Dirk Poelman, Philippe F. Smet

  *The 4*th *international conference on the physics of optical materials and devices (ICOM 2015)*, Budva, Montenegro, 31/08/2015-04/09/2015.

- **Cathodoluminescence in electron microscopy: from phosphor evaluation to single particle analysis**

  Philippe F. Smet, Lisa I. D. J. Martin, Jeroen Wattez, Filip Strubbe, Jonas J. Joos, Jonas Botterman, Katleen Korthout, Sofie Abe, Heleen F. Sijbom, Dirk Poelman

  *The 4*th *international conference on the physics of optical materials and devices (ICOM 2015)*, Budva, Montenegro, 31/08/2015-04/09/2015.

- **Hybrid remote phosphors for white LEDs: combining quantum dots and rare earth doped phosphors**

  Sofie Abe, Jonas J. Joos, Philippe F. Smet, Zeger Hens

  Nanotech 2015, Washington DC, USA, 14/06/2015-17/06/2015.

- **I-III-VI_2 semiconductor nanocrystals as remote color converting alternatives for white LEDs**

  Sofie Abe, Jonas J. Joos, Philippe F. Smet, Zeger Hens

  European Materials Research Society (E-MRS) Spring Meeting, Lille, France, 11/05/2015-15/05/2015.

- **Hybrid remote phosphors for white LEDs: combining quantum dots and rare earth doped phosphors**

  Sofie Abe, Jonas J. Joos, Philippe F. Smet, Zeger Hens

  European Materials Research Society (E-MRS) Spring Meeting, Lille, France, 11/05/2015-15/05/2015.

- **Explaining green emission of Eu^{2+} in $ZnGa_2S_4$**

  Jonas J. Joos, Katleen Korthout, Dirk Poelman, Philippe F. Smet

  *16*th *International Krutyń Summer School: Lanthanide-based photonic materials and structures : breakthrough applications and cutting edge systems*, Krutyń, Poland, 31/08/2014-06/09/2014.

- **Energy level modeling of lanthanide defects in $SrGa_2S_4$**

  Jonas J. Joos, Philippe F. Smet

  *PRE'14: 5*th *international workshop on photoluminescence in rare earths : photonic materials and devices*, San Sebastian, Spain, 13/05/2014-16/05/2014.

- **On the incorporation of europium in $SrAl_2O_4$**

  Jonas J. Joos, Jonas Botterman, Dirk Poelman, Philippe F. Smet

PRE'14: 5th international workshop on photoluminescence in rare earths : photonic materials and devices, San Sebastian, Spain, 13/05/2014-16/05/2014.

- **Temperature and wavelength dependent trap filling in $SrAl_2O_4$:Eu,Dy**

  Jonas Botterman, Jonas J. Joos, Dirk Poelman, Philippe F. Smet

  PRE'14: 5th international workshop on photoluminescence in rare earths : photonic materials and devices, San Sebastian, Spain, 13/05/2014-16/05/2014.

- **Synthesis, characterization and emission tuning of I-III-VI_2 semiconductor nanocrystals as color converting alternatives for white LEDs**

  Sofie Abe, Jonas J. Joos, Philippe F. Smet, Zeger Hens

  European Materials Research Society (E-MRS) Spring Meeting, Lille, France, 26/05/2014-30/05/2014.

- **Structure and luminescence of Eu^{2+} in $ZnGa_2S_4$**

  Jonas J. Joos, Katleen Korthout, Dirk Poelman, Philippe F. Smet

  4th International workshop on Advances Spectroscopy and Optical Materials (IWASOM 2013), Gdansk, Poland, 14/07/2013-19/07/2013.

- **On the luminescence centers in $SrAl_2O_4$:Eu,Dy and their role in the persistent luminescence process**

  Jonas Botterman, Koen Van den Eeckhout, Jonas J. Joos, Dirk Poelman, Philippe F. Smet

  2nd International workshop on Persistent and Photostimulable Phosphors (WPPP 2013), Guangzhou, PR China, 17/11/2013-21/11/2013.

- **Thiogallate phosphors for phosphor-converted LEDs: saturated green emission**

  Philippe F. Smet, Jonas J. Joos, Dirk Poelman

  Society for Information Displays (SID) Mid-Europe Spring Meeting 2013, Gent, 15/04/2013-16/04/2013.

- **Revisiting rare-earth doped sulfide phosphors**

  Philippe F. Smet, Anthony B. Parmentier, Jonas J. Joos, Nurcen Avci, Katleen Korthout, Dirk Poelman

  79th Annual meeting of the Japanese Electrochemical Society ; Phosphor symposium, Hamamatsu, Japan, 29/03/2012-31/03/2012.

- **Luminescence of 5d-4f emitting rare earth ions in sulfide hosts**

  Philippe F. Smet, Anthony B. Parmentier, Nurcen Avci, Katleen Korthout, Jonas J. Joos, Dirk Poelman

  PRE'12: 4th International workshop on Photoluminescence in Rare Earths, Kyoto, Japan, 28/03/2012-30/03/2012.

Contribution at national conferences

- **Systematic in the luminescence of ns^2 ions**
  David Van der Heggen, Jonas J. Joos, Dirk Poelman, Philippe F. Smet
  Belgian Physical Society, General scientific meeting, Gent, 18/05/2016.

- **Hybrid remote quantum dot/powder phosphors for display applications**
  Sofie Abe, Jonas J. Joos, Lisa I. D. J. Martin, Philippe F. Smet, Zeger Hens
  Photonics@be : Towards smart photonics in 2020, Eindhoven, The Netherlands, 16/10/2015.

- **Energy level modeling of lanthanide defects in $SrAl_2O_4$**
  Jonas J. Joos, Dirk Poelman, Philippe F. Smet
  Belgian Physical Society, General scientific meeting, Liège, 13/05/2015.

- **Connecting crystal structure and luminescence, the case of $SrAl_2O_4$:Eu^{2+}**
  Jonas J. Joos, Jonas Botterman, Philippe F. Smet
  8th Belgian Crystallography symposium (BCS-8), Brussels, 15/10/2014.

- **Hybrid remote phosphors for white LEDs**
  Sofie Abe, Jonas J. Joos, Dorian Dupont, Heleen F. Sijbom, Yolanda Justo, Mickael D. Tessier, Koen Van den Eeckhout, Guido Huyberechts, Philippe F. Smet, Zeger Hens
  NB Photonics Annual Meeting 2014, Gent, 08/09/2014.

- **Designing phosphors for brighter LEDs**
  Jonas J. Joos, Dirk Poelman, Philippe F. Smet
  Belgian Physical Society, General scientific meeting, Leuven, 28/05/2014.

- **Designing phosphors for brighter LEDs**
  Jonas J. Joos, Dirk Poelman, Philippe F. Smet
  Doctoraatssymposium Faculteit Wetenschappen 2014, Gent, 20/03/2014.

- **Macroscopic and microscopic investigation of a blue oxynitride phosphor**
  Jonas J. Joos, Jonas Botterman, Dirk Poelman, Philippe F. Smet
  NB Photonics Annual Meeting 2014, Gent, 20/09/2013.

- **Evaluation of a novel blue oxynitride conversion phosphor**
  Jonas Botterman, Jonas J. Joos, Dirk Poelman, Philippe F. Smet
  Belgian Physical Society, General scientific meeting, Louvain-La-Neuve, 22/05/2013.

- **Saturated green phosphors for LED applications**
  Jonas J. Joos, Katrien W. Meert, Anthony B. Parmentier, Jonas Botterman, Dirk

Poelman, Philippe F. Smet

NB Photonics Annual Meeting 2014, Gent, 21/09/2012.

- **Saturated green phosphors for LED applications**

  Jonas J. Joos, Katrien W. Meert, Anthony B. Parmentier, Jonas Botterman, Dirk Poelman, Philippe F. Smet

  Belgian Physical Society, General scientific meeting, Brussel, 30/05/2012.

A GROUP THEORY

Modern physics, and more specific quantum mechanics, has an intimate connection with the mathematical machinery of group theory. This appendix enumerates the aspects of group theory which are most important for the application to the spectroscopy of metal impurities. The symmetry group of the Hamiltonian is established and it is shown how group theory offers meaningful labels for the physical states of the system under study.

This chapter is mainly based on the following books:

- A. Frank, J. Jolie and P. Van Isacker. *Symmetries in atomic nuclei: from isospin to supersymmetry*. Springer, New York, 2008.
- R. Penrose. *The road to reality - A complete guide to the laws of the universe*. Alfred A. Knoph, New York, 2005 .
- G. B. Arfken and H. J. Weber. *Mathematical methods for physicists*. Elsevier, 2005.

A.1 Definitions

A group, G, is a mathematical concept, constructed of several elements, $g_1,\ldots,g_n$ which can be combined with the *multiplication* $\circ$, satisfying following conditions:

- Closure: $g_i \circ g_j \in G$.
- Associativity: $(g_i \circ g_j) \circ g_k = g_i \circ (g_j \circ g_k)$.
- Unity element: $g_i \circ E = E \circ g_i = g_i$.
- Inverse element: $g_i \circ g_i^{-1} = g_i^{-1} \circ g_i = E$.

A group is therefore not necessarily commutative. The latter is examined through the group commutator, $g_1 g_2 g_1^{-1} g_2^{-1}$, which yields E for a commutative group. Commutative groups are also known as Abelian groups, after the tragically short-lived Norwegian mathematician Niels Henrik Abel [453].

The number of elements, n, can be finite, countable finite or uncountable finite, yielding finite, infinite discrete and continuous groups respectively. In the last case, which is often referred to as Lie groups[1], a set of algebraically defined and continuously varying parameters $\boldsymbol{a} = a_1, \ldots, a_r$ can be used to represent the group elements[2]. In this work, both discrete groups, describing the symmetry of crystals, and Lie groups, describing atomic states, are required. In the case of finite groups, the number of elements n is called the order of the group, while for Lie groups, the order refers to the number of parameters, r.

A group G can be mapped onto/into another group G'. This is formally written down by ϕ for which $g' = \phi(g)$. Some special mappings are important and have hence received a distinct name. If a mapping is bijective, *i.e.* one-to-one, it is said to be faithful and the inverse mapping can be defined. When ϕ conserves the group multiplication, $\phi(g_i \circ g_j) = \phi(g_i) \circ \phi(g_j)$, it is called a homomorphism. An isomorphic mapping is a homomorphism which is also faithful.

A group G can contain a subgroup H, denoted as $H \subset G$. Here, H is composed of a selection of elements of G which fulfill the group axioms for the same multiplication and inversion operation as G. A subgroup is called normal when each element of G commutes with all the elements of H.

A.2 Symmetry and quantum mechanics - representation theory

Assume that a physical system is invariant for a group G of symmetry operations g_i. These can be geometrical symmetries, such as rotations, translations or reflections, but are not restricted to these. For instance, the operation of charge conjugation, where each particle is replaced by its anti-particle is also a symmetry for certain systems. Another example of a non-geometrical symmetry is the gauge symmetry of electromagnetic theory (see §2.2.1). These symmetry operations are quantum mechanically encoded as unitary transformation in the Hilbert space, mapping a state vector onto another state vector. Unitarity of U is required as the norm of state vectors is conserved during the symmetry operations.:

$$|\Psi'\rangle = U(g_i)|\Psi\rangle. \tag{A.1}$$

If a basis for the Hilbert space is introduced, $|\psi_i\rangle$, each symmetry operation can be represented by a matrix:

$$U(g_i)|\psi_n\rangle = \sum_m [\Gamma(g_i)]_{mn} |\psi_m\rangle. \tag{A.2}$$

These matrices necessarily fulfill the group axioms:

$$\Gamma(g_i \circ g_j) = \Gamma(g_i)\Gamma(g_j), \tag{A.3}$$

[1] Named after the Norwegian, 19$^{\text{th}}$ century mathematician Sophus Lie.

[2] All possible rotations along a fixed axis form a Lie group, parametrized by the rotation angle. For all rotations in 3D space, three parameters are required, *e.g.* the Euler angles.

where the group multiplication is simply the matrix multiplication. The dimension of these matrices is equal to the dimension of Hilbert space, while the order of the matrix group equals the order of G. In general, a group of matrices that satisfy Eq. A.2 are called a matrix representation, or in short a representation of the group G. A representation is at least homomorphic with G. When the mapping is isomorphic in addition, the representation is called faithful. The different types of matrix groups are discussed in §A.3.3. Often, the symbol of the matrix group is used to denote the associated group for which the representations are studied.

Representations which are connected through a similarity transformation[3] are considered as equivalent. If a representation can be brought into block diagonal form upon a similarity transformation, it is said to be reducible:

$$\Gamma' = S^{-1}\Gamma S = \begin{pmatrix} \Gamma_1 & \mathbf{0} & \cdots \\ \mathbf{0} & \Gamma_2 & \cdots \\ \vdots & \vdots & \ddots \end{pmatrix} = \Gamma_1 \oplus \Gamma_2 \oplus \ldots, \tag{A.4}$$

with $\mathbf{0}$ matrices containing only zeros. The direct sum, $\oplus$, was introduced to simplify notation. By reducing representations, Hilbert space is divided in invariant subspaces for the group operations $U(g_i)$. If a group operation works on a state vector in an invariant subspace, the result will necessarily be a linear combination of the states in the same invariant subspace. If a representation cannot be brought into block diagonal form, it is called an irreducible representation, abbreviated as irrep.

Consider a physical observable, given by the operator $\mathcal{A}$, with eigenvalues a_n,

$$\mathcal{A}|\psi_n\rangle = a_n|\psi_n\rangle. \tag{A.5}$$

The eigenstates of $\mathcal{A}$ can be used as basis for the Hilbert space, which is divided in invariant subspaces, the different eigenspaces of $\mathcal{A}$, corresponding to the different eigenvalues. If it is further assumed that the commutators of the observable $\mathcal{A}$ and the operations of G vanish:

$$[\mathcal{A}, U(g_i)] = \mathcal{A}U(g_i) - U(g_i)\mathcal{A} = 0, \qquad \forall i, \tag{A.6}$$

it is found that:

$$\mathcal{A}U(g_i)|\psi_n\rangle = a_n U(g_i)|\psi_n\rangle. \tag{A.7}$$

So, $U(g_i)|\psi_n\rangle$ and $|\psi_n\rangle$ have the same eigenvalue and they therefore are part of the same invariant subspace. In most physical problems, the operator for which the spectrum is inspected, is the Hamiltonian, $\mathcal{A} = \mathcal{H}$. With a similar argument, it is easy to show that if the commutator of two operators vanishes, they can be diagonalized simultaneously.

Summarized, Hilbert space is divided in several invariant subspaces which form irreducible representations of the symmetry group G. The states within the invariant

[3] $\Gamma' = S^{-1}\Gamma S$, with S an invertible matrix.

subspace correspond to the same eigenvalue of the considered operator, *i.e.* the energy in typical quantum mechanical problems. The irreps of the symmetry groups can in other words be used to label the energy eigenvalues of the Hamiltonian and the eigenfunctions of the Hamiltonian within each eigenspace can be used as basis for the representation spaces. Every basis function or partner is characterized by a so-called row index, denoted γ. The degeneracy of the eigenvalue is then given by the dimension of the associated representation space.

These results are very useful when the effect of symmetry lowering on the energy eigenvalues is studied. A representation which is irreducible for a group G does not necessarily remain irreducible when the symmetry is lowered to $H \subset G$. When the representation has to be reduced, the invariant subspaces of G are divided in new invariant subspaces of H. This is associated with a lifting of degeneracy in the eigenvalues. Group theoretical arguments can consequently be used to predict the degeneracies of physical eigenstates. This is fully exploited in chapter 4.

The direct or Kronecker product of representations is an often encountered construction. When $\psi_n^{(1)}$ and $\psi_k^{(2)}$ are the basis functions of two representations, Γ_1 and Γ_2 of a group G and are considered to be linearly independent, *e.g.* depending on different variables, the direct product representation is found from:

$$\begin{aligned} U(g_i)(|\psi_n^{(1)}\rangle|\psi_k^{(2)}\rangle) &= \left(\sum_m [\Gamma_1(g_i)]_{mn}\,|\psi_m^{(1)}\rangle\right)\left(\sum_l [\Gamma_2(g_i)]_{lk}\,|\psi_l^{(2)}\rangle\right) \\ &= \sum_{ml} [\Gamma(g_i)]_{ml,\,nk}\,|\psi_m^{(1)}\rangle|\psi_l^{(2)}\rangle \end{aligned} \tag{A.8}$$

where Γ is the direct product of Γ_1 and Γ_2 and is itself a representation of G:

$$\Gamma_{ml,\,nk} = (\Gamma_1 \otimes \Gamma_2)_{ml,\,nk} = \Gamma_{1,\,mn}\,\Gamma_{2,\,lk}. \tag{A.9}$$

The product representation is in general reducible, also when it is composed of irreps.

A.3 Lie groups and Lie algebra's

A.3.1 Generators

The elements of continuous or Lie groups, $g(\boldsymbol{a})$, are uniquely defined by a set of r continuously varying real parameters, $\boldsymbol{a} = a_1, \ldots, a_\mu, \ldots, a_r$. The identity corresponds to $\boldsymbol{a} = \mathbf{0}$, $E = g(\mathbf{0})$. The number of parameters, r, is called the order of the group. Lie's treatment of continuous groups focuses on the local structure of the group, by means of a set of infinitesimal group elements which define a kind of algebra. This Lie algebra contains all information on the local structure of the group, although not necessarily all information of the global structure of the group. However, the latter is generally of less importance for physics applications.

Consider that a matrix $I+\Gamma[g(\delta a)]$ represents an infinitesimal operation $g(\delta\boldsymbol{a})$ of the continuous group G, with $\delta\boldsymbol{a}$ a small parameter. The product of two infinitesimal operations is given by:

$$U(g(\delta\boldsymbol{a}))\circ U(g(\delta\boldsymbol{b})) \quad \rightarrow \tag{A.10}$$
$$(I+\Gamma[g(\delta\boldsymbol{a})])(I+\Gamma[g(\delta\boldsymbol{b})]) = I+\Big(\Gamma[g(\delta\boldsymbol{a})]+\Gamma[g(\delta\boldsymbol{b})]\Big)+\Gamma[g(\delta\boldsymbol{a})]\Gamma[g(\delta\boldsymbol{b})].$$

If the term of second order in the small matrices is ignored, the group multiplication $g(\delta\boldsymbol{a})g(\delta\boldsymbol{b})$ is represented by the sum $\Gamma[g(\delta\boldsymbol{a})]+\Gamma[g(\delta\boldsymbol{b})]$. This is problematic if the group is non-Abelian, as matrix summation is commutative. For this, the group commutator is evaluated by inserting the geometric series[4]:

$$\begin{aligned} U(g(\delta\boldsymbol{a}))\circ U(g(\delta\boldsymbol{b}))\circ U(g^{-1}(\delta\boldsymbol{a}))\circ U(g^{-1}(\delta\boldsymbol{b})) \quad &\rightarrow \\ (I+\Gamma[g(\delta\boldsymbol{a})])(I+\Gamma[g(\delta\boldsymbol{b})])(I+\Gamma[g(\delta\boldsymbol{a})])^{-1}&(I+\Gamma[g(\delta\boldsymbol{b})])^{-1} \\ = \quad I+&\Big(\Gamma[g(\delta\boldsymbol{a})]\Gamma[g(\delta\boldsymbol{b})]-\Gamma[g(\delta\boldsymbol{b})]\Gamma[g(\delta\boldsymbol{a})]\Big) \\ = \quad I+&\Big[\Gamma[g(\delta\boldsymbol{a})],\,\Gamma[g(\delta\boldsymbol{b})]\Big] \end{aligned} \tag{A.11}$$

where the commutator in its *quantum mechanical disguise* is found. In this context, it is referred to as the Lie bracket. The Lie algebra $\mathfrak{g}$ is constructed by the repeated application of addition, subtraction, scalar multiplication and the Lie bracket operation. The Lie algebra has the structure of a linear vector space, it closes under commutation. If a basis is chosen for the $\Gamma[g(\delta\boldsymbol{a})]$'s, denoted as X_μ, one has:

$$\Big[X_\mu, X_\nu\Big] = \sum_{\sigma=1}^{r} c_{\mu\nu}^{\sigma} X_\sigma, \tag{A.12}$$

which describes the structure of the Lie algebra. The numbers $c_{\mu\nu}^{\sigma}$ and the basis vectors X_μ are called respectively the structure constants and the generators of the Lie algebra. The Lie bracket satisfies following properties:

- Bilinearity: $\Big[\alpha X_\mu+\beta X_\nu, X_\sigma\Big] = \alpha\Big[X_\mu, X_\sigma\Big]+\beta\Big[X_\nu, X_\sigma\Big] \qquad (\alpha,\ \beta\in\mathbb{C})\,.$
- Alternativity: $\Big[X_\mu, X_\mu\Big] = 0.$
- Jacobi identity: $\Big[X_\mu,\Big[X_\nu, X_\sigma\Big]\Big]+\Big[X_\nu,\Big[X_\sigma, X_\mu\Big]\Big]+\Big[X_\sigma,\Big[X_\mu, X_\nu\Big]\Big] = 0.$
- Antisymmetry: $\Big[X_\mu, X_\nu\Big] = -\Big[X_\nu, X_\mu\Big]$

These properties put restrictions on the values of the structure constants. A finite element of the Lie group can be constructed from the elements of the Lie algebra by the exponential map:

$$U(g_i(\boldsymbol{a})) = \sum_{i=0}^{\infty}\frac{1}{i!}\sum_{\mu=1}^{r}\Big(a_\mu X_\mu\Big)^i = \exp\,\mathrm{i}\sum_{\mu=1}^{r} a_\mu X_\mu, \tag{A.13}$$

[4] $(I+\Gamma[g(\delta\boldsymbol{a})])^{-1} = I-\Gamma[g(\delta\boldsymbol{a})]+\Gamma[g(\delta\boldsymbol{a})]^2-\Gamma[g(\delta\boldsymbol{a})]^3+\ldots$

where the basis vectors are chosen according to:

$$X_\mu = \left.\frac{\partial U(g(\boldsymbol{a}))}{\partial a_\mu}\right|_{a_\mu=0}, \tag{A.14}$$

which is the more appropriate form of the expressions that introduced this paragraph. Because of Eq. A.13, the X_μ's are called the generators of the Lie group. This shows that the study of representation theory of continuous groups can be largely transferred to the study of the representations of Lie algebras, which is common practice in physics because the Lie algebra's matrices are usually simpler than the Lie group's matrices and satisfy linear rather than nonlinear restrictions. For this reason, the designations Lie group and Lie algebra are often interchanged. Interestingly, the Lie generators can be proven to be hermitic and often have a direct physical interpretation (see *e.g.* §A.3.5).

A.3.2 Root figures

It proves to be insightful to elaborate on the Lie algebra by performing a well-chosen basis transformation. Graphical representations of the Lie algebra are constructed which can be exploited to find the irreps and their partners of the Lie group.

First, a maximal set of mutually commuting generators are searched for, which are denoted as H_i and called the Cartan generators,

$$\left[H_i, H_j\right] = 0 \qquad (i = 1 \ldots m < r). \tag{A.15}$$

The order of this subalgebra m is called the rank of the original Lie algebra. From Eq. A.15, it follows that the H_i's can be simultaneously diagonalized implying that their eigenvalues can be used to label the partners of a given irrep. The m-dimensional vectors that are found by combining the eigenvalues of the Cartan generators are referred to as weight vectors and they form the so-called weight diagram. The m-dimensional vector space is called weight space. A weight $(h_1, \ldots, h_m)$ is higher than another weight $(h'_1, \ldots h'_m)$ when the first nonzero $h_i - h'_i$ is positive, starting at $i = 1$. According to the theory of semi-simple groups[5], an irrep is unambiguously labeled by its highest weight. The weights themselves can be used to label the different partners that belong to the irrep.

Second, the remaining generators of the Lie algebra are used to construct raising and lowering operators. Within Lie group theory it can be shown that all remaining generators are used for this. The obtained linear combinations are denoted as E_α and are referred to as the Weyl generators. They satisfy by definition:

$$[H_i, E_\alpha] = \alpha_i E_\alpha \qquad (i = 1 \ldots m < r, \alpha = 1 \ldots r - m) \tag{A.16}$$

[5] A Lie group is simple when it possesses no non-trivial normal subgroups, it is semi-simple when its Lie-algebra is the direct sum of simple Lie algebras.

and the m-dimensional vectors composed of the α_i are called the root vectors, forming the root figure in the m-dimensional root space. A root figure can be considered as a graphical representation of the Lie algebra.

Along with the Cartan and Weyl generators, the Casimir operators, $\mathcal{G}_i$, are also defined. These operators commute with the full Lie algebra and it can be shown that the number of Casimir operators equals the rank of the Lie algebra. The first Casimir operator is a bilinear function of the generators, while the other have a more complicated form. The Cartan generators and the Casimir operators all mutually commute, implying that their eigenvalues can be used to label a general eigenfunction:

$$H_i \left|g_1 \dots g_m, h_1 \dots h_m\right\rangle = h_i \left|g_1 \dots g_m, h_1 \dots h_m\right\rangle \tag{A.17}$$

$$\mathcal{G}_i \left|g_1 \dots g_m, h_1 \dots h_m\right\rangle = g_i \left|g_1 \dots g_m, h_1 \dots h_m\right\rangle \tag{A.18}$$

From the definition of the Weyl generators, Eq. A.16, it follows that they indeed behave as raising/lowering operators:

$$\begin{aligned} H_i E_\alpha \left|g_1 \dots g_m, h_1 \dots h_m\right\rangle &= \left(E_\alpha H_i + [H_i, E_\alpha]\right) \left|g_1 \dots g_m, h_1 \dots h_m\right\rangle \\ &= (h_i + \alpha_i) E_\alpha \left|g_1 \dots g_m, h_1 \dots h_m\right\rangle \\ \Leftrightarrow E_\alpha \left|g_1 \dots g_m, h_1 \dots h_m\right\rangle &\propto \left|g_1 \dots g_m, h_1 + \alpha_1 \dots h_m + \alpha_m\right\rangle. \end{aligned} \tag{A.19}$$

In summary, the eigenvalues of the Casimir operators can be used to label the irreducible representations, while the eigenvalues of the Cartan generators can be used to label the partners of the irrep. The Weyl generators are raising and lowering operators that allow to change from one partner to another within the same irrep.

A.3.3 Matrix groups

In this paragraph, some subgroups of the general linear group of degree n, GL(n) are enumerated. GL(n) is the group of all invertible $n \times n$ matrices with the matrix multiplication as group multiplication. These matrices can be defined over a field of choice such as the real or complex numbers. Some interesting subgroups of GL(n) are:

- Special linear group SL(n). The matrices of GL(n) for which the determinant is one.
- Orthogonal group O(n). The matrices of GL(n) for which the inverse matrix equals the transposed matrix: $O^T = O^{-1}$ or $O_{ki} O_{kj} = \delta_{ij}$ which implies $\det O = \pm 1$. Orthogonal transformations preserve the inner product and can represent either rotations or reflections in the n-dimensional space R^n.
- Special orthogonal group SO(n). The matrices of O(n) for which the determinant is one. Only the n-dimensional rotations are left.
- Unitary group U(N). The matrices of GL(n) for which the inverse matrix equals the hermitian conjugate matrix: $U^\dagger = U^{-1}$ or $U^*_{ki} U_{kj} = \delta_{ij}$ which implies $\det U = \mathrm{e}^{\mathrm{i}\phi}$. Obviously, the unitary group is defined over the field C^n.

- Special unitary group SU(n). The matrices of U(n) for which the determinant is one.

- Symplectic group Sp(n). The matrices of GL(n) which preserve the non-singular antisymmetric matrix

$$M = \begin{pmatrix} 0 & I_{n/2} \\ -I_{n/2} & 0 \end{pmatrix},$$

i.e. $S^T M S = M$. As M can only be non-singular for even n, odd n values are excluded.

The associated semi-simple Lie algebras $\mathfrak{sl}(n+1)$, $\mathfrak{so}(2n+1)$, $\mathfrak{sp}(2n)$ and $\mathfrak{so}(2n)$ are often alternatively denoted as A_m, B_m, C_m and D_m respectively. Here, the degree is written such that n is the rank of the Lie algebra. In addition to these four classes, five exceptional Lie algebras, associated with the groups E_6, E_7, E_8, F_4 and G_2, are found to complete the enumeration of the semi-simple Lie algebras over the complex numbers.

A.3.4 Noether's theorem

To conclude the general discussion on continuous symmetries, we take a step back to physics. Consider that the Hamiltonian features a continuous symmetry. Then Eq. A.13 can be filled in Eq. A.6 to obtain

$$\left[\mathcal{A}, X_\mu\right] = 0 \qquad (\forall \mu). \tag{A.20}$$

This means that when a physical system is invariant for a continuous symmetry group, the Hamiltonian commutes with the generators of the group. Another important result can be derived upon calculating the time dependence of the expectation value of the generator by means of the time-dependent Schrödinger equation[6]:

$$\frac{\mathrm{d}}{\mathrm{d}t}\langle\Psi| X_\mu |\Psi\rangle = \langle\Psi| \frac{\partial X_\mu}{\partial t} |\Psi\rangle + \frac{\mathrm{i}}{\hbar}\langle\Psi| \left[\mathcal{H}, X_\mu\right] |\Psi\rangle. \tag{A.21}$$

If the generator is not explicitly time dependent, the first term vanishes. If furthermore the generator corresponds to the symmetry group of $\mathcal{H}$, the second term also vanishes because of the above result and the quantity to which X_μ corresponds is a constant of motion for the physical system. The fact that a quantity is conserved when its operator commutes with the Hamiltonian is known as Ehrenfest's theorem. The more profound result that for every continuous symmetry of a physical system, a conserved quantity can be found is known as Noether's theorem.

[6] $\mathrm{i}\hbar\frac{\mathrm{d}|\Psi\rangle}{\mathrm{d}t} = \mathcal{H}|\Psi\rangle$.

A.3.5 Spherical symmetry

Angular momentum algebra

Consider a system which shows spherical symmetry. This means that rotations, R, form the symmetry operations of the group:

$$\boldsymbol{r}' = R(\alpha,\beta,\gamma)\boldsymbol{r}. \tag{A.22}$$

When applied on a function of the spatial coordinates,

$$U(R)(\alpha,\beta,\gamma)f(x,y,z) = f'(x,y,z) = f(x',y',z'). \tag{A.23}$$

Rotations in three-dimensional space can be specified by three angles, *e.g.* the Euler angles. Consider here the simplified case of an infinitesimal rotation about the z axis,

$$R_z(\delta\phi) = \lim_{\phi\to\delta\phi}\begin{pmatrix}\cos\phi & \sin\phi & 0\\ -\sin\phi & \cos\phi & 0\\ 0 & 0 & 1\end{pmatrix} = \begin{pmatrix}1 & \delta\phi & 0\\ -\delta\phi & 1 & 0\\ 0 & 0 & 1\end{pmatrix} \tag{A.24}$$

yielding

$$\begin{aligned} U(R_z)(\delta\phi)f(x,y,z) &= f(x+y\delta\phi, y-x\delta\phi, z)\\ &= f(x,y,z) + \delta\phi\left[y\frac{\partial}{\partial x} - x\frac{\partial}{\partial y}\right]f(x,y,z)\\ &= (1-\mathrm{i}\delta\phi L_z)\,f(x,y,z) \end{aligned} \tag{A.25}$$

where a Taylor expansion was used in the first step and the definition of orbital angular momentum, $\boldsymbol{L} = \boldsymbol{r}\times\boldsymbol{p}$, was used in the second step. Composing a finite and an infinitesimal rotation yields:

$$U(R_z)(\phi+\delta\phi)f(x,y,z) = U(R_z)(\delta\phi)U(R_z)(\phi)f(x,y,z) = (1-\mathrm{i}\delta\phi L_z)\,U(R_z)(\phi)f(x,y,z) \tag{A.26}$$

upon rearranging and taking the limit $\delta\phi\to 0$, a derivative of the operator is found:

$$\frac{\mathrm{d}U(R_z)(\phi)}{\mathrm{d}\phi} = \lim_{\delta\phi\to 0}\frac{U(R_z)(\phi+\delta\phi) - U(R_z)(\phi)}{\delta\phi} = -\mathrm{i}L_z U(R_z)(\phi), \tag{A.27}$$

which can be integrated to yield

$$U(R_z)(\phi) = \exp(-\mathrm{i}\phi L_z). \tag{A.28}$$

This shows that the components of the angular momentum vector are the generators for rotations. Their commutation relation can be found from the definition of $\boldsymbol{L}$:

$$\left[L_i, L_j\right] = \mathrm{i}\epsilon_{ijk}L_k \tag{A.29}$$

yielding immediately the structure of the associated Lie algebra. This happens to be exactly the structure of the Lie algebra $\mathfrak{so}(3)$. For this reason, SO(3) is often referred

to as the rotation group. This is not surprising because rotation matrices are indeed orthogonal (see §A.3.3). From the Noether theorem, it follows that angular momentum is conserved for spherically symmetric systems.

The dimension of the Lie algebra is three, given the three generators L_x, L_y and L_z. The rank is one as none of the generators commute. Conventionally, L_z is chosen as the Cartan generator, having the weights as eigenvalue. Furthermore, it is easy to show that L^2 commutes with all L_i, hence L^2 is the Casimir operator of $\mathfrak{so}(3)$, *i.e.* its eigenvalues will label the irreps. The Cartan and Casimir operator can be diagonalized simultaneously. Their eigenvalues and eigenvectors are denoted as:

$$L^2|\ell m_\ell\rangle = \ell(\ell+1)\hbar^2|\ell m_\ell\rangle \tag{A.30}$$

$$L_z|\ell m_\ell\rangle = m_\ell\hbar|\ell m_\ell\rangle. \tag{A.31}$$

The Weyl operators are found as $L_\pm = L_x \pm \mathrm{i}L_y$:

$$L_\pm|\ell m_\ell\rangle = \sqrt{\ell(\ell+1) - m_\ell(m_\ell \pm 1)}\hbar|\ell m_\ell \pm 1\rangle. \tag{A.32}$$

This angular momentum algebra was derived for orbital angular momentum. For spin angular momentum the same commutation relations are however found, as well as for composite angular momenta. Now, the irreps for the rotation group can be written down. These are labeled by the eigenvalue of the Casimir operator, ℓ:

$$U(R)|\ell m\rangle = \sum_{m'} \mathcal{D}^{(\ell)}_{m'm}(R)|\ell m'\rangle \tag{A.33}$$

and are called the Wigner-$\mathcal{D}$ matrices. When the direct product of two irreps is reduced, the expansion is known as the Clebsch-Gordan series:

$$\begin{aligned}(\mathcal{D}^{(\ell_1)} \otimes \mathcal{D}^{(\ell_2)})_{m_1 m_2, m_1' m_2'} &= \mathcal{D}^{(\ell_1)}_{m_{\ell 1} m_{\ell 1'}}(R)\,\mathcal{D}^{(\ell_2)}_{m_{\ell 2} m_{\ell 2'}}(R) \\ &= \sum_{\ell=|\ell_1-\ell_2|}^{\ell_1+\ell_2} \sum_{m,m'=-\ell}^{\ell} \langle \ell_1\ell_2 m_1 m_2|\ell_1\ell_2\ell m\rangle \\ &\qquad \times \langle \ell_1\ell_2 m_1' m_2'|\ell_1\ell_2\ell m'\rangle \mathcal{D}^{(\ell)}_{mm'}(R)\end{aligned} \tag{A.34}$$

where the coefficients $\langle \ell_1\ell_2 m_1 m_2|\ell_1\ell_2\ell m\rangle$ are known as the Clebsch-Gordan coefficients.

Homomorphism between SO(3) and SU(2)

In previous section, rotations were represented by real orthogonal 3x3 matrices, *i.e.* elements of SO(3). Alternatively, one can also use complex-valued unimodular unitary matrices, *i.e.* elements of SU(2).

A general SU(2) matrix can be written as

$$u = \begin{pmatrix} a & b \\ -b^* & a^* \end{pmatrix} \qquad \text{with} \qquad |a|^2 + |b|^2 = 1 \tag{A.35}$$

and can be expanded in terms of the unit matrix and the three Pauli matrices,

$$\sigma_1 = \begin{pmatrix} 0 & 1 \\ 1 & 0 \end{pmatrix}, \quad \sigma_2 = \begin{pmatrix} 0 & -\mathrm{i} \\ \mathrm{i} & 0 \end{pmatrix}, \quad \sigma_3 = \begin{pmatrix} 1 & 0 \\ 0 & -1 \end{pmatrix}, \tag{A.36}$$

which are the generators of SU(2). The Pauli matrices satisfy the same algebraic structure as the angular momentum operators:

$$\left[\frac{\sigma_i}{2}, \frac{\sigma_j}{2}\right] = \mathrm{i}\epsilon_{ijk}\frac{\sigma_k}{2} \tag{A.37}$$

Furtherore, it can be shown that a general rotation in three dimensional space about an angle ϕ around an arbitrary axis $\boldsymbol{n} = (n_1, n_2, n_3)$ (with $|n| = 1$) is equivalent to a rotation in two-dimensional complex space, given by the SU(2) matrix:

$$u(R(\boldsymbol{n}, \phi)) = I_2 \cos\frac{\phi}{2} + \mathrm{i}\,(n_1\sigma_1 + n_2\sigma_2 + n_3\sigma_3)\sin\frac{\phi}{2} \tag{A.38}$$

The correspondence is however not one-to-one. If the angle is altered according to $\phi \to \phi + 2\pi$, the same result is obtained for the 3x3 orthogonal matrix, while $u \to -u$ is found for the 2x2 unitary matrix. Only after a rotation over 4π, the same result is found. For this reason, the map between SO(3) and SU(2) is not isomorphic, it is a 2:1 homomorphism. The double group of SO(3) can be used to obtain an isomorphism nevertheless (see §A.4.2) .

A particle in a spherical potential

Finally, the angular momentum eigenfunctions are considered in three-dimensional coordinate space, *i.e.* $\langle \boldsymbol{r}|\ell m_\ell\rangle$. This is an interesting toolbox because the eigenfunctions of a spherically symmetric Hamiltonian will be exactly the eigenfunctions of the angular momentum operators (see §A.3.4). Symmetry dictates that spherical coordinates (r, θ, ϕ) are used for this. Some elaboration learns that the angular momentum operators do not alter the radial part of the wave function such that only the $\Omega = (\theta, \phi)$ dependence matters. Solving the eigenvalue equation yields:

$$\langle \Omega\,|\ell m_\ell\rangle = Y^{(\ell)}_{m_\ell}(\Omega) = (-1)^{m_\ell}\sqrt{\frac{2\ell+1}{4\pi}\frac{(\ell-m)!}{(\ell+m)!}}P_{\ell m_\ell}(\cos\theta)\mathrm{e}^{\mathrm{i}m_\ell\phi}. \tag{A.39}$$

where $P_{\ell m_\ell}$ are the associated Legendre polynomials [32]. The eigenfunctions $Y^{(\ell)}_{m_\ell}(\Omega)$ are widely known as the spherical harmonics.

The eigenfunctions of a spherically symmetric Hamiltonian can be obtained by realizing that the Hamiltonian forms together with L^2 and L_z a set of commuting operators, yielding eigenfunctions that are labeled $|E\ell m_\ell\rangle$. In coordinate space, the eigenfunction factorizes according to:

$$\langle r\theta\phi\,|E\ell m_\ell\rangle = \psi_{E\ell m_\ell}(r, \theta, \phi) = R_{E_\ell}(r)Y^{(\ell)}_{m_\ell}(\Omega). \tag{A.40}$$

The problem is hence solved when the radial wave function is obtained from the radial Schrödinger equation:

$$\left[\frac{\mathrm{d}^2}{\mathrm{d}r^2}+\frac{2}{r}\frac{\mathrm{d}}{\mathrm{d}r}-\frac{\ell(\ell+1)}{r^2}+\frac{2m}{\hbar^2}\left[E-V(r)\right]\right]R_{E\ell}(r)=0. \tag{A.41}$$

$R_{E\ell}$ is indeed independent of m_ℓ, which could be expected because the Hamiltonian commutes with the Weyl generators. A $(2\ell+1)$-fold degeneracy is hence expected for every energy-eigenvalue.

A.4 Discrete groups

In this section, some specific features of discrete groups are collected. Their representation theory has plenty of similarities to the representation theory of Lie groups which was described above, but also some unique aspects.

A.4.1 Point groups: representation theory and application

A point group is a collection of symmetry operations that keep one point fixed. In physics, they describe the symmetry of molecules or point defects in crystals. Here, discrete point groups are discussed, where the number of symmetry elements, h, called the order, is a finite number.

Two group elements, g_1 and g_2 are said to be conjugate if they are connected by a third group element, g_3 such that:

$$g_2=g_3^{-1}g_1g_3. \tag{A.42}$$

Conjugate elements are hence equivalent. Conjugacy classes are formed by elements which are all mutually conjugate.

Consider now a matrix representation for the point group. As all elements of a class are equivalent up to a similarity transformation, the representation matrices of elements of the same class will automatically have the same trace which is an invariant for similarity transformations:

$$\chi^{(\Gamma)}(R)=\mathrm{Tr}\left[\Gamma(R)\right]=\sum_{i=1}^{l_\Gamma}\Gamma(R)_{ii}, \tag{A.43}$$

with l_Γ the dimension of the representation Γ. Because of its distinguished role in point group representation theory, the trace gets a special name in this context, *i.e.* the character.

A discrete point group has a finite number of irreps. From the representation theory it can be shown that the number of irreps is exactly equal to the number of conjugacy

classes, r. The classes, irreducible representations and their characters are the work horses when point groups are applied. For this reason, so-called character tables for the different point groups can be found anywhere, including in this work. In §A.4.3, the character tables that were used in this text can be found.

A straightforward, but important application of point groups is to inspect the splitting of energy levels, *i.e.* the eigenvalues of the Hamiltonian, upon symmetry lowering. Group theoretically, the energy level is initially labeled by an irrep of the supergroup, Γ (see §A.2). Upon lowering of the symmetry, Γ will in general be a reducible representation of the subgroup. Upon reducing, multiple irreps of the subgroup are found,

$$\Gamma = \bigoplus_{j=1}^{r} a_j \Gamma^{(j)}, \tag{A.44}$$

corresponding to the splitting of the energy level. It can be shown that the integer coefficients can be found from the characters:

$$a_j = \frac{1}{h} \sum_{i=1}^{h} \chi(g_i) \left[\chi^{(j)}(g_i) \right]^*. \tag{A.45}$$

When the supergroup corresponds to the rotation or rotation-inversion group, the representations of SU(2) can be used for which the characters are:

$$\chi^{(j)}(\alpha) = \frac{\sin(2j+1)\frac{\alpha}{2}}{\sin\frac{\alpha}{2}}. \tag{A.46}$$

for a general angular momentum j.

A.4.2 Double point groups

If the angular momentum in Eq. A.46 is an integer number, no problems are encountered. However, when j is half-integer, *e.g.* in cases where spin is added to the description, a complication occurs. Consider a rotation about $\alpha + 2\pi$. The associated character is:

$$\chi^{(j)}(\alpha + 2\pi) = (-1)^{2j} \chi^{(j)}(\alpha). \tag{A.47}$$

For half-integer j, the sign of χ changes after a rotation of 2π. This is a consequence of the 2:1 isomorphism of SU(2) and SO(3) (see A.3.5).

To circumvent this problem, a new group element is introduced, R, which signifies a rotation about 2π and which is explicitly different to the unity operation E:

$$R \neq E \tag{A.48}$$

$$R^2 = E. \tag{A.49}$$

The introduction of this operation, and the combination of this operation with the other original operation of the symmetry group G gives rise to the double group G^*.

The order of G^* is doubled with respect to the order of G. This does however not mean that the number of classes/irreps doubles as some of the new symmetry operations can be added to original classes. This is governed by the rules of Opechowski. As in the case of single groups, character tables can be constructed for the double groups. Their application is completely analogous.

A.4.3 Character tables of point groups

Below, the character tables of the point groups that are used in this text can be found. Schönflies notation was used for the names of the point groups, while Mulliken symbols were used for the irreps.

Two tables can be found for each symmetry. The first table is the conventional character table that can be found at many places. The second table contains the relevant part of the associated double group, *i.e.* the characters of the additional irreps. The remaining characters of the double group can be copied from the character table of the single group. Double groups allow to describe the symmetry of spin wave functions.

T_d

Table A.1:

T_d	E	$8C_3$	$3C_2$	$6\sigma_d$	$6S_4$
A_1	1	1	1	1	1
A_2	1	1	1	-1	-1
E	2	-1	2	0	0
T_1	3	0	-1	-1	1
T_2	3	0	-1	1	-1
$\mathcal{D}^{(2+)}$	5	-1	1	1	-1

Table A.2:

T_d^*	E	R	$8C_3$	$8RC_3$	$3C_2+3RC_2$	$6\sigma_d+6R\sigma_d$	$6S_4$	$6RS_4$
$E_{1/2}$	2	-2	1	-1	0	0	$\sqrt{2}$	$-\sqrt{2}$
$E_{5/2}$	2	-2	1	-1	0	0	$-\sqrt{2}$	$\sqrt{2}$
$G_{3/2}$	4	-4	-1	1	0	0	0	0
$\mathcal{D}^{(1/2)}$	2	-2	1	-1	0	0	$\sqrt{2}$	$-\sqrt{2}$
$\mathcal{D}^{(7/2)}$	8	-8	1	-1	0	0	0	0

C_{3v}

Table A.3:

C_{3v}	E	$2C_3$	$3\sigma_v$
A_1	1	1	1
A_2	1	1	-1
E	2	-1	0
$\mathcal{D}^{(2+)}$	5	-1	1

Table A.4

C^*_{3v}	E	R	$2C_3$	$2RC_3$	$3\sigma_v$	$3R\sigma_v$
$E_{1/2}$	2	-2	1	-1	0	0
$E_{3/2}$	1	-1	-1	1	i	$-i$
	1	-1	-1	1	$-i$	i
$\mathcal{D}^{(1/2)}$	2	-2	1	-1	0	0
$\mathcal{D}^{(7/2)}$	8	-8	1	-1	0	0

D_{4d}

Table A.5:

D_{4d}	E	$2S_8$	$2C_4$	$2S_8^3$	C_2	$4C_2'$	$4\sigma_d$
A_1	1	1	1	1	1	1	1
A_2	1	1	1	1	1	-1	-1
B_1	1	-1	1	-1	1	1	-1
B_2	1	-1	1	-1	1	-1	1
E_1	2	$\sqrt{2}$	0	$-\sqrt{2}$	-2	0	0
E_2	2	0	-2	0	2	0	0
E_3	2	$-\sqrt{2}$	0	$\sqrt{2}$	-2	0	0
$\mathcal{D}^{(2+)}$	5	$1-\sqrt{2}$	-1	$1+\sqrt{2}$	1	1	1

Table A.6:

D_{4d}^{*}	E	R	$2S_8$	$2RS_8$	$2C_4$	$2RC_4$	$2S_8^3$	$2RS_8^3$	C_2+RC_2	$4C_2'+4RC_2'$	$4\sigma_d+4R\sigma_d$
$E_{1/2}$	2	-2	$\sqrt{2+\sqrt{2}}$	$-\sqrt{2+\sqrt{2}}$	$\sqrt{2}$	$-\sqrt{2}$	$\sqrt{2-\sqrt{2}}$	$-\sqrt{2-\sqrt{2}}$	0	0	0
$E_{3/2}$	2	-2	$\sqrt{2-\sqrt{2}}$	$-\sqrt{2-\sqrt{2}}$	$-\sqrt{2}$	$\sqrt{2}$	$-\sqrt{2+\sqrt{2}}$	$\sqrt{2+\sqrt{2}}$	0	0	0
$E_{7/2}$	2	-2	$-\sqrt{2+\sqrt{2}}$	$\sqrt{2+\sqrt{2}}$	$\sqrt{2}$	$-\sqrt{2}$	$-\sqrt{2-\sqrt{2}}$	$\sqrt{2-\sqrt{2}}$	0	0	0
$E_{5/2}$	2	-2	$-\sqrt{2-\sqrt{2}}$	$\sqrt{2-\sqrt{2}}$	$-\sqrt{2}$	$\sqrt{2}$	$\sqrt{2+\sqrt{2}}$	$-\sqrt{2+\sqrt{2}}$	0	0	0
$\mathcal{D}^{(1/2)}$	2	-2	$\sqrt{2+\sqrt{2}}$	$-\sqrt{2+\sqrt{2}}$	$\sqrt{2}$	$-\sqrt{2}$	$\sqrt{2-\sqrt{2}}$	$-\sqrt{2-\sqrt{2}}$	0	0	0
$\mathcal{D}^{(7/2)}$	8	-8	0	0	0	0	0	0	0	0	0

O_h

Table A.7:

O_h	E	$8C_3$	$6C_2'$	$6C_4$	$3C_2$	i	$8S_6$	$6\sigma_d$	$6S_4$	$3\sigma_h$
A_{1g}	1	1	1	1	1	1	1	1	1	1
A_{2g}	1	1	-1	-1	1	1	1	-1	-1	1
E_g	2	-1	0	0	2	2	-1	0	0	2
T_{1g}	3	0	-1	1	-1	3	0	-1	1	-1
T_{2g}	3	0	1	-1	-1	3	0	1	-1	-1
A_{1u}	1	1	1	1	1	-1	-1	-1	-1	-1
A_{2u}	1	1	-1	-1	1	-1	-1	1	1	-1
E_u	2	-1	0	0	2	-2	1	0	0	-2
T_{1u}	3	0	-1	1	-1	-3	0	1	-1	1
T_{2u}	3	0	1	-1	-1	-3	0	-1	1	1
$\mathcal{D}^{(2+)}$	5	-1	1	-1	1	5	-1	1	-1	1

Table A.8:

O_h^*	E	R	$8C_3$	$8RC_3$	$6C_2'$ $+6RC_2'$	$6C_4$	$6RC_4$	$3C_2$ $+3RC_2$	i	Ri	$8S_6$	$8RS_6$	$6\sigma_d$ $+6R\sigma_d$	$6S_4$	$6RS_4$	$3\sigma_h$ $+3R\sigma_h$
$E_{1/2g}$	2	-2	1	-1	0	$\sqrt{2}$	$-\sqrt{2}$	0	2	-2	1	-1	0	$\sqrt{2}$	$-\sqrt{2}$	0
$E_{5/2g}$	2	-2	1	-1	0	$-\sqrt{2}$	$\sqrt{2}$	0	2	-2	1	-1	0	$-\sqrt{2}$	$\sqrt{2}$	0
G_g	4	-4	-1	1	0	0	0	0	4	-4	-1	1	0	0	0	0
$E_{1/2u}$	2	-2	1	-1	0	$\sqrt{2}$	$-\sqrt{2}$	0	-2	2	-1	1	0	$-\sqrt{2}$	$\sqrt{2}$	0
$E_{5/2u}$	2	-2	1	-1	0	$-\sqrt{2}$	$\sqrt{2}$	0	-2	2	-1	1	0	$\sqrt{2}$	$-\sqrt{2}$	0
G_u	4	-4	-1	1	0	0	0	0	-4	4	1	-1	0	0	0	0
$\mathcal{D}^{(1/2)}$	2	-2	1	-1	0	$\sqrt{2}$	$-\sqrt{2}$	0	2	-2	1	-1	0	$\sqrt{2}$	$-\sqrt{2}$	0
$\mathcal{D}^{(7/2)}$	8	-8	1	-1	0	0	0	0	8	-8	1	-1	0	0	0	0

B Racah's toolbox

The elaboration of angular integrals in atomic spectroscopy relies strongly on a few powerful calculation techniques such as irreducible tensor operators and the associated angular momentum algebra, the theory of Lie groups and coefficients of fractional parentage. The intention of this appendix is twofold, namely to refresh the most important formulas to those who are familiar with these techniques and to offer a basic introduction for the less experienced user. This appendix is mainly based on

- B. R. Judd. *Operator techniques in atomic spectroscopy*. Princeton University Press, New Jersey, 1998.
- A. R. Edmonds. *Angular momentum in quantum mechanics*. Princeton University Press, New Jersey, 1996.

B.1 Wigner-nj symbols

The calculation of angular integrals by means of the Wigner-Eckart theorem (see §B.2) is standard practice in atomic spectroscopy. Due to the algebraic structure of the rotation group, angular momenta are frequently encountered, often in the form of so-called Wigner-nj symbols ($n = 3, 6, 9$). Here, the most important identities pertaining to these symbols are reviewed.

B.1.1 Wigner-3j symbols

The Wigner-3j symbol is directly related to the Clebsch-Gordan coefficients of SO(3):

$$\begin{pmatrix} j_1 & j_2 & j_3 \\ m_1 & m_2 & m_3 \end{pmatrix} = \frac{(-1)^{j_1-j_2-m_3}}{\sqrt{2j_3+1}} \langle j_1 j_2 m_1 m_2 | j_1 j_2 j_3 - m_3 \rangle \tag{B.1}$$

and hence couple two angular momenta. Some useful symmetries of the Wigner-3j symbol are that even permutation of the columns keep it invariant, while odd permutations yield a factor $(-1)^{j_1+j_2+j_3}$. Changing the signs of all m-values yields the same factor. The Wigner-3j symbol has some selection rules. It vanishes when one of the m_i cannot correspond to a projection (weight, see §A.3) of the corresponding

j_i, when $m_1 + m_2 + m_3 = 0$ or $|j_1 - j_2| \leq j_3 \leq j_1 + j_2$ (the so-called triangular inequality, often denoted as $\Delta(j_1 j_2 j_3)$) is not fulfilled. Finally, $j_1 + j_2 + j_3$ must be an integer number.

B.1.2 Wigner-6j symbols

The Wigner-6j symbols are encountered when three angular momenta need to be coupled:

$$|(j_1(j_2 j_3)j_{23})jm\rangle = \sum_{j_{12}} (-1)^{j_1+j_2+j_3+j} \sqrt{(2j_{12}+1)(2j_{23}+1)} \begin{Bmatrix} j_1 & j_2 & j_{12} \\ j_3 & j & j_{23} \end{Bmatrix} |((j_1 j_2)j_{12} j_3)jm\rangle. \tag{B.2}$$

They can be expressed as Wigner-3j symbols:

$$\begin{Bmatrix} j_1 & j_2 & j_3 \\ j_4 & j_5 & j_6 \end{Bmatrix} = \sum_{m_1 \ldots m_6} (-1)^{j_4+j_5+j_6+m_4+m_5+m_6} \begin{pmatrix} j_1 & j_2 & j_3 \\ m_1 & m_2 & m_3 \end{pmatrix} \tag{B.3}$$
$$\begin{pmatrix} j_1 & j_5 & j_6 \\ m_1 & m_5 & -m_6 \end{pmatrix} \begin{pmatrix} j_4 & j_2 & j_6 \\ -m_4 & m_2 & m_6 \end{pmatrix} \begin{pmatrix} j_4 & j_5 & j_3 \\ m_4 & -m_5 & m_3 \end{pmatrix}$$

and are hence bound to the triangular conditions $\Delta(j_1 j_2 j_3)$, $\Delta(j_1 j_5 j_6)$, $\Delta(j_4 j_2 j_6)$ and $\Delta(j_4 j_5 j_3)$. Furthermore, they are invariant for every permutation of the columns and when the upper and lower arguments of two columns are interchanged. A 6j symbol with a zero entry reduces to:

$$\begin{Bmatrix} j_1 & j_2 & j_3 \\ j_4 & j_5 & 0 \end{Bmatrix} = \frac{(-1)^{j_1+j_2+j_3}}{\sqrt{(2j_1+1)(2j_2+1)}} \delta_{j_1 j_5} \delta_{j_2 j_4}. \tag{B.4}$$

Useful is Racah's sum rule:

$$\sum_{j_6} (-1)^{j+j_3+j_6} (2j_6+1) \begin{Bmatrix} j_1 & j_2 & j_3 \\ j_4 & j_5 & j_6 \end{Bmatrix} \begin{Bmatrix} j_1 & j_4 & j \\ j_2 & j_5 & j_6 \end{Bmatrix} = \begin{Bmatrix} j_1 & j_2 & j_3 \\ j_5 & j_4 & j \end{Bmatrix}. \tag{B.5}$$

Similar and well-known is the Biedenharn-Elliot sum rule [454].

B.1.3 Wigner-9j symbols

Finally, the Wigner-9j symbol occurs upon the coupling of four momenta:

$$|[(j_1 j_3)j_{13}(j_1 j_4)j_{24}]jm\rangle = \sum_{j_{12} j_{34}} \sqrt{(2j_{12}+1)(2j_{34}+1)(2j_{13}+1)(2j_{24}+1)} \tag{B.6}$$
$$\times \begin{Bmatrix} j_1 & j_2 & j_{12} \\ j_3 & j_4 & j_{34} \\ j_{13} & j_{24} & j \end{Bmatrix} |[(j_1 j_2)j_{12}(j_3 j_4)j_{34}]jm\rangle$$

and can be expressed in terms of $6j$ symbols:

$$\begin{Bmatrix} j_1 & j_2 & j_3 \\ j_4 & j_5 & j_6 \\ j_7 & j_8 & j_9 \end{Bmatrix} = \sum_r (-1)^{2r}(2r+1) \begin{Bmatrix} j_1 & j_4 & j_7 \\ j_8 & j_9 & r \end{Bmatrix} \begin{Bmatrix} j_2 & j_5 & j_8 \\ j_4 & r & j_6 \end{Bmatrix} \begin{Bmatrix} j_3 & j_6 & j_9 \\ r & j_1 & j_2 \end{Bmatrix}. \tag{B.7}$$

Hence, the selection rules of the found $6j$ symbols also relate to the $9j$ symbol. It is furthermore invariant for even permutations of rows and columns, while a factor $(-1)^{\sum j_i}$ is added for odd permutations. A $9j$ symbol with a vanishing argument reduces to a $6j$ symbol:

$$\begin{Bmatrix} j_1 & j_2 & j \\ j_3 & j_4 & j \\ j' & j' & 0 \end{Bmatrix} = \frac{(-1)^{j_2+j_3+j+j'}}{\sqrt{(2j+1)(2j'+1)}} \begin{Bmatrix} j_1 & j_2 & j \\ j_4 & j_3 & j' \end{Bmatrix}. \tag{B.8}$$

B.2 Irreducible tensor operators

Irreducible tensors were introduced by Racah in order to simplify atomic structure calculations. Thanks to their well-defined transformation properties, the application of Wigner-Eckart's theorem reduces the arithmetic labor in computing matrix elements to a large extent if the operator can be identified with such a tensor [1] .

B.2.1 Definition

Irreducible tensors are a generalization of spherical harmonics in terms of their transformation properties under coordinate rotations, R:

$$U(R)\mathcal{T}^{(k)}_q U(R)^{-1} = \sum_{q'=-k}^{k} [\mathcal{D}^{(k)}(R)]_{q'q} \mathcal{T}^{(k)}_{q'}, \tag{B.9}$$

where the Wigner-$\mathcal{D}$ matrices are re-encountered. The irreducible tensor of rank k, $\mathcal{T}^{(k)}$ has $2k+1$ components q and forms the basis of a the irrep $\mathcal{D}^{(k)}$ of SO(3).

The angular momenta J_i generate rotations, implying that:

$$\left[J_z, \mathcal{T}^{(k)}_q\right] = q\mathcal{T}^{(k)}_q \quad \text{and} \quad \left[J_\pm, \mathcal{T}^{(k)}_q\right] = \sqrt{(k \mp q)(k \pm q + 1)}\mathcal{T}^{(k)}_{q\pm 1}, \tag{B.10}$$

which is equivalent to the definition Eq. B.9.

[1] ''*But the method ... necessitates very long calculations. It appeared therefore more convenient to develop a new method.*'' [455].

The reason why irreducible tensors simplify calculations is that the Wigner-Eckart theorem can be directly applied, given their transformation property:

$$\langle \alpha JM | \mathcal{T}_q^{(k)} | \alpha' J' M' \rangle = (-1)^{J-M} \begin{pmatrix} J & k & J' \\ -M & q & M' \end{pmatrix} \langle \alpha J \| \mathcal{T}^{(k)} \| \alpha' J' \rangle. \tag{B.11}$$

In the following subsections, some examples are given which are applied when calculating matrix elements, illustrating the power of the technique.

B.2.2 Special tensors

In the calculation of matrix elements, it is common practice to reformulate the operator in terms of special irreducible tensor operators for which the reduced matrix elements are easily calculated.

Spherical harmonics

The Gaunt coefficients, which are nothing more than the integral of three spherical harmonics having the same argument, are often encountered objects in quantum mechanics:

$$\langle \ell m | Y_q^{(k)} | \ell' m' \rangle = (-1)^m \sqrt{\frac{(2\ell+1)(2k+1)(2\ell'+1)}{4\pi}} \begin{pmatrix} \ell & k & \ell' \\ -m & q & m' \end{pmatrix} \begin{pmatrix} \ell & k & \ell' \\ 0 & 0 & 0 \end{pmatrix}. \tag{B.12}$$

Here, the middle spherical harmonic is regarded as an irreducible tensor operator. Applying the Wigner-Eckart theorem on the left-hand side yields immediately the reduced matrix element:

$$\langle \ell \| Y^{(k)} \| \ell' \rangle = (-1)^\ell \sqrt{\frac{(2\ell+1)(2k+1)(2\ell'+1)}{4\pi}} \begin{pmatrix} \ell & k & \ell' \\ 0 & 0 & 0 \end{pmatrix}. \tag{B.13}$$

Angular momentum

Matrix elements of the components of $\boldsymbol{j}$ are evaluated. The component along the quantization axis is straightforward:

$$\langle jm | j_z | j' m' \rangle = m \delta_{jj'} \delta_{mm'}. \tag{B.14}$$

The vector $\boldsymbol{j}$ transforms as an irreducible tensor of rank-1, for which j_z is the $q = 0$ component. With the Wigner-Eckart theorem, one obtains alternatively:

$$\langle jm | j_z | j' m' \rangle = (-1)^{j-m} \begin{pmatrix} j & 1 & j \\ -m & 0 & m' \end{pmatrix} \langle j \| \boldsymbol{j} \| j' \rangle \tag{B.15}$$

$$= \frac{m \delta_{mm'}}{\sqrt{(2j+1)(j+1)j}} \langle j \| \boldsymbol{j} \| j' \rangle, \tag{B.16}$$

yielding:

$$\langle j \| \boldsymbol{j} \| j' \rangle = \delta_{jj'} \sqrt{(2j+1)(j+1)j} \tag{B.17}$$

and finally:

$$\langle jm | j_q | j'm' \rangle = (-1)^{j-m} \, \delta_{jj'} \, \sqrt{(2j+1)(j+1)j} \begin{pmatrix} \ell & 1 & \ell \\ -m & q & m' \end{pmatrix}. \tag{B.18}$$

For $j = s = 1/2$, one obtains:

$$\langle s \| \boldsymbol{s} \| s' \rangle = \sqrt{\frac{3}{2}}. \tag{B.19}$$

Unit tensor

The unit tensor operator is defined as:

$$U_q^{(k)} = \sum_{i=1}^{N} u_q^{(k)}(i) \qquad \text{for which} \qquad \langle \alpha j \| u^{(k)} \| \alpha' j' \rangle = \delta_{\alpha\alpha'} \delta_{jj'}. \tag{B.20}$$

It is a convenient tool in the calculation of matrix elements as it can be used to replace single-particle operators, of course upon inclusion of the correct reduced matrix element. For a spherical harmonic as an example, one has symbolically,

$$u_q^{(k)} = \frac{Y_q^{(k)}}{\langle \ell \| Y^k \| \ell \rangle}, \tag{B.21}$$

with ℓ the relevant angular momentum. The validity of Eq. B.21 can be easily verified from the Wigner-Eckart theorem.

Finally, the object $V_{q\lambda}^{k1}$ is mentioned. It is a direct product of two tensors working in different Hilbert spaces (see §B.2.3), and is like $U^{(k)}$ defined through its reduced matrix element:

$$V_{q\lambda}^{(k1)} = \sum_{i=1}^{N} v_{q\lambda}^{(k1)}(i) \qquad \text{for which} \qquad \langle \alpha \ell s \| v^{(k1)} \| \alpha' \ell' s' \rangle = \langle \alpha \ell \| u^{(k)} \| \alpha' \ell' \rangle \langle s \| \boldsymbol{s} \| s' \rangle. \tag{B.22}$$

B.2.3 Products of irreducible tensors

Scalar product

The scalar product of two irreducible tensors is defined as:

$$\mathcal{S}^{(k)} \cdot \mathcal{T}^{(k)} = \sum_{q=-k}^{k} (-1)^q \mathcal{S}_q^{(k)} \mathcal{T}_{-q}^{(k)}. \tag{B.23}$$

Matrix elements of such products can be simplified thanks to the Wigner-Eckart theorem:

$$\begin{aligned}\langle \alpha JM|\mathcal{S}^{(k)}\cdot\mathcal{T}^{(k)}|\alpha' J'M'\rangle &= \sum_{\alpha'' J'' M''}\sum_{q=-k}^{k}\langle \alpha JM|\mathcal{S}^{(k)}_q|\alpha'' J'' M''\rangle\langle \alpha'' J'' M''|\mathcal{T}^{(k)}_{-q}|\alpha' J'M'\rangle \\ &= \sum_{\alpha'' J'' M''}\sum_{q=-k}^{k}(-1)^{q+J+J''-M-M''}\begin{pmatrix} J & k & J'' \\ -M & q & M''\end{pmatrix}\begin{pmatrix} J'' & k & J' \\ -M'' & -q & M'\end{pmatrix} \\ &\qquad\times\ \langle \alpha J\|\mathcal{S}^{(k)}\|\alpha'' J''\rangle\langle \alpha'' J''\|\mathcal{T}^{(k)}\|\alpha' J'\rangle \\ &= \sum_{\alpha'' J''}(-1)^{J-J''}\frac{\delta_{JJ'}\delta_{MM'}}{2J+1}\langle \alpha J\|\mathcal{S}^{(k)}\|\alpha'' J''\rangle\langle \alpha'' J''\|\mathcal{T}^{(k)}\|\alpha' J'\rangle \qquad \text{(B.24)}\end{aligned}$$

where in the last step, symmetry properties and the orthogonality relation of the Wigner-3j symbols were used.

Tensor product

The tensor product of two irreducible tensors is defined as:

$$\begin{aligned}\mathcal{X}^{(K)}_Q = \left[\mathcal{S}^{(k_1)}\,\mathcal{T}^{(k_2)}\right]^{(K)}_Q &= \sum_{q_1,q_2}\langle k_1 q_1\, k_2 q_2|KQ\rangle\,\mathcal{S}^{(k_1)}_{q_1}\mathcal{T}^{(k_2)}_{-q_2} \qquad \text{(B.25)} \\ &= \sum_{q_1,q_2}(-1)^{k_1-k_2-Q}\sqrt{2K+1}\begin{pmatrix} k_1 & k_2 & K \\ q_1 & q_2 & -Q\end{pmatrix}\mathcal{S}^{(k_1)}_{q_1}\mathcal{T}^{(k_2)}_{-q_2}.\end{aligned}$$

and transforms according to the irrep $\mathcal{D}^{(K)}$ of SO(3). $\mathcal{X}^{(K)}_Q$ is therefore an irreducible tensor operator itself and commutation relations like Eq. B.10 exist. The possible K values are given by the Clebsch-Gordan series:

$$\mathcal{D}^{(k_1)}\otimes\mathcal{D}^{(k_2)} = \bigoplus_{K=-|k_1-k_2|}^{k_1+k_2}\mathcal{D}^{(K)}. \qquad \text{(B.26)}$$

The evaluation of tensor products is a rewarding effort.

Assume that both tensors in the product act in different Hilbert spaces, with (j_1, m_1) and (j_2, m_2) labels for the respective bases, *i.e.* they commute. The basis of the direct product space is labeled by (J, M). Application of the Wigner-Eckart theorem yields:

$$\langle \alpha j_1 j_2 JM|\mathcal{X}^{(K)}_Q|\alpha' j_1' j_2' J'M'\rangle = (-1)^{J-M}\begin{pmatrix} J & K & J' \\ -M & Q & M'\end{pmatrix}\langle \alpha j_1 j_2 J\|\mathcal{X}^{(K)}\|\alpha' j_1' j_2' J'\rangle. \qquad \text{(B.27)}$$

This can be evaluated in terms of $\mathcal{S}^{(k_1)}$ and $\mathcal{T}^{(k_2)}$ when the bra and ket are decoupled. Together with definition Eq. B.25, this yields three Wigner-3j symbols:

$$\begin{aligned}\langle \alpha j_1 j_2 JM|\mathcal{X}^{(K)}_Q|\alpha' j_1' j_2' J' M'\rangle &= \sum_{m_1 m_2 m_1' m_2' q_1 q_2} (-1)^{j_1-j_2+M+j_1'-j_2'+M'+k_1-k_2+Q} \\ &\times \begin{pmatrix} j_1 & j_2 & J \\ m_1 & m_2 & -M \end{pmatrix}\begin{pmatrix} j_1' & j_2' & J' \\ m_1' & m_2' & -M' \end{pmatrix}\begin{pmatrix} k_1 & k_2 & K \\ q_1 & q_2 & -Q \end{pmatrix} \\ &\times \sqrt{(2J+1)(2J'+1)(2K+1)}\,\langle \alpha j_1 m_1 j_2 m_2|\mathcal{S}^{(k_1)}_{q_1}\mathcal{T}^{(k_2)}_{-q_2}|\alpha' j_1' m_1' j_2' m_2'\rangle \\ = \sum_{m_1 m_2 m_1' m_2' q_1 q_2} &\sum_{\alpha'' j_1'' m_1'' j_2'' m_2''} (-1)^{j_1-j_2+M+j_1'-j_2'+M'+k_1-k_2+Q} \\ &\times \begin{pmatrix} j_1 & j_2 & J \\ m_1 & m_2 & -M \end{pmatrix}\begin{pmatrix} j_1' & j_2' & J' \\ m_1' & m_2' & -M' \end{pmatrix}\begin{pmatrix} k_1 & k_2 & K \\ q_1 & q_2 & -Q \end{pmatrix} \\ &\times \sqrt{(2J+1)(2J'+1)(2K+1)}\,\langle \alpha j_1 m_1|\mathcal{S}^{(k_1)}_{q_1}|\alpha'' j_1'' m_1''\rangle\langle j_2 m_2| j_2'' m_2''\rangle \\ &\times \langle j_1'' m_1''| j_1' m_1'\rangle\langle \alpha'' j_2'' m_2''|\mathcal{T}^{(k_2)}_{-q_2}|\alpha' j_2' m_2'\rangle. \end{aligned} \tag{B.28}$$

Two more 3j symbols appear upon applying the Wigner-Eckart theorem on both irreducible tensor operators:

$$\begin{aligned} = \sum_{m_1 m_2 m_1' m_2' q_1 q_2 \alpha''} &(-1)^{j_1-j_2+M+j_1'-j_2'+M'+k_1-k_2+Q+j_1-m_1+j_2-m_2} \\ &\times \begin{pmatrix} j_1 & j_2 & J \\ m_1 & m_2 & -M \end{pmatrix}\begin{pmatrix} j_1' & j_2' & J' \\ m_1' & m_2' & -M' \end{pmatrix}\begin{pmatrix} k_1 & k_2 & K \\ q_1 & q_2 & -Q \end{pmatrix} \\ &\times \begin{pmatrix} j_1 & k_1 & j_1' \\ -m_1 & q_1 & m_1' \end{pmatrix}\begin{pmatrix} j_2 & k_2 & j_2' \\ -m_2 & q_2 & m_2' \end{pmatrix}\sqrt{(2J+1)(2J'+1)(2K+1)} \\ &\times \langle \alpha j_1\|\mathcal{S}^{(k_1)}\|\alpha'' j_1'\rangle\langle \alpha'' j_2\|\mathcal{T}^{(k_2)}\|\alpha' j_2'\rangle. \end{aligned} \tag{B.29}$$

Finally, both Eq. B.27 and B.29 are multiplied by

$$(-1)^{J-M}\begin{pmatrix} J & K & J' \\ -M & Q & M' \end{pmatrix}, \tag{B.30}$$

and summed over the row indices M, M' and Q. For Eq. B.27, the Wigner-3j symbols vanish because of the orthogonality relation and only the reduced matrix element remains. For Eq. B.29, some rearranging of rows and columns with the symmetry relations of the 3j symbols is required. When this is done in an appropriate way, one recognizes the definition of the Wigner-9j symbol, to obtain:

$$\begin{aligned}\langle \alpha j_1 j_2 J\|\mathcal{X}^{(K)}\|\alpha' j_1' j_2' J'\rangle &= \sqrt{(2J+1)(2J'+1)(2K+1)}\begin{Bmatrix} j_1 & j_1' & k_1 \\ j_2 & j_2' & k_2 \\ J & J' & K \end{Bmatrix} \\ &\times \sum_{\alpha''}\langle \alpha j_1\|\mathcal{S}^{(k_1)}\|\alpha'' j_1'\rangle\langle \alpha'' j_2\|\mathcal{T}^{(k_2)}\|\alpha' j_2'\rangle. \end{aligned} \tag{B.31}$$

The matrix element of the scalar product in the coupled scheme $|j_1 j_2 JM\rangle$ is obtained by setting $K = Q = 0$, implying $k_1 = k_2 = k$. A $9j$ symbol with a vanishing argument reduces to a $6j$ symbol (Eq. B.8), yielding:

$$\begin{aligned}\langle \alpha j_1 j_2 J \| \mathcal{S}^{(k)} \cdot \mathcal{T}^{(k)} \| \alpha' j_1' j_2' J' \rangle &= (-1)^{j_1'+j_2+J} \delta_{JJ'} \delta_{MM'} \begin{Bmatrix} j_1' & j_2' & J \\ j_2 & j_1 & k \end{Bmatrix} \\ &\times \sum_{\alpha''} \langle \alpha j_1 \| \mathcal{S}^{(k)} \| \alpha'' j_1' \rangle \langle \alpha'' j_2 \| \mathcal{T}^{(k)} \| \alpha' j_2' \rangle. \end{aligned} \tag{B.32}$$

Another useful reduced matrix element is that of a single operator working only on one part of the coupled basis. This is obtained by putting $k_2 = 0$ and $\mathcal{T}^{(k)} = 1$ or $k_1 = 0$ and $\mathcal{S}^{(k)} = 1$, yielding respectively:

$$\begin{aligned}\langle \alpha j_1 j_2 J \| \mathcal{S}^{(k)} \| \alpha' j_1' j_2' J' \rangle &= \delta_{j_2 j_2'} (-1)^{j_1+j_2+J'+k} \sqrt{(2J+1)(2J'+1)} \\ &\times \begin{Bmatrix} J & k & J' \\ j_1' & j_2 & j_1 \end{Bmatrix} \langle \alpha j_1 \| \mathcal{S}^{(k)} \| \alpha' j_1' \rangle \\ \langle \alpha j_1 j_2 J \| \mathcal{T}^{(k)} \| \alpha' j_1' j_2' J' \rangle &= \delta_{j_1 j_1'} (-1)^{j_1'+j_2'+J+k} \sqrt{(2J+1)(2J'+1)} \\ &\times \begin{Bmatrix} J & k & J' \\ j_2' & j_1 & j_2 \end{Bmatrix} \langle \alpha j_2 \| \mathcal{T}^{(k)} \| \alpha' j_2' \rangle. \end{aligned} \tag{B.33}$$

Direct product

The direct product of two irreducible tensor operators is defined as:

$$\mathcal{X}^{(k_1 k_2)}_{q_1 q_2} = \mathcal{S}^{(k_1)}_{q_1} \mathcal{T}^{(k_2)}_{q_2} \tag{B.34}$$

and does in general not satisfy Eq. B.9.

If $\mathcal{S}^{(k_1)}$ and $\mathcal{T}^{(k_1)}$ act in different Hilbert spaces, $\mathcal{X}^{(k_1 k_2)}_{q_1 q_2}$ behaves as an irreducible tensor of rank k_1 with respect to the first Hilbert space, while it behaves as an irreducible tensor of rank k_2 with respect to the second Hilbert space. In this case, a reduced matrix element of $\mathcal{X}^{(k_1 k_2)}_{q_1 q_2}$ is *defined* as:

$$\langle j_1 j_2 \| \mathcal{X}^{(k_1 k_2)} \| j_1' j_2' \rangle = \langle j_1 \| \mathcal{S}^{(k_1)} \| j_1' \rangle \langle j_2 \| \mathcal{T}^{(k_2)} \| j_2' \rangle. \tag{B.35}$$

Applying the Wigner-Eckart theorem on both tensors yields:

$$\begin{aligned}\langle j_1 m_1 j_2 m_2 | \mathcal{X}^{(k_1 k_2)}_{q_1 q_2} | j_1' m_1' j_2' m_2' \rangle &= (-1)^{j_1 - m_1 + j_2 - m_2} \begin{pmatrix} j_1 & k_1 & j_1' \\ -m_1 & q_1 & m_1' \end{pmatrix} \begin{pmatrix} j_2 & k_2 & j_2' \\ -m_2 & q_2 & m_2' \end{pmatrix} \\ &\times \langle j_1 j_2 \| \mathcal{X}^{(k_1 k_2)} \| j_1' j_2' \rangle. \end{aligned} \tag{B.36}$$

This shows that $V^{(k1)}_{q,\lambda}$ (Eq. B.22) is indeed a direct product of ranks $k1$. The scalar product of two direct products with the same ranks is given by:

$$\mathcal{X}^{(k_1 k_2)} \cdot \mathcal{Y}^{(k_1 k_2)} = \sum_{q_1 q_2} (-1)^{q_1+q_2} \mathcal{X}^{(k_1 k_2)}_{q_1 q_2} \mathcal{Y}^{(k_1 k_2)}_{-q_1\ -q_2}. \tag{B.37}$$

If it is assumed that $\mathcal{X}^{(k_1k_2)}$ works only on the momenta ℓ_1 and s_1 and $\mathcal{Y}^{(k_1k_2)}_{q_1q_2}$ works exclusively on ℓ_2 and s_2, while the k_1 part of both tensors transforms as a irreducible tensor in the ℓ Hilbert space and similar for the k_2 parts with the s Hilbert space, Eq. B.24 can be applied twice:

$$\begin{aligned}\langle \alpha \ell_1 s_1,\, \ell_2 s_2;\, LSM_LM_S|\mathcal{X}^{(k_1k_2)}\cdot\mathcal{Y}^{(k_1k_2)}|\alpha'\ell_1' s_1',\, \ell_2' s_2';\, L'S'L'_MS'_M\rangle \\ = \quad (-1)^{\ell_1'+\ell_2+L+s_1'+s_2+S}\delta_{LL'}\delta_{SS'}\begin{Bmatrix}\ell_1' & \ell_2' & L\\ \ell_2 & \ell_1 & k_1\end{Bmatrix}\begin{Bmatrix}s_1' & s_2' & S\\ s_2 & s_1 & k_2\end{Bmatrix} \\ \times\sum_{\alpha''}\langle \alpha\ell_1 s_1\|\mathcal{X}^{(k_1k_2)}\|\alpha''\ell_1' s_1'\rangle\langle\alpha''\ell_2 s_2\|\mathcal{Y}^{(k_1k_2)}\|\alpha'\ell_2' s_2'\rangle \quad \text{(B.38)}\end{aligned}$$

B.3 Coefficients of fractional parentage

Another useful concept that was launched by Racah are the coefficients of fractional parentage (CFP). They are a clever way to circumvent the expansion of mp basis states in terms of Slater determinants. This was standard practice in pre-1940s atomic physics, prohibiting a serious investigation of configurations with more than two electrons.

B.3.1 Definition

One-particle CFPs relate mp basis functions of configuration ℓ^N to those of configuration ℓ^{N-1}. In the RS basis,

$$\begin{aligned}|\ell^N\,\alpha LSM_LM_S\rangle \quad = \sum_{\overline{\alpha}\,\overline{L}\,\overline{S}\,\overline{M}_L\,\overline{M}_S m_\ell m_s} & \langle \overline{L}\,\overline{M}_L\,\ell m_\ell|LM_L\rangle\,\langle\overline{S}\,\overline{M}_S\,sm_s|SM_S\rangle \\ & \times\langle \ell^{N-1}\,\overline{\alpha}\,\overline{L}\,\overline{S};\,\ell s|\}\,\ell^N\,\alpha LS\rangle \\ & \times|\ell^{N-1}\,\overline{\alpha}\,\overline{L}\,\overline{S}\,\overline{M}_L\,\overline{M}_S\rangle|\ell s m_\ell m_s\rangle, \quad \text{(B.39)}\end{aligned}$$

where the third coefficient is the CFP. For nonzero CFPs, $|\ell^N\,\alpha LS\rangle$ is called a daughter term of $|\ell^{N-1}\,\overline{\alpha}\overline{LS}\rangle$, while $|\ell^{N-1}\,\overline{\alpha}\overline{LS}\rangle$ is called a parent term of $|\ell^N\,\alpha LS\rangle$.

Below, it will be shown that the difficulty in calculating matrix elements is shifted to the difficulty in calculating CFPs. The advantage of using CFPs is that they have to be calculated only once after which they can be employed for different kinds of matrix elements. Racah obtained the one-particle CFPs for d^N and f^N configurations by factorizing them according to the irreps of a chain of Lie groups. This text will not go into the details of their calculation, but will take the results for granted. CFPs can be found in the famous tables by Nielson and Koster [111].

When the techniques of second quantization became more in use, the interpretation of the CFPs as reduced matrix element of the fermion creation and annihilation operators was evident [116].

B.3.2 Matrix elements

Knowledge of the CFPs allows one to calculate matrix element of mp states in a very straightforward way as the calculation is effectively reduced to a single-particle matrix element. This is demonstrated below for single- and two-particle operators in the RS basis.

Single-particle operator

A single-particle operator acts only on one electron. For an N-electron shell, it reads:

$$F = \sum_{i=1}^{N} f(i). \tag{B.40}$$

The electrons in the same shell are equivalent, yielding for the matrix element:

$$\langle \ell^N\, \alpha LSM_LM_S|F|\ell^N\, \alpha' L'S'M'_LM'_S\rangle = N\langle \ell^N\, \alpha LSM_LM_S|f(i)|\ell^N\, \alpha' L'S'M'_LM'_S\rangle, \tag{B.41}$$

where the index i is arbitrary and can be omitted.

One could directly insert the CFP expansion, Eq. B.39,

$$\begin{aligned} = \; N \sum_{\substack{\overline{\alpha}\ \overline{L}\ \overline{S}\ \overline{M}_L\ \overline{M}_S m_\ell m_s \\ \overline{\alpha}'\ \overline{L}'\ \overline{S}'\ \overline{M}'_L\ \overline{M}'_S m'_\ell m'_s}} & \langle LM_L|\overline{L}\ \overline{M}_L\ \ell m_\ell\rangle\ \langle \overline{L}'\ \overline{M}'_L\ \ell m'_\ell|L'M'_L\rangle \\ & \times\langle SM_S|\overline{S}\ \overline{M}_S\ sm_s\rangle\ \langle \overline{S}'\ \overline{M}'_S\ sm'_s|S'M'_S\rangle \\ & \times\langle \ell^{N-1}\ \overline{\alpha}'\overline{L}'\overline{S}';\ \ell s|\}\ \ell^N\ \alpha' L'S'\rangle\ \langle \ell^N\ \alpha LS\{|\ell^{N-1}\ \overline{\alpha}\ \overline{L}\ \overline{S};\ \ell s\rangle \\ & \times\underbrace{\langle \ell^{N-1}\ \overline{\alpha}\ \overline{L}\ \overline{S}\ \overline{M}_L\ \overline{M}_S|\ell^{N-1}\ \overline{\alpha}'\overline{L}'\overline{S}'\overline{M}'_L\overline{M}'_S\rangle}_{\delta_{\overline{\alpha}\,\overline{\alpha}'}\ \delta_{\overline{L}\,\overline{L}'}\ \delta_{\overline{S}\,\overline{S}'}\ \delta_{\overline{M}_L\,\overline{M}'_L}\ \delta_{\overline{M}_S\,\overline{M}'_S}}\langle \ell m_\ell sm_s|f|\ell m'_\ell sm'_s\rangle, \end{aligned} \tag{B.42}$$

showing that the matrix element is reduced to a single-particle matrix element. If the operator transforms according to Eq. B.9, it can be regarded as an irreducible tensor operator and the Wigner-Eckart theorem can be applied. Then, the sums over the angular momentum projections in Eq. B.42 should have the same dependency on M_L, M_S, M'_L, M'_S and the rank and index of the operator as dictated by the Wigner-Eckart theorem. Then, the projections can be left out of the equations when the reduced matrix elements are calculated.

As an example, it is assumed that $f_q^{(k)}(i)$ works only on the orbital angular momentum. Applying the Wigner-Eckart theorem yields:

$$\begin{aligned} \langle \ell^N\, \alpha LS\|F^{(k)}\|\ell^N\, \alpha' L'S'\rangle \;\; = \;\; & N\delta_{SS'} \sum_{\overline{\alpha}\ \overline{L}\ \overline{S}} \langle \ell^{N-1}\ \overline{\alpha}\ \overline{L}\ \overline{S};\ \ell s|\}\ \ell^N\ \alpha' L'S\rangle \\ & \times\langle \ell^N\ \alpha LS\{|\ell^{N-1}\ \overline{\alpha}\ \overline{L}\ \overline{S};\ \ell s\rangle\langle \ell^{N-1}\ \overline{\alpha}\ \overline{L};\ \ell\ \|\ f^{(k)}\ \|\ \ell^{N-1}\ \overline{\alpha L};\ \ell\rangle. \end{aligned} \tag{B.43}$$

The last factor is a coupled representation L, while $f^{(k)}(i)$ works only on ℓ, therefore, Eq. B.33 can be used:

$$\begin{aligned}\langle \ell^N\, \alpha LS \| F^{(k)} \| \ell^N\, \alpha' L' S' \rangle &= N\delta_{SS'} \sqrt{(2L+1)(2L'+1)} \sum_{\overline{\alpha}\,\overline{L}\,\overline{S}} (-1)^{L+\ell+\overline{L}+k} \begin{Bmatrix} L & k & L' \\ \ell & \overline{L} & \ell \end{Bmatrix} \\ &\times \langle \ell^{N-1}\, \overline{\alpha}\, \overline{L}\, \overline{S};\, \ell s | \}\, \ell^N\, \alpha' L' S \rangle \langle \ell^N\, \alpha LS \{ | \ell^{N-1}\, \overline{\alpha}\, \overline{L}\, \overline{S};\, \ell s \rangle \langle \ell \| f^{(k)} \| \ell \rangle. \end{aligned} \tag{B.44}$$

Matrix elements of the unit tensor, $F^{(k)} = U^{(k)}$, Eq. B.20, can be calculated if the CFP's are available:

$$\begin{aligned}\langle \ell^N\, \alpha LS \| U^{(k)} \| \ell^N\, \alpha' L' S' \rangle &= N\delta_{SS'} \sqrt{(2L+1)(2L'+1)} \sum_{\overline{\alpha}\,\overline{L}\,\overline{S}} (-1)^{L+\ell+\overline{L}+k} \begin{Bmatrix} L & k & L' \\ \ell & \overline{L} & \ell \end{Bmatrix} \\ &\times \langle \ell^{N-1}\, \overline{\alpha}\, \overline{L}\, \overline{S};\, \ell s | \}\, \ell^N\, \alpha' L' S \rangle \langle \ell^N\, \alpha LS \{ | \ell^{N-1}\, \overline{\alpha}\, \overline{L}\, \overline{S};\, \ell s \rangle. \end{aligned} \tag{B.45}$$

In the case of a scalar operator, *i.e.* $k = 0$, the $6j$ symbol in Eq. B.44 can be evaluated:

$$\begin{Bmatrix} L & 0 & L \\ \ell & \overline{L} & \ell \end{Bmatrix} = (-1)^{\overline{L}+\ell+L} \frac{\delta_{LL'}}{\sqrt{(2\ell+1)(2L+1)}}. \tag{B.46}$$

If furthermore the matrix element is diagonal, $\alpha = \alpha'$, a short expression is obtained thanks to the normalization of the CFPs:

$$\langle \ell^N\, \alpha LS \| F^{(0)} \| \ell^N\, \alpha LS \rangle = N \sqrt{\frac{2L+1)}{2\ell+1}} \langle \ell \| f^{(0)} \| \ell \rangle. \tag{B.47}$$

For the direct product $V^{(k1)}$ (B.22), one obtains:

$$\langle \ell^N\, \alpha LS \| V^{(k1)} \| \ell^N\, \alpha' L' S' \rangle \tag{B.48}$$

$$\begin{aligned} &= N \sum_{\overline{\alpha}\,\overline{L}\,\overline{S}} \langle \ell^{N-1}\, \overline{\alpha}\, \overline{L}\, \overline{S};\, \ell s | \}\, \ell^N\, \alpha' L' S \rangle \langle \ell^N\, \alpha LS \{ | \ell^{N-1}\, \overline{\alpha}\, \overline{L}\, \overline{S};\, \ell s \rangle \\ &\qquad \times \langle \ell^{N-1}\, \overline{\alpha}\, \overline{L}\, \overline{S};\, \ell s \parallel v^{(k1)} \parallel \ell^{N-1}\, \overline{\alpha}\, \overline{L}\, \overline{S};\, \ell s \rangle \\ &= N \sum_{\overline{\alpha}\,\overline{L}\,\overline{S}} \langle \ell^{N-1}\, \overline{\alpha}\, \overline{L}\, \overline{S};\, \ell s | \}\, \ell^N\, \alpha' L' S \rangle \langle \ell^N\, \alpha LS \{ | \ell^{N-1}\, \overline{\alpha}\, \overline{L}\, \overline{S};\, \ell s \rangle \\ &\qquad \times \langle \ell^{N-1}\, \overline{\alpha}\, \overline{L}\, \overline{S};\, \ell s \parallel u^{(k)} \parallel \ell^{N-1}\, \overline{\alpha}\, \overline{L}\, \overline{S};\, \ell s \rangle \\ &\qquad \times \langle \ell^{N-1}\, \overline{\alpha}\, \overline{L}\, \overline{S};\, \ell s \parallel s^{(1)} \parallel \ell^{N-1}\, \overline{\alpha}\, \overline{L}\, \overline{S};\, \ell s \rangle \\ &= N \sqrt{\frac{3}{2}} \sqrt{(2S+1)(2S'+1)(2L+1)(2L'+1)} \sum_{\overline{\alpha}\,\overline{L}\,\overline{S}} \begin{Bmatrix} S & S' & 1 \\ \frac{1}{2} & \frac{1}{2} & \overline{S} \end{Bmatrix} \begin{Bmatrix} L & L' & k \\ \ell & \ell & \overline{L} \end{Bmatrix} \\ &\qquad \times (-1)^{\overline{L}+\overline{S}+L+S+\ell+\frac{1}{2}+k+1} \langle \ell^{N-1}\, \overline{\alpha}\, \overline{L}\, \overline{S};\, \ell s | \}\, \ell^N\, \alpha' L' S \rangle \langle \ell^N\, \alpha LS \{ | \ell^{N-1}\, \overline{\alpha}\, \overline{L}\, \overline{S};\, \ell s \rangle \end{aligned}$$

where in the final step, Eq. B.33 was used twice and the expression for the reduced matrix element Eq. B.19 was filled in.

C VALUES OF EMPIRICAL PARAMETERS

In this appendix, values for the different empirical parameters that are required to construct band diagrams containing lanthanide impurity levels are given. For more information, see chapter 6.

Ln	$E_{4f}(Ln^{2+}, free)$	$E_{4f}(Ln^{3+}, free)$
La	-18.29	—
Ce	-20.20	-36.76
Pr	-21.62	-38.98
Nd	-22.10	-40.6
Pm	-22.37	-41.2
Sm	-23.60	-41.6
Eu	-24.92	-42.97
Gd	-20.34	-44.5
Tb	-21.91	-39.37
Dy	-22.89	-41.2
Ho	-22.84	-42.4
Er	-22.74	-42.5
Tm	-23.68	-42.4
Yb	-25.03	-43.56
Lu	—	-45.25

Table C.1 – Ionization potentials of the free lanthanide ions [216]. All values in eV.

Ln	$\overline{\Delta E(Ln, Eu, 2)}$	$\overline{\Delta E(Ln, Eu, 3)}$
La	5.61	—
Ce	4.13	5.24
Pr	2.87	3.39
Nd	2.43	1.90
Pm	2.34	1.46
Sm	1.25	1.27
Eu	0.00	0.00
Gd	4.56	-1.34
Tb	3.21	3.57
Dy	2.27	2.15
Ho	2.40	1.05
Er	2.58	1.12
Tm	1.72	1.28
Yb	0.43	0.24
Lu	—	-0.98

Table C.2 – Shape of the 4f zig-zag curves with respect to the europium ion [216]. All values in eV.

Ln	$E^{fd}(Ln^{2+}, free)$	$E^{fd}(Ln^{3+}, free)$
La	-0.94	—
Ce	-0.35	6.12
Pr	1.56	7.63
Nd	1.93	8.92
Pm	1.96	9.24
Sm	3.00	9.34
Eu	4.22	10.50
Gd	-0.20	11.80
Tb	1.19	7.78
Dy	2.17	9.25
Ho	2.25	10.10
Er	2.12	9.86
Tm	2.95	9.75
Yb	4.22	10.89
Lu	—	12.26

Table C.3 – Energy of the first spin-allowed $4f^{N-1}5d^1$ multiplet with respect to the $4f^N$ ground state of the free lanthanide ions [216]. All values in eV.

Ln	$E^{fs}(Ln^{2+}, free)$	$E^{fs}(Ln^{3+}, free)$
La	0.79	—
Ce	2.39	10.74
Pr	3.52	12.43
Nd	3.76	13.65
Pm	3.65	13.76
Sm	4.49	13.66
Eu	5.95	14.53
Gd	0.84	15.55
Tb	2.19	10.92
Dy	2.86	12.29
Ho	2.71	12.98
Er	2.40	12.84
Tm	3.14	12.27
Yb	4.30	13.14
Lu	—	14.48

Table C.4 – Energy of the first spin-allowed $4f^{N-1}6s^1$ multiplet with respect to the $4f^N$ ground state of the free lanthanide ions [307]. All values in eV.

D Light units

Photometric quantities and units are often used in the field of illumination engineering and by consequence also this text. In contrast to the more common radiometric quantities, photometric quantities are defined by means of the spectral eye sensitivity of the (average) human.

Radiometric or energetic quantities can in general be used to describe all types of radiation. The total integrated power, emitted by a source, is called the radiant flux (Φ_E [W]). When the emitted power is restricted to a specific direction, *i.e.* per unit of solid angle, one obtains the radiant intensity (I_E (W/sr)). If the radiation source is extended in space, one can define the emitted power per unit of surface area, the radiant exitance (M_E (W/m^2)). Finally, when the emitted power of an extended source, expressed per unit of surface area, is considered in a specific direction, *i.e.* per unit of solid angle, one obtains the radiance (L_E (W/m^2/sr)).

The above quantities pertain to radiation sources. When radiation is observed, the incident power per unit surface is defined as the irradiance (E_E (W/m^2)).

For all enumerated quantities, one can introduce a spectral density, *e.g.* the spectral radiant flux:

$$\Phi_E = \int \Phi_{E\lambda} \, \mathrm{d}\lambda, \tag{D.1}$$

where λ is the wavelength of the light.

A photometric quantity can be associated with every radiometric quantity. These are only relevant in the visible part of the electromagnetic spectrum (± 380-780 nm). To obtain a photometric quantity, a weighted integration of the spectral radiometric quantity is performed. The weight function, $K(\lambda)$ is defined as:

$$K(\lambda) = K_m V(\lambda) \tag{D.2}$$

where $V(\lambda)$ is the spectral eye sensitivity or luminosity function, normalized to the maximum and K_m is a proportionality constant. The photometric quantity X_P is hence obtained from the radiometric spectral density $X_{E,\lambda}$ as follows:

$$X_P = K_m \int V(\lambda) X_{E,\lambda} \, \mathrm{d}\lambda. \tag{D.3}$$

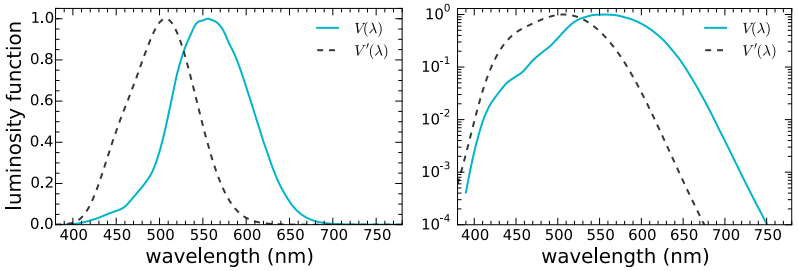

Figure D.1 – Luminosity functions for photopic ($V(\lambda)$ and scotopic ($V'\lambda$)) vision, displayed on linear and logarithmic scales.

Thus far, photopic vision was implicitly assumed. In this case, the luminosity function $V(\lambda)$ peaks around 550 nm and $K_m = 683$ lm/W, where the lumen (lm) was introduced as unit for luminous flux, the photometric analogue of radiant flux. For scotopic vision, the spectral eye sensitivity is different and one uses the notation $K'(\lambda)$, $V'(\lambda)$ and K'_m. The scotopic luminosity function peaks at 505 nm and $K'_m = 1754$ lm/W[1]. The functions $V(\lambda)$ and $V'(\lambda)$ are shown in Fig. D.1. More elaboration on the origin of these functions is given in appendix E. An overview of the most common radiometric and photometric quantities is given in Tab. D.1.

Spectra that are commonly found in scientific literature, including this text, are typically expressed as *intensity* as function of wavelength. The intensity typically scales with the power incident on the detector, *i.e.* the irradiance. Alternatively, the intensity can scale with the number of detected photons. Both are not equivalent, but are connected by the photon energy (Eq. 2.13).

For specific cases, *e.g.* when energy level schemes are envisioned, it can be more useful to study spectra as a function of photon energy instead of wavelength. What can then be easily passed over is the fact that the equidistant wavelength intervals, $\Delta\lambda$, in which emission spectra are measured are not equidistant on energy scale due to Eq. 2.13 which is to be regarded as a coordinate transformation in this context. For this reason, also the ordinates of the data points have to be rescaled according to:

$$\int_{\Delta E} I(E)\,\mathrm{d}E = \int_{\Delta\lambda} I\left[E(\lambda)\right]\left|J(\lambda,E)\right|\,\mathrm{d}\lambda, \tag{D.4}$$

where ΔE are the corresponding -non-equidistant- energy intervals and J is the Jacobian of the transformation *i.e.* $\frac{\partial E}{\partial \lambda}$, yielding an factor $\frac{hc}{E^2}$ which needs to be multiplied to the ordinates of emission scans, measured in equidistant wavelength intervals, to obtain the correct spectrum on energy scale [456].

[1] The nominal values for K_m and K'_m were determined at the General Conference on Weights and Measures in 1979 and based on the historical definition of the candela (cd), stating that the luminous intensity of a a candle flame is 1 cd.

Table D.1 – Overview of radiometric and photometric quantities. ϕ represents the angle between the surface normal and the line of sight [458].

radiometric	definition	unit	photometric	definition	unit
radiant flux	Φ_E	W	luminous flux	Φ_P	lm
radiant exitance	$M_E = \frac{d\Phi_E}{dS}$	W/m^2	luminous exitance	$M_P = \frac{d\Phi_P}{dS}$	lm/m^2
radiant intensity	$I_E = \frac{d\Phi_E}{d\Omega}$	W/sr	luminous intensity	$I_P = \frac{d\Phi_P}{d\Omega}$	lm/sr [cd]
radiance	$L_E = \frac{d\Phi_E}{dS\cos\phi}$	$W/m^2/sr$	luminance	$L_P = \frac{d\Phi_P}{dS\cos\phi}$	cd/m^2 [nit]
irradiance	$E_E = \frac{d\Phi_E}{dS}$	W/m^2	illuminance	$E_P = \frac{d\Phi_P}{dS}$	lm/m^2 [lux]

Absorption and excitation scans on the other hand do not require this Jacobian conversion. The reason for this is the fact that these spectra are measured in a relative fashion with respect to the spectrum of the light source used during the measurement. Both the measured signal as the reference signal of the light source are subject to the same Jacobian conversion which cancel each other [457].

A surface is said to be a Lambertian radiator or to have a Lambertian reflectance if the radiance is isotropic (or alternatively when the radiant intensity obeys a cosine behavior with respect to the surface normal). For completeness, some alternative quantities are given in tables D.2 and D.3.

Table D.2 – Alternative units for luminance [458].

lambert [L]	$1\,\text{mL} = 3.183\,\text{cd/m}^2$
footlambert [fL]	$1\,\text{fL} = 3.426\,\text{cd/m}^2$

Table D.3 – Alternative unit for illuminance [458].

footcandle [fc]	$1\,\text{fc} = 10.76\,\text{lux}$

E QUANTIFYING COLOR

This text utilizes concepts from color theory on multiple places. This appendix is meant to briefly introduce the basic ideas of the extensive domain of colorimetry.

E.1 Physiological origin of color

The human eye contains two types of photoreceptor cells which have the ability to convert ambient light, a visual stimulus, into an electrical signal. The neural network, composed of the optic nerve and the brains are responsible for the further signal processing. The photoreceptor cells are called rods and cones. Both have a strongly differing spectral sensitivity and resolution. Under conditions of low luminances, it is thanks to the rods that one can see, *i.e.* scotopic vision, as these cells are about 100 times more sensitive than cones in the range between 400 nm and 500 nm. When the luminance increases, the rods get saturated while the cones get active, *i.e.* photopic vision[1]. As three different types of cones occur, all having a different spectral sensitivity, a small part of the spectral information can be processed by the neural network. This information is called *color*.

E.1.1 Scotopic vision

Assume that $\alpha'(\lambda)$ is the absorption characteristic of the rods. Their response to a visual stimulus with spectral irradiance $S(\lambda)$ is then described by the number:

$$A' = \int \alpha'(\lambda) S(\lambda) \mathrm{d}\lambda. \tag{E.1}$$

In this number, which describes scotopic vision, no wavelength dependent information is left, *i.e.* scotopic vision is color blind. A' solely measures the subjective brightness of the stimulus[2].

The absorption coefficient $\alpha'(\lambda)$ is the basis for the definition of the photometric properties that were discussed in appendix D. The eye sensitivity curve $K'(\lambda)$ was

[1] The intermediate regime between photopic and scotopic vision, *i.e.* mesopic vision is not discussed here.

[2] The true experienced brightness will be the result of the data processing of A' by the whole visual system, a complex, nonlinear system.

constructed from experiments where subjects were asked to adapt the intensities of light sources with different spectral distributions until the perceived brightnesses were are equal.

E.1.2 Photopic vision

Analogous as for scotopic vision, the response of the cones for a stimilus $S(\lambda)$ can be described by means of the numbers:

$$A_i = \int \alpha_i(\lambda) S(\lambda) \mathrm{d}\lambda \qquad (i = 1, 2, 3), \tag{E.2}$$

where the index runs over the three different types of cones.

In color matching experiments, subjects are asked to alter the relative intensities of three different light sources with spectra $P_j(\lambda)$, the so-called primary colors, to achieve a mixing color which corresponds visually to a fourth light source with spectrum $S(\lambda)$. This is expressed by following relation:

$$S(\lambda) \quad \leftrightarrow \quad \sum_{j=1}^{3} c_j P_j(\lambda), \tag{E.3}$$

where the numbers c_j are the so-called tristimulus coefficients. These coefficients can become negative, meaning that the corresponding spectrum $P_j(\lambda)$ has to be added to the target spectrum $S(\lambda)$. Two spectra have the same color when the A_i values are equal. The above relationship can hence be formulated as

$$\int \alpha_i(\lambda) S(\lambda) \mathrm{d}\lambda = \sum_{i=1}^{3} c_j \int \alpha_i(\lambda) P_j(\lambda) \mathrm{d}\lambda. \tag{E.4}$$

This system of three equations and three unknowns (c_j) has a unique solution when the primary colors are independent, *i.e.* when the determinant of the system is nonzero. The linearity of the map Eq. E.3 was experimentally verified.

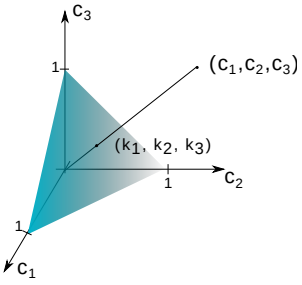

Figure E.1 – Chromatic space (k_j) as a subspace of the total color space (c_j)

The tristimulus coefficients can hence be interpreted as the components of a vector, describing the color of $S(\lambda)$ in a three-dimensional linear vector space, *color space*. The primary colors $P_j(\lambda)$ can be conceived as basis vectors. Changing the primary colors, *i.e.* a basis transformation, corresponds to changing the tristimulus values. The new c_j values can be calculated with the 3x3 matrix describing the basis transformation. The relative intensities of the primary colors is conventionally chosen such that the tristimulus coefficients for a uniform white

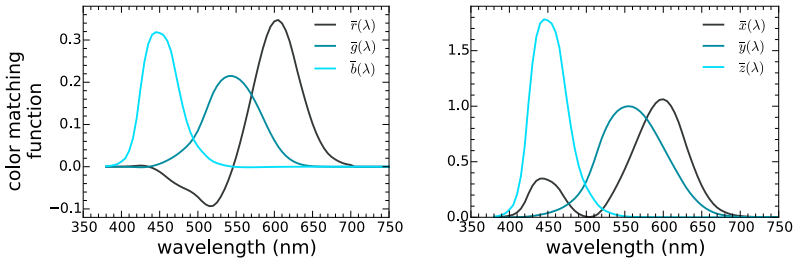

Figure E.2 – Color matching functions for both standards in the CIE 1931 space.

spectrum are equal.

To determine the coordinates of a color, a color matching experiment has to be performed in principle. However, thanks to the linear character of the model it is sufficient to determine the tristimulus values for monochromatic, *i.e.* spectral, colors once. The tristimulus values that are obtained in this way for every wavelength are referred to as the color matching functions $m_j(\lambda)$. These allow to determine the color coordinates of an arbitrary spectrum $S(\lambda)$:

$$c_j = \int m_j(\lambda) S(\lambda) \mathrm{d}\lambda. \tag{E.5}$$

The c_j values also carry information on the brightness of the stimulus. Because the brightness can be determined from the luminosity function $K(\lambda)$, the tristimulus coefficients are typically normalized:

$$k_j = \frac{c_j}{\sum_{i=1}^{3} c_i}, \tag{E.6}$$

implying that a color can be described by only two independent values. The k_j values are referred to as the trichromatic coordinates or color coordinates. The luminance, measuring the brightness of the stimulus, is the third independent variable allowing to reproduce tristimulus coefficients from color coordinates. Summarized, the three-dimensional vector space breaks up into a (2+1)-dimensional (color + luminance)-space. The two-dimensional subspace is called chromatic space[3]. The connection between the three-dimensional color space and the two-dimensional chromatic space is illustrated in Fig. E.1.

[3]When two sets of tristimulus values are given, it is trivial to calculate the tristimulus values of the mixed color thanks to the linearity of the model, *i.e.* $c_j^{(\mathrm{mix})} = c_j^{(1)} + c_j^{(2)}$. Calculating mixed colors in the chromatic subspace is less trivial, requiring a correct accounting of the luminances. What is known is that a mixed color is always on the line connecting both primary colors. From more than two primaries, all colors inside the defining polygon can be made by suitable color tuning.

E.2 CIE (x, y, Y) (1931)

To achieve a unique set of color coordinates, it is still required to define primary colors as well as a standard observer. This was done in 1931 by the CIE (*Comité Internationale de l'Eclairage*). Monochromatic primaries for red (700.0 nm), green (546.1 nm) and blue (435.8 nm) were defined and color matching functions, $\bar{r}(\lambda)$, $\bar{g}(\lambda)$ and $\bar{b}(\lambda)$, were determined in accordance (see Fig. E.2(a)). The tristimulus values that are determined for an arbitrary stimulus are denoted as (R, G, B), the trichromatic coordinates as (r, g, b).

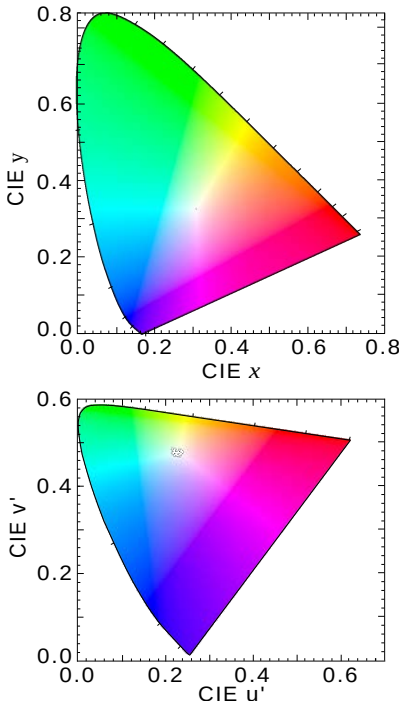

Figure E.3 – The CIE 1931 (x, y) and CIE 1976 (u', v') chromatic spaces.

As can be seen in Fig. E.2(a), the function $\bar{r}(\lambda)$ is negative in the region around 500 nm. This means that the c_j and k_j values can also take negative values. To avoid this, alternative primary colors were derived from the above standard. The corresponding color matching functions $\bar{x}(\lambda)$, $\bar{y}(\lambda)$ and $\bar{z}(\lambda)$ are positive over the full visible spectrum by construction. The tristimulus and trichromatic coordinates are respectively denoted as (X, Y, Z) and (x, y, z) and are positive for all physical colors. The consequence of this construction is that the newly defined primary colors are no physical colors[4]. This is however not problematic as both standards are related by a linear transformation. Additional, one has chosen the new primaries such that the function $\bar{y}(\lambda)$ is equal to the luminosity function $V(\lambda)$. Altering slightly the definition, Eq. E.5, it is put that:

$$\begin{pmatrix} X \\ Y \\ Z \end{pmatrix} = \mathcal{K} \int \begin{pmatrix} \bar{x}(\lambda) \\ \bar{y}(\lambda) \\ \bar{z}(\lambda) \end{pmatrix} S(\lambda)\, \mathrm{d}\lambda \qquad \text{(E.7)}$$

with $\mathcal{K} = K_m = 683$ lm/W for a radiating surface and with Y the luminance of the surface. Until today, the (x, y, Y) coordinates are frequently used to characterize colors even though better alternatives are available such as the CIELUV and CIELAB (1976) (u, v) and (u', v') color coordinates. An important shortcoming of the CIE (x, y) coordinates is that distances do not encode perceived color differences in a uniform way across chromatic space. Figure E.3 displays the chromaticity diagram in terms of the (x, y) and the more uniform (u', v') coordinates.

[4] *"It was octarine, the color of magic. It was alive and glowing and vibrant and it was the undisputed pigment of the imagination, because wherever it appeared it was a sign that mere matter was a servant of the powers of the magical mind. It was enchantment itself. But Rincewind always thought it looked a sort of greenish-purple.* - The Color of Magic, Terry Pratchett (1983).

BIBLIOGRAPHY

[1] E.N. Harvey. *A History of Luminescence: From the Earliest Times Until 1900*. CreateSpace Independent Publishing Platform, 2015.

[2] B.H. Bransden and C.J. Joachain. *Quantum Mechanics*. Prentice Hall, 2000.

[3] Wikipedia, the free encyclopedia. `https://en.wikipedia.org/wiki/Main_Page`, 2016.

[4] Annalen der physik. `http://annalen-der-physik.org/`, 2016.

[5] P. F. Smet, I. Moreels, Z. Hens, and D. Poelman. Luminescence in Sulfides: A Rich History and a Bright Future. *Materials*, 3(4):2834–2883, 2010.

[6] H. F. Brito, J. Hölsä, T. Laamanen, M. Lastusaari, M. Malkamäki, and L. C. V. Rodrigues. Persistent luminescence mechanisms: human imagination at work. *Optical Materials Express*, 2(4):371–381, 2012.

[7] S. Shionoya, W.M. Yen, and H. Yamamoto. *Phosphor Handbook*. CRC Press, 2006.

[8] Hans E. Suess and Harold C. Urey. Abundances of the Elements. *Rev. Mod. Phys.*, 28:53–74, 1956.

[9] China consolidates grip on rare earths.

[10] A. Meijerink. Van Kröger tot Blasse, Luminescentie van tl-buis en kleuren-tv. *KNAW/KNCV*, 2001.

[11] N.W. Ashcroft and N.D. Mermin. *Solid State Physics*. Cengage Learning, 2011.

[12] Grosso, G. and Parravicini, G.P. *Solid State Physics*. Elsevier Science, 2000.

[13] P. F. Smet, A. B. Parmentier, and D. Poelman. Selecting conversion phosphors for white light-emitting diodes. *Journal of the Electrochemical Society*, 158(6):R37–R54, 2011.

[14] S. Ye, F. Xiao, Y. X. Pan, Y. Y. Ma, and Q. Y. Zhang. Phosphors in phosphor-converted white light-emitting diodes Recent advances in materials, techniques and properties. *Materials Science & Engineering R-Reports*, 71(1):1–34, 2010.

[15] E.F. Schubert. *Light-Emitting Diodes*. SPIE - The International Society for Optical Engineering, 2002.

[16] International Telecommunication Union. Parameter values for ultra-high difinition television systems for production and international programme exchange. *Recommendation ITU-R BT-2020*, 1:1–8, 2015.

[17] S. Abé. *Colloidal quantum dots: from reaction chemistry to light emitting devices*. Thesis, Ghent University, 2016.

[18] K. A. Gschneidner. The Rare Earth Crisis - The Supply/Demand Situation for 2010-2015. *Material Matters*, 6(2), 2011.

[19] R. E. Peierls. Wolfgang Ernst Pauli. 1900-1958. *Biographical Memoirs of Fellows of the Royal Society*, 5:174–192, 1960.

[20] Kurt Lejaeghere, Gustav Bihlmayer, Torbjörn Björkman, Peter Blaha, Stefan Blügel, Volker Blum, Damien Caliste, Ivano E. Castelli, Stewart J. Clark, Andrea Dal Corso, Stefano de Gironcoli, Thierry Deutsch, John Kay Dewhurst, Igor Di Marco, Claudia Draxl, Marcin Duak, Olle Eriksson, José A. Flores-Livas, Kevin F. Garrity, Luigi Genovese, Paolo Giannozzi, Matteo Giantomassi, Stefan Goedecker, Xavier Gonze, Oscar Grånäs, E. K. U. Gross, Andris Gulans, Franois Gygi, D. R. Hamann, Phil J. Hasnip, N. A. W. Holzwarth, Diana Iuşan, Dominik B. Jochym, Franois Jollet, Daniel Jones, Georg Kresse, Klaus Koepernik, Emine Kkbenli, Yaroslav O. Kvashnin, Inka L. M. Locht, Sven Lubeck, Martijn Marsman, Nicola Marzari, Ulrike Nitzsche, Lars Nordström, Taisuke Ozaki, Lorenzo Paulatto, Chris J. Pickard, Ward Poelmans, Matt I. J. Probert, Keith Refson, Manuel Richter, Gian-Marco Rignanese, Santanu Saha, Matthias Scheffler, Martin Schlipf, Karlheinz Schwarz, Sangeeta Sharma, Francesca Tavazza, Patrik Thunstrm, Alexandre Tkatchenko, Marc Torrent, David Vanderbilt, Michiel J. van Setten, Veronique Van Speybroeck, John M. Wills, Jonathan R. Yates, Guo-Xu Zhang, and Stefaan Cottenier. Reproducibility in density functional theory calculations of solids. *Science*, 351(6280):aad3000, 2016.

[21] K. Bird and M.J. Sherwin. *American Prometheus: The Triumph and Tragedy of J. Robert Oppenheimer*. Vintage. Knopf Doubleday Publishing Group, 2007.

[22] M. Dolg. *Computational Methods in Lanthanide and Actinide Chemistry*. Wiley, 2015.

[23] L. J. Norrby. Why Is Mercury Liquid - or, Why Do Relativistic Effects Not Get into Chemistry Textbooks. *Journal of Chemical Education*, 68(2):110–113, 1991.

[24] J. D. Jackson. *Classical Electrodynamics*. John Wiley, 1975.

[25] J. Biggus. *Sketches of a History of Classical Electromagnetism: (optics, Magnetism, Electricity, Electromagnetism)*. HyperJeff network. Jeff Biggus, 1996.

[26] D.A. Bromley and W. Greiner. *Quantum Mechanics: Special Chapters*. Springer Berlin Heidelberg, 2012.

[27] Greiner, W. and Bromley, D.A. and Reinhardt, J. *Field Quantization*. Springer Berlin Heidelberg, 2013.

[28] P. A. M. Dirac. *The principles of quantum mechanics*. International series of monographs on physics. The Clarendon Press, 1930.

[29] M.E. Peskin and D.V. Schroeder. *An Introduction To Quantum Field Theory*. Frontiers in physics. Westview Press, 1995.

[30] B. Henderson and G.F. Imbusch. *Optical spectroscopy of inorganic solids*. Oxford University Press, Incorporated, 2006.

[31] Kun Huang and Avril Rhys. Theory of Light Absorption and Non-Radiative Transitions in F-Centres. *Proceedings of the Royal Society of London A: Mathematical, Physical and Engineering Sciences*, 204(1078):406–423, 1950.

[32] G.B. Arfken and H.J. Weber. *Mathematical Methods for Physicists*. Elsevier Science, 2013.

[33] F. Duschinsky. The importance of the electron spectrum in multi atomic molecules. Concerning the Frank-Condon principle. *Acta Physicochimica URSS*, 7:551, 1937.

[34] Alberto Baiardi, Julien Bloino, and Vincenzo Barone. General Time Dependent Approach to Vibronic Spectroscopy Including Franck-Condon, Herzberg-Teller, and Duschinsky Effects. *Journal of Chemical Theory and Computation*, 9(9):4097–4115, 2013.

[35] J. Franck and E. G. Dymond. Elementary processes of photochemical reactions. *Trans. Faraday Soc.*, 21:536–542, 1926.

[36] Edward U. Condon. Nuclear Motions Associated with Electron Transitions in Diatomic Molecules. *Phys. Rev.*, 32:858–872, Dec 1928.

[37] A. von Hippel. Einige prinzipielle Gesichtspunkte zur Spektroskopie der Ionenkristalle und ihre Anwendung auf die Alkalihalogenide. *Zeitschrift für Physik*, 101(11):680–720, 1936.

[38] A. von Hippel. Electronic Conduction In Insulating Crystals Under Very High Field Strength. *Phys. Rev.*, 54:1096–1102, Dec 1938.

[39] Frederick Seitz. Interpretation of the Properties of Alkali Halide-Thallium Phosphors. *The Journal of Chemical Physics*, 6(3):150–162, 1938.

[40] N. F. Mott. On the Absorption of Light by Crystals. *Proceedings of the Royal Society of London. Series A, Mathematical and Physical Sciences*, 167(930):384–391, 1938.

[41] Thomas H. Keil. Shapes of Impurity Absorption Bands in Solids. *Phys. Rev.*, 140:A601–A617, Oct 1965.

[42] C. W. Struck and W. H. Fonger. Temperature Quenching of Luminescence for Linear and Derivative Nuclear Operators. *Journal of Luminescence*, 14(4):253–279, 1976. Ck404 Times Cited:19 Cited References Count:10.

[43] C. Manneback. Computation of the intensities of vibrational spectra of electronic bands in diatomic molecules. *Physica*, 17(11):1001–1010, 1951.

[44] W. H. Fonger and C. W. Struck. Eu^{3+} ^5D Resonance Quenching to Charge-Transfer States in Y_2O_2S, La_2O_2S, and LaOCl. *Journal of Chemical Physics*, 52(12):6364–6372, 1970. G6525 Times Cited:151 Cited References Count:19.

[45] C. W. Struck and W. H. Fonger. Thermal Quenching of Tb^{3+}, Tm^{3+}, Pr^{3+}, and Dy^{3+} $4f^n$ Emitting States in La_2O_2S. *Journal of Applied Physics*, 42(11):4515–, 1971. K5959 Times Cited:46 Cited References Count:8.

[46] C. W. Struck and W. H. Fonger. Unified Model of Temperature Quenching of Narrow-Line and Broad-Band Emissions. *Journal of Luminescence*, 10(1):1–30, 1975. V9740 Times Cited:216 Cited References Count:53.

[47] I. B. Bersuker. *The Jahn-Teller Effect*. Cambridge University Press, 2006.

[48] H. A. Jahn and E. Teller. Stability of Polyatomic Molecules in Degenerate Electronic States. I. Orbital Degeneracy. *Proceedings of the Royal Society of London. Series A - Mathematical and Physical Sciences*, 161(905):220–235, 1937.

[49] H. A. Jahn. Stability of Polyatomic Molecules in Degenerate Electronic States. II. Spin Degeneracy. *Proceedings of the Royal Society of London. Series A - Mathematical and Physical Sciences*, 164(916):117–131, 1938.

[50] P. Thyssen. *Symmetry and Symmetry Breaking in the Periodic Table, Towards a Group-Theoretical Classification of the Chemical Elements*. Thesis, KU Leuven, 2013.

[51] W.H. Dickhoff and D. Van Neck. *Many-body Theory Exposed!: Propagator Description of Quantum Mechanics in Many-body Systems*. World Scientific, 2005.

[52] A. Frank, J. Jolie, and P. van Isacker. *Symmetries in Atomic Nuclei: From Isospin to Supersymmetry*. Springer Tracts in Modern Physics. Springer New York, 2008.

[53] B. R. Judd. Complex Atomic Spectra. *Reports on Progress in Physics*, 48(7):907–954, 1985.

[54] B.R. Judd. *Operator technqiues in atomic spectroscopy*. Mcgraw-Hill Advanced Physics Monograph Series. Princeton University Press, 1963.

[55] R. E. Trees. Configuration Interaction in Mn II. *Physical Review*, 83(4):756–760, 1951.

[56] R. Trees. The $L(L+1)$ Correction to the Slater Formulas for the Energy Levels. *Physical Review*, 85(2):382–382, 1952.

[57] G. Racah and Y. Shadmi. Q Correction in the Spectra of the Iron Group. *Physical Review*, 119(1):156–158, 1960.

[58] K. Rajnak and B. G. Wybourne. Configuration Interaction Effects in Ln Configurations. *Physical Review*, 132(1):280–290, 1963.

[59] B. R. Judd. Three-Particle Operators for Equivalent Electrons. *Physical Review*, 141(1):4–, 1966.

[60] K. Rajnak and B. G. Wybourne. Electrostatically Correlated Spin-Orbit Interactions in Ln-Type Configurations. *Physical Review a-General Physics*, 134(3A):A596–, 1964.

[61] B. R. Judd, H. M. Crosswhite, and H. Crosswhite. Intra-Atomic Magnetic Interactions for f Electrons. *Physical Review*, 169(1):130–138, 1968.

[62] H.A. Bethe and E.E. Salpeter. *Quantum Mechanics of One- and Two-Electron Atoms*. Springer Berlin Heidelberg, 2013.

[63] H. H. Marvin. Mutual Magnetic Interactions of Electrons. *Physical Review*, 71(2):102–110, 1947. PR.

[64] V. Hurtubise and K. F. Freed. The algebra of effective Hamiltonians and operators: Truncated operators and computational aspects. *The Journal of Chemical Physics*, 99:7946, 1993.

[65] C. Froese-Fischer, T. Brage, and P. Johnsson. *Computational Atomic Structure: An MCHF Approach*. Taylor & Francis, 1997.

[66] W. T. Carnall. A systematic analysis of the spectra of trivalent actinide chlorides in D_{3h} site symmetry. *Journal of Chemical Physics*, 96(12):8713–8726, 1992.

[67] C.K. Jørgensen. *Modern aspects of ligand field theory*. North-Holland Pub. Co., 1971.

[68] B.G. Wybourne. *Spectroscopic properties of rare earths*. Interscience Publishers, 1965.

[69] D. J. Newman. Matrix Mutual Orthogonality and Parameter Independence. *Journal of Physics a-Mathematical and General*, 14(11):L429–L431, 1981.

[70] D.J. Newman and B. Ng. *Crystal Field Handbook*. Cambridge University Press, 2007.

[71] D. J. Newman. Operator Orthogonality and Parameter Uncertainty. *Physics Letters A*, 92(4):167–169, 1982.

[72] B. R. Judd, J. E. Hansen, and A. J. J. Raassen. Parametric Fits in the Atomic d Shell. *Journal of Physics B-Atomic Molecular and Optical Physics*, 15(10):1457–1472, 1982.

[73] D. J. Newman and S. S. Bishton. Theory of the correlation crystal field. *Chemical Physics Letters*, 1(13):616–618, 1968.

[74] B. R. Judd. Ligand-Field Theory for Actinides. *Journal of Chemical Physics*, 66(7):3163–3170, 1977.

[75] M. F. Reid. Correlation Crystal-Field Analyses with Orthogonal Operators. *Journal of Chemical Physics*, 87(5):2875–2884, 1987.

[76] B. R. Judd. Correlation Crystal Fields for Lanthanide Ions. *Physical Review Letters*, 39(4):242–244, 1977.

[77] H. Bethe. Termaufspaltung in Kristallen. *Annalen der Physik*, 395(2):133–208, 1929.

[78] S. Sugano. *Multiplets of Transition-Metal Ions in Crystals*. Elsevier Science, 2012.

[79] M. I. Bradbury and D. J. Newman. Ratios of crystal field parameters in rare earth salts. *Chemical Physics Letters*, 1(2):44–45, 1967.

[80] D. J. Newman and B. Ng. The Superposition Model of Crystal Fields. *Reports on Progress in Physics*, 52(6):699–763, 1989.

[81] Claus E. Schäffer and C. K. Jørgensen. The angular overlap model, an attempt to revive the ligand field approaches. *Molecular Physics*, 9(5):401–412, 1965.

[82] Erik Larsen and Gerd N. La Mar. The angular overlap model. How to use it and why. *Journal of Chemical Education*, 51(10):633, 1974.

[83] Z. I.; Aizenberg I. B. Malkin, B. Z.; Ivanenko. *Fizika Tverdogo Tela*, 12:1873, 1970.

[84] B. Z. Larionov, A. L.; Malkin. Effective Hamiltonian of valence electrons of rare-earth elements in ionic crystals. *Optics and Spectroscopy*, 39(6):637–639, 1975.

[85] N.M. Avram and M.G. Brik. *Optical Properties of 3d-Ions in Crystals: Spectroscopy and Crystal Field Analysis*. Springer, 2013.

[86] A. L. Tchougreeff and R. Dronskowski. Nephelauxetic Effect Revisited. *International Journal of Quantum Chemistry*, 109(11):2606–2621, 2009.

[87] A. Atanasov, C. A. Daul, and C. Rauzy. A DFT based ligand field theory. *Optical Spectra and Chemical Bonding in Inorganic Compounds, Vol 1*, 106:97–125, 2004.

[88] M. Atanasov and C. Daul. Theoretical studies on the electronic properties and the chemical bonding of transition metal complexes using DFT and ligand field theory. *Chimia*, 59(7-8):504–510, 2005.

[89] M. Atanasov and C. A. Daul. Modeling properties of molecules with open d-shells using density functional theory. *Comptes Rendus Chimie*, 8(9-10):1421–1433, 2005.

[90] A. Canning, A. Chaudhry, R. Boutchko, and N. Grønbech-Jensen. First-principles study of luminescence in Ce-doped inorganic scintillators. *Physical Review B*, 83(12):125115, 2011.

[91] S. Derenzo, G. Bizarri, R. Borade, E. Bourret-Courchesne, R. Boutchko, A. Canning, A. Chaudhry, Y. Eagleman, G. Gundiah, S. Hanrahan, M. Janecek, and M. Weber. New scintillators discovered by high-throughput screening. *Nuclear Instruments & Methods in Physics Research Section a-Accelerators Spectrometers Detectors and Associated Equipment*, 652(1):247–250, 2011.

[92] A. M. Souza, I. Rungger, C. D. Pemmaraju, U. Schwingenschlogl, and S. Sanvito. Constrained-DFT method for accurate energy-level alignment of metal/molecule interfaces. *Physical Review B*, 88(16), 2013.

[93] A. Chaudhry, R. Boutchko, S. Chourou, G. Zhang, N. Grønbech-Jensen, and A. Canning. First-principles study of luminescence in Eu^{2+}-doped inorganic scintillators. *Physical Review B*, 89(15):155105, 2014.

[94] C. Freysoldt, B. Grabowski, T. Hickel, J. Neugebauer, G. Kresse, A. Janotti, and C. G. Van de Walle. First-principles calculations for point defects in solids. *Reviews of Modern Physics*, 86(1):253–305, 2014.

[95] E. Runge and E. K. U. Gross. Density-Functional Theory for Time-Dependent Systems. *Physical Review Letters*, 52(12):997–1000, 1984.

[96] M.A.L. Marques, N.T. Maitra, F.M.S. Nogueira, E.K.U. Gross, and A. Rubio. *Fundamentals of Time-Dependent Density Functional Theory*. Lecture Notes in Physics. Springer Berlin Heidelberg, 2012.

[97] L. González, D. Escudero, and L. Serrano-Andrés. Progress and Challenges in the Calculation of Electronic Excited States. *Chemphyschem*, 13(1):28–51, 2012.

[98] Ab Initio Calculations on Excited States of Lanthanide Containing Materials. volume 50. Elsevier, 2016.

[99] L. Seijo and Z. Barandiarán. Intervalence charge transfer luminescence: The anomalous luminescence of cerium-doped $Cs_2LiLuCl_6$ elpasolite. *Journal of Chemical Physics*, 141(21), 2014.

[100] R. Shi, M. M. Qi, L. X. Ning, F. J. Pan, L. Zhou, W. J. Zhou, Y. C. Huang, and H. B. Liang. Combined Experimental and ab Initio Study of Site Preference of Ce^{3+} in $SrAl_2O_4$. *Journal of Physical Chemistry C*, 119(33):19326–19332, 2015.

[101] Z. Barandiarán and L. Seijo. Metal-to-metal charge transfer between dopant and host ions: Photoconductivity of Yb-doped CaF_2 and SrF_2 crystals. *Journal of Chemical Physics*, 143(14), 2015.

[102] D. Kulesza, J. Cybińska, L. Seijo, Z. Barandiarán, and E. Zych. Anomalous Red and Infrared Luminescence of Ce^{3+} Ions in SrS:Ce Sintered Ceramics. *Journal of Physical Chemistry C*, 119(49):27649–27656, 2015.

[103] B. R. Judd. Optical Absorption Intensities of Rare-Earth Ions. *Physical Review*, 127(3):750–, 1962.

[104] G. S. Ofelt. Intensities of Crystal Spectra of Rare-Earth Ions. *Journal of Chemical Physics*, 37(3):511–, 1962.

[105] J. D. Axe. Radiative Transition Probabilities within $4f^n$ Configurations - Fluorescence Spectrum of Europium Ethylsulfate. *Journal of Chemical Physics*, 39(5):1154–, 1963.

[106] M. P. Hehlen, M. G. Brik, and K. W. Krämer. 50^{th} anniversary of the Judd-Ofelt theory: An experimentalist's view of the formalism and its application. *Journal of Luminescence*, 136:221–239, 2013.

[107] C. Görller-Walrand and K. Binnemans. *Spectral intensities of f-f transitions*, volume 25, book section 167. North-Holland, 1998.

[108] O.K. Moune, M.D. Faucher, and N. Edelstein. Spectroscopic investigations and configuration-interaction-assisted crystal field analysis of Pr^{3+} in YPO_4 single crystal. *Journal of Luminescence*, 96(1):51 – 68, 2002.

[109] W. Wang, G. K. Liu, M. G. Brik, L. Seijo, and D. Shi. 5f-6d orbital hybridization of trivalent uranium in crystals of hexagonal symmetry: Effects on electronic energy levels and transition intensities. *Physical Review B*, 80(15), 2009.

[110] Python Software Foundation, Python Language Reference, version 2.7. `http://www.python.org`.

[111] C.W. Nielson and G.F. Koster. *Spectroscopic Coefficients for the p^n, d^n, and f^n Configurations*. MIT Press, 1963.

[112] G. Racah. Theory of Complex Spectra. IV. *Physical Review*, 76(9):1352–1365, 1949.

[113] J. A. Nelder and R. Mead. A Simplex-Method for Function Minimization. *Computer Journal*, 7(4):308–313, 1965.

[114] A. K. Kerman. Pairing Forces and Nuclear Collective Motion. *Annals of Physics*, 12(2):300–329, 1961.

[115] K. Helmers. Symplectic Invariants and Flowers Classification of Shell Model States. *Nuclear Physics*, 23(4):594–611, 1961.

[116] G. Gaigalas, S. Fritzsche, and Z. Rudzikas. Reduced coefficients of fractional parentage and matrix elements of the tensor $W^{(k_q k_j)}$ in jj-coupling. *Atomic Data and Nuclear Data Tables*, 76(2):235–269, 2000.

[117] G. Gaigalas and S. Fritzsche. Maple procedures for the coupling of angular momenta. VI. LS-jj transformations. *Computer Physics Communications*, 149(1):39–60, 2002.

[118] R. D. Lawson and M. H. Macfarlane. Quasi-Spin Formalism and Dependence of Nuclear Matrix Elements on Particle Number. *Nuclear Physics*, 66(1):80–96, 1965.

[119] J. M. Kaniauskas and Z. B. Rudzikas. Quasi-Spin Method for Jj Coupling in the Theory of Many-Electron Atoms. *Journal of Physics B-Atomic Molecular and Optical Physics*, 13(18):3521–3533, 1980.

[120] Y. Tanabe and S. Sugano. On the Absorption Spectra of Complex Ions. I. *Journal of the Physical Society of Japan*, 9(5):13, 1954.

[121] Y. Tanabe and S. Sugano. On the Absorption Spectra of Complex Ions II. *Journal of the Physical Society of Japan*, 9(5):13, 1954.

[122] Y. Tanabe and S. Sugano. On the Absorption Spectra of Complex Ions, .III. The Calculation of the Crystalline Field Strength. *Journal of the Physical Society of Japan*, 11(8):864–877, 1956.

[123] Y. Tanabe and H. Kamimura. On the Absorption Spectra of Complex Ions .IV. The Effect of the Spin-Orbit Interaction and the Field of Lower Symmetry on d Electrons in Cubic Field. *Journal of the Physical Society of Japan*, 13(4):394–411, 1958.

[124] J. R. Hester, E. N. Maslen, N. Spadaccini, N. Ishizawa, and Y. Satow. Accurate Synchrotron-Radiation Delta-Rho Maps for K_2SiF_6 and K_2PdCl_6. *Acta Crystallographica Section B-Structural Science*, 49:967–973, 1993.

[125] S. Adachi and T. Takahashi. Direct Synthesis of K_2SiF_6:Mn^{4+} Red Phosphor from Crushed Quartz Schist by Wet Chemical Etching. *Electrochemical and Solid State Letters*, 12(2):J20–J23, 2009.

[126] J. H. Oh, H. Kang, Y. J. Eo, H. K. Park, and Y. R. Do. Synthesis of narrow-band red-emitting K_2SiF_6:Mn^{4+} phosphors for a deep red monochromatic LED and ultrahigh color quality warm-white LEDs. *Journal of Materials Chemistry C*, 3(3):607–615, 2015.

[127] L. L. Wei, C. C. Lin, M. H. Fang, M. G. Brik, S. F. Hu, H. Jiao, and R. S. Liu. A low-temperature co-precipitation approach to synthesize fluoride phosphors K_2MF_6:Mn^{4+} (M = Ge, Si) for white LED applications. *Journal of Materials Chemistry C*, 3(8):1655–1660, 2015.

[128] H. F. Sijbom, J. J. Joos, L. I. D. J. Martin, K. Van den Eeckhout, D. Poelman, and P. F. Smet. Luminescent Behavior of the K_2SiF_6:Mn^{4+} Red Phosphor at High Fluxes and at the Microscopic Level. *ECS Journal of Solid State Science and Technology*, 5(1):R3040–R3048, 2016.

[129] R. Kasa and S. Adachi. Red and Deep Red Emissions from Cubic K_2SiF_6:Mn^{4+} and Hexagonal K_2MnF_6 Synthesized in HF/$KMnO_4$/KHF_2/Si Solutions. *Journal of the Electrochemical Society*, 159(4):J89–J95, 2012.

[130] C.J. Ballhausen. *Introduction to Ligand Field Theory*. McGraw-Hill, 1970.

[131] T. Takahashi and S. Adachi. Mn^{4+}-Activated Red Photoluminescence in K_2SiF_6 Phosphor. *Journal of the Electrochemical Society*, 155(12):E183–E188, 2008.

[132] C.A. Morrison. *Crystal Fields for Transition-Metal Ions in Laser Host Materials*. Springer Berlin Heidelberg, 2012.

[133] W. Li. Magnetic interactions in transition metal ions: Part I. Electronic configurations d^2, d^3 and d^4. *Atomic Data and Nuclear Data Tables*, 2:45–56, 1970.

[134] G.H. Dieke, H.M. Crosswhite, and H. Crosswhite. *Spectra and energy levels of rare earth ions in crystals*. Interscience Publishers, 1968.

[135] W. T. Carnall, G. L. Goodman, K. Rajnak, and R. S. Rana. A Systematic Analysis of the Spectra of the Lanthanides Doped into Single-Crystal LaF_3. *Journal of Chemical Physics*, 90(7):3443–3457, 1989.

[136] P. S. Peijzel, A. Meijerink, R. T. Wegh, M. F. Reid, and G. W. Burdick. A complete $4f^n$ energy level diagram for all trivalent lanthanide ions. *Journal of Solid State Chemistry*, 178(2):448–453, 2005.

[137] M. F. Reid, L. van Pieterson, R. T. Wegh, and A. Meijerink. Spectroscopy and calculations for $4f^n \rightarrow 4f^{n-1}5d$ transitions of lanthanide ions in $LiYF_4$. *Physical Review B*, 62(22):14744–14749, 2000.

[138] M. F. Reid, L. van Pieterson, and A. Meijerink. Trends in parameters for the $4f^N \leftrightarrow 4f^{N-1}5d$ spectra of lanthanide ions in crystals. *Journal of Alloys and Compounds*, 344(1-2):240–245, 2002.

[139] L. van Pieterson, M. F. Reid, G. W. Burdick, and A. Meijerink. $4f^n \rightarrow 4f^{n-1}5d$ transitions of the heavy lanthanides: Experiment and theory. *Physical Review B*, 65(4), 2002.

[140] L. van Pieterson, M. F. Reid, R. T. Wegh, S. Soverna, and A. Meijerink. $4f^n \rightarrow 4f^{n-1}5d$ transitions of the light lanthanides: Experiment and theory. *Physical Review B*, 65(4), 2002.

[141] C. K. Duan and M. F. Reid. A simple model for $f \rightarrow d$ transitions of rare-earth ions in crystals. *Journal of Solid State Chemistry*, 171(1-2):299–303, 2003.

[142] L. X. Ning, C. K. Duan, S. D. Xia, M. F. Reid, and P. A. Tanner. A model analysis of $4f^n$-$4f^{n-1}5d$ transitions of rare-earth ions in crystals. *Journal of Alloys and Compounds*, 366(1-2):34–40, 2004.

[143] C. G. Ma, M. F. Reid, C. K. Duan, S. D. Xia, and M. Yin. Recent advances in simple model for 4f-5d transitions of lanthanide ions in solids. *Journal of Rare Earths*, 25:262–267, 2007.

[144] C. G. Ma, C. K. Duan, S. D. Xia, M. Yin, and M. F. Reid. Application of point-group bases to f^N-$f^{N-1}d$ transitions of lanthanide and actinide ions doped in crystals. *Journal of Physics and Chemistry of Solids*, 69(10):2578–2583, 2008.

[145] C. G. Ma, M. G. Brik, W. Ryba-Romanowski, H. C. Swart, and M. A. Gusowski. Spectroscopy and Calculations for $4f^n \rightarrow 4f^{n-1}5d$ Transitions of Lanthanide Ions in K_3YF_6. *Journal of Physical Chemistry A*, 116(36):9158–9180, 2012.

[146] C. G. Ma, M. G. Brik, V. Kiisk, and I. Sildos. Analysis of f-d excitation spectra of heavy lanthanide ions in various crystals based on the simple model for f-d transition and its correction caused by the 5d spin-orbit interaction. *Journal of Luminescence*, 133:39–44, 2013.

[147] C. G. Ma, M. G. Brik, Y. Tian, and Q. X. Li. Systematic analysis of spectroscopic characteristics of the lanthanide and actinide ions with the $4f^{N-1}5d$ and $5f^{N-1}6d$ electronic configurations in a free state. *Journal of Alloys and Compounds*, 603:255–267, 2014.

[148] M. J. Freiser, S. Methfess, and F. Holtzber. Multiplet Structure in Absorption Spectrum of Eu^{2+}. *Journal of Applied Physics*, 39(2p2):900–902, 1968.

[149] A. Meijerink and G. Blasse. Luminescence Properties of Eu^{2+}-Activated Alkaline-Earth Haloborates. *Journal of Luminescence*, 43(5):283–289, 1989.

[150] J. E. Van Haecke, P. F. Smet, and D. Poelman. Luminescent characterization of $CaAl_2S_4$:Eu powder. *Journal of Luminescence*, 126(2):508–514, 2007.

[151] M. Suta, P. Larsen, F. Lavoie-Cardinal, and C. Wickleder. Photoluminescence of $CsMBr_3$:Eu^{2+} (M=Mg, Ca, Sr)-A novel strategy for the development of low-energy emitting phosphors. *Journal of Luminescence*, 149:35–44, 2014.

[152] S. J. Camardello, P. J. Toscano, M. G. Brik, and A. M. Srivastava. Optical spectroscopy, thermal quenching and electron-vibrational interaction of the octahedrally coordinated Eu^{2+} ion in $SrAl_2B_2O_7$. *Journal of Luminescence*, 151:256–260, 2014.

[153] H. A. Weakliem. Electronic Interactions in $4f^6$5d Configuration of Eu^{2+} in Crystals. *Physical Review B*, 6(7):2743–2748, 1972.

[154] A. Yanase and T. Kasuya. Magneto-Optical Effect Due to Eu^{2+} Ion. *Progress of Theoretical Physics*, 46:388–410, 1970.

[155] C. K. Duan, M. F. Reid, and G. Ruan. A simple model for the f-d transition of actinide and heavy lanthanide ions in crystals. *Current Applied Physics*, 6(3):359–362, 2006.

[156] P. Dorenbos. Mechanism of persistent luminescence in Eu^{2+} and Dy^{3+} codoped aluminate and silicate compounds. *Journal of the Electrochemical Society*, 152(7):H107–H110, 2005.

[157] F. Clabau, X. Rocquefelte, S. Jobic, P. Deniard, M. H. Whangbo, A. Garcia, and T. Le Mercier. On the phosphorescence mechanism in $SrAl_2O_4$:Eu^{2+} and its codoped derivatives. *Solid State Sciences*, 9(7):608–612, 2007.

[158] K. Van den Eeckhout, P. F. Smet, and D. Poelman. Persistent Luminescence in Eu^{2+}-Doped Compounds: A Review. *Materials*, 3(4):2536–2566, 2010.

[159] K. Korthout, K. Van den Eeckhout, J. Botterman, S. Nikitenko, D. Poelman, and P. F. Smet. Luminescence and x-ray absorption measurements of persistent $SrAl_2O_4$:Eu,Dy powders: Evidence for valence state changes. *Physical Review B*, 84(8):085140, 2011.

[160] K. Van den Eeckhout, D. Poelman, and P. F. Smet. Persistent Luminescence in Non-Eu^{2+}-Doped Compounds: A Review. *Materials*, 6(7):2789–2818, 2013.

[161] P. F. Smet, K. Van den Eeckhout, O. Q. De Clercq, and D. Poelman. Persistent phosphors. In J.C.G. Bünzli and V.K. Pecharsky, editors, *Handbook on the Physics and Chemistry of Rare Earths*, number v. 48 in Handbook on the Physics and Chemistry of Rare Earths, chapter 48. Elsevier Science, 2015.

[162] C. Tydtgat, K. W. Meert, D. Poelman, and P. F. Smet. Optically stimulated detrapping during charging of persistent phosphors. *Optical Materials Express*, 6(3):844–858, 2016.

[163] A. R. Schulze and H. Müller-Buschbaum. Zur Struktur von monoklinem $SrAl_2O_4$. *Zeitschrift Fur Anorganische Und Allgemeine Chemie*, 475(4):205–210, 1981.

[164] S. H. M. Poort, W. P. Blokpoel, and G. Blasse. Luminescence of Eu^{2+} in Barium and Strontium Aluminate and Gallate. *Chemistry of Materials*, 7(8):1547–1551, 1995.

[165] F. Clabau, X. Rocquefelte, S. Jobic, P. Deniard, M. H. Whangbo, A. Garcia, and T. Le Mercier. Mechanism of phosphorescence appropriate for the long-lasting phosphors Eu^{2+}-doped $SrAl_2O_4$ with codopants Dy^{3+} and B^{3+}. *Chemistry of Materials*, 17(15):3904–3912, 2005.

[166] J. Hölsä, T. Laamanen, M. Lastusaari, M. Malkamki, and P Novák. Anomalous low-temperature luminescence of $SrAl_2O_4$:Eu^{2+} persistent luminescence material. *Desy annual report*, 2009.

[167] P. Dorenbos. $f \rightarrow d$ transition energies of divalent lanthanides in inorganic compounds. *Journal of Physics-Condensed Matter*, 15(3):575–594, 2003.

[168] P. Dorenbos. Energy of the first $4f^7 \rightarrow 4f^6 5d$ transition of Eu^{2+} in inorganic compounds. *Journal of Luminescence*, 104(4):239–260, 2003.

[169] V. Bachmann, C. Ronda, and A. Meijerink. Temperature quenching of yellow Ce^{3+} luminescence in YAG:Ce. *Chemistry of Materials*, 21(10):2077–2084, 2009.

[170] M. Kamada, J. Murakami, and N. Ohno. Excitation spectra of a long-persistent phosphor $SrAl_2O_4$:Eu, Dy in vacuum ultraviolet region. *Journal of Luminescence*, 87-9:1042–1044, 2000.

[171] W. T. Carnall, P. R. Fields, and K. Rajnak. Electronic Energy Levels of Trivalent Lanthanide Aquo Ions. IV. Eu^{3+}. *Journal of Chemical Physics*, 49(10):4450–4455, 1968.

[172] J. Sugar and N. Spector. Spectrum and Energy-Levels of Doubly Ionized Europium (Eu III). *Journal of the Optical Society of America*, 64(11):1484–1497, 1974.

[173] P. Dorenbos. Relation between Eu^{2+} and Ce^{3+} $f \leftrightarrow d$-transition energies in inorganic compounds. *Journal of Physics-Condensed Matter*, 15(27):4797–4807, 2003.

[174] P. Dorenbos. Crystal field splitting of lanthanide $4f^{n-1}5d$-levels in inorganic compounds. *Journal of Alloys and Compounds*, 341(1-2):156–159, 2002.

[175] P. Dorenbos, J. Andriessen, and C. W. E. van Eijk. $4f^{n-1}5d$ centroid shift in lanthanides and relation with anion polarizability, covalency, and cation electronegativity. *Journal of Solid State Chemistry*, 171(1-2):133–136, 2003.

[176] C. A. Morrison. Host Dependence of the Rare-Earth Ion Energy Separation $4f^n$-$4f^{n-1}$nl. *Journal of Chemical Physics*, 72(2):1001–1002, 1980.

[177] R. D. Shannon. Revised effective ionic-radii and systematic studies of interatomic distances in halides and chalcogenides. *Acta Crystallographica Section A*, 32(Sep1):751–767, 1976.

[178] J. Bierwagen, S. Yoon, N. Gartmann, B. Walfort, and H. Hagemann. Thermal and concentration dependent energy transfer of Eu^{2+} in $SrAl_2O_4$. *Optical Materials Express*, 6(3):793–803, 2016.

[179] H. Hagemann, D. Lovy, S. Yoon, S. Pokrant, N. Gartmann, B. Walfort, and J. Bierwagen. Wavelength dependent loading of traps in the persistent phosphor $SrAl_2O_4$:Eu^{2+}, Dy^{3+}. *Journal of Luminescence*, 170:299 – 304, 2016.

[180] M. Nazarov, M.G. Brik, D. Spassky, and B. Tsukerblat. Crystal field splitting of 5d states and luminescence mechanism in $SrAl_2O_4$:Eu^{2+} phosphor. *Journal of Luminescence*, 182:79 – 86, 2017.

[181] R. Evarestov. *Quantum Chemistry of Solids: The LCAO First Principles Treatment of Crystals*. Springer Series in Solid-State Sciences. Springer Berlin Heidelberg, 2007.

[182] Bilbao Crystallographic Server. http://www.cryst.ehu.es/.

[183] R.J.D. Tilley. *Defects in Solids*. Wiley, 2008.

[184] M. Lannoo and J. Bourgoin. *Point Defects in Semiconductors I: Theoretical Aspects*. Springer Berlin Heidelberg, 1981.

[185] K.A. Kikoin and V.N. Fleurov. *Transition Metal Impurities in Semiconductors: Electronic Structure and Physical Properties*. World Scientific, 1994.

[186] J. M. Luttinger and W. Kohn. Motion of Electrons and Holes in Perturbed Periodic Fields. *Phys. Rev.*, 97:869–883, Feb 1955.

[187] W. Kohn and J. M. Luttinger. Theory of Donor States in Silicon. *Phys. Rev.*, 98:915–922, May 1955.

[188] G. F. Koster and J. C. Slater. Wave Functions for Impurity Levels. *Physical Review*, 95(5):1167–1176, 1954.

[189] G. F. Koster and J. C. Slater. Simplified Impurity Calculation. *Physical Review*, 96(5):1208–1223, 1954.

[190] F. D. M. Haldane and P. W. Anderson. Simple Model of Multiple Charge States of Transition-Metal Impurities in Semiconductors. *Physical Review B*, 13(6):2553–2559, 1976.

[191] V. N. Fleurov and K. A. Kikoin. Multiple-Charge Impurity States of the Transition and Noble-Metal Ions in Semiconductors. *Journal of Physics C-Solid State Physics*, 12(1):61–77, 1979.

[192] W. Shockley and J. T. Last. Statistics of the Charge Distribution for a Localized Flaw in a Semiconductor. *Phys. Rev.*, 107:392–396, Jul 1957.

[193] S. B. Zhang and J. E. Northrup. Chemical-Potential Dependence of Defect Formation Energies in GaAs - Application to Ga Self-Diffusion. *Physical Review Letters*, 67(17):2339–2342, 1991.

[194] G. Kresse and J. Furthmüller. Efficiency of ab-initio total energy calculations for metals and semiconductors using a plane-wave basis set. *Computational Materials Science*, 6(1):15–50, 1996.

[195] G. Kresse and D. Joubert. From ultrasoft pseudopotentials to the projector augmented-wave method. *Physical Review B*, 59(3):1758–1775, 1999.

[196] J. Hafner. Ab-initio simulations of materials using VASP: Density-functional theory and beyond. *Journal of Computational Chemistry*, 29(13):2044–2078, 2008.

[197] A. J. Cohen, P. Mori-Sanchez, and W. T. Yang. Challenges for Density Functional Theory. *Chemical Reviews*, 112(1):289–320, 2012.

[198] D. Van Neck, S. Verdonck, G. Bonny, P. W. Ayers, and M. Waroquier. Quasiparticle properties in a density-functional framework. *Physical Review A*, 74(4), 2006.

[199] A. De Vos, K. Lejaeghere, D. E. P. Vanpoucke, J. J. Joos, P. F. Smet, and K. Hemelsoet. First-Principles Study of Antisite Defect Configurations in $ZnGa_2O_4$:Cr Persistent Phosphors. *Inorganic Chemistry*, 55(5):2402–2412, 2016.

[200] John P. Perdew, Robert G. Parr, Mel Levy, and Jose L. Balduz. Density-Functional Theory for Fractional Particle Number: Derivative Discontinuities of the Energy. *Phys. Rev. Lett.*, 49:1691–1694, Dec 1982.

[201] E. Pavarini, E. Koch, A. Frithjof, and Jarrell M. *Correlated Electrons: From Models to Materials*. Forschungszentrum Jlich GmbH Institute for Advanced Simulation, 2012.

[202] A. I. Liechtenstein, V. I. Anisimov, and J. Zaanen. Density-Functional Theory and Strong-Interactions - Orbital Ordering in Mott-Hubbard Insulators. *Physical Review B*, 52(8):R5467–R5470, 1995.

[203] S. L. Dudarev, G. A. Botton, S. Y. Savrasov, C. J. Humphreys, and A. P. Sutton. Electron-energy-loss spectra and the structural stability of nickel oxide: An LSDA+U study. *Physical Review B*, 57(3):1505–1509, 1998.

[204] G. Kresse, M. Marsman, and J. Furthmüller. VASP the guide. `http://cms.mpi.univie.ac.at/VASP/`.

[205] K. Lejaeghere. *Ab initio screening of suitable tungsten alloys as first-wall material in nuclear fusion reactors*. Thesis, Ghent University, 2014.

[206] P. E. Blöchl, O. Jepsen, and O. K. Andersen. Improved Tetrahedron Method for Brillouin-Zone Integrations. *Physical Review B*, 49(23):16223–16233, 1994.

[207] M. Leslie and M. J. Gillan. The Energy and Elastic Dipole Tensor of Defects in Ionic-Crystals Calculated by the Supercell Method. *Journal of Physics C-Solid State Physics*, 18(5):973–982, 1985.

[208] G. Makov and M. C. Payne. Periodic Boundary-Conditions in Ab-Initio Calculations. *Physical Review B*, 51(7):4014–4022, 1995.

[209] S. Baroni and R. Resta. Abinitio Calculation of the Macroscopic Dielectric-Constant in Silicon. *Physical Review B*, 33(10):7017–7021, 1986.

[210] M. Gajdos, K. Hummer, G. Kresse, J. Furthmüller, and F. Bechstedt. Linear optical properties in the projector-augmented wave methodology. *Physical Review B*, 73(4), 2006.

[211] A. Janotti and C. G. Van de Walle. Oxygen vacancies in ZnO. *Applied Physics Letters*, 87(12):122102, 2005.

[212] A. Janotti and C. G. Van de Walle. Native point defects in ZnO. *Physical Review B*, 76(16):165202, 2007.

[213] F. de Groot and A. Kotani. *Core Level Spectroscopy of Solids*. Advances in Condensed Matter Science. CRC Press, 2008.

[214] P. Boutinaud and E. Cavalli. Predicting metal-to-metal charge transfer in closed-shell transition metal oxides doped with Bi^{3+} or Pb^{2+}. *Chemical Physics Letters*, 503(4-6):239–243, 2011.

[215] J. W. Verhoeven. Glossary of terms used in photochemistry. *Pure and Applied Chemistry*, 68(12):2223–2286, 1996.

[216] P. Dorenbos. A Review on How Lanthanide Impurity Levels Change with Chemistry and Structure of Inorganic Compounds. *ECS Journal of Solid State Science and Technology*, 2(2):R3001–R3011, 2013.

[217] M. Nazarov, D. Y. Noh, and H. Kim. Structural and luminescent properties of calcium, strontium and barium thiogallates. *Materials Chemistry and Physics*, 107(2-3):456–464, 2008.

[218] M. Nazarov, B. Tsukerblat, and D. Y. Noh. Electron-vibrational interaction in 4f-5d optical transitions. in Ba, Ca, Sr thiogallates doped with Eu^{2+} ions. *Journal of Luminescence*, 128(9):1533–1540, 2008.

[219] A. Garcia, F. Guillen, and C. Fouassier. Charge-Transfer Excitation of the Nd^{3+}, Sm^{3+}, Dy^{3+}, Ho^{3+}, Er^{3+}, and Tm^{3+} Emission in $CaGa_2S_4$. *Journal of Luminescence*, 33(1):15–27, 1985.

[220] A. Bessière, P. Dorenbos, C. W. E. van Eijk, E. Yamagishi, C. Hidaka, and T. Takizawa. Spectroscopy and lanthanide impurity level locations in $CaGa_2S_4$:Ln^{3+} (Ln = Ce, Pr, Tb, Er, Tm). *Journal of the Electrochemical Society*, 151(12):H254–H260, 2004.

[221] Linus Pauling. Photo-Ionization in Liquids and Crystals and the Dependence of the Frequency of X-Ray Absorption Edges on Chemical Constitution. *Physical Review*, 34(6):954–963, 1929.

[222] C. Pedrini, D. S. McClure, and C. H. Anderson. Photo-Ionization Thresholds of Divalent Rare-Earth Ions in Alkaline-Earth Fluorides. *Journal of Chemical Physics*, 70(11):4959–4962, 1979.

[223] D. S. McClure and C. Pedrini. Photoionization of Divalent Rare-Earth Ions in Fluorite-Type Crystals. *Journal De Physique*, 46(C-7):397–401, 1985.

[224] C. Pedrini, F. Rogemond, and D. S. McClure. Photoionization Thresholds of Rare-Earth Impurity Ions - Eu^{2+}-CaF_2, Ce^{3+}-YAG, and Sm^{2+}-CaF_2. *Journal of Applied Physics*, 59(4):1196–1201, 1986.

[225] C. W. Thiel, H. Cruguel, H. Wu, Y. Sun, G. J. Lapeyre, R. L. Cone, R. W. Equall, and R. M. Macfarlane. Systematics of 4f electron energies relative to host bands by resonant photoemission of rare-earth ions in aluminum garnets. *Physical Review B*, 64(8):085107, 2001.

[226] C. W. Thiel, H. Cruguel, Y. Sun, G. J. Lapeyre, R. M. Macfarlane, R. W. Equall, and R. L. Cone. Systematics of 4f electron energies relative to host bands by resonant photoemission of rare earth doped optical materials. *Journal of Luminescence*, 94:1–6, 2001.

[227] C. W. Thiel. *Energies of Rare-Earth Ion States Relative to Host Bands in Optical Materials from Electron Photoemission Spectroscopy*. Thesis, `http://scholarworks.montana.edu/xmlui/handle/1/2416`, Montana State University, 2003.

[228] C. W. Thiel and R. L. Cone. Investigating material trends and lattice relaxation effects for understanding electron transfer phenomena in rare-earth-doped optical materials. *Journal of Luminescence*, 131(3):386–395, 2011.

[229] P. Dorenbos. Modeling the chemical shift of lanthanide 4f electron binding energies. *Physical Review B*, 85(16):165107, 2012.

[230] P. Boutinaud, E. Cavalli, and M. Bettinelli. Emission quenching induced by intervalence charge transfer in Pr^{3+}- or Tb^{3+}-doped $YNbO_4$ and $CaNb_2O_6$. *Journal of Physics-Condensed Matter*, 19(38):386230, 2007.

[231] A. H. Krumpel, P. Boutinaud, E. van der Kolk, and P. Dorenbos. Charge transfer transitions in the transition metal oxides ABO_4:Ln^{3+} and APO_4:Ln^{3+} (A=La, Gd, Y, Lu, Sc; B=V, Nb, Ta; Ln=lanthanide). *Journal of Luminescence*, 130(8):1357–1365, 2010.

[232] P. Dorenbos. Ce^{3+} 5d-centroid shift and vacuum referred 4f-electron binding energies of all lanthanide impurities in 150 different compounds. *Journal of Luminescence*, 135(0):93–104, 2013.

[233] Pieter Dorenbos. Lanthanide 4f-electron binding energies and the nephelauxetic effect in wide band gap compounds. *Journal of Luminescence*, 136(0):122–129, 2013.

[234] P. Dorenbos. Relating the energy of the $[Xe]5d^1$ configuration of Ce^{3+} in inorganic compounds with anion polarizability and cation electronegativity. *Physical Review B*, 65(23):235110, 2002.

[235] J. Sugar and J. Reader. Ionization Energies of Doubly and Triply Ionized Rare-Earths. *Journal of Chemical Physics*, 59(4):2083–2089, 1973.

[236] P. Dorenbos. Systematic behaviour in trivalent lanthanide charge transfer energies. *Journal of Physics-Condensed Matter*, 15(49):8417–8434, 2003.

[237] P. Dorenbos. Lanthanide charge transfer energies and related luminescence, charge carrier trapping, and redox phenomena. *Journal of Alloys and Compounds*, 488(2):568–573, 2009.

[238] P. Dorenbos, A. H. Krumpel, E. van der Kolk, P. Boutinaud, M. Bettinelli, and E. Cavalli. Lanthanide level location in transition metal complex compounds. *Optical Materials*, 32(12):1681–1685, 2010.

[239] Y. Toyozawa, K.S. Song, and R.T. Williams. *Self-Trapped Excitons*. Springer Berlin Heidelberg, 1996.

[240] M. Cardona and L. Ley. *Photoemission in solids: General principles*. Springer-Verlag, 1978.

[241] P. Dorenbos. The Eu^{3+} charge transfer energy and the relation with the band gap of compounds. *Journal of Luminescence*, 111(1-2):89–104, 2005.

[242] P. Dorenbos. The Electronic Structure of Lanthanide Impurities in TiO_2, ZnO, SnO_2, and Related Compounds. *Ecs Journal of Solid State Science and Technology*, 3(3):R19–R24, 2014.

[243] P. Dorenbos. Valence stability of lanthanide ions in inorganic compounds. *Chemistry of Materials*, 17(25):6452–6456, 2005.

[244] M. R. MacDonald, J. E. Bates, J. W. Ziller, F. Furche, and W. J. Evans. Completing the Series of +2 Ions for the Lanthanide Elements: Synthesis Of Molecular Complexes of Pr^{2+}, Gd^{2+}, Tb^{2+}, and Lu^{2+}. *Journal of the American Chemical Society*, 135(26):9857–9868, 2013.

[245] M. R. MacDonald, M. E. Fieser, J. E. Bates, J. W. Ziller, F. Furche, and W. J. Evans. Identification of the+2 Oxidation State for Uranium in a Crystalline Molecular Complex, [K(2.2.2-Cryptand)][$(C_5H_4SiMe_3)_3U$]. *Journal of the American Chemical Society*, 135(36):13310–13313, 2013.

[246] P. Dorenbos. The $4f^n \leftrightarrow 4f^{n-1}5d$ transitions of the trivalent lanthanides in halogenides and chalcogenides. *Journal of Luminescence*, 91(1-2):91–106, 2000.

[247] C. K. Jørgensen. Electron Transfer Spectra of Lanthanide Complexes. *Molecular Physics*, 5(3):271–277, 1962.

[248] J. L. Ryan and C. K. Jørgensen. Absorption Spectra of Octahedral Lanthanide Hexahalides. *Journal of Physical Chemistry*, 70(9):2845–2857, 1966.

[249] M. J. J. Lammers and G. Blasse. Luminescence of Tb^{3+}-Activated and Ce^{3+}-Activated Rare-Earth Silicates. *Journal of the Electrochemical Society*, 134(8A):2068–2072, 1987.

[250] P. Dorenbos. The 5d level positions of the trivalent lanthanides in inorganic compounds. *Journal of Luminescence*, 91(3-4):155–176, 2000.

[251] J. J. Joos, K. W. Meert, A. B. Parmentier, D. Poelman, and P. F. Smet. Thermal quenching and luminescence lifetime of saturated green $Sr_{1-x}Eu_xGa_2S_4$ phosphors. *Optical Materials*, 34(11):1902–1907, 2012.

[252] T. L. Barry. Fluorescence of Eu^{2+}-activated phases in binary alkaline earth orthosilicate systems. *Journal of the Electrochemical Society*, 115(11):1181–1184, 1968.

[253] A. Zych, J. Ogieglo, C. Ronda, C. D. Donega, and A. Meijerink. Analysis of the shift of zero-phonon lines for f-d luminescence of lanthanides in relation to the Dorenbos model. *Journal of Luminescence*, 134:174–179, 2013.

[254] G. Blasse, W. Schipper, and J. J. Hamelink. On the Quenching of the Luminescence of the Trivalent Cerium Ion. *Inorganica Chimica Acta*, 189(1):77–80, 1991.

[255] M. Ando and Y. A. Ono. Temperature Effects in the Emission Characteristics of CaS:Eu Thin-Film Electroluminescent Devices. *Journal of Crystal Growth*, 117(1-4):969–974, 1992.

[256] M. Raukas, S. A. Basun, W. van Schaik, W. M. Yen, and U. Happek. Luminescence efficiency of cerium doped insulators: The role of electron transfer processes. *Applied Physics Letters*, 69(22):3300–3302, 1996.

[257] U. Happek, S. A. Basun, J. Choi, J. K. Krebs, and M. Raukas. Electron transfer processes in rare earth doped insulators. *Journal of Alloys and Compounds*, 303:198–206, 2000.

[258] P. Dorenbos. Thermal quenching of Eu^{2+} 5d-4f luminescence in inorganic compounds. *Journal of Physics-Condensed Matter*, 17(50):8103–8111, 2005.

[259] P. Dorenbos and E. G. Rogers. Vacuum Referred Bining Energies of the Lanthanides in Transition Metal Oxide Compounds. *ECS Journal of Solid State Science and Technology*, 3(8):R150–R158, 2014.

[260] W. B. Fowler and D. L. Dexter. Relation between Absorption and Emission Probabilities in Luminescent Centers in Ionic Solids. *Physical Review*, 128(5):2154–2165, 1962.

[261] S. H. M. Poort, A. Meijerink, and G. Blasse. Lifetime measurements in Eu^{2+}-doped host lattices. *Journal of Physics and Chemistry of Solids*, 58(9):1451–1456, 1997.

[262] P. Dorenbos. Anomalous luminescence of Eu^{2+} and Yb^{2+} in inorganic compounds. *Journal of Physics-Condensed Matter*, 15(17):2645–2665, 2003.

[263] A. Lecointre, A. Bessière, A. J. J. Bos, P. Dorenbos, B. Viana, and S. Jacquart. Designing a Red Persistent Luminescence Phosphor: The Example of YPO_4:Pr^{3+},Ln(3+) (Ln = Nd, Er, Ho, Dy). *Journal of Physical Chemistry C*, 115(10):4217–4227, 2011.

[264] P. Dorenbos, A. J. J. Bos, N. R. J. Poolton, and F. T. You. Photon controlled electron juggling between lanthanides in compounds. *Journal of Luminescence*, 133:45–50, 2013.

[265] L. C. V. Rodrigues, H. F. Brito, J. Hölsä, R. Stefani, M. C. F. C. Felinto, M. Lastusaari, T. Laamanen, and L. A. O. Nunes. Discovery of the Persistent Luminescence Mechanism of $CdSiO_3$:Tb^{3+}. *Journal of Physical Chemistry C*, 116(20):11232–11240, 2012.

[266] J. Botterman, J. J. Joos, and P. F. Smet. Trapping and detrapping in $SrAl_2O_4$:Eu,Dy persistent phosphors: Influence of excitation wavelength and temperature. *Physical Review B*, 90(8):085147, 2014.

[267] A. B. Parmentier, J. J. Joos, P. F. Smet, and D. Poelman. Luminescence of ytterbium in CaS and SrS. *Journal of Luminescence*, 154:445–451, 2014.

[268] G. Sánchez-Sanz, L. Seijo, and Z. Barandiarán. Electronic spectra of Yb^{2+}-doped $SrCl_2$. *Journal of Chemical Physics*, 133(11):114506, 2010.

[269] G. Sánchez-Sanz, L. Seijo, and Z. Barandiarán. Yb^{2+}-doped $SrCl_2$: Electronic structure of impurity states and impurity-trapped excitons. *Journal of Chemical Physics*, 133(11):114509, 2010.

[270] B. Eisenmann, M. Jakowski, W. Klee, and H. Schafer. The Structure of $CaAl_2S_4$, $CaGa_2S_4$, $SrAl_2S_4$, $SrGa_2S_4$ and $BaIn_2S_4$. *Revue De Chimie Minerale*, 20(2):255–263, 1983.

[271] C. F. Guo, Q. Tang, D. X. Huang, C. X. Zhang, and Q. A. Su. Tunable color emission and afterglow in $CaGa_2S_4$: Eu^{2+}, Ho^{3+} phosphor. *Materials Research Bulletin*, 42(12):2032–2039, 2007.

[272] C. F. Guo, Q. Tang, C. X. Zhang, D. X. Huang, and Q. Su. Thermoluminescent properties of Eu^{2+} and RE^{3+} co-doped phosphors $CaGa_2S_4$: Eu^{2+}, RE^{3+} (RE = Ln, excluding Pm, Eu and Lu). *Journal of Luminescence*, 126(2):333–338, 2007.

[273] Chiharu Hidaka and Takeo Takizawa. Trap levels in $CaGa_2S_4$ co-doped with Eu and rare earth elements. *Physica Status Solidi C*, 10(7-8):1123–1126, 2013.

[274] Z. J. Zhang, A. Feng, X. Y. Chen, and J. T. Zhao. Photoluminescence properties and energy levels of RE (RE = Pr, Sm, Er, Tm) in layered-CaZnOS oxysulfide. *Journal of Applied Physics*, 114(21):213518, 2013.

[275] VítJarý, Lubomír Havlák, Jan Bárta, Maksym Buryi, Eva Mihóková, Martin Rejman, Valentin Laguta, and Martin Nikl. Optical, Structural and Paramagnetic Properties of Eu-Doped Ternary Sulfides $ALnS_2$ (A = Na, K, Rb; Ln = La, Gd, Lu, Y). *Materials*, 8(10):5348, 2015.

[276] J. Ueda, P. Dorenbos, A. J. J. Bos, K. Kuroishi, and S. Tanabe. Control of electron transfer between Ce^{3+} and Cr^{3+} in the $Y_3Al_{5-x}Ga_xO_{12}$ host via conduction band engineering. *Journal of Materials Chemistry C*, 3(22):5642–5651, 2015.

[277] L. X. Ning, C. C. Zhou, W. P. Chen, Y. C. Huang, C. K. Duan, P. Dorenbos, Y. Tao, and H. B. Liang. Electronic Properties of Ce^{3+}-Doped $Sr_3Al_2O_5Cl_2$: A Combined Spectroscopic and Theoretical Study. *Journal of Physical Chemistry C*, 119(12):6785–6792, 2015.

[278] A. D. Sontakke, J. Ueda, Y. Katayama, P. Dorenbos, and S. Tanabe. Experimental insights on the electron transfer and energy transfer processes between Ce^{3+}-Yb^{3+} and Ce^{3+}-Tb^{3+} in borate glass. *Applied Physics Letters*, 106(13):131906, 2015.

[279] J. He, R. Shi, M. G. Brik, P. Dorenbos, Y. Huang, Y. Tao, and H. B. Liang. Luminescence and multi-step energy transfer in $GdAl_3(BO_3)_4$ doped with Ce^{3+}/Tb^{3+}. *Journal of Luminescence*, 161:257–263, 2015.

[280] A. Dobrowolska, E. C. Karsu, A. J. J. Bos, and P. Dorenbos. Spectroscopy, thermoluminescence and afterglow studies of $CaLa_4(SiO_4)_3O$:Ln (Ln=Ce, Nd, Eu, Tb, Dy). *Journal of Luminescence*, 160:321–327, 2015.

[281] W. L. Warren, K. Vanheusden, M. A. Rodriguez, C. H. Seager, D. R. Tallant, P. D. Rack, P. H. Holloway, B. K. Wagner, C. J. Summers, and P. N. Yocom. Luminescence, absorption, and site symmetry of Ce activated $SrGa_2S_4$ phosphors. *Applied Physics Letters*, 70(4):478–480, 1997.

[282] T. Matsuzawa, Y. Aoki, N. Takeuchi, and Y. Murayama. New long phosphorescent phosphor with high brightness, $SrAl_2O_4$:Eu^{2+},Dy^{3+}. *Journal of the Electrochemical Society*, 143(8):2670–2673, 1996.

[283] T. Aitasalo, J. Hölsä, H. Jungner, J. C. Krupa, M. Lastusaari, J. Legendziewicz, and J. Niitykoski. Effect of temperature on the luminescence processes of $SrAl_2O_4$:Eu^{2+}. *Radiation Measurements*, 38(4-6):727–730, 2004.

[284] D. D. Jia. Relocalization of Ce^{3+} 5d electrons from host conduction band. *Journal of Luminescence*, 117(2):170–178, 2006.

[285] D. D. Jia, X. J. Wang, W. Jia, and W. M. Yen. Temperature-dependent photoconductivity of Ce^{3+}-doped $SrAl_2O_4$. *Journal of Luminescence*, 119:55–58, 2006.

[286] Y. Q. Li, G. de With, and H. T. Hintzen. Luminescence properties of Ce^{3+}-activated alkaline earth silicon nitride $M_2Si_5N_8$ (M = Ca, Sr, Ba) materials. *Journal of Luminescence*, 116(1-2):107–116, 2006.

[287] Agata Lazarowska, Sebastian Mahlik, Marek Grinberg, Chiao-Wen Yeh, and Ru-Shi Liu. Spectroscopic properties and energy level location of Eu^{2+} in $Sr_2Si_5N_8$ phosphor. *Optical Materials*, 37(0):734–739, 2014.

[288] Y. Q. Li, J. E. J. van Steen, J. W. H. van Krevel, G. Botty, A. C. A. Delsing, F. J. DiSalvo, G. de With, and H. T. Hintzen. Luminescence properties of red-emitting $M_2Si_5N_8$:Eu^{2+} (M=Ca, Sr, Ba) LED conversion phosphors. *Journal of Alloys and Compounds*, 417(1-2):273–279, 2006.

[289] X. Q. Piao, T. Horikawa, H. Hanzawa, and K. Machida. Characterization and luminescence properties of $Sr_2Si_5N_8$:Eu^{2+} phosphor for white light-emitting-diode illumination. *Applied Physics Letters*, 88(16):161908, 2006.

[290] R. J. Xie, N. Hirosaki, N. Kimura, K. Sakuma, and M. Mitomo. 2-phosphor-converted white light-emitting diodes using oxynitride/nitride phosphors. *Applied Physics Letters*, 90(19):191101, 2007.

[291] S. E. Brinkley, N. Pfaff, K. A. Denault, Z. J. Zhang, H. T. Hintzen, R. Seshadri, S. Nakamura, and S. P. DenBaars. Robust thermal performance of $Sr_2Si_5N_8$:Eu^{2+}: An efficient red emitting phosphor for light emitting diode based white lighting. *Applied Physics Letters*, 99(24):241106, 2011.

[292] R.-J. Xie and H. T. Hintzen. Optical Properties of (Oxy)Nitride Materials: A Review. *Journal of the American Ceramic Society*, 96(3):665–687, 2013.

[293] Rong-Jun Xie, Naoto Hirosaki, T. Takeda, and T. Suehiro. On the Performance Enhancement of Nitride Phosphors as Spectral Conversion Materials in Solid State Lighting. *ECS Journal of Solid State Science and Technology*, 2(2):R3031–R3040, 2013.

[294] O. M. ten Kate, Z. Zhang, P. Dorenbos, H. T. Hintzen, and E. van der Kolk. 4f and 5d energy levels of the divalent and trivalent lanthanide ions in $M_2Si_5N_8$ (M=Ca, Sr, Ba). *Journal of Solid State Chemistry*, 197:209–217, 2013.

[295] T. Schlieper, W. Milius, and W. Schnick. Nitrido-Silicates 2. High-Temperature Syntheses and Crystal-Structures of $Sr_2Si_5N_8$ and $Ba_2Si_5N_8$. *Zeitschrift Fur Anorganische Und Allgemeine Chemie*, 621(8):1380–1384, 1995.

[296] R. Hoppe. Effective Coordination Numbers (Econ) and Mean Fictive Ionic-Radii (Mefir). *Zeitschrift Fur Kristallographie*, 150(1-4):23–52, 1979. Jf409 Times Cited:512 Cited References Count:50.

[297] C. W. Yeh, W. T. Chen, R. S. Liu, S. F. Hu, H. S. Sheu, J. M. Chen, and H. T. Hintzen. Origin of Thermal Degradation of $Sr_{2-x}Si_5N_8$:Eu_x Phosphors in Air for Light-Emitting Diodes. *Journal of the American Chemical Society*, 134(34):14108–14117, 2012.

[298] R. Roques, R. Rimet, J. P. Declercq, and G. Germain. Determination of Crystal-Structure of $EuGa_2S_4$. *Acta Crystallographica Section B-Structural Science*, 35(Mar):555–557, 1979.

[299] Jonas J. Joos, Katleen Korthout, Sergey Nikitenko, Dirk Poelman, and Philippe F. Smet. Origin of saturated green emission from europium in zinc thiogallate. *Opt. Mater. Express*, 3(9):1338–1350, 2013.

[300] P. Benalloul, C. Barthou, and J. Benoit. $SrGa_2S_4$:RE phosphors for full colour electroluminescent displays. *Journal of Alloys and Compounds*, 275:709–715, 1998.

[301] J. C. Souriau, Y. D. Jiang, J. Penczek, H. G. Paris, and C. J. Summers. Cathodoluminescent properties of coated $SrGa_2S_4$:Eu^{2+} and ZnS:Ag,Cl phosphors for field emission display applications. *Materials Science and Engineering B-Solid State Materials for Advanced Technology*, 76(2):165–168, 2000.

[302] C. Chartier, P. Benalloul, C. Barthou, J. M. Frigerio, G. O. Mueller, R. Mueller-Mach, and T. Trottier. Photoluminescence and cathodoluminescence properties of green emitting $SrGa_2S_4$:Eu^{2+} thin film. *Journal of Physics D-Applied Physics*, 35(4):363–368, 2002.

[303] C. Chartier, C. Barthou, P. Benalloul, and J. M. Frigerio. Photoluminescence of Eu^{2+} in $SrGa_2S_4$. *Journal of Luminescence*, 111(3):147–158, 2005.

[304] Y. Arai, H. Kominami, Y. Nakanishi, and Y. Hatanaka. Luminescent properties of $SrGa_2S_4$:Eu thin film phosphors deposited by two electron beam evaporation. *Applied Surface Science*, 244(1-4):473–476, 2005.

[305] I. Kitajima, T. Takizawa, C. Hidaka, and S. Nomura. ESR study of Ce^{3+} ions in a $CaGa_2S_4$ single crystal. *Physica Status Solidi C*, 10(7-8):1119–1122, 2013.

[306] M. Iwamaru, H. Nakajima, H. Kominami, Y. Nakanishi, and Y. Hatanaka. Luminescent properties of $SrGa_2S_4$:Sm thin-film phosphors under low-voltage excitation. *Journal of Vacuum Science & Technology B*, 22(3):1382–1385, 2004.

[307] J. J. Joos, D. Poelman, and P. F. Smet. Energy level modeling of lanthanide materials: review and uncertainty analysis. *Physical Chemistry Chemical Physics*, 17(29):19058–19078, 2015.

[308] C. Kittel. *Introduction to Solid State Physics*. Wiley, 2004.

[309] P.J. Goodhew, J. Humphreys, and R. Beanland. *Electron Microscopy and Analysis, Third Edition*. Taylor & Francis, 2000.

[310] P. F. Smet, J. E. van Haecke, and D. Poelman. Spatially resolved cathodoluminescence of luminescent materials using an EDX detector. *Journal of Microscopy*, 231(1):1–8, 2008.

[311] A. B. Parmentier, P. F. Smet, F. Bertram, J. Christen, and D. Poelman. Structure and luminescence of $(Ca,Sr)_2SiS_4$:Eu^{2+} phosphors. *Journal of Physics D-Applied Physics*, 43(8):085401, 2010.

[312] B. Ravel and M. Newville. ATHENA, ARTEMIS, HEPHAESTUS: data analysis for X-ray absorption spectroscopy using IFEFFIT. *Journal of Synchrotron Radiation*, 12:537–541, 2005.

[313] G. Derbyshire, K. C. Cheung, P. Sangsingkeow, and S. S. Hasnain. A low-profile monolithic multi-element Ge detector for X-ray fluorescence applications. *Journal of Synchrotron Radiation*, 6:62–63, 1999.

[314] P. Kubelka and F. Munk. Ein Beitrag zur Optik der Farbanstriche. *Zeitschrift für technische Physik*, 12:8, 1931.

[315] J. Torrent and V. Barrón. *Diffuse Reflectance Spectroscopy*, book section 13. Soil Science Society of America, 2008.

[316] A. Miller. *Fundamental optical properties of solids*, volume 1, book section 9. McGraw-Hill, Optical Society of America, 1995.

[317] J. Tauc. Absorption Edge and Internal Electric Fields in Amorphous Semiconductors. *Materials Research Bulletin*, 5(8):721–729, 1970.

[318] Y.P. Raizer, V.I. Kisin, and J.E. Allen. *Gas Discharge Physics*. Springer Berlin Heidelberg, 2011.

[319] E. Hecht. *Optics*. Pearson education. Addison-Wesley, 2002.

[320] Edinburgh Photonics. `http://www.edinburghphotonics.com/`.

[321] R.W. Engstrom and RCA Corporation. *Photomultiplier handbook*. RCA Corp., 1980.

[322] S. Leyre, E. Coutino-González, J. J. Joos, J. Ryckaert, Y. Meuret, D. Poelman, P. F. Smet, G. Durinck, J. Hofkens, G. Deconinck, and P. Hanselaer. Absolute determination of photoluminescence quantum efficiency using an integrating sphere setup. *Review of Scientific Instruments*, 85(12):123115, 2014.

[323] J. Botterman. *Trapping and detrapping in persistent phosphors*. Thesis, `https://biblio.ugent.be/publication/5879288`, Ghent University, 2014.

[324] N. Avci, J. Musschoot, P. F. Smet, K. Korthout, A. Avci, C. Detavernier, and D. Poelman. Microencapsulation of Moisture-Sensitive CaS:Eu^{2+} Particles with Aluminum Oxide. *Journal of the Electrochemical Society*, 156(11):J333–J337, 2009.

[325] V. Bachmann, C. Ronda, O. Oeckler, W. Schnick, and A. Meijerink. Color point tuning for (Sr,Ca,Ba)$Si_2O_2N_2$:Eu^{2+} for white light LEDs. *Chemistry of Materials*, 21(2):316–325. 396QC ISSN = 0897-4756, year = 2009, type = Journal Article.

[326] Y. Q. Li, A. C. A. Delsing, G. de With, and H. T. Hintzen. Luminescence properties of Eu^{2+}-activated alkaline-earth silicon-oxynitride $MSi_2O_{2-\delta}N_{2+2/3\delta}$ (M = Ca, Sr, Ba): A promising class of novel LED conversion phosphors. *Chemistry of Materials*, 17(12):3242–3248, 2005.

[327] J. Botterman, K. Van den Eeckhout, A. J. J. Bos, P. Dorenbos, and P. F. Smet. Persistent luminescence in $MSi_2O_2N_2$:Eu phosphors. *Optical Materials Express*, 2(3):341–349, 2012.

[328] V. Bachmann, T. Jüstel, A. Meijerink, C. Ronda, and P. J. Schmidt. Luminescence properties of $SrSi_2O_2N_2$ doped with divalent rare earth ions. *Journal of Luminescence*, 121(2):441–449, 2006.

[329] I. H. Cho, G. Anoop, D. W. Suh, S. J. Lee, and J. S. Yoo. On the stability and reliability of $Sr_{1-x}Ba_xSi_2O_2N_2:Eu^{2+}$ phosphors for white LED applications. *Optical Materials Express*, 2(9):1292–1305, 2012.

[330] X. F. Song, H. He, R. L. Fu, D. L. Wang, X. R. Zhao, and Z. W. Pan. Photoluminescent properties of $SrSi_2O_2N_2:Eu^{2+}$ phosphor: concentration related quenching and red shift behaviour. *Journal of Physics D-Applied Physics*, 42(6):065409, 2009.

[331] Markus Seibald, Tobias Rosenthal, Oliver Oeckler, and Wolfgang Schnick. Highly Efficient pc-LED Phosphors $Sr_{1-x}Ba_xSi_2O_2N_2:Eu^{2+}$ $(0 \leq x \leq 1)$ - Crystal Structures and Luminescence Properties Revisited. *Critical Reviews in Solid State and Materials Sciences*, 39(3):215–229, 2014.

[332] H. A. Höppe, F. Stadler, O. Oeckler, and W. Schnick. $Ca[Si_2O_2N_2]$ - A novel layer silicate. *Angewandte Chemie-International Edition*, 43(41):5540–5542, 2004.

[333] O. Oeckler, F. Stadler, T. Rosenthal, and W. Schnick. Real structure of $SrSi_2O_2N_2$. *Solid State Sciences*, 9(2):205–212, 2007.

[334] J. A. Kechele, O. Oeckler, F. Stadler, and W. Schnick. Structure elucidation of $BaSi_2O_2N_2$ - A host lattice for rare-earth doped luminescent materials in phosphor-converted (pc)-LEDs. *Solid State Sciences*, 11(2):537–543, 2009.

[335] J. Botterman, K. Van den Eeckhout, I. De Baere, D. Poelman, and P. F. Smet. Mechanoluminescence in $BaSi_2O_2N_2$:Eu. *Acta Materialia*, 60(15):5494–5500, 2012.

[336] L. Zhang, C. Xu, and H. Yamada. Strong Mechanoluminescence from Oxynitridosilicate Phosphors. *IOP Conference Series: Materials Science and Engineering*, 18(212001):212001, 2011.

[337] M. Seibald, T. Rosenthal, O. Oeckler, F. Fahrnbauer, A. Tücks, P. J. Schmidt, and W. Schnick. Unexpected Luminescence Properties of $Sr_{0.25}Ba_{0.75}Si_2O_2N_2:Eu^{2+}$ - A Narrow Blue Emitting Oxonitridosilicate with Cation Ordering. *Chemistry-a European Journal*, 18(42):13446–13452, 2012.

[338] Markus Seibald, Tobias Rosenthal, Oliver Oeckler, Christian Maak, Andreas Tücks, Peter J. Schmidt, Detlef Wiechert, and Wolfgang Schnick. New polymorph of the highly efficient LED-phosphor $SrSi_2O_2N_2:Eu^{2+}$ polytypism of a layered oxonitridosilicate. *Chemistry of Materials*, 25(9):1852–1857, 2013.

[339] F. Stadler, O. Oeckler, H. A. Höppe, M. H. Moller, R. Pottgen, B. D. Mosel, P. Schmidt, V. Duppel, A. Simon, and W. Schnick. Crystal structure, physical properties and HRTEM investigation of the new oxonitridosilicate $EuSi_2O_2N_2$. *Chemistry-a European Journal*, 12(26):6984–6990, 2006.

[340] Y. Q. Li, K. V. Ramanujachary, S. E. Lofland, G. de With, and H. T. Hintzen. Optical and magnetic properties of $EuSi_2O_2N_2$. *Journal of Materials Research*, 21(2):396–401, 2006.

[341] B. G. Yun, Y. Miyamoto, and H. Yamamoto. Luminescence properties of $(Sr_{1-u}Ba_u)Si_2O_2N_2:Eu^{2+}$, yellow or orange phosphors for white LEDs, synthesized with $(Sr_{1-u}Ba_u)_2SiO_4$: Eu^{2+} as a precursor. *Journal of the Electrochemical Society*, 154(10):J320–J325, 2007.

[342] L. H. Liu, R.-J. Xie, C. N. Zhang, and N. Hirosaki. Role of Fluxes in Optimizing the Optical Properties of $Sr_{0.95}Si_2O_2N_2:0.05Eu^{2+}$ Green-Emitting Phosphor. *Materials*, 6(7):2862–2872, 2013.

[343] F. Stadler, R. Kraut, O. Oeckler, S. Schmid, and W. Schnick. Synthesis, crystal structure and solid-state NMR spectroscopic investigation of the oxonitridosilicate $BaSi_6N_8O$. *Zeitschrift Fur Anorganische Und Allgemeine Chemie*, 631(10):1773–1778, 2005.

[344] C. Braun, M. Seibald, S. L. Börger, O. Oeckler, T. D. Boyko, A. Moewes, G. Miehe, A. Tücks, and W. Schnick. Material properties and structural characterization of $M_3Si_6O_{12}N_2:Eu^{2+}$ (M = Ba, Sr) - A comprehensive study on a promising green phosphor for pc-LEDs. *Chemistry-a European Journal*, 16(31):9646–9657, 2010.

[345] F. Stadler and W. Schnick. The new layer-silicates $Ba_3Si_6O_9N_4$ and $Eu_3Si_6O_9N_4$. *Zeitschrift Fur Anorganische Und Allgemeine Chemie*, 632(6):949–954, 2006.

[346] R.-J. Xie, N. Hirosaki, Y. Q. Li, and T. Takeda. Photoluminescence of $(Ba_{1-x}Eu_x)Si_6N_8O$ ($0.005 \leq x \leq 0.2$) phosphors. *Journal of Luminescence*, 130(2):266–269, 2010.

[347] M. Mikami, S. Shimooka, K. Uheda, H. Imura, and N. Kijima. New Green Phosphor $Ba_3Si_6O_{12}N_2$:Eu for White LED: Crystal Structure and Optical Properties. *Key Engineering Materials*, 403:11–14, 2009.

[348] M. Seibald, O. Oeckler, V. R. Celinski, P. J. Schmidt, A. Tücks, and W. Schnick. Real structure and diffuse scattering of $Sr_{0.5}Ba_{0.5}Si_2O_2N_2:Eu^{2+}$ - A highly efficient yellow phosphor for pc-LEDs. *Solid State Sciences*, 13(9):1769–1778, 2011.

[349] P. F. Smet, J. Botterman, A. B. Parmentier, and D. Poelman. Thermal quenching at the microscopic level in multi-phase thiosilicate phosphors. *Optical Materials*, 35(11):1970–1975, 2013.

[350] D. Poelman and P. F. Smet. Time resolved microscopic cathodoluminescence spectroscopy for phosphor research. *Physica B-Condensed Matter*, 439:35–40, 2014.

[351] A. A. Setlur, J. J. Shiang, and U. Happek. Eu^{2+}-Mn^{2+} phosphor saturation in 5 mm light emitting diode lamps. *Applied Physics Letters*, 92(8):081104, 2008.

[352] W. Davis and Y. Ohno. Color quality scale. *Optical Engineering*, 49(3):033602, 2010.

[353] R. Mueller-Mach, G. Mueller, M. R. Krames, H. A. Höppe, F. Stadler, W. Schnick, T. Jüstel, and P. Schmidt. Highly efficient all-nitride phosphor-converted white light emitting diode. *Physica Status Solidi A*, 202(9):1727–1732, 2005.

[354] T. Jüstel, H. Bechtel, W. Mayr, and D. U. Wiechert. Blue emitting $BaMgAl_{10}O_{17}$:Eu with a blue body color. *Journal of Luminescence*, 104(1-2):137–143, 2003.

[355] K. C. Mishra, M. Raukas, G. Marking, P. Chen, and P. Boolchand. Investigation of fluorescence degradation mechanism of hydrated $BaMgAl_{10}O_{17}:Eu^{2+}$ phosphor. *Journal of the Electrochemical Society*, 152(11):H183–H190, 2005.

[356] M. H. Crawford. LEDs for solid-state lighting: performance challenges and recent advances. *IEEE Journal of Selected Topics in Quantum Electronics*, 15(4):1028–1040, 2009.

[357] Rong-Jun Xie, N. Hirosaki, and T. Takeda. Wide color gamut backlight for liquid crystal displays using three-band phosphor-converted white light-emitting diodes. *Applied Physics Express*, 2(2):022401, 2009.

[358] T. E. Peters. Luminescent properties of thiogallate phosphors II. Ce^{3+}-activated phosphors for flying spot scanner applications. *Journal of the Electrochemical Society*, 119(12):1720–1723, 1972.

[359] K. T. Lethi, A. Garcia, F. Guillen, and C. Fouassier. Investigation of the MS-Al_2S_3 systems (M = Ca, Sr, Ba) and luminescence properties of europium-doped thioaluminates. *Materials Science and Engineering B-Solid State Materials for Advanced Technology*, 14(4):393–397, 1992.

[360] L. Eichenauer, B Jarofke, H.-C. Mertins, J. Dreyhsig, W. Busse, H.-E. Gumlich, P. Benalloul, C. Barthou, Benoît, C. Fouassier, and A. Garcia. Optical characterization of europium and cerium in strontium thiogallate thin films and powders. *Physica Status Solidi C*, 153(2):515–527, 1996.

[361] P. Benalloul, C. Barthou, C. Fouassier, A. N. Georgobiani, L. S. Lepnev, Y. N. Emirov, A. N. Gruzintsev, B. G. Tagiev, O. B. Tagiev, and R. B. Jabbarov. Luminescence of Eu^{2+} in calcium thiogallate. *Journal of the Electrochemical Society*, 150(1):G62–G65, 2003.

[362] R. B. Jabbarov, C. Chartier, B. G. Tagiev, O. B. Tagiev, N. N. Musayeva, C. Barthou, and P. Benalloul. Radiative properties of Eu^{2+} in $BaGa_2S_4$. *Journal of Physics and Chemistry of Solids*, 66(6):1049–1056, 2005.

[363] Ariyuki Kato, Khikmet Nadjafov, Ryuichiro Hayashi, Tamao Matsumoto-Aoki, Makoto Yamazaki, Bakhadur Tagiev, Oktai Tagiev, Rasim Dzhabbarov, Ayaz Bayramov, Nazim Mamedov, and Seishi Iida. Effects of Ce Doping on Phosphor Characteristics of $CaGa_2S_4$:Eu. *Japanese Journal of Applied Physics*, 39(S1):440, 2000.

[364] C. Hidaka and T. Takizawa. Optical properties of $Sr_{1-x}Eu_xGa_2S_4$ mixed compounds. *Journal of Physics and Chemistry of Solids*, 69(2-3):358–361, 2008.

[365] R. J. Yu, J. Wang, M. Zhang, H. B. Yuan, W. J. Ding, Y. An, and Q. Su. Luminescence properties of $Ca_{1-x}Sr_x(Ga_{1-y}Al_y)_2S_4 : Eu^{2+}$ and their potential application for white LEDs. *Journal of the Electrochemical Society*, 155(10):J290–J292, 2008.

[366] P. T. Anderson. *Luminescent sulfides and solution-deposited oxide thin films*. Thesis, https://ir.library.oregonstate.edu/xmlui/bitstream/handle/1957/7992/Anderson_dissertation.pdf?sequence=1, Oregon State University, 2008.

[367] S. Iida, A. Kato, M. Tanaka, H. Najafov, and H. Ikuno. Photoluminescence characterization of rare-earth stoichiometric compounds of $EuGa_2S_4$. *Journal of Physics and Chemistry of Solids*, 64(9-10):1815–1819, 2003.

[368] R. J. Yu, H. K. Yang, B. K. Moon, B. C. Choi, and J. H. Jeong. Luminescence properties of stoichiometric EuM_2S_4 (M = Ga, Al) conversion phosphors for white LED applications. *Physica Status Solidi A*, 209(12):2620–2625, 2012.

[369] Ruijin Yu, Hyeon Mi Noh, Byung Kee Moon, Byung Chun Choi, Jung Hyun Jeong, Kiwan Jang, Soung Soo Yi, and Jun Kyu Jang. Photoluminescence Characteristics of a New Thiogallate-Based Green-Emitting Phosphor: $MgGa_2S_4$:Eu^{2+}. *Journal of the American Ceramic Society*, 96(6):1821–1826, 2013.

[370] P. F. Smet, J. E. Van Haecke, R. L. Van Meirhaeghe, and D. Poelman. Crystallographic and luminescent properties of orthorhombic $BaAl_2S_4$:Eu powder and thin films. *Journal of Applied Physics*, 98(4):043512, 2005.

[371] P. F. Smet, D. Poelman, and R. L. Van Meirhaeghe. Blue electroluminescence from multilayered BaS:Eu/Al_2S_3 thin films. *Journal of Applied Physics*, 95(1):184–190, 2004.

[372] C. Wickleder, S. Zhang, and H. Haeuseler. Photoluminescence of $ZnGa_2S_4$:Eu^{2+}. *Zeitschrift Fur Kristallographie*, 220(2-3):277–280, 2005.

[373] C. K. Lowe-Ma and T. A. Vanderah. Structure of $ZnGa_2S_4$, a defect sphalerite derivative. *Acta Crystallographica Section C*, 47(5):919–924, 1991.

[374] Harry Hahn and Wilhelm Klingler. Über die Kristallstruktur einiger ternärer Sulfide, die sich vom Indium(III)-sulfid ableiten Mit 8 Abbildungen. *Zeitschrift fr anorganische und allgemeine Chemie*, 263(4):177–190, 1950.

[375] B. Eisenmann and A. Hofmann. Crystal structure of strontium phyllotetrathioindate(III). *Zeitschrift fuer Kristallographie*, 197:167–168, 1991.

[376] P. C. Donohue and J. E. Hanlon. Synthesis and photoluminescence of $M^{II}M_2^{III}(S,Se)_4$. *Journal of the Electrochemical Society*, 121:137–142, 1974.

[377] M. Kawanishi, Y. Ono, R. Nakagawa, N. Miura, H. Matsumoto, and R. Nakano. Possibility of RGB emission by Eu^{2+} ion doped IIa-$IIIb_2$-S_4 phosphors for full color inorganic electroluminescent displays. *Proceedings of the 11$^{\text{th}}$ international workshop on inorganic and organic electroluminescence*, pages 239–242, 2002.

[378] C. Romers, B. A. Blaisse, and D. J. W. Ijdo. Complex sulphur compounds. I. The crystal structure of $MgGa_2S_4$. *Acta Crystallographica*, 23:634, 1967.

[379] P. F. Smet, N. Avci, B. Loos, J. E. Van Haecke, and D. Poelman. Structure and photoluminescence of $(Ca, Eu)_2SiS_4$ powders. *Journal of Physics-Condensed Matter*, 19(24):246223, 2007.

[380] A. N. Georgobiani, B. G. Tagiev, O. B. Tagiev, S. A. Abushov, F. A. Kazymova, T. S. Gashimova, and X. R. Xu. Temperature effect on the photoluminescence intensity and Eu^{2+} excited state lifetime in $EuGa_2S_4$ and $EuGa_2S_4$:Er^{3+}. *Inorganic Materials*, 45(2):116–122, 2009.

[381] C. Barthou, P. Benalloul, B. B. Tagiev, O. G. Tagiev, S. Abushov, F. A. Kazimova, and A. N. Georgobiani. Energy transfers between Eu^{2+} and Er^{3+} in $EuGa_2S_4$: Er^{3+}. *Journal of Physics-Condensed Matter*, 16(45):8075–8084, 2004.

[382] A. B. Parmentier, P. F. Smet, and D. Poelman. Europium doped thiosilicate phosphors of the alkaline earth metals Mg, Ca, Sr and Ba: Structure and luminescence. *Optical Materials*, 33(2):141–144, 2010.

[383] N. Avci, I. Cimieri, P. F. Smet, and D. Poelman. Stability improvement of moisture sensitive CaS:Eu^{2+} micro-particles by coating with sol-gel alumina. *Optical Materials*, 33(7):1032–1035, 2011.

[384] E.L. Wolf. *Nanophysics and Nanotechnology: An Introduction to Modern Concepts in Nanoscience*. Wiley, 2015.

[385] M. Cirillo, T. Aubert, R. Gomes, R. Van Deun, P. Emplit, A. Biermann, H. Lange, C. Thomsen, E. Brainis, and Z. Hens. "Flash" Synthesis of CdSe/CdS Core-Shell Quantum Dots. *Chemistry of Materials*, 26(2):1154–1160, 2014.

[386] G. J. Supran, Y. Shirasaki, K. W. Song, J. M. Caruge, P. T. Kazlas, S. Coe-Sullivan, T. L. Andrew, M. G. Bawendi, and V. Bulovic. QLEDs for displays and solid-state lighting. *Mrs Bulletin*, 38(9):703–711, 2013.

[387] K. J. Chen, C. C. Lin, H. V. Han, C. Y. Lee, S. H. Chien, K. Y. Wang, S. H. Chiu, Z. Y. Tu, J. R. Li, T. M. Chen, X. L. Li, M. H. Shih, and H. C. Kuo. Wide-Range Correlated Color Temperature Light Generation From Resonant Cavity Hybrid Quantum Dot Light-Emitting Diodes. *IEEE Journal of Selected Topics in Quantum Electronics*, 21(4), 2015.

[388] Y. Ohno. Spectral design considerations for white LED color rendering. *Optical Engineering*, 44(11), 2005.

[389] J. Y. Woo, K. Kim, S. Jeong, and C. S. Han. Enhanced Photoluminance of Layered Quantum Dot-Phosphor Nanocomposites as Converting Materials for Light Emitting Diodes. *Journal of Physical Chemistry C*, 115(43):20945–20952, 2011.

[390] M. M. Yuta and W. B. White. Photoluminescence of sulfide phosphors with the MB_2S_4 composition. *Journal of the Electrochemical Society*, 139(8):2347–2352, 1992.

[391] J. W. Kim and Y. J. Kim. Synthesis and luminescent characterization of zinc thiogallate. *Journal of the European Ceramic Society*, 27(13-15):3667–3670, 2007.

[392] Y. K. Kim, D. H. Cho, Y. K. Jeong, M. K. Nah, K. B. Kim, and J. G. Kang. Luminescence characterization of $(Ca_{1-x}Zn_x)Ga_2S_4$:Eu^{2+} phosphors for a white light-emitting diode. *Materials Research Bulletin*, 45(8):905–909, 2010.

[393] R. Yu, R. X. Luan, C. F. Wang, J. T. Chen, Z. X. Wang, B. K. Moon, and J. H. Jeong. Photoluminescence properties of green emitting $ZnGa_2S_4$:Eu^{2+} phosphor. *Journal of the Electrochemical Society*, 159(5):J188–J192, 2012.

[394] Y. K. Jeong, D. H. Cho, K. B. Kim, and J. G. Kang. Highly luminescent $(Zn_{0.6}Sr_{0.3}Mg_{0.1})_2Ga_2S_5$:$Eu^{2+}$ green phosphors for a white light-emitting diode. *Bulletin of the Korean Chemical Society*, 33(8):2523–2528, 2012.

[395] J. W. Kim and Y. J. Kim. Optical properties of Eu doped M-Ga_2S_4 (M : Zn, Ca, Sr) phosphors for white light emitting diodes. *Journal of Nanoscience and Nanotechnology*, 7(11):4065–4068, 2007.

[396] B. G. Tagiev, G. G. Guseinov, R. B. Dzhabbarov, O. B. Tagiev, N. N. Musaeva, and A. N. Georgobiani. Synthesis and luminescent properties of $ZnGa_2S_4$:Eu,F and $ZnGa_2O_4$:Eu,F. *Inorganic Materials*, 36(12):1189–1191, 2000.

[397] H. A. Höppe. Recent developments in the field of inorganic phosphors. *Angewandte Chemie-International Edition*, 48(20):3572–3582, 2009.

[398] B. G. Yacobi and D. B. Holt. Cathodoluminescence scanning electron-microscopy of semiconductors. *Journal of Applied Physics*, 59(4):R1–R24, 1986. Ayv81 Times Cited:129 Cited References Count:231.

[399] A. Eifler, G. Krauss, V. Riede, V. Kramer, and W. Grill. Optical phonon modes and structure of $ZnGa_2Se_4$ and $ZnGa_2S_4$. *Journal of Physics and Chemistry of Solids*, 66(11):2052–2057, 2005.

[400] Vitalij K. Pecharsky and Peter Y. Zavalij. *Fundamentals of powder diffraction and structural characterization of materials*. Springer, 2005.

[401] T. Kobayashi, K. Susa, and S. Taniguchi. Preparation and semiconductive properties of rock salt type solid-solution systems, $Cd_{1-x}M_xS$ (M=Sr, Ca, Mg, Pb, Sn). *Journal of Physics and Chemistry of Solids*, 40(10):781–785, 1979.

[402] Ferdinand Anne Kröger. *Some Aspects of the Luminescence of Solids*. Elsevier Publishing Company, 1948.

[403] H. C. Froelich. Manganese Activated Calcium Silicate Phosphors. *Journal of the Electrochemical Society*, 93(4):101–113, 1948.

[404] H. H. Haft and W. A. Thornton. High Performance Fluorescent Lamps. *Journal of the Illuminating Engineering Society*, 2(1):29–35, 1972.

[405] W. Lehmann. Phosphor Deterioration in Fluorescent Lamps. *Journal of the Electrochemical Society*, 130(2):426–431, 1972.

[406] C. J. Duan, A. C. A. Delsing, and H. T. Hintzen. Photoluminescence Properties of Novel Red-Emitting Mn^{2+}-Activated MZnOS (M = Ca, Ba) Phosphors. *Chemistry of Materials*, 21(6):1010–1016, 2009.

[407] T. Sambrook, C. F. Smura, S. J. Clarke, K. M. Ok, and P. S. Halasyamani. Structure and physical properties of the polar oxysulfide CaZnOS. *Inorganic Chemistry*, 46(7):2571–2574, 2007.

[408] B. P. Chandra. Development of mechanoluminescence technique for impact studies. *Journal of Luminescence*, 131(6):1203–1210, 2011.

[409] B. P. Chandra, V. D. Sonwane, B. K. Haldar, and S. Pandey. Mechanoluminescence glow curves of rare-earth doped strontium aluminate phosphors. *Optical Materials*, 33(3):444–451, 2011.

[410] B.P. Chandra, C.N. Xu, H. Yamada, and X.G. Zheng. Luminescence induced by elastic deformation of ZnS:Mn nanoparticles. *Journal of Luminescence*, 130(3):442 – 450, 2010.

[411] B.P. Chandra, V.K. Chandra, and Piyush Jha. Piezoelectrically-induced trap-depth reduction model of elastico-mechanoluminescent materials. *Physica B: Condensed Matter*, 461:38 – 48, 2015.

[412] D. Tu, C. N. Xu, Y. Fujio, S. Kamimura, Y. Sakata, and N. Ueno. Phosphorescence quenching by mechanical stimulus in CaZnOS:Cu. *Applied Physics Letters*, 105(1):011908, 2014.

[413] D. Tu, C. N. Xu, Y. Fujio, and A. Yoshida. Mechanism of mechanical quenching and mechanoluminescence in phosphorescent CaZnOS:Cu. *Light-Science Applications*, 4:e356, 2015.

[414] D. Tu, C. N. Xu, Y. Fujio, and A. Yoshida. Tuning the mechano-optical conversion in CaZnOS with Cu ion concentration. *Journal of Physics D-Applied Physics*, 48(47):475105, 2015.

[415] J. C. Zhang, L. Z. Zhao, Y. Z. Long, H. D. Zhang, B. Sun, W. P. Han, X. Yan, and X. S. Wang. Color Manipulation of Intense Multiluminescence from CaZnOS:Mn^{2+} by Mn^{2+} Concentration Effect. *Chemistry of Materials*, 27(21):7481–7489, 2015.

[416] Bolong Huang. Energy harvesting and conversions mechanisms for intrinsic upconverted-mechano-persistent-luminescence in CaZnOS. *Physical Chemistry Chemical Physics*, 18:25946–25974, 2016.

[417] Bolong Huang, Dengfeng Peng, and Caofeng Pan. "energy relay center" for doped mechanoluminescence materials: a case study on cu-doped and mn-doped caznos. *Physical Chemistry Chemical Physics*, 19:1190–1208, 2017.

[418] S. A. Petrova, V. P. Mar'evich, R. G. Zakharov, E. N. Selivanov, V. M. Chumarev, and L. Y. Udoeva. Crystal structure of zinc calcium oxysulfide. *Doklady Chemistry*, 393(1-3):255–258, 2003.

[419] X. G. Zhang, L. Y. Zhou, Q. Pang, J. X. Shi, and M. L. Gong. Tunable Luminescence and $Ce^{3+} \rightarrow Tb^{3+} \rightarrow Eu^{3+}$ Energy Transfer of Broadband-Excited and Narrow Line Red Emitting Y_2SiO_5:Ce^{3+}, Tb^{3+}, Eu^{3+} Phosphor. *Journal of Physical Chemistry C*, 118(14):7591–7598, 2014.

[420] Zhongxian Qiu, Chunying Rong, Wenli Zhou, Jilin Zhang, Chengzhi Li, Liping Yu, Shubin Liu, and Shixun Lian. A Strategy for Synthesizing CaZnOS:Eu^{2+} Phosphor and Comparison of Optical Properties with CaS:Eu^{2+}. *Journal of Alloys and Compounds*, 583:335 – 339, 2014.

[421] T. Yamamoto. Assignment of pre-edge peaks in K-edge x-ray absorption spectra of 3d transition metal compounds: electric dipole or quadrupole? *X-Ray Spectrometry*, 37(6):572–584, 2008.

[422] I. Hernández, Fernando Rodríguez, and H. D. Hochheimer. Pressure-induced two-color photoluminescence in mnf_2 at room temperature. *Phys. Rev. Lett.*, 99:027403, Jul 2007.

[423] C. Barthou, J. Benoit, P. Benalloul, and A. Morell. Mn^{2+} concentration effect on the optical properties of zn_2sio_4:mn phosphors. *Journal of the Electrochemical Society*, 141:524–528, 1994.

[424] C. R. Ronda and T. Amrein. Evidence for exchange-induced luminescence in zn_2sio_4:mn. *Journal of Luminescence*, 69:245–248, 1996.

[425] M. J. Caldas, A. Fazzio, and A. Zunger. A Universal Trend in the Binding-Energies of Deep Impurities in Semiconductors. *Applied Physics Letters*, 45(6):671–673, 1984.

[426] A. Zunger and U. Lindefelt. Substitutional 3d Impurities in Silicon - a Self-Regulating System. *Solid State Communications*, 45(4):343–346, 1983.

[427] H. Raebiger, S. Lany, and A. Zunger. Charge self-regulation upon changing the oxidation state of transition metals in insulators. *Nature*, 453(7196):763–766, 2008.

[428] M. Jansen and U. Wedig. A Piece of the Picture-Misunderstanding of Chemical Concepts. *Angewandte Chemie-International Edition*, 47(52):10026–10029, 2008.

[429] M. H. Du. Chemical trends of mn4+ emission in solids. *Journal of Materials Chemistry C*, 2(14):2475–2481, 2014.

[430] K. E. Lawson. Optical Studies of Electronic Transitions in Hexa- and Tetracoordinated Mn^{2+} Crystals. *Journal of Chemical Physics*, 47(9):3627–3633, 1967.

[431] D. T. Palumbo and J. J. Brown. Electronic States of Mn^{2+}-Activated Phosphors .1. Green-Emitting Phosphors. *Journal of the Electrochemical Society*, 117(9):1184–1188, 1970.

[432] D. T. Palumbo and J. J. Brown. Electronic States of Mn^{2+}-Activated Phosphors .2. Orange-to-Red Emitting Phosphors. *Journal of the Electrochemical Society*, 118(7):1159–1164, 1971.

[433] D. Curie, C. Barthou, and B. Canny. Covalent Bonding of Mn^{2+} Ions in Octahedral and Tetrahedral Coordination. *Journal of Chemical Physics*, 61(8):3048–3062, 1974.

[434] S. Koide and M. H. L. Pryce. Intensity Calculation of Some Optical Absorption Lines in Hydrated Manganous Salts. *Philosophical Magazine*, 3(30):607–624, 1958.

[435] B. Ng and D. J. Newman. A Linear-Model of Crystal-Field Correlation-Effects in Mn^{2+}. *Journal of Chemical Physics*, 84(6):3291–3296, 1986.

[436] J. Hubbard, D. E. Rimmer, and F. R. A. Hopgood. Weak Covalency in Transition Metal Salts. *Proceedings of the Physical Society of London*, 88(559p):13–36, 1966.

[437] D. J. Newman, B. Ng, and Y. M. Poon. Parametrization and Interpretation of Paramagnetic Ion Spectra. *Journal of Physics C-Solid State Physics*, 17(31):5577–5584, 1984.

[438] G. K. Liu, X. Y. Chen, N. M. Edelstein, M. F. Reid, and J. Huang. Analysis of f-element multiphonon vibronic spectra. *Journal of Alloys and Compounds*, 374(1-2):240–244, 2004.

[439] W. E. Bron. Bound-Electron-Lattice Coupling and Vibronic Spectra. *Physical Review*, 140(6a):2005–2014, 1965.

[440] M. Wagner and W. E. Bron. Rare-Earth Ions in Alkali Halides .II. Pseudolocalized Vibrational Frequencies. *Physical Review*, 139(1a):A223–A233, 1965.

[441] W. E. Bron and M. Wagner. Rare-Earth Ions in Alkali Halides .III. Electron-Lattice Coupling and Details of Vibronic Spectra. *Physical Review*, 139(1a):A233–A241, 1965.

[442] Lianhua He, Fang Liu, Geoffroy Hautier, Micael J. T. Oliveira, Miguel A. L. Marques, Fernando D. Vila, J. J. Rehr, G.-M. Rignanese, and Aihui Zhou. Accuracy of generalized gradient approximation functionals for density-functional perturbation theory calculations. *Phys. Rev. B*, 89:064305, Feb 2014.

[443] S. Poncé, G. Antonius, P. Boulanger, E. Cannuccia, A. Marini, M. Côté, and X. Gonze. Verification of first-principles codes: Comparison of total energies, phonon frequencies, electronphonon coupling and zero-point motion correction to the gap between ABINIT and QE/Yambo. *Computational Materials Science*, 83:341 – 348, 2014.

[444] Jonathan M. Skelton, Davide Tiana, Stephen C. Parker, Atsushi Togo, Isao Tanaka, and Aron Walsh. Influence of the exchange-correlation functional on the quasi-harmonic lattice dynamics of II-VI semiconductors. *The Journal of Chemical Physics*, 143(6), 2015.

[445] Z. Barandiarán, A. Meijerink, and L. Seijo. Configuration coordinate energy level diagrams of intervalence and metal-to-metal charge transfer states of dopant pairs in solids. *Phys. Chem. Chem. Phys.*, 17:19874–19884, 2015.

[446] X. Piao, K. Machida, T. Horikawa, H. Hanzawa, Y. Shimomura, and N. Kijima. Preparation of $CaAlSiN_3$:Eu^{2+} phosphors by the self-propagating high-temperature synthesis and their luminescent properties. *Chemistry of Materials*, 19(18):4592–4599, 2007.

[447] S. H. Park, K. H. Lee, S. Unithrattil, H. S. Yoon, H. G. Jang, and W. B. Im. Melilite-Structure $CaYAl_3O_7$:Eu^{3+} Phosphor: Structural and Optical Characteristics for Near-UV LED-Based White Light. *Journal of Physical Chemistry C*, 116(51):26850–26856, 2012.

[448] A. J. J. Bos. Theory of thermoluminescence. *Radiation Measurements*, 41:S45–S56, 2006.

[449] T. Maldiney, A. Bessiere, J. Seguin, E. Teston, S. K. Sharma, B. Viana, A. J. J. Bos, P. Dorenbos, M. Bessodes, D. Gourier, D. Scherman, and C. Richard. The in vivo activation of persistent nanophosphors for optical imaging of vascularization, tumours and grafted cells. *Nature Materials*, 13(4):418–426, 2014.

[450] H. Dixit, N. Tandon, S. Cottenier, R. Saniz, D. Lamoen, and B. Partoens. First-principles study of possible shallow donors in $ZnAl_2O_4$ spinel. *Physical Review B*, 87(17), 2013.

[451] J. J. Joos, D. Poelman, and P. F. Smet. Nonequivalent lanthanide defects: Energy level modeling. *Optical Materials*, 61:50–58, 2016.

[452] B. Huang. Unraveling energy conversion modeling in the intrinsic persistent upconverted luminescence of solids: a study of native point defects in antiferromagnetic Er_2O_3. *Physical Chemistry Chemical Physics*, 18(19):13564–13582, 2016.

[453] R. Penrose. *The Road To Reality: A Complete Guide to the Laws of the Universe*. Random House, 2016.

[454] A.R. Edmonds. *Angular Momentum in Quantum Mechanics*. Investigations in Physics. Princeton University Press, 2016.

[455] G. Racah. Theory of Complex Spectra. II. *Physical Review*, 62(9-10):438–462, 1942.

[456] G. Blasse and B.C. Grabmaier. *Luminescent materials*, book Appendix 4. Springer-Verlag, 1994.

[457] Jonathan Mooney and Patanjali Kambhampati. Correction to "Get the Basics Right: Jacobian Conversion of Wavelength and Energy Scales for Quantitative Analysis of Emission Spectra". *The Journal of Physical Chemistry Letters*, 5(20):3497–3497, 2014.

[458] Philips. Philips CE BCU TV Innovation lab. Beeldschermtechnologie.